Studies of the Crack Initiation and Notch Sensitivity Behaviour of Gilsocarbon



M.S.L. Jordan
St Edmund Hall, University of Oxford

A thesis submitted for the degree of D.Phil. in Materials

Hilary Term 2019

Studies of the Crack Initiation and Notch Sensitivity Behaviour of Gilsocarbon

M.S.L. Jordan
St Edmund Hall, University of Oxford
A thesis submitted for the degree of D.Phil. in Materials,
Hilary Term 2019

Abstract

To better understand the initiation of axial cracks in the graphite moderator bricks of advanced gas-cooled nuclear reactors, the development of a test suitable for measuring notch sensitivity from small specimens would be valuable. The test geometry is constrained, currently, to be under 20 mm in two dimensions. There is limited data on the notch sensitivity of Gilsocarbon, particularly after exposure to a nuclear environment. For the potential small specimen test geometries the microstructural scale is expected to significantly affect the fracture behaviour, which could make understanding of the component-scale behaviour difficult. The material science challenges in defining a suitable test will be outlined in this thesis, with studies of how crack initiation of the Gilsocarbon-grade graphite depends on the notch sensitivity.

Geometries based on a notched 6 x 6 x 19 mm beam will be prototyped, with over 100 beams of seven different notch geometries tested. Multi-scale, multi-camera *in situ* imaging will be combined with image correlation and finite element techniques to calculate the specimens' states at fracture, and potential fracture criteria evaluated (notch strengthening factors and strain energy density, SED). Comparison with historical results will demonstrate an increased insensitivity to notch radius (from 0.05 mm to 2.00 mm), and notch depth (up to 4.50 mm). The need for non-linear simulations will be highlighted and a potential material model tested, with limited success. SED calculation from digital image correlation measurements will be evaluated as a suitable monitoring technique, agreeing with the simulations but suffering from lack of reliable coverage for predictive capability. *In situ* volumetric imaging will be used to understand the interactions of the microstructural phases. A non-linear, non-recoverable stress-strain response will be observed, with anomalous deformation identified and attributed to damage at the filler particle peripheries. The origin of the insensitivity of Gilsocarbon to notch radii less than 2.0 mm will be explained by the observation of a notch radius-independent fracture process zone that extends over several millimetres. This understanding will support the development of a notch sensitivity test, and the outstanding challenges and potential future work will also be identified.

In memory of

Pauline and Geoff White

and dedicated to

Zoë Jordan.

Thank you for helping when I needed you.

Acknowledgements

A great many people deserve thanks for supporting this D.Phil. and in the production of this thesis. Family, friends, colleagues and collaborators have all helped me greatly since I started this research, and so thank you to you all. In particular I wish to thank my supervisors, James and David. Both have been supportive, keen to help me develop, and encouraged me to take on new challenges. I have always felt very lucky to be your student. The research group has changed completely since I began my time at Oxford. At the start, the group comprised only myself and one post-doc, and I thank Mahmoud for your kind guidance in those early days. I've had the pleasure of working alongside brilliant researchers, including (and in no particular order) Selim, Luis, Yelena, Dong, Phil, Matt, Ahmet, Liye, Shixiang, Chloe, Ashley, Dave, Ridhi, Vivian and Thomas. It has been a pleasure to work with you all and I've enjoyed the heated technical debates, the innovation, and the social gatherings.

I wish to thank all the technical staff who have gone out of their way to help me; your insightful comments and suggestions have always made life easier. There are too many of you to mention, but I hope you have realised how thankful I am. I also thank the researchers who have given time and effort to help generate the presented results: Selim, Luis and Yelena have all written code; Zoë and Ashley have contributed analysis; and many of the people mentioned above were involved in running my synchrotron experiments or helped to prepare complicated experimental set-ups.

I have had a good interaction with industry throughout this ICASE Award Studentship, including with the Award sponsor, EDF Energy. Many EDF Energy staff have been supportive, and I particularly thank Alan Steer, for providing encouragement and insight, and having been understanding of the delays to the project. Similarly, I thank the National Nuclear Laboratory (NNL) staff, and particularly Nassia Tzelepi, Samantha Wilkinson, Maureen Haverty and Adam Qaisar, for help during my secondment and since. As my employer since 2016, I'm grateful for the understanding and support of my NNL colleagues that have enabled me to complete this thesis. Other people and institutions that have been supportive during my D.Phil are Brian Connolly, Abbie Jones, Peter Flewitt, and the staff at the Diamond Light Source, the University of Birmingham, the University of Manchester, and the Dalton Cumbria Facility. I'm grateful for all the behind-the-scenes efforts of the staff and fellows at St Edmund Hall, the Oxford Materials department and the University that have made my time at Oxford relatively smooth, despite complications.

Lastly, particular family and friends deserve recognition for being there when things have been painful: my parents, grandparents, siblings and in-laws, who have always been supportive without really understanding what I've been doing; the many friends who've been available to offer encouragement, kind words and consolation; Lotte and Hazel who gave up their Easter weekends to get this work finished; and finally my wife, Zoë, who's had to be artistic, critical, supportive, practical, patient, and at times has 'been my hands'. I can't thank you all enough, and so I hope you know how much you all mean to me.

Two things are to be remembered: that a man whose opinions and theories are worth studying may be presumed to have had some intelligence, but that no man is likely to have arrived at complete and final truth on any subject whatever. When an intelligent man expresses a view which seems to us obviously absurd, we should not attempt to prove that it is somehow true, but we should try to understand how it ever came to seem true. This exercise of historical and psychological imagination at once enlarges the scope of our thinking, and helps us to realize how foolish many of our own cherished prejudices will seem to an age which has a different temper of mind.

– Bertrand Russell, A History of Western Philosophy (1945)

i. Contents

Abstract iii
Acknowledgements vi
i. Contents viii
ii. Symbols xi
iii. Abbreviations xiv
iv. A note on numerical nomenclature xv
v. Disclaimer xvii

I The Problem of Axial Cracking 1

I.1 Introduction 1
I.2 AGR design 3
I.3 Determining crack initiation in a reactor 11
I.3.1 General methodology for predicting initiation of axial cracks 11
I.3.2 Material science considerations in the general methodology 12
I.4 Towards development of a notch sensitivity test 28

II The Properties of Nuclear Graphites 31

II.1 Nuclear graphite grades 31
II.2 Fabrication and microstructure 33
II.2.1 Artificial graphite manufacture 33
II.2.2 Microscopic structure 34
II.3 Physical properties of virgin Gilsocarbon 39
II.3.1 Crystal structures 40
II.3.2 Composite properties of the large-scale phases 41
II.4 Effects of the nuclear environment 55
II.4.1 Effects of fast neutron and gamma irradiation 55
II.4.2 Effects of radiolytic-oxidation 60
II.5 Modelling fracture and notch sensitivity 69
II.5.1 Analytical models 70
II.5.2 Numerical simulations 84
II.6 Challenges in implementing the general methodology 87

III Crack Initiation in Notched Small Specimens 91

III.1 Introduction 91
III.2 Experiment description 95
III.2.1 Specimens 95
III.2.2 Loading and imaging 99
III.3 Data processing 103
III.3.1 Load-displacement behaviour 104
III.3.2 Optical image processing 110
III.4 Finite element simulations 124
III.4.1 Geometry and boundary condition definition 124
III.4.2 Stiffness models 126
III.4.3 Simulation predictions 134

III.5 Analysis 149
III.5.1 Notch sensitivity 149
III.5.2 Strain energy density 155
III.5.3 Stress and SED calculation from DIC 164
III.6 Discussion 172
III.6.1 Experiment setup and analysis procedure 173
III.6.2 Simulation 178
III.6.3 Crack initiation criteria 182
III.7 Conclusions 192
IV Microstructural Response to Crack Initiation in Gilsocarbon 195
IV.1 Introduction 195
IV.2 Experiment 197
IV.2.1 Specimen geometry 197
IV.2.2 Mechanical loading 199
IV.2.3 X-ray imaging 205
IV.2.4 Observations from tomography 212
IV.3 Analysis 216
IV.3.1 Radiograph 2D digital image correlation 217
IV.3.2 Keyhole notch finite element simulation 223
IV.3.3 Tomograph 3D digital volume correlation 232
IV.3.4 Linear deviations 257
IV.4 Discussion 316
IV.4.1 Experiment set-up and analysis procedure 317
IV.4.2 Strain concentration behaviour 321
IV.4.3 Non-linear response 324
IV.4.4 Damage (non-recoverable strain) 325
IV.4.5 Implications for damage modelling 329
IV.5 Conclusions 331
V Progress Towards a Notch Sensitivity Test 333
V.1 Assessment of challenges in implementing the general methodology 333
V.1.1 Assessment matrix 334
V.2 Size effect tests in notched four-point bend 341
V.2.1 Statistical distributions from other loading modes 342
V.2.2 Full field 3D boundary conditions volumetric analyses 347
V.2.3 Filler particle identification 350
V.2.4 Multi-scale simulation of Gilsocarbon crack initiation 351
V.2.5 DVC sensitivity dependence on oxidation 352
V.3 Summary 354
VI Appendices 357
A1. Determining the minimum number of short beam specimens 357
Experimental 358
Analysis 360
Conclusions and recommendations 367

A2. Tomograph projection normalisation and partial angle tomography 368
Use of frame-average radiographs 368
Reconstruction of partial angle tomograph 369
A3. Linear elastic predictions for DLENT geometries 370
Calculation of effective stress 370
Calculation of stress reduction factor 371
Surface stresses 372
Implications for future work 373

VII References 377

ii. Symbols

a	Total notch depth
b	Boolean operator
C	Slot offset (beam centre)
D	Beam depth
E	Young's modulus
E_{FLE}	Fitted Young's modulus used for linear elastic simulation
E_{TLE}	Tensile Young's modulus used for linear elastic simulation
E_{UMAT}	UMAT modulus formulation used for non-linear elastic simulation
F	Applied load
F^*	Previously applied maximum load
F_C	Critical load
f_j	The j^{th} UMAT fitting constant
F_M	Maximum applied load
F_P	Applied load at pop-in
G	Acceleration due to gravity
g	Notch tip geometry, "Blunt" or "Sharp"
$H^{KNi}(F)$	Hotspot displacement field, filtered from U_{Dev} for geometry KNi at F or F^*
J_{IC}	Mode I J-integral
k	Notch strengthening factor
K	Stress intensity factor
K_I	Mode I stress intensity factor
K_{IC}	Mode I fracture toughness
k_{FLE}	Notch strengthening factor calculated from σ_{FLE}
k_o	Notch strengthening factor observed
k_{RL}	Notch strengthening factor calculated from σ_{RL}
k_t	Notch strengthening factor theoretical
k_{UMAT}	Notch strengthening factor calculated from σ_{UMAT}
L	Beam length
L_C	Critical distance ahead of crack tip
l_{in}	Half-span of inner rollers in four-point bend testing
l_{out}	Half-span of outer rollers in bend testing
m	Number of predictors
N	Total number of specimens
n	Number of specimens per geometry (sample size)
P	Parallel notch depth
P_0	Porous fraction
R	Radius of notch tip
R_0	Radius of the strain energy density measurement volume locus
r_0	Offset radius of the strain energy density measurement volume locus centre

S	Slot width of notch
s_i	Sample standard deviation of variable *i*, see § iv
T	Notch half opening angle
$t(n)$	Critical values from the t-test distribution
U	A displacement field
$\vec{U}$	Vector within U
U_{Corr}	Correlation displacement field
U_{Def}	Deformation displacement field
$U_{Dev}^{KNi}(F)$	Deviation displacement field, for geometry KNi at F or F^*
U_{Disp}	Rigid body displacement field
$U_{Exp}^{KNi}(F)$	Experimental (from tomography-DVC) displacement field, for geometry KNi at F or F^*
$U_{RG}^{KNi}(F)$	Experimental (from radiograph-DIC) displacement field, for geometry KNi at F or F^*
$\vec{U}_{Roll}$	Vertical displacement of roller
U_{Rot}	Rigid body rotation field
$U_{Sim}^{KNi}(F)$	Simulation displacement field, for geometry KNi at F or F^*
U_{Uncert}	Measurement uncertainty field displacement field
V	Volumetric region of interest
W	Beam width
w	Weight loss
w_{eff}	Effective weight loss
x	Distance from crack tip
x_{CZ}	Extent of the strain concentration zone along the notch bisecting profile.
X, Y, Z	Spatial coordinates
α	Significance level
β	Statistical power
γ	Ratio of $\vec{U}_{Roll}$ to δ_C
γ_{wof}	Work of fracture
δ	Crosshead displacement
δ_C	Critical crosshead displacement
δ_M	Crosshead displacement at maximum load
δ_p	Crosshead displacement at pop-in load
$\measuredangle\epsilon$	Deviation strain
ϵ	Strain
ϵ_1	Maximum principal strain
$\epsilon_{Dev}^{KNi}(F)$	Deviation strain field, for geometry KNi at F or F^*
$\epsilon_{Exp}^{KNi}(F)$	Experimental (from tomography-DVC) strain field, for geometry KNi at F or F^*
ϵ_{max}	Nominal failure strain
$\epsilon_{Sim}^{KNi}(F)$	Simulation displacement field, for geometry KNi at F or F^*
ϵ_y	Yield strain
ζ_i	Measurement uncertainty of variable *i*, see § iv

λ	Notch sensitivity ratio
ν	Poisson ratio
ξ_{Corr}	Standard error of image correlation measurement
ξ_i	Specimen standard deviation of variable *i* at 95%ile, see § iv
ϱ	Strain energy density
ϱ_c	Critical strain energy density
σ	Stress
σ_{eff}	Effective stress
σ_{FLE}	Linear elastic stress calculated using the E_{FLE}
σ_{LE}	Linear elastic stress
σ_{max}	Nominal maximum stress
σ_n	Strength (maximum) of notched sample
σ_{RL}	Reduced ligament stress
σ_{TLE}	Linear elastic stress calculated using the E_{TLE}
σ_u	Maximum axial stress in unnotched beam
σ_{UMAT}	UMAT stress
σ_1	Maximum principle stress
ϕ	Diameter

iii. Abbreviations

3PB ..... *Three-point bend*
4PB ..... *Four-point bend*
AGR ..... *Advanced gas-cooled reactor*
ASTM *American Society for Testing and Materials*
Blackstone.. *An MTR experiment that accelerates oxidation and irradiation of virgin and ex-reactor Gilsocarbon*
CCD..... *Charge-coupled device*
CMOD ..... *Crack mouth opening displacements*
CZM ..... *Cohesive zone model*
DIC..... *Digital image correlation*
DLENT ..... *Double ligament edge notched tensile*
DLS..... *Diamond Light Source*
DVC ..... *Digital volume correlation*
EDF Energy .. *EDF Energy Nuclear Generation Limited*
EDND ..... *Equivalent Dido nickel dose*
ESPI..... *Electronic speckle pattern interferometry*
FE ..... *Finite element*
FFT..... *Fast Fourier transform*
FOV..... *Field of view*
FPZ..... *Fracture process zone*
GFMM ..... *Graphite Fracture Mechanics Model*
HAIL ..... *High-accuracy iteration limit*
IQR..... *Inter-quartile range*
KN..... *Keyhole notch*
KWRC..... *Keyway root crack*
LE..... *Linear elastic*
LEFM..... *Linear elastic fracture mechanics*
Magnox .... *A Generation II CO_2-cooled, graphite-moderated reactor design named after the Magnox fuel cladding, a contraction of 'magnesium non-oxidising'*
MTR ..... *Material test reactor*
NLE ..... *Non-linear elastic*
NNL..... *National Nuclear Laboratory*
NSF ..... *Notch strengthening factor*
PEEQ..... *Equivalent Plastic Energy*
PGA . *Pile Grade A, a nuclear graphite grade used in the Magnox reactors*
PIE ..... *Post irradiation examination*
RBD ..... *Rigid body displacement*
RBM..... *Rigid body motion*
ROI..... *Region of interest*
SCZ..... *Stress concentration zone*
SED..... *Strain energy density*
SIF ..... *Stress intensity factor*
SRF..... *Stress reduction factor*
UCAR..... *Union Carbide, a graphite manufacturer*
UMAT..... *User-defined material*
XCT..... *X-ray computed tomograph*
ϵCZ ..... *Strain concentration zone*

iv. A note on numerical nomenclature

Throughout this thesis, measured parameters will be presented with an estimate of the statistical spread using the following nomenclature to describe the distributions.

For any parameter, i, the mean value is indicated using the hat accent, $\hat{\imath}$. Statistical scatter will be described by: (1) presenting all measurements individually; (2) describing the measurement range, in either absolute values or percent; or preferably, when the number of specimens measured, n, is sufficient to calculate a representative statistic, (3) a standard deviation.

The mean and uncertainties, at the 95-percentile level (95%ile), ξ_i, are presented as

$$\hat{\imath} \pm \xi_i$$

Where ξ_i is calculated assuming the property is normally distributed with the sample standard deviation, s_i, by equation (1).

$$\xi_i = s_i * 1.96 \quad (1)$$

The values are given to a precision that reflects the accuracy of the measurement technique, ζ_i. If the spread of the data were smaller than the measurement precision, 95%ile values would be presented as $\xi = 0.0$, for example. ζ_i was determined based on various sources, notably: accuracies quoted by manufacturers; estimated errors due to image artefacts; and repeatability of a given measurement. Where sources of error were expected to compound, the values were summed in quadrature; in general, the calculation of ζ_i will not be presented.

In figures, the error bars are similarly presented at the 95%ile, such that the interval estimates the range of the population data intuitively.

If more than five specimens were tested in a sample, the standard error of the mean is also given, where appropriate, as the 95% confidence interval (95%CI) of the mean, and in the following bracketed form to differentiate these values from the 95%ile measure:

(minimum estimate of $\hat{\imath}$, maximum estimate of $\hat{\imath}$)

The standard error of the mean is calculated by (2), where $t_{0.95}(n)$ is a critical value of the t-test distribution to achieve 95% confidence, dependent on the number of degrees of freedom, which is related to number of specimens in the sample; for example, for 14 specimens, $t_{0.95}(14) \approx 2.16$.

(2) $$Standard\ error\ (95\%CI) = \frac{s_i}{\sqrt{n}} * t_{0.95}(n)$$

For example, the estimated mean of the acceleration due to gravity on Earth, *G*, based on 14 fictitious measurements with $s_G = 0.50$ m.s^{-2} at $\zeta_G = 0.01$ m.s^{-2}, would be quoted $G = 9.81 \pm 0.98$ (9.52, 10.10) m.s^{-2}. For brevity the units will only be given at the end of the measurement, rather than after each value.

Where a range of numbers is quoted, the values will be in square brackets. This nomenclature is to differentiate the values from the standard error description and saves the use of a hyphen (as for example, 5-6) to prevent confusion with a subtraction. For example,

[minimum value in range, maximum value in range]

v. Disclaimer

This work was sponsored by EDF Energy Nuclear Generation Limited ("EDF Energy"), as part of the EPSRC Industrial CASE Studentship award 11220486. EDF Energy also supplied the Gilsocarbon billet characterised in this work. A three-month industrial secondment that started at the end of 2015 was undertaken at the National Nuclear Laboratory's Central Laboratory, work from which is presented in the final chapter of this thesis. Practical support to the secondment was given by Professor Abbie Jones, the University of Manchester and the Dalton Cumbria Facility. The author has been employed by the National Nuclear Laboratory since 2016. Some of the presented experimental work was conducted during beam time on beamline I12 JEEP at the Diamond Light Source (experiments EE8519-1 and EE9478-1). The data collected during experiment EE9036-1 on the same beamline has also been important to this thesis. The loading rig used in the tomography experiments was on long-term loan from Dr Brian Connolly at the University of Birmingham. This D.Phil was supervised by Professors T. James Marrow (James Martin Chair in Energy Materials) and David Nowell (Chair in Machine Dynamics and Director of the VUTC, Imperial College London). This thesis has been the examined by *viva voce* by Professors Abbie Jones (Chair in Nuclear Graphite, University of Manchester) and David Armstrong (Associate Professor of Materials, University of Oxford)

The views presented here are solely the author's, and not necessarily those of any of the people or institutions mentioned above.

© Matthew SL Jordan, 2019. All rights reserved.

I The Problem of Axial Cracking

I.1 Introduction

Hunterston B Reactor 3, a graphite-moderated nuclear reactor in Scotland, has been offline since March 2018, and as of March 2019 is not forecast to return to service until at least June 2019. The reactors at Hunterston B are of the British-designed advanced gas-cooled reactor, AGR, class (see § I.2).[1] The principal cause of the prolonged outage was the discovery of c. 370 axial cracks in the graphite bricks forming the fuel channels of the core, which exceeded the agreed 'operational limit' of a maximum of 350 axial cracks. The structural integrity of the graphite core, and particularly the requirement to guarantee shutdown by control rod insertion in the event of a 1-in-10,000-year earthquake, is a key safety requirement in the licence to operate. Since beginning its statutory outage, the most extensive inspection ever of an AGR core has been conducted in Reactor 3, and Reactor 4 was also taken offline for a precautionary inspection. Demonstrating to the regulator and the general public that the reactors are safe to operate with many more than the 350 crack limit, and that the rate of cracking is predictable, is clearly important for the continued operation of graphite-moderated reactors [1, 2].

[1] The AGR is a Generation III–design fission-based reactor class built solely in the UK. The seven commercial AGR power stations each contain two reactors and are owned and operated by EDF Energy. The first reactors were connected to the power grid in 1976, with initial outputs of around 1500 MWt driving 660 MWe turbines.

Nuclear power is a cornerstone of the UK's electricity supply, providing a low carbon baseload supply and energy security, as well as generating employment for local communities and revenue for the licensee and their shareholders. Fourteen AGRs were built during the 1970s and 1980s, and form the majority of the UK civil nuclear fleet. They are all currently forecasted to remain operational until at least 2023, following a number of plant life extensions. To enable the reactors to reach their forecast end of generation dates, and potentially exceed them, accurate predictions of cracking rates and the associated operational implications will be necessary. Both of these requirements are governed by the graphites' response to the core distortions arising from continual fast neutron irradiation and radiolytic oxidation.

Axial cracking had been predicted for many years before being first detected at Hunterston B, and a significant amount of work, both empirical and theoretical, had been conducted to try and predict the phenomenon [3-5]. Despite this, the number of cracks observed at the March 2018 inspection showed that the cracking rates were under-predicted. Further work is therefore required to better understand the mechanisms leading to crack initiation, and to improve predictions of axial crack formation. Part of this work is the continual monitoring of the graphite's physical properties and particularly how the sensitivity to stress-raising features, 'notch sensitivity', might evolve.

The fuel channels in the reactor core are characterised by multiple techniques during the regular inspections, including extraction of c. ϕ 19 x 70 mm 'trepanned' cores from the bore face of the bricks.[2] The cores contain a steep density gradient due to the oxidation, requiring them to be machined into small specimens typically 6 mm thick. As such, the post irradiation examination, or PIE, techniques are constrained to use small specimens, often of a geometry and scale incompatible with accepted standards, for example from ASTM.

[2] The core inspections include passing a variety of probes down the fuel (and control rod) channels into the core. Measurements include video capture, eddy current and the removal of small volumes of graphite by trepanning for subsequent inspection. Necessarily, these inspections monitor the centre of the bricks only; there is no access to the brick periphery.

Graphite technology has been proven in nuclear industry, and has the potential for use in nuclear generation in the Generation IV+ fission and fusion reactor schemes [6, 7]. In these reactor systems, similar problems will be faced to those in the Magnox and AGRs stations.[3] As such, the outcomes of this research will also be relevant to future builds.

This thesis will consider the effect of stress concentrations on the graphite bricks, the sensitivity to stress raising features, and the feasibility of measuring the notch sensitivity during the PIE.

I.2 AGR design

To understand the problem of axial cracking, the design of the AGRs and the role of graphite must first be appreciated. Graphite technology has been key to the nuclear industry since the Manhattan Project, as graphite has excellent nuclear moderation properties, is a solid, is easily machined, can be load-bearing at operational temperatures to form part of the reactor structure, and is relatively inexpensive. Graphite moderation was employed in the earliest reactors, including Chicago Piles 1 and 2,[4] the X-10 Graphite Reactor,[5] the Windscale Piles,[6] and Calder Hall.[7] Calder Hall was the first of the Magnox power stations, and marked the start of over sixty years of commercial operation of graphite-moderated reactors in the UK, which is now comprised solely of AGRs.

[3] Magnox refers to the world's first commercial graphite-moderated, CO_2-cooled reactor fleet. The term 'Magnox' derives from the 'magnesium non-oxidising' alloy used for fuel cladding. A Generation II–design, the Magnox reactors were used for plutonium breeding and power generation, and were the predecessor to the AGR fleet. In total, thirteen Generation II Magnox power stations (totalling twenty-six reactor units) were operated in the UK, plus one in Tōkai, Japan and one in Latina, Italy (a further two units); all stations are now being decommissioned.
[4] Chicago Pile 1 (1942 – 1954), an experiment led by Enrico Fermi at the University of Chicago, was a proof of principle demonstration of controlled nuclear fission. Pile 2 was a subsequent evolution of the design.
[5] The X-10 Graphite Reactor (1943 – 1963) was developed following the success of Chicago Pile I at Oak Ridge for the purpose of breeding plutonium. X-10 was the first reactor to demonstrate electricity generation from nuclear fission was possible.
[6] The Windscale Piles (1950 – 1957), built in West Cumbria, now part of the Sellafield estate, were the UK's first nuclear reactors, built for plutonium breeding. The use of graphite, and the need to periodically anneal out Wigner energy, contributed directly to the 'Windscale fire' nuclear event. See [8] W. Penney, B.F.J. Schonland, J.M. Kay, J. Diamond, D.E.H. Peirson, Report on the accident at Windscale No. 1 Pile on 10 October 1957, Journal of Radiological Protection 37(3) (2017) 780-796.
[7] The Calder Hall power station (1956 – 2003), also now part of the Sellafield estate, was the world's first nuclear power plant, designed and built to generate electricity commercially

Though there are a several variants,[8] all AGRs comprise a steel-lined concrete pressure vessel of a domed cylinder geometry with internal dimensions of approximate diameter, ϕ, and height of ϕ 11 x 11 m (see Figure 1). Permanently sealed within are several thousand graphite bricks, predominantly in two types arranged to form vertical channels. The larger bricks, forming channels for fuel rods, are tubes of outer dimensions c. ϕ 0.4 x 0.9 m with a ϕ 0.2 m central bore, while the smaller bricks, tubes with an external c. 0.4 x 0.4 m square cross sections, form the control rod channels. Figure 2 shows how the bricks are positioned in an orthogonal array with a system of fixed and loose keys to maintain the relative positioning of the bricks. The keys fit into vertical grooves, 'keyways', cut into the bricks' outer surfaces. The graphite, Gilsocarbon, was selected and purpose-made for the AGRs (see Chapter II) and machined by standard cutting practices, such as lathes, drills and saws [9-12]. For the earliest stations, tolerances on the corner radii (known as the 'keyway' roots) were specified as low as 0.25 mm maximum (no minimum), while later stations tolerated radii in the range [1.5, 2.5] mm [9-12]. The billets will have distorted with irradiation and the actual root radii cannot be measured.

To maintain criticality, the graphite reduces the fast neutron energy to thermal levels. The CO_2-rich coolant gas is pumped through the reactor at 40 bar pressure, maintaining the graphite temperature in the range [600, 723] K and transferring the excess heat to the boiler. The high-energy irradiation promotes radiolytic oxidation, where the pure carbon graphite is corroded by CO_2 radiolysis species [3, 13-16]. The mechanisms are described in detail by Best *et al.* [3], and summarised as

$$C_{(s)} + CO_{2\,(g)} + \text{neutron radiation} + \text{gamma radiation} + \text{heat} \rightarrow 2\,CO_{(g)}$$

Some control of oxidation rate is achieved by tuning the gas composition, particularly with the inclusion of methane [3, 9-13], but differential oxidation rates are still expected, as in Figure 3 [3].

[8]The AGR construction rights were put to tender, with each company providing their own specific design for each station. Both in construction and operation there are only two paired stations with similar operational histories: Hunterston B and Hinkley Point B; and Heysham 2 and Torness.

To date, the peak (localised) reduction in graphite density due to radiolytic-oxidation from the virgin material (a measurement termed 'weight-loss') exceeds 36 % at Hinkley Point B and Hunterston B [16, 17] and has dramatically altered the microstructure and mechanical properties. Under the currently agreed structural integrity assessment limits, the reactors will be shut down when weight-loss reaches 43 %.

Combined irradiation and oxidation of the graphite causes the component volume to shrink initially, and then expand; the transition is termed 'turn around'. This behaviour was seen in the Magnox stations and is well understood; the causes will be explored in § II.4.2. For a Hookean material (see § I.3.2.1.3 for further details), the predicted consequence of the turnaround behaviour is that the hoop (tangential) stresses would go from compressive to tensile (see Figure 4). Stress-raising features in the brick periphery, like the corners of the keyways, could become points of crack initiation, with the cracks propagating axially. A crack associated with the keyway corners is commonly referred to a keyway root crack, KWRC. The formation of a KWRC raises the possibility of large channel distortions [18] or debris falling into the fuel or control rod channels, either of which is envisaged as a potential hazard affecting control rod insertion. A cracked brick might also induce damage in the neighbouring bricks via the key mechanism; this appears to have occurred in Hunterston B, as seen in the panorama of the channel bore (a 'chanorama') in Figure 5, where the cracking in layer 4 is associated with crack formation in layer 3 [19]. Axial cracking of a significant proportion of the core is expected to limit AGR life.

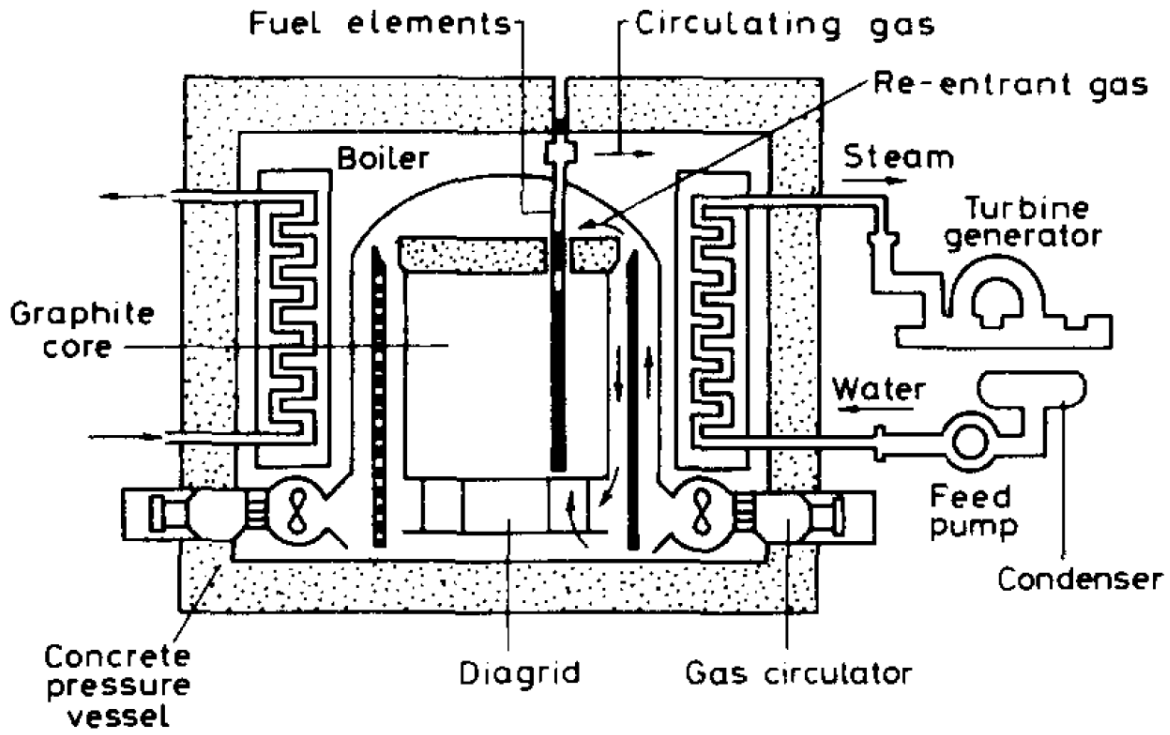


Figure 1: Schematic of an AGR showing the fluid flows, with only a single fuel stringer is shown. Reprinted from [3] with permission from Elsevier.

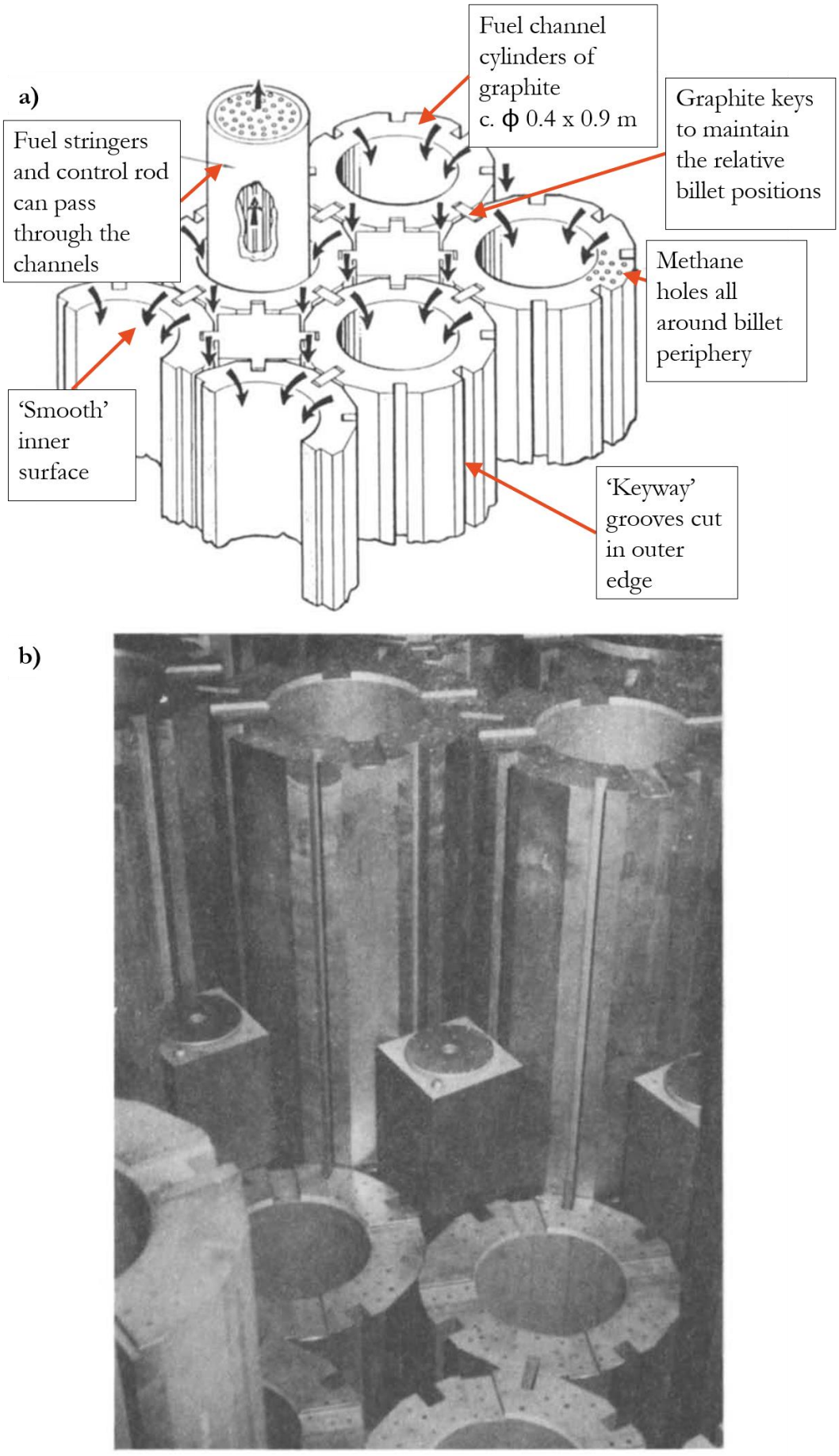


Figure 2:Schematic (a) and corresponding photograph (b) of the AGR moderator billet arrangement. Black arrows indicate CO_2 flow direction. Reprinted from [3] with permission from Elsevier.

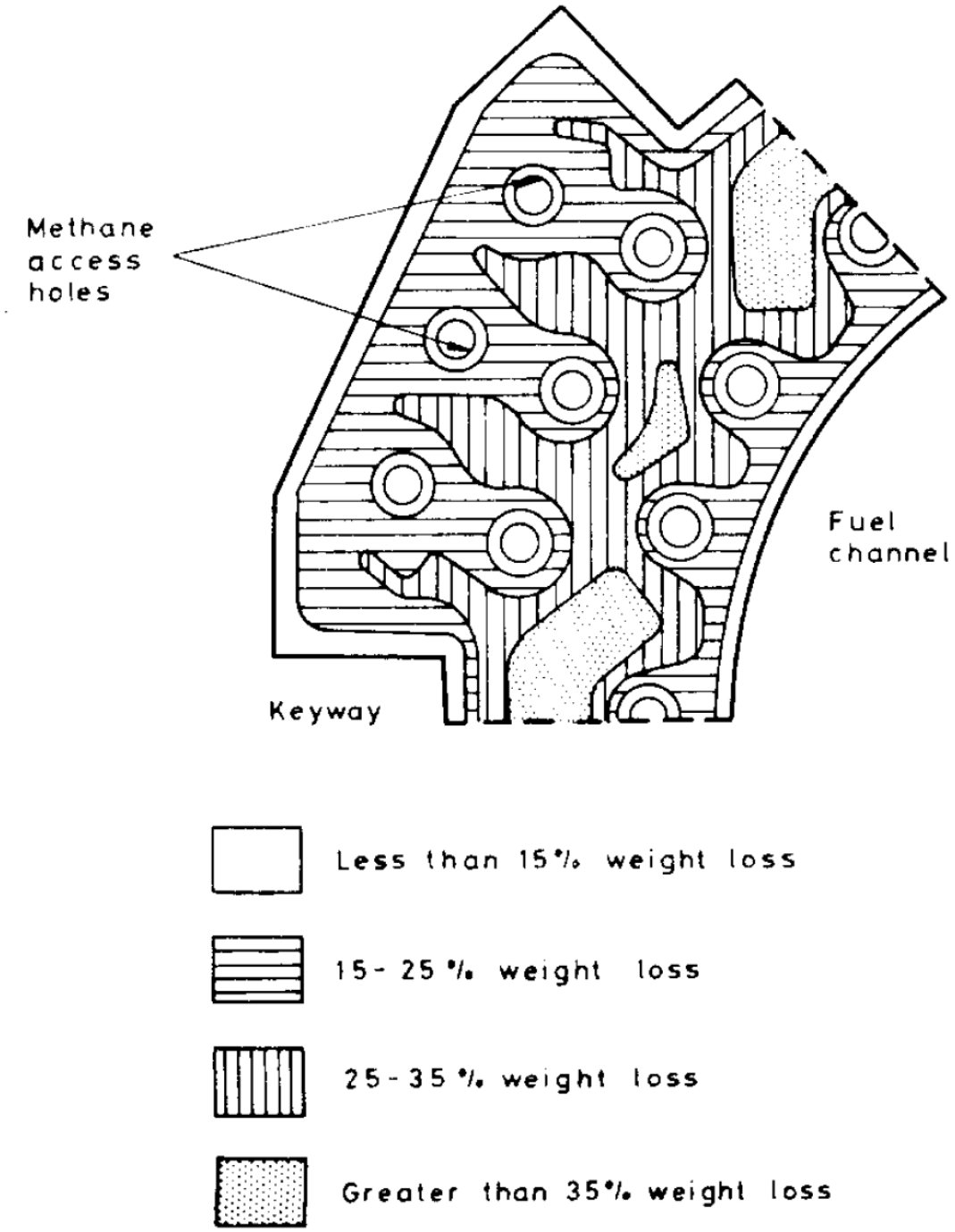


Figure 3: Predicted weight-loss profile in an early graphite billet design due to methane depletion. Reprinted from [3] with permission from Elsevier.

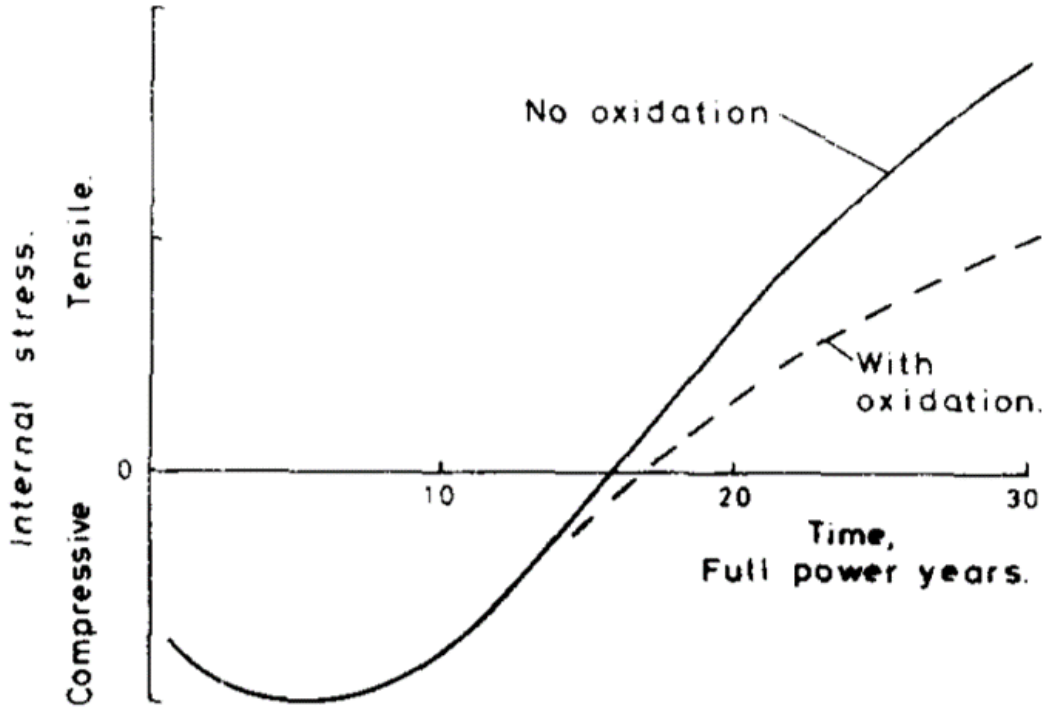


Figure 4: Qualitative predictions of the changing stress state in keyway-roots (from 1984). The solid line represents the changes due to neutron induced shrinkage, and the dashed line indicates the delaying effect of radiolytic oxidation. Reprinted from [3] with permission from Elsevier.

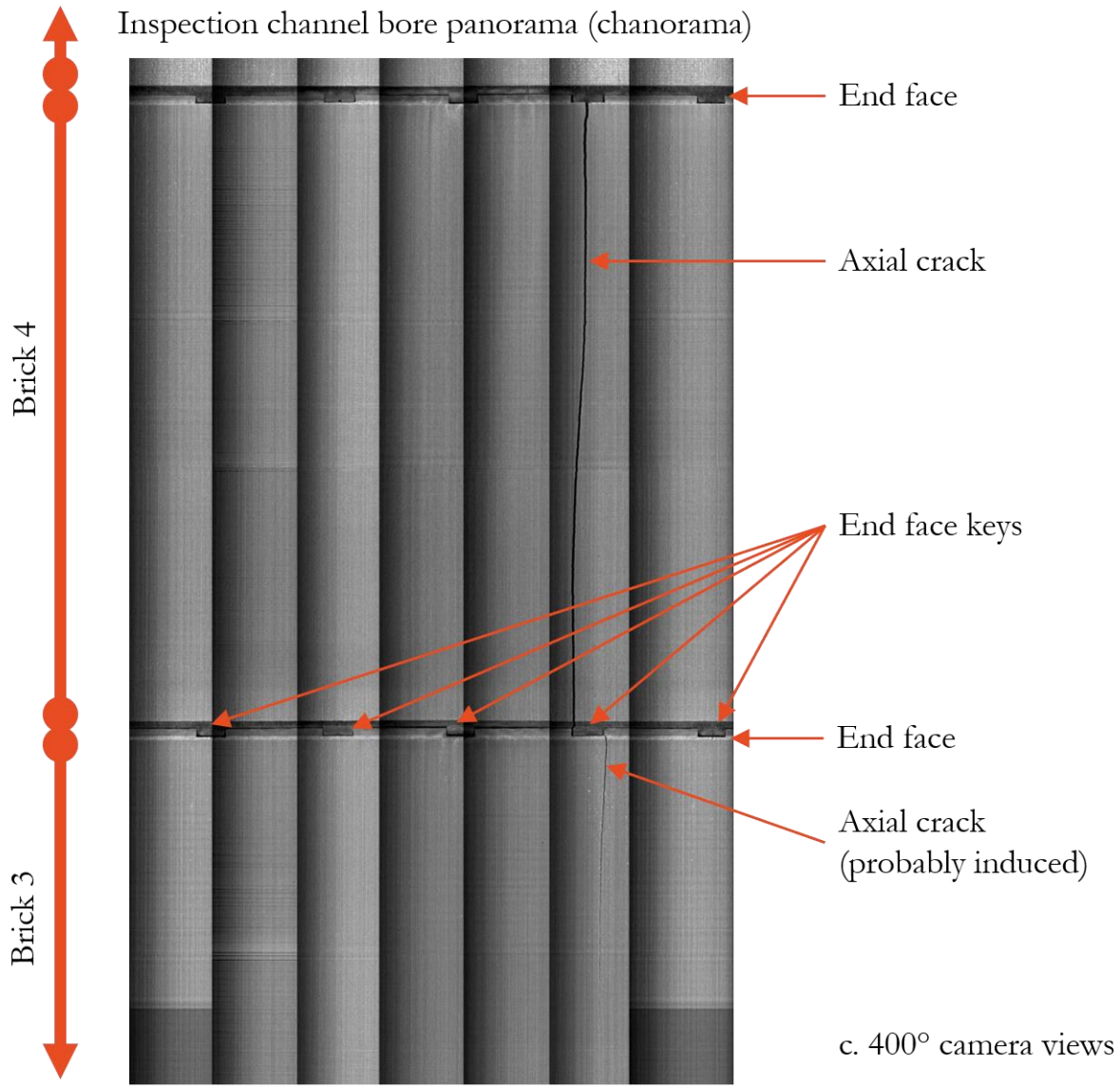


Figure 5: Channel bore panorama (a 'chanorama') of Hunterston B Reactor 3 showing an axial crack in brick 4. A secondary axial crack appears to have been induced in brick 3, and is associated with the end face key structure. The image is composed of six independent camera feeds as the camera is moved vertically, and the images stitched to give a c. 400° view, with the far-left hand feed repeated on the right. Image courtesy of EDF Energy; (part of) the original inspection footage may be viewed as a video in [1].

I.3 Determining crack initiation in a reactor

A general methodology for predicting the onset of axial fracture in a given AGR brick is outlined in § I.3.1, based loosely on BS 7910.[9] Some of the principal considerations associated with each stage are described in § I.3.2; this list is not exhaustive, and particularly focuses on the material science.

I.3.1 General methodology for predicting initiation of axial cracks

The initiation of axial cracks might be determined by the following stages:

For a given time-dose-oxidation-temperature state:

1. Simulate the strain state at each point in the brick
2. Calculate stress state at each point in the brick
3. Identify potential initiation points in the brick based on the accepted fracture criterion
4. Apply notch strengthening factors based on geometry
5. Determine if the fracture initiates
    - If fracture has not initiated, iterate to the next time-dose-oxidation-temperature state of interest.
6. Determine if the fracture propagates
    - If fracture has not propagated, iterate to the next time-dose-oxidation-temperature state of interest.[10]

In practice, the strain and stress states are interdependent and are solved iteratively, currently by using finite element, FE, solvers.

[9] BS 7910:2013+A1:2015 "Guide to methods for assessing the acceptability of flaws in metallic structures" is a code of practice for assessing the maximum dimension of flaws that may exist in a metallic structure under a given loading condition without precipitating failure. The standard is based on the assumption that by demonstrating that the strain intensifying effect due to the largest flaw in the structure is below the fracture criterion, using energetic crack growth principles, all flaws are subcritical. The general application of standards for metallic structures to ceramics or composites is rarely acceptable, but the underlying principles may be applicable.

[10] A flaw extension rule could be applied to simulate the changing state of the flaws, but this is beyond the scope of this thesis.

I.3.2 Material science considerations in the general methodology

Every stage of the proposed methodology, including defining the input data for the time-dose-oxidation-temperature state, presents many industrial challenges. Focusing on the material science aspects, the principal considerations will be highlighted. These topics will then be addressed in the following chapters.

I.3.2.1 Stress-strain response

Although the word strain is used in ordinary language indiscriminately to denote relative molecular displacement, and the force by which it is produced… I shall… use it, throughout this paper, in the restricted sense of relative displacement of particles, whether consisting in dilatation, condensation, or distortion…

– W. J. M. Rankine (1850) [20]

We have now to consider the very important kinematical conditions presented by the changes of volume or figure experienced by a solid... Any such definite alteration of form or dimensions is called a Strain

– W. Thomson & P. G. Tait (1879) [21]

Stages 1 and 2 of the general methodology concern the calculation of strains and stresses. From the above definitions, the strains in a body depend on the equilibrium balance of forces acting on infinitesimal elements within the material, which in turn depend on the nature of those forces, the geometries to which they are applied, and the kinematical response of the material, which are explored further in § I.3.2.1.1 and I.3.2.1.2. Stresses are then the distribution of forces within the body, due to the strains (see § I.3.2.1.3). It is important to further account for evolving stress and strain behaviours due to the nuclear environment around the body (see § I.3.2.1.4).

I.3.2.1.1 Loading considerations

In a given body under arbitrary loading, the strains may be separated into orthogonal components by the principle of superposition and described as normal or shear. Loading may combine any set of components as tensile or compressive deformations, for example as uniaxial, biaxial, triaxial, flexural, torsional, or shear; multiaxial loading states may be reduced to the orthogonal components by tensor transformations. To fully characterise a material every combination should be considered, though for practical application defining a subset is typically sufficient. For a detailed definition of the strain calculations, see Filonenko-Borodich's *Theory of Elasticity* (translated) [22].

I.3.2.1.2 Geometric considerations

From an engineering perspective, geometry constrains the stress-strain response. For example, in plane stress there is no stress component perpendicular to a surface, such that only the orthogonal in-plane stresses act, while in the plane strain state at the centre of a symmetrically-loaded body, only strains orthogonal to the symmetry axis are possible. A geometric feature that causes localised deviations from 'planar flow' conditions (that is the 'flow' lines of equal force through the body), results in a strain concentration zone, ϵCZ, and, if the stiffness behaviour permits, a complementary stress concentration zone, SCZ. The behaviour in the vicinity of these features is determined by the stress intensity factor, SIF (symbol *K*).

I.3.2.1.3 Stress response considerations

The stresses within the body then depend on the material's response to strain in terms of linear elasticity, non-linearity, damage (non-elastic) mechanisms, anisotropy, and the degree of homogeneity, each arising as described below.

The elastic response is the Hookean behaviour where all strain is recovered at unload. The stress is governed by the stiffness tensor, and as a first-order approximation is linear, hence linear elastic, or LE. The non-linear elastic, or NLE, response refers to a strain-dependent stiffness, in which strain is fully recoverable but the stress is no longer linearly dependent. Damage mechanisms (including plasticity) act to dissipate energy during loading, such that the response is non-linear, and permanently affect the mechanical properties; this may result in non-recoverable damage in the form of permanent strains at unload. Materials may respond anisotropically, such that in addition to the loading configuration, the relative orientation of the material must also be accounted for when determining the response. The degree of homogeneity refers to the multiphase nature of the material, and the associated stiffness response. If the material is composed of multiple phases, each individual phase will have a unique stress-strain response, and the properties of the bulk will be a volume-averaged response. The bulk response will depend on the specific mechanical interactions of the phases and is likely to be non-linear and/or anisotropic. For further details, see Hollister's *Experimental Stress Analysis* [23].

Fracture behaviour under quasi-static loading is then determined by the activation of any damage, and subsequently fracture, mechanisms. Where no such mechanisms are active, fracture is brittle (no yield, instantaneous crack growth, with no energy dissipation). Where such mechanisms exist and can operate over large length scales relative to the size of the strain concentration zone, fracture is plastic (yield, inhibited crack growth, with large energy dissipation). Material in the intermediate category is termed quasi-brittle (yield may be observed rapid crack growth, with limited energy dissipation). The post-yield and fracture behaviour may therefore indicate the active mechanisms at crack initiation.

I.3.2.1.4 Nuclear environment considerations

In an AGR, the effects of fast neutron irradiation and radiolytic-oxidation on the material's stiffness response must be considered. High energy radiation damage and chemical corrosion of the material typically modify a material's physical properties significantly, including the elastic properties and damage mechanisms. The future state of the reactors may only be estimated, since no other graphite-moderated reactors have been run for as long or to as high levels of irradiation dose and oxidation weight-loss. While measurements of the current state may be made, currently only a subset of the fuel channels are sampled, of which only a further subset are trepanned. Trepanning can only remove material from the bore of the bricks and, in general, this is limited to one core per brick per outage.[11] No measurements are collected from the outside the fuel channels. This means that, at best, the simulation input conditions are validated against historical trends.

Other mechanisms that may change the physical properties with a time dependence are fatigue and dynamic fracture, but these will not be examined in this review.

I.3.2.2 Fracture criterion

Cracks initiate once a material-specific criterion is met. Stage 3 of the general methodology requires the identification of potential crack initiation sites. A complete fracture criterion must correspond to initiation in any loading condition such that all components and loading modes are accounted for. For a given criteria (see also § I.3.2.4), identification of the potential crack initiation sites may be achieved algorithmically from a computer simulation

In practice, a criterion is generally determined by testing the material in a series of different geometries and loading states, and a failure locus defined (in orthogonal stress space, for example); the criterion should then correspond to fracture in every possible configuration.

[11] This is a nominal rule to protect the structural integrity of the brick, and generally bricks have only ever been trepanned once, if ever. A small number of bricks have been trepanned multiple times, but these cases are exceptional.

I.3.2.2.1 Fracture modes

As with stress and strain, fracture modes may be considered as orthogonal components linked to the deformation mode across a planar discontinuity, such as a crack or notch. The three principal modes (see Figure 6) may be described as: Mode I (opening) – a tensile loading across the discontinuity plane; Mode II (sliding) – an in-plane shear; and Mode III (tearing) – an out-of-plane shear [24]. From the external loading on the body, it is common that one mode will dominate around the discontinuity, and mode-specific fracture criteria may be tested. Recognised test geometries are designed to accentuate a particular fracture mode to determine the mode-specific fracture criteria.

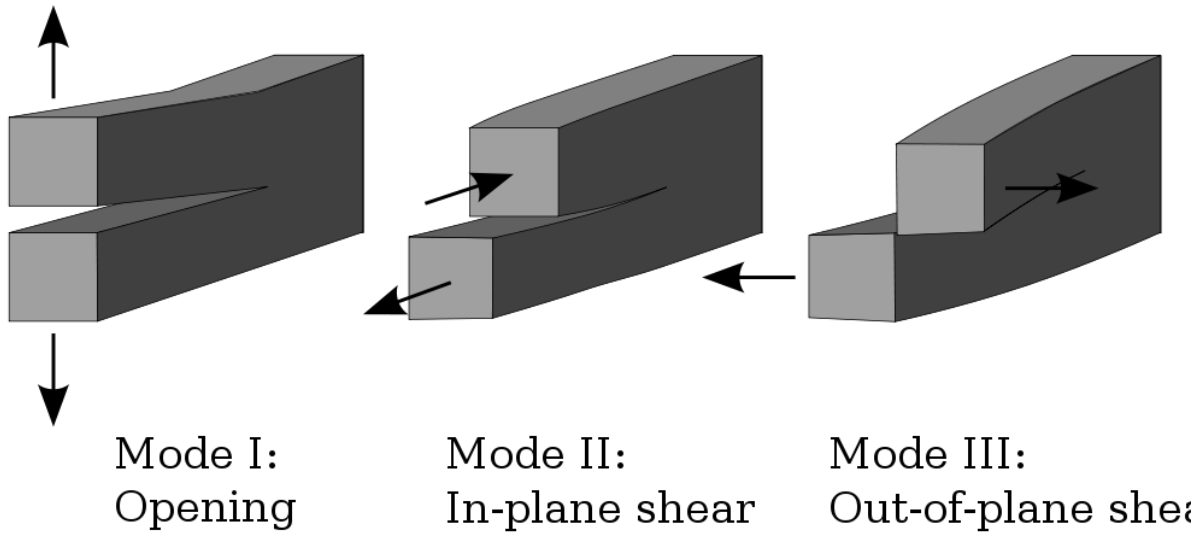


Figure 6: Crack opening modes from [25], after [24].

I.3.2.2.2 Fracture criteria considerations

A fracture criterion must be based on a property that increases with increasing strain, such that the threshold is not passed in the unstrained state. Typical criteria are stress, strain or strain energy based: maximum stress, point strain or total strain energy, for example. The criterion may be based on point measurements or area (or volume) averages, such as strain energy density, SED, in which case the area (or volume) must be defined. To demonstrate the applicability of a criterion, a consistent value of the measured property should be determined for every geometry.

Crack initiation and propagation may be governed by different material responses. Crack propagation is an energetic process and best understood [26], and stress-based approaches to propagation are inadequate [24]. It is often considered that crack initiation should be considered as merely the growth of sub-critical cracks beyond a critical point. The cracks exist in the material from manufacture and are thermodynamically metastable until an energy barrier is overcome due to additional strain energy.

Rather than the LEFM approach, an energetic criterion may be defined where the material can dissipate a certain amount of energy before fracture initiates, quantified by the energy needed to overcome the 'fracture toughness' (K_C) which may be defined for the different modes, such as K_{IC} [24]. This is the basis of the BS 7910 approach [27]. During fracture, the related concept (see (3)) of work of fracture (symbol γ_{wof}) is also considered, loosely defined as "the total energy consumed to produce a unit area of fracture surface during a complete fracture" [28]. Practical measurement may be made using the J-integral techniques, where a strain field is integrated to measure the energy changes in crack extension on a closed contour encompassing the crack tip [29-33]. The Mode I J-integral (J_{IC}) is related to K_{IC} by (4). K_{IC}, J_{IC} and γ_{wof} may be decomposed linearly to account for any energy dissipating mechanisms separately from the elastic straining.

(3) $$\gamma_{wof} \propto \frac{K_{Ic}^2}{E}$$

(4) $$K_{IC} = \sqrt{\frac{J_{IC}\, E}{1 - \nu^2}}$$

It is useful to briefly outline the different fracture behaviours. In the review of Gilsocarbon's properties given in Chapter II, various criteria will be defined and tested against the empirical data.

I.3.2.2.2.1 Brittle fracture

In brittle fracture, the energetic resistance to crack growth is constant, so once a threshold strain energy is surpassed crack growth is unconstrained [26]. Crack paths may be predicted by thermodynamic principles [32, 34-36].

I.3.2.2.2.2 Plastic fracture

In plastic fracture, the microstructural mechanisms absorb strain energy by permanently deforming around a stress raising feature in a ductile manner to form a fracture process zone, FPZ. Mechanisms include dislocation movement, phase transformations, twinning and grain boundary sliding [37-39]. An FPZ effectively blunts any crack tips and maintains the material in a state below the criterion for crack propagation, raising the bulk fracture strength. The stresses decay to near the macroscopic stress levels with distance from the crack, (Figure 7), while the shape depends on the type of loading and shape of the flaw [40, 41]. The deformation is permanent, such that the FPZ stretches the surrounding material at unload.

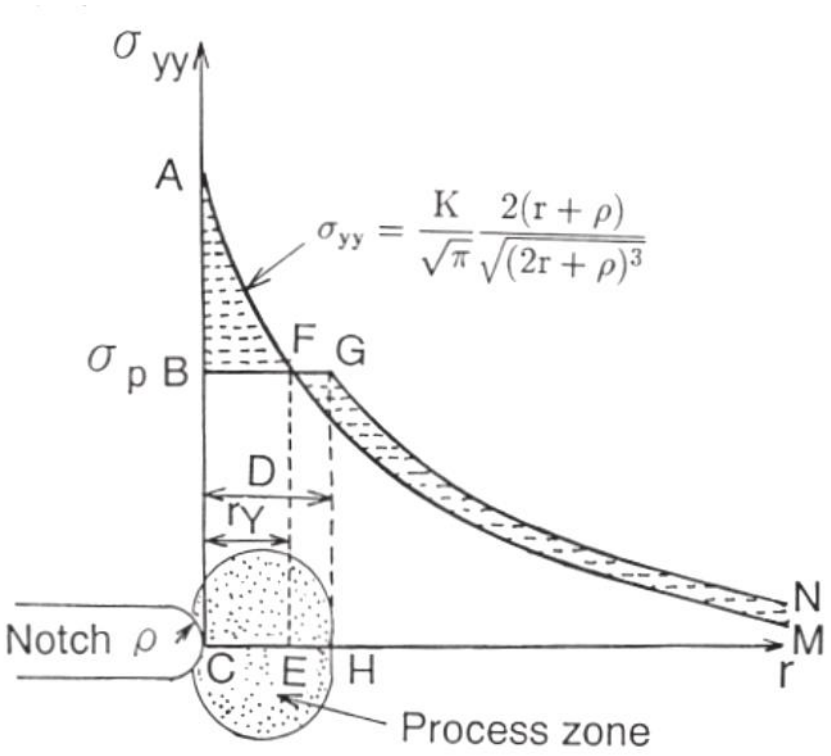


Figure 7: In a plastic material a process zone develops, such that the stress profile, σ, at distance r ahead of a notch tip (of radius ϱ) modified. In this figure, the elastic stress field (σ_{yy}), defined in terms of the stress intensity factor (K) and notch geometry, is reduced above the line BF to the constant plastic stress (σ_p), so that the region of high stress is broadened (from r_Y to D), but the maximum stress at the notch tip is lower. Reprinted from [41] with permission from John Wiley and Sons.

I.3.2.2.2.3 Quasi-brittle

Between these two extremes, quasi-brittle materials have a small capacity to dissipate energy, developing an FPZ, but high levels of ductility (over, say, 1 % strain) cannot be achieved. Suggested mechanisms for this behaviour include crystal cleavage, micro-cracking, crack bridging, ligament pull-out and delamination [42-44]. Although there are virtually no materials that fail in a perfectly brittle manner, the term 'quasi-brittle' is most often associated with composites: bone, concrete, fibre-reinforced polymers and graphite, for example. The material response of these composites is highly dependent on the microstructural features, and particularly the volume fractions of the different phases, any degrees of anisotropy, and their dispersion through the material.

I.3.2.3 Notch strengthening behaviour

Where a material has a non-elastic response, a body with a strain concentrating feature may fail with an apparent peak stress greater than expected for a comparable linear elastic material; the body appears to have been strengthened to notches. For notch strengthening, it is necessary that the material can dissipate strain energy by a damage or fracture mechanism, otherwise the stress and strain energy at the notch tip would tend to infinity as the stress concentration increased. Numerical corrections may be defined to compensate for this insensitivity to notches and applied to the predicted behaviour at the crack initiation sites.

I.3.2.3.1 Reduced-ligament notch tip stress

Determining the maximum stress at the notch tip stress is non-trivial for a material with a non-linear stress response. For testing in flexure, one method is to calculate the stress by assuming the beam is linear elastic and unnotched, with a reduction in the ligament (the material ahead of the notch). This 'reduced-ligament' method, as used in Peterson's Stress Concentration Factors [45] and by Brocklehurst and Birch [46] and Brown *et al.* [47], assumes the maximum axial stress as though generated by an infinitely blunt tip. For flexure the reduced ligament stress (σ_{RL}) may be calculated as a modified version of the standard maximum stress equation. For example, (5) is the four-point bend, 4PB, reduced-ligament variation where the beam has dimensions of width (W), breadth (D), notch depth (a), with a load (F) applied across the rollers with outer and inner half-spans of l_{out} and l_{in}, respectively. This formulation relies on the assumptions behind the standard equations remaining valid.

(5) $$\sigma_{RL} = \frac{3\,F\,(l_{out} - l_{in})}{D\,(W-a)^2}$$

I.3.2.3.2 Notch strengthening factor and sensitivity

For a given geometry and loading state, empirical testing is required to determine the peak stresses at failure for notched (σ_n) and unnotched bodies(σ_u); the ratio in (6) is termed the notch strengthening factor, NSF (symbol k), also known as the stress concentration factor [47].

(6) $$k = \frac{\sigma_n}{\sigma_u}$$

A further correction factor for more general application is the notch sensitivity (λ), which relates the measured NSF of the material (k_o) to the NSF of a perfect linear elastic material (k_t), as per (7). k_t for a range of geometries may be derived analytically, for example in Peterson's Stress Concentration Factors [45], or simulated, by FE modelling for example.

(7) $$\lambda = \frac{k_o}{k_t}$$

I.3.2.3.2.1 Energy-based NSF alternative

Notch insensitivity may be similarly defined when considering an energetic fracture criterion. The equivalent correction factor to the NSF would recognise that, for notches of radii below a given threshold, the energy dissipation was disproportionate to that of blunter features.

Notch sensitivity effects for brittle materials have been well studied, for example [32, 34, 35, 48-51]. The actual behaviour can be distinguished in terms of the shape of the notch, which can be either a sharp V-notch, or a blunt U-notch. The failure stress in a V-notch is dependent on the notch tip angle, bound by a reciprocal function, as per Figure 8. For a U-shaped notch the behaviour is dependent on the notch tip radius (R). For fine-grained materials, such as ceramics, a characteristic notch sensitivity curve is observed with fracture toughness, $K_{IC} \propto \sqrt{R}$, and tending to the smooth specimen strength.

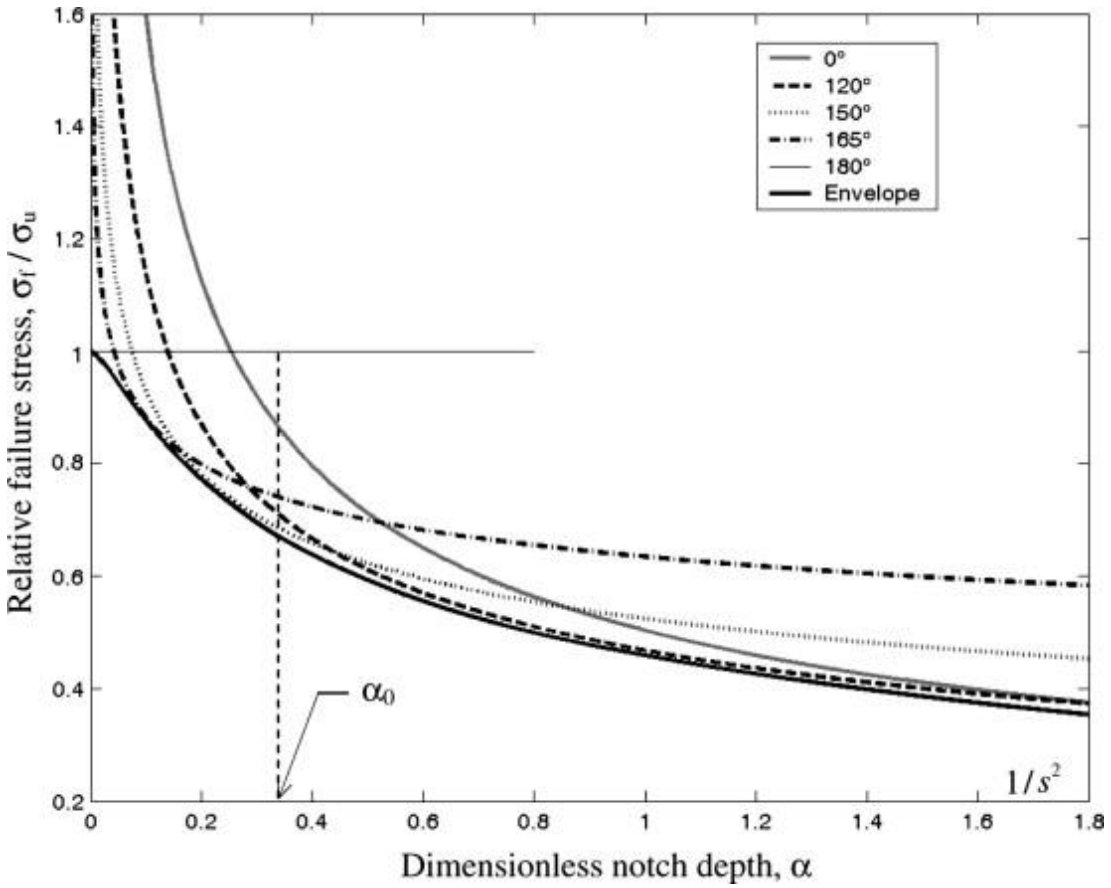


Figure 8: Theoretical notch sensitivity, plotting stress-concentration factor (y-axis) against the depth with respect to notch depth and opening angle for a brittle material. The fitted curve is $\propto 1/s^2$ where s is a 'brittleness number' here. Reprinted from [48] with permission from Elsevier.

I.3.2.3.3 Size and scale considerations

Notch strengthening behaviour may have a size dependence, such that the notch strengthening factor has a notch radius dependence and becomes progressively more insensitive to features below a given radius. Similarly, there may be a scale dependence where a body becomes insensitive to notches with the linear dimensions (depth, for example) below a threshold. Both size and scale affects may be associated with microstructural features. From an engineering perspective, the behaviour is commonly recognised in composite materials where the multiphase interactions affect the localised behaviour of the material; the microstructure is considered to impose a certain length scale, such that mechanisms that act at that length scale are altered. When measuring notch strengthening behaviour it is vital to understand how the microstructure influences the size and scale effects, and test geometries need to be selected based of the ductility of the material.

For deep and/or blunt notches, compared with the microstructural length scale, quasi-brittle materials behave as if brittle. However, when the depth (shallowness) is comparable to the inherent length-scale, the fracture strength commonly deviates from the ideal brittle behaviour – σ_{max} becomes invariant with further reduction in depth, and the sample no longer fails reliably at the notch. Similarly, below a critical notch radius, the fracture strength and toughness deviate from the brittle case [52].

Berto *et al.* showed that the J-integral is related to the average strain energy density in a general but non-trivial manner. This was particularly defined for use with U-shaped (blunt) notches, where a relatively large control volume must be considered (compared to the notch radius), especially for quasi-brittle and plastic materials (see Figure 9) [33].

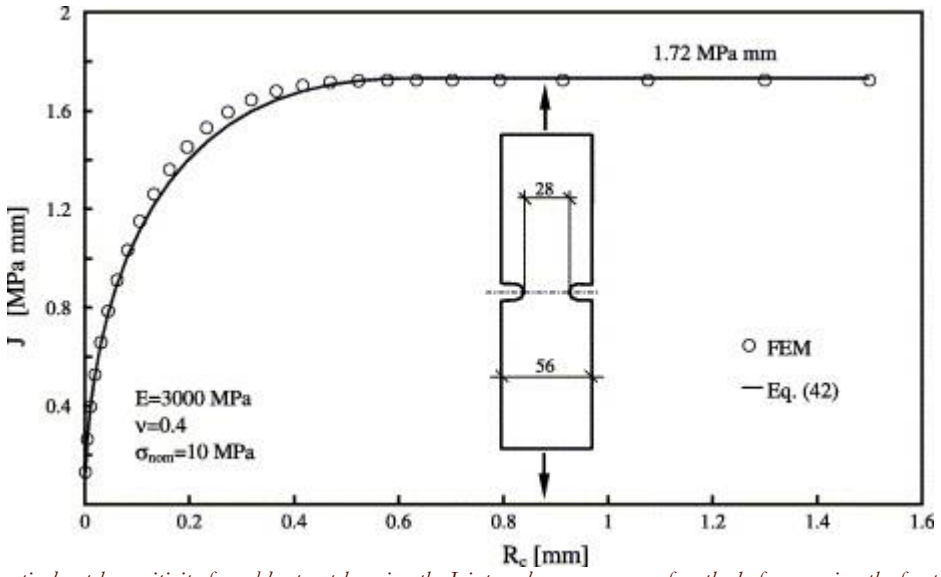


Figure 9: Theoretical notch sensitivity for a blunt notch, using the J-integral as a measure of method of measuring the fracture toughness. Here, R_C is the critical radius, for a notch root radius of R = 1.0 mm. Reprinted from [33] with permission from Elsevier.

I.3.2.4 Determining fracture initiation

In Stage 5 of the general methodology the corrected stress/strain/energy state etc. at each of the potential initiation points is compared to the fracture criterion in a pass/fail test. While conceptually simple, this test must consider the potential for a multiphase or scale-dependent response, including the potential need for multiple fracture criteria to be met.

I.3.2.4.1 Composite failure considerations

In a heterogeneous material, a series of fracture criteria may be required such that fracture occurs in multiple phases before catastrophic failure; as with the damage mechanisms (and the two may be related, for example in micro-cracking), the fracture criteria depend on the phase interactions.

For example, a typical failure route for a long fibre composite (a glass fibre reinforced polymer, for instance) loaded parallel to the fibre direction could be: 1) the load bearing glass fibre absorbs significant elastic energy preventing the polymer from distorting; 2) the fibre fractures, but the strong fibre-polymer interface prevents crack growth; 3) fibre pull-out occurs as the interface breaks down, absorbing more energy and further preventing polymer distortion; 4) finally, the polymer deforms plastically (absorbing more energy), fails, and the crack extends to the next fibre and the process is repeated. For each stage a different damage mechanism and fracture criterion must be considered such that macroscopic fracture can only occur when multiple fibres fail (either serially, as described, or simultaneously).

Crack initiation in composites must therefore be considered at the appropriate scale for the fracture mechanisms.

I.3.2.4.2 Measuring fracture properties

The simplest recognised approaches to measuring bulk fracture properties are by using surface strain gauges or clip gauges to measure crack mouth opening displacements, CMOD [53]. These approaches are contact methods, so can only characterise the response in a 'point' location or the bulk, are limited to usually flat or carefully-machined surfaces, have size limitations determined by the material, and cannot develop understanding of any heterogeneous response in general [23]. Care must be taken using these surface contact methods that the material response is not modified, and so they are difficult to prepare, both in general and particularly for aggregate materials like graphite. Even correctly applied, no subsurface strains are measured.

'Full-field' area analysis techniques, such as photo-elastic coatings, and Moiré grids [23], can analyse surface deformations to an accuracy comparable to a strain gauge. The techniques of digital image correlation, DIC [29, 54][12], and electronic speckle pattern interferometry, ESPI [55], may be completely non-contact, avoiding issues of intimate bonding, and can analyse surface deformations to an accuracy approaching that of strain gauges. These latter techniques are highly flexible and deployable but do require a suitably patterned and/or reflective surface, so some surface treatment may be required, though this is less likely to influence the stress response.

[12] DIC uses signal cross-correlation techniques to 'track' features in image data, in either image or Fourier space. Features must be well defined by contrast differences. The algorithms identify features within a specified interrogation window in a reference image, and then the same features in a distorted image. The features must therefore be well dispersed across the region of interest and preferably with a size distribution broader than the displacement distribution, such that representative features can be correlated at all length-scales. Multiple image sources may be combined to measure surface displacements (stereo DIC), or internal displacements measured from volumetric images using the 3D analogue called digital volume correlation, or DVC.

To measure internal strains, non-destructive techniques are preferred; methods such as micro-sectioning and fractography not only require external stresses to be removed, relaxing elastic strains, but may also damage the fracture surface. X-rays are suitable for penetrating bulk materials to examine structures from crystals (using X-ray diffraction) to metres (using X-ray radiographs) in scale. For analysis of component scale specimens, the resolution of radiography is of the order of 1 μm which may be achieved using laboratory sources or more brilliant synchrotron sources such as the Diamond Light Source, DLS.[13] A radiograph is a differential absorption map of transmitted X-rays. Using a Radon transfer to combine radiographs taken at different angular positions, an X-ray computed tomograph, XCT, may be produced (see Figure 10) [56, 57], which is a 3D contrast map of the internal structure, or a virtual microstructure, with each voxel[14] reflecting the density and chemistry in the equivalent position in the material [56]. Mechanical testing may be performed *in situ*, with the displacements of greyscale features tracked between virtual images by digital volume correlation, DVC, the 3D analogue of DIC. The detectable feature size and resultant strain resolution is limited by the brilliance of the X-ray source, experimental method and sample size; sub-voxel displacements may be routinely measured, as in [58] and [59] from 2012 and 2013. Where the microstructure is heterogeneous, the resultant strain field might be similarly diverse, with different loading modes operating at different length scales. DVC can capture all of this behaviour but must be optimised for the microstructure [60].

[13] The Diamond Light Source, part of the Harwell Science and Innovation Campus, UK, can generate collimated mono-chromatic X-ray beams with energies up to 150 keV.
[14] A voxel is the equivalent of a 3D pixel, the size of which is dependent on the context. In XCT, it depends on the spatial discretisation of the charge coupled device, CCD, in the detector.

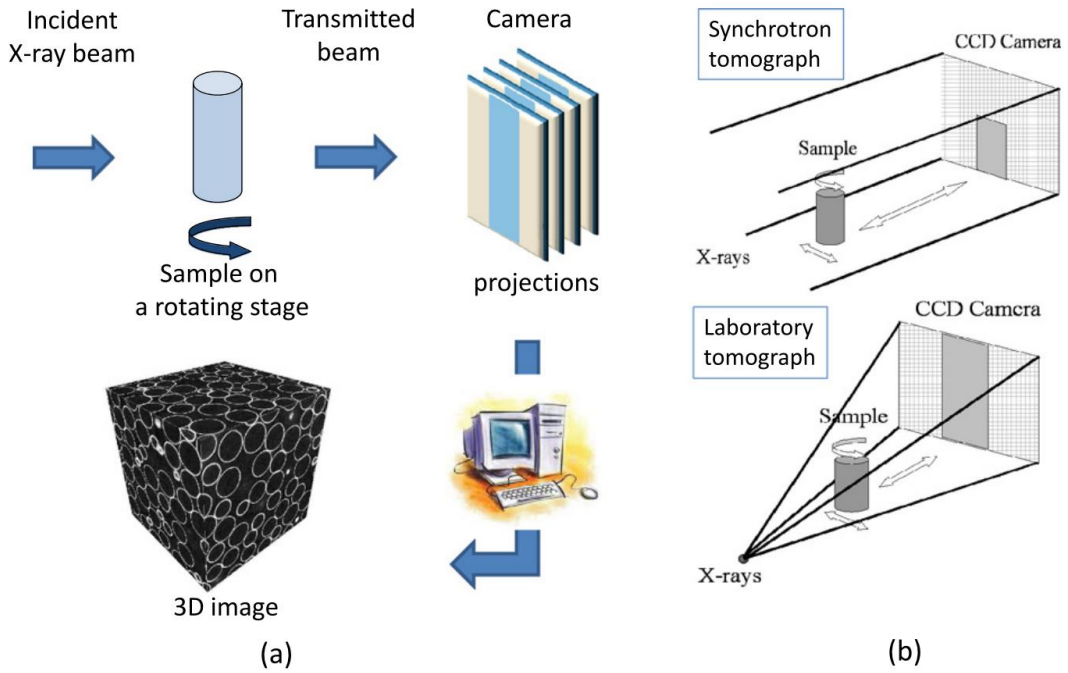


Figure 10: The principles of X-ray computed tomography: (a) the basic imaging method where transmission projections are numerically reconstructed into a 3D virtual microstructure; and (b) the different magnifying effects between a collimated synchrotron source and a cone-shaped laboratory source; conical beam magnification must be corrected numerically during reconstruction. Reprinted from [57] with permission from Elsevier.

I.3.2.5 Determining fracture propagation

For the fracture propagation calculation in Stage 6 energetic principles must be considered. As alluded to in § I.3.2.4.1, it is possible for a fracture to initiate, forming a proto-crack, but then cease to grow to catastrophic failure. This is an entirely energetic process, dependent on the thermodynamics of crack growth, and there is no requirement for heterogeneous properties; should the body attain a metastable state after the crack initiates, the crack will arrest. If the arrest is due to microstructural mechanisms, this is often described as the 'rising R-curve' phenomenon, where resistance to fracture is a function of crack length and crack tip position.

While there are a number of material considerations related to crack propagation, a detailed examination is beyond the scope of this thesis. For understanding crack initiation, additional information may be gained from studying the stress-strain behaviour around arrested cracks as they may be used to infer the effect of an 'infinitely sharp' stress raising feature.

I.4 Towards development of a notch sensitivity test

This thesis will consider how the evolution of notch sensitivity may be measured during a practical PIE test, such that confidence in the predictions of crack initiation due to stress concentrations might be improved. The development of a suitable test method will be considered in the context of the material science considerations outlined in § I.3.2. In Chapter II the known physical properties of the AGR graphite Gilsocarbon relevant to measuring notch sensitivity will be described, including how these properties are known to evolve in the nuclear environment. From the considerations highlighted in this chapter, the material science challenges not addressed in the available literature will be identified.

In Chapter III, trials with a possible notch sensitivity test will be reported, based on 6 x 6 x 19 mm beam geometry loaded in four-point bend. The notch sensitivity will be measured in virgin (as-manufactured) Gilsocarbon, which will highlight the relative notch insensitivity to notch radius (from 0.05 mm to 2 mm), and the effect of notch depth (up to 4.5 mm). Over 100 specimens were tested, and hence these results will provide a statistical basis for future analyses. Full field measurements based on multi-scale, multi-camera *in situ* imaging will be combined with DIC techniques and FE simulation to determine the stress, strain and energy states of the specimens at fracture. Stress and energy-based approaches to considering the fracture criteria and notch strengthening effect will be evaluated, including calculating the notch strengthening factors and strain energy density using full field data. By comparison with historical results, the 6 mm samples will be shown to underestimate notch sensitivity. Furthermore, it will be shown that linear elasticity and the effective-ligament theories are deficient, and a non-linear material model is required. A non-linear, but elastic, model, previously fitted to Gilsocarbon's empirical behaviour will be tested, though not fully evaluated due to numerical instability in the simulations. Additionally, consistent behaviour will be shown between the SED measurements from simulation and DIC, despite incomplete empirical data, which is an important result in the development of PIE techniques and has potential for the real-time monitoring of graphite components.

To better explain the notch insensitivity in small specimens, an experiment utilising *in situ* volumetric imaging during crack initiation will be examined in Chapter IV. By further combining multi-scale image correlation and simulation, the presence of sub-millimetre heterogeneous behaviour of the microstructure will be demonstrated to deviate from the predicted linear elastic response. A non-linear, non-recoverable stress-strain response will be identified, with deformation due to residual strains identified and associated with microstructural features. Furthermore, the formation of a strain concentration zone extending over several millimetres will be argued to be the origin of the insensitivity of Gilsocarbon to notch radii less than 2 mm.

Chapter V will then consider the additional insights into measuring notch sensitivity arising from these observations, and the implications of a changing microstructure for the conclusions due to the reactor environment will be considered.

II The Properties of Nuclear Graphites

II.1 Nuclear graphite grades

This review will focus on the gilsonite-based graphite grades used as the AGR moderator and will touch on historical results measured on other grades. Gilsonite coke is the feedstock on which the near-isotropic AGR moderator graphites were based, hence the generic term Gilsocarbon. Pertinent properties of other grades will also be discussed. The feedstock and manufacture of each grade is different and the properties are unique; Table 1 broadly classifies a relevant selection.

In the context of notch sensitivity, virgin Gilsocarbon may be summarised as having: a heterogeneous microstructure formed of spherical filler particles (ϕ < 1 mm) in a binder phase (classified by the ASTM microscopy definitions as medium-fine grained); a significant pore network extending over many length scales; near-isotropic behaviour; a non-linear plastic stress-strain response, with quasi-brittle failure; and an insensitivity to features below a c. 1 mm radius. There is a significant distribution in properties measured from both a single brick, and between bricks in a given core. The effect of neutron irradiation on the crystal and nano-structures causes a volume contraction and expansion (and stress reversal at the brick periphery); increased stiffness and linearity of the stress response; and increased brittleness and strength. Radiolytic-oxidation additionally expands the bulk pore network, preferentially attacking the binder phase, causing a modification to the dimensional change rates [3], and an overall reduction in bulk stiffness and strength [15].

Table 1: A selection of graphite grades discussed in this review grouped according to their microstructure, properties and use in historical reactor environments. This list is not exhaustive for the graphites used in nuclear applications.

Group	Grade	Notable structure	Isotropy	Typical (or potential) application in reactor	Refs
Gilsocarbon-type	IM1-24, NP4, UCAR's GCMB	Spherical filler particles from gilsonite feedstock (up to c. 2 mm diameter), Porosity up to 20 %	(Near) isotropic	AGR moderator, fuel sleeves	[29, 43, 47, 61]
PGA-type	PGA	Needle-like filler particles (up to c. 2 mm across), Low porosity (c. 10 %)	Anisotropic	Magnox moderator	[13, 43, 61]
Fuel sleeve type	SGL's EK78, VFT, NSCC; UCAR's VFT, NSCC; Pechiney, Pitchcoke	Very low porosity due to multiple impregnation cycles	Extruded (anisotropic)	Fuel sleeves	[43, 47, 61, 62]
Fine grained	IG-11	Fine grained particles (< 0.5 mm)	Quasi-isotropic	HTR-10 structure	[14, 63]
Isotropic	SM2-24	Blended needle coke and gilsonite	Isotropic	AGR Reflector	[61]

II.2 Fabrication and microstructure

A key aspect of the graphite grades outlined in Table 1 is that these are synthetic composites formed by high-temperature calcination of graphite coke coated in pitch (see § II.2.1). Many industrial graphites, Gilsocarbon included, have an almost fractal collection of phases ranging from the millimetre to the nanometre length scales, which have been well reviewed in [15], for example. The principal phases of interest in this review are the particles, referred to here as 'filler particles', and the calcined pitch, 'binder', which have different properties due to the underlying crystallinity and porous structures (see § II.2.2). The finer scale behaviour will only be mentioned briefly where it is applicable to the stress concentration behaviour.

II.2.1 Artificial graphite manufacture

While globally available, natural graphite grades are unsuitable for engineering components in a reactor. Artificial grades are mass produced via the Acheson process in which the physical properties of the graphite may be tailored, particularly the degrees of anisotropy and porosity [64].

The 'Pile Grade A', PGA, grade used for Magnox moderation had large lath-like filler particles and was formed by extrusion; this resulted in uneven dimensional change and restricted control of the neutron flux and the cooling gases. To increase isotropy for the AGR fleet, the Gilsocarbon group of artificial graphites was developed based on the gilsonite coke feedstock and isobaric moulding during manufacture.

Naturally, the gilsonite comprised of globules of coke, which were often found clumped together. The globules were graded by size to spheres of nominally [0.3, 1.0] mm and purified chemically to remove neutron-absorbing elements leaving 'green coke'. The exact graphite manufacturing process differed between reactors and feedstock, but for the AGRs the general stages were [13]:

1. Coke calcination

   The green coke was heated to [1200, 1350] °C to remove further impurities and moisture. For some reactors the coke was then crushed and re-sieved. The resulting solid particles, crushed or uncrushed, formed the 'filler'.

2. Moulding or extrusion

   The particulate filler was mixed with liquid pitch at [165, 170] °C, then formed by extrusion (PGA, for example) or iso-moulding (such as Gilsocarbon) while cooling naturally, and finally water-quenched.

3. Baking

   The solid mixture was baked at [750, 1000] °C for [20, 70] days, resulting in a c. 33 % volume reduction and a series of interconnected pores from vapour escape.

4. Pitch impregnation

   The billets were repeatedly impregnated with more liquid pitch and re-baked, reducing the porosity to c. 8 % and increasing its strength.

5. Graphitisation.

   Electrical resistance heating was used to reach [2800, 3000] °C. At these temperatures, the random 2D crystallites reorder into 3D crystals.

II.2.2 Microscopic structure

Manufactured in this fashion, graphite is a hierarchical composite material with a microstructure that may be classified on a wide range of length scales (see Figure 11 – Figure 14). Three large-scale feature sets may be identified, described for Gilsocarbon as:

1. Filler particles
   Resulting directly from the original coke, these are large (up to 2 mm across), approximately spherical units, containing 'onion' layered or cross-like voids. As they often clumped together, some manufacturers tended to crush these particles, as seen in Figure 11.
2. Binder:
   Formed from the graphitised pitch, the binder is the matrix surrounding and connecting the filler particles.
3. Pores
   Created by oxidation and distillation of the pitch, pores sizes range from the nano-scale up to 3 mm across [65, 66].

In many grades, the filler particles are needle-like or blocky in form and tend to align during the processing, leading to strong anisotropy. In gilsonite, the coke particle morphology arises from the crystal's basal planes forming an enclosed surface, which eliminates weak end boundaries, increases the filler strength, and is naturally isotropic. The shrinkage following distillation causes the distinctive void shapes (Figure 13).

The chemical complexity of the pitch is reflected in the structural intricacy of the matrix after graphitisation [67-69]. The matrix may be divided into 'binder' and 'flour'. The substructure of the binder may then be described based on the continuity of basal plane alignment into 'domains' (continuity for ≥ 100 μm), and 'mosaics' (continuity for ≤ 10 μm). The most fine-scale feature (< 10 μm) of the matrix, the flour, is found at crystallite boundaries. Studies in the 1970s demonstrated that the matrix may be regarded as pure graphite [69]. The following nano-scale features have been imaged, as collated in [70]:

- Well graphitised material (Figure 14a)
- Quinoline insoluble particles, found in and on the surface of mesophase spheres (Figure 14b,c,d)
- Nano-sized graphitised particles (Figure 14e)
- Non-graphitised carbon (Figure 14f)

The majority of pores form between crystallite regions, where the packing between filler particles and the binder is imperfect [71, 72]. Pores may be categorised by their size [65], but at a microscopic level are rarely observed in isolation, forming instead extensive networks that are either 'open' if they are surface contacting, or 'closed' if not. Gilsocarbon is approximately 20 % porous, of which [14, 19] % is open porosity [72].

When cooling from 2000 °C to 1500 °C after graphitisation, differential crystal contraction of results in nano-scale cracking, known as Mrozowski cracking [15, 73].

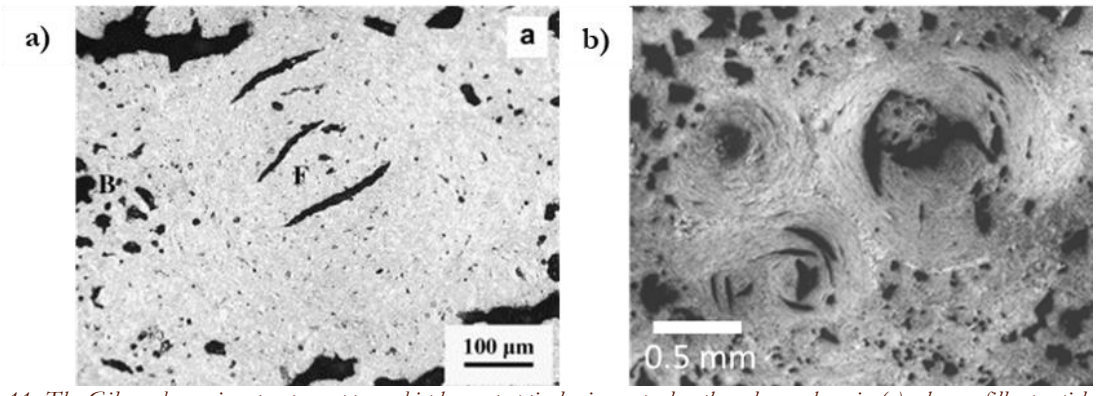


Figure 11: The Gilsocarbon microstructure appears bi-phase at optical microscopy length scales, such as in (a) where a filler particle, F, and the binder, B, are identified by their pore shapes: filler particle pores are typically elongated and often concentric, while the binder pores are more equiaxed. Filler particles often clump together, as seen in (b). Reprinted from (a) [74] and (b) [70] with permissions from Elsevier.

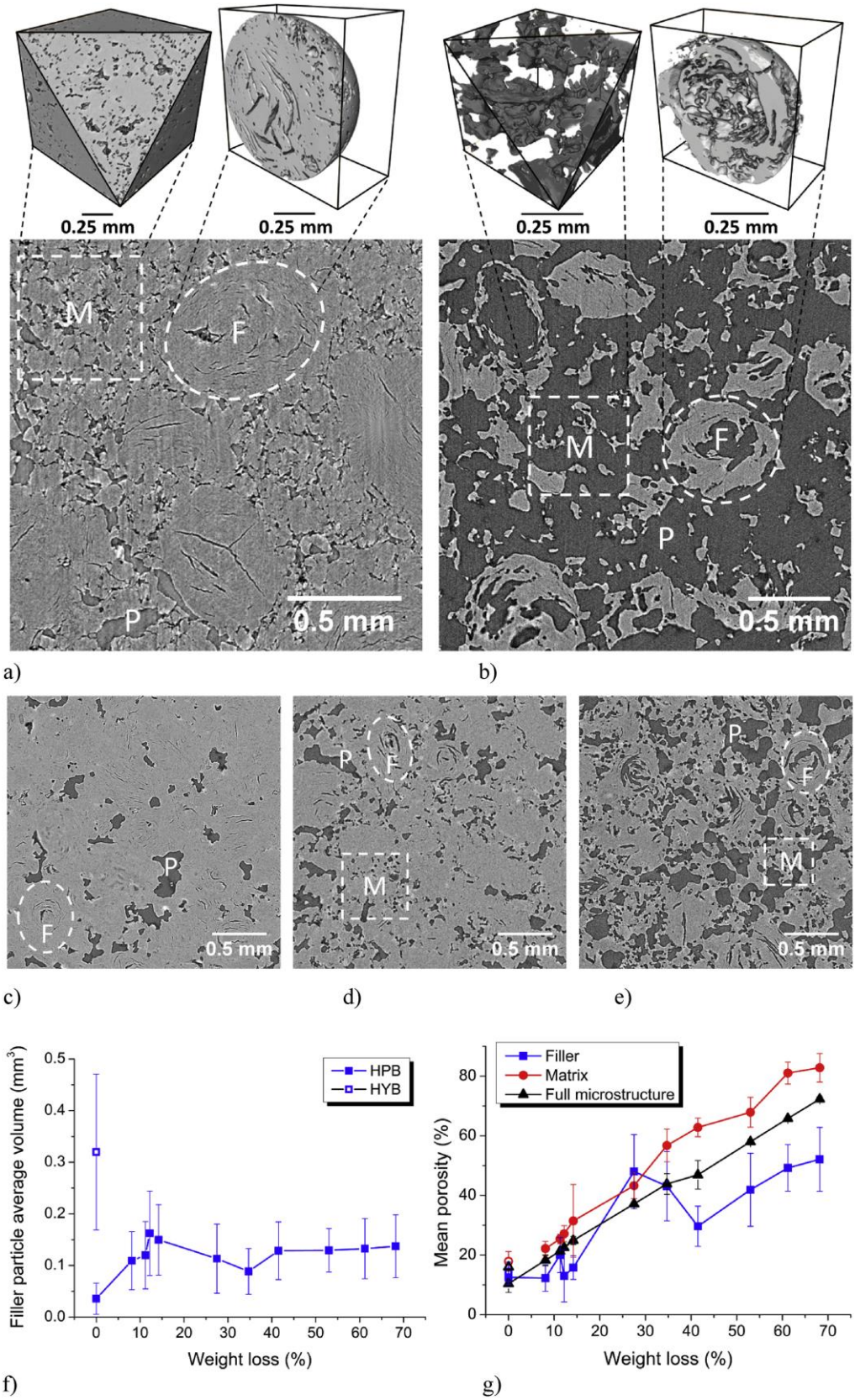


Figure 12: The evolution of the Gilsocarbon microstructure with radiolytic oxidation: (a) 2D X-ray tomography slices of virgin Heysham 2 graphite; (b) Hinkley Point B graphite with weight loss of 68.2 %, (c) 0 % weight loss, (d) low 8.1 % weight loss and, (e) 27.5 % weight loss. 3D reconstructions of the extracted filler particles (F) and matrix (M) sub-volumes are shown inset, with pores are denoted by 'P'. Segmentation analysis the evolving behaviour of (f) the average sizes of the extracted filler particles, and (g) the measured porosities of the selected sub-volumes and full microstructures. Error bars correspond to standard deviation. Hinkley Point B graphite is shown by solid points, Heysham 2 graphite is represented by open points. Reprinted from [75] with permission from Elsevier.

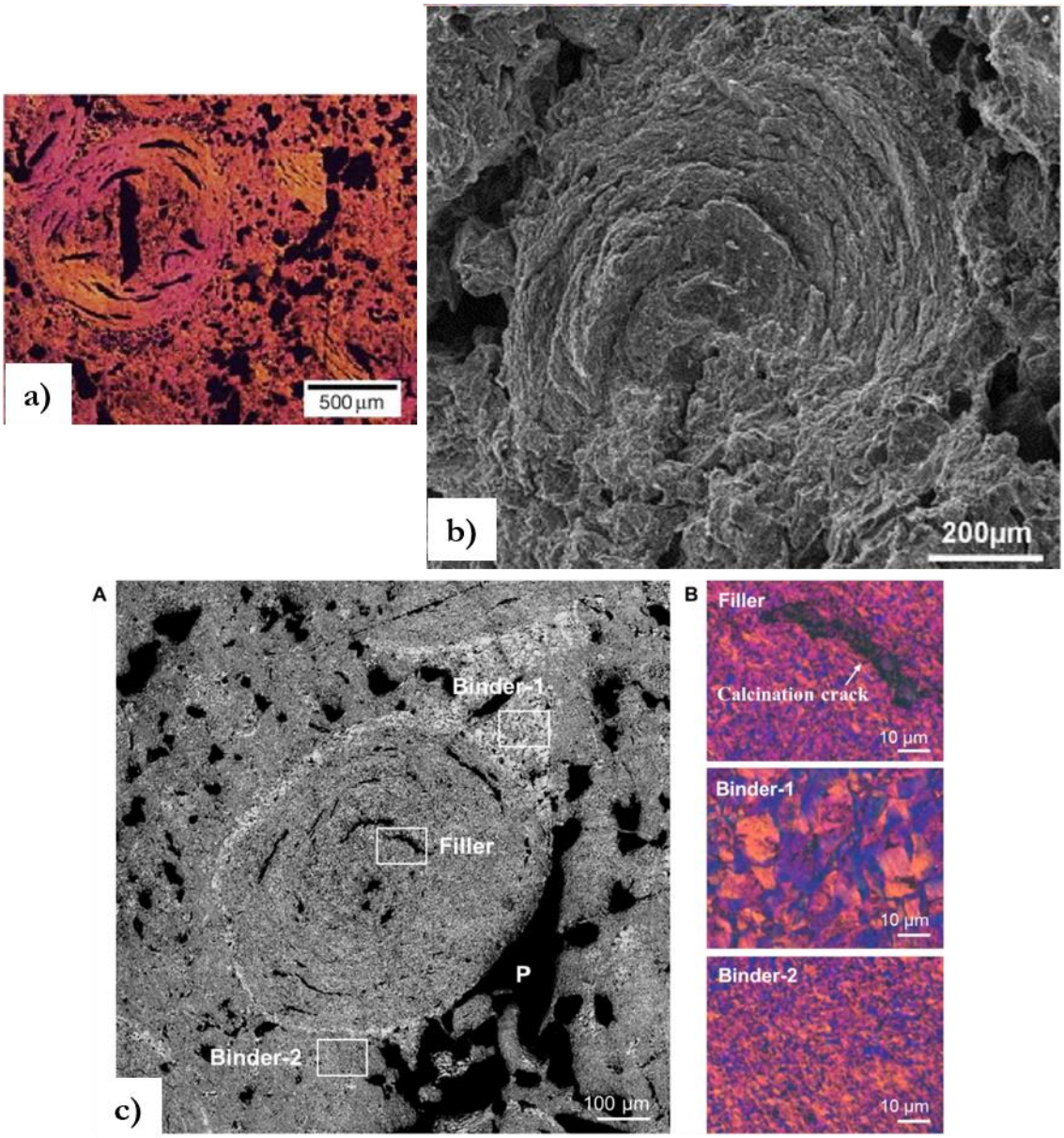


Figure 13: The nano-crystalline texture in Gilsocarbon's phases leads to the variety microstructural features at the micrometre length scales. Polarised optical microscopy (a) indicates the alignment of the nano-crystallites over domains up to 500 µm within both the filler particles and the binder; it is notable the aligned domains are not defined strictly be the pores and that the alignment domains in the particles are larger than in the binder. The higher resolution SEM in (b), shows the 3D surface structure and demonstrates the 'onion-like' structure of a filler particle distinct from the binder. Similar, features are seen at even higher resolution using polarised optical microscopy in (c). Reprinted from (a) [15], (b)[76], and (c) [77] with permissions from Elsevier. .

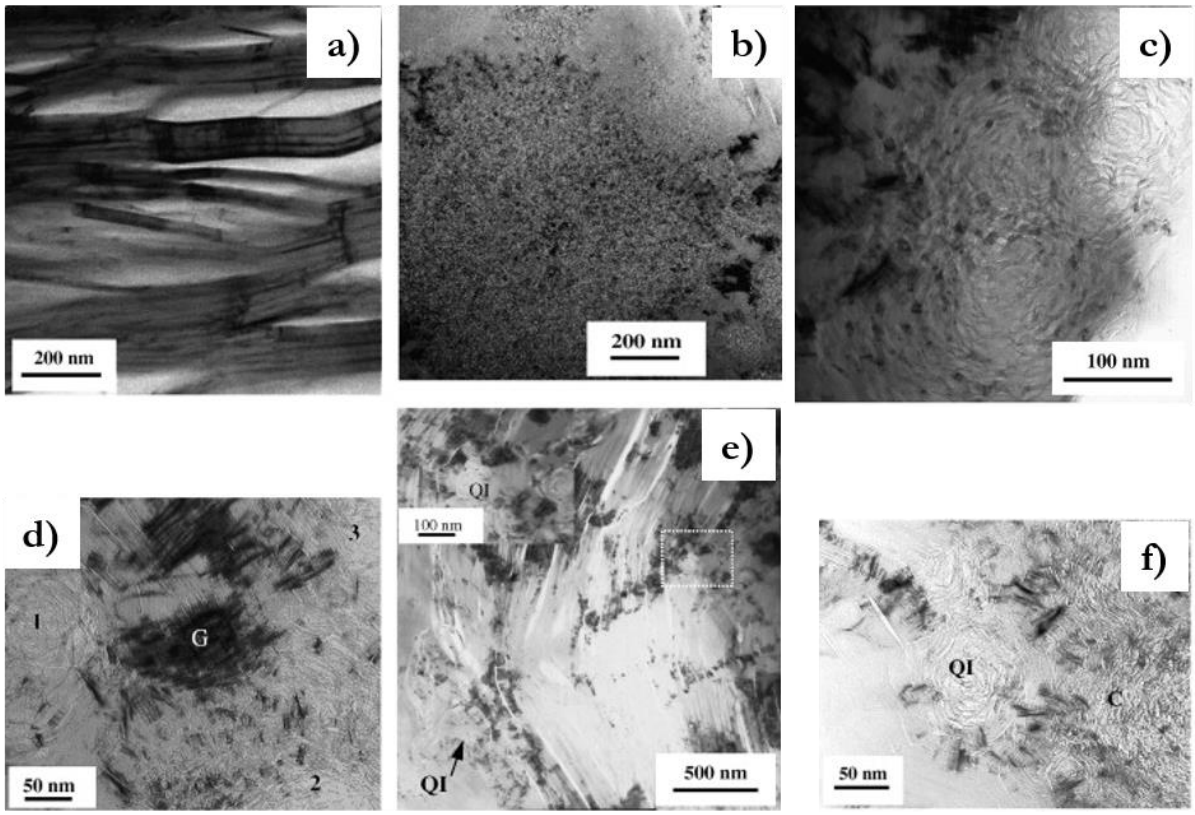


Figure 14: Various fine-scale features observed in the Gilsocarbon binder phase using transmission electron microscopy: a) well graphitized crystallites showing alignment of the basal planes over an appreciable area; (b) a large area with a chaotic structure; (c) an aggregate of four quinoline insoluble, QI, particles; (d and e) bulk well graphitized graphite carbon interspersed with QI particles with higher magnification inset in (e) showing that the graphite basal planes were deflected by a QI particle; and (f) the QI particles may exist in contact with carbon of a chaotic structure (C). Figure parts reprinted from [74] with permission from Elsevier.

II.3 Physical properties of virgin Gilsocarbon

To understand notch sensitivity of features at the millimetre length scale, it is necessary to consider the properties of comparably sized features. The properties of these large features have a hierarchical dependence on the fine scale features, right down to the crystal level. The properties of crystalline graphite will be reviewed in § II.3.1, and the properties of the bulk nuclear graphite in § II.3.2.

II.3.1 Crystal structures

Several allotropes of pure carbon are thermodynamically metastable, including diamond, graphite, the fullerenes and amorphous carbon (see Figure 15); of these, crystalline graphite is the most stable at the temperatures and pressures of AGR operation. Graphite has a layered hexagonal close-packed structure with a dihexagonal dipyramidal crystal class and space group $P6_3/mmc$ (see Figure 16). With sp^2 hybridised atoms, the properties are highly anisotropic with short and strong intra-layer bonds, but longer and weaker inter-plane bonding [13, 65, 78].

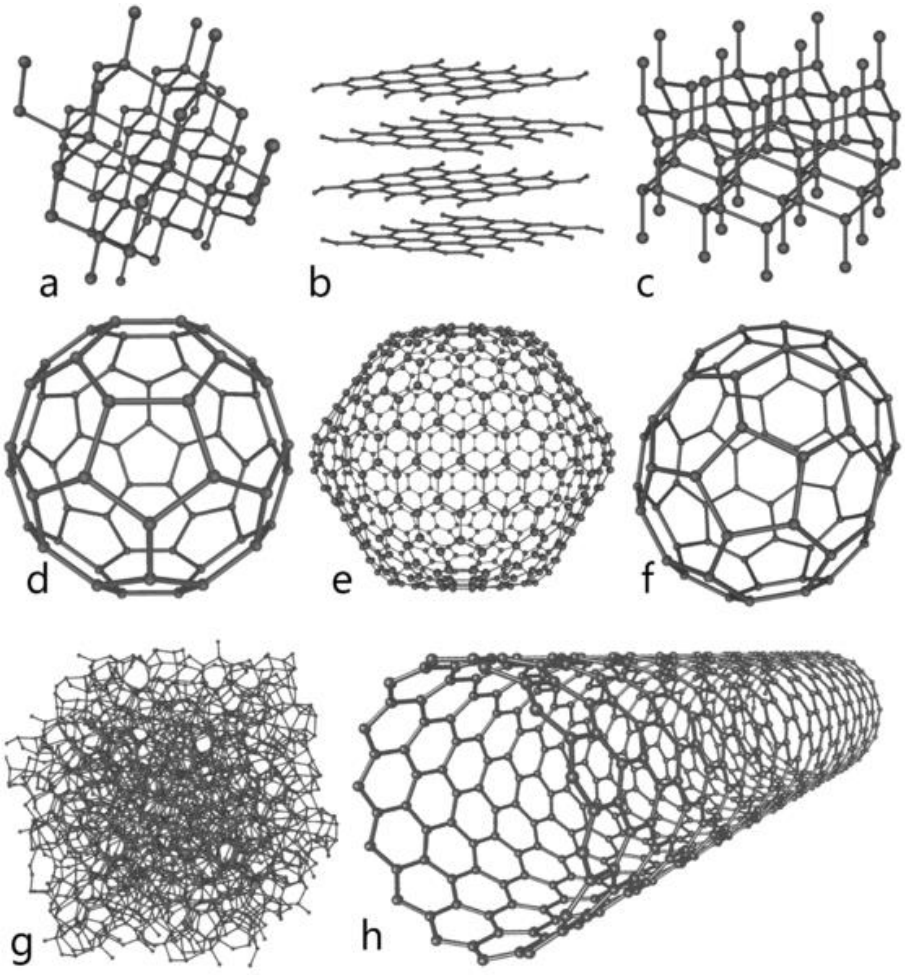


Figure 15: Eight allotropes of pure carbon: a) diamond; b) graphite; c) Lonsdaleite; d) C60 (Buckminsterfullerene); e) C540 (a fullerene); f) C70 (a fullerene); g) amorphous carbon; and h) a carbon nanotube (here, single-walled). This list is not exhaustive. At ambient pressure and temperatures below 1000 °C, graphite is the thermodynamically stable allotrope, but all could exist metastably in an AGR. Reprinted from [79] under Creative Commons Attribution ShareAlike license v. 2.5.

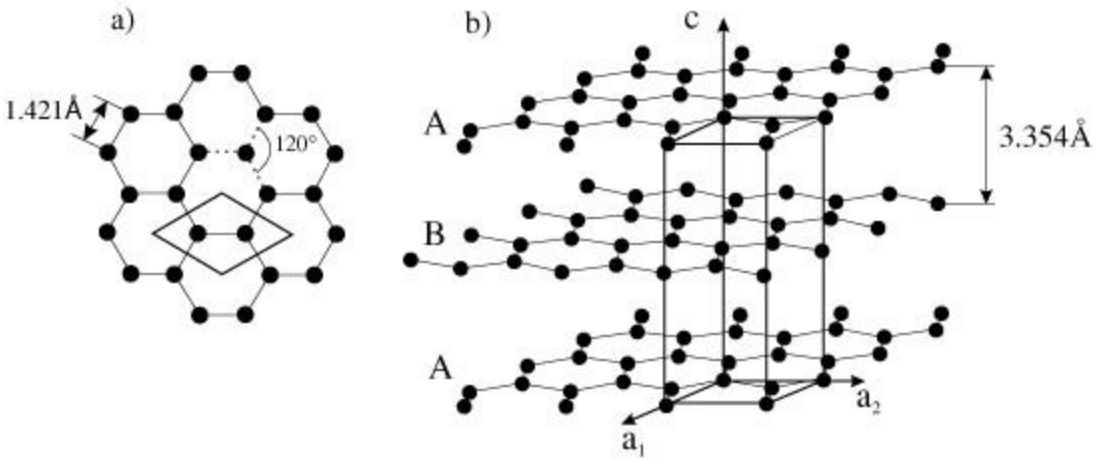


Figure 16: The unit cell of graphite with dimensions, in which (a) the layered structure results from three planar σ-bonds, and (b) delocalised 'planes' of π-bonding that exist between the atomic planes forming a 3D staggered structure. Reprinted from [80] with permission from IOP Science.

II.3.2 Composite properties of the large-scale phases

Due to the manufacturing method, the properties of the individual microstructural phases cannot be known uniquely, only inferred from their impact of the bulk material. For example, for the stress-strain behaviour, the individual phases of Gilsocarbon are believed to have a Poisson ratio in keeping with most ceramics, $\nu \approx 0.3$, but the composite graphite is able to absorb uniaxial strains with a bulk $\nu \approx 0.2$. Both E and ν are found to change with applied load [81].

Table 2 lists representative properties of bulk Gilsocarbon; having been made to different specifications for each AGR, no single set of material properties can be specified for 'reactor grade' Gilsocarbon. Properties are known to vary within a single billet, and between billets [82]. These data show that graphite is a low density, porous material with moderate stiffness. Although Young's modulus is commonly quoted as 11 GPa, this is found to vary experimentally. The elastic stiffness of artificial graphite is affected by the heat treatment during manufacture, test temperature, the degree of crystallite orientation, and porosity [83-85]. Furthermore, the presence of Mrozowski cracks is used to explain unusual observations of the coefficient of thermal expansion, thermal shock resistance [3] and the hysteresis effect of temperature dependence of Young's modulus, such as the stiffness response of PGA at elevated temperatures in Figure 17 [83]. Theories to account for all these effects have been reviewed by Roberts *et al.* [86] and Mason and Knibbs [83, 87].

The stress-strain (σ-ϵ) behaviour of virgin Gilsocarbon is distinctly non-linear, even far below the peak fracture load, and different in tension and compression. Using the transmission X-ray techniques of radiography and diffraction, Marrow *et al.* demonstrated that for Gilsocarbon in uniaxial tension, the bulk strains were correlated with the change in basal plane distance ($d_{(00.2)}$). Neutron diffraction was further used to study the strain response in flexure, where both tension and compression were compared. In the compressive state a linear response was measured, but the bulk elastic modulus was non-linear and exhibited non-recoverable strains that resulted in a permanent set, assuming the crystals were undamaged by the loading. The combined strain response from the diffraction elements is shown in Figure 18, which highlighted the nonlinear strain response in tension, associated with damage. The bulk strains were further related to the nominal stress behaviour, such as in Figure 19 and a study by Hodgekins that further showed non-recoverable strain, Figure 20. Marrow *et al.* rationalised the behaviour as the redistribution of elastic and non-elastic strains due to significant residual strains from the initial heat treatment; microcracking was then proposed as the mechanism for the formation of the permanent set [88].

Barhli *et al.*, [89], formulated a user-defined material, UMAT, based on the response observed by Marrow *et al.*, and suitable for use in finite element simulations. Simplifying the stiffness tensor to the dominant uniaxial component, a strain dependent form of the Young's modulus, E_{UMAT}, was fitted empirically to the power law in (8), described in a form suitable for FE analysis and shown in Figure 21. The modulus is dependent on the maximum principal strain, ϵ_1, with the porous fraction, P, and fitting constants, f_1, f_2, f_3, f_4 and f_5, determined as: f_1 = 28.3 GPa, f_2 = 1, f_3 = 36.34, f_4 = 6.8e-7, f_5 = 4.12 and P_0 = 0.18. The strain limits were defined based on the empirical findings, and also numerical and practical considerations for modelling.

(8)
$$E_{UMAT}(\epsilon_1) = \begin{Bmatrix} 11.93 \\ f_1(1 - f_2(P + f_3\epsilon_1 + f_4)^{f_5}) \\ 0.001 \end{Bmatrix} [GPa] \; for \begin{Bmatrix} \epsilon_1 \leq 0.0002 \\ 0.0002 < \epsilon_1 < 0.0224 \\ 0.0224 \leq \epsilon_1 \end{Bmatrix}$$

In compression, industrial graphites are strong enough to form a self-supporting core, even at high temperatures, but are approximately only a quarter as strong in tension [13, 90]. Graphites fail in a quasi-brittle manner, and the strength is sensitive to the microstructural features, such as the volume fraction, size and form, of the porosity and filler particles [3, 91, 92]. High-resolution mapping of the surface strains in Brazilian disc specimens (discs compressed on their edge to cause biaxial stress) revealed that damage generally initiates at defects, such as pores [81]. Prior to failure, regions of permanent deformation were observed; these were assumed to contain micro-cracks that coalesced until a critical defect was formed [70].

Brown *et al.* measured the fracture strengths for smooth tensile and three-point bend, 3PB, specimens of several graphite grades (Figure 22) [47, 93]. In graphite, the strain to failure (ϵ_{max}) is greatest in bending, while σ_{max} in flexure is around 1.5 times greater than in tension. The smallest dimensions of the specimens were significantly larger than the inherent microstructural scale (> 12 mm compared to the c. 1 mm scale, as determined by [94]). Far from conclusive in themselves, Brown *et al.* claimed that the fracture strength decreased with decreasing specimen size, a counterintuitive result. The claim is supported by Mason [95], though the counter claim is made for other grades [96]. Using a critical volume approach, Brocklehurst compared the size effects in 4PB and tension on strength [93] (Figure 23). For static 4PB, above volumes of 1 cm^3, Weibull statistics were obeyed (with m = 16) where smaller volumes increased the failure strength, but for volumes below 1 cm^3 the strength decreased. In tension, above 10 cm^3 size had no effect, but the strength decreased for smaller specimens. For PIE measurements, fracture strength is measured by 3PB of 6 x 6 x 19 mm beams. This geometry is squat compared to normal flexure geometries, and requires a 7 % correction to the measured stress (derived from beam theory) to account for the size effect [97, 98].

Data on graphite γ_{wof} is limited. For stable crack growth from the double torsion technique, Becker *et al.*, [29], and Molteno *et al.*, [99], measured the resistance to crack growth via the J-integral method. A clear increase in toughness was observed, attributed to the development of the FPZ and micro-cracking [29]. Brown *et al.* related the inherent microstructural length scale to the fracture toughness; in the fine-grained EK78, a very low K_{IC} was observed (1 MN.m$^{-1.5}$) for both impact and static loading. The static loading results suggest that γ_{wof} increases smoothly following initiation and then levels off at a stable crack length [47, 94]. Similarly, Barhli *et al.* [89] used J-integral measurements based on DIC displacements and the UMAT formulation for the material ahead of a growing crack to determine the work of fracture, $J_{IC} \approx 200$ J.m^{-2} (a value in line with other measurements in the literature). A recently-developed PIE technique for graphite γ_{wof} based on fracture from a chevron-notch in a 6 x 6 x 19 mm beam (or beam-like) specimen (see also [100]), indicated a size effect with a linear dependence on ligament size; this behaviour was not seen in the homogeneous ceramic Macor® or the porous filter carbon PC45 [17].

Brown *et al.* (1986) reviewed notch sensitivity of several graphite grades, including a near-isotropic gilsonite-based grade (NP4), tested in static 4PB and impact 3PB [47]. For both geometries, single-edge notched samples with notch depths of 2.5 mm were used with notch radii varying over [< 0.1, 10] mm. In the static loading, all but the shallowest of the notched samples failed at the notch; the standard deviation of the scatter was up to 9 % (for six samples). In 3PB testing, the NSF was found to follow the general trends shown in Figure 24, and for a given graphite grade, the NSF determined from 3PB and 4PB loading showed good agreement. The grades tested appeared insensitive to loading rate (Figure 25) [47], but this was disputed for the fine-grained grades [101]. NP4 appeared to be insensitive to notch radii below 0.6 mm (the inherent scale). An alternative estimation for various Gilsocarbon grades in notched flexure testing (see Figure 26) and analysed in the method proposed by Tucker [102], puts the average defect size at 1.5 mm [46], in agreement with [103, 104]. It has been suggested that the inherent defect size in the material negates the effect of artificial defects smaller than this [47].

An early report by Mason showed that the fracture toughness, K_c, tends to a maximum with increasing notch depth [94]. His analysis showed that by adding an artificial nominal notch depth, when calculating the fracture toughness, the average values of K_c are independent of the artificial notch depths, *viz* the natural notch ceases to have any effect on the fracture toughness when significantly less that the artificial notch depth.

An explanation for the notch insensitivity is that micro-cracking ahead of the crack-tip facilitates ductility prior to σ_{max} [70, 81, 105]. These cracks are distributed across the FPZ and tend to accumulate in ligaments, in order to relieve the greatest stresses [106]. For Gilsocarbon, a correlation between the lowest σ_{max} and the deepest surface cracks present in the sample surface (up to 1 mm) was demonstrated by *in situ* XCT of flexure experiments; the initiating defects were often sub-surface [107].

The physical properties of Gilsocarbon are known to show significant spatial variation on the centimetre length scale, an effect which is likely related to the variation in the microstructure, in terms of size and position distributions of filler particles and pores [82, 108]. For component scale predictions using measured properties from small geometries, it is vital to account for the potential variation with meaningful statistical distributions.

Table 2: Representative physical properties of Gilsocarbon at room temperature [109, 110].

Property	Value	Unit
Density	1.8	$g.cm^{-3}$
Young's modulus, *E*	11	GPa
Poisson ratio, ν	0.21	-
Hardness (Vicker's)	16.5	$kg.mm^{-2}$
Thermal conductivity,	131	$W.m^{-1}.K^{-1}$
Coefficient of thermal expansion, (over [20, 120] °C)	3.7	$x10^{-6}\ K^{-1}$
Ratio $\sigma_{compression}/\sigma_{tension}$	4	-
Work of fracture, γ_{wof}	200	$J.m^{-2}$

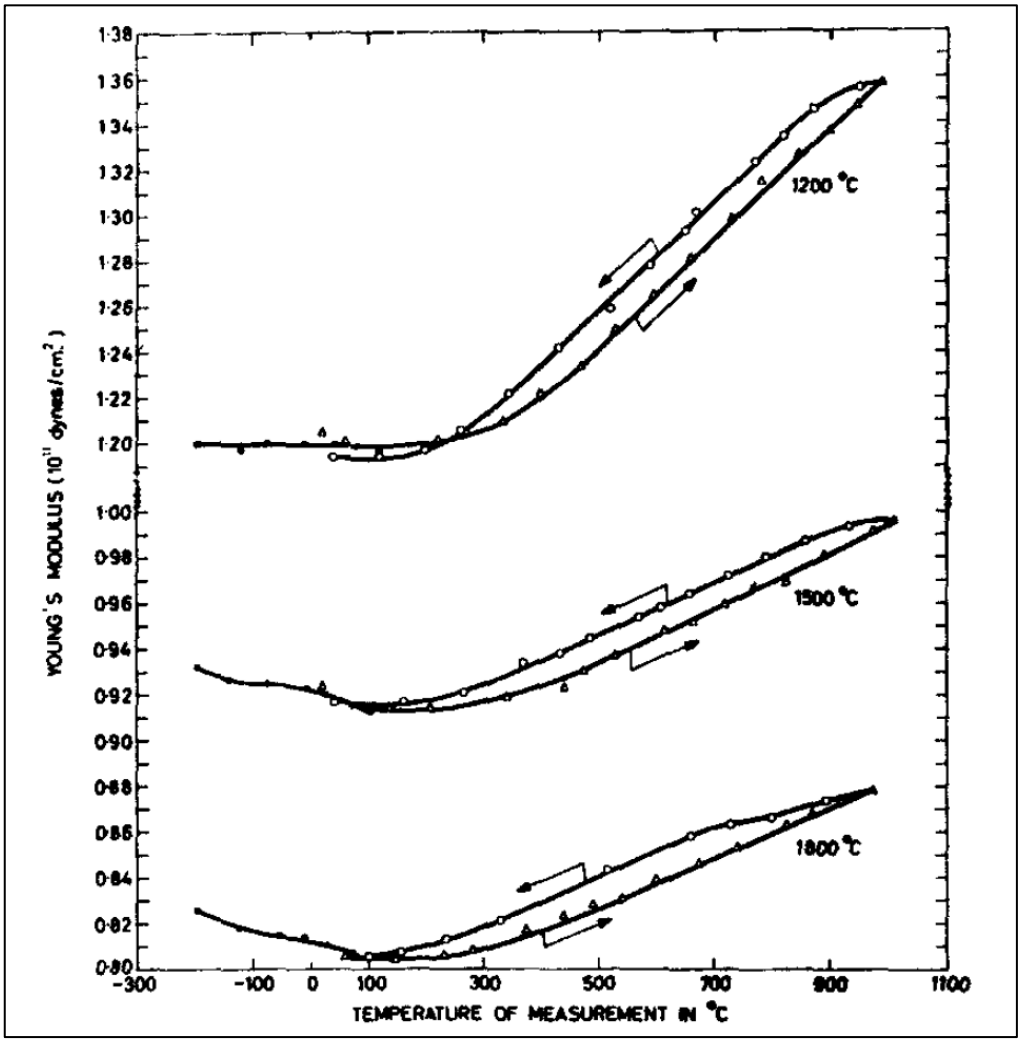


Figure 17:The effect of temperature on Young's modulus in PGA tested at elevated temperatures (parallel to the extrusion axis). Reprinted from [83] with permission from Elsevier.

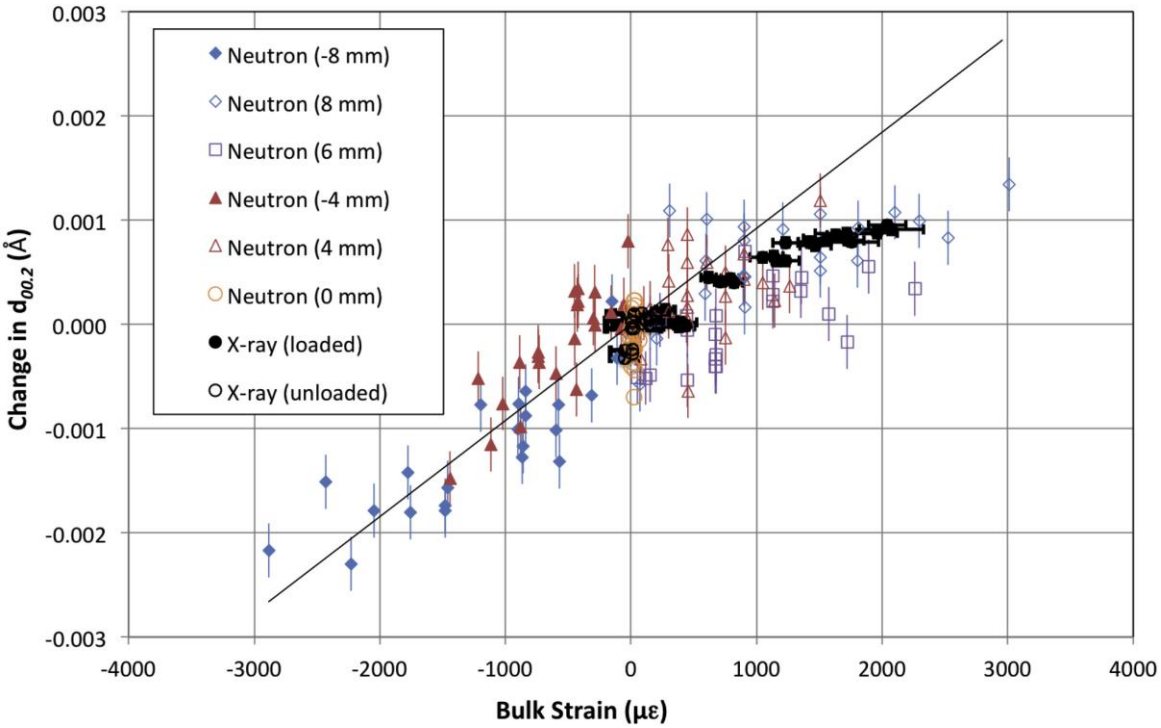


Figure 18: Comparison between bulk strain and differences in $d_{(00.2)}$ in Gilsocarbon loaded in uniaxial tension and measured by X-ray diffraction and radiography, and in four-point bend and measured by strain gauges and neutron diffraction. A linear fit is made to the compressive neutron data. Reprinted from [88] under a Creative Commons CC-BY license.

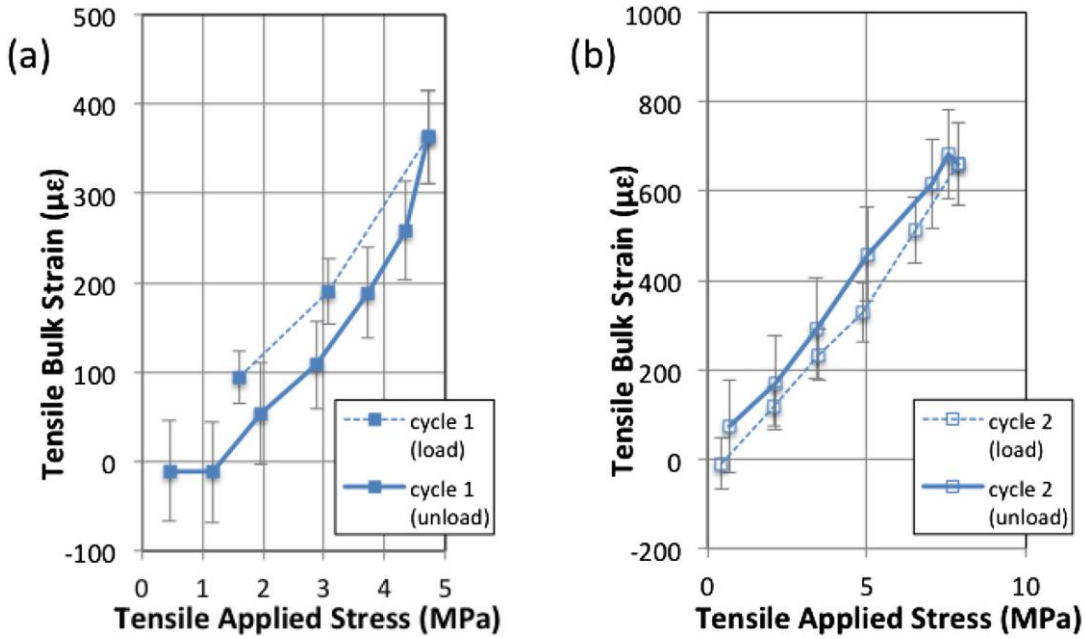


Figure 19: The stress (nominal)-strain (bulk) response of Gilsocarbon in uniaxial tension, showing load and subsequent unload behaviour to progressively higher applied stresses, as (a) first cycle and (b) second cycle. Reprinted from [88] under a Creative Commons CC-BY license.

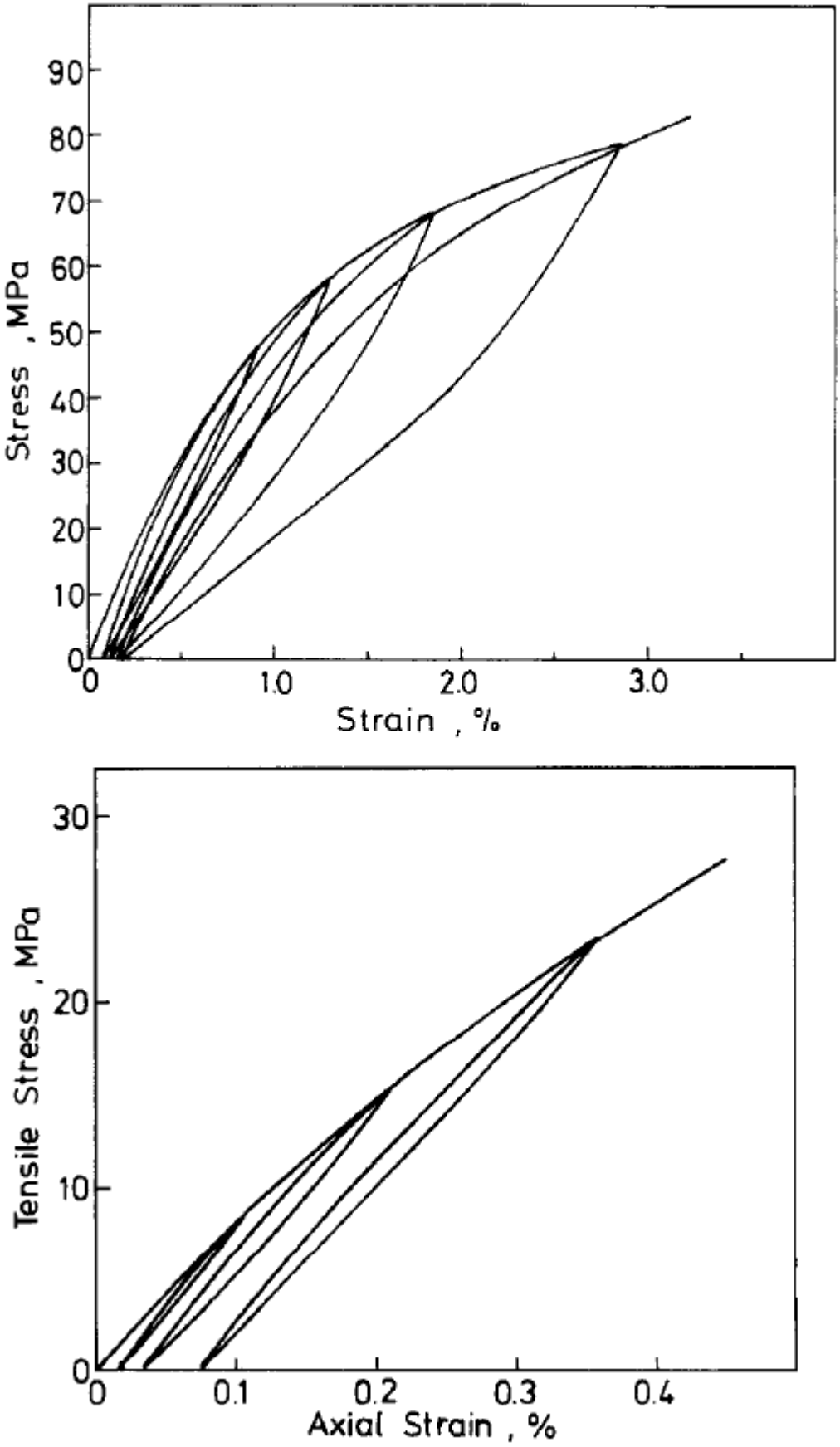


Figure 20: Load-unload curves of Gilsocarbon (IG-11). Since σ(0) monotonically increases with subsequent cycling, permanent deformation must be occurring prior to peak load. Reprinted from [111] with permission from Elsevier.

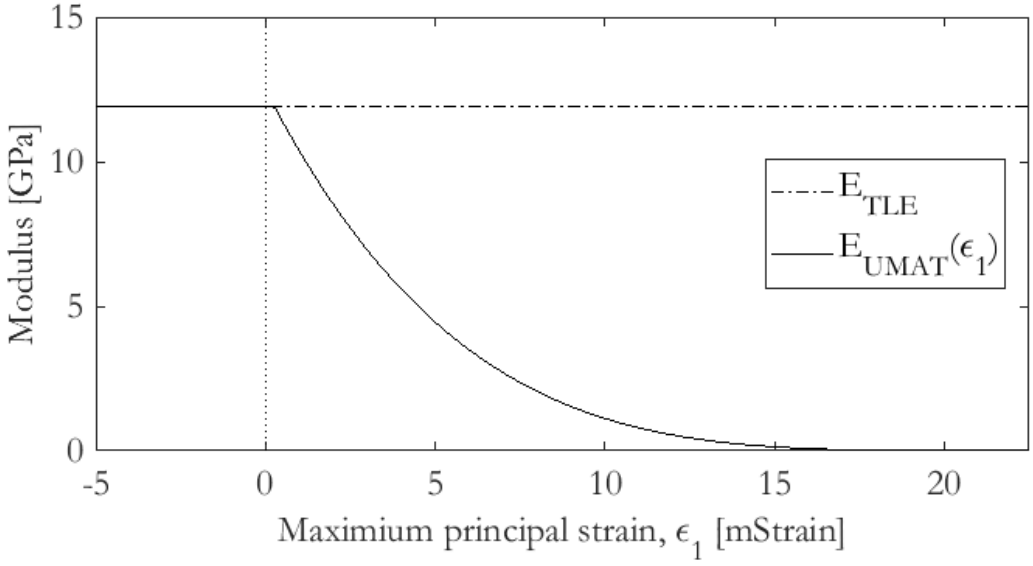


Figure 21: Non-linear elastic user-defined material routine defined by Barbli et al. where the Young's modulus, ($E_{UMAT}(\epsilon_1)$) is degraded from the tensile linear elastic modulus (E_{TLE}) by progressive tensile straining. In compression, the models are identical.

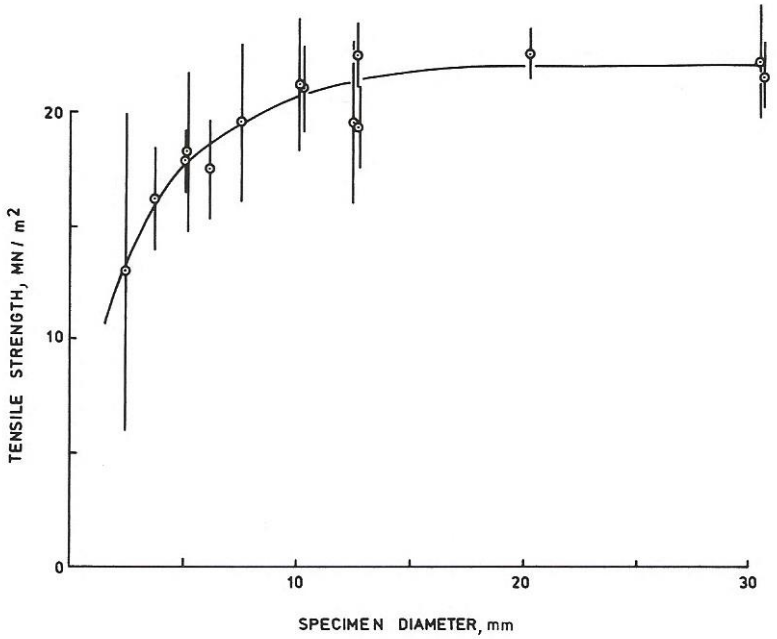


FIG. 9. Effect of specimen diameter on tensile strength of IM1-24 graphite.

TABLE 3

Some 4-point Bend Strength Data at Small Specimen Sizes for IM1-24 Graphite

	Thickness (mm)		
Width (mm)	6.3	3.2	1.6
	Strength (MN/m^2) with SEM for six specimens		
12.7	37.0 ± 0.7	36.2 ± 0.6	36.8 ± 1.2
6.3	38.1 ± 0.9	36.0 ± 1.2	37.0 ± 0.7
3.2		34.9 ± 1.8	

Figure 22: The variation of tensile (figure, top) and flexural (table, bottom) strength with specimen cross-section in Gilsocarbon graphite. Reprinted from [93], with permission from Marcel Dekker.

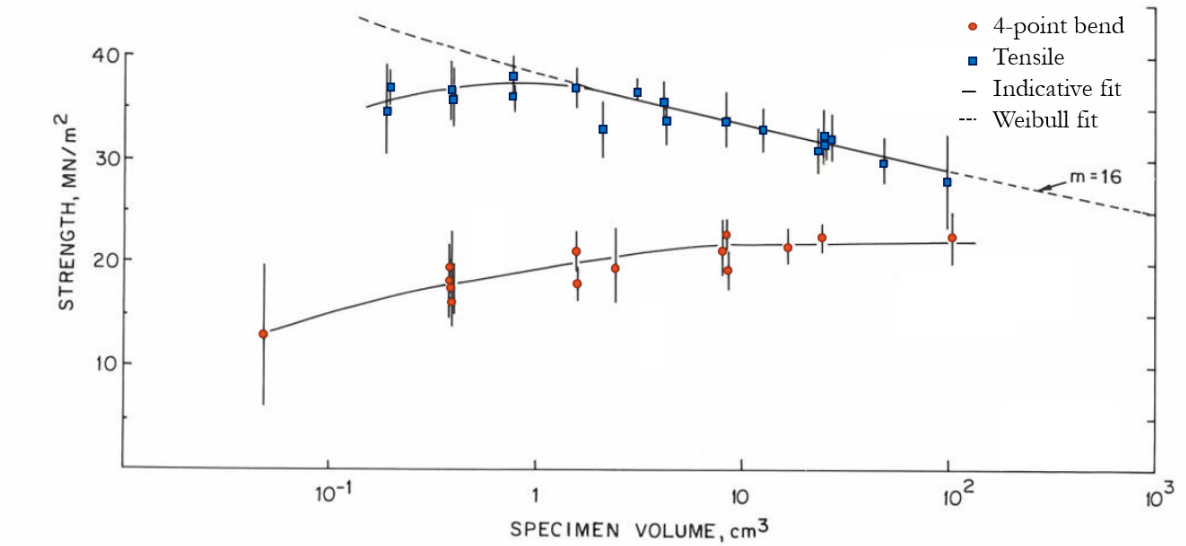


Figure 23: The dependence of smooth specimen strength on critical volume for tensile and 4PB geometries. For the 4PB data, a Weibull prediction is fitted to the strengths for the specimens with volumes > 1 cm^3. Reprinted from [93], with permission from Marcel Dekker.

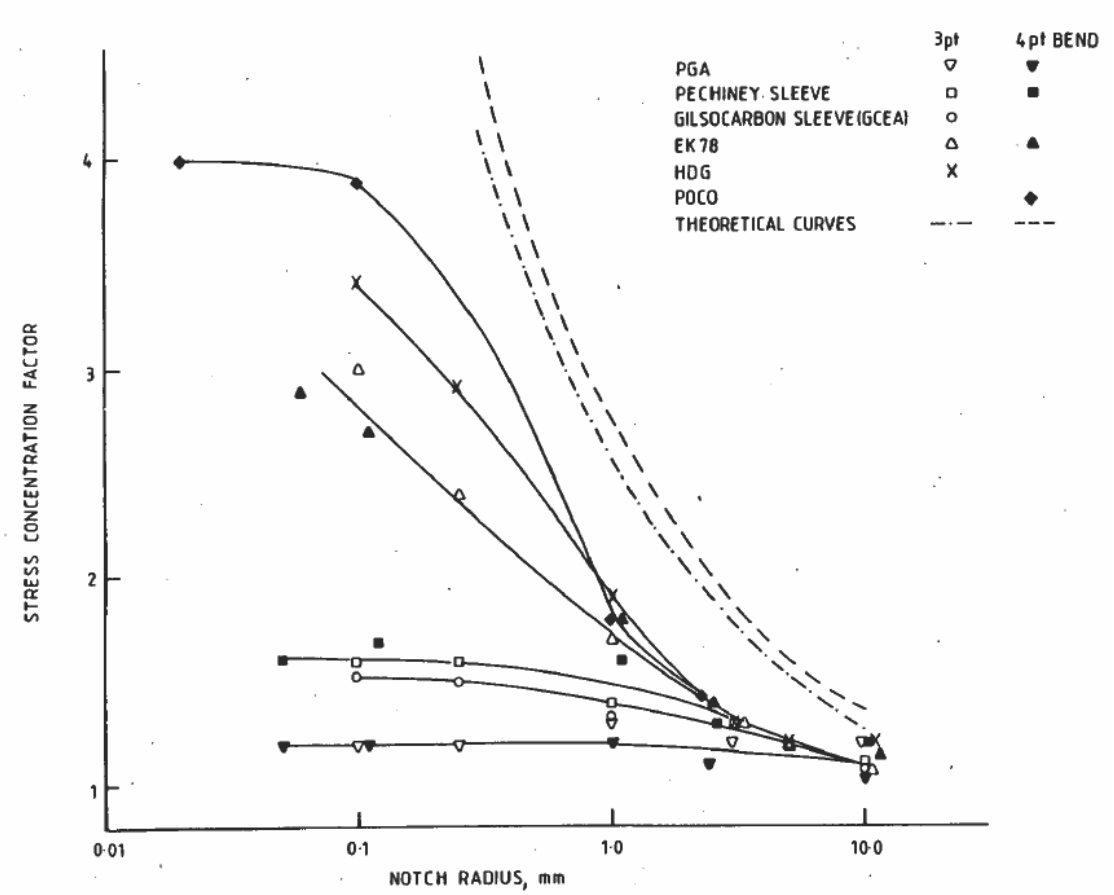


Figure 24: The variation of stress concentration factor (notch strengthening factor) with notch radius for different graphite grades tested in three- and four-point bending modes. Reprinted from [47] with permission of UKAEA.

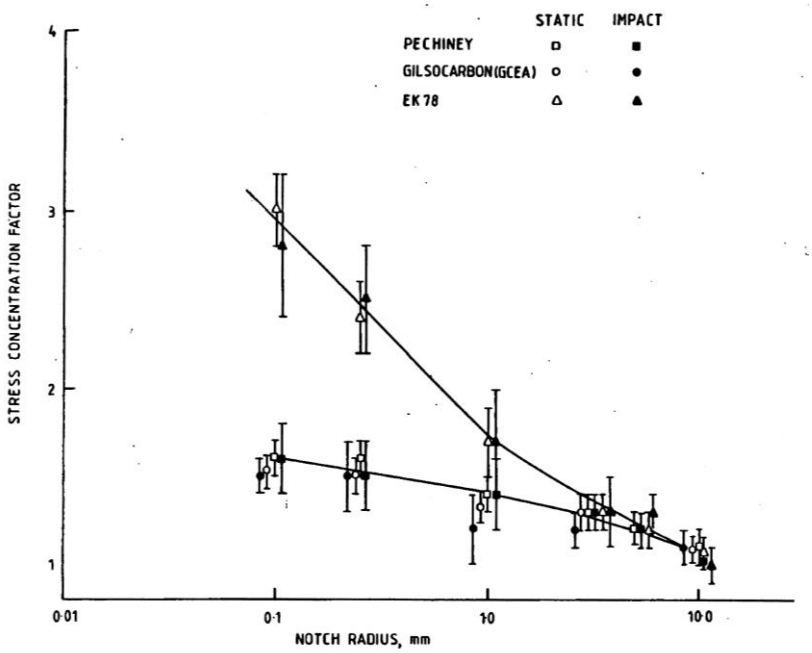


Figure 25: Comparison of stress concentration factors (notch strengthening factors) in impact and standard three-point bend tests (for clarity, some of the data points have been slightly offset from their exact notch radius in this figure). Reprinted from [47] with permission of UKAEA.

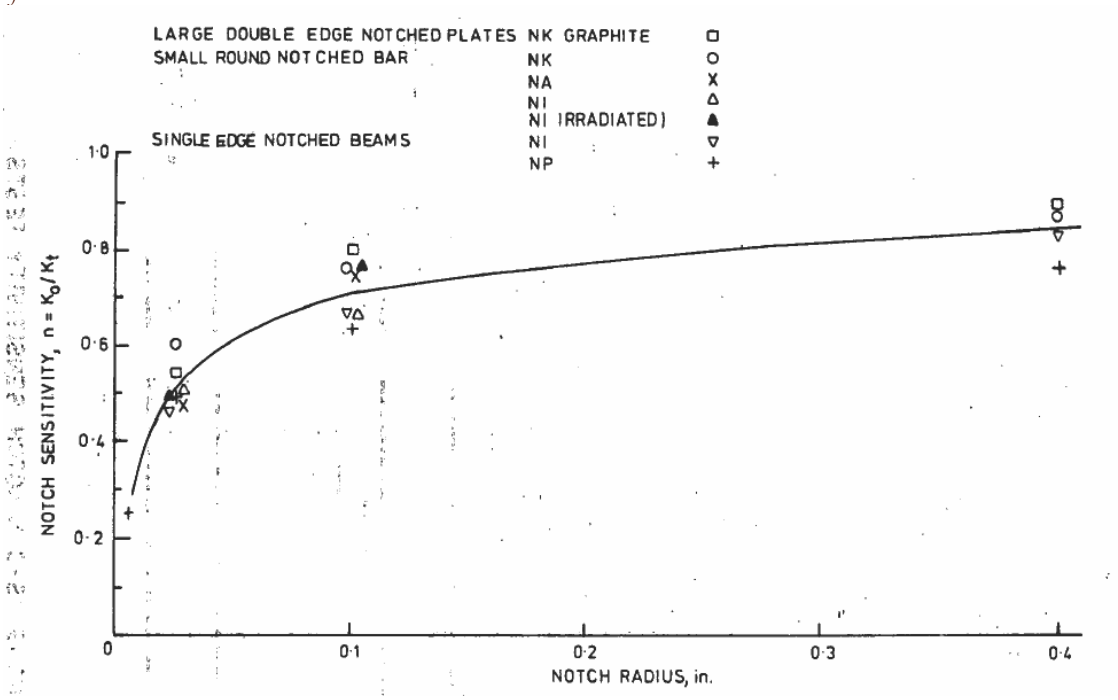


Figure 26: The notch sensitivity of a range of isotropic AGR graphite grades, including the effect of irradiation (0.1×10^{20} n.cm^{-2} EDND at 50 °C). Reprinted from [93], with permission from Marcel Dekker.

II.3.2.1 Notch sensitivity in other graphites

The trends in notch sensitivity behaviour are broadly similar between various graphite grades once filler particle size and anisotropy are accounted for [92]. Temperature has no effect on notch sensitivity [101].

In his review of fracture in polycrystalline graphite, Brocklehurst showed that the relationship between SIF and notch radius is similar for all graphite grades [112]. In both tension and flexure, the SIF rises as the radius decreases, until a characteristic SIF limit is reached (see Figure 27). Below this radius, the samples ceased to reliably fail at the notch. Brocklehurst noted that the inherent defect size is dependent on the geometry, with flexure defects c. 33 % larger than in tension.

Table 3 lists estimates (from experiment and fracture mechanics modelling) of the effective inherent defect size, the maximum value of the NSF and the tensile strength for various grades. These data indicate that for all the grades shown, the inherent defect size is at least as great as the filler particle dimension (not given), and that the maximum SIF (notch sensitivity) correlates with tensile strength [47, 92, 105]. Thus, as the inherent defect size increases, [104] a drop in notch sensitivity is predicted [101].

For very coarse-grained graphite, with filler particles of largest dimension > 2 mm, Allard *et al.* showed that the FPZ formation is more sensitive to residual strains than to crack bridging [113]. It has been suggested by some that any interactions between the sub-critical cracks are insignificant in the overall crack growth [104], though others dispute this [13].

Many sources propose a sensitivity to the applied stress profile and particularly to gradient which is geometry and microstructure dependent (e.g. Figure 28). Predicting the profiles is difficult, but it has been demonstrated that a steep gradient in flexure leads to a lower fracture stress [101, 103, 104, 112].

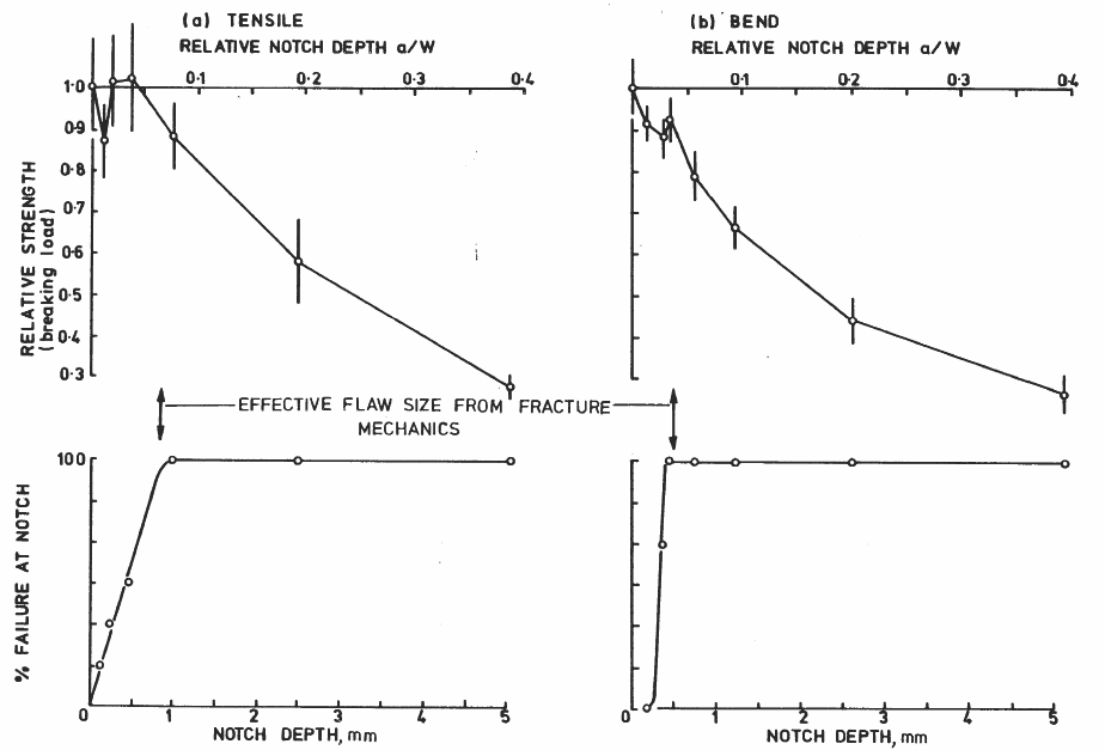


Figure 27: The effect of notch depth of tensile and bend specimens of SM2-24 graphite, and the % of samples that failed at the notch for a given notch depth. Reprinted from [93], with permission from Marcel Dekker.

Table 3: The estimated effective inherent flaw size, for several graphite grades [47, 94].

Graphite	Effective inherent flaw size	Failure stress (smooth)	Notch strengthening factor (maximum)
	[mm]	[MPa]	[-]
Gilsocarbon	0.6	41 ± 2.0	1.74 ± 0.2
PGA	1.5	12 ± 2.0	1.24 ± 0.2
POCO	0.06	94 ± 4.0	4.01 ± 0.2

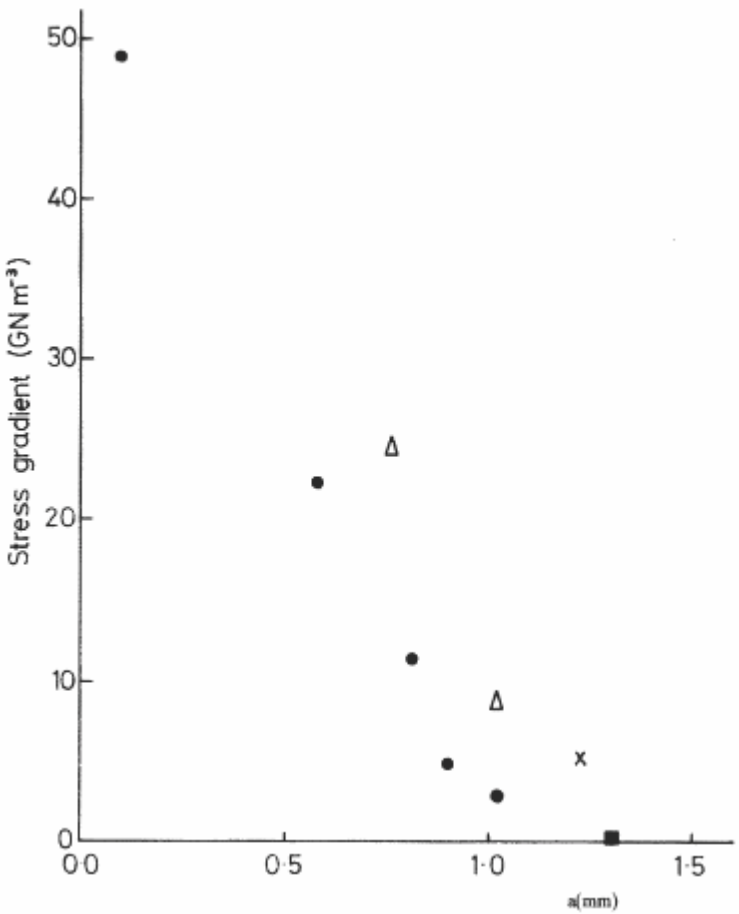


Figure 28: Effect of stress gradient on the calculated effective (inherent) defect size (here, a), derived assuming a constant K_{IC}. Closed circles are 4PB, open triangles are internal pressure tests, crosses are diametral pressure tests, and closed squares are uniaxial uniform tensile tests. Reprinted from [114] with permission from Springer Nature.

II.4 Effects of the nuclear environment

The effects of pure irradiation on the mechanical and fracture properties of graphite at both ambient and elevated temperature will be considered in § II.4.1, and the additional effects of radiolytic-oxidation in § II.4.2.

II.4.1 Effects of fast neutron and gamma irradiation

The effect of irradiation on the crystalline behaviour is strongly anisotropic, reflecting the crystal structure and virgin properties. Further details on the atomic damage and recovery processes, including the phenomenon of Wigner energy, are well described in reviews, for example by Kelly [13], and Burchell [115] and Marsden and Hall [15].

In Gilsocarbon, the effect of irradiation varies between the component phases due to their crystallinity levels. The dimensional changes result in macroscopic shrinkage, with *c*-direction swelling absorbed by the pores. Due to the spherical morphology of the filler particles, the bulk behaviour is approximately isotropic. By contrast, the extruded PGA shrank differently along the major and minor axes (see Figure 29) [116]. Turn around in Gilsocarbon is at fluences of c. 1.3 x 10^{22} n.cm^{-2} equivalent Dido nickel dose, EDND, when the majority of voids have collapsed and volume shrinkage has reached several percent (Figure 29) [3]. Doses of up to 2.2 x 10^{22} n.cm^{-2} EDND stiffen the graphite, but beyond this the modulus decreases (Figure 30) [3, 61]. During reactor design these effects were poorly understood; now, understanding the implications of this behaviour is of the upmost importance for ensuring the safe life extension of the AGR fleet [3].

At applied stresses far below the peak stress, σ_{max}, irradiation results in the plastic deformation of graphite at temperatures where thermal creep is negligible – the phenomenon of 'irradiation creep'. The effects, mechanisms and degree to which creep occurs has been debated since it was first observed during the material test reactor, MTR, programmes in the 1960s [117-119]. The large deformations possible (around ten times the maximum strain in the virgin material, see Figure 31) are regarded as necessary for the safe operation of the reactors; if creep did not occur, stresses due to the distortion of the core (bowing, for example [13]) could not otherwise be accommodated.

Neutron irradiation is found to increase σ_{max} (Figure 38) and γ_{wof} of graphite components [13, 109]. The stress-strain behaviour becomes increasingly linear (Figure 32). Brocklehurst and Brown showed that low level irradiation causes no change to the inherent defect size calculated from the notch sensitivity [46].

In PGA, the crack paths are unaffected by irradiation (Figure 33). Micro-cracking and plastic deformation remain apparent and are sensitive to the micro-structure and depend on the tensile axis orientation [120].

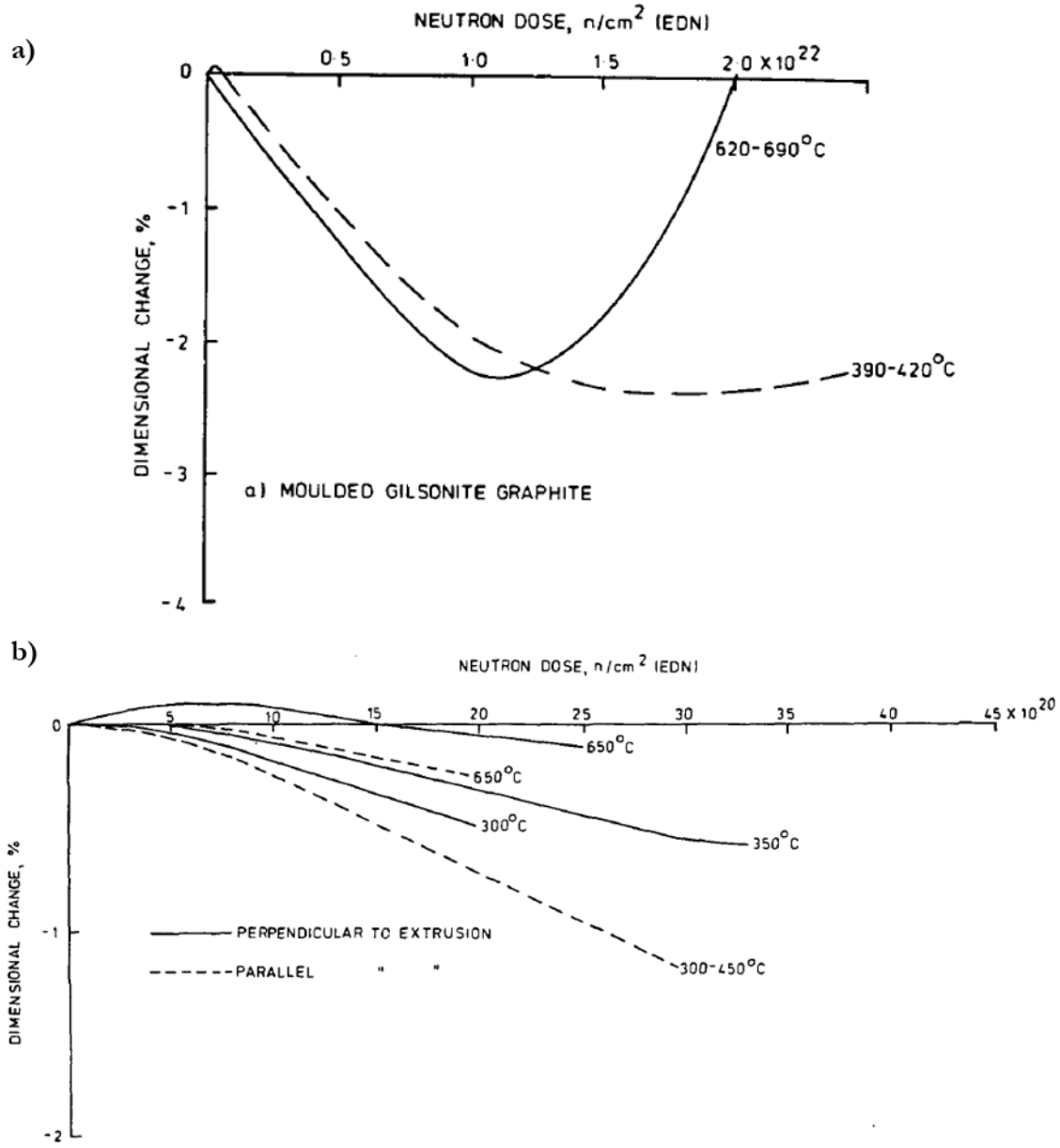


Figure 29: Dimension changes in (a) Gilsocarbon and (b) PGA due to pure irradiation at different temperatures. Reprinted from [13] with permission from Elsevier.

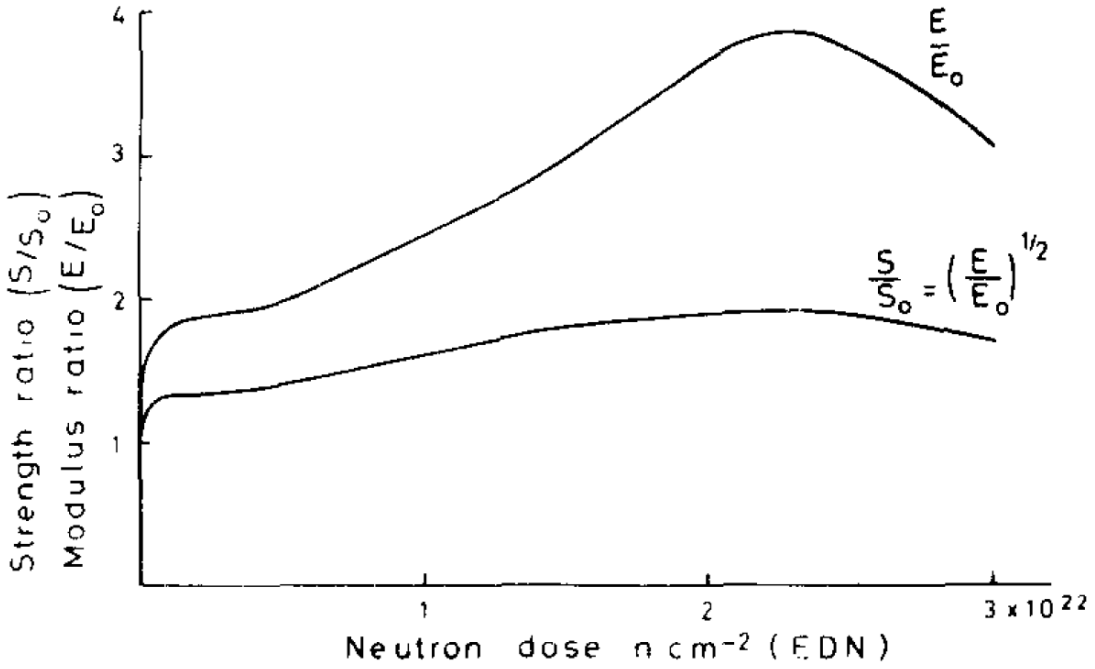


Figure 30: The effect of irradiation (at a flux of 5 × 10^{20} n.cm^{-1} EDN) on the stiffness and strength of graphite. E_o and S_o refer to the modulus and strength of virgin materials, respectively. Reprinted from [3] with permission from Elsevier.

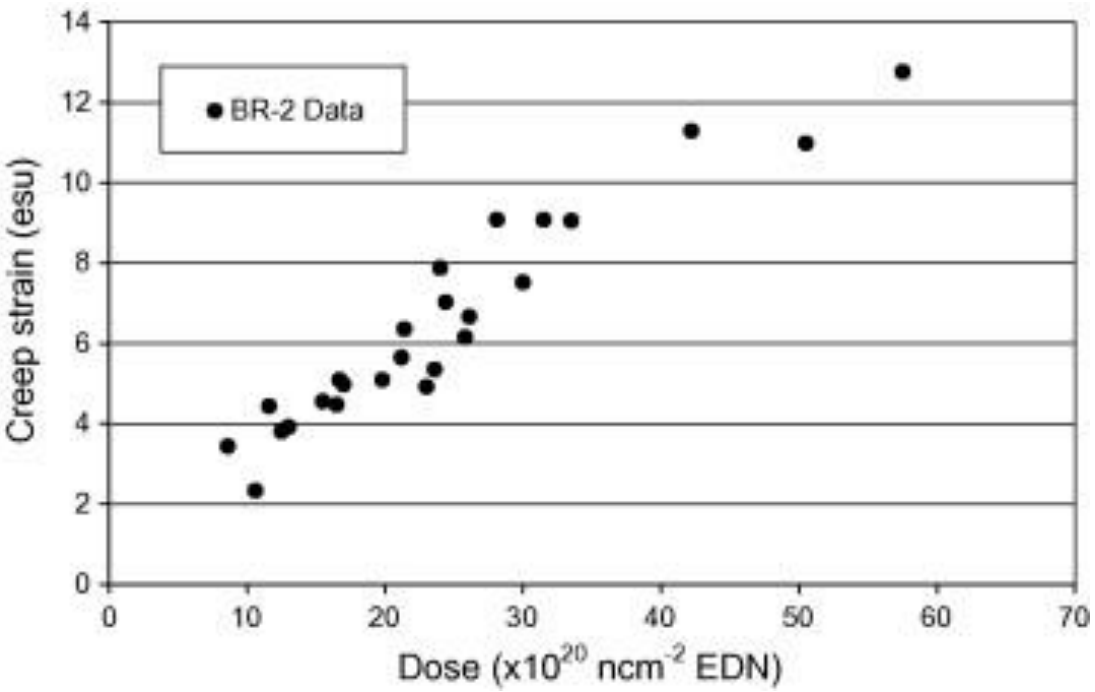


Figure 31: The effect of neutron irradiation creep can lead to strains around ten times the mechanical strain found in virgin material. Reprinted from [119] with permission from Elsevier.

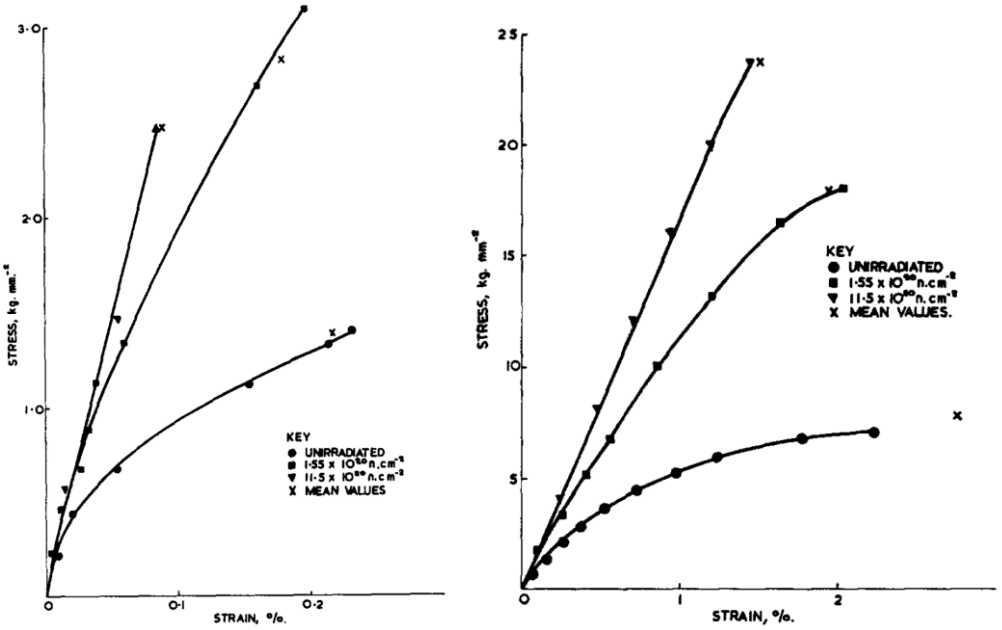


Figure 32: The stress-strain behaviour of an isotropic graphite with spherical coke particles up to ϕ 1 mm becomes increasingly linear with irradiation dose in tension (Left) and compression (Right). Reprinted from [109] with permission from Elsevier.

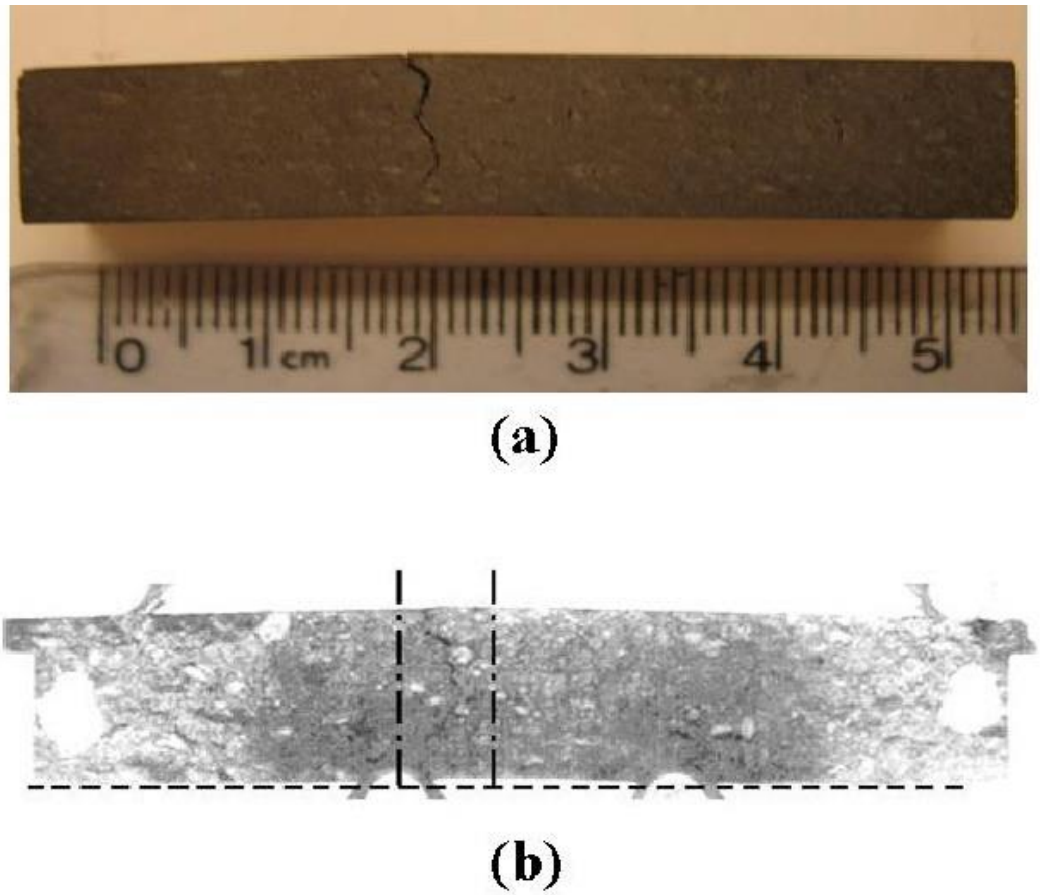


Figure 33: Crack paths in PGA in the (a) virgin and (b) irradiated state. Reprinted from [120] with permission from the Taylor and Francis Group.

II.4.2 Effects of radiolytic-oxidation

When considering the effects of simultaneous radiolytic-oxidation and fast neutron irradiation, it is prudent to separate the known behaviour in the AGRs measured from PIE to date, from predicted behaviour from accelerated MTR studies (the EDF Energy 'Blackstone' experiment,[15] for instance), serial irradiation and radiolytic-oxidation studies, and thermal oxidation (with and without irradiation). The relevance of the observed behaviour diminishes in that order due to the (suspected) complex interactions of the two mechanisms and any related rate effects. Measurement of the PGA from the Magnox reactors, while temporally realistic, is of limited value due to strikingly different oxidation behaviour.

There is limited published data on Gilsocarbon PIE data, especially for weight-losses above 30 %. There is a marked effect on the Gilsocarbon microstructure, as radiolytic-oxidation causes the growth and coalescence of internal voids, making the graphite more skeletal in form (see Figure 34) [3, 120]. The oxidation preferentially grows the smallest pores, which have been suggested to be particularly important in controlling the dimensional change [121]. As pore size is increased, and beyond turn around when pore generation is non-negligible, weight-loss accelerates. For effective modelling, the effects of pore coalescence therefore need to be captured, as shown in Figure 35 [3]. The high weight-losses achieved in Blackstone have demonstrated that the binder is preferentially corroded leaving relatively intact filler particles; eventually 'breakthrough' occurs where the closed internal pores of a filler particle are connected to the extended pore network, and the corrosion behaviour is thereafter consistent (see Figure 12) [75].

[15] The EDF Energy Blackstone MTR experiment that has been investigating the effects of radiolytic oxidation and irradiation on Gilsocarbon since 2009. The MTR will take the graphite to conditions beyond the forecast end of AGR generation in the High Flux Reactor, Petten, Netherlands. The samples include virgin material manufactured at the same time as that used in the AGRs, and pre-irradiated/pre-oxidised material from trepanned PIE samples, and material from older MTR experiments. Dose rates are increased by a factor of up to 17 and weight loss by up to 1.7 compared to the AGRs. To date, over 800 samples have been irradiated and characterised.

Diffusion via the pore networks and the influence of methane results in gradients of weight-loss around the bricks' features, with predicted behaviour like that in Figure 3. In their 2012 review [15], Marsden and Hall summarised the following effects on the physical properties (see also Figure 36), providing much greater detail on each than is reported here:

- "Stored energy – a function of fast neutron damage and temperature, due to damage to the graphite crystallites, but not affected by radiolytic oxidation other than by a reduction in mass.
- Specific heat – a function of temperature but not affected by fast neutron irradiation or radiolytic oxidation other than by stored energy, which may be considered separately.
- Dimensional changes – a function of fast neutron damage and irradiation temperature. There is also some evidence of modification by radiolytic oxidation. It is also modified by stress [and associated with irradiation creep].
- CTE – a function of temperature, fast neutron damage, irradiation temperature, and stress. There is evidence that it is not modified by radiolytic weight-loss.
- Thermal conductivity – a function of temperature, fast neutron damage, and irradiation temperature. It is significantly modified by radiolytic weight-loss.
- Young's modulus – a function of temperature, fast neutron damage, and irradiation temperature. It is significantly modified by radiolytic weight-loss.
- Strength (tensile, compressive, flexural, and fracture) – a function of temperature, fast neutron damage, and irradiation temperature. It is significantly modified by radiolytic weight-loss.
- Irradiation creep – a function of fast neutron damage, irradiation temperature, and stress."

The effect on dimensional change (extension of the shrinkage regime and turn around delay) impact on the stress behaviour (see Figure 37 and Figure 4).

Correlated trends in electrical and thermal resistivity were shown for AGR weight-losses up to 36 %, and extended using Blackstone data to 59 % weight-loss [16]. Radiolytic oxidation caused changes in electrical resistivity comparable to thermal oxidation. For the mechanical properties, the measured effects of thermal oxidation have only a poor correlation with radiolytic-oxidation; considering the different mechanisms, this is not unexpected [3, 13, 122-126]. PIE γ_{wof} measurements-on reactor-extracted Gilsocarbon showed a linear effect with dose and weight loss for doses up to 143 x10^{20} n.cm^{-2} EDND [17].

Using separate oxidation and irradiation stages, Kelly radiolytically oxidised pre-irradiated graphite samples and showed reduced oxidation rates compared to un-irradiated control samples [121, 127]. Brocklehurst showed that simple multiplication of the individual effects conservatively predicted strength [91]; the irradiation-oxidation interaction is highly complex, with mechanistic explanations revolving around the changing distributions of pore size and connectivity. These step-wise studies provide insight into the mechanisms, but cannot be used for accurate prediction [3].

For fracture prediction, Pickup *et al.* demonstrated that surface energy is practically invariant with oxidation [128]. Kelly *et al.* [127] and Adam and Brocklehurst [129] showed that Young's modulus and compressive and tensile strengths decay exponentially with increasing weight-loss, w, (Figure 38) according to (9) and (10), where E_o and S_0 are the initial modulus and strength. Stiffness is considered directly proportional to strength [130, 131], though a square root relationship has also been proposed, see [15].

(9) $$E = E_o\, e^{-3.68w}$$

(10) $$S = S_o\, e^{-5.1\,w}$$

Data on the effects of radiolytic-oxidation, and particularly on the notch sensitivity, on graphite is sparse. Best *et al.* in 1984 [3] presented Figure 39 indicating the predicted effects of combined irradiation and oxidation on Gilsocarbon, and how this affected the strength safety factor of the reactor (a reactor was deemed safe if the factor was greater than unity).

Adam (1988) highlighted that the data collected from reactor-extracted samples are sensitive to the operating environment and difficult to compare in a meaningful manner. By normalising the fractional losses of strength against that of virgin graphite, based on the dose and weight loss, a geometry-independent relationship between weight-loss and notch sensitivity was determined. The 'oxidised' specimens included drilled, thermally oxidised and radiolytically-oxidised samples. With increasing weight-loss the former two specimen types became progressively notch-insensitive. This trend was not observed during radiolytic-oxidation, but few data are presented (Figure 40) [126].

In 2017, Tzelepi *et al.* [98] presented data for 3PB notch sensitivity measurements of 8 x 8 x 38 mm beams machined from AGR 'installed sets' with weight losses in the range [3, 8] % and neutron doses of c. 20 x 10^{20} n.cm^{-2} EDND. The notches were blunt with notch radii of 2 mm. NSF values were calculated comparable to the virgin results reported by Brocklehurst and Darby [103]. Tests in PGA showed similar results. 6 x 6 x 19 mm beams with the same notch radius were machined from the W = 8 mm beams and were found to be completely insensitive with an NSF of c. 1.0.[16] There are no measurements of Gilsocarbon at high doses or weight losses.

[16] The measurements reported by Tzelepi *et al.* were made by the UK National Nuclear Laboratory during an Innovate UK project closely related to the work presented in this thesis. The strength data were analysed almost identically to the data that will be presented in Chapter III. Notably, the tests were performed in three-point bend, in line with the strength PIE techniques.

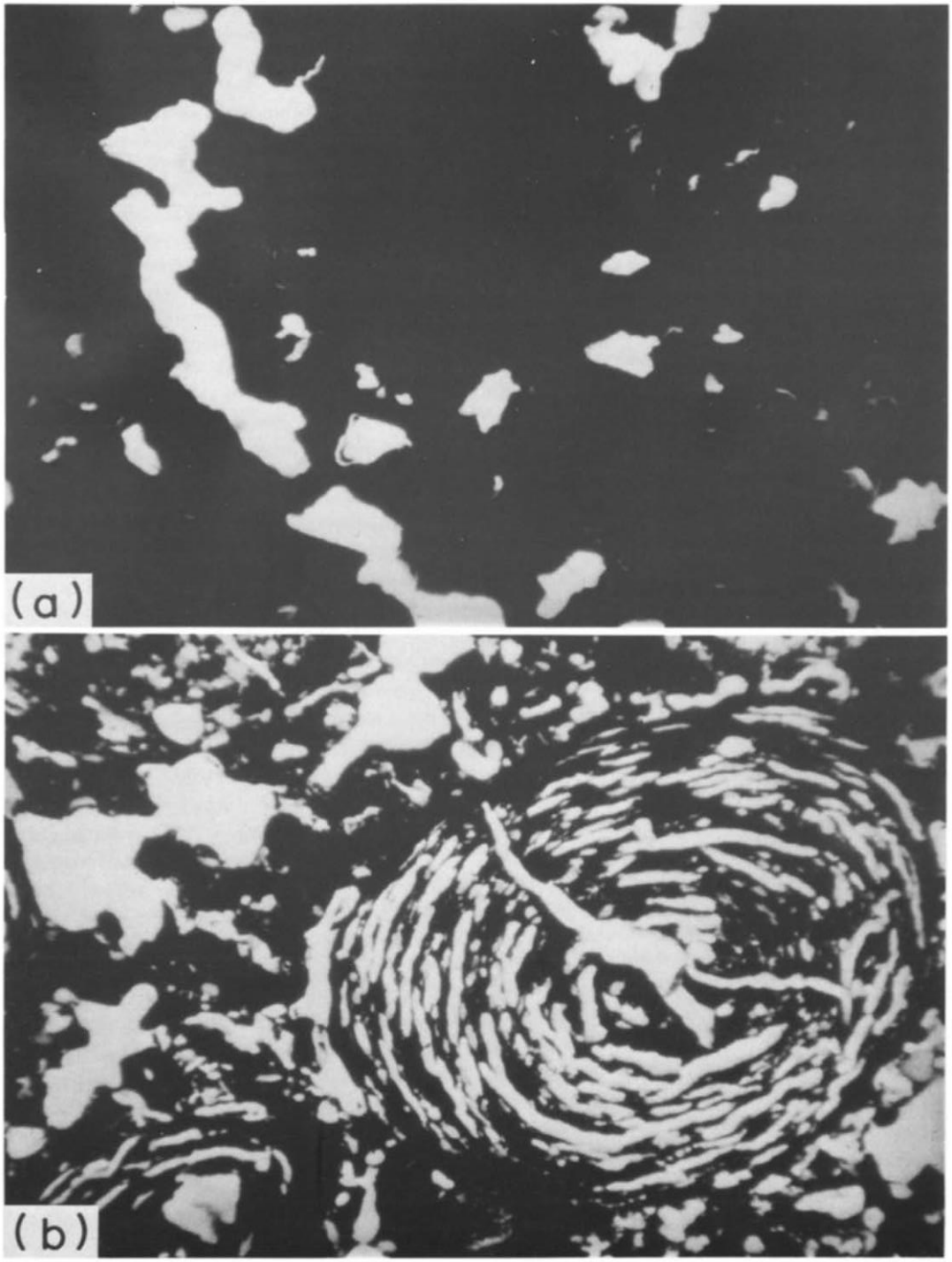


Figure 34: Micrographs of fluorescent resin impregnated Gilsocarbon: (a) virgin graphite and (b) after 21.5 % weight-loss. Reprinted from [3] with permission from Elsevier.

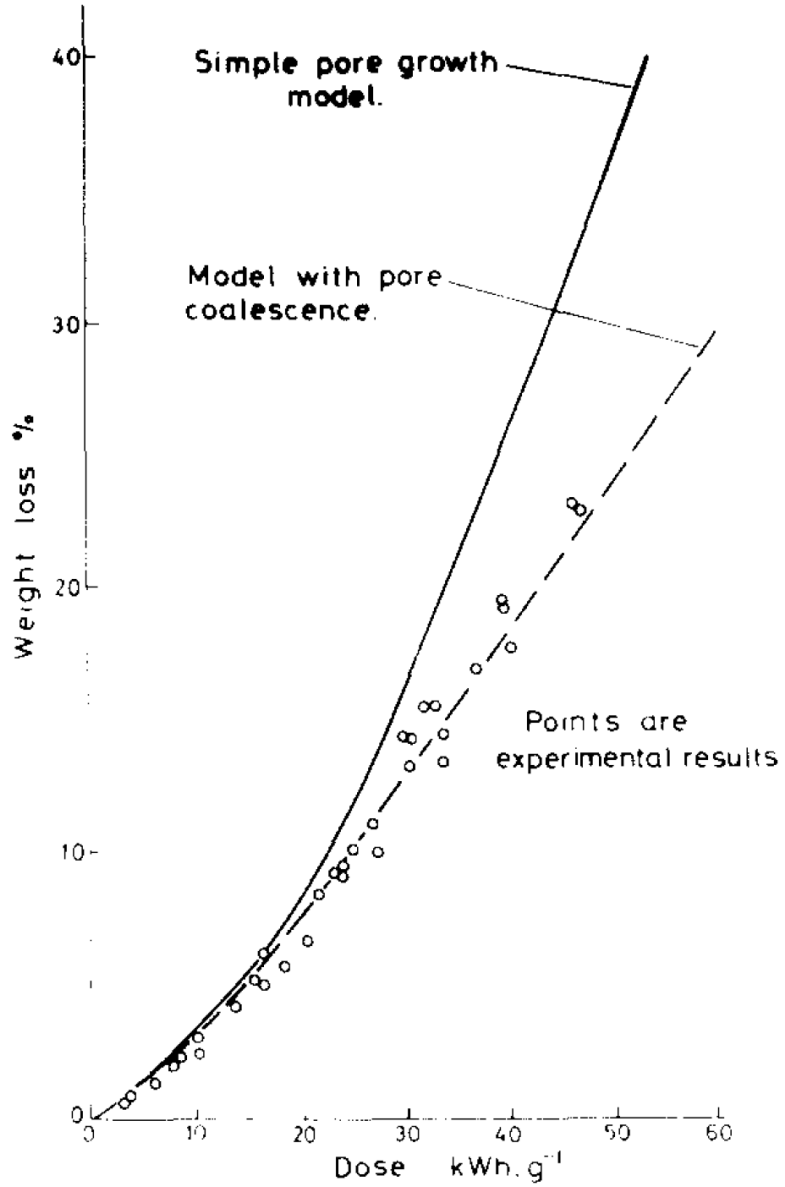


Figure 35: The relationship between radiolytic-oxidation and weight-loss in a CO_2/2.0 % CO/200 ppm (volumetric) methane atmosphere. Reprinted from [3] with permission from Elsevier.

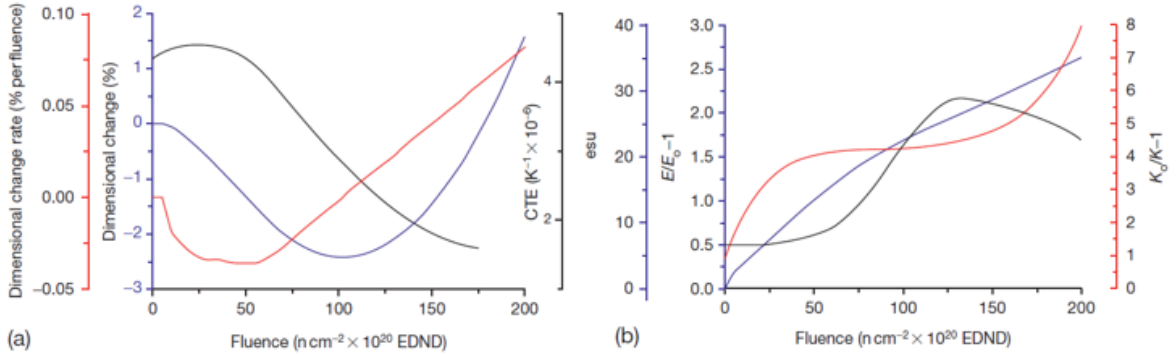


Figure 36: Schematic behaviour of the effect of irradiation on the properties of Gilsocarbon irradiated at 550 °C. At other temperatures, the curves would be similar: (a) dimensional change (blue), dimensional change rate (red), and coefficient of thermal expansion (black), and (b) factorial change in Young's modulus (E/E₀-1) (blue) and thermal conductivity (K₀/K-1) (red), and irradiation creep (elastic strain units, esu) (black). Reprinted from [15] with permission from Elsevier.

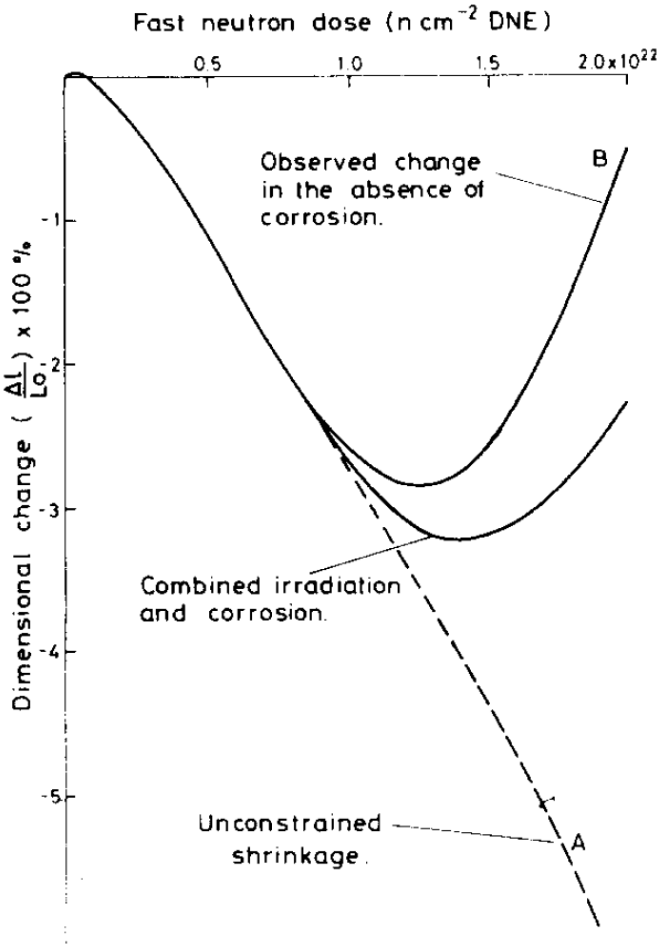


Figure 37: Net dimensional change on: A, unconstrained graphite crystallites and B, on a Gilsocarbon billet, highlighting the delay in turn around caused by radiolytic-oxidation. Reprinted from [3] with permission from Elsevier.

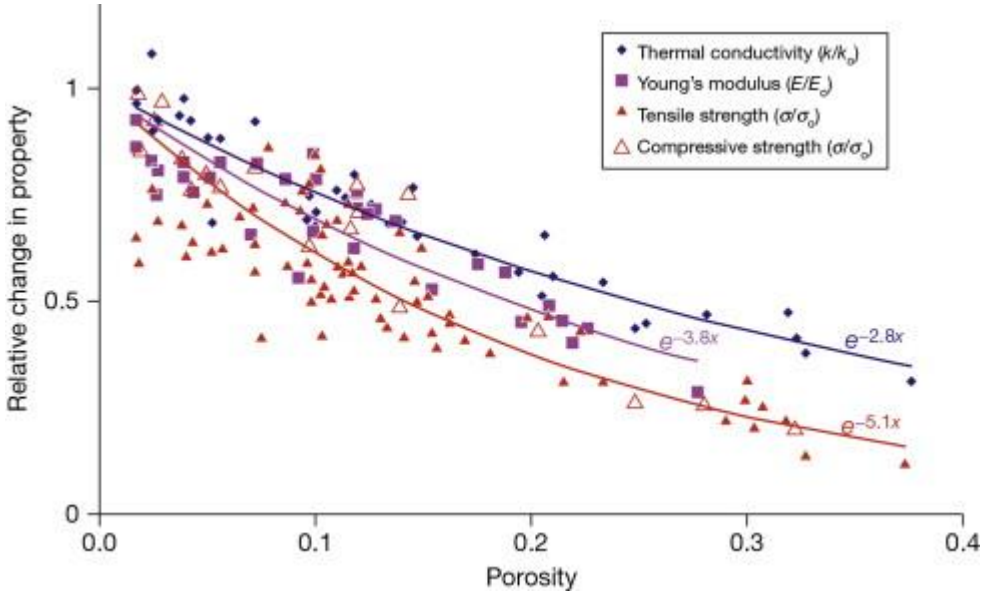


Figure 38: Comparison of the effects of Gilsocarbon radiolytic oxidation on thermal conductivity, Young's modulus, and strength. Reprinted from [15] with permission from Elsevier after [129].

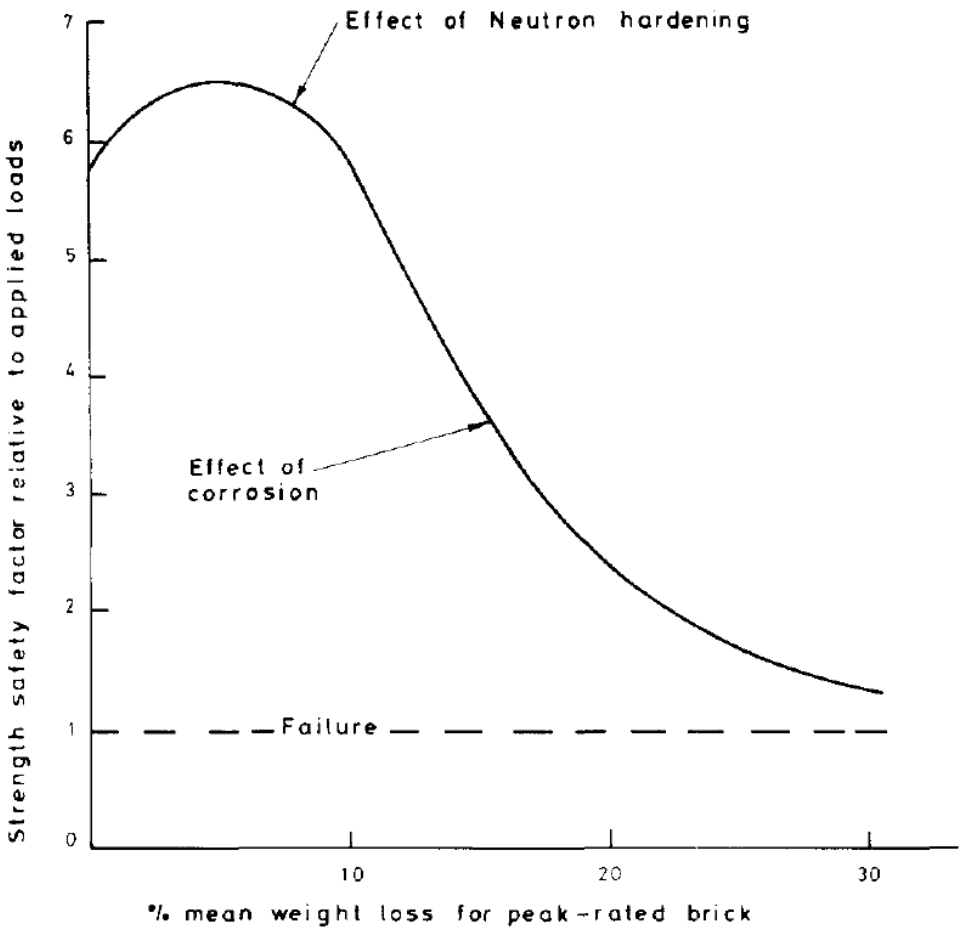


Figure 39: The combined predicted effect of neutron hardening and corrosion. Reprinted from [3] with permission from Elsevier.

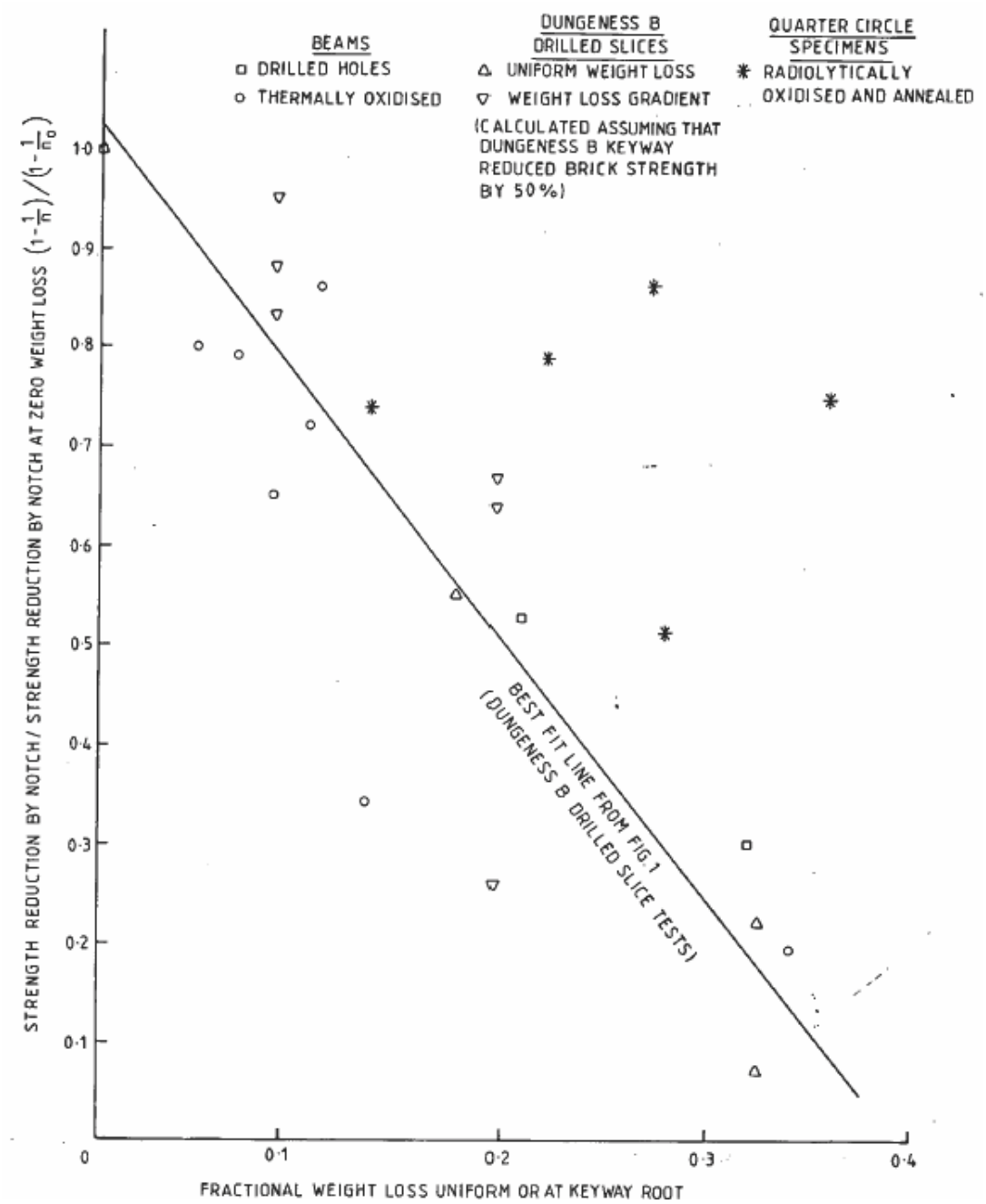


Figure 40: The strength reduction in Gilsocarbon grades of graphite due to weight-loss. Reprinted from [126] with permission from UKAEA.

II.5 Modelling fracture and notch sensitivity

Small-scale testing of extracted radioactive material is routinely conducted at significant cost and exposure risk to operators, but the data remains limited. Scaling the measured behaviour from the small geometries to make predictions of future axial cracking requires a simulation method capable of predicting failure reliably across all the engineering length scales that is adaptable to any degree of irradiation or radiolytic oxidation. Historically, generic failure predictors were applied analytically to Gilsocarbon tests, including: the fracture mechanics concepts of maximum stress or strain, and critical distance limits (§ II.5.1.1); statistical methods such as Weibull (§ II.5.1.2); and energetic methods such as strain energy density (§ II.5.1.3). While these methods had strengths, they were unable to fully capture the behaviour of the different test geometries, different graphite grades or the effects of the nuclear environment. Adaptations of the generic methods to include graphite specific concepts were evolved which were better predictors, but were still applied analytically (§ II.5.1.4). An excellent assessment of these methods was produced by Tucker *et al.* [43], which will be summarised below.

With advances in computing power and computational solvers, numerical simulation of highly-defined components and multiple component interactions have become possible. These methods can incorporate arbitrary property evolutions, arbitrary damage and failure criteria, and may be coupled to produce multiscale analyses, as required for heterogeneous microstructures. Statistical distributions of the fracture properties may be computed directly based on the input property distributions, such that high-order interactions may be properly captured. Simulating fracture is a very broad research field, and only the models pertinent to graphite fracture will be touched on.

II.5.1 Analytical models

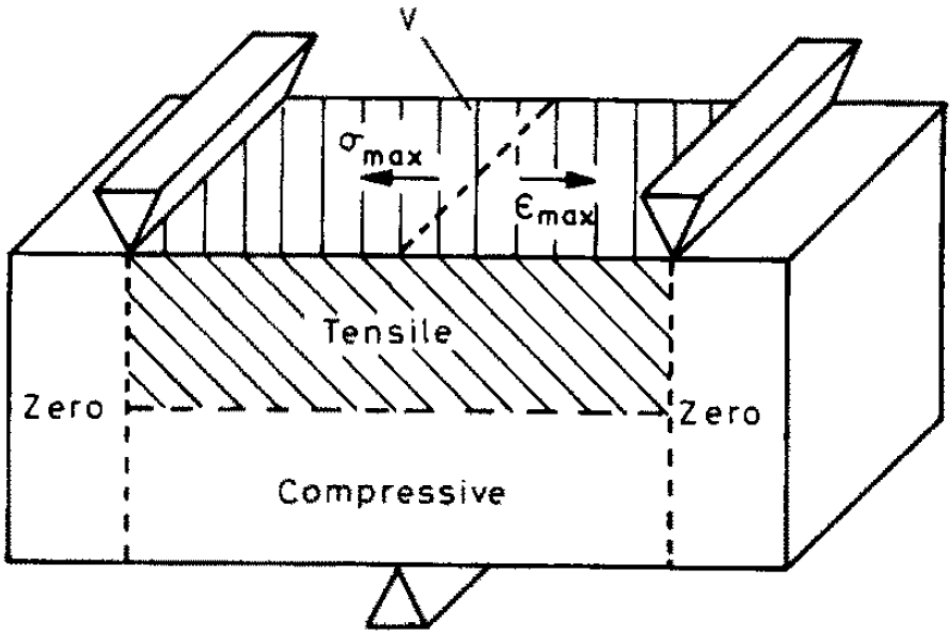
II.5.1.1 Critical stress and strain, and length scale criteria

The simplest initiation criterion would be when the local stress or strain exceeds a given critical value (see Figure 41). A homogeneous material obeying continuum elasticity is assumed; the 'critical stress' and 'critical strain' models ignore microstructural contributions, except that the macroscopic stiffness may be adjusted by volume weighting (for stress) [43]. Furthermore, the critical stress and critical strain models are incapable of predicting specimen size effects, microstructural length scales, notch sensitivity or stress profile gradients [43]. In multi-axial loading, contributions from all but the maximum principal stress, σ_1, or strain, ϵ_1, are ignored, which is a poor predictor of failure in Gilsocarbon; consider the predictions of biaxial loading in Figure 42, for example [32, 43]. Despite these limitations, critical strain is the only model considered by Tucker *et al.* to quantitatively predict tensile strength changes due to radiolytic-oxidation, and to qualitatively predict irradiation changes (Figure 43). The critical stress model is insensitive to modulus changes, and incapable of predicting irradiation effects [43].

The length scale and point stress models acknowledge the presence of an FPZ, with failure dependent on whether the FPZ has attained a threshold size, or whether the stress at critical distance has met a threshold level, respectively [132]. Correlation with a single micro-structural parameter, such as grain size, is insufficient for this definition [41]. It is implicitly assumed that the FPZ size is dependent only on the geometry of the notch tip, with the critical distance, L_C, defined based on the material interaction with the damage zone stresses. In [132] L_C was defined as twice the distance from the crack tip to the stress contour equal to the ultimate tensile strength, though this definition seems arbitrary, and relies on an accurate stiffness model meaning it is likely to be self-consistent at best.

In elastic-plastic fracture mechanics the FPZ size changes with multi-axial loading state. The critical distance models account for this by summing contributions from all tensile stresses within the damage zone [50, 132]. By using the above definition of L_C, the SIF becomes equal to the fracture toughness in pure Mode I opening (11), and can be argued to be mathematically equivalent to damage accumulation criteria in the general case, with some validity for fine-grained graphites[133, 134]. The response to the nuclear environment would be captured by changes in K_{IC} and σ, though no evidence was found for testing this behaviour on ex-reactor material.

(11) $$\boldsymbol{L} \propto \left(\frac{K_{IC}}{\sigma}\right)^2$$



Critical strain energy density.

$\int_V (\sigma^2 / 2E)\, dV/V$ = critical energy.

Critical stress.

σ_{max} = tensile strength.

Critical strain.

ϵ_{max} = tensile failure strain.

Figure 41: Definition of the critical stress, stain and loading geometry strain energy density models for a three-point bend geometry. Reprinted from [43] with permission from Elsevier.

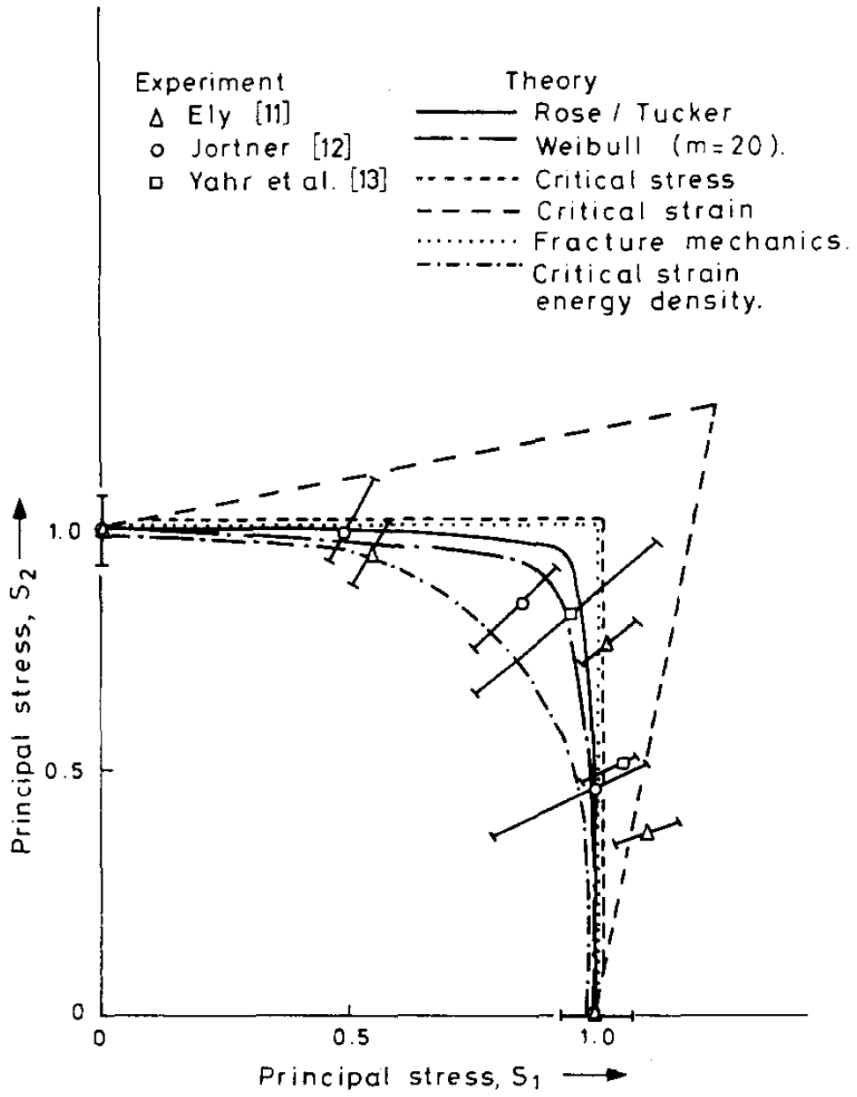


Fig. 21. Failure envelopes in biaxial tension.

Figure 42: Predictions of Gilsocarbon's biaxial strength compared to experimental data. Reprinted from [43] with permission from Elsevier.

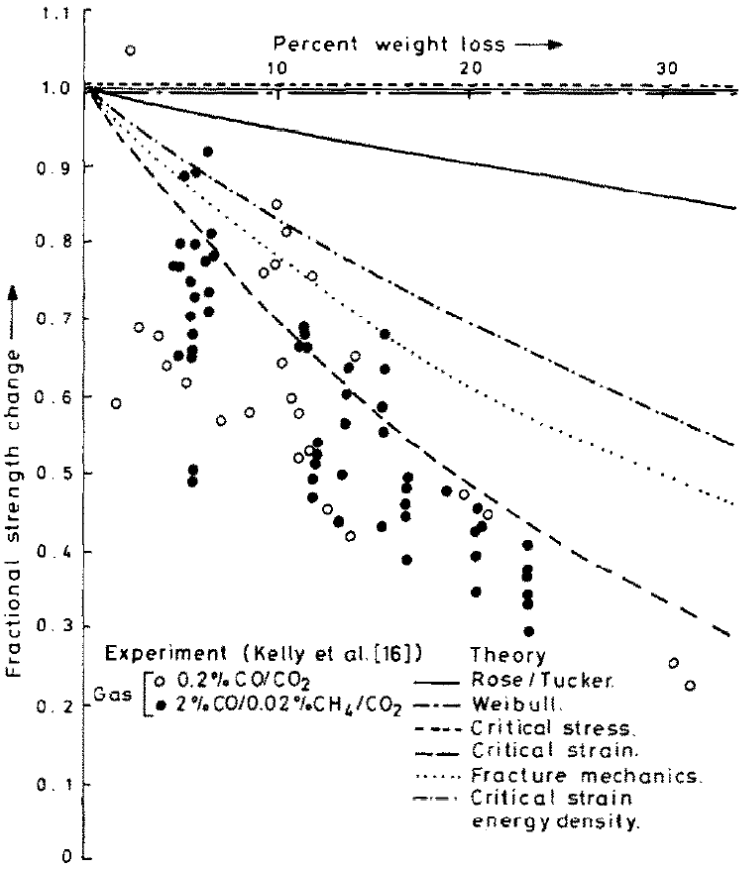


Figure 43: The effects of radiolytic-oxidation as predicted by several models and compared to experimental data; the Rose and Taylor model can explicitly adapt for changes in porosity, while the other models just scale the modulus appropriately (see also Figure 38) . Reprinted from [43] with permission from Elsevier.

II.5.1.2 Weibull

Weibull analysis is the most common technique used for size-effect extrapolation by the ceramics community. A purely statistical method, it is based on the 'weakest link' concept described by Figure 44. Physically, as the volume of the component increases, it is increasingly more likely that it contains a flaw that will fail at a given applied stress and initiate the crack. The analysis benefits from the statistical basis, enabling strength distribution predictions, and is able to account (partially) for the variability of defects in a real material. With only two fitted parameters, the analysis excels in predicting failure strengths due to scaling effects (with scaling parameter *m*), but is insensitive to loading geometry; for a given critical volume, the probability distribution of failure strengths is identical in all geometries [43].

Although reliable for approximately homogeneous and continuous media, such as fine-grained ceramics, the model has no capacity for predicting the failure of significantly heterogeneous materials (such as aggregate based, or porous materials) with a range of microstructural scales (see Figure 42, Figure 43, Figure 45, and Figure 46) [43].

Other methods of predicting failure in small- and medium-scale samples exist, including that of Bažant [135], though their applicability to graphite is unknown.

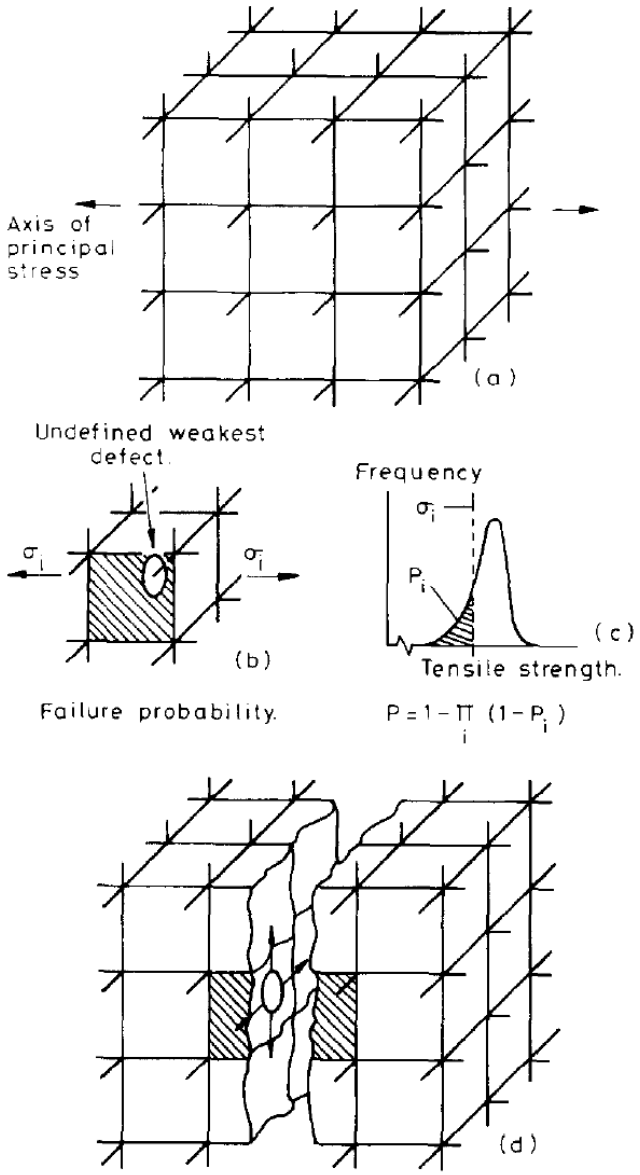


Figure 44: Representation of the Weibull 'weakest link' analysis: (a) the loaded material is defined by connected volumes of material; (b) each volume contins a defect(s), and failue of that volume will occur if the size is greater than a critical threshold; (c) the probability of volume failure is then a distribution related to the liklihood (described here by the function for P) of each containing a critical defect; and (d) when one volume fails, the whole body fails, hence the 'weakest link' theory. Reprinted from [43] with permission from Elsevier.

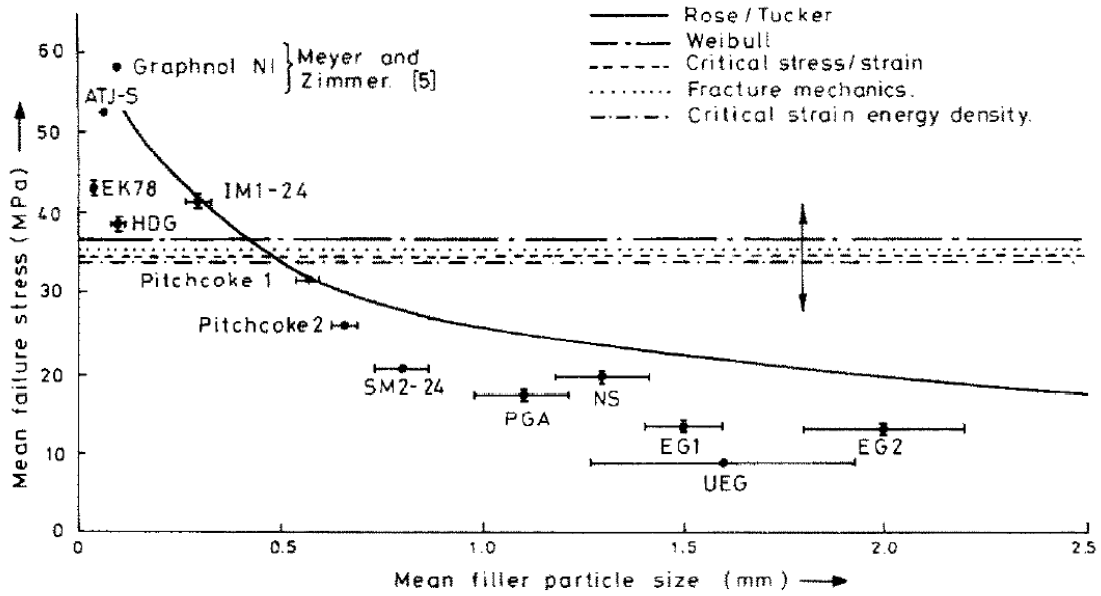


Figure 45: The Rose and Taylor model was able to predict the variation in fracture strength with microstructural strength, unlike any previous model. Reprinted from [43] with permission from Elsevier.

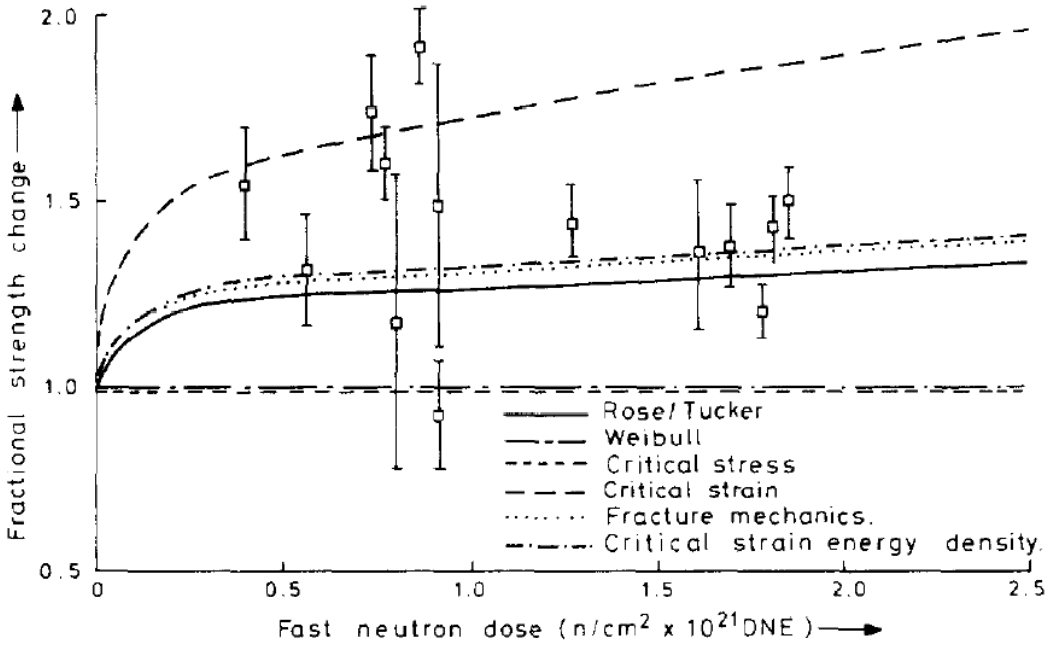


Figure 46: The effects of irradiation as predicted by several models and compared to experimental data; the Rose and Taylor model can explicitly adapt for changes in fracture strength, while the other models just scale the modulus appropriately. Reprinted from [43] with permission from Elsevier.

II.5.1.3 Strain energy density

The critical stress/strain approach may be extended to consider a critical strain energy criterion. An energetic criterion implicitly accounts for the applied strain and materials' stiffness response, but energy must be integrated over a given volume by definition. An appropriately defined 'control volume' to integrate over is important for accurate determination. To account for energy dispersion within an FPZ, this volume must be of a significant size, and measuring strain energy density, SED (ϱ), is more appropriate as defined by (12), comprising an integral of the stress over a volumetric region of interest, ROI (symbol V), with spatial coordinate X and over the strain domain, $\epsilon = [0, \epsilon_{max}]$. Crack initiation is assumed when strain energy density passes a critical threshold, ϱ_c, that is when (13) is true. The criterion is highly sensitive to the choice of this volume, and two definitions will be considered.

(12) $$\rho = \frac{1}{V}\int_0^{\epsilon_{max}} \iiint_V \sigma(\epsilon, X)\, dV d\epsilon$$

(13) $$\rho \geq \rho_c$$

In the 'loading geometry' definition, the volume in which tensile stresses are most likely to contribute to fracture is identified [43]. In some geometries this is a straightforward definition, but for others it is contentious. For instance, in 4PB of a plain beam the ROI is defined as the cuboid region of tensile stresses (demarked by the neutral axis) between the inner rollers as used by Brocklehurst and Darby [103]; in this region, the bending moment is constant, such that this naturally arising ROI is generally accepted for slender beams. In contrast, for 3PB the tensile volume between the outer rollers, as in (Figure 41), is much larger with a constantly varying bending moment, such that the ROI is less naturally defined. In tension, an appropriate definition is even less clear. For standard geometries, the SED may be calculated using simple analytical formulae, such as (14) for plain beam 4PB [103]; specifically, this assumes a linear elastic isotropic and homogeneous body.

(14) $$\rho = \frac{{\sigma_{max}}^2}{6\,E}$$

For a 'notch geometry' definition, Yosibash *et al.* [136], Lazzarin and Berto [137], Torabi *et al.* [138] and Gomez *et al.* [139] have proposed and validated an alternative ROI defined by prismatic circular loci ahead of the notch tip with specimen-specific radii (R_0) and centres offset from the notch tip by distance r_0, as per Figure 47. For notches under plane stress and plane strain with opening angle $T \leq 90°$ (for U-notches, $T = 0°$), R_0 may be calculated by (15) and (16), respectively, in which σ_{max} is a nominal maximum stress commonly taken as the ultimate tensile strength for *a priori* predictions (see [137, 138]). r_0 is a function of notch tip radius (R) and T, see (17), as defined by Lazzarin and Berto [137].

(15) $$R_0 = \frac{(1+\nu)(5-8\nu)}{4\pi}\left(\frac{K_{IC}}{\sigma_{max}}\right)^2 \text{ for plane stress}$$

(16) $$R_0 = \frac{(5-3\nu)}{4\pi}\left(\frac{K_{IC}}{\sigma_{max}}\right)^2 \text{ for plane strain}$$

(17) $$r_0 = \frac{\pi - T}{2\pi - T} R$$

Comparing the suitability of these ROI definitions, the loading geometry definition depends on the specimen geometry and the loading conditions, and requires no material parameters. For standard smooth geometries it is simple to calculate analytically. Brocklehurst and Darby used this definition to explain why the flexural strength of Gilsocarbon exceeds the tensile strength with the assertion that, for flexure, although the applied stress may be large, the average strain energy could still be insufficient for catastrophic failure [103]. Included as part of Tucker *et al.*'s review, contributions from multi-axial loading may be included, but strength is under-predicted (Figure 42) [32, 43]. There is no variable to account for the presence of a notch. The nuclear environment would be accounted for by changing stiffness, with appreciable predictive power (Figure 46). Tucker *et al.* summarised the loading geometry method as "remarkably unsuccessful". The notch geometry definition could potentially be a more robust definition than considered by Tucker *et al.* and may overcome many of the shortcomings. The definition is loading geometry-independent, and fully able to account for notches of different geometries. The ROI outer radius is material-dependent and would be modified by changes in the material properties in the nuclear environment. A knowledge of more material parameters and the location of crack initiation is required, complicating *a priori* prediction for fracture in smooth geometries. This method has not been tested on Gilsocarbon before, but has been demonstrated for other brittle and quasi-brittle materials, including fine-grained graphites, in a variety of loading modes [139-141].

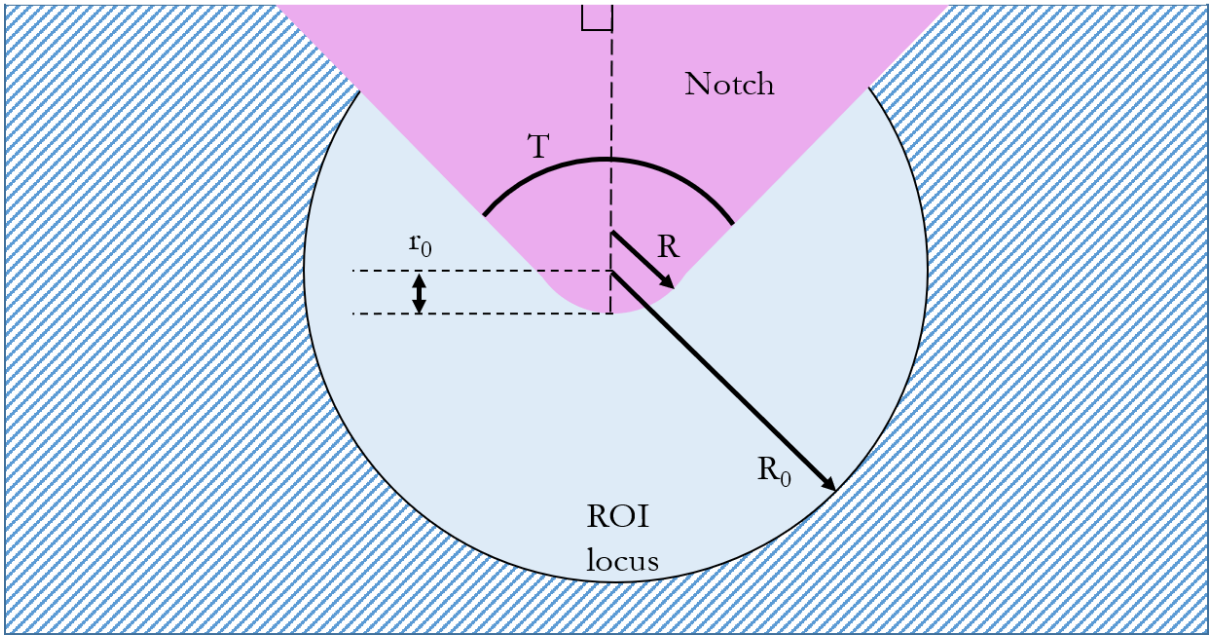


Figure 47: Geometric definition of parameters R_0 and r_0 based on the measured notch tip geometry (based on Lazzarin et al. [137]).

II.5.1.4 Graphite specific models

Brocklehurst and Brown (1973) determined that LEFM overestimated the NSF in graphite, suggesting that a damage mechanism results in a lower sensitivity to notching [46]. It was suggested that during propagation the crack extends and sharpens at a distance related to the microstructural features. They developed a critical distance model that had reasonable predictive power for notched flexure specimens, but failed to predict failure of circumferentially-notched bars [46].

The Graphite Fracture Mechanics Model, GFMM, was developed by Tucker to account for graphite's intrinsic defects. The applied stress required to form the most damaging crack in an elastic body from a single representative defect was conservatively predicted (see Figure 48). Rose and Tucker added multiple defects to statistically simulate reduced strength, akin to Weibull, from which statistical strength distributions were calculated [142]. The GFMM and Rose and Tucker model are both capable of predicting fracture in many geometries, and account for irradiation and weight-loss to some degree but neither is ideal for all geometries (see Figure 43, Figure 45, Figure 46, Figure 49). A notch sensitivity analysis with the Tucker model predicted a 1.5 mm Gilsocarbon microstructural length-scale agreeing with the empirical values, though made no estimate of the failure distributions [43, 103, 104]. Combined as the Tucker and McLachlan model [143], accurate experimental predictions were made from a single set of parameters, including the effect of notch depth on the probability of failures at the notch which is important for evaluating scale dependence (Figure 50 - Figure 51). Burchell also proposed a model that aimed to embody the effects of pore size distributions, crack initiation from pores and sub-critical crack growth, with reasonable success in predicting scale effects (for example, see Figure 52) [41]. Both the Tucker and McLachlan and Burchell models were criticised for the number of required many fitting parameters, many of which are difficult to measure [5]. There are no reports of these latter models being applied to either irradiation damage or radiolytic-oxidation, possibly due to the complexity in obtaining the necessary parameters.

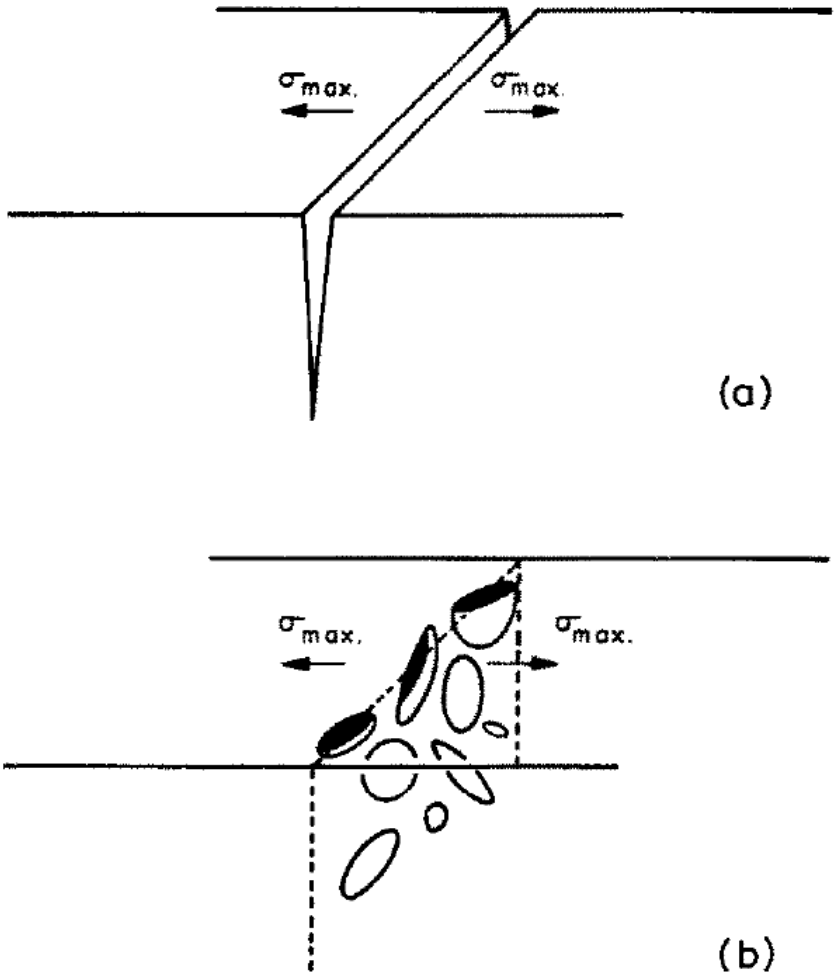


Figure 48: The GFMM applied to a tensile specimen. Rather than assuming a pre-existing crack, as in (a), the natural heterogeneity of the microstructure (b) is replaced with a single plane in the most damaging orientation, reducing the effective cross-section and load bearing capacity. Reprinted from [43] with permission from Elsevier.

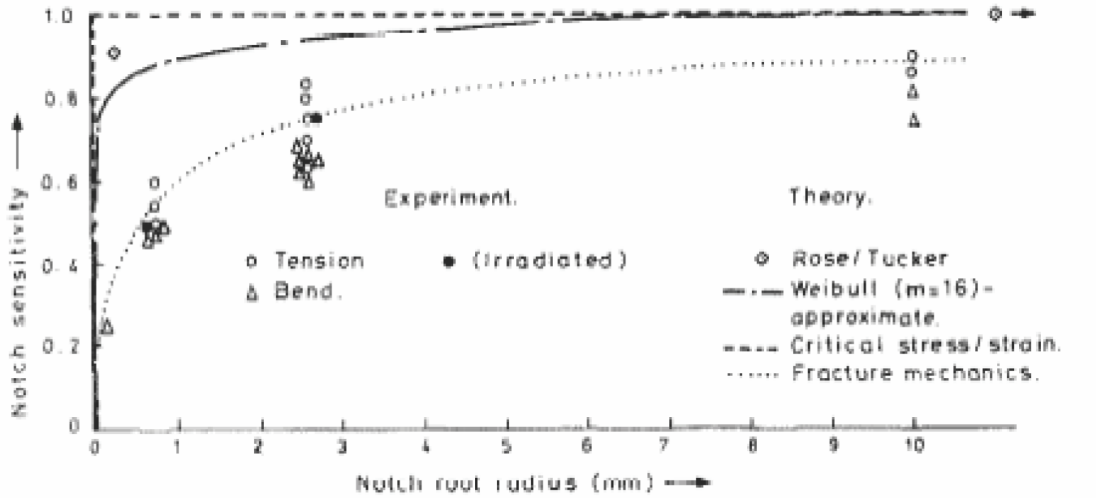


Figure 49: The GFMM can predict the effect of notch sensitivity in virgin and irradiated notched flexure. Reprinted from [43] with permission from Elsevier.

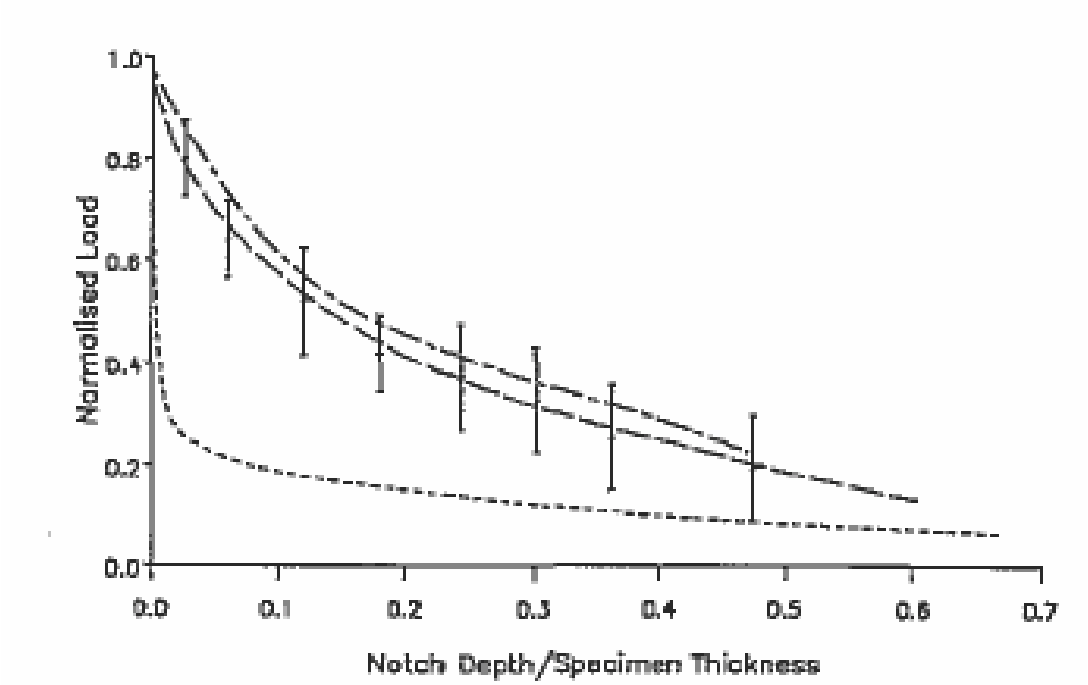


Figure 50: Use of the Tucker and McLachlen model (long dash-dot) in predicting the formation of stress gradients in bend specimens, compared to the GFFM (long dashes) and Rose and Taylor (short dashes) models. Reprinted from [143] with permission from IOP Publishing.

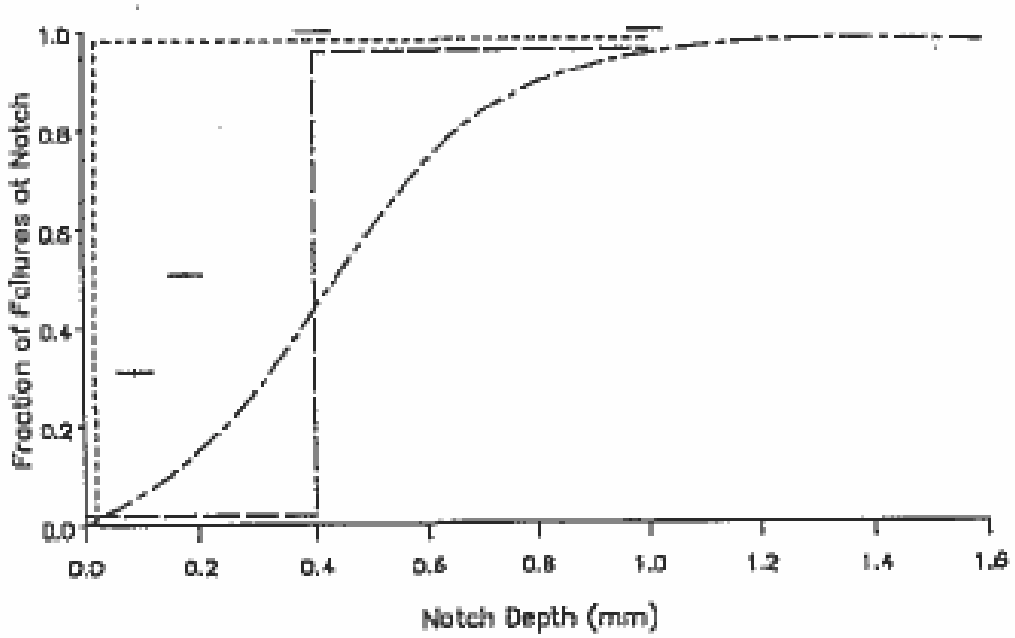


Figure 51: An improvement on all previous models, the Tucker and McLachlen model (same patterning as Figure 50) is able to predict the distribution of flexure samples that fail at the notch with respect to notch depth. Reprinted from [143] with permission from IOP Publishing.

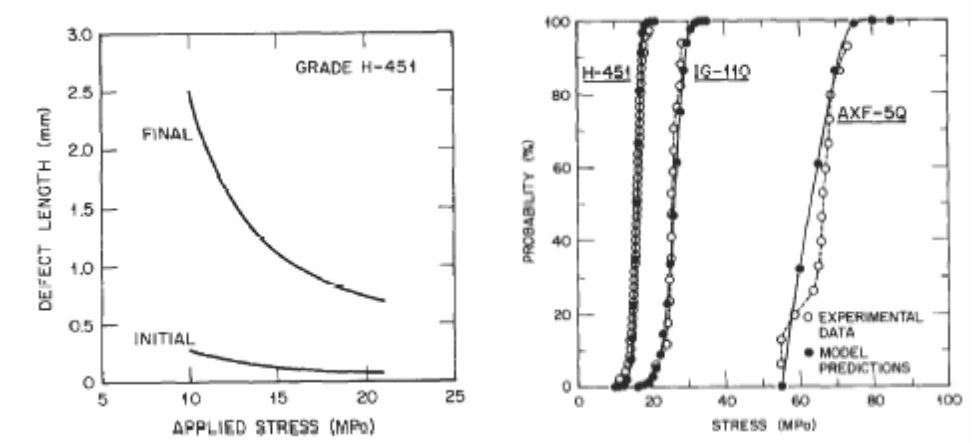


Figure 52: The Burchell model is capable of making good predictions of the tensile strength with various sized microstructures. Reprinted from [144] with permission from Elsevier.

II.5.2 Numerical simulations

II.5.2.1 Cohesive zone-type algorithms

An extension of the length-scale criterion is the 'cohesive zone' model, CZM, which incorporates more advanced deformation and failure laws in computer simulations. These are area- or volume-averaging methods, suitable for materials with limited energy dissipation mechanisms. In their simplest form they assume continuum materials and may be extended to composites, with each phase failing in a unique fashion according to an arbitrary yield surface. Examples include, with increasing degree of physicality and computational complexity, the 'smeared cracking', 'cohesive zone' [145] and 'damaged plasticity' [146] models. In each model, a mechanical property (tensile stress, for example) is integrated over a volume comparable to the FPZ size. To simulate softening and fracture, when the integral passes a threshold criterion (critical stress, for example) the volume is damaged, and its load-bearing capacity degraded proportionately. At high levels of damage, when the stiffness is very low, the elements are removed completely; a physical analogy would be dispersed micro-cracking until critical flaw formation [134, 147]. Although using stress-based criteria, iterative relaxation of the model is equivalent to an energetic solution.

For the simplest models, the behaviour is non-linear elastic, where the stiffness is recovered on unloading, and crack paths are arbitrarily defined. The Barhli *et al.* NLE UMAT formulation (see § II.3.2) used this approach, and was able to successfully predict strain profiles ahead of a growing crack [89]. As complexity increases, the model stiffness may be permanently degraded, non-recoverable strains introduced (proportional to the damage), and cracks paths defined implicitly by the most failed regions [148-150].

Cohesive models are extensively applied in simulating concrete fracture, with reasonable agreement to experiment, for example [151]. Successful application has been made to graphite, particularly for modelling component fracture [152, 153]. By assuming brittle behaviour, fracture due to blunt notches has been modelled using a combination of SED and CZM – the non-linear stiffness of virgin graphite in multi-mode loading was captured in un-notched samples, while linear behaviour was predicted in notched samples [35]. From XCT-DVC data on chevron-notch samples, Mostafavi *et al.* demonstrated that linear elastic fracture mechanics, LEFM, can correctly simulate CMOD but not crack lengths. The *J*-integral was extracted from the calibrated model, and the SIF compared to the DVC measurements, clearly indicating strain-softening which they attributed to cohesive zone formation. The CZM predicted the behaviour more accurately than the linear elastic formulation (Figure 53) [58, 100]. Since the strain energy release rate appeared to vary across the crack front, they argued that K_{IC} is constraint dependent in quasi-brittle materials [100].

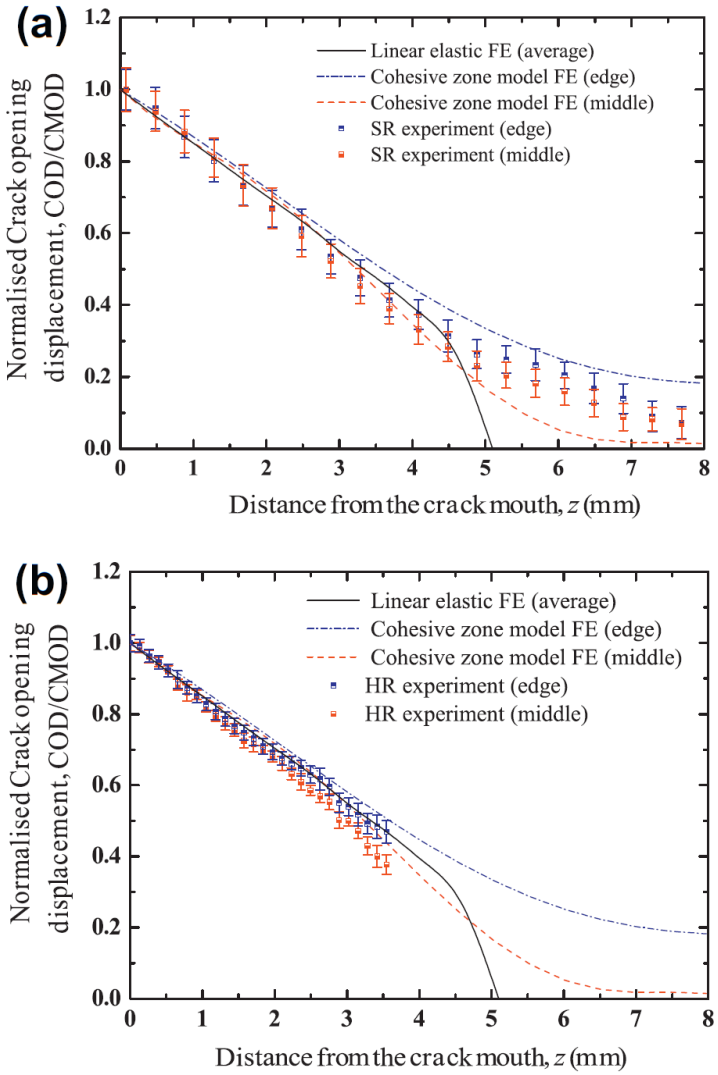


Figure 53: Comparison of the experimental measurements of a crack profile in graphite with predictions from LEFM and CZM techniques. Experimental data is from 'standard resolution', SR, and 'high resolution', HR, XCT observations. Reprinted from [100] with permission from Elsevier.

II.5.2.2 Multi-scale models

Recent advances in computational power allow microstructurally-realistic models of components to be simulated as composite models combining an arbitrary number of phases and material responses. Furthermore, models may be embedded to benefit from complementary techniques at different scales, or computation speeds. As an example, the FEMME model by Saucedo-Mora simulates large scale properties with a coarse mesh and linear elastic properties and is combined with localised cohesive zone behaviour that seeds automatically in regions likely to be damaged, and is solved separately, but simultaneously. Composite or multiphase behaviour may be simulated without computational difficulties, and the criteria for damage and failure in each phase are defined separately so may represent different mechanisms. This approach has successfully simulated fracture in engineering composites, including concrete [154] and silicon carbide composites [155, 156]. For all multi-scale models, it is vital that properties vary smoothly and continuously between the different length scales to prevent energetic anomalies.

For application to graphite, the FEMME model was combined with the cellular automata model by Vertyagina and Marrow [157], becoming CA-FEMME [158]. This model can simulate components such as full Gilsocarbon bricks with realistic distributions of filler particles (measured from XCT), heterogeneous non-linear stiffnesses, localised non-recoverable damage, and phase failure reflecting observations from experiment. The damage and failure behaviour may be applied stochastically to make predictions of strength distributions. The stochastic distributions in the fine-scale cellular automata may be tuned for irradiated or oxidised material as required [157].

II.6 Challenges in implementing the general methodology

This chapter has summarised the empirical evidence and historical attempts to rationalise and predict the behaviour of Gilsocarbon in both the virgin state and reactor environment.

In the virgin state, Gilsocarbon is a complex material. The structure is strongly heterogeneous and irregular, with features covering at least six orders of magnitude. The natural anisotropy of the crystal structure is reflected in the bulk properties, despite the structure of the gilsonite coke chosen to maximise isotropy. Mechanically, the bulk stress-strain response of Gilsocarbon is asymmetric, non-linear, and partially non-recoverable. Gilsocarbon fails in a quasi-brittle manner with the formation of a fracture process zone, possibly mediated by microcracking. The strength, particularly in flexure, exhibits a size effect that diverges from the Weibull formulation for PIE relevant sizes (critical volumes < 1 cm^3). In terms of notch sensitivity, for components and beams of over 12.5 mm depth, Gilsocarbon obeys a $K_{IC} \propto \sqrt{R}$ relationship for notch radii above c. 1 mm (as predicted by linear elasticity), and is notch insensitive below this limit with a constant apparent strength. Gilsocarbon is also insensitive to notches with depths below a similar threshold. These insensitivities appear to be dependent on the microstructural scale. In other materials, such an effect is attributed to crack tip blunting mechanisms, which result in FPZ formation. The respective sizes and distributions of pores and filler particles have the strongest influence on the fracture properties.

Low-level irradiation increases the strength and stiffness, while elastic deformation becomes increasingly linear. Notch sensitivity and the microstructural length-scale are invariant. By contrast, radiolytic-oxidation results in a more open pore network, with maximum growth in the smallest voids. An exponential reduction in both strength and modulus is observed. The available notch sensitivity data of radiolytically-oxidised specimens relates to only a small number of relatively low dose, low weight loss specimens. A potential size effect in notch sensitivity exists. For forward prediction, the limited property data available comes from accelerated MTR programmes, and the lack of understanding of the kinetic effects limits their predictive usefulness.

Models are validated against empirical notch sensitivity data defined in terms of stress, but the models deemed most appropriate for scalable predictions use an energy-based approach. The loading geometry critical SED, Weibull analysis and GFMM are microstructure independent and so although successful predictions are made of certain failure geometries in graphite, the results are not transferrable [94]. As such, even where the models agree with the effects of irradiation or oxidation, they cannot be considered predictive. Critical distance and cohesive zone models are able to capture FPZ evolution and with implementation in FE analysis, any geometry or loading conditions may be modelled, with evolving material properties. Due to computational limitations, the properties tend to be averaged, making the output more applicable to the engineering scale than microstructural scale, but heterogeneous and multi-scale approaches have been successful, and are perhaps most suited to predictions of failure at different engineering scales.

Considering the general methodology for predicting axial crack initiation outlined in § I.3.1, the following challenges are highlighted as requiring further investigation:

1. Define constraints for a suitable PIE test for notch sensitivity
2. Prototype a PIE test to demonstrate whether notch sensitivity can be measured at suitable scales
3. Obtain statistical data suitable for simulation such that the variability in notch sensitivity of components can be predicted
4. Characterise notch sensitivity in multiaxial loading and multimodal failure applicable to the conditions in the bricks
5. Further characterise the unique mechanical properties of the individual microstructural phases (filler particle and binder), particularly related to non-recoverable strains, damage and crack initiation criteria
6. Identify mechanisms related to how the phases interact and the critical length scales for predicting stress concentration behaviour
7. Identify the failure mechanism 'critical path' for the bulk material
8. Create a microstructurally-realistic simulation enabling scalable prediction
9. Confirm notch sensitivity trends with irradiation and radiolytic oxidation continue to end of generation conditions
10. Refine a PIE test, and demonstrate industrial validity

To further develop a notch sensitivity test, these challenges will be addressed in the following chapters, using first an 'engineering' approach to understand small specimen behaviour, and then the microstructural effects assessed from a 'materials' perspective. The limitations of these approaches and the understanding gained will be discussed in the final chapter.

III Crack Initiation in Notched Small Specimens

III.1 Introduction

Regular monitoring of the notch sensitivity of the reactor graphite could contribute to the safety case for continued operation. This would be an additional technique in the current PIE. For current monitoring, cores of diameter, ϕ 19 mm are trepanned from the reactor's fuel channel bores and machined into the specimens of appropriate geometries. With a maximum core length of c. 100 mm, the volume of material available for PIE is very limited, and due to the presence of density gradients and the need to measure a significant number of properties, test specimens are always constrained to be on the centimetre length scale. Three-point bend, 3PB, is used for fracture strength PIE of 6 x 6 x 19 mm beams, since these beams are too squat to measure in four-point bend, 4PB, whilst complying with industrial standards such as "ASTM C651: Four-point bending of plain graphite beams". For Gilsocarbon, ASTM C651 would require plain beams with minimum dimensions of 10 x 10 x 80 mm [159].

There are no suitable industrial standards for PIE notch sensitivity measurements in Gilsocarbon and there is a lack of published research in the field. Machining notches into the 6 x 6 x 19 mm beams is a potential test geometry, and some early investigations on irradiated material have indicated that the test methodology may be viable on ex-reactor material [98]. To develop confidence in such a test, it would be necessary to validate whether the notch sensitivity behaviours seen in small specimens are in line with historical measurements on larger specimens including those by Brocklehurst and Brown [46] and Brown *et al.* [47]. The historical studies tested large beams, where the smallest dimensions were greater than 12 mm and had relatively slender geometries, and component-scale specimens (known as 'feature tests'). As outlined in § II.3.2, these studies used elementary beam theory to calculate properties such as strain, stress and strain energy density at failure. The material was assumed to be brittle linear elastic and failure stresses were calculated using the reduced-ligament method, from which NSFs and notch sensitivity parameters were calculated. These experimental datasets provide benchmark datasets for understanding potential size effects in the behaviour. Key limitations of these techniques are the requirements for a linear elastic, LE, homogenous response, where analytical equations are well defined. With small squat beams, especially with the introduction of significant notches, the assumptions behind the elementary equations are no longer valid, and the calculated values could diverge from reality.

Various crack initiation criteria were presented, in § II.5, though none were truly satisfactory. A more general fracture criterion with potential application to Gilsocarbon is the notch geometry critical SED (§ II.5.1.3), since it: 1) relies on an areal measurement, which does not require knowledge of the precise stresses at the crack/notch tip, nor empirical point measurements to be representative; 2) considers a relatively large critical volume, which can account for variable responses from a heterogeneous microstructure; and 3) includes contributions from both stress and strain, with no requirement for uniaxial deformation. While the loading definition critical SED was evaluated as having limited applicability, the notch definition version has not been evaluated on Gilsocarbon. To be a valid criterion, a consistent SED value would be calculated for a notch of any geometry in any loading configuration.

Innovations in imaging capability, data storage and processing, and strain measurement techniques such as DIC have enabled significant advances in small specimen characterisation in recent decades. Similarly, multi-part 3D finite element simulations using user-defined material, UMAT, formulations can be performed and interpreted routinely, for detailed comparison with experimental data. By combining these techniques with fracture test data of a 'statistically-valid' sample of small specimens, the notch sensitivity behaviour of small specimens will be determined, compared to historical data and the critical SED criterion re-evaluated.

Crack initiation data will be obtained from 4PB testing of over 100 Gilsocarbon specimens with notches in seven geometries, based on 6 x 6 x 19 mm beams. The tested parameters will be notch depth and notch tip geometry, comparing blunt U-notches with sharp V-notches. Multi-camera imaging and digital image correlation will be used to track the deformation of the specimens: low-resolution stereo imaging will be used to uniquely define the sample deflection based on the vertical displacements along a surface profile, and strain fields will be calculated from high-resolution monoscopic imaging. FE simulations of the beams, fitted to agree with the measured deflection, and demonstrated to agree with the calculated strain fields, will be used to predict stresses. Strain softening from the uniaxial tensile modulus with increasing deflection will be demonstrated. Multiple models will be tested for stress prediction to attempt to simulate this behaviour: LE models with moduli that bound the apparent stiffness degradation, and a non-linear elastic, NLE, model that enables prediction of local strain softening. NSF and notch sensitivity trends will be compared to the historical studies to demonstrate comparable trends with notch geometry, but a potential size effect. Simulated strain energy density, SED, will also be compared with the historical reports to show similar behaviour for the small samples, raising the possibility of revisiting the use of SED as the crack initiation criterion for Gilsocarbon. Strain data determined by DIC will be shown as a good first-order SED measurement, despite the inability to measure strains immediately adjacent to the notch tip.

III.2 Experiment description

III.2.1 Specimens

Single edge-notched Gilsocarbon beams were prepared from a single billet of graphite manufactured by Union Carbide, UCAR, as used in Heysham 2 and characterised previously [75, 88, 89]. The specimens had gross dimensions of width, W = 6.00 mm, depth, D = 6.00 mm and length, L = 19.00 mm, as per Figure 54. Seven unique geometries were designed with the two geometric variables of notch depth, a, and notch tip geometry; the beams were unnotched, or notched with slots of width, S = 2.0 mm with either a blunt (full radius) 'U' or a sharp '90° V' notch tip. Machining was performed by milling, with the sharp notches cut using a bespoke profile saw. The nominal depths were shallow (a = 1.00 mm), half-depth (a = 3.00 mm), and deep (a = 4.50 mm). Six of each the half-depth sharp and blunt specimens were prepared for preliminary testing which is described in § A1. The results of the preliminary testing provided the statistical basis for machining a further 14 specimens in each of the seven geometries;[17] 18 specimens of the unnotched geometry were prepared as that geometry was considered the experiment control, and so benefited from increased confidence.

[17]The specimens were cut from a cross-section of a single billet. The location of each sample was stipulated to ensure that each geometry sampled the full volume. Subsequent analysis of the data presented in this thesis could seek to identify significant spatial variation of billet strength or notch sensitivity.

The specimens were baked at 140 °C for two hours and then stored in a desiccated atmosphere. Prior to testing, dimensions *L*, *D* and *W* were measured on every specimen using Vernier callipers; all specimens were found to be correctly machined, with visibly parallel faces. Dimensions *W* (for calibration of the image resolution), *S*, *P*, *T*, *R* and *a* were measured from photographs of one face of each geometry with estimated measurement accuracies, ζ_i. Only the notch depths of the shallow blunt notch specimens (SF-B100) were outside tolerance, where $\hat{a} = 1.12$ mm (95%CI: 1.08 mm, 1.16 mm) and 95%ile $\xi_a = \pm$ 0.14 mm. The means and pooled standard deviations are recorded in Table 4. The mean radius for the sharp notch tip specimens was $\hat{r} = 0.05$ mm (95%CI: 0.04 mm, 0.06 mm), with 95%ile $\xi_r = \pm$ 0.02 mm.

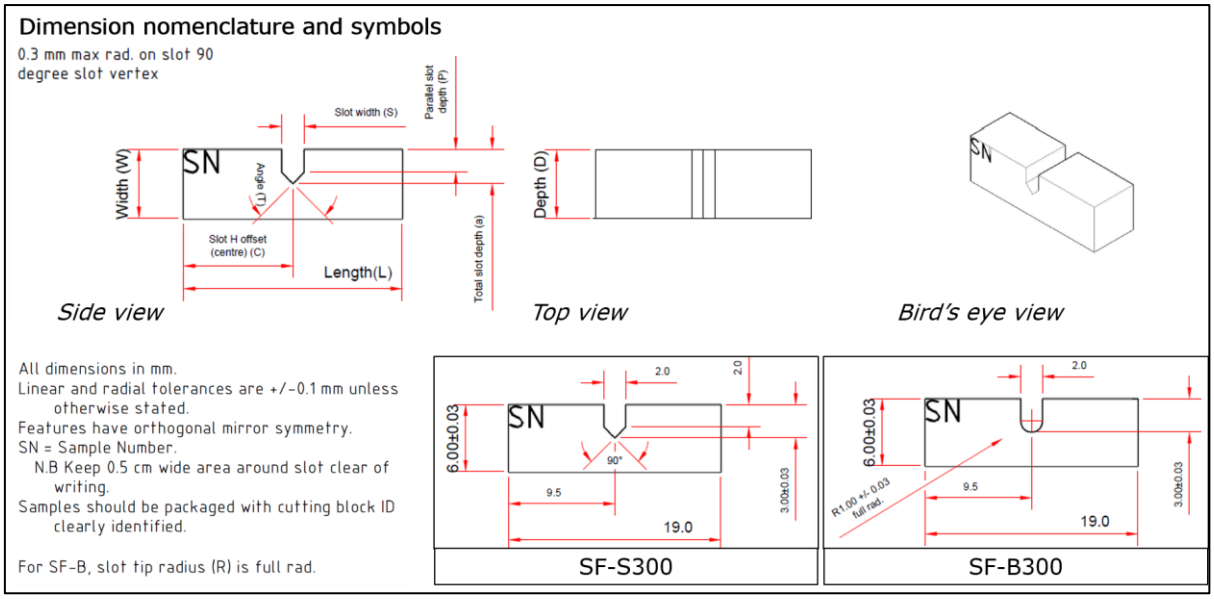


Figure 54: Dimension definitions, nomenclature and symbols for the SF series. Drawings for the half-depth sharp (SF-S300) and blunt (SF-B300) notch geometries are shown inset to indicate the design of the two notch tips. Notch tip radius, R, is the radius of the blunt tip or the sharp tip 90° vertex.

Table 4: Dimension distributions for the specimens and the estimated measurement accuracy. Standard deviations and measurement accuracy quoted at the 95%ile, numbers in () are 95%CI, where applicable; see § iv. †Measured radius of sharp notches was 0.05 ± 0.02 (95%CI 0.04, 0.06) mm based on measurements of eight specimens, including at least two specimens from each of the three geometries.

Notch geometry	Drawing code	Number of specimens, n	Width, W	Depth, D	Length, L	Slot width, S	Parallel slot height, P	Ligament, $(W-a)$	Notch depth, a	Notch radius, R	Vertex angle, T
	-	-	mm	mm	mm	mm	mm	mm	mm	mm	°
Blunt shallow notch	SF-B100	14	6.00 (6.00, 6.00)	6.00 (6.00, 6.00)	19.00 (19.00, 19.00)	n/a	n/a	4.88 (4.84, 4.92)	1.12 (1.08, 1.16)	0.98 (0.98, 0.98)	n/a
Blunt half-depth notch	SF-B300	14	6.00 (6.00, 6.00)	6.00 (6.00, 6.00)	19.00 (19.00, 19.00)	1.97 (1.96, 1.98)	n/a	2.93 (2.89, 2.97)	3.07 (3.03, 3.11)	0.97 (0.97, 0.98)	n/a
Blunt deep notch	SF-B450	14	6.00 (6.00, 6.00)	6.00 (6.00, 6.00)	19.00 (19.00, 19.00)	1.99 (1.98, 2.00)	n/a	1.42 (1.38, 1.46)	4.58 (4.54, 4.62)	0.98 (0.98, 0.99)	n/a
Sharp shallow notch	SF-S100	14	6.00 (6.00, 6.00)	6.00 (6.00, 6.00)	19.00 (19.00, 19.00)	n/a	n/a	5.03 (4.99, 5.07)	0.97 (0.93, 1.01)	n/a†	89.8 (89.2, 90.4)
Sharp half-depth notch	SF-S300	14	6.00 (6.00, 6.00)	6.00 (6.00, 6.00)	19.00 (19.00, 19.00)	1.96 (1.96, 1.97)	2.00 (1.96, 2.04)	3.03 (2.99, 3.07)	2.97 (2.93, 3.01)	n/a†	90.4 (89.7, 91.1)
Sharp deep notch	SF-S450	13	6.00 (6.00, 6.00)	6.00 (6.00, 6.00)	19.00 (19.00, 19.00)	1.98 (1.97, 1.99)	3.55 (3.51, 3.59)	1.48 (1.44, 1.52)	4.52 (4.48, 4.56)	n/a†	89.7 (88.8, 90.5)
Un-notched	SF-U000	18	6.00 (6.00, 6.00)	6.00 (6.00, 6.00)	19.00 (19.00, 19.00)	n/a	n/a	n/a	n/a	n/a	n/a
Estimated standard deviation in measured data (pooled, 95%ile), ξ		n/a	± 0.00	± 0.00	± 0.00	± 0.03	± 0.01	± 0.01	± 0.01	± 0.02	± 2.4
Measurement accuracy, ζ		n/a	0.02 mm	0.02 mm	0.02 mm	0.03 mm	1.4%	0.9%	0.9%	0.03 mm	2.4°

III.2.2 Loading and imaging

The specimens were tested in the 4PB geometry shown in Figure 55 with an inner span, $2l_{in}$, of 5.33 mm, and outer span, $2l_{out}$, of 16.00 mm, using ϕ 4.00 mm steel rollers. The tests were conducted using a *Grip Engineering* TH238 adjustable span jig mounted on a *Shimadzu* AGS-X universal test machine (Figure 55). Multiple mechanical degrees of freedom were permitted to minimise eccentric loads and the lower anvils were greased to reduce contact friction. Loading was quasi-static with a maximum loading rate of 0.5 $\mu m.s^{-1}$. Periodic unloads were performed to monitor changes in specimen compliance; at 25 N intervals, the specimen was unloaded by up to 15 N (peak load dependent), up to a final unload at 200 N (loading continued beyond this load, but no further partial unloads were conducted). Load-displacement data were logged at 10 ms intervals and all tests continued until final failure was recorded.

The wide face of all the specimens was imaged by a stereo pair of Toshiba-Teli (CSB4000CL-10A) cameras and a higher-resolution *FLIR* Grasshopper® 3 (GS3-U3-416C) camera, as arranged in the photograph and accompanying schematic in Figure 56. The stereo pair, separated by c. 30°, captured at an interval of 1.5 s with a 16.9 μm.pixel^{-1} resolution, with fields of view shown in Figure 57. The c. 14 mm width of the bi-focussed region was sufficient to completely include several millimetres outside of each inner roller; the remainder of the specimen was visible, but out of focus. The Grasshopper® 3 was positioned centrally, perpendicular to the specimen face, and was used to image two specimens of each geometry at an interval of 0.5 s with a 3.19 μm.pixel^{-1} resolution and a 6.6 x 6.6 mm field of view, with an example frame in Figure 57. Camera calibrations were performed using *LaVision*'s Micro Calibration Plate (part number 1108939) mounted on the focal plane. Concentrated lighting was provided by an axially-mounted annular halogen light around the Grasshopper® 3 lens extender. Additionally, two LED banks with built-in diffusing panes were mounted with the Toshiba cameras to illuminate the specimens at a more oblique angle. All the cameras captured 16-bit greyscale images, with the Grasshopper® 3 recording 2048 x 2048 pixel frames, and the Toshiba pair recording 2008 x 2047 pixel frames.

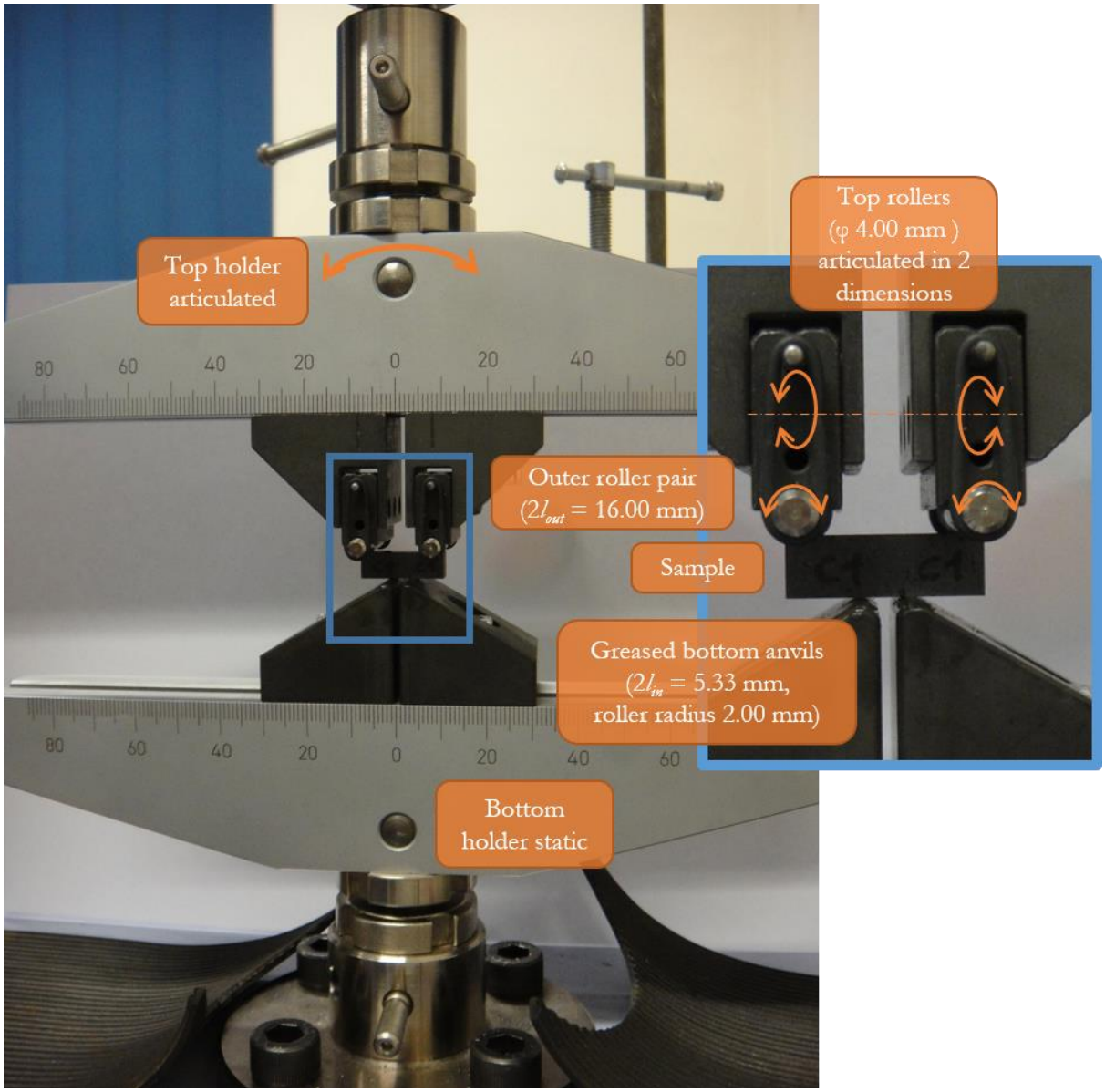


Figure 55: Four-point flexure jig used for short beam testing, with inset to highlight the roller arrangement. Rotational degrees of freedom are indicated by the orange arrows.

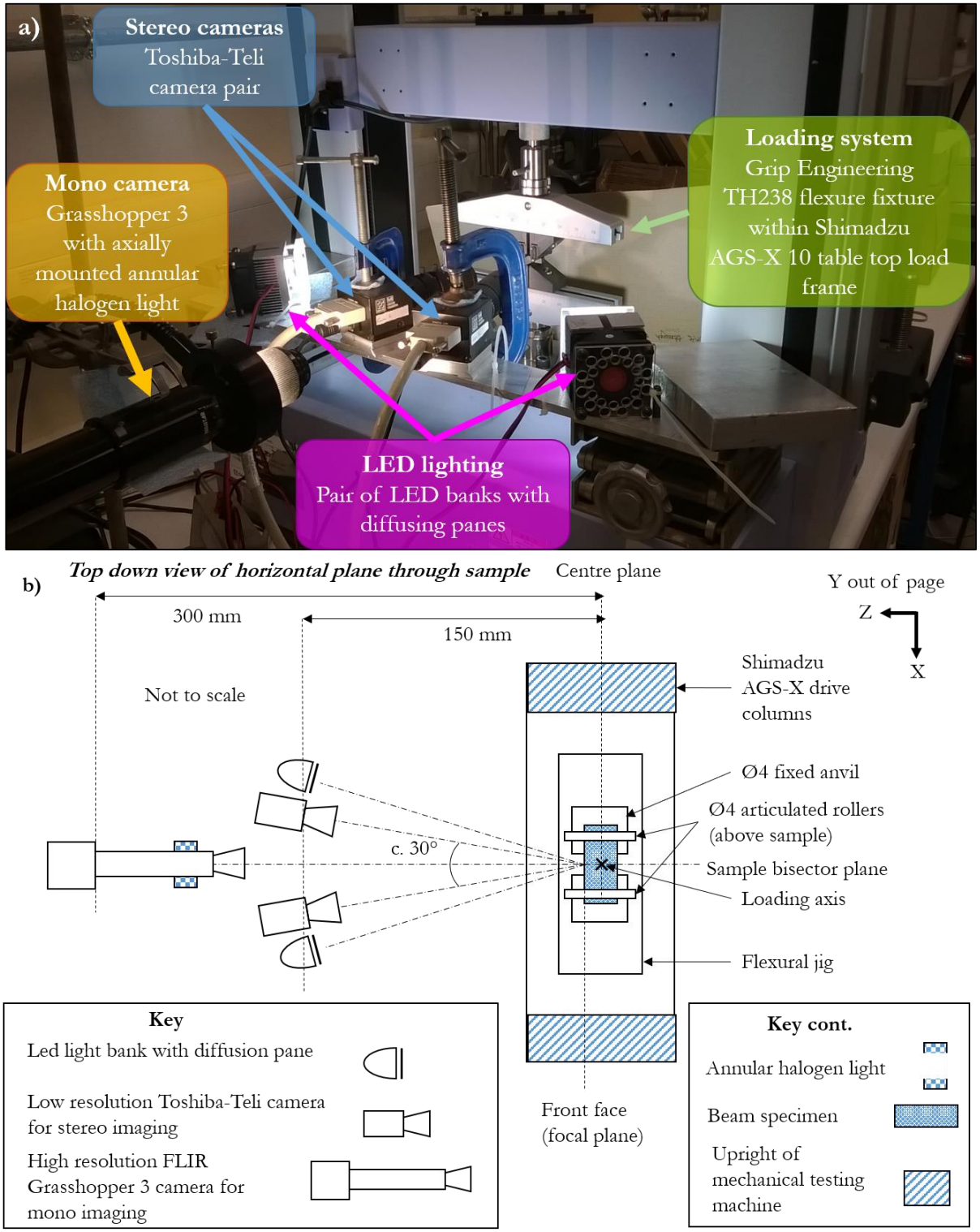


Figure 56:The three-camera and load frame imaging set-up used for the short beam testing: (a) as seen and (b) schematically. Positions and orientations of the cameras, lighting, loading system and the loading axes definition are indicated.



Figure 57: Example views from the three-camera system of a blunt half-depth sample.

III.3 Data processing

The rich datasets of load, crosshead displacement and multiscale imaging, were combined to measure the behaviour at crack initiation. Using the process described in § III.3.1, the load displacement data were cleaned, and pop-in events detected that would indicate crack initiation. For later statistical comparisons, the parameters describing the statistical distributions of the loads and crosshead displacements were also calculated. The various image data were also post-processed, as described in § III.3.2, with specific frames selected for digital image correlation, DIC. From the DIC, the beam deflection was parameterised, and full-field strains calculated for later analysis in § III.3.2.2.3 and § III.4.3.

III.3.1 Load-displacement behaviour

For clarity and to permit automatic detection of fracture, the load-displacement data were cleaned to remove both the initial slack in the jig and the partial unload-reload intervals; see the example for a half-depth blunt notch tip in Figure 58. After cleaning, relatively consistent load behaviour was observed for all the bend tests except for the deep notched specimens. All the load data below 15 N was excluded, since this was mainly mechanical artefacts, and Figure 58(b) shows that beneath loads of around 50 N a period of decreasing compliance (increasing gradient) was observed, which was attributed to the jig settling and achieving full alignment. Above 50 N, the load response was approximately linear; for some specimens no significant deviation from linearity was observed before failure until instantaneous fracture, but deviations were visible for others from about 80 % peak load, F_M. Beyond the limit of the linear response, the compliance increased following apparently instantaneous load drops. These load drops could be attributed to one of the following causes: a fracture event, where they are termed 'pop-ins'; electronic noise in the load cell; or further settling of the specimen on the loading jig. Here, it is assumed that the significant load drops that occurred above 40 %F_M resulted from a non-catastrophic fracture, and therefore represent the crack initiation; this was supported by visual and DIC assessments of surface imaging that indicated the simultaneous appearance of cracking or localised high strains. Crack growth would reduce the load-bearing cross-section of the body; this further accounts for the decrease in compliance.

In this study, potential pop-ins ("events") were identified as load drops detected above 40 %F_M with an associated increase in compliance exceeding 4 %. For each event, the pre- and post-event compliances were the load-displacement gradients of linear fits to 100 load data points (equivalent to 1 s) before and after the event, respectively. The post-event gradient calculation was relaxed for either very gradual events, or where multiple or very severe events occurred within the 100-point domain, such that the gradients were non-representative. From the fits, an 'effective load drop' was calculated as the predicted load difference in the linear behaviours at the event displacement. The standard deviation of the load data about the pre-event fit was calculated (such that the 95%ile standard deviation was typically $\zeta < 0.1$ N) and the pop-in was deemed to be the first of the events where the effective load drop exceeded three standard deviations. This definition was implemented in a semi-automatic MATLAB® [160] script that detected the earliest event algorithmically, with confirmation by manual inspection. While the general load-displacement behaviour of the deep notched specimens was consistent with the other geometries, peak loads were comparable to the settling load of the jig, and other artefacts attributed to the mechanical loading system. It was therefore not possible to confidently separate the load drops caused by pop-ins and those arising from the rig self-adjustment, and so the pop-in data are not available for the deep-notched specimens.

The distributions of the maximum load, F_M, and the corresponding crosshead displacement, δ_M, and the equivalent values at pop-in, F_P and δ_P, respectively, are described in Table 5. For analysing crack initiation, the pop-in properties are of most importance, where available. In all subsequent calculations these values will be used and referred to as the critical loads and extensions (subscript C) comprising pop-in values where available, or maximums otherwise. The F_M, F_C, δ_M and δ_C distributions are shown in the box and whisker plots in Figure 59 and Figure 60, and indicated that the distributions were all approximately symmetric; in the figures, the red lines are the median, the box indicates the inter-quartile range, IQR, and the whiskers extend to the maximum data limits within the 95%ile, with red crosses marking any data points as potential outliers. Generally, the critical point distributions were seen to be more symmetric than the corresponding maximum point distributions in both figures, though the differences were relatively minor. For a few of the geometries, potential outliers were detected, though the distributions remained approximately symmetric and the crosses were less than twice the IQR, so no further action was taken, and the values were included in the statistical properties. In Table 5, consistent $\hat{F}_M : \hat{F}_P$ ratios of 0.96 ± 0.11 and 0.98 ± 0.04 and were calculated for the blunt and sharp geometries, respectively, though the variances of these distributions were unphysical for a symmetric distribution. The comparative extension ratios, $\hat{\delta}_M : \hat{\delta}_P$ of 0.93 and 0.96, respectively, were less consistent, though there was a positive correlation between F_M:F_C and δ_M:δ_C for the individual geometries.

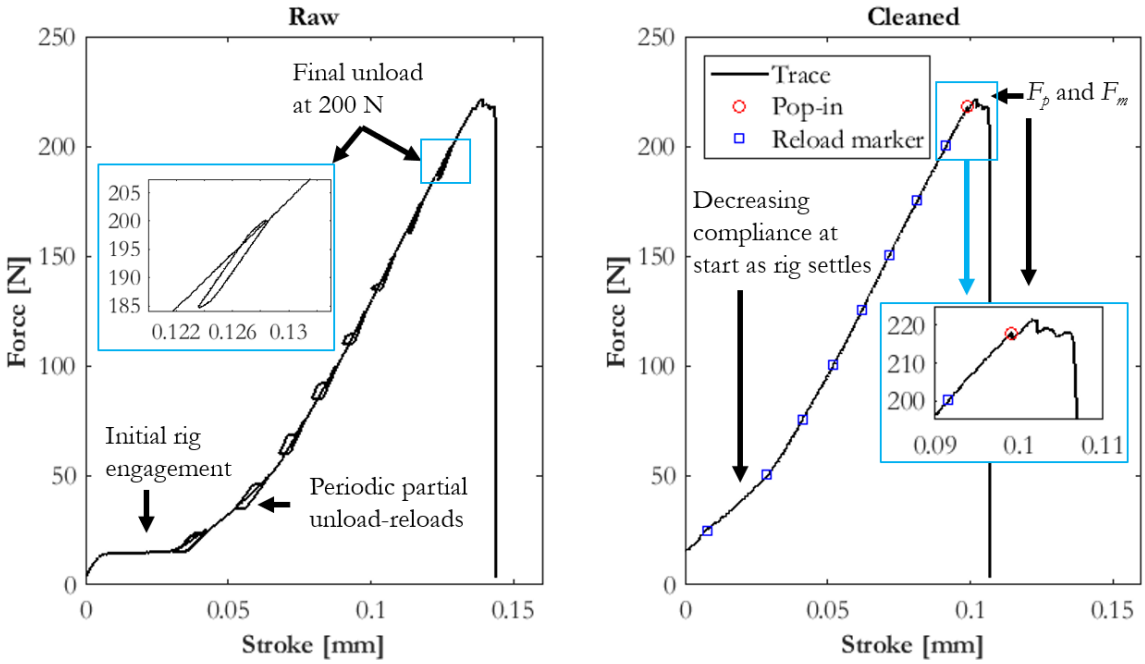


*Figure 58: Example raw and cleaned load-displacement traces for a shallow blunt notch tip specimen. To clean the traces, the initial rig settling and partial unload-reload cycles (*inset left*) were removed, before the maximum and pop-in loads were then automatically determined (*inset right*).*

Table 5: Load-extension distribution properties for geometries, calculated for the failure criterion of either '4 % pop-in' or maximum load, and the ratios of these mean values. Scatter is described by ξ the 95%ile, and the standard error of the mean in brackets at the 95%CI, as described in § iv. No outliers were excluded from the distributions.

Geometry		Pop-in (4 % definition) criterion		Max load criterion		Pop-in: Maximum ratios	
ID	**Notch description**	**Load, F_P**	**Extension (cleaned), δ_P**	**Load, F_M**	**Extension (cleaned), δ_M**	F_P/F_M	δ_P/δ_M
		[N]	**[µm]**	**[N]**	**[µm]**	**[%]**	**[%]**
SF-B100	Blunt, shallow	224 ± 26 (208, 239)	105 ± 11 (99, 111)	232 ± 24 (218, 246)	110 ± 9 (105, 115)	96	96
SF-B300	Blunt, half-depth	94 ± 15 (85, 103)	70 ± 10 (65, 76)	99 ± 13 (92, 106)	78 ± 5 (75, 81)	95	90
SF-B450	Blunt, deep	-	-	26 ± 2 (25, 28)	34 ± 5 (31, 37)	-	-
SF-S100	Sharp, shallow	205 ± 16 (195, 214)	97 ± 7 (94, 101)	210 ± 16 (200, 219)	101 ± 6 (97, 104)	98	97
SF-S300	Sharp, half-depth	88 ± 09 (82, 93)	62 ± 7 (58, 66)	90 ± 9 (84, 95)	66 ± 5 (63, 69)	98	94
SF-S450	Sharp, deep notch	-	-	30 ± 4 (27, 32)	32 ± 8 (27, 37)	-	-
SF-U000	Unnotched	341 ± 33 (324, 357)	149 ± 16 (142, 157)	344 ± 34 (327, 360)	151 ± 16 (143, 159)	99	99
Mean	Blunt	-	-	-	-	96 ± 11	93
	Sharp	-	-	-	-	98 ± 4	96

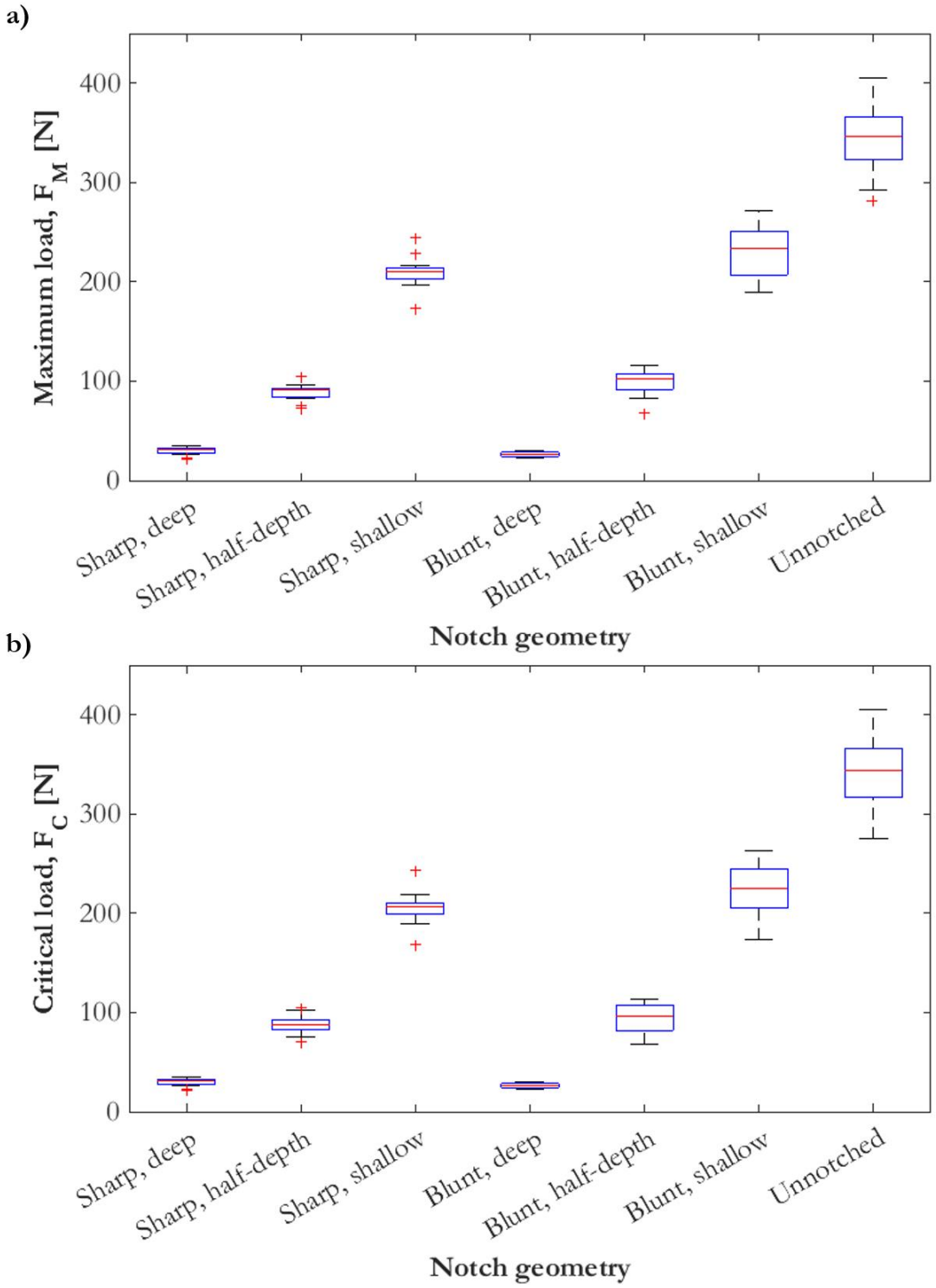


Figure 59: Fracture property distributions as box and whisker plots of a) maximum load, F_M, and b) critical load, F_C. For each box the centre line indicates the distribution median, and the box bottom and top edges indicate the 25th and 75th percentile, respectively. The whiskers indicate the extent of the data within the 95%ile. Data points outside the 95%ile are indicated by red crosses.

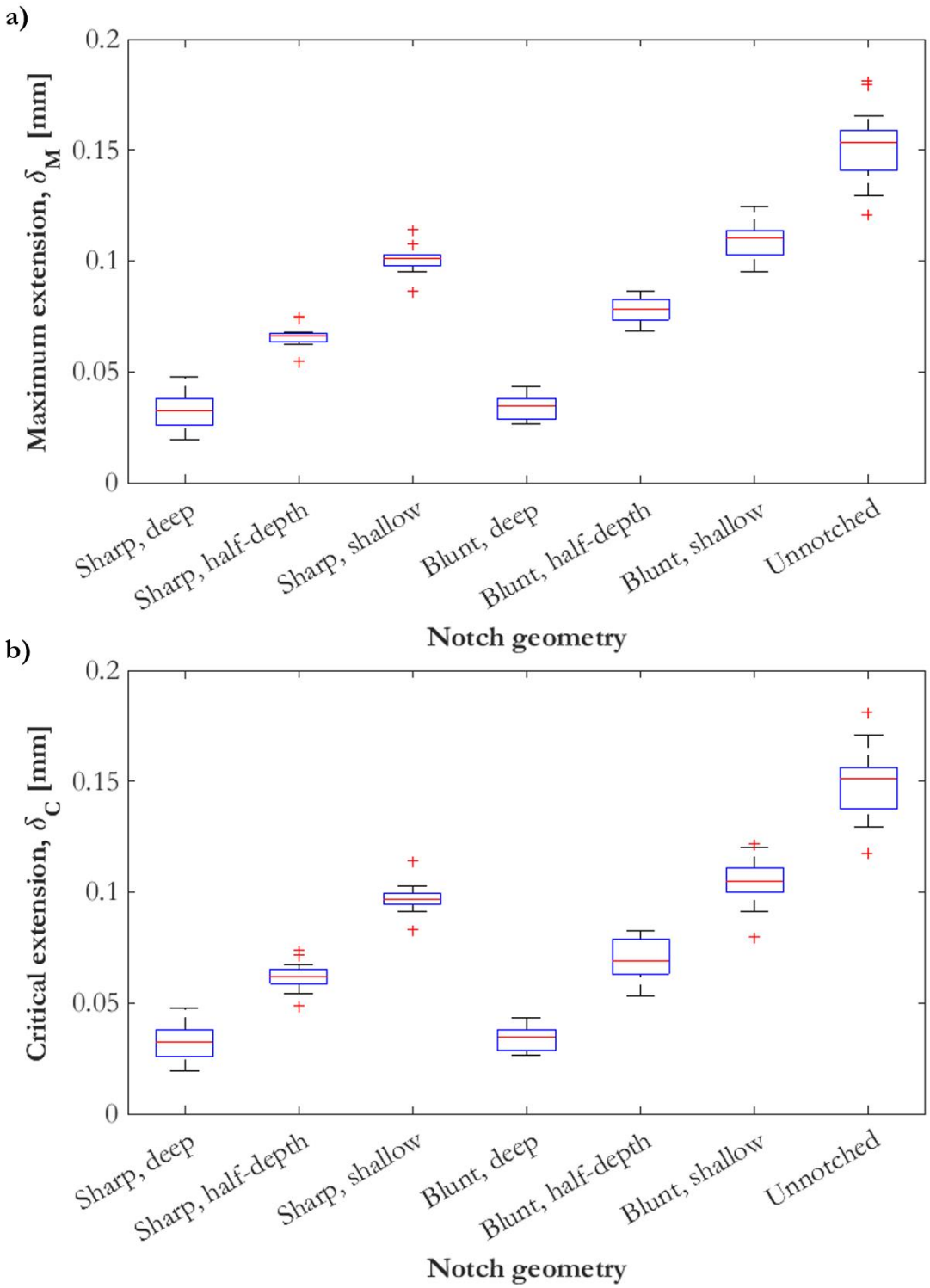
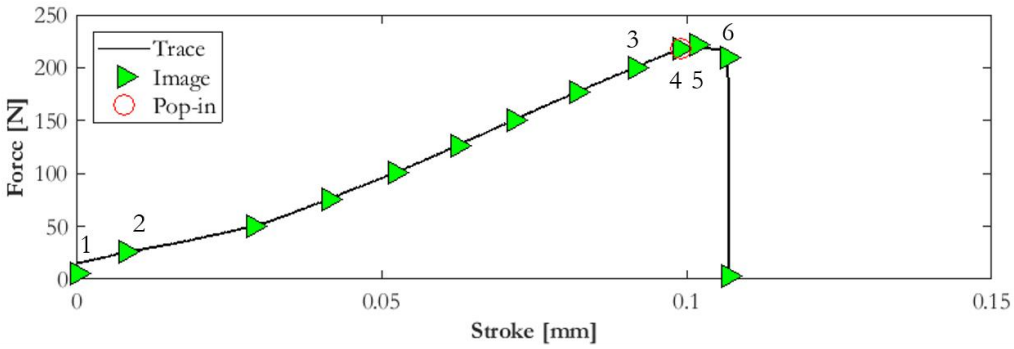


Figure 60: Fracture property distributions as box and whisker plots of a) maximum extension, δ_M, and b) critical extension, δ_C. For each box the red centre line indicates the distribution median, and the box bottom and top edges indicate the 25th and 75th percentile, respectively. The whiskers indicate the extent of the data within the 95%ile. Data points outside the 95%ile are indicated by red crosses.

III.3.2 Optical image processing

III.3.2.1 Image selection

For each specimen imaged by all three cameras, a subset of the monoscopic and corresponding stereoscopic images were selected for analysis by DIC. In addition to an initial image for reference (pre-loaded to < 10 N), the subset consisted of frames at regular load intervals, and the frames immediately before the pop-in, at the maximum load and following failure. The frames were selected by an automated process, with the regular intervals of 12.5 N for the half-depth geometries and 25 N for the shallow notched and unnotched specimens. Figure 61 and Figure 62 show typical images from the loading sequence of a shallow blunt tip specimen. The ultimate crack paths for all specimens were located within the inner roller region.



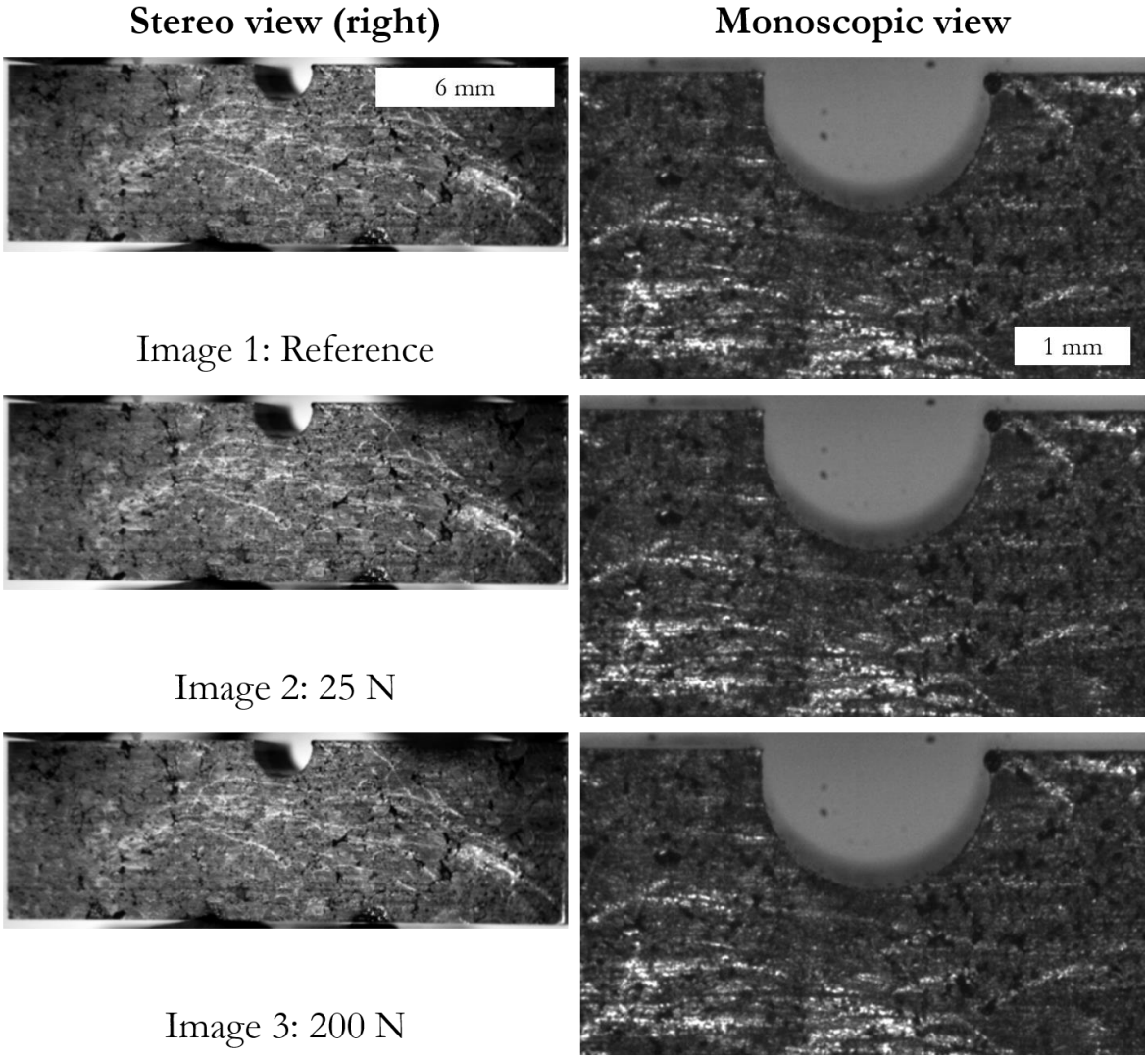


Figure 61: Frames selected from the stereo and monoscopic datasets for DIC at regular load intervals and also just prior to load trace features, including pop-in, peak load and complete failure. An example load-displacement trace and images for a blunt shallow notch specimen (as in Figure 58) are shown. As indicated on the trace, 13 frames were correlated for this specimen, but only the right-hand view and monoscopic frames numbered on the trace are shown. For clarity, both views have been cropped to show pertinent features. Continues in Figure 62.

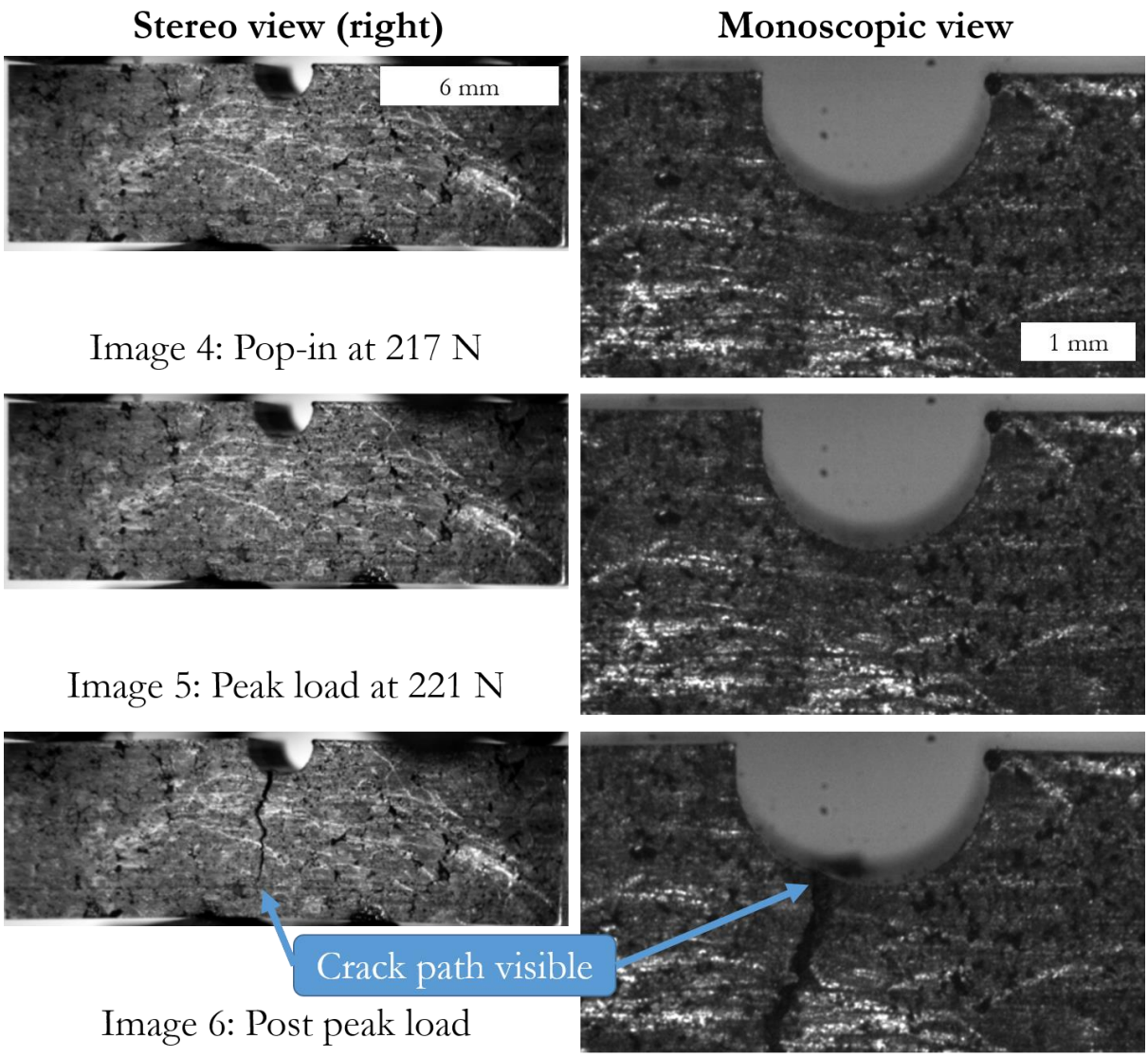


Figure 62: Continued from Figure 61. Frames selected from the stereo and monoscopic datasets for DIC at regular load intervals and also just prior to load trace features, including pop-in, peak load and complete failure. An example load-displacement trace and images for a blunt shallow notch specimen (as in Figure 58) are shown. As indicated on the trace, 13 frames were correlated for this specimen, but only frames numbered on the trace are shown for the right-hand view and monoscopic cameras. For clarity, both views have been cropped to show pertinent features.

III.3.2.2 Digital image correlation processing

DIC was used to characterise the experimental deformations of the specimens, based on the three-camera imaging. The DIC method uses multi-dimensional signal correlation to determine the most likely displacement of a small region of pixels (the 'interrogation window') between a reference image and subsequent image during the loading tests. The process is localised, with each displacement determined independently, and the resultant vectors combined to describe full field displacements. The stereo and monoscopic images were correlated separately, as described in § III.3.2.2.1 and III.3.2.2.1. Pre- and post-correlation corrections were made to the images and correlations, respectively. Most of these processing steps are functions of the commercial software *LaVision*'s DaVis, but the post-correlation correction to remove rigid body motion, RBM, was enhanced in MATLAB®, as described in § III.3.2.2.3. A sensitivity analysis was performed on each dataset to determine the technique's uncertainty. From the monoscopic correlations, the evolving strain fields were measured, while § III.3.2.2.4 describes how specimen deflections were quantified from the stereo imaging.

III.3.2.2.1 Monoscopic imaging

Processed in ImageJ [161], using a custom macro that incorporated standard ImageJ tools, the monoscopic images were first filtered using a small kernel Gaussian filter (sigma = 0.75 pixel) to compensate for slight temporal variation in background lighting and image noise that otherwise prevented accurate DIC. To prevent spurious correlations at specimen and image edges, geometric masking of the reference image excluded pixels within the notch, in the free space above and below the specimen and along the image borders.

The least-squares 'direct correlation' time series 2D DIC algorithm in DaVis 8.3.1 was employed, using a $(155 \text{ pixel})^2$ square DIC interrogation window, with a 2 pixel vector spacing. Vectors with outlier displacements (exceeding 2.5 times the mean of a 5 x 5 kernel) or with correlation coefficients below 0.85 were deleted, and iteratively replaced where possible.

Vector displacement fields and displacement gradient maps ('normal' components dU_X/dX and dU_Y/dY, and 'shear' components dU_Y/dX and dU_X/dY) were extracted for subsequent analysis in MATLAB®. The displacement gradients were converted to engineering strains by (18), after Holister [162].

$$\begin{cases} \epsilon_{XX} = {\partial U_X}/{\partial X} \\ \epsilon_{YY} = {\partial U_Y}/{\partial Y} \\ \epsilon_{XY} = {\partial U_X}/{\partial Y} + {\partial U_X}/{\partial Y} \end{cases} \quad (18)$$

Since strain is a derivative property it is strongly susceptible to noise and artefacts in the displacement calculations, particularly at mask boundaries in the image where the direct correlation algorithm fails to measure displacements accurately. 'Hotspots' were identified and suppressed in the first correlation of each loading series as regions with strains exceeding 1 mStrain. Correlation noise was then reduced using a Gaussian filter (sigma = 3 pixel), and the mask dilated by 155 pixel (c. 0.5 mm) to exclude artefacts at the edge of the masked regions and adjacent to the hotspots. The same masking was applied to every image in the series. The evolution of maximum principal strain, ϵ_1, for a shallow blunt notch tip specimen is shown in Figure 63.

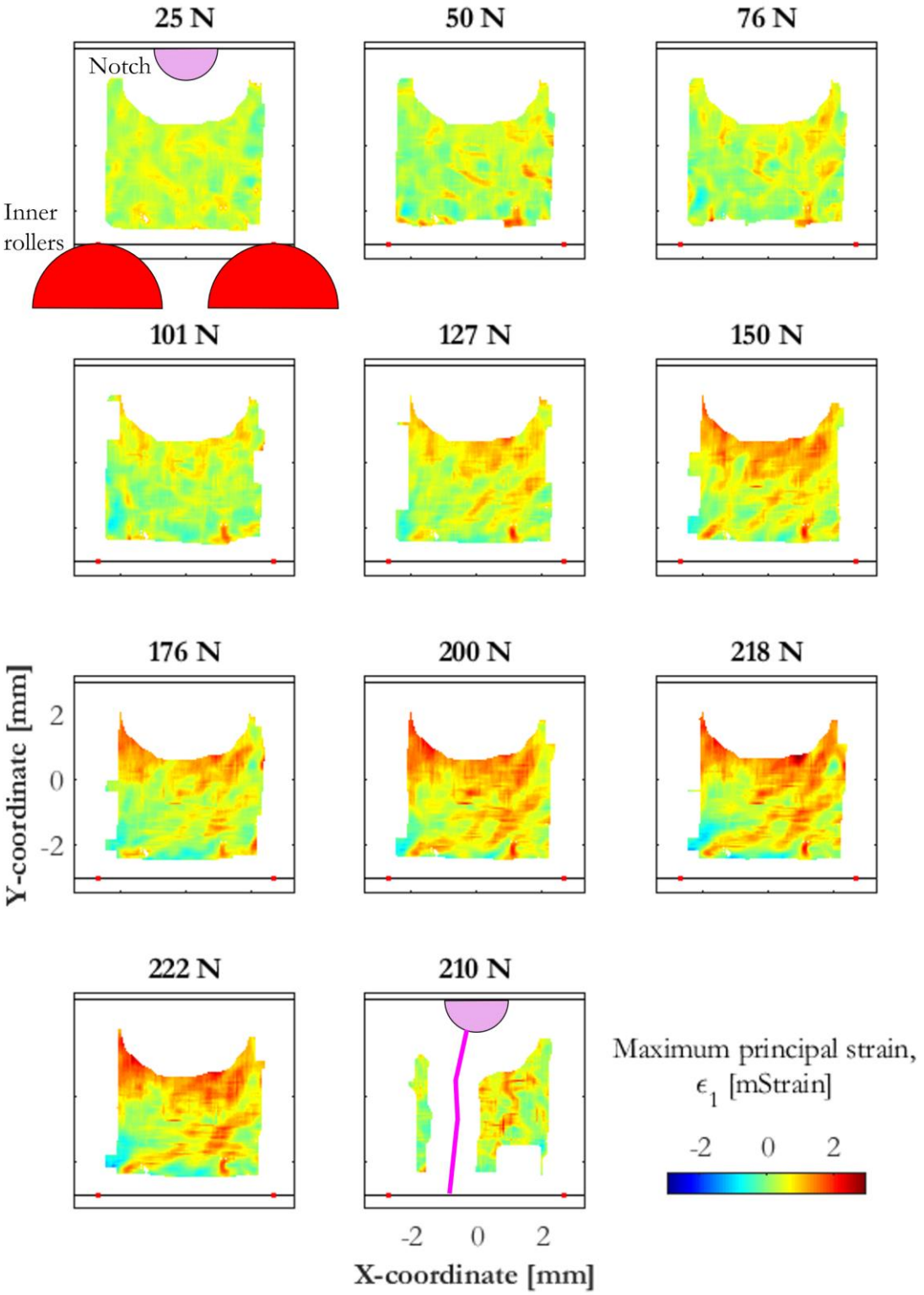


Figure 63: Evolution of ϵ_1 with increasing deformation measured by monoscopic DIC for the blunt shallow specimen images shown in Figure 61 and Figure 62. The deformation increases left-to right, top-to-bottom, captioned with the corresponding load. Black lines at the top and bottom of each map are the upper and lower edges of the sample and on the first map the position of the notch tip is indicated in pink and the inner rollers in red. The approximate crack path is indicated on the final map. For display, strains were capped at ± 3 mStrain.

III.3.2.2.2 Stereoscopic images

No pre-processing was necessary for high-quality correlation of the stereoscopic images. For each load, the image pair was correlated by the least-squares 3D time series stereo DIC algorithm in DaVis, with an interrogation window size of (101 pixel)^2 and vector spacing of 1 pixel. As with the monoscopic DIC, outlier vectors were removed, and vectors with correlation values less than 0.85 replaced. Only the vector displacement fields were required.

The correlation algorithm first determined the 3D coordinates of every correlation point in the reference images, and then calculated the vector displacements to subsequent images. Poor correlation of a small number of the surface points resulted in non-physical Z-coordinates. These points were excluded using a bespoke difference-to-nearest-neighbours algorithm coded in MATLAB®, with a Gaussian filter width of 10 correlation pixels and threshold of ± 1 μm. A further Gaussian filter with a width of 3 correlation pixels was applied to the Z coordinates to improve numerical stability of subsequent calculation. As specimen edges were easily defined and naturally avoided in stereo DIC due to the difference in illumination, the mask dilation used in the monoscopic processing was not required.

III.3.2.2.3 Theory of image correlation displacement field correction and uncertainty calculation

The displacement fields measured by image correlation, U_{Corr}, are considered as the linear summation in (19) of the experimental deformations, U_{Def} the RBM of displacement, U_{Disp}, and rotation, U_{Rot}, and also an uncertainty term that accounts for errors arising from the experimental conditions and correlation artefacts, U_{Uncert}. U_{Def} is the parameter of interest, but RBM and noise obscure this behaviour and are incompatible with the global reference frame used for finite element modelling.

$$U_{Corr} = \left(U_{Def} + U_{Uncert}\right) + \left(U_{Disp} + U_{Rot}\right) \tag{19}$$

Each component has a distribution of values, which compound to form the measurable U_{Corr} distribution. Changes to the component fields has a predictable effect on the U_{Corr} distribution: rigid body displacement, RBD, would shift the mean without changing the distribution shape, while rigid body rotation and random noise would broaden the distribution without changing the mean value. As no contribution would narrow the U_{Corr} histogram,[18] the variance of U_{Corr} is always greater than the variance of U_{Def}.

To remove the RBM artefacts from correlated vector fields, Mostafavi *et al.* [163] achieved good results by using an algorithm based on the rotation correction proposed by Shoemake *et al.* [164] and coded in MATLAB®. However, this implementation was sensitive to correlation noise and artefacts, and to the presence of discontinuities in the displacement field, limiting its general applicability. An enhanced version of Mostafavi's algorithm was developed. For instance, recognising that DIC is often erroneous near surfaces/image boundaries, the RBM correction parameters (and errors) were determined for only a subset of vectors in the centre of the displacement field, the confident 'core region' (for example, see Figure 64). Also, Mostafavi *et al.* used a simple estimate of the sample rotation, so an improved definition of the centre of rotation based on the physical requirements of the specimen movement, and a non-linear least squares solver (MATLAB®'s LSQNONLIN function [165]) were added to determine the most appropriate rotation angles.

[18] A systematic error in the measurement could feasibly reduce U_{Corr}, but such an error could only be quantified by an independent study, and a detailed analysis into the effects on U_{Corr} is beyond the scope of this work. From review of all the available data, no evidence for systematic errors was detected that would affect the rotation correction by causing the U_{Corr} variance to reduce.

The RBM corrections were calculated from the core region of U_{Corr} and subtracted from every vector in the dataset, leaving the U_{Def} and U_{Uncert} fields. The benefit of these corrections is seen in the example correction in Figure 64, both as improved visual clarity in specimen deformations for the majority of the specimen, and a narrowing of the U_{Corr} histogram for the core region in Figure 65. For the correction to be valid, it is a necessary condition that the statistical spread of the displacements in the core region vectors is reduced.

Algorithms based on this method have been developed for both two- or three-dimensional data. If $U_{Def} = 0$ (or a constant value when it is known *a priori*), these algorithms may be applied to calculate the correlation uncertainty, ξ_{Corr} (at the 95%ile), by (20), arising from U_{Uncert} and the RBM correction error. Practically, this is approximated by performing a rigid body displacement (or rotation) on the specimen and analysing as though it were a deformation.

$$\xi_{Corr} = 1.96 * StDev\left(\left|U_{Corr} - \left(U_{Disp} + U_{Rot}\right)\right|\right) \quad (20)$$

ξ_{Corr} is a function of the image correlation interrogation window dimensions, the feature geometry and dispersion, and the noise-to-signal ratio present in the image. For a given rigid body test, the function can be determined and then an appropriate interrogation window size selected to achieve a predetermined level of error.

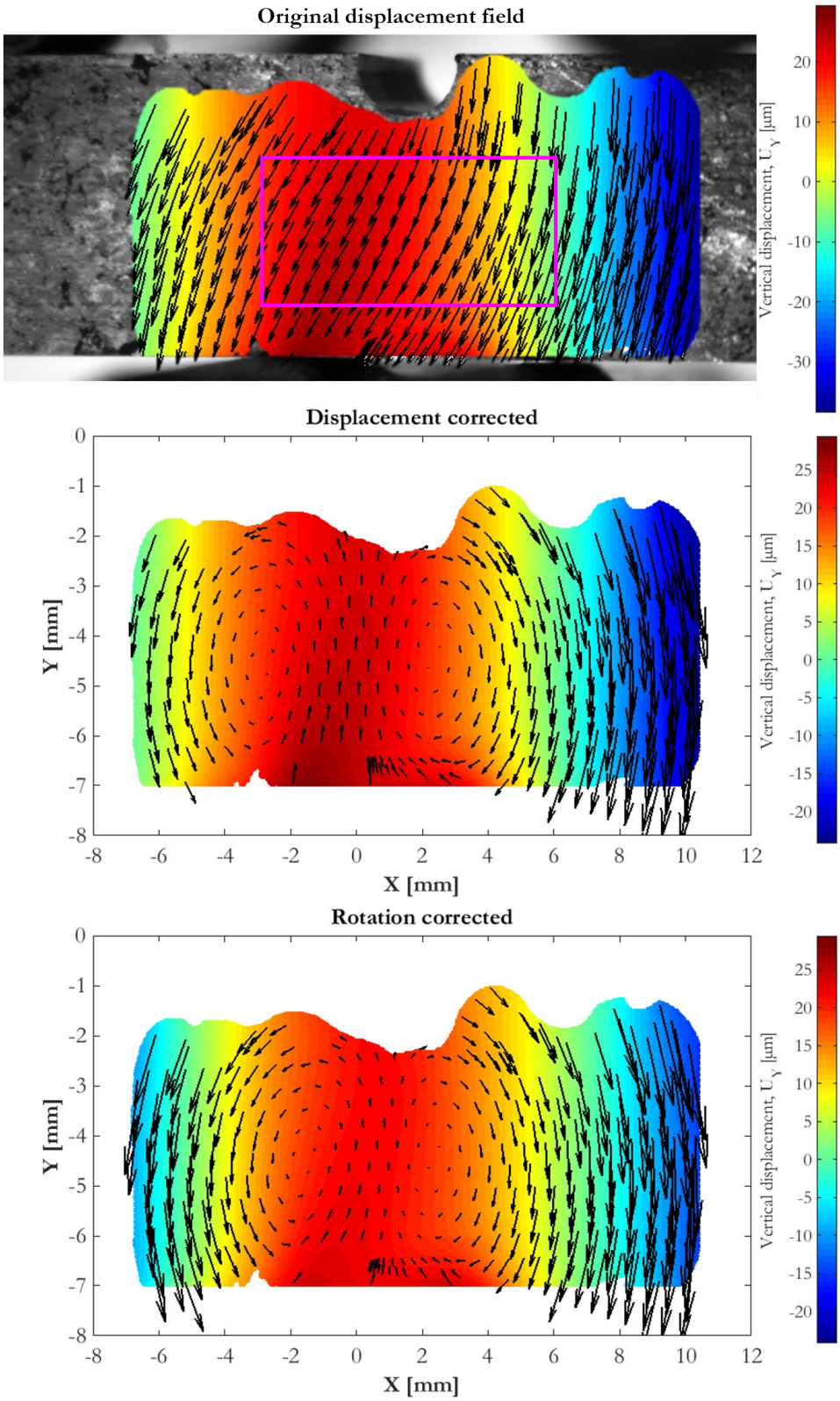


Figure 64: Stages of rigid body movement correction for DIC fields, as applied to one of the correlations of the blunt shallow sample shown in Figure 61. Arrows indicate the two-dimensional vector displacement, though for clarity only a subset is shown, with the colour maps displaying the U_Y components. Top *The as-correlated data superimposed on one frame of the original stereo image, with the confident core region indicated by a pink rectangle;* Middle *the mean displacement is removed to correct for RBD*; Bottom *the rotation is then removed, to show the underlying deformation behaviour.*

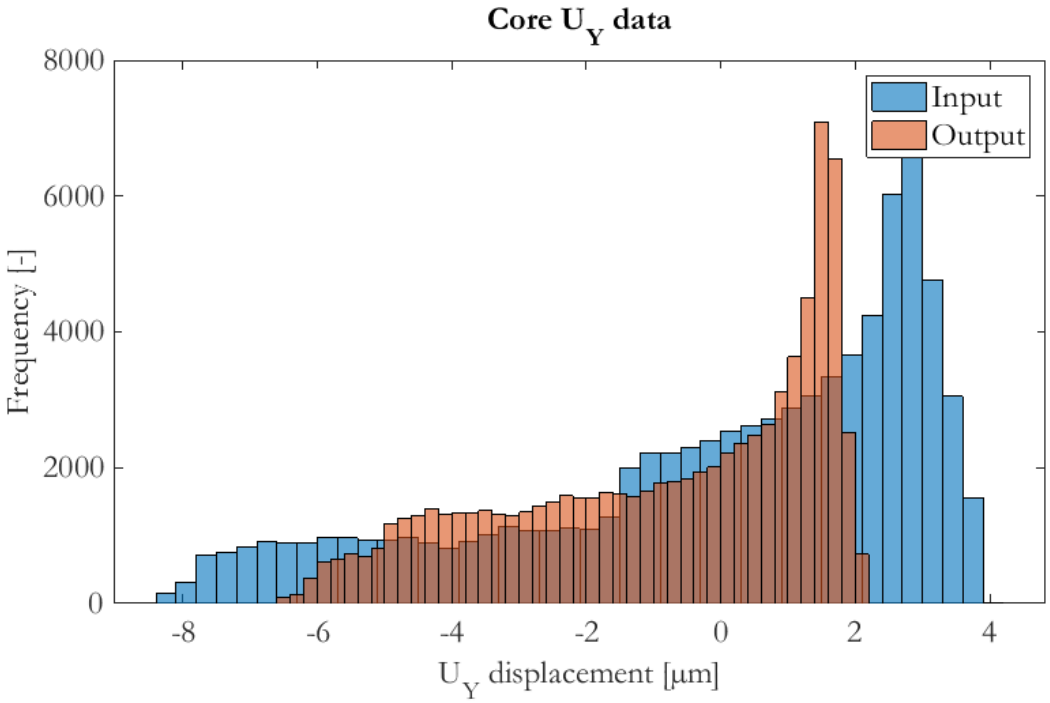


Figure 65: Histograms of the U_Y distributions in the confident core subset of vectors before ("Input") and after ("Output") the rotation correction, for the U_Y vector fields in Figure 64, showing that the correction reduced the breadth of the distribution, as required.

III.3.2.2.4 Parameterising specimen deformation

The stereo DIC is used to define the specimen deflection as a function of load, rather than using the crosshead extension, which, due to the load train compliance, is not a direct measurement. Deflections were parameterised in terms of the horizontal surface profile 1.33 mm from the smooth face (when unloaded), indicated on the vector map in Figure 66. The map shows the vector locations in the RBM-corrected stereo correlation fields (in blue, from Figure 64), with the vectors within the confident core coloured by surface height; the confident core omitted vectors within 1 mm of the notch tip or far face in the *Y*-direction, and more than 5 mm either side of the notch in the *X*-direction. Vertical displacements (U_Y) along the horizontal profile were selected as the deflection descriptor, rather than the conventional relative roller displacement due to shadows in the stereo images caused by the rollers, which prevented reliable DIC in these regions.

For the profile, Figure 66 shows the variation in Z-coordinate and each of the orthogonal displacement components. Most of the deflection was in the Y-direction, with a U_Y range here of c. 20 μm, four times greater than U_X. Maximum U_Y ranges (for the unnotched beams at pop-in) were c. 70 μm. The U_Y profile may be summarised as an arc between the inner rollers, and linear between the inner and outer rollers. The measured profiles were not entirely symmetric, with this specimen showing a greater displacement above the left inner roller than the right (as viewed). Such behaviour existed despite the jig's degrees of freedom and may be explained by a minor discrepancy in the roller positions about the centre. Since the behaviour of the material between the inner roller was most sensitive to any poor positioning or material damage during loading, the deflection was characterised in terms of the mean (absolute) gradient of the linear regime, dU_Y/dX. Specifically, dU_Y/dX was measured as the mean in the horizontal domain X = [4.0, 5.0] mm either side of the notch tip, as indicated on the U_Y profile in Figure 66.

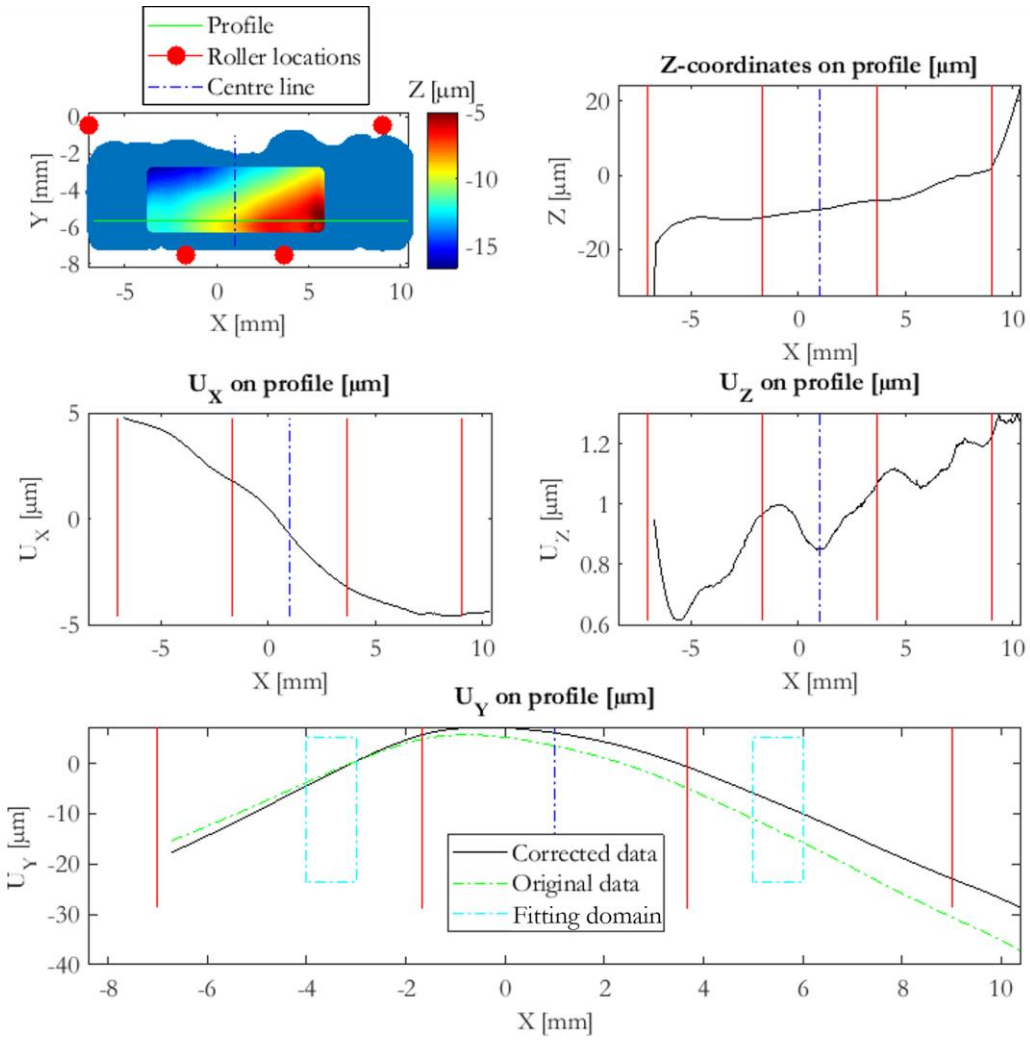
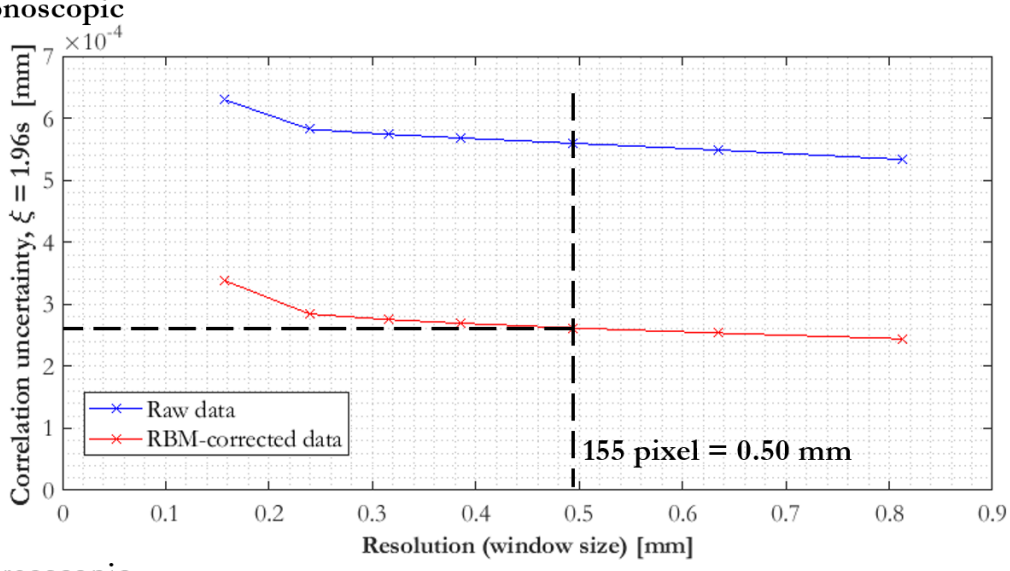


Figure 66: Displacement profiles for the corrected displacement field shown in Figure 64 and Figure 65. The region of valid DIC vectors for the sample is indicated in blue on the map Top-left, as per *Figure 64* Top*, with the core subset region indicated by the contour map (coloured by Z-coordinate). Along the profile indicated the Z-coordinate, and U_X, U_Y and U_Z displacements are plotted on separate graphs. In each plot the roller locations and centre-line are indicated, for reference. The U_Y graph shows the raw and corrected profiles and indicates the domains ("Fitting domain") over which the profile was averaged to calculate the gradients for fitting the deflection. The diameters of the red points indicating the roller locations in the vector map are not to scale for the size of the rollers.*

III.3.2.2.5 Correlation uncertainty

The uncertainties in the correlation and corrections of the two DIC processing routes were determined by (20). For the processing settings described in § III.3.2.2.1 and § III.3.2.2.2, the 95%ile uncertainty for the monoscopic DIC displacement was $\xi_{Corr,Mono}$ = 0.25 µm, equivalent to 0.4 mStrain, and for the stereo DIC was $\xi_{Corr,Stereo}$ = 6.7 µm. The sensitivity of the two uncertainties to interrogation window size is shown in Figure 67.

a) Monoscopic



b) Stereoscopic

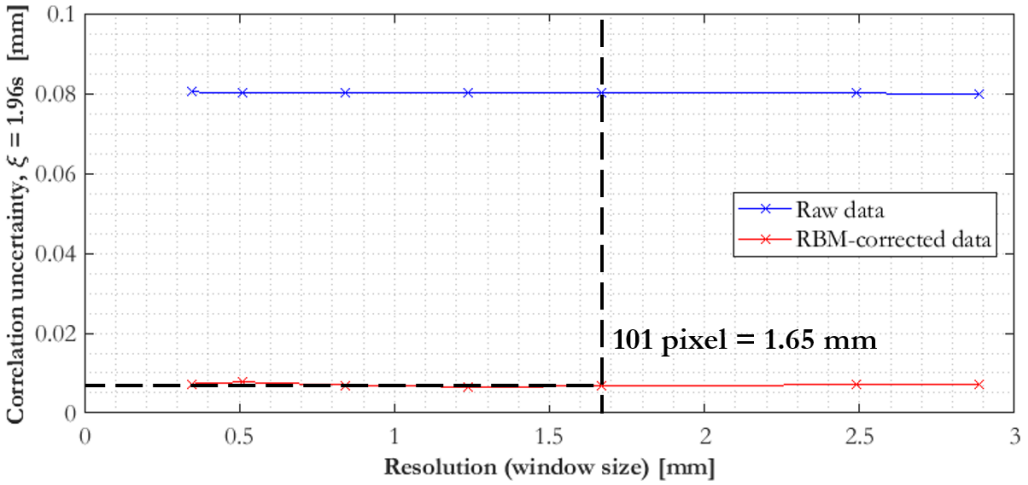


Figure 67: Uncertainty in digital image correlation and correction calculated from a rigid body motion for (a) monoscopic, and (b) stereoscopic.

III.4 Finite element simulations

III.4.1 Geometry and boundary condition definition

A quarter-symmetry geometry was generated for each of the specimen designs, with dimensions in Figure 54 and Table 4. The sharp notch tip radii agreed with the mean measured values (R = 0.05 mm), but no correction was made for the over-cutting of the shallow blunt notches, as the numerical errors arising from this inaccuracy were deemed less than the experimental error. Loads were applied via rigid rollers with frictional contacts (small-sliding formulation with a coefficient of friction of 0.1 [166]) that emulated the experimental degrees of freedom. Quadratic meshes were generated with refinement around the notch tips, the far face of the ligament and the roller contact regions, as seen in Figure 68(a) which shows the example simulation for the shallow blunt notch tip specimen analysed in § III.3. The mesh refinement was defined such that strain increments were ≤ 10 % between nodes at the expected pop-in deflections with a LE material model. Hexahedral elements were used for the blunt and unnotched geometries with the element edge lengths varying from 0.05 to 0.50 mm, but a greater level of refinement was required for the sharp-tip geometries, so a tetrahedral mesh was used with element edges as small as 0.002 mm. Initial FE modelling was performed in Simulia's *Abaqus Standard* version 6.14, and used an LE simulation with the tensile Young's modulus, E_{TLE} = 11.93 GPa, from Marrow *et al.* [88] (see also § III.4.2). A constant Poisson's ratio, ν = 0.21, was used for all simulations.

Figure 68(b) shows the pattern of the U_Y displacement in a loaded beam and indicates the location of the profile in the 3D system. Assuming the material and test rig had a Hookean response, the applied crosshead displacement was directly proportional to the specimen curvature (and dU_Y/dX) and independent of stiffness. The constant of proportionality was unique to each geometry and assumed to be valid for Gilsocarbon under all applied loads. Each of the geometries were modelled under displacement control, by vertically displacing the outer roller. The roller displacement for which the simulated and empirical dU_Y/dX at pop-in were in agreement was termed $\vec{U}_{Roll}$. A scaling parameter, γ, was then defined as the ratio of $\vec{U}_{Roll}$ to δ_C.

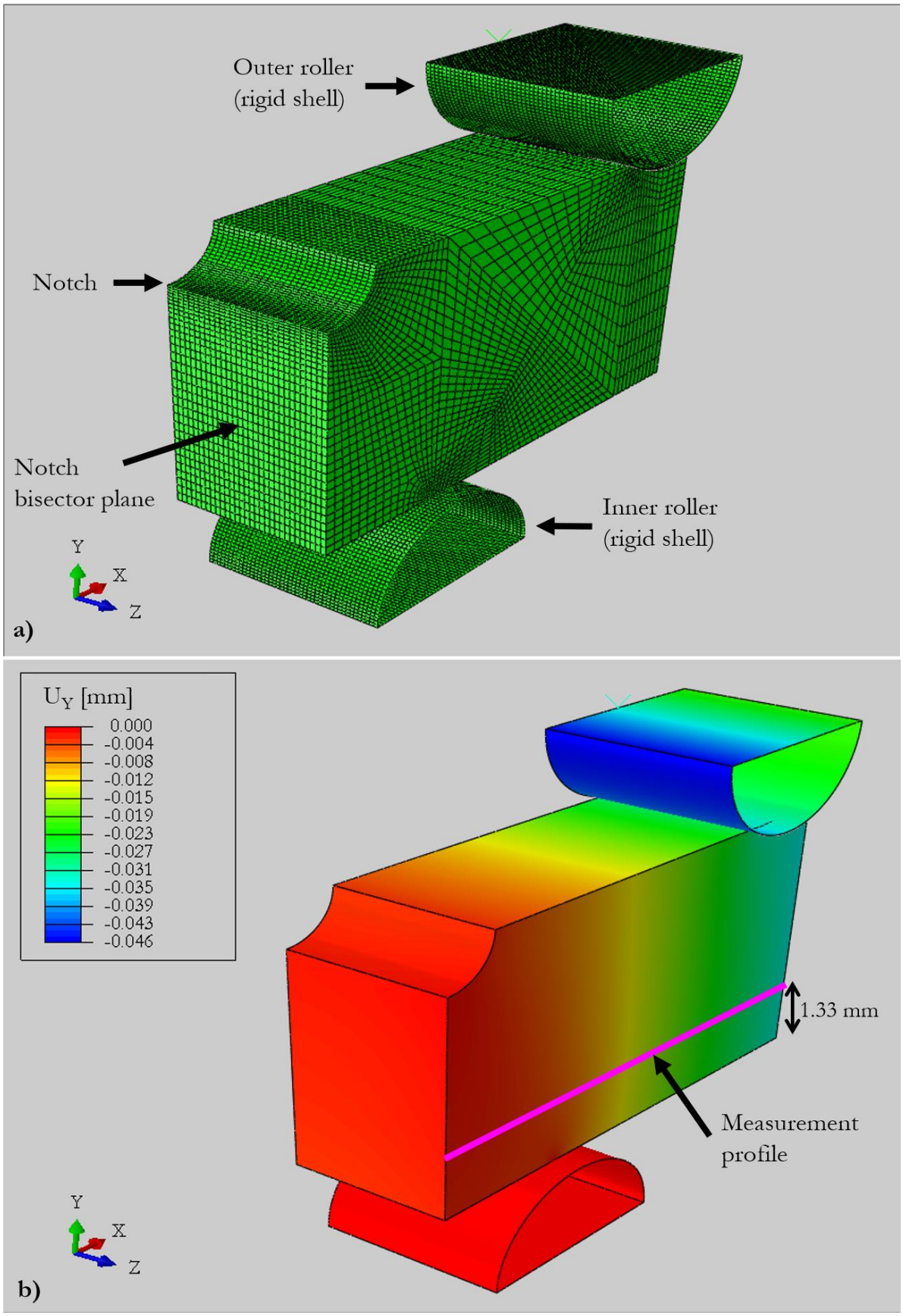


Figure 68: Quarter-symmetry finite element simulation of a shallow blunt notch tip specimen, with (a) mesh showing significant refinement around the notch tip and the roller contact regions, and (b) pattern of U_Y displacements and the location of the measurement profile on external surface.

III.4.2 Stiffness models

One purpose of the FE simulations is the prediction of stress and stress-dependent properties, which are sensitive to the stiffness definition. Strain prediction from a LE simulation is independent of stiffness, provided that an order-of-magnitude estimate of Young's modulus is used. To predict stress an accurate modulus is necessary. For non-linear simulations, accurate definition is necessary for both stress and strain prediction. It will be demonstrated that a simple LE simulation using E_{TLE} is insufficient to understand the behaviour of graphite with increasing strain, due to an apparent stiffness degradation. The simulations were therefore run using both linear elastic (§ III.4.2.1) and a non-linear elastic UMAT (§ III.4.2.2) stiffness.

III.4.2.1 Linear elasticity

The deflection-matched simulations all overestimated the reaction force on the rollers by up to 73 %, as detailed in Table 6. The simulations in poorest agreement were the unnotched beams, Specimens 9 and 10 in the table. For Specimen 9, reaction load as a function of increasing dU_Y/dX (and also $\vec{U}_{Roll}$) was plotted in Figure 69(a). The green crosses are for progressive E_{TLE} simulation iterations as the roller displacement was increased linearly from zero to $\vec{U}_{Roll}$; equivalent roller displacement is indicated on the lower X-axis. The FE-predicted load increased from zero linearly with dU_Y/dX (and hence $\vec{U}_{Roll}$). The black circles are the DIC series data and show non-linear behaviour. At low deflections, the E_{TLE} simulation was a good predictor of the experimental loads, but the curves diverged with progressive deflection, suggesting a continuous degradation in apparent stiffness. To account for the degradation, the Young's modulus was proportionally reduced (by a factor of 0.57) such that load agreement was achieved at the critical load (F_C = 292 N, when dUY/dX= 6.23 μm.mm^{-1}); the load-response of the linear elastic simulation with this fitted modulus, E_{FLE} = 6.82 GPa, was also plotted in Figure 69(a) using blue crosses. The E_{TLE} and E_{FLE} simulations were bounding cases on the specimen modulus (to pop-in), and the evolution between the two is shown in Figure 69(b), where the ratio of the experimental and E_{TLE}-simulated loads was used to calculate a normalised stiffness. All the geometries showed a comparable stiffness degradation, and a unique E_{FLE} was calculated for each specimen, as listed in Table 6.

To calculate the mean properties each geometry, the remainder of the specimens in each geometry were assumed to obey the same linear relationships so that the property distribution could be scaled. For each geometry, γ and the failure moduli were defined as the average for the two specimens weighted by their positions within the experimental F_C distributions (assuming normal distributions), see Table 6. The estimated moduli values at crack initiation ranged from 6.90 ± 1.93 MPa to 8.20 ± 2.52 MPa (excluding the deep notched geometries).

Stress, strain and strain energy density predictions will be presented in § III.4.3.

Table 6: Fitting parameters for the linear elastic models, using the tensile and fitted elastic moduli, and estimated mean properties for each geometry at the critical load.

Geometry	Specimen	Target load, F_C	Target gradient, dU_Y/dx	Fitted roller displacement, $\vec{U}_{Roll}$	Displacement ratio, γ	Load simulated with E_{TLE}, F_{TLE}	Fitted modulus, E_{FLE}
		N	**[µm/mm]**	**[µm]**	**[mm/mm]**	**[N]**	**GPa**
SF-B100	Specimen 1	244	5.43	-40.2	0.36		7.90
	Specimen 2	218	4.49	-33.6	0.34		8.54
	Est. population mean	224	n/a	-36.6 ± 10.9	0.35 ± 0.03	325	8.20 ± 2.52
SF-B300	Specimen 3	106	6.25	-38.2	0.50		8.07
	Specimen 4	85	5.66	-34.7	s0.51		7.13
	Est. population mean	94	n/a	-35.6 ± 8.8	0.51 ± 0.01	140	8.00 ± 3.34
SF-S100	Specimen 5	209	4.56	-34.4	0.35		7.76
	Specimen 6	207	5.14	-38.4	0.37		6.80
	Est. population mean	205	n/a	-34.8 ± 9.3	0.36 ± 0.04	314	7.80 ± 1.62
SF-S300	Specimen 7	90	5.17	-32.3	0.51		7.42
	Specimen 8	75	4.56	-28.6	0.53		7.04
	Est. population mean	88	n/a	-31.6 ± 5.1	0.51 ± 0.03	137	7.68 ± 2.27
SF-U000	Specimen 9	292	6.23	-48.2	0.37		6.82
	Specimen 10	274	5.64	-43.9	0.37		7.07
	Est. population mean	341	n/a	-55.2 ± 10.8	0.37 ± 0.00	590	6.90 ± 1.93

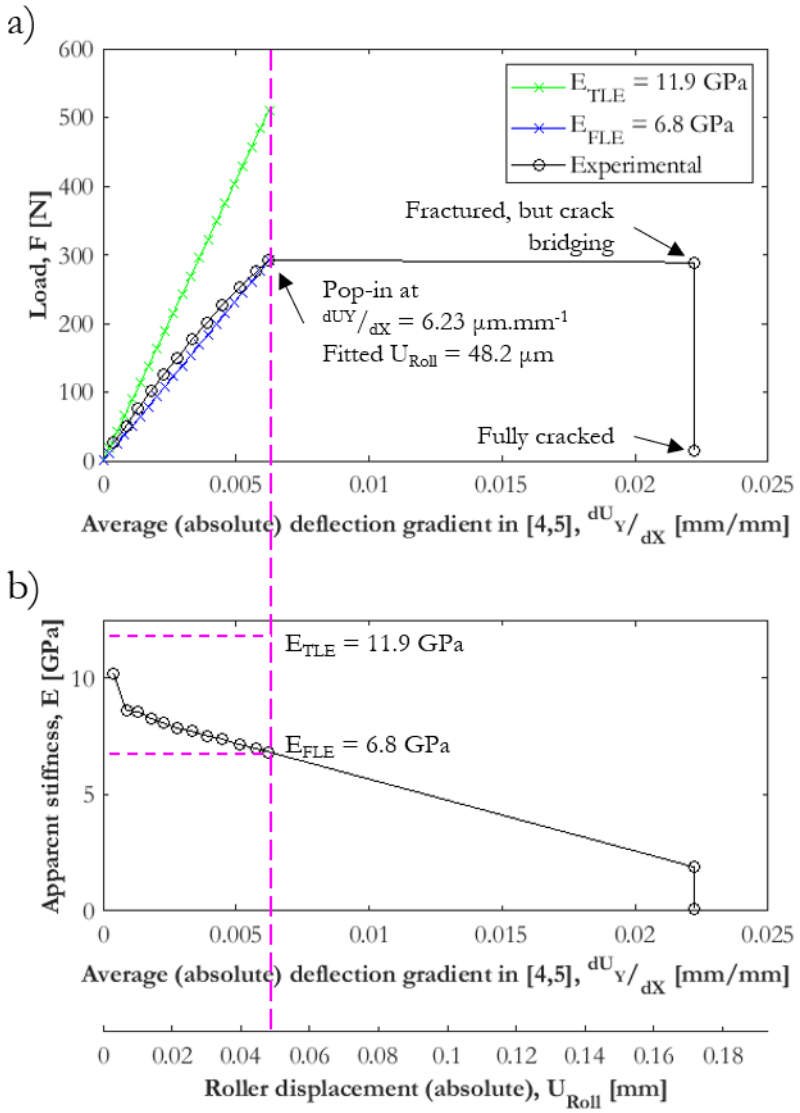


Figure 69: Effect of increasing deflection on an unnotched beam (Specimen 9 in Table 6), measured as either the deflection profile gradient dU_Y/dX, or equivalently $\vec{U}_{Roll}$, and the effect on (a) load and (b) apparent linear elastic stiffness. In (a), linear elastic FE predictions are given for the bounding moduli: the tensile modulus, E_{TLE} and pop-in fitted modulus, E_{FLE}.

III.4.2.1.1 Comparison to standard FE method

The presented method of fitting the beam's gross deflection and then adjusting the stiffness to match the failure load is a non-standard method of calculating stress in a flexure sample. A more common method is to simulate a nominal $\vec{U}_{Roll}$ and tensile stiffness (11.93 GPa) and extract the maximum predicted stress. The predicted stress is then scaled by the ratio of the predicted and experimentally-measured load; alternatively, the simulation may be run in load-control to the same effect. The standard approach relies on only the linear relationship between F_M and the peak stress. For maximum stress calculations, the two methods are equivalent, since F is also directly proportional to dU_Y/dX, which is in turn proportional to $\vec{U}_{Roll}$ (see Figure 69).

For example, the maximum stresses at pop-in for the specimen fitted in Figure 69 (unnotched Specimen 9 in Table 6) were 22.3 MPa and 39.0 MPa using the fitted and tensile moduli respectively, but these values were based on *a priori* knowledge of the displacement field, and particularly that $\vec{U}_{Roll}$ = 48.2 μm. If, instead, the beam were modelled with a nominal $\vec{U}_{Roll}$ = 100 μm, the predicted maximum stress would be 80.9 MPa, at a load of 1,060 N. Re-scaling the model to match the experimental load of 292 N, the predicted stress would be 22.3 MPa, in agreement with the fitting routine. This rescaling routine is equivalent to running the model to a pre-set point on the green curve in Figure 69, then moving along the green curve to achieve the same load as the target load.

The standard method is an underdetermined solution, and so does not guarantee equivalent strains. Therefore, the more sophisticated fitting of dU_Y/dX was employed for most geometries. In fact, for the specimens tested here, the tensile stiffness curve was always as under-prediction of experimental deflection at pop-in (load-matched). dU_Y/dX were not available for the deep notched beams so the standard method was used to predict the mean maximum stress for these geometries.

III.4.2.2 UMAT: Non-linear elastic stiffness

The non-linear elastic UMAT routine defined by Barhli *et al.* and based on the results of Marrow *et al.* was defined in § II.3.2. This model defined a Young's modulus (E_{UMAT}) that degraded as the tensile maximum principal strain increased, but was invariant in compression. The strain limits were defined based on the empirical findings, and also upon numerical and practical considerations for modelling; with a degradation in stiffness by a factor of 10^5, the most strained elements lost numerical stability when the $\epsilon_1 \gtrsim 0.02$, resulting in high fictitious strains (see Figure 70). A single UMAT simulation was run for each geometry. At $\vec{U}_{Roll}$, the maximum strains in the linear elastic FE models were below the strain threshold, but for the UMAT simulations excessive strains were predicted in the least stiff regions of the notched geometries. For simulations that ran beyond the threshold, the model reliability was degraded; generally, for areal calculations, up to 12 % of the nodes exceeded the strain threshold in the entire model, and less than 5 % in the area of interest was deemed tolerable. For each simulation, details on the state of the model at the iteration at which the model begins to exceed the strain limit (the 'high-accuracy iteration limit' or HAIL) and the final iteration were recorded in Table 7. The sharp notched beams were most affected, with a HAIL at c. 50 %$\vec{U}_{Roll}$. To match the dU_Y/dX, the models would generally be required to run beyond the HAIL.

On average, at 50 %$\vec{U}_{Roll}$ the UMAT simulations overestimated the load by 30 ± 2 %. No attempt was made to alter the UMAT modulus definition to achieve load agreement. The pop-in state for the simulations was instead selected as the iteration that most closely predicted F_C ('load-matched'), described in Table 7. Hence, the mean specimen deflection for the UMAT simulations was 29 % less than the empirical and linear elastic simulations.

Where the HAIL was exceeded to achieve load matching, the strain of individual elements (averaged at the nodes) was capped at 0.021 for subsequent calculations.

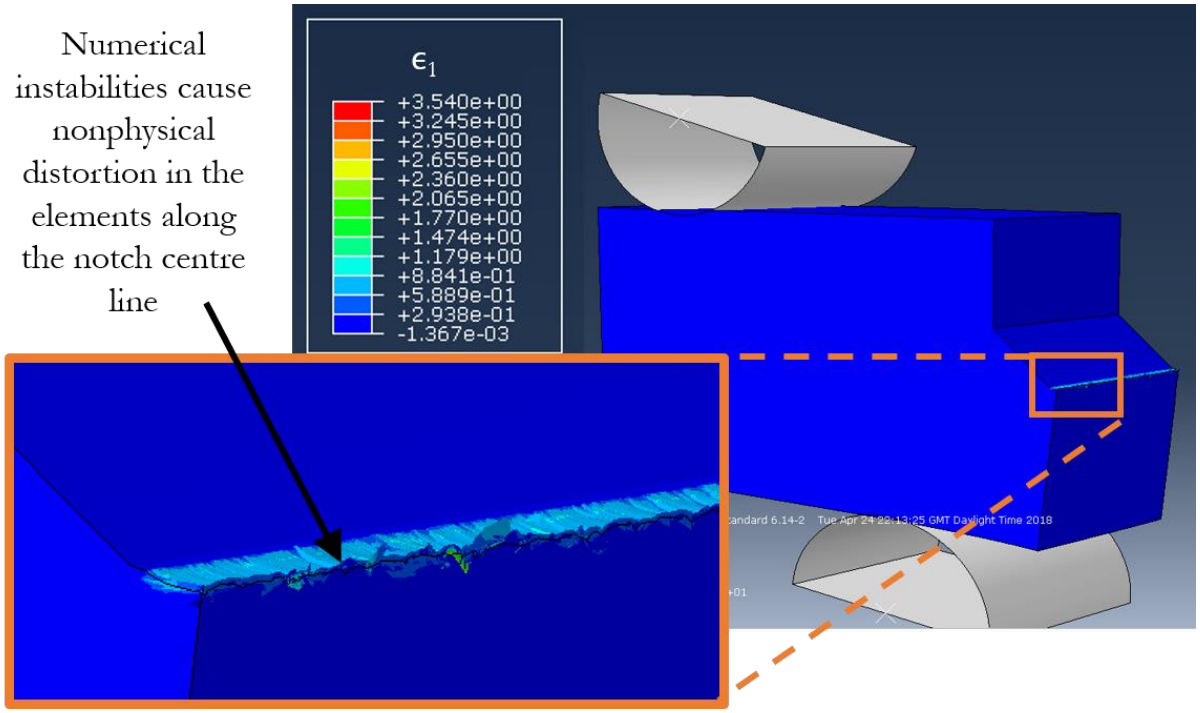


Figure 70: When simulating with the UMAT stiffness definition with the $\vec{U}_{Roll}$ derived for the linear elastic models, the elements in the most strained regions lost numerical stability, and deformed non-physically. Point measurement of these elements was therefore nonsensical, and the accuracy of the rest of the model was degraded. Element definition is not shown for clarity.

Table 7: Properties of the UMAT simulations. Numerical instability caused model breakdown for applied roller displacements beyond the high-accuracy iteration limit (HAIL). UMAT simulations were instead load-matched to F_C and the control properties are given for each specimen in Table 6. Load-matched displacements are highlighted in red where they exceed the corresponding HAIL displacement.

Geometry	**$\vec{U}_{Roll}$ Iteration**	**Properties at HAIL (Roller displacement ≤ $\vec{U}_{Roll}$)**			**Load matched iteration (Roller displacement ≤ $\vec{U}_{Roll}$)**				
	Iteration number	**Iteration Number**	**Roller displacement**	**Load**	**Specimen #**	**Iteration number**	**Roller displacement**	**Load**	**Load error (c.f. *Fc*)**
	[-]	**[-]**	**[µm]**	**[N]**	**[-]**	**[-]**	**[µm]**	**[N]**	**[N]**
Blunt, shallow (SF-B100)	20	18	-0.036	310	1	15	-0.030	250	6
					2	13	-0.026	219	1
Blunt, half-depth (SF-B300)	21	20	-0.037	124	3	16	-0.030	106	1
					4	13	-0.024	86	3
Sharp, shallow (SF-S100)	22	9	-0.013	113	5	16	-0.025	212	3
					6	16	-0.025	212	6
Sharp, half-depth (SF-S300)	22	9	-0.013	52	7	17	-0.025	92	1
					8	13	-0.019	75	0
Unnotched (SF-U000)	12	12	-0.046	434	9	8	-0.031	305	13
					10	7	-0.027	259	15

III.4.3 Simulation predictions

To use FE modelling for material property extraction or response prediction, the selected models must agree with the available empirical data. FE predictions for the linear elastic and UMAT material models will be shown to agree with the empirical displacement fields (§ III.4.3.1) and strain profiles (§ III.4.3.2), and example stress maps for different geometries presented (§ III.4.3.3).

III.4.3.1 FE Displacements

Line profiles of the displacement components from the simulations were compared to the stereoscopic and monoscopic DIC to ensure consistency. For the pop-in load of Specimen 2 in Table 6, the mean DIC, linear elastic and UMAT simulated displacements along the line profile shown in Figure 68(b) are compared in Figure 71 as the (a) U_Y and (b) U_X components. The 'mean DIC' profiles are the point-wise average of the 'left' (-ve) and 'right' (+ve) halves of the profile, to account for asymmetry (see Figure 66); the U_X profiles are the means of the absolute values. Where they overlapped, the two DIC datasets showed excellent agreement, despite the independent measurements.

At any given load until F_C, the profiles for the linear elastic simulations compared well with the experiment; after fracture the simulations were invalid, as the crack was not modelled. Figure 71(a) showed that between the inner and outer roller, the empirical and simulation U_Y curves were parallel, with the simulation curve appearing slightly offset in X. Within the inner roller region, the curves were almost identical, and the differences were well within the bounds of the two halves of the DIC displacement for all X. For the much smaller U_X component, overall the trends are similar in Figure 71(b), but there are minor differences between the LE simulation and the DIC, particularly around the inner roller. The consistency of the U_Y curves was considered a demonstration of the fit to the entire model, and the differences in the U_X were not considered significant. Since the geometries and the profiles outside of the gradient fitting regions also agree, the use of the LE FE models is supported.

As the UMAT simulations could not be run to achieve the correct deflection gradient, the deflection was expected to be lower than in the experimental data. The load-matched UMAT profiles in Figure 71 were clearly an underestimation of the sample deflection; this was the case for every sample.

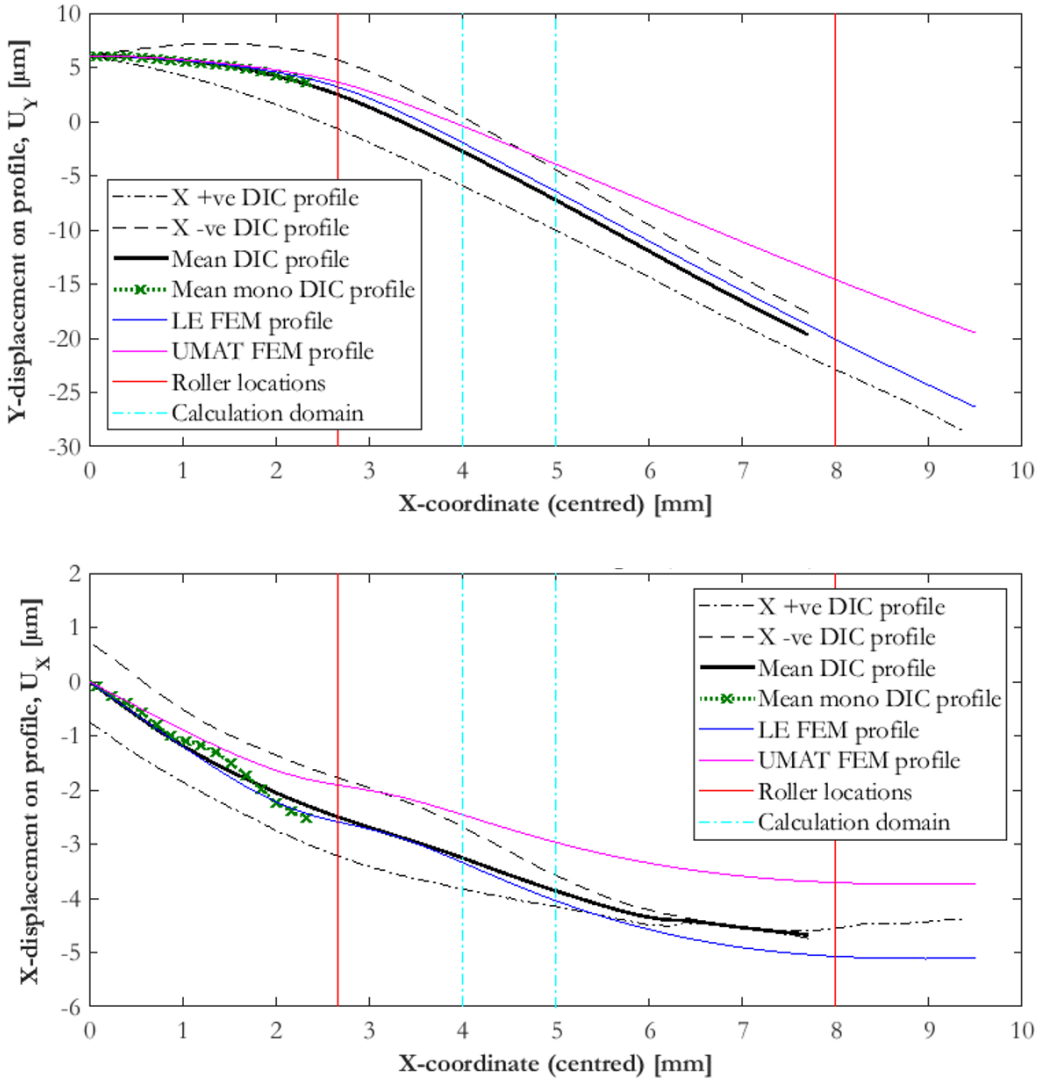


Figure 71: Displacement component (U_Y and U_X) half profiles from stereo and monoscopic DIC and linear elastic and UMAT finite element simulations for the shallow blunt notch tip specimen at pop-in analysed in Figure 64-Figure 66, with the notch centred at X = 0 mm. The two halves of the stereoscopic DIC profile 'X +ve' and 'X -ve' are reflected back about the centre line for clarity and averaged in the 'mean DIC' profile; for clarity only the mean monoscopic DIC profiles are shown. The gradients of the profiles (dU_Y/dX) are calculated in the X = [4.0, 5.0] mm domain indicated.

III.4.3.2 FE Strains

The simulated maximum principal strains at pop-in for one specimen of each geometry are shown in Figure 72 for the linear elastic models, and in Figure 73 for the UMAT models. The strains shown for the blunt shallow sample in Figure 72 were the equivalent of the empirical data shown in the 218 N frame in Figure 63, though the contours are presented at different with different limits. Qualitative agreement was observed, though the simulated patterns are more homogeneous and smoother. The 218 N map is replotted in Figure 74(a) showing the location of profile AB shown on Figure 72. ϵ_1 along this profile predicted by the LE and NLE simulations were compared with the monoscopic DIC in Figure 74 and Figure 75. In each geometry, the largest orthogonal component of strain in the beams was the axial strain (ϵ_{XX}).

For both simulation models, the unnotched beams (for Specimen 9) show a broad 3D prismatic region of increased tensile strain between the inner rollers. Heightened strains are seen at the roller contacts. The LE profile in Figure 75(a) shows that ϵ_1 from the 'far face' (point A) to the beams' neutral axis (c. 3 mm) was approximately zero, then smoothly increased to a maximum value of ϵ_1 = 2.9 mStrain. The UMAT profile was similar but only reached 1.8 mStrain.

For the notched beams, outside the inner rollers the behaviour is comparable with the unnotched beams for both material models. Strain concentrations are seen around the notch tips. The concentration regions were broader around the blunt notches than the sharp notch tips, and were always seen in the 3D images to be well-contained by the inner roller region. The profiles for the blunt notch tip specimens show that the LE and UMAT strain predictions were almost identical, despite the different deflections used. For the sharp notch geometries, the LE simulation predicted a monotonic and smooth but very rapid increase in strain ahead of the notch, with a greater maximum strain than the blunt notches. The UMAT 3D simulations also predicted a strong strain concentration ahead of the sharp notch tip. The peak UMAT strains were at a maxima ($\epsilon_{1,max}$ = 10 mStrain on the profiles) with the strain then began to reduce towards the tip. Near the tip the strains behave unrealistically, reaching $\epsilon_1 \gg$ 22.4 mStrain, and continuity is lost between neighbouring nodes, with almost zero strain on the inclined notch face. This behaviour is due to passing the HAIL. The maxima appear to be a real phenomenon of the stiffness definition, but the absolute values of the strains between the maxima and the notch tip are probably erroneous. Interpretation of the NLE strains immediately adjacent to the notch tips is therefore impossible.

To estimate the extent of the strain concentration zone, ϵCZ, in each profile a threshold of 2.9 mStrain was applied. 2.9 mStrain was chosen such that the unnotched beam had no ϵCZ. For the LE, the distance along the profile was $x_{CZ,LE} \approx$ 0.1 mm for both the sharp notch geometries, $x_{CZ,LE}$ = 0.2 mm for the blunt shallow notch and $x_{CZ,LE}$ = 0.3 mm for the blunt half-depth notch. With similar profiles, the UMAT-predicted ϵCZ for the blunt geometries are the same as the LE. $x_{CZ,UMAT}$ for the sharp notch-tip geometries was consistent at 0.2 mm, and therefore comparable to that of the blunt geometries.

Comparing strains to empirical data is a more sensitive measure for model validation than the displacement test in § III.4.3.1. For the region covered by monoscopic DIC, the ϵ_1 was well predicted for all the geometries. The DIC profiles contained small fluctuations that were not present in either simulations, but it was not possible to demonstrate whether either material model was a better predictor. The best differentiator would be to match the strains in the notch tip region, but due to the 0.5 mm border masking, this information was not present in the DIC. Based on the good agreements shown for the displacements and strains, the FE was therefore accepted as a first-order predictor.

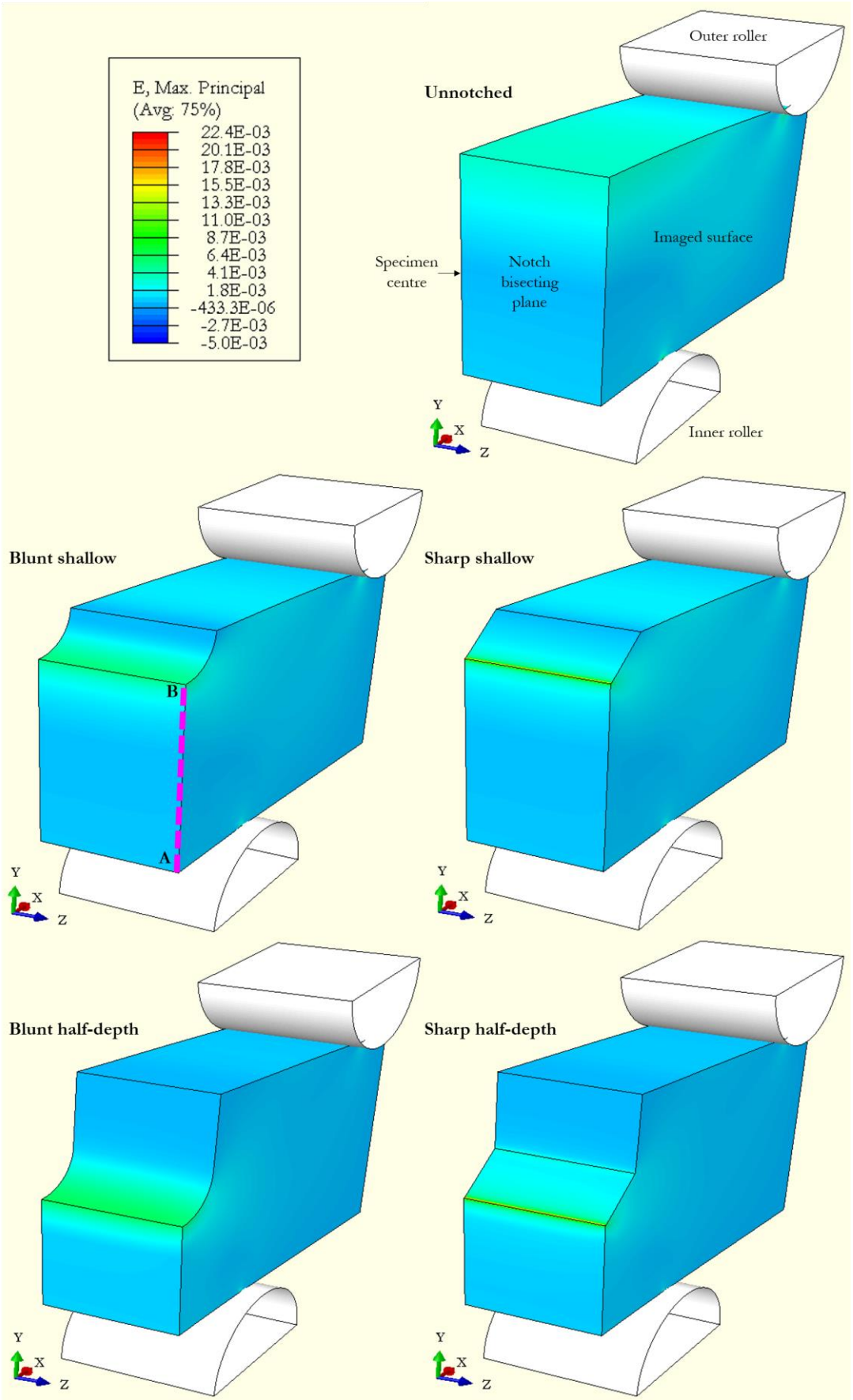


Figure 72: 3-D predictions of the maximum principal strain for one specimen of each of the geometry. See also Figure 74 and Figure 75. Deformations shown with a 10 × scale factor.

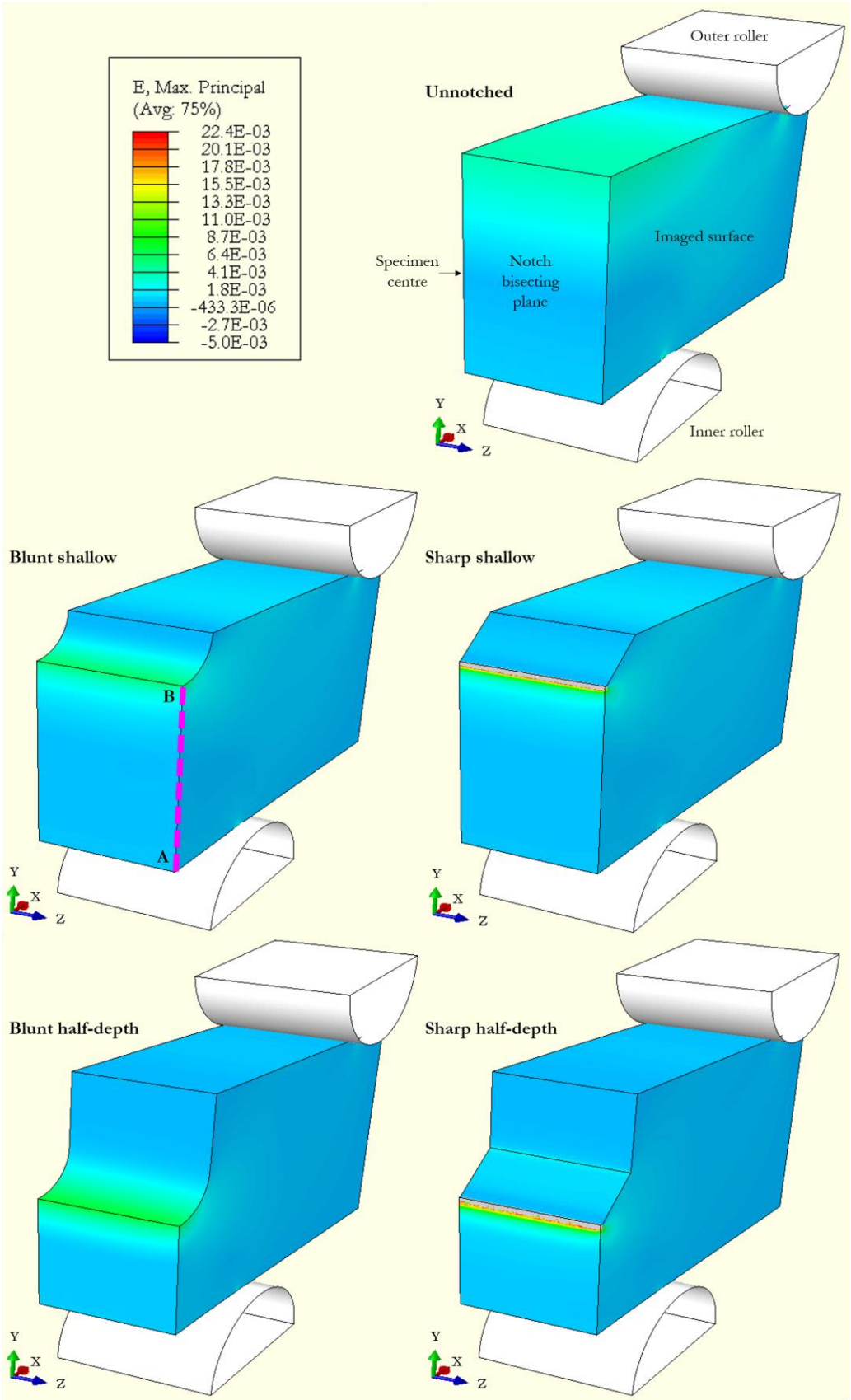


Figure 73: 3-D predictions of the maximum principal strain for one specimen of each of the geometry. See also Figure 74 and Figure 75 for the profiles along AB. Deformations shown with a 10 × scale factor.

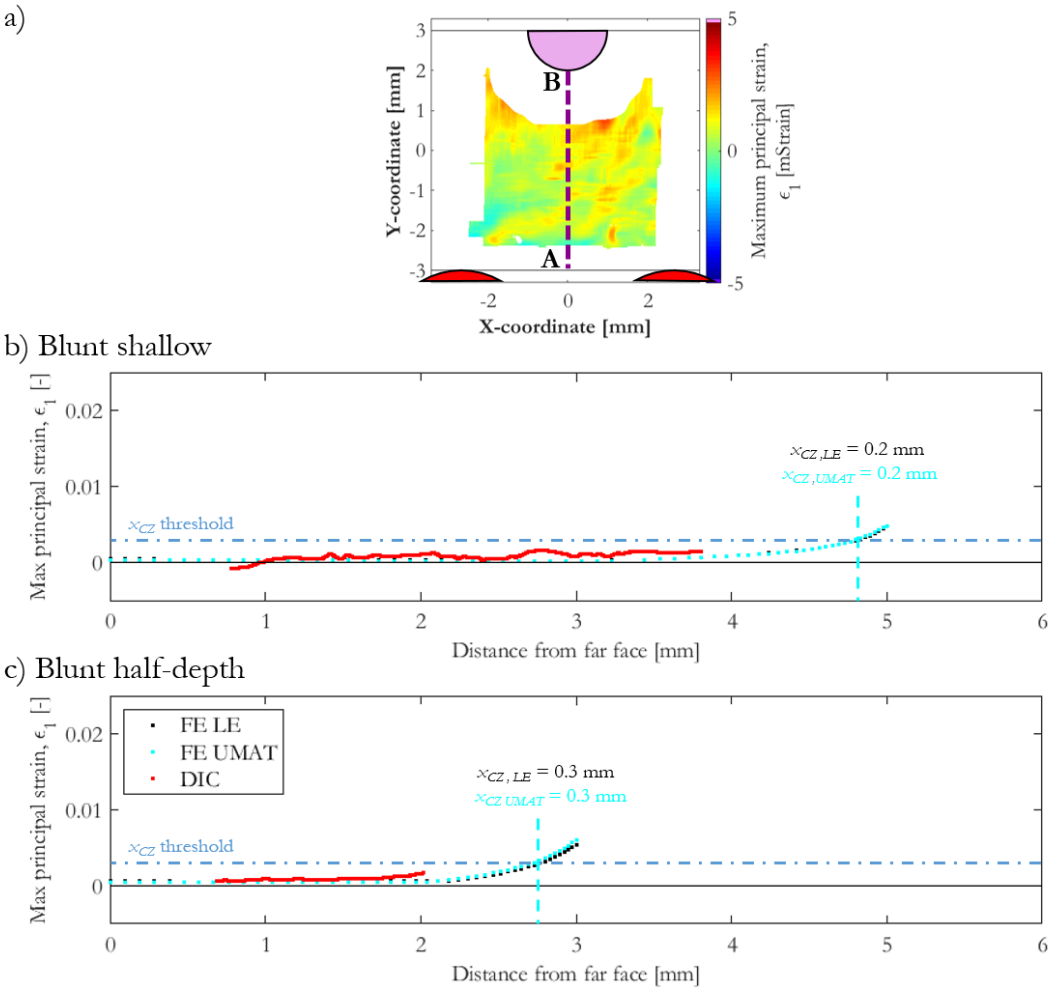


Figure 74: Maximum principal strains (ϵ_1) at pop-in along surface profile AB ahead of each notch tip/crack initiation point, predicted by the linear elastic and UMAT FE simulations (see Figure 72 and Figure 73) and measured by monoscopic DIC of one specimen in the blunt notch tip geometries. The profile definition is indicated on the monoscopic DIC strain map in (a) for Specimen 2 (blunt shallow notch tip), which replots the 218 N map in Figure 63. The notch is indicated in pink and inner roller locations in red. The extent along the profiles of the strain concentration zones (x_{CZ}) is indicated on the profiles for the two simulations. Simulation strains were capped at 0.021.

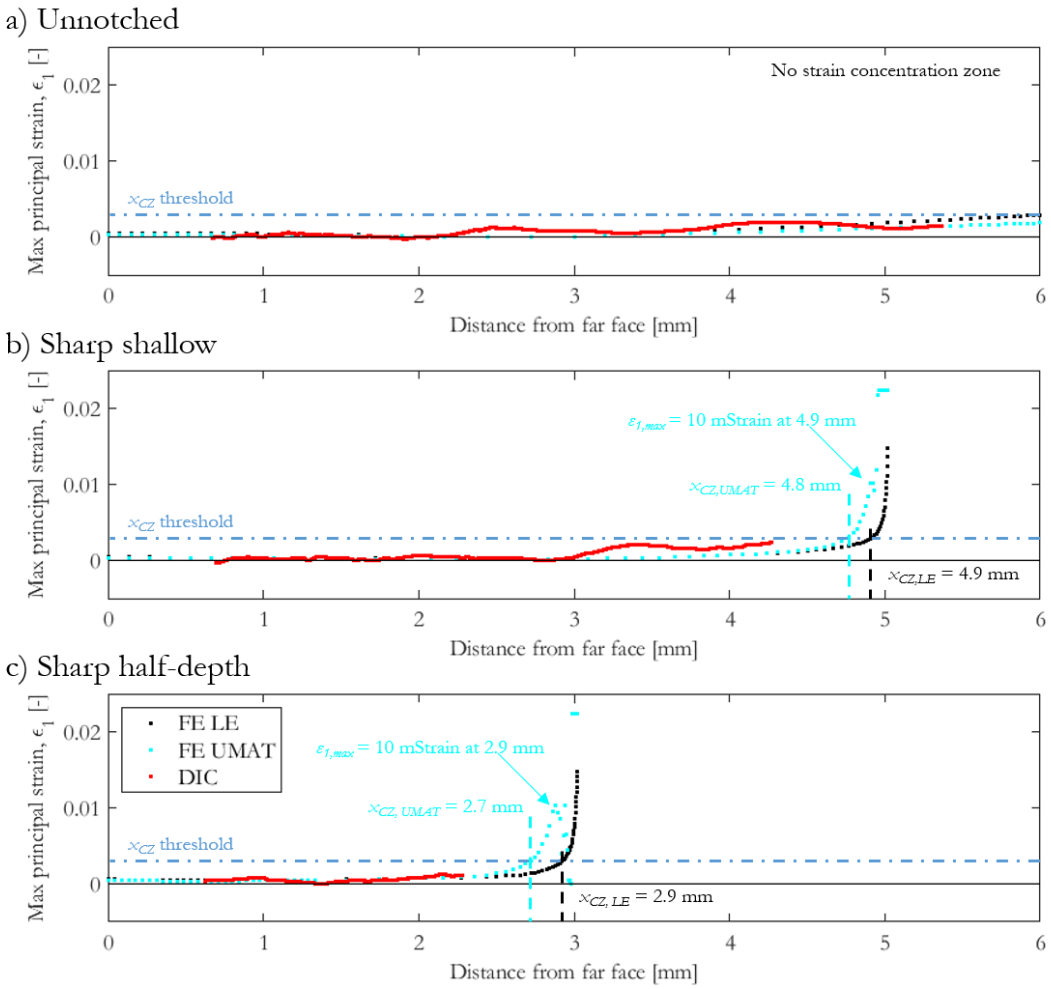


Figure 75: Maximum principal strains (ϵ_1) at pop-in along surface profile AB ahead of each notch tip/crack initiation point (see Figure 74) at pop-in, predicted by the linear elastic and UMAT FE simulations (see Figure 72 and Figure 73) and measured by monoscopic DIC of one specimen in the unnotched and sharp notch tip geometries. The extent along the profiles of the strain concentration zones (x_{CZ}) is indicated on the profiles for the two simulations. Simulation strains were capped at 0.021.

III.4.3.3 FE Stresses

The corresponding stress field predictions for the strain fields shown in Figure 72 and Figure 73 are shown in Figure 76 using the LE model with fitted moduli, and in Figure 77 using the UMAT model.

The patterns in the linear elastic predictions are unremarkable, since they are only scaled strains, and the maximum stresses occurred at the notch tip with a modulus dependent value. Similarly, the UMAT-simulated unnotched beams are similar to the LE predictions, with only a slight strain softening along the tensile edge.

For the blunt notched samples, the stress concentration region is larger, though with a lower maximum stress; the high stresses are distributed over a larger volume, and the maximum is located very close to the notch tip (within the $x_{CZ,LE}$). For the sharp notch-tip samples, the volume of the stress concentration is comparable to the LE, but the maxima has moved away from the notch tip. With limited confidence in the strains at the sharp notch tips, the stresses at the tip are uncertain.

Despite the lack of confidence at the tip, the peak stress can still be predicted based on the evolution of stresses with applied strain. Figure 78(a) shows the stress-strain response for a general 1D element with both the LE material model (with E_{TLE}), and the UMAT model. In compression, the stress response of the two models is identical. With tensile strain, the linear elastic stress rises proportionally, while the UMAT attains a natural maximum of 22.5 MPa, before decaying until the limit of the UMAT definition in (8). For the simulation iterations corresponding to low loads, Figure 78(b) shows the stress maximum at the notch tip, as in the linear elastic models. With increasing load, the strain at the tip continues to increase, rising beyond the maximum in Figure 78(a), such that the notch tip stress drops in Figure 78(c)-(h), as the region of maximum stress moves away from the notch tip, but maintains a constant value of c. 35 MPa. Despite the inability to attain the correct deflection, the maximum stress can still be predicted as 35 MPa.

The largest orthogonal component of stress in the beams was the axial stress (σ_{XX}), which is also the most important stress in Mode I fracture, and relates to the historical methods used for strength prediction. Table 8 records the maximum axial stresses for the linear elastic and UMAT finite element simulations, σ_{FLE} and σ_{UMAT}, respectively. The statistics in the table for the LE predictions are based on the scaling of the fracture distributions, assuming all properties scale linearly and have a normal distribution. For the UMAT, the properties do not scale linearly and the distributions can no longer be estimated in the same fashion, hence only the means (of the two load-matched simulations per geometry) are quoted. The stresses predicted by the UMAT for the pair in each geometry showed much better agreement than the linear elastic predictions which was a consequence of the natural stress maximum; the largest difference was 1.6 MPa for the stresses in the unnotched beams (where $\hat{\sigma}_{UMAT}$ = 22.6 MPa). The trends of stress with notch geometry will be explored further in § III.5.1.

From the definition of the UMAT (see § III.4.2.2), strain softening is only observed in regions of high tensile strain. For a notched beam, the strain concentrating effect is such that significant strain softening only occurs within a c. 1.0 mm radius of the notch tip. The rest of the beam retains the uniaxial modulus, and responds in an essentially linear elastic manner comparable to the purely linear elastic simulations. With the uniaxial modulus, the reaction forces of the simulated beams are, however, too high. Since the correct deflections cannot be reliably attained, the simulations are load-matched at reduced deflections, and the beams are strained to a lower degree. The result is that the strain patterning for most of the beam is similar to the purely linear elastic responses, but with lower magnitudes. Differences in the patterns are seen adjacent to the stress concentration, where the strain and modulus gradients conflict: softening occurs to such an extent that the elements at the tip become so compliant as to cease to carry appreciable load (and losing numerical stability in the solver). This effectively reduces the cross-section and requires a load redistribution (like the formation of a plastic hinge in a metallic system), which results in the enlarged concentration zone, and a stress maximum that moves away from the notch tip, despite the lower beam deflection. Further deflection would cause further load redistribution, keeping the same peak load.

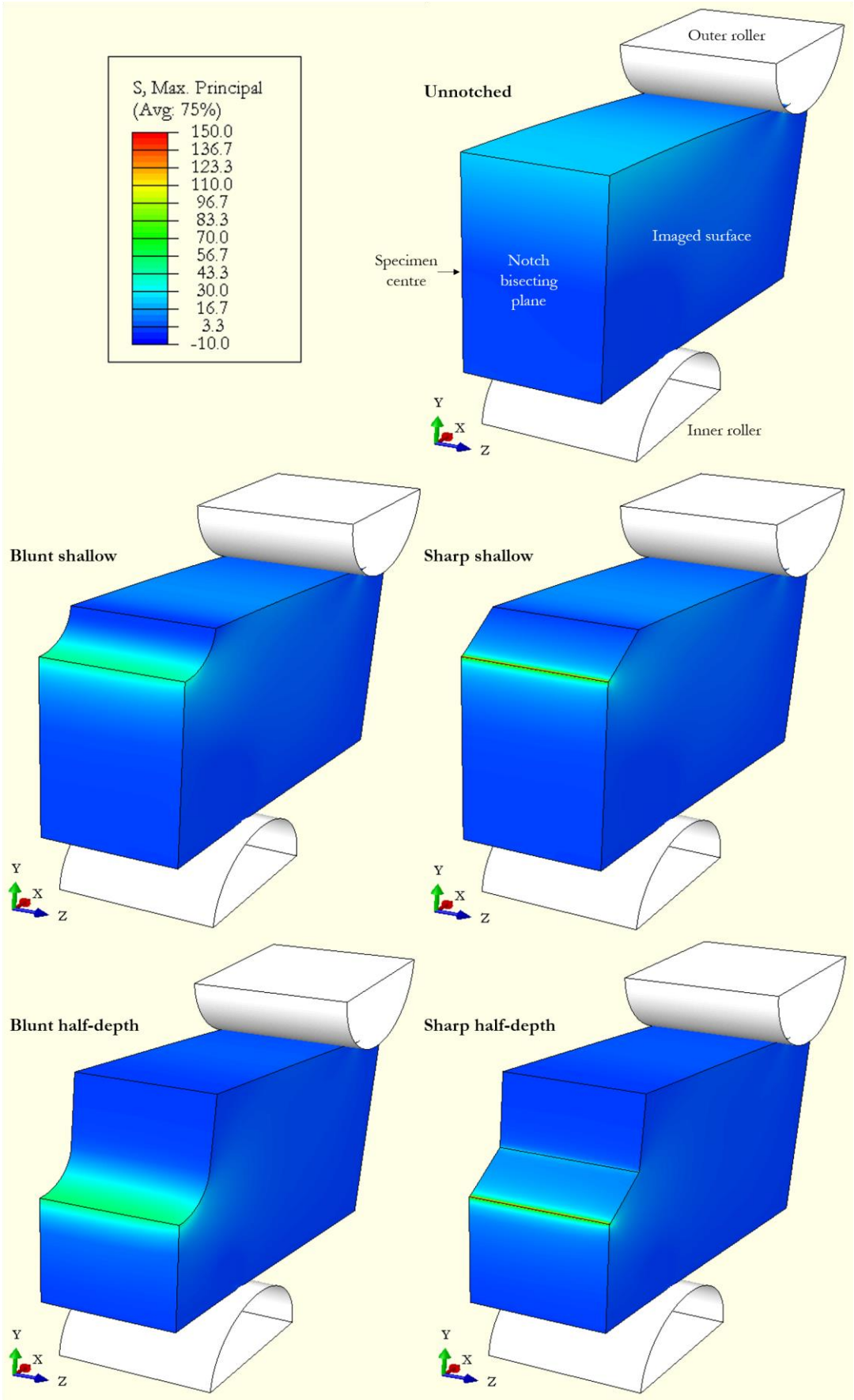


Figure 76: Linear elastic (using E_{FLE}) predictions of the maximum principal stress for one specimen of each of the geometry. Deformations shown with a 10 × scale factor, with stress in units of MPa.

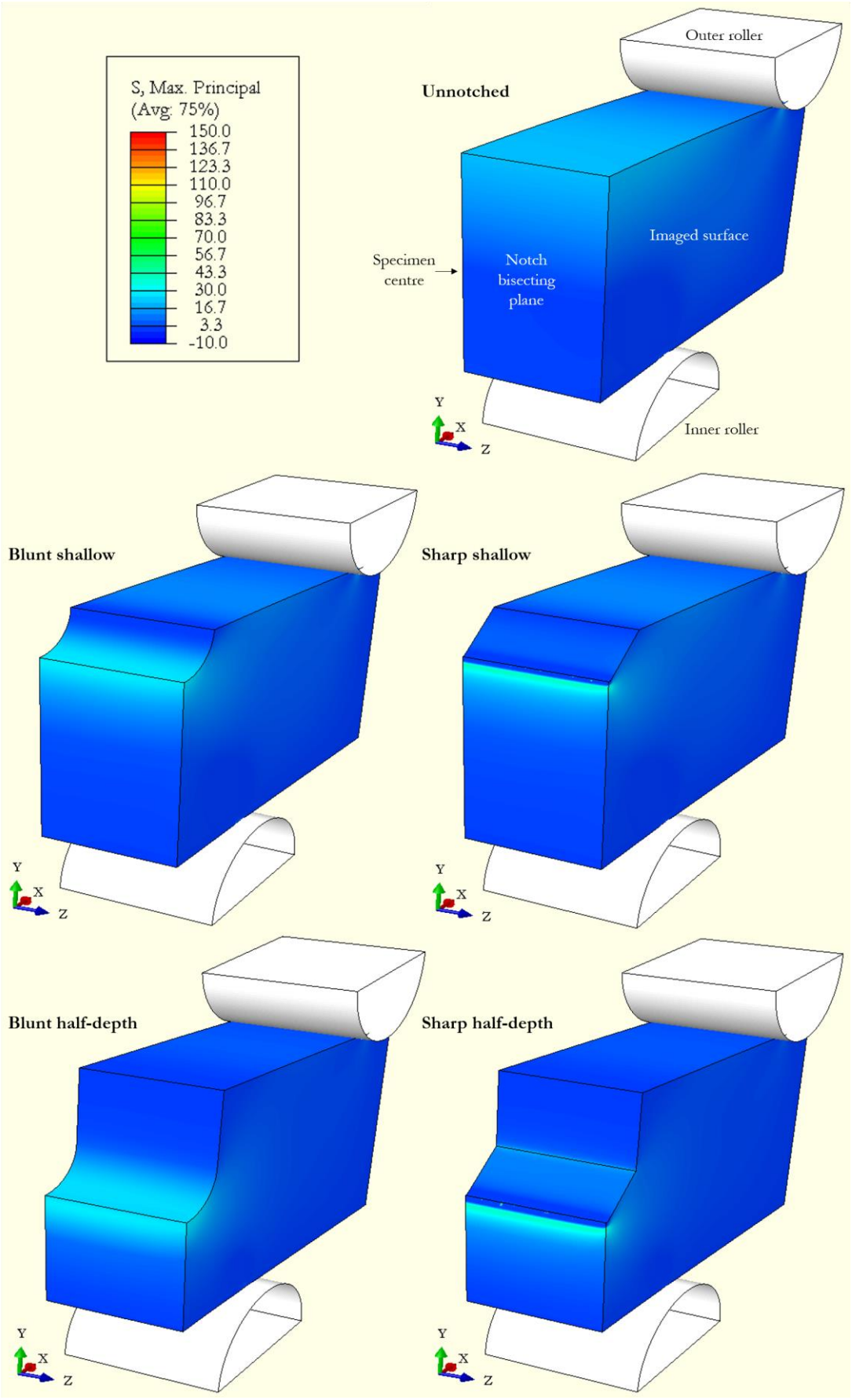


Figure 77: Non-linear elastic (using E_{UMAT}) predictions of the maximum principal stress for one specimen of each of the geometry. Deformations shown with a 10 × scale factor, with stress in units of MPa.

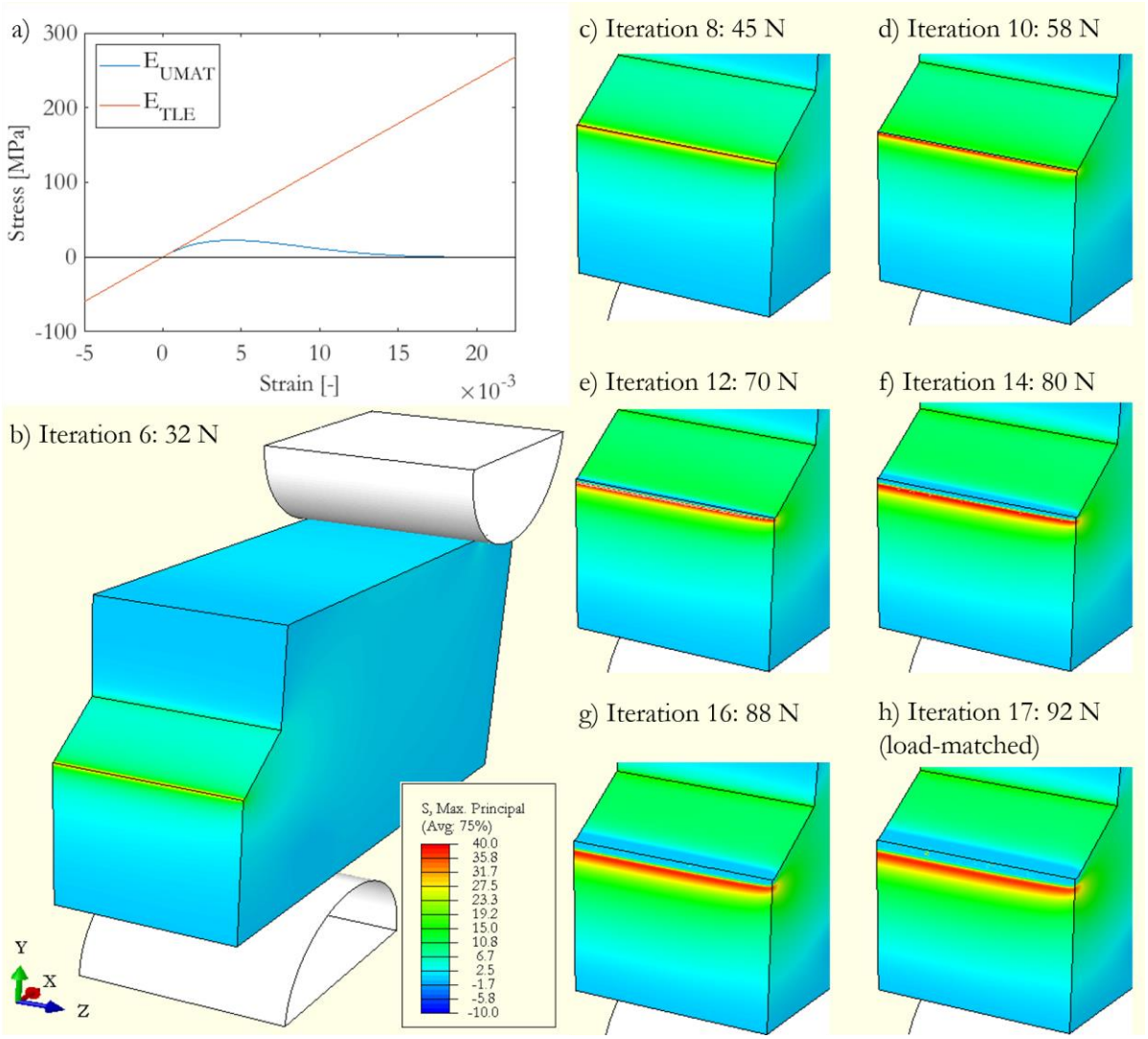


Figure 78: Evolution of maximum principal stress, based on the UMAT definition. Unlike the linear elastic model, the UMAT definition limits the maximum stress (a) such that the peak stress moves from the notch tip in (b)-(h). Deformations shown with a 10 × scale factor, with stress in units of MPa.

Table 8: Predicted maximum axial stresses (σ_{zz}) for each geometry at pop-in simulated with linear elasticity and the UMAT. For the UMAT simulations passing the HAIL, values are estimated, as indicated. See also § iv.

Geometry	Fitted linear elastic stress, σ_{FLE}	UMAT (load-matched) stress, σ_{UMAT}
	[MPa]	[MPa]
Blunt shallow	47.6 ± 10.8 (44.4, 50.8)	27.7
Blunt half-depth	45.9 ± 14.4 (41.7, 50.2)	27.0
Blunt deep	40.5 ± 7.1 (38.4, 42.6)	N/A
Sharp shallow	149.2 ± 29.3 (140.5, 157.8)	c. 35
Sharp half-depth	148.5 ± 30.2 (139.6, 157.4)	c. 35
Sharp deep	149.2 ± 41.7 (136.3, 162.1)	N/A
Unnotched	26.1 ± 5.1 (24.9, 27.4)	22.6

III.5 Analysis

Combining the empirical load and DIC data (§ III.3) and the finite element simulations (§ III.4) is a powerful tool for exploring the crack initiation in the small specimens. Historical and modern analysis techniques will now be employed to explore the apparent notch sensitivity, using the definitions for NSF and notch sensitivity given in § I.3.2.3.2 (§ III.5.1) and the applicability of critical strain energy density as a potential crack initiation criteria (§ III.5.2). The different material models will be compared to understand the bounding behaviour, and the effect of localised strain softening. A comparison will be made with the SED fields calculated from the empirical DIC directly, whereby the FE simulation stages are omitted (§ III.5.3).

III.5.1 Notch sensitivity

The notch tip stresses were simulated in (§ III.4.3.3) using linear elasticity, which is the usual approach, and also for the non-linear UMAT material models. For comparison, the notch tip stresses will also be calculated by the reduced-ligament formulation that was used in the historical measurements described in § I.3.2.3.1 (§ III.5.1.1). From these stresses, the NSFs and notch sensitivities will be determined in § III.5.1.3 using the definitions for NSF and notch sensitivity given in § I.3.2.3.2.

III.5.1.1 Reduced ligament stresses

The squat nature of the test geometries could have invalidated application of the reduced-ligament formulation. Estimates of peak axial stress in unnotched beams with reduced height were verified to be within 5 % (± 1 MPa) of the value predicted by corresponding LE-FE models, and so the application was considered valid (data not presented).

Table 9 lists the mean and estimated distribution of the reduced ligament stress for each geometry, where the statistical spread, $\xi_{\sigma RL}$, were calculated in quadrature as the 95%ile using (21). For these calculations, the spread was calculated based on standard deviation of the dimensions (see § III.2.1) and the failure load distributions (see § III.3.1), and it was assumed that the errors in setting the roller positions, l_{out} and l_{in}, were each 0.1 mm; see also § iv.

$$\xi_{\sigma RL} = \sigma_{RL} * \sqrt{\left(\frac{\xi_F}{F}\right)^2 + \left(\frac{\xi_D}{D}\right)^2 + \frac{{\xi_{lout}}^2 + {\xi_{lin}}^2}{(l_{out} - l_{in})^2} + \frac{{\xi_W}^2 + {\xi_a}^2}{(W - a)^2}} \quad (21)$$

From Table 9, the mean flexural strength of the Gilsocarbon billet from the unnotched specimens was σ_{RL} = 25.3 ± 2.5 (24.0, 26.5) MPa, and agreed well with the simulation predictions for the unnotched beams in Table 8. The value is also in agreement with the flexural stress of 26.4 MPa (with an estimated scatter of 6 % to 10 %) measured by Marrow *et al.* on larger beams [88]. The uniaxial tensile strength of the sample in that study, machined from the same billet as the specimens tested here, was 15.8 MPa, and the preliminary samples had a scatter of ξ_{UT} = 2.9 MPa.

Table 9: Reduced-ligament stresses for each geometry. See also § iv.

Geometry	Reduced-ligament stress, σRL
	[MPa]
Blunt shallow	25.0 ± 6.0 (23.3, 26.8)
Blunt half-depth	29.2 ± 9.5 (26.4, 32.0)
Blunt deep	34.7 ± 7.2 (32.5, 36.8)
Sharp shallow	21.6 ± 3.6 (20.6, 22.7)
Sharp half-depth	25.4 ± 5.6 (23.7, 27.0)
Sharp deep	36.3 ± 10.8 (33.0, 39.6)
Unnotched	25.3 ± 5.0 (24.0, 26.5)

III.5.1.2 Notch strengthening factors

Notch strengthening factors, NSF, were calculated for the different geometries by (6) and are presented in Table 10 and Figure 79. Separate NSF values, k_{LE}, k_{UMAT} and k_{RL}, were calculated for the stresses from each prediction method: respectively, linear elastic FE using E_{FLE}, UMAT FE (see Table 8) and reduced-ligament (see Table 9); linear elastic FE using the tensile modulus were not calculated since these were neither load- nor deflection- matched.

NSFs predicted by the linear elastic behaviour were the largest values for each geometry and increased monotonically as notch radius reduced, with no significant dependence of notch depth; $\hat{k}_{FLE} \approx 1.7$ for the blunt and $\hat{k}_{FLE} \approx 5.7$ for the sharp notch-tip geometries.

From the reduced ligament formulation, $\hat{k}_{RL} \approx 1$ for the half-depth sharp and shallow blunt notch specimens, indicating at the 95%CI that no effect of notch concentration occurred as their mean critical stresses were in agreement with the unnotched beams. The critical stresses in the deep notched and half-depth blunt notch specimens exceeded that of the unnotched beam, indicating a slight notch concentration effect, where $k_{RL} = 1.16 \pm 0.44$ (1.03, 1.29) for the half-depth blunt, $k_{RL} = 1.37 \pm 0.39$ (1.26, 1.49) for the deep blunt, and $k_{RL} = 1.44 \pm 0.51$ (1.28, 1.60) for the deep sharp notch geometries. The shallow sharp notch geometry had a lower predicted strength at pop-in, at the 5 % significance level, than the unnotched beam, with $k_{RL} = 0.86 \pm 0.22$ (0.79, 0.92).

The UMAT-predicted values fell between the other two predictions, showing only a small notch concentrating effect, with $\hat{k}_{UMAT} \approx 1.2$ for the blunt and $\hat{k}_{UMAT} \approx 1.6$ for the sharp notch-tip geometries.

Table 10: Notch strengthening factors for each geometry calculated relative to the unnotched critical axial stress for each method. See also § iv.

Geometry	k_{FLE}	k_{UMAT}	k_{RL}
	[-]	[-]	[-]
Blunt shallow	1.82 ± 0.54 (1.66, 1.98)	1.22	0.99 ± 0.31 (0.90, 1.08)
Blunt half-depth	1.76 ± 0.65 (1.57, 1.95)	1.19	1.16 ± 0.44 (1.03, 1.29)
Blunt deep	1.55 ± 0.41 (1.43, 1.67)	N/A	1.37 ± 0.39 (1.26, 1.49)
Sharp shallow	5.71 ± 1.58 (5.24, 6.17)	c. 1.55	0.86 ± 0.22 (0.79, 0.92)
Sharp half-depth	5.68 ± 1.60 (5.21, 6.15)	c. 1.55	1.00 ± 0.30 (0.92, 1.09)
Sharp deep	5.71 ± 1.94 (5.11, 6.31)	N/A	1.44 ± 0.51 (1.28, 1.60)
Unnotched	1.00 ± 0.20 (0.95, 1.05)	1.00	1.00 ± 0.20 (0.95, 1.05)

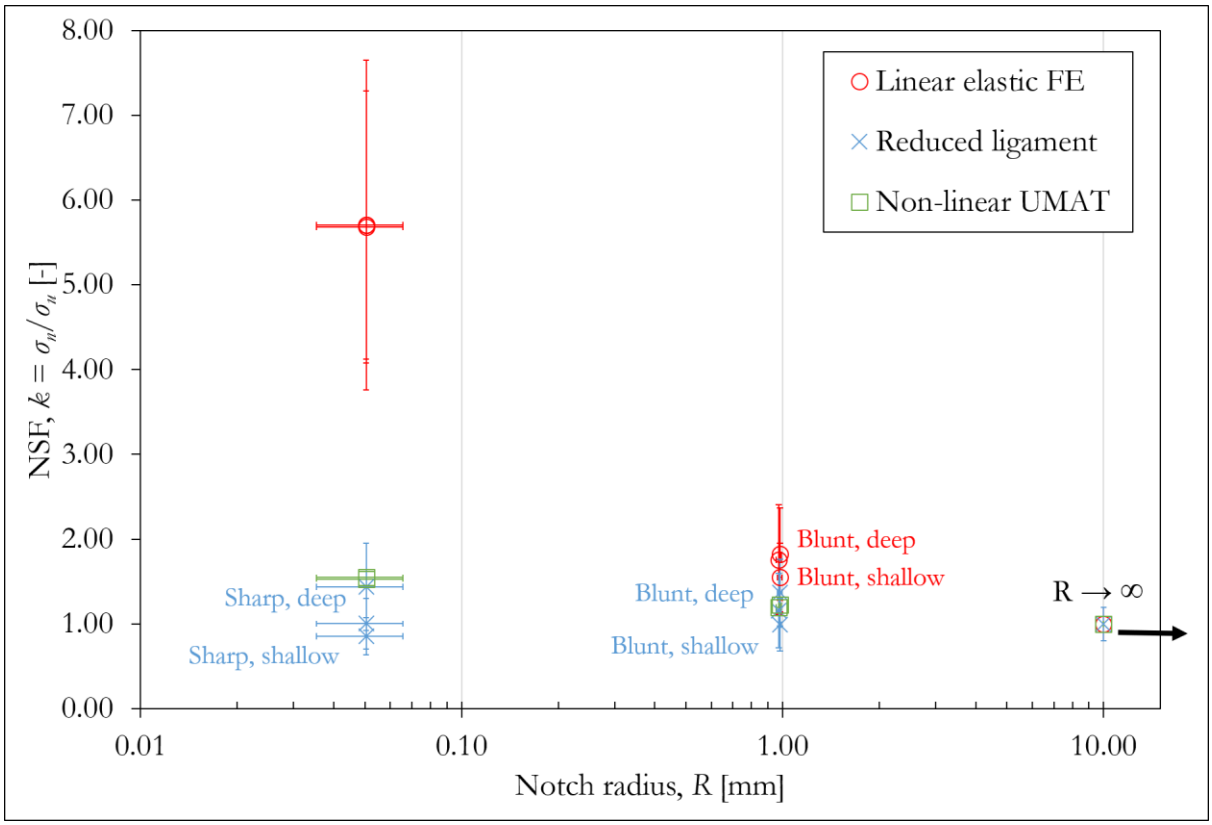


Figure 79: Notch strengthening factors calculated by linear elastic, non-linear elastic and reduced ligament stress methods (see also Figure 93 for comparison to literature values).

III.5.1.3 Notch sensitivity

Notch sensitivities for the reduced ligament and UMAT critical axial stresses, taking the linear elastic predictions as the 'theoretical' results, are recorded in Table 11, and plotted against specimen ligament in Figure 80. Again, no estimate of the scatter or confidence interval is given for the UMAT-predicted values. For the different notch-tip geometries, the UMAT values were within the ranges predicted by the reduced ligament method, though showed virtually no sensitivity to notch depth. The different notch-tip geometries had different sensitivities, with the blunt geometries exhibiting a greater sensitivity of $\hat{\lambda} \approx 0.7$ compared to $\hat{\lambda} \approx 0.2$ for the sharp geometries. In both notch tip geometries, $\hat{\lambda}$ decreased for the larger ligaments consistently. $\hat{\lambda}$ for the unnotched beams is unity by construction. For the reduced ligament predictions, only the 95%CI on $\hat{\lambda}$ for the blunt deep notch overlapped with the unnotched the $\hat{\lambda}$ interval for the unnotched specimen (and then Welch's t-test [167] concluded only a 6 % likelihood). This implies that the NSF predicted by linear elastic models is not realised in Gilsocarbon for with $R \leq 1.00$ mm, at the 7 % significance level (and for most at the 5 %). Similarly, considering the geometries in the two sets, it is statistically unlikely that $\hat{\lambda}$ for the deep notch and the shallow notch geometries (in both notch tip geometries) are from the same population (and the half-depth value is expected in the interval), which suggests that a real trend exists.

The notch sensitivity ratios are replotted in Figure 81 against notch radius, and appears to show that notch radius has a strong effect on the ratio, with the sensitivity rapidly falling below radius of 1 mm. No trendline has been added to this figure, as with only two finite radii tested it is not possible to understand the trend with any confidence, but a logarithmic function might be considered appropriate.

Table 11: Notch sensitivities calculated relative to the linear elastic simulated critical axial stresses, $\lambda = k/k_{LE}$. See also § iv.

Geometry	λ_{RL}	λ_{UMAT}
	[-]	[-]
Blunt shallow	0.54 ± 0.23 (0.47, 0.61)	0.67
Blunt half-depth	0.66 ± 0.35 (0.57, 0.74)	0.68
Blunt deep	0.89 ± 0.34 (0.82, 0.95)	N/A
Sharp shallow	0.15 ± 0.06 (0.14, 0.16)	c. 0.27
Sharp half-depth	0.18 ± 0.07 (0.16, 0.19)	c. 0.27
Sharp deep	0.25 ± 0.12 (0.22, 0.28)	N/A
Unnotched	1.00 ± 0.28 (0.93, 1.07)	1.00

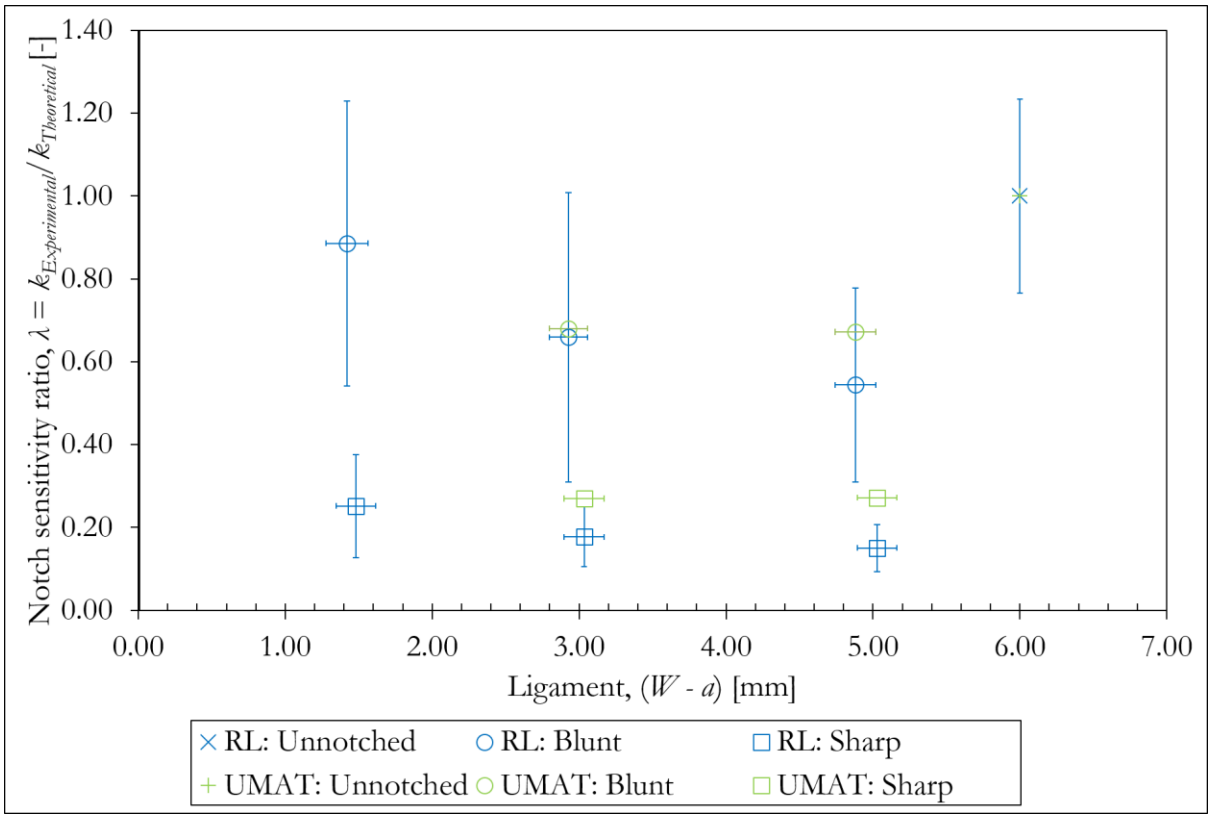


Figure 80: Notch sensitivity, λ, calculated by the UMAT and reduced ligament stress methods relative to the linear elastic predictions, as a function on specimen ligament.

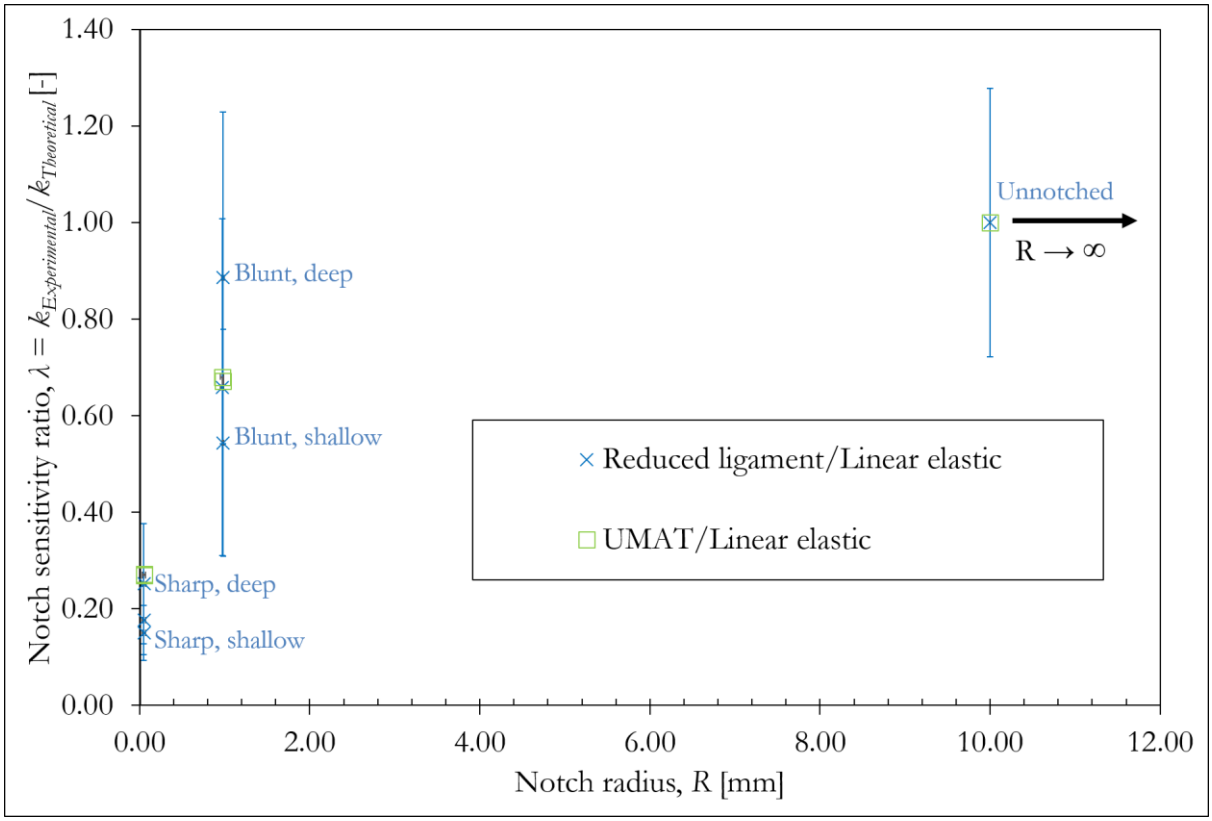


Figure 81: Notch sensitivity, λ, calculated by the UMAT and reduced ligament stress methods relative to the linear elastic predictions, as a function of notch radius (see also Figure 94 for a comparison with literature values).

III.5.2 Strain energy density

The notch sensitivity analysis in § III.5.1 relied only upon estimated or modelled point stresses, and did not require accurate knowledge of the strains. More sophisticated crack initiation criteria definitions require knowledge of stress and/or strain to be measured over a region or at a distance from the notch tip, and so point measurements are insufficient. The notch geometry critical SED (defined in § II.5.1.3) will be calculated from the simulations (§ III.5.2.1). The quadratic evolution of SED with load will be demonstrated for both linear and non-linear elasticity (§ III.5.2.2), from which a critical strain energy density related to the onset threshold for initiation will be defined (§ III.5.2.3).

III.5.2.1 SED calculation from FE

Starting from (12), by rearranging the order of integration into the form in (22), the compound integral can be written in terms of a spatial integral over the integrated SED (over the strain domain) in discrete elements of space, $\varrho^e(X)$, as defined in (23).

(22) $$\rho = \frac{1}{V}\iiint_V \rho^e(X)dV$$

(23) $$\rho^e(X) = \int_0^{\epsilon_{max}} \sigma(\epsilon, X)\, d\epsilon$$

Failure is expected due to tensile energy contributions in a limited volume only, so only the SED for points of positive maximum principal strain, $\epsilon_1 > 0$, in the ROI were averaged, where N_e is the number of valid elements in the ROI. Where each element corresponds to a relatively small area (volume) of material of identical size, the volume integral in (22) is then approximated by (24).

(24) $$\rho = \frac{\sum_e^{Ne} \rho^e(\varepsilon_{MP}>0)}{N_e} \; for\; e \in V$$

The ROI loci were assumed to be prismatic parallel to the notch, and therefore the values could be averaged over 2D planes. R_0 was assumed to be independent of notch tip geometry, but calculated separately for the specimen surface (in plane stress) and centre (in plane strain) using (15) and (16), respectively. All the SED calculations were based on the same K_{IC} and R_0 values using measured data for this billet: an ultimate tensile strength of 15.8 MPa [88], and K_{IC} was computed by (4) using the J-integral value measured by Barhli *et al.* of $J_{IC} \approx 200$ J.m^{-2} [89] (a value in line with other measurements in the literature) as $K_{IC} = 1.2$ MPa.m$^{0.5}$. For plane stress and plane strain $R_0 = 2.2$ mm and $R_0 = 2.0$ mm, respectively, such that the diameters of the circular loci were therefore around twice the 2.0 mm slot width (dimension S). r_0 was defined using (17).

For each FE simulation, the natively-calculated SED for each node in both the surface or centre planes were interpolated onto the DIC coordinate grid using MATLAB®'s SCATTEREDINTERPOLANT function [160] such that each element was cuboidal, with a volume of 260 μm^3. Figure 82 shows example ρ fields within the ROIs for a shallow blunt notch simulated using the E_{FLE} and E_{UMAT} material properties integrated to pop-in (for brevity, the E_{TLE} results are not shown, as they were merely a linear scaling of the E_{FLE} results by the ratio E_{TLE}/E_{FLE}). For clarity, the regions around the notch tip are redrawn magnified in Figure 83 with the identical colour scheme. The loci were all circular, but since the elements near the far face were under compressive strain due to the loading geometry and hence the imposed distortion, they did not contribute to ρ.

The figure shows that the SED fields were broadly similar for both planes and material models. The strain concentration was reflected in an SED concentration about the notch. In the elements adjacent to the notch tip, the centre planes exhibited greater values of ρ^e than the surface planes, and the range of ρ^e values was greater when simulating with E_{FLE} rather than E_{UMAT} (the E_{TLE} range was greater still). The SED concentration region in the UMAT-simulated fields was broader than the linear elastic. In the centre plane fields, the shape of the concentration is more equiaxed than the two-lobe form seen on the surface planes.

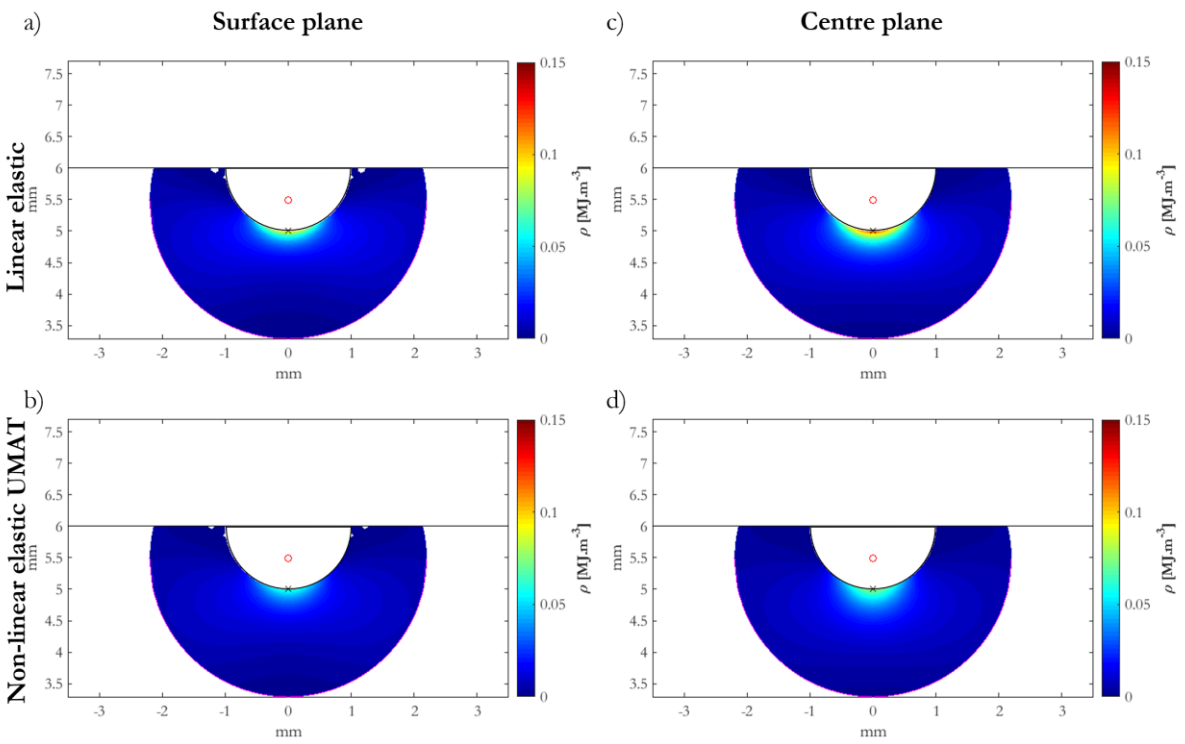


Figure 82: Example maps of the strain energy density fields for a blunt shallow notch sample integrated to the pop-in simulated with linear elasticity and the NLE UMAT within the surface ((a) and (b)) and centre ((c) and (d)) ROIs. In each map, the sample edge and notch are drawn schematically with the pink line indicating the ROI locus centred on the red circle. See also Figure 83 for magnified notch tip regions.

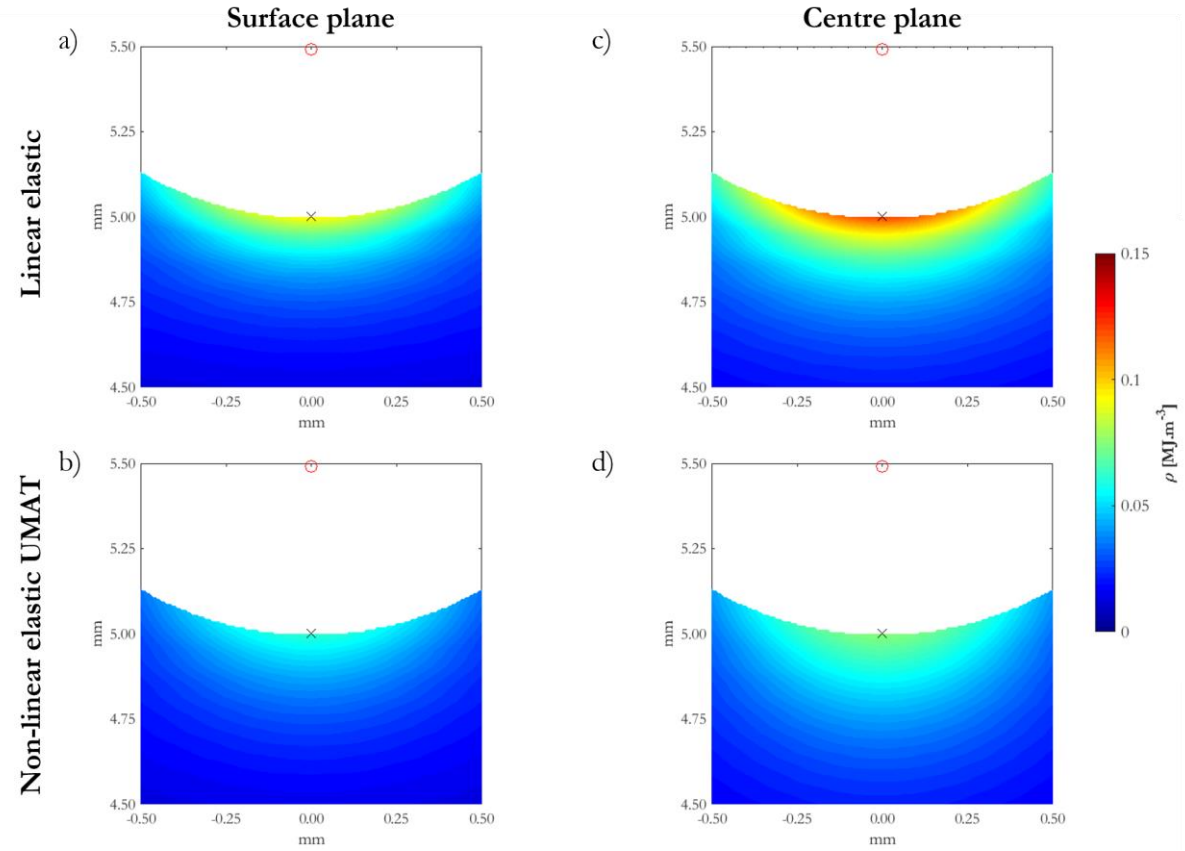


Figure 83: Notch tip contributions in the example strain energy density maps shown in Figure 82. Maps are for a blunt shallow notch sample integrated to the pop-in simulated with linear elasticity and the NLE UMAT within the surface ((a) and (b)) and centre ((c) and (d)) ROIs. In each map, the cross indicates the notch tip and the red circle the ROI locus centre.

III.5.2.2 SED evolution

The evolution of the ROI-averaged ϱ values is an integral function with increasing strain. In Figure 84, ϱ is plotted as a function of load, averaged over the same ROI, for the same modelling configurations as in Figure 82. In each evolution profile, the SED at pop-in is indicated by a star symbol. The E_{TLE} predictions (with scaled gradients) were again omitted for brevity.

All the simulation data in Figure 84 increased smoothly with a quadratic-type curve. Considering the linear elastic simulations, the curves' rate of increase was predicted to be sensitive to notch geometry, with the blunt notched samples rising marginally faster than the sharp notched counterparts. Similarly, a dependence of notch depth was observed, with curves for the half-depth notches rising faster than for their shallow-notched counterparts. The unnotched geometry rose slowest of all. For the non-linear elastic behaviour, the relative trends were comparable in each case, even beyond the HAIL. For both material models, the form of the SED evolution in plane stress was comparable to plane strain, though with a slightly faster rate, implying SED on the centre plane was always c. 10 % greater than on the surface.

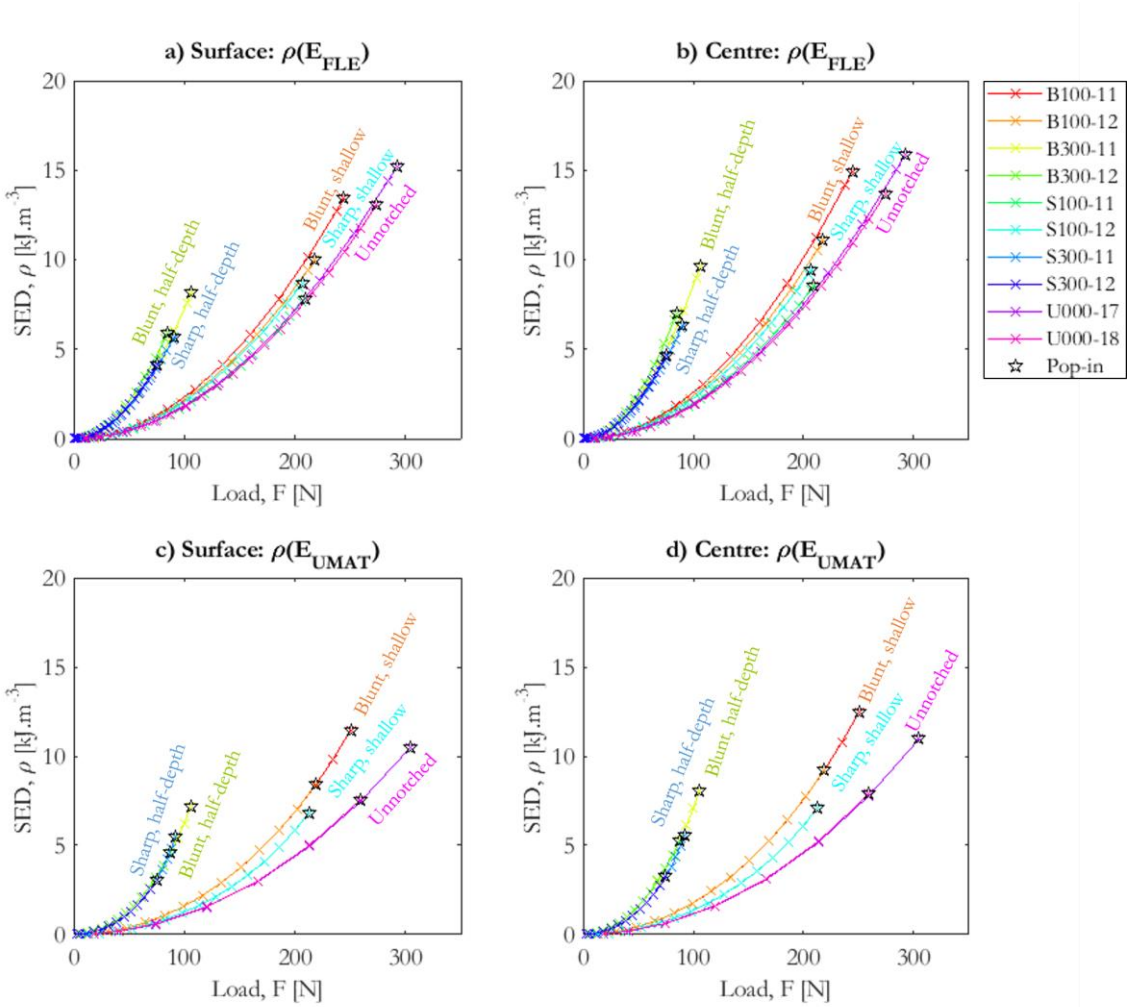


Figure 84: ρ as a function of loaf, F (averaged over the ROI) until pop-in within the surface and centre ROIs, simulated with linear elasticity ((a) and (b)) and the NLE UMAT ((c) and (d)).

III.5.2.3 Crack initiation SED

The FE-simulated crack initiation SED values are tabulated in Table 12. Figure 85 compares the SED predictions on the surface to the centre plane values, where each connected open red circle, filled red circle, and filled black circles were the E_{TLE}, E_{FLE} and E_{UMAT} predictions, respectively, for a given specimen, with a 1:1 guideline plotted. For the linear elastic predictions, the plane strain SED values (from the centre plane) were consistently c. 10 % greater than the plane stress predictions (from the surface). The offset was marginally smaller for the non-linear elastic simulations (c. 7 %).

To identify trends between the different geometries, the values in Table 12 are plotted in Figure 86. The loading geometry SED was calculated using Brocklehurst and Darby definition as $\rho_{TLE}^{B\&D}$ = 9.5 kJ.m^{-3} using the tensile modulus and the unnotched flexural stress from the FE simulations, and $\rho_{FLE}^{B\&D}$ = 16.4 kJ.m^{-3} if calculated using the mean pop-in fitted modulus for the unnotched beams in Table 6. These SED estimates are indicated on Figure 86 for comparison.

Figure 86 highlights the appreciable degree of scatter in SED estimates across the specimens and methods. The surface SED value ranges were significant across the geometries and differed between models, with $\hat{\rho}_{TLE}^{FE}$ = [7.0, 26.6] kJ.m^{-3}, $\hat{\rho}_{FLE}^{FE}$ = [4.2, 15.2] kJ.m^{-3} and $\hat{\rho}_{UMAT}^{FE}$ = [3.1, 11.5] kJ.m^{-3}, always with a sharp half-depth specimen the lowest and an unnotched beam the highest (except for the UMAT, where a blunt shallow notched beam was highest). To evaluate whether a particular value could be used for ρ_c the mean predicted values will be compared; of the different calculation methods, the FE surface plane predictions are the most pertinent for comparison. From comparison with the Brocklehurst and Darby approximation, the linear elastic simulation showed good agreements with the mean values, with $\hat{\rho}_{FLE}^{FE}$ = 9.2 ± 7.2 (6.6, 11.8) kJ.m^{-3} ≈ $\rho_{TLE}^{B\&D}$ and $\hat{\rho}_{TLE}^{FE}$ = 14.8 ± 12.3 (10.3, 19.3) kJ.m^{-3} ≈ $\rho_{FLE}^{B\&D}$, both within the 95%CI on the mean; note the moduli model reversal in these comparisons. Taking the linear elastic material models as the bounding cases, the true value of ρ_C lies in the range ρ_C = [9.2, 14.8] kJ.m^{-3}. The UMAT means were below both of the Brocklehurst and Darby predictions, with $\hat{\rho}_{UMAT}^{FE}$ = 7.2 ± 5.0 (5.4, 9.0) kJ.m^{-3}.

The non-linear model reduced the crack initiation SED prediction for all the geometries, and particularly the unnotched beams where the mean reduction was 21 % compared to the E_{FLE} predictions. Visually, the crack initiation SED values were more consistent across the geometries, with a smaller statistical scatter.

The values in Table 12 were averaged by geometry, and plotted in Figure 87 as a function of radius and ligament. These figures indicated that consistent trends might exist, particularly with ligament depth, for which linear trend lines have been added to the plot, suggesting that mean SED decreases as ligament is reduced for all the material models. However, given the small number of specimens and high level of scatter, it was difficult to draw more meaningful conclusions as to the effect of notch geometry, and determining which material model is most appropriate.

Table 12: Simulated crack initiation SED values averaged over the centre and surface ROIs. For nomenclature of the mean values see § iv.

Geometry	Specimen number	Strain energy density, ϱ					
		Surface			Centre		
		E_{TLE}	E_{FLE}	E_{UMAT}	E_{TLE}	E_{FLE}	E_{UMAT}
		[kJ.m^{-3}]	[kJ.m^{-3}]	[kJ.m^{-3}]	[kJ.m^{-3}]	[kJ.m^{-3}]	[kJ.m^{-3}]
Blunt shallow	1	20.3	13.4	11.5	22.6	14.9	12.5
	2	13.9	10.0	8.4	15.5	11.1	9.2
Blunt half-depth	3	12.1	8.2	7.1	14.3	9.7	8.1
	4	9.9	5.9	4.6	11.7	7.0	5.3
Sharp shallow	5	12.0	7.8	6.8	13.1	8.5	7.1
	6	15.2	8.7	6.8	16.5	9.4	7.1
Sharp half-depth	7	9.1	5.6	5.5	10.2	6.3	5.6
	8	7.0	4.2	3.1	7.9	4.7	3.2
Unnotched	9	26.6	15.2	10.5	27.8	15.9	11.0
	10	22.1	13.1	7.6	23.1	13.7	7.9
Mean		14.8 ± 12.3 (10.3, 19.3)	9.2 ± 7.2 (6.6, 11.8)	7.2 ± 5.0 (5.4, 9.0)	16.3 ± 12.4 (11.7, 20.8)	10.1 ± 7.4 (7.4, 12.8)	7.7 ± 5.3 (5.7, 9.6)

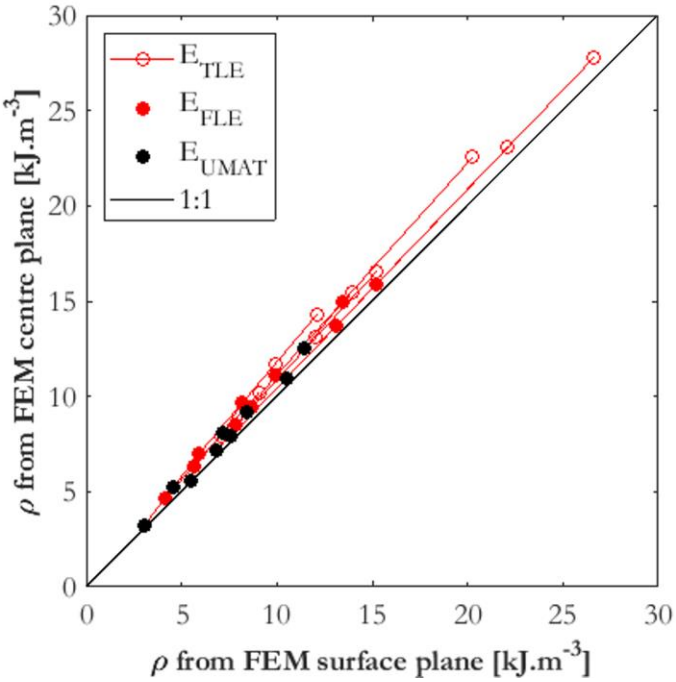


Figure 85: Comparison plot of the simulated SED values from the surface and centre planes at pop-in. For each geometry, the complementary predictions from the different material models are connected: the linear elasticity using the tensile modulus, E_{TLE}, and the fitted modulus, E_{FLE}, and the non-linear UMAT, E_{UMAT}.

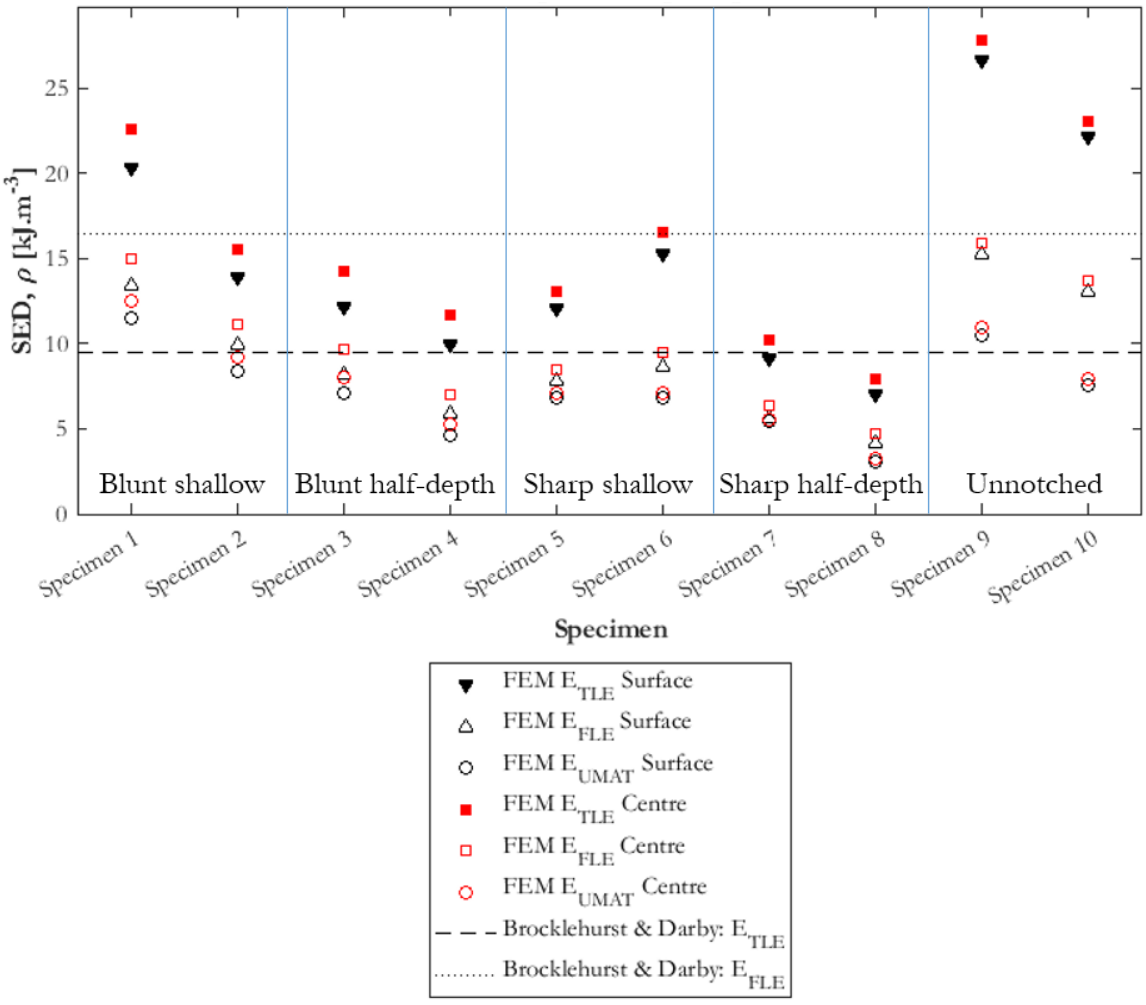


Figure 86: Linear elastic mean SED values at pop-in for each geometry, comparing the surface and centre ROIs, and calculated using tensile linear elasticity, fitted linear elasticity and non-linear elastic UMAT.

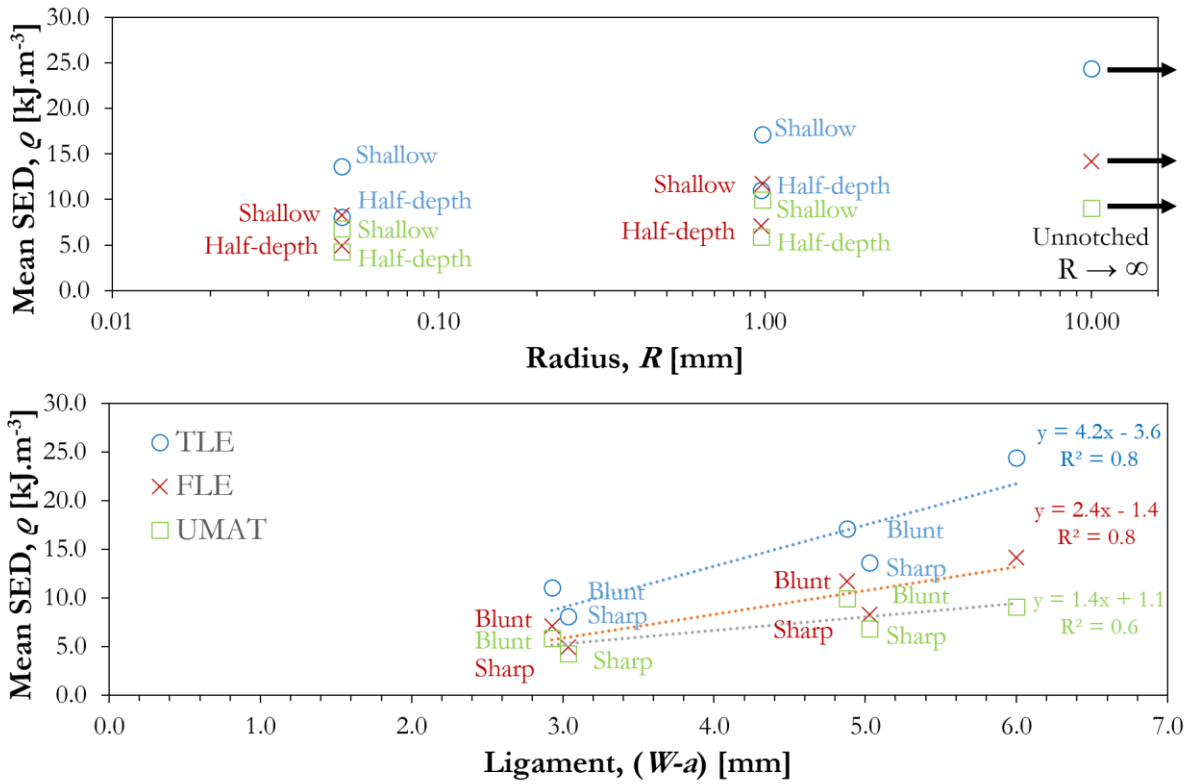


Figure 87: Variation of SED with geometric variables radius and ligament, as simulated using the material models of E_{TLE}, E_{FLE} and E_{UMAT}. For the linear fitting in the ligament comparison, y = Mean SED, and x = Ligament. R^2 is the square of the residual of the fit.

III.5.3 Stress and SED calculation from DIC

The SED calculation method in § III.5.2 uses an areal (or volumetric) average, but requires precise and time-consuming finite element simulation. DIC is a suitable technique for processing image data to obtain experimental strain fields directly, such that areal properties could be calculated in 'real-time'. The limitations of DIC prevent point strain measurement, and therefore stress prediction, close to surfaces including stress-concentrating features. By prediction of stresses from DIC strain fields, the potential to calculate $\rho^{e,DIC}$ fields directly will be explored (see § III.5.3.1), from which the evolution and critical SED values will be determined for the different material models (§ III.5.3.2).

III.5.3.1 SED calculation from DIC

The in-plane stress components at each DIC interrogation point were calculated from the Young's modulus and Poisson ratio by (25) from [162] to form a partial stress tensor. For the bounding cases of linear elastic behaviour, stresses were calculated using both E_{TLE} and E_{FLE}; the same modulus was assumed at every point. For calculating the E_{UMAT} stresses, at every interrogation point the ϵ_I-dependent stiffness was determined by (8) and substituted into (25), assuming ν was invariant with damage.

(25)
$$\begin{cases} \sigma_{xx} = \frac{E\,(\epsilon_{xx} + \nu\,\epsilon_{yy})}{1-\nu^2} \\ \sigma_{yy} = \frac{E\,(\epsilon_{yy} + \nu\,\epsilon_{xx})}{1-\nu^2} \\ \sigma_{xy} = \frac{E\,\epsilon_{xy}}{2\,(1+\nu)} \end{cases}$$

For the calculation of ϱ in (22), first integral calculation of ϱ^e in (23) is required over $[0, \epsilon]$ for each element. For the linear elastic cases, calculation of $\rho^e_{LE}(\epsilon)$ simplifies to (26) (written in tensor notation) for any given ϵ, which for the approximation from DIC data was implemented as (27); this formulation ignored out-of-plane tensor components, but through component-wise comparison with the native FE values the error due to this approximation was found to be insignificant. Again, ϱ was calculated for the bounding elasticity cases as ρ^{DIC}_{TLE} and ρ^{DIC}_{FLE}.

(26)
$$\rho^e_{LE} = \frac{1}{2}\sigma_{ij}\varepsilon_{ij}\ for\ i,j = 1(\equiv x), 2(\equiv y), 3(\equiv z)$$

(27)
$$\rho^{e,DIC}_{LE} \cong \frac{1}{2}\left(\sigma_{xx}\varepsilon_{xx} + \sigma_{yy}\varepsilon_{yy} + \sigma_{xy}\varepsilon_{xy}\right)$$

For the UMAT simulations, $\rho^e_{UMAT,DIC}$ was calculated by discrete integration of the component fields for every correlation step in $[0, \epsilon]$ using MATLAB®'s CUMTRAPZ function which implements the trapezium rule for numerical integration.

The equivalent surface SED maps to Figure 82(a) and (b), are shown in Figure 88(a) and (b) calculated using the E_{FLE} and the E_{UMAT} models. A significant number of the DIC vectors were suppressed, due to the DIC exclusion borders, the hotspot masking, and requirement for tensile-only strain contributions. For comparison of the available data, Figure 88(c) and (d) shows Figure 82(a) and (b) masked to exclude the same vectors as the DIC maps. The patterns in the DIC maps that are visible compare well with the FE for both LE and UMAT, though the data was noisier and less well defined. It was notable that the masking almost completely excluded the SED concentration regions seen in Figure 82(a) and (b). This was true for all the specimens analysed.

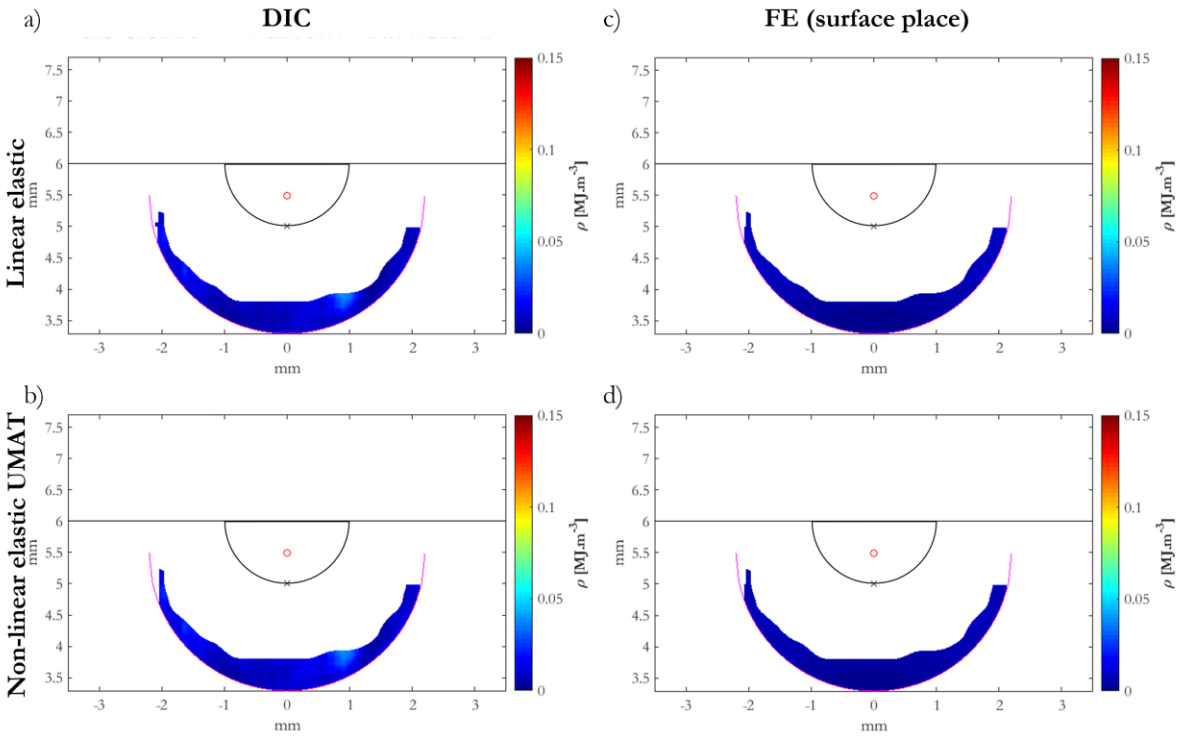


Figure 88: Example maps of the strain energy density fields for a blunt shallow notch sample integrated to the pop-in using the linear elasticity and the NLE UMAT material models, calculated from DIC ((a) and (b)) and masked FE ((c) and (d)) (both use the surface ROI). The sample edge and notch are drawn schematically with the pink line indicating the ROI locus centred on the red circle.

III.5.3.2 DIC-SED evolution and critical value determination

The evolution of the DIC-calculated SED with strain is shown in Figure 89 for comparison with the SED calculated for the (unmasked) surface in Figure 84. In Figure 89, both the E_{FLE} and E_{UMAT} model DIC-measured evolutions increased in a generally quadratic-type manner but were non-monotonic and appeared to have significant scatter. The maximum measured SED for all the specimens (from an unnotched specimen) significantly exceeded any of the FE predictions for both the material models, though this specimen's behaviour appeared anomalous. For the other specimens the curvature and SED at pop-in were comparable between the E_{UMAT} and E_{FLE} predictions.

Comparing Figure 89 with Figure 84 shows that the behaviour of most of the specimens was similar to the FE predictions, suggesting a good first order prediction. Several of the DIC measured profiles in Figure 89 showed a marked and inconsistent increase between the penultimate and pop-in correlations, exceeding 100 % in some cases. Such an increase was considered unphysical and artefacts of the analysis method, and so future discussion of the DIC pop-in properties are based on the penultimate correlation for all specimens. While this approximation introduced uncertainty, the image selection criteria ensured that this correlation did not represent a significantly different (in time) loading state, and the error may be estimated by considering the difference in ϱ shown in Figure 89 between the consecutive datapoints. The SED values from the penultimate correlations were tabulated in Table 13. The values in Table 13 were compared to the FE surface values given in Table 12 in the 1:1 comparison plot in Figure 90, where each connected open blue circle, filled blue circle, and filled black circle were the E_{TLE}, E_{FLE} and E_{UMAT} predictions, respectively, for a given specimen. With all points close to the 1:1 guideline, the DIC-calculated data is further demonstrated as a good predictor. On average, the linear elastic DIC measurements were c. 15 % lower, and the UMAT values were 42 % greater. These patterns reflect the use of the penultimate correlation, and the underpredicted strains of the UMAT simulation.

Figure 91 replots Figure 86 including the DIC data and omitting the centre plane averages. The average values from DIC are in tolerable agreement with the FE and Brocklehurst and Darby estimates for ϱ_C: $\hat{\rho}_{TLE}^{DIC}$ = 11.1 kJ.m^{-3}, $\hat{\rho}_{FLE}^{DIC}$ = 7.0 kJ.m^{-3} and $\hat{\rho}_{UMAT}^{DIC}$ = 9.5 kJ.m^{-3}. However, there was no obvious trend of the agreement in the measured and predicted values of ϱ each material model with specimen geometry, and the scatter about the mean values is very high; for the linear elastic models the 95%ile scatter was greater than the mean. The geometric effects on the DIC-predicted values are shown in Figure 92, showing similar trends to the FE behaviour in Figure 86. While the overall range in values is significant, there is arguably a clearer dependence on ligament shown in these plots.

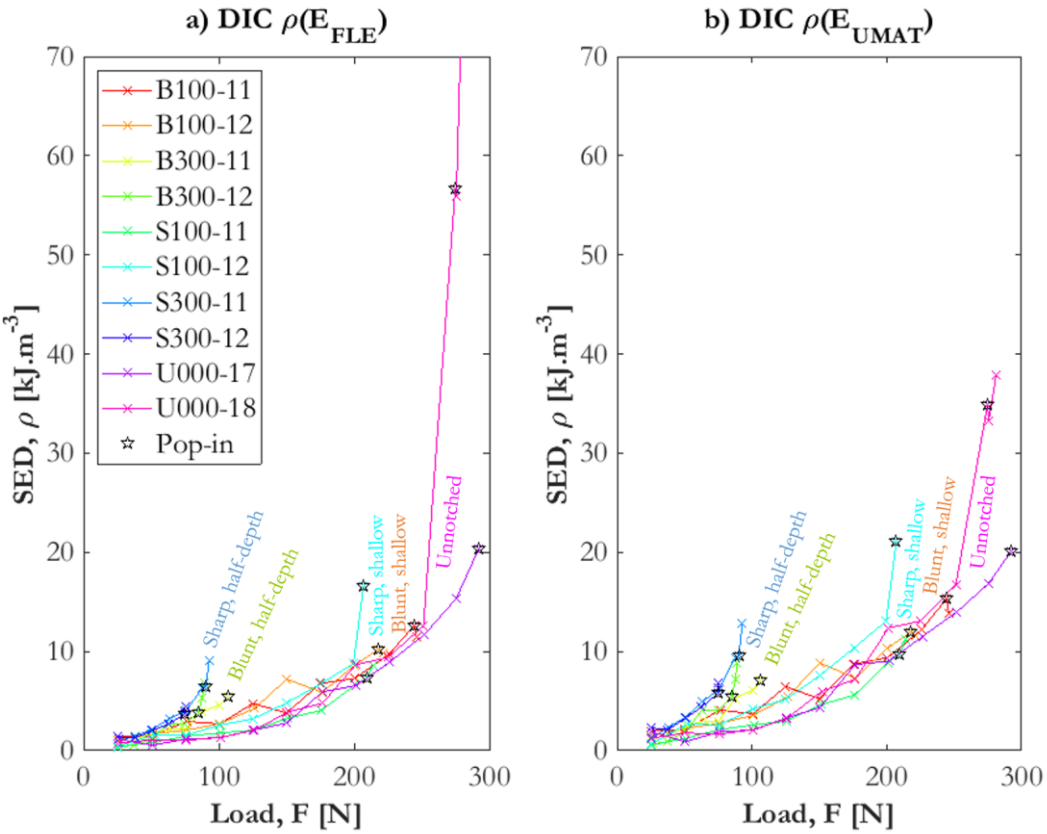


Figure 89: ϱ as a function of median axial strain, ϵ_{XX}, (averaged over the ROI) for the surface SED calculated from the DIC by (a) LE and (b) UMAT material models.

Table 13: Crack initiation surface SED values calculated from DIC for the penultimate correlation to pop-in, and the masked FE. For nomenclature of the mean values see § iv.

Geometry	Specimen	DIC-based strain energy density, ϱ		
		E_{TLE}	E_{FLE}	E_{UMAT}
		[kJ.m^{-3}]	[kJ.m^{-3}]	[kJ.m^{-3}]
Blunt shallow	1	14.7	9.7	12.2
	2	12.0	8.6	10.3
Blunt half-depth	3	6.8	4.6	6.1
	4	4.6	2.7	4.1
Sharp shallow	5	10.2	6.7	8.9
	6	15.4	8.8	13.1
Sharp half-depth	7	10.1	6.3	9.4
	8	4.6	2.7	4.4
Unnotched	9	26.8	15.3	16.9
	10	21.2	12.6	16.8
Mean		12.6 ± 14.0 (7.5, 17.8)	7.8 ± 8.0 (4.9, 10.7)	10.2 ± 9.0 (6.9, 13.5)

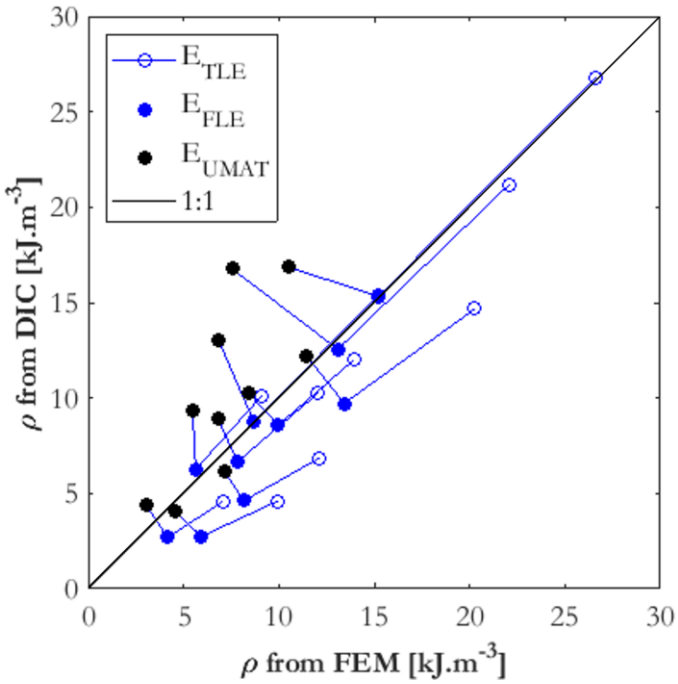


Figure 90: Comparison plot of the DIC and simulated SED values from the surface planes at the penultimate correlation to pop-in. For each geometry, the complementary predictions from the different material models are connected: the linear elasticity using the tensile modulus, E_{TLE}, and the fitted modulus, E_{FLE}, and the non-linear UMAT, E_{UMAT}.

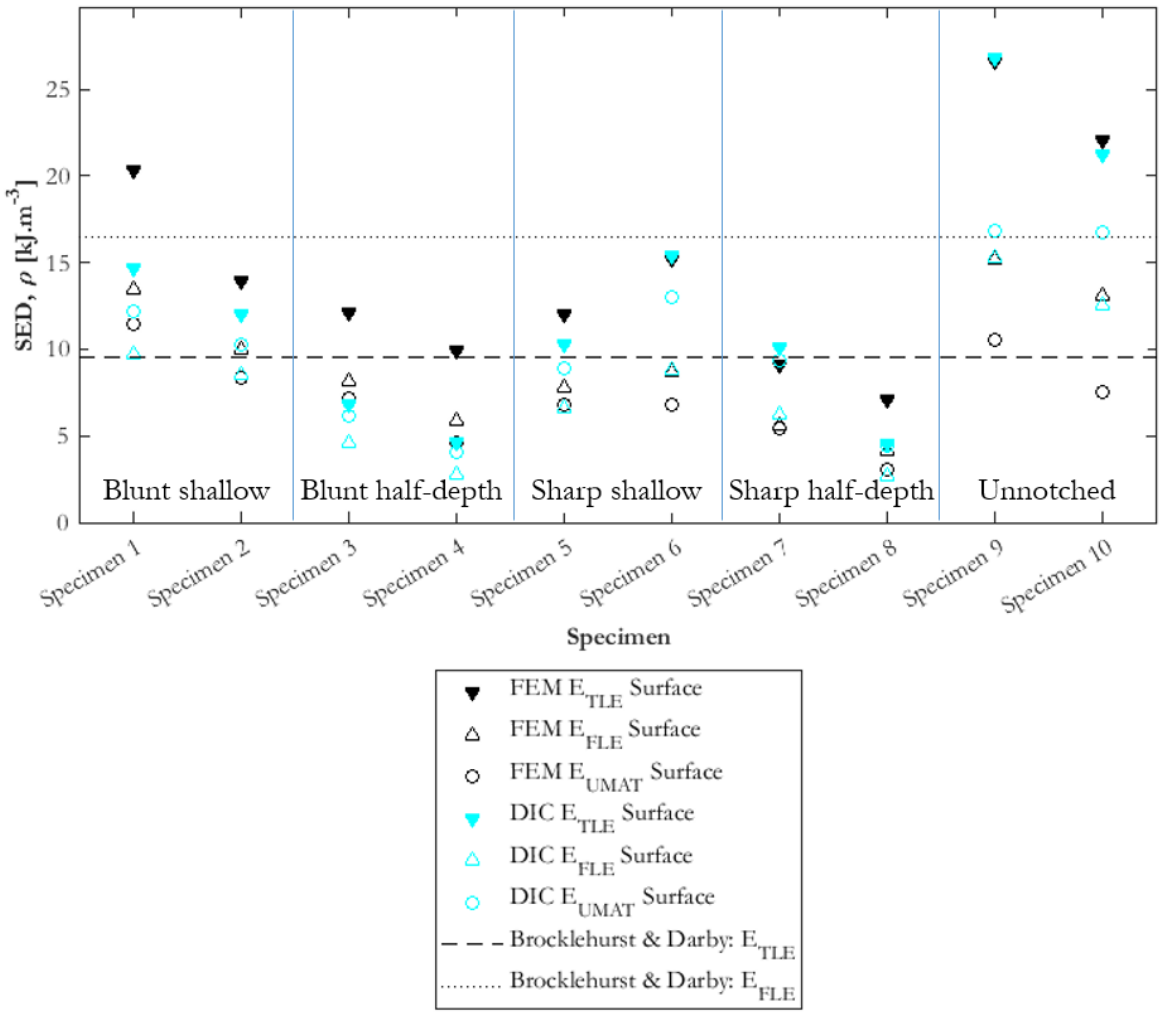


Figure 91: Mean SED values, comparing the surface DIC calculations using E_{TLE}, E_{FLE} and E_{UMAT} to their FE (surface) counterparts

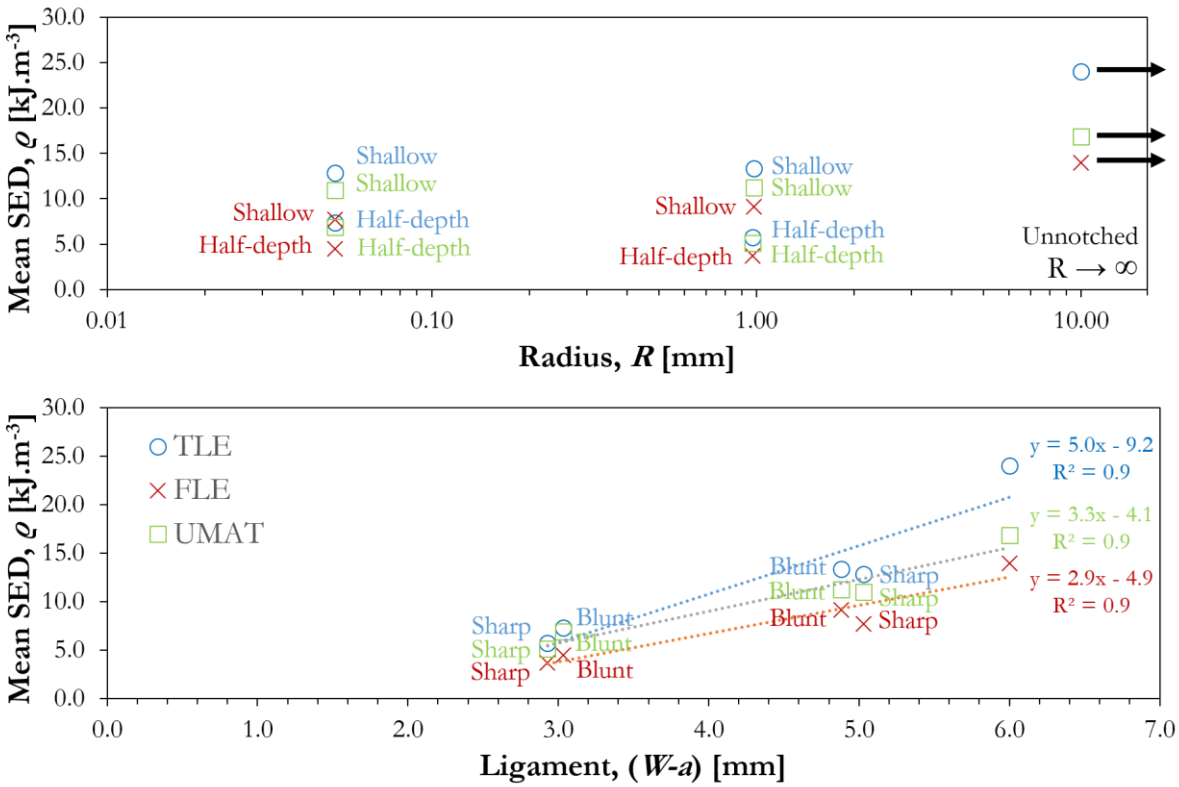


Figure 92: Variation of SED with geometric variables radius and ligament, as measured from the DIC data using the material models of E_{TLE}, E_{FLE} and E_{UMAT}. For the linear fitting in the ligament comparison, y = Mean SED, and x = Ligament. R^2 is the square of the residual of the fit.

III.6 Discussion

This small-size specimen campaign had three aims to establish: firstly, whether the behaviour in historical testing was observed, despite different specimen volumes; secondly, whether the strain energy density could be applied as a fracture criterion for differently notched geometries, using modern measurement techniques; and thirdly, whether SED calculated from DIC without FE simulation is reliable. The coupling of detailed experimental measurements with advanced finite element modelling has been demonstrated to be a powerful tool in understanding the notch sensitivity of small specimens of Gilsocarbon (§ III.6.1). By using an *in situ* multi-camera imaging system during small specimen fracture testing, precise full field displacements were determined, from which stresses were predicted by FE modelling using two material models, and a strain-dependent stiffness degradation demonstrated (§ III.6.2). The stresses were then used as the basis for considering fracture criteria, testing the sensitivity of graphite crack initiation in small beams. Seven different notch geometries were tested to explore the dependence on notch radius and depth, and with over 100 specimens fractured, a meaningful statistical comparison was conducted (§ III.6.3). The analysis demonstrated that in four-point bend, Gilsocarbon beams of 6 x 6 x 19 mm, with a loading span of only 5.33 mm, were relatively insensitive to notches with radii between 0.05 and 1.00 mm, in keeping with the literature results for specimens with double the linear dimensions. Furthermore, a range for the critical mean strain energy density for use in a fracture criterion was derived, though a possible dependence on geometry was indicated. The use of a non-linear elastic stiffness model reduced the variability between geometries. In addition, it was possible to use DIC-only methods to estimate the SED, despite an incomplete measurement field. The findings from the study further the understanding of crack initiation and notch sensitivity in Gilsocarbon, which will better inform post-irradiation examination (PIE) techniques for Gilsocarbon removed from the advanced gas-cooled reactors (AGRs). Furthermore, the techniques and trends could be applied to understand the notch sensitivity and size effects in coarse-grained materials tested at small scales.

III.6.1 Experiment setup and analysis procedure

III.6.1.1 Specimen geometries

Flexure testing of materials using specimens of only a 6 x 6 mm cross-section is not usually recommended when the microstructure is as coarse as that found in Gilsocarbon; ASTM C561-17 recommends a 10 x 10 x 80 mm beam. The 6 x 6 x 19 mm geometry adopted here was selected to agree with the routine PIE standard flexure strength test geometry, which in turn is determined by the trepanning techniques deployed in the reactors and the desire to avoid gradients of oxidation in the material.

The notch tip geometries considered were blunt U-notches and 90° sharp V-notches (see Figure 54). The geometries were selected to represent the keyway root features found in the AGR's, and to complement historical studies, such as those by Brown *et al.* [47] and Brocklehurst and Brown [46]. Those studies have shown a significant degree of insensitivity to notch radius in virgin Gilsocarbon, but had only tested large beams, or component scale specimens. They also demonstrated that Gilsocarbon is insensitive to notch depth, $a \lesssim 1$ mm, and tested notches up to half the depth of their beams ($a/W \leq 0.5$). The depths in this study bounded and exceeded those designs with nominal depths of 1.0 mm (shallow), 3.0 mm (half-depth) and 4.5 mm (deep). The ligament ahead of the deep notches was therefore only 1.5 mm, which was selected due to the coarse microstructure.

III.6.1.2 Load data and pop-in definition

Flexure testing in 4PB, was selected over the established PIE method of 3PB so that:

1. The alignment of the notch and load axis of the test machine was less critical
2. Crushing behaviour ahead of the central roller (in 3PB) would not directly interact with any damage zone preceding the notch
3. The 'critical volume' size, as defined by classical flexure theory, was controlled, and should have been sufficient to sample multiple filler particles.

As explored in §I.3.2.2, the latter justification relates to the critical volume fracture theory where the stress gradients about the centre roller results in a narrow critical volume, as opposed to the 4PB case where the volume is as wide as the inner-roller-span (5.33 mm). Naïvely, a notch of 2 mm width will therefore be fully contained in the 4PB volume, but could extend outside the 3PB volume. Good control of the mechanical alignment was demonstrated by consistent deformation patterns seen in the DIC analyses, but the mechanical freedom also led to non-linearities and abnormalities in the load traces, particularly below 25 N (§ III.3.1) . Despite the careful approach, experimental issues meant that the properties of the deep notched beams could be only partially determined.

Crack initiation was analysed with the assumption that the onset was observed by pop-ins in the load displacement curve, rather than peak load (Figure 58). This assumption ensured that any substantial but subcritical cracks could not form in the porous microstructure that might have altered the stress concentrating fracture behaviour. For example, if the surface of the notch were to break down and the pores beneath the notch spread the strain, a lower concentrating effect might have been observed.

The statistical scatter in the measurements of the pop-in load and crosshead displacements were all c. 10 % (at the 95%ile level) of the mean values, for all the geometries (Figure 59 and Table 5). With a significant sample size, totalling over 100 specimens, this indicated a reliable test and a robust analytical approach, providing a sound foundation for the comparison of derived properties. When linear elasticity was later assumed in the analysis, these levels of scatter could be directly scaled to the stress and strain predictions, so that the notch sensitivity factors could be statistically compared (§ III.5.1.3).

It is notable that the mean pop-in load and extension for each geometry were within 5 % and 10 % of the values at peak load, respectively. Several authors have suggested that graphite begins to fail at very low applied loads [81, 168-170]. This analysis shows that while the load displacement curve may lose linearity at low strains, and so does not contradict the idea of early onset damage, substantial fracture around stress concentrators does not initiate until near the ultimate failure. The data supports the use of peak load properties from flexural testing for predictions of crack initiation, but also demonstrates that these should be treated as only a first-order approximation.

III.6.1.3 Image capture and analysis

The unconventional geometries, particularly with an inner roller span less than specimen width, meant that confidence in strains and stresses derived from load, applied displacement, and elementary beam theory was low, and so integrated image measurement and simulation techniques were employed. The complementary camera system combined large field-of-view stereo and high-resolution monoscopic imaging of the larger face of the sample.

DIC of the stereo cameras and an enhanced correction algorithm (Figure 64) provided a non-contact measurement of the gross deflection, characterised by the mean profile gradient (dU_Y/dX) measured between the inner and outer rollers. A measure based on displacements within the relatively narrow inner roller region (that could otherwise have been measured from the monoscopic DIC), could have been compromised by the effects of a damage mechanism that could have resulted in non-linear behaviour. The height of the profile was also far enough for the far face to be included in the monoscopic DIC (with excellent comparison of the displacements), but near enough to be below the middle of the ligament of the half-depth notch samples. The dU_Y/dX uniquely defined the beam's deformation, and from agreement with the linear elastic modelling, always increased in proportion to the roller displacement. As such, it was selected as the fitting parameter for the FE simulations for the unnotched, shallow and half-depth notched geometries. A potentially more accurate approach would have been to fit the FE using all the measured vectors on the imaged face of the sample, known as 'full-face fitting', rather than the subset in the profile used here. Other studies have used suchtechniques, for example Farsi *et al.* [171].The profile fitting employed here appears to have been sufficiently robust for Gilsocarbon specimens. The beam deflection for Gilsocarbon was relatively low compared to many engineering materials; for materials with a greater yield strength, a full-face fitting method (using DIC or ESPI data) might be more appropriate.

The high resolution monoscopic camera was suitable for capturing microstructural deformations (Figure 57), though only imaged between the inner rollers. Elementary beam theory suggests that outside the inner rollers there is zero moment, resulting in a constant stress and therefore the load rollers bound the critical volume. While this theory may not be entirely correct for the small specimens, the shape of the surface profiles followed the classical formulation and linear elastic simulations (Figure 71), and so it is likely to be a good assumption that the monoscopic field of view fully contained the critical volume. The instant of formation of the macroscopic surface cracks surface was determined from these images, which was used for calibration of the loading and imaging systems and justified the pop-in detection criteria. Such criteria could have been calculated from a purely theoretical energy analysis, but the complexity of the material and non-standard loading geometries made such a calculation non-trivial. Instead, by refining an empirically based definition, a robust method was employed (§ III.3.1).

The DIC of the high-resolution series data provided detailed mapping of the evolution of surface strains with applied deflection (Figure 63). Despite sympathetic pre-and post-processing (§ III.3.2.2.1), significant regions of the specimen images could not be analysed, since the correlation quality in these areas was insufficient or suffered from technique artefacts. It is a failing of the technique that these regions coincide with the regions of greatest interest, such as the notch tips. The DIC approach employed was based on a localised, but area-averaged, analysis that was incapable of correctly mapping any discontinuities (such as microcracks) that might have been present in the strain field.

It was a significant limitation of the imaging system that the Toshiba-Teli stereo cameras could only capture images with a minimum interval of 1.5 seconds. The Grasshopper® 3 was capable of significantly higher frame rate than the two frames per second used but was limited by the disc write speed of the computer. As such there was a granularity in the imaging that was reflected by the uncertainty in assigning the exact frames related to pop-in; the potential 1.5 s offset error for the pop-in frame was equivalent to up to c. 2 N or 0.75 μm for the unnotched beams. While significant effort was devoted to ensuring agreement of the images for every sample, the results using the frames captured nominally immediately prior to pop-in proved to be unreliable (Figure 89), and so analysis was conducted on the preceding frame. If a faster stereo imaging or alternative strain measurement system were employed, ESPI for example, it might be possible to get more robust measurement of the pop-in state.

III.6.2 Simulation

Linear elastic finite element simulations were developed where the roller displacement was fitted to achieve the empirical deflection. The simulations were then run with the uniaxial tensile modulus and separately with a modulus fitted to match the empirical reaction force. This multipart fitting routine enabled stresses and strains to be calculated in a more accurate manner than fitting just the load data, as is usually done, and provided bounding cases for the behaviour. The fitted simulations were shown to be good representations of the experimental state (§ III.4.3).

The modelling approach relied on explicit definition of the rollers and beam, with contact surfaces defined between the two materials, including an assumed friction coefficient. This approach is in line with other models of graphite-steel contacts. The effect of axial friction due to the roller contact will always be speculative, and may be the cause of the slight difference between the DIC and linear elastic FE profiles seen in Figure 71, though there are other potentially more significant sources of error, arising from the DIC measurement and fitting procedure. A more accurate method of model fitting would be to use the displacements measured directly by image correlation as the input boundary conditions for the model. For these experiments, with only surface imaging available, such a method would have been feasible, but subject to significant inaccuracies. For a more complex geometry, where the contact surface is less easily defined, such a method would be a valuable tool for exploring the evolution of stress and strain.

Comparing the predicted strain profiles ahead of the notch from the LE and UMAT simulations, the reducing modulus apparently increased the volume of material subjected to high tensile strain, especially in the sharp geometries. The size of the stress concertation zones was estimated for the linear elastic and UMAT models from Figure 72, Figure 73, Figure 74 and Figure 75. The largest zone from the UMAT and LE simulations was for the half-depth blunt geometries at 0.3 mm. For the blunt samples there were no significant differences between the predicted strains, with only a slight increase in the zone size for the smaller ligaments. In contrast, the size of the UMAT-predicted zones around the sharp tips were ligament independent, but significantly broader than the LE predictions (up to 0.2 mm), dissipating the high strains. If the UMAT correctly simulate the degradation behaviour, this would indicate the size of a 'damage' zone. The size of the zone is not discredited by the DIC profile data.

III.6.2.1 Stiffness

In the linear elastic simulations an important stage was to adapt the global linear elastic material stiffness to achieve the pop-in load agreement. The tensile stiffness was shown to be a good estimate to the initial flexible stiffness, and the specimens became progressively more compliant with increasing sample deflection (Figure 69). The change was found to be initially rapid, and then approximately linear with increasing deflection, with the stiffness at pop-in reducing to around half the tensile stiffness (for the unnotched beam shown). This loss of stiffness is widely recognised in the literature of graphite fracture. It is unclear whether the origin was some damage or failure mechanism, or non-linear elasticity. In this study, models were run with both the tensile and fitted moduli such that the simulated behaviour bounds behaviour of the beams. Many authors also show unloading curves to demonstrate this increase in compliance; partial unloading was included in the load cycles for these tests to accommodate this behaviour, but, due to concerns over the influence of mechanical settling in the loading setup, the data for these unload cycles could not be analysed satisfactorily.

The progressive deviation from the tensile stiffness supported the use of a material model where the modulus is strain dependent. By changing the Young's modulus of a linear elastic model, the stiffness in every part of the beam was reduced. Such changes are unrealistic if the damage is concentrated around stress concentrators, and the fitted moduli may therefore be an average of the moduli in the beam at the pop-in deflection. This is problematic for the calculation of point-wise properties, such as the NSF and notch sensitivity, since the stress may be significantly overestimated at the notch tip; areal averaged properties, such as SED, would be less affected. In contrast, the non-linear elastic UMAT enabled localised softening such that while most of the beam, including all the regions of compressive stress, maintained the tensile modulus, regions most likely to be subjected damage were able to soften to the point where they effectively offered no resistance. If the form of the stiffness softening curve were appropriately derived this would have the effect of matching the apparent stiffness reduction.

The UMAT was derived from a uniaxial tensile experiment on the same graphite billet. As a function of maximum principal strain, the UMAT was extrapolated by a factor of c. 10 compared to the original tensile experiment for notched flexure loading, and so can only be considered as indicative. Furthermore, despite mesh refinement, the models could not all be run to achieve the expected deflection without a numerical instability (Figure 70), and would have significantly overestimated the load if they had. The UMAT simulations were instead run to load-match the empirical data, so had a lower beam deflections (Figure 71). For the blunt and unnotched geometries, this allowed for numerically stable predictions, but not the sharp geometries where the simulations still exceeded the HAIL, and so require careful interpretation.

The effect of the UMAT was to create a region of dispersed stresses ahead of the stress raising feature in Figure 76 and Figure 77. The sharp geometries particularly exhibited a maximum stress value, which moved away from the notch tip with progressive deflection (Figure 78); this was directly related to the definition of the UMAT.

No attempt was made to modify the UMAT to allow the simulations to run to the full extent required and achieve the correct load. It is unclear whether a simple modification could be made to the existing UMAT; the definition was derived specifically for the graphite used in this study, and any change would also have to be compatible with the original tensile data. Compared to other material models described in § II.5.1, a key strength is the simplicity of the damage definition (a single parameter based on ϵ_1). However, as demonstrated here, it is also the cause of numerical instability in FE simulations. ϵ_1 is an isotropic variable, has no temporal history in the simulation and is highly simplistic. For a uniaxial tensile system this is physically acceptable, but for a flexural system where biaxial or shear strains may be nontrivial, its applicability is questionable.

III.6.3 Crack initiation criteria

Two important aspects of this study were to consider whether small scale testing was appropriate for measuring notch sensitivity in Gilsocarbon, and whether any new information about the crack initiation criteria in Gilsocarbon could be derived. Since only small tests specimens were used in these experiments, it is necessary to compare with historical data to verify that the effect is not scale sensitive.

III.6.3.1 Maximum notch stress criterion

For each of the notched geometries the linear elastic notch concentration factor was calculated at pop-in. This approach was intended to replicate the study by Brown *et al.* 1986 [47]. That study used single edge notched beams of dimensions 117 x 15.5 x 6 mm, with a 13 mm ligament (a/W = 0.16), tested in four-point bend, with an outer roller span of 100 mm an inner roller span of 50 mm. The Gilsocarbon tested (grade NP4) was determined to have an effective inherent flaw size of 0.6 mm [94], and flexural strength of 41 MPa. Figure 93 replots the data from Figure 79 overlaid on the figure from Brown *et al.* [47].

Brown *et al.* demonstrated Gilsocarbon notch strengthening factors calculated by the reduced-ligament formulation of 1.74 ± 0.2 for a notch radius of 0.02 mm, reducing to 1.57 ± 0.08 for a radius of 1.0 mm. This represents a significant insensitivity to stress raising features in these relatively large specimens. In the current study, an even smaller sensitivity was observed also calculated using the reduced-ligament formulation with linear elastic stiffness, with the largest mean NSF values for the deep notched samples (with ligaments of c. 1.5 mm, $a/W = 0.75$), with notch tip averaged values of $k_{RL} = 1.37 \pm 0.39$ (1.26, 1.49) and $k_{RL} = 1.44 \pm 0.51$ (1.28, 1.60) for the blunt and sharp geometries, respectively. The mean NSF values for the half-depth and shallow notches were even closer to unity, suggesting a complete insensitivity at the 95% confidence level. While the difference might be explained by the different Gilsocarbon grades tested, Figure 93 suggests that the samples in this study were even less sensitive than the coarser grained PGA. This is an important result when considering a PIE test, since it may indicate a lower bound on the specimen size from which notch sensitivity could be measured.

The calculation of the reduced ligament NSF using a non-linear stiffness is also an important result, as no evidence has been found for such a calculation previously for any material. The UMAT predictions appear to follow the historical Gilsocarbon curve in the figure, and were insensitive to ligament size (due to the maximum stress limiting behaviour). The UMAT may therefore capture sufficient information to be useful for predicting scalable results, but the accuracy is, of course, degraded beyond the HAIL. This relationship should be investigated further, including a size effect study.

In Figure 80 and Figure 81, the notch sensitivity ratio was shown to be sensitive to notch radius, and notch depth. Brocklehurst and Brown [46] made a similar study of several Gilsocarbon grades using a variety of geometries that included square cross-section beams. For the beams, the cross-section dimensions were W = 0.5 ” (12.3 mm). Across the notched geometries, with a/W = [0.1, 0.4], and the notch tip radii, R = [c. 0.001 ” (0.025 mm), 0.4 ” (10.2 mm)]. Stresses were calculated using the reduced ligament method. The data in Figure 81 is re-plotted over the results from the Brocklehurst and Brown study in Figure 94, where a mean value is plotted for each graphite grade at different radii. The λ values calculated in this study are comparable, and the trendline they proposed appears to be a good fit to the half-depth geometries despite the different scale of the beams. It is difficult to extrapolate the proposed fitting curve to the radius of the sharp notches, so only a qualitative comparison can be made. The Brocklehurst and Brown notch sensitivities for the blunt notches is estimated from the trend line as $\hat{\lambda} = 0.58$. The UMAT simulated values stand out as being exactly on trend for all the notched geometries, though no uncertainty is given for these values. For the reduced ligament predictions, at the 5 % significance level, only the shallow and blunt half-depth geometries would be expected to exhibit the same notch sensitivity as the larger specimens, while the blunt deep-notched beams are quantitatively more sensitive, *viz* they behave more similarly to the linear elastic prediction.

The favourable comparison with these historical studies suggests that using small-scale specimens is not prohibitive in measuring the notch sensitivity of crack initiation in virgin Gilsocarbon. The size of the specimens in the studies represented in Figure 93 and Figure 94 is at least double that of the geometries in this study. The notch tip radii are comparable, for both blunt and sharp notches, but the ligaments are considerably larger, especially compared to the half-depth and deep notched samples in this study. The UMAT formulation appears particularly well-suited for matching the behaviour predicted by the large beams.

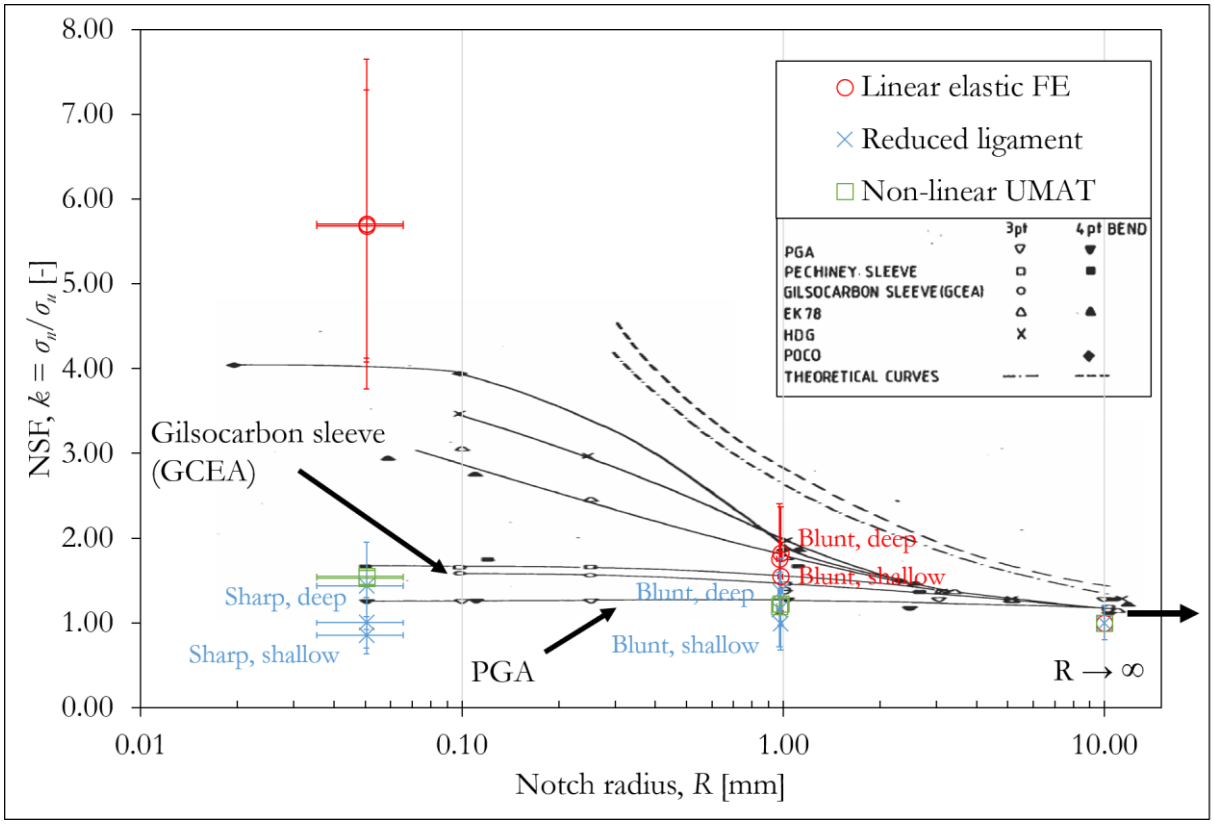


Figure 93: Notch strengthening factors, k, calculated by linear elastic and reduced ligament stress methodologies, replotted from Figure 79, and compared to notch sensitivity study by Brown et al. [47] (see § II.3.2).

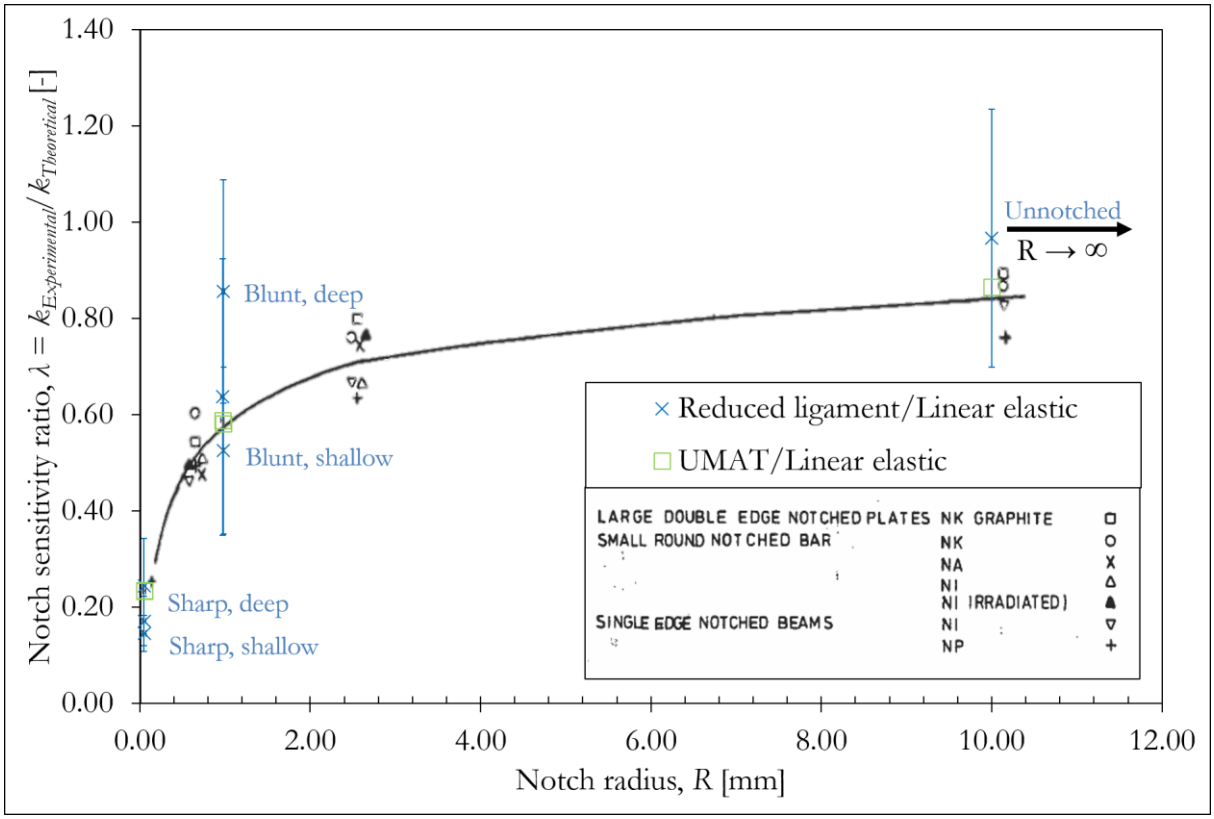


Figure 94: Notch sensitivity ratio, λ, calculated by linear elastic and reduced ligament stress methodologies, replotted from Figure 81, and compared to notch sensitivity study by Brocklehurst and Brown [46] (see § II.3.2). Original image reprinted from [93], with permission from Marcel Dekker.

III.6.3.2 Critical strain energy density criterion

Strain energy density was calculated and averaged over the critical volume defined by Lazzarin and Berto's formulation, which was dependent on the stress state (plane strain or plane stress), notch geometry and material properties.

The c. 10 % higher mean SED in plane strain than in plane stress (Figure 85) implies that if the fracture criterion is dependent on mean SED rising above a threshold, the crack might be expected to initiate in the plane strain region, that is, the centre of the specimen, especially for a larger specimen. As such, any proto crack may not be visible to surface observation, as conducted here. Since these data points relate to cracks observed on the surface plane, the mechanisms for energy release during crack formation must require that the proto-crack is sub-critical in the location that it forms, or else the crack immediately grows to the surface.

The non-linear elastic stiffness further accentuated these differences. This is in part explained by the UMAT-FE being load-matched, so the gross deflections and strains were not equivalent. To estimate the error in the gross strain behaviour arising from the load-matching, consider the linear elastic unnotched beam, for which the relationship between load and deflection (or $\vec{U}_{Roll}$) was described in Figure 69(a). For the E_{TLE} curve, if the simulation was stopped at the iteration that achieved load matching, the strains would be reduced by c. 40 %. For the LE case, this would proportionally reduce the SED (since $\varrho \propto \sigma.\epsilon$). The UMAT would be less affected due to the strain softening and stress redistribution, such that a 40 % correction is bounding approximation.

From the linear elastic simulations using bounding moduli, the critical strain energy density for the crack initiation of Gilsocarbon was estimated to lie in the range $\rho_{LE,C}^{DIC}$ = [9.2, 14.8] kJ.m^{-3}, in agreement with the predictions by Brocklehurst and Darby despite the simplistic assumptions behind that estimation. The mean value for the non-linear elastic stiffness was slightly lower, at $\rho_{UMAT,C}^{FE}$ = 7.2 ± 5.0 (5.4, 9.0) kJ.m^{-3}, which increased to $\rho'^{FE}_{UMAT,C}$ ≈ 12 kJ.m^{-3} if the 40 % strain correction is applied (hence these are bounding values). Comparing the geometries there was a significant scatter in the measured values using all the material models. Consideration of the dependence on geometry indicated that critical SED may be particularly dependent on ligament, though the available data is too sparse to draw firm conclusions (Figure 87).

As a pragmatic approach, ϱ_C will be assumed to be the central value of the LE range, ϱ_C = 12.0 kJ.m^{-3} (agreeing with $\rho'^{FE}_{UMAT,C}$). Using this value, and the quadratic relations between SED and both load and $\vec{U}_{Roll}$ (for example, see Figure 84 (a) and (c)), the critical loads and displacements can be back-calculated to test the sensitivity to the estimated values. The experimental crack initiation parameters are predicted for three different geometries in Table 14; the example specimens chosen were selected to include the extreme SED predictions. In the table the predicted values were compared (and coloured) as percentage differences relative to the experimental data taken from Table 5 and Table 6, and also plotted as 1:1 comparisons in Figure 95. The figure shows that for the blunt and unnotched specimens considered, (E_{FLE}) linear elasticity can be used to predict both the load and displacement to within ± 10 %. The E_{UMAT} and E_{TLE} predictions were also in reasonably good agreement for the specimens (within ± 30 %) and predicted consistently higher or lower values than the E_{FLE} simulations. The predictions for the sharp half depth specimen were less accurate, with the E_{UMAT} over predicting load by 92 %. It is unclear why the sharp notch estimate was so far off, but the specimen may just have outlier behaviour (it has the lowest SED in Figure 86). No attempt was made to compensate for the potential effect of notch geometry shown in Figure 87; such a correction is likely to improve the estimates, but since the dataset defining the trends is sparse, testing the model against the data it is fitted to is nonsensical. Refining the potential geometric trends is an area for future investigation.

The use of the Lazzarin and Berto definition of the ROI makes the technique more generally applicable, since there is no assumption about the critical volume based on the test geometry, only on the material properties and the notch geometry. The Brocklehurst and Darby-type approach was suitable for unnotched beams, and bounded the critical SED as tightly as the linear elastic simulation predictions. However, that method cannot be used to measure the SED evolution prior to fracture in an arbitrary geometry. Overall, the use of critical SED with ϱ_C is demonstrated to be a good first-order criterion for Gilsocarbon crack initiation.

The area-averaging basis of the SED calculation makes it relatively insensitive to microstructure, but assumes a homogeneous and isotropic medium. Questions therefore remain as to how the strains build up within the heterogeneous microstructure under an applied deformation, since these could affect the stress distributions and ultimate failure of the specimens. Measurements of this type were not possible from the surface imaging, and so this behaviour will be explored the following chapter using 3D imaging of the internal microstructure of specimens under *in situ* loading.

Table 14:Predicted critical loads and roller displacements, assuming a critical strain energy density criterion with ϱ_C = 12.0 kJ.m^{-3}, for each material model: tensile linear elastic, E_{TLE}, fitted linear elastic, E_{FLE}, and the non-linear elastic UMAT, E_{UMAT}. Each prediction is compared to the measured load and extension from Table 5 with a percentage difference relative to the measured value given. For ease of reference, the cells are coloured by the absolute percentage difference (darkest cells being the largest differences). For the U_{Roll} prediction, the linear elastic models are equivalent.

Specimen	Load, F_C [N]				Roller displacement, U_{Roll} [µm]		
	Measured	E_{TLE}	E_{FLE}	E_{UMAT}	Measured	E_{LE}	E_{UMAT}
1 (Blunt shallow)	244	187 (-23 %)	231 (-6 %)	258 (5 %)	40.2	38.1 (-5 %)	30.9 (-23 %)
2 (Blunt shallow)	218	202 (-7 %)	239 (10 %)	261 (20 %)	33.6	36.8 (9 %)	31.0 (-8 %)
8 (Sharp half-depth)	75	99 (31 %)	129 (71 %)	144 (92 %)	28.6	48.2 (68 %)	37.2 (30 %)
10 (Unnotched)	275	201 (-27 %)	262 (-5 %)	326 (19 %)	43.9	42.2 (-4 %)	33.2 (-24 %)

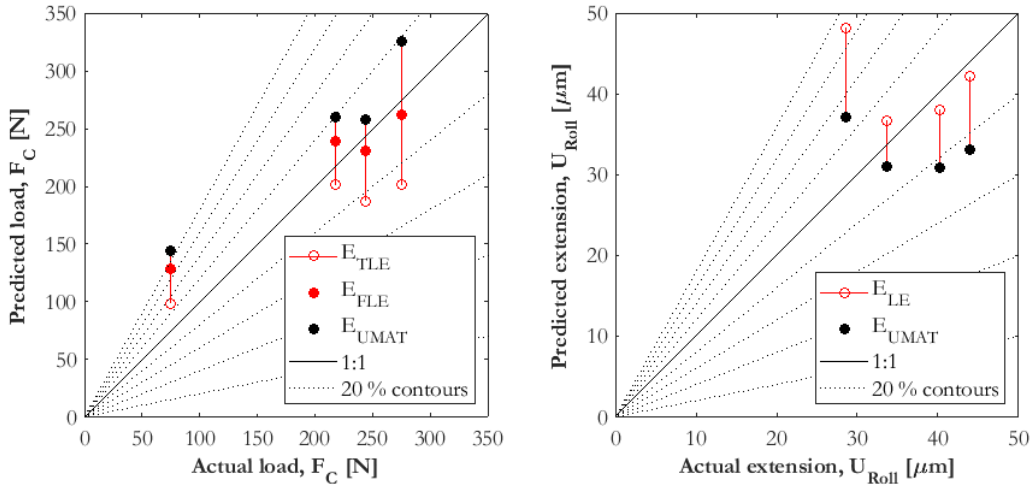


Figure 95: Predicted critical loads and roller displacements, assuming a critical strain energy density criterion with ϱ_C = 12.0 kJ.m^{-3}, plotted relative to the measured value for each specimen using the different material models. For each geometry, the complementary predictions from the different material models are connected: linear elasticity using the tensile modulus, E_{TLE}, and the fitted modulus, E_{FLE}, and the non-linear UMAT, E_{UMAT}. For the U_{Roll} prediction, the linear elastic models are equivalent.

III.6.3.3 Use of DIC in SED monitoring

DIC is a valuable tool for making noncontact, *in situ* and near real-time measurements of displacement from which small strains may be trivially derived. As a technique to define the boundary conditions for FE simulation, the power and significant benefits of DIC were demonstrated in § III.4.3 compared to relying on contact measurements. DIC has several limitations, including that it requires good patterning on the sample for reliable correlation, it is sensitive to sample and image boundaries, and, in this study, the high-resolution data was monoscopic such that out-of-plane strains could not be measured. It should be noted that combining DIC and FE accurately, for real-time monitoring SED evolution during a fracture test for example, is likely to be a time consuming and computationally expensive approach.

In § III.5.3, estimates of the surface SED based only on DIC were shown to be in very good agreement with the FE simulations from § III.5.2.3, as seen in Figure 90. This agreement was seen despite the limitations of DIC meaning that both the stress and strain fields were incomplete (Figure 88). The slight under-prediction of the E_{FLE} SED values may be explained by the necessity of selecting the correlation penultimate to pop-in; this issue might be avoided with careful consideration of which traces in Figure 89 showed anomalous increases, and only reselecting the pop-in correlation for those specimens.

A major benefit of SED calculated from DIC only using the E_{UMAT} was that the issues of FE simulation numerical instability beyond the HAIL were avoided. Direct measurements of strains meant that the predicted stresses, and hence SED, reflected both load- and deflection-matched state. The apparent over-prediction of the E_{UMAT} values in Figure 90 by 31 % on average may be explained by recalling that the E_{UMAT} FE simulations, which were only load-matched, were estimated to underpredict the strains by up to 40 % (§ III.6.3.2); this offset would also apply to the SED, given that the stresses were self-limiting.

The FE-derived ϱ_C of 12 kJ.m^{-3} is bounded by the geometry-averaged LE SEDs ($\rho_{LE,C}^{DIC}$ = [7.8, 12.6] kJ.m^{-3}), and falls in the 95%CI of $\hat{\rho}_{UMAT,C}^{DIC}$, supporting the ϱ_C selection. However, it must be noted that the 95%ile scatter is very large; again, this might be reduced by developing a notch geometry-dependent ϱ_C. The key finding is that the ϱ values compared well to the simulation predictions, supporting the use of DIC to measure SED as a first-order predictor for Gilsocarbon fracture.

The results of Gomez *et al* [139] and Lazzarin and Berto *[137]* appear to confirm that the SED calculation technique is scalable and applicable to any geometry, and may be used to easily calculate K_{IC} or J_{IC} by (15) and (4) without requiring any FE analysis. Their testing has only been conducted on fine-grained materials. Never-the-less, the methodology has potential for use in real-time monitoring of SED evolution, and hence *in situ* crack initiation detection. In this study only four-point flexural specimens were tested, and so for more general application to other loading modes, further work would be required to validate the theory. Once validated, SED monitoring from visual inspection could have significant application, since it would permit real-time calculation of the SED, without requiring any sophisticated FE software, or the simulation time involved. As a fracture predictor, real-time calculation of SED could be used during damage monitoring of equipment to detect imminent failure of graphite components, and so prevent catastrophic cracking. While this would not be feasible for an AGR, since continuous visual monitoring is not possible, there may be application in other sectors which employ graphite components. For the AGR's, SED measurement could be conducted during PIE testing to ensure that the behaviour under radiolytic oxidation and fast neutron irradiation was consistent with the understanding of the virgin material, and possibly deployed by applying DIC to the images captured during regular fuel channels inspections at reactor shutdown to observe any long-term SED evolution.

III.7 Conclusions

This small-size specimen campaign had three purposes: firstly, to establish whether the behaviour in historical testing was observed, despite different specimen volumes; secondly, whether the strain energy density (SED) could be applied as a fracture criterion for differently notched geometries, using modern SED simulation techniques; and thirdly, whether (near) real-time monitoring of graphite components might be possible to detect imminent crack initiation using non-contact DIC without relying on finite element simulation. The coupling of detailed experimental measurements with advanced finite element modelling was demonstrated to be a powerful tool in understanding the notch sensitivity of small specimens of Gilsocarbon. Over 100 small beams machined with seven different notch geometries were fractured in four-point bend. The geometries explored the dependence on notch radius and depth, aiming to simulate the possible keyway root radii. By using an *in situ* multi-camera imaging system during small specimen fracture testing, precise full field displacements were determined, from which stresses were predicted by FE modelling using both linear and non-linear stiffness models.

The analysis demonstrated that in four-point bend, Gilsocarbon beams of 6 x 6 x 19 mm with a loading span of only 5.33 mm were relatively insensitive to notches with radii between 0.05 and 1.00 mm, in keeping with the literature results for specimens with double the linear dimensions. Bounding values of the critical SED were derived from finite element simulation, using fitted moduli, from which the central value (12.0 $kJ.m^{-3}$) was shown to provide a relatively reliable fracture criterion, especially with the application of a non-linear elastic stiffness model. Further improvement may be made by developing a geometry-dependent criterion, but that was not explored in detail. An equation for SED based on elementary beam theory was shown to be a good predictor even for notched beams of squat geometry and a coarse microstructure, bounding the critical SED as tightly as the simulated values. The DIC measured values were shown to be in very good agreement to the FE simulated values. The findings from the study further the understanding of crack initiation and notch sensitivity in Gilsocarbon, which will better inform post irradiation examination techniques for Gilsocarbon removed from the advanced gas cooled reactors. Furthermore, the techniques and trends could be applied to understand the notch sensitivity and size effects in coarse-grained materials tested at small scales.

In summary, a large sample of specimens has been tested to determine the statistical distributions of stresses and strains at crack initiation ahead of notches of different geometries. Simple and generic homogeneous fracture behaviour was assumed, and it was demonstrated that Gilsocarbon is somewhat insensitive to notches even with small geometries; the notch sensitivity of the sharp-notched specimens was far less than expected for a linear elastic brittle material, and comparable to those with blunt notches, or even unnotched.

Questions remain as to how the strains build up within the heterogeneous microstructure under an applied deformation, since these could affect the stress distributions and ultimate failure of the specimens. Measurements of this type were not possible from the surface imaging, and so this behaviour will be explored the following chapter using 3D imaging of the internal microstructure of specimens under *in situ* loading.

IV Microstructural Response to Crack Initiation in Gilsocarbon

IV.1 Introduction

In this chapter the response of the Gilsocarbon microstructure to external loading will be explored, focusing on the deformation ahead of a blunt notch tip prior to crack initiation. In the previous chapter, a large sample of specimens was tested to determine the statistical distributions of stresses and strains at crack initiation ahead of notches of different geometries. Simple and generic homogeneous fracture behaviour was assumed, and it was demonstrated that Gilsocarbon is somewhat insensitive to notches even with small geometries; the notch sensitivity of the sharp-notched specimens was far less than expected for a linear elastic brittle material, and comparable to those with blunt notches, or even unnotched.

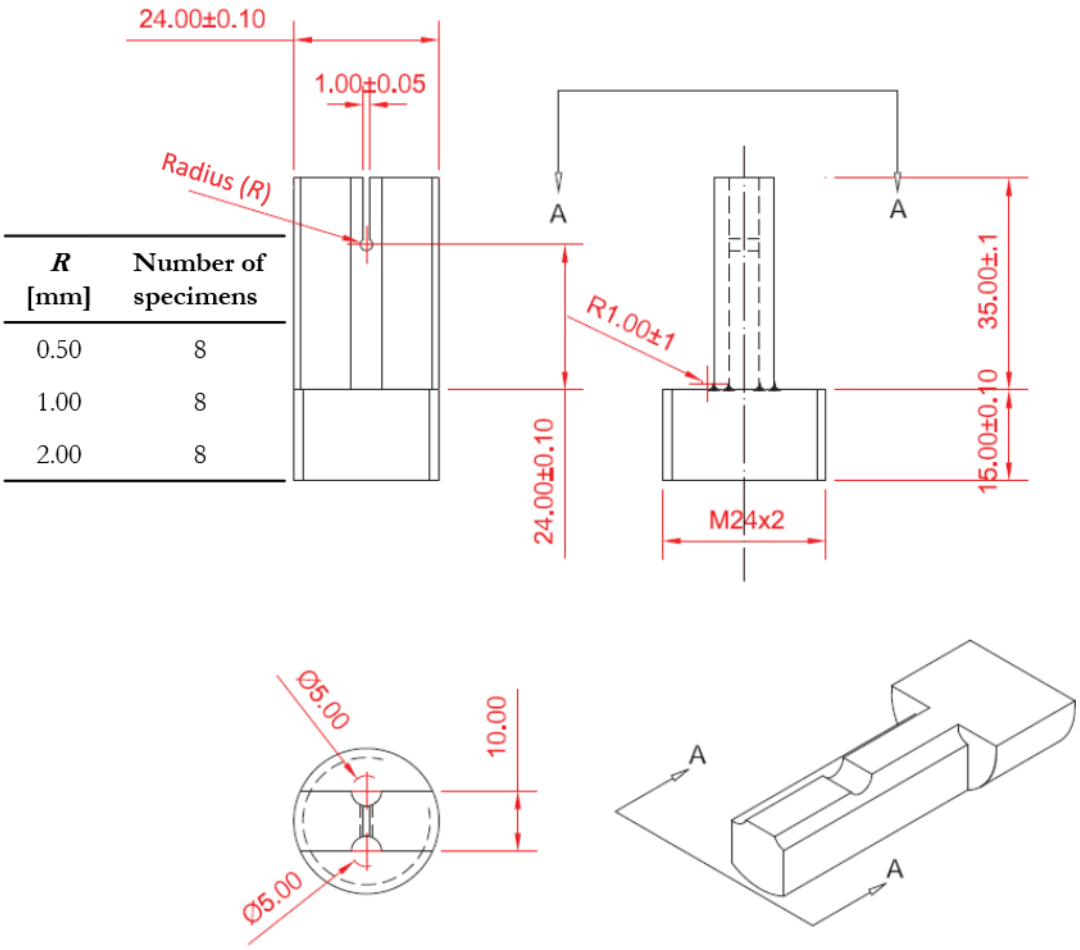
Commercial graphite grades used for reactor moderation are heterogeneous materials, where the physical properties of the binder and filler are known to be different, and so a heterogeneous response to applied strains would be expected. This assumption has been used to justify the non-linear tensile and compressive behaviour in bulk, the quasi-brittle failure and to loosely explain the notch insensitivity of graphites, including Gilsocarbon. These assertions are generally based on 1) the correlation between the nominal filler particle size and the notch dimension (radius or depth) at which the strength of a notched beam saturates, and 2) the microstructural observation that propagated cracks arrest inside or avoid filler particles. An understanding of how non-linear strains develop is yet to mature; formation of a regional 'plastic zone' or sub-critical cracking after exceeding some yield criterion is a potential mechanism, and studies have inferred the presence and size (several millimetres) of a 'damage' zone, but how these zones might be linked is undefined.

Determining how the microstructure responds to an applied deformation and any potential mechanisms of damage will support predictions of crack initiation. From these observations, an understanding of Gilsocarbon's notch insensitivity could be derived. 3D X-ray imaging and image correlation techniques will be used to measure the internal deformations of loaded graphite ahead of a blunt feature, using a novel keyhole notch geometry. By calculating the deviations between the empirical deformations and linear elastic simulation, the heterogeneous nature of Gilsocarbon's microstructure will be demonstrated, with different damage behaviours associated with the microstructural phases. The non-linear and non-recoverable nature of these deviations will be assessed. The boundary of a permanent strain concentration zone will be proposed, and used to explain the origin of the notch insensitivity. The ϵCZ is fully-formed ahead of the notch at very low loads and the size is approximately consistent with the size of zone expected ahead of a 2.00 mm radius notch from the linear elastic simulation.

IV.2 Experiment

IV.2.1 Specimen geometry

Keyhole notched, KN, specimens of virgin Gilsocarbon were prepared according to Figure 96. The gross geometry was constrained for compatibility with X-ray imaging, and particularly that signal attenuation would not significantly affect tomography. In general terms, the geometry was a 24.00 x 35.00 mm plate with a 1.00 mm slot cut in the narrow edge. Three variants of the circular notch tips were selected to simulate the stipulated keyway root machining, as radii (*R*) of 0.50, 1.00 and 2.00 mm. Around the notch, the 10.00 mm thick plate was thinned to 5.00 mm. By inserting a 10° wedge into the slot, the notches could be opened progressively and precisely until a pop-in was detected (as outlined in § III.3.1), with the geometry encouraging thermodynamically stable crack initiation and planar propagation. Eight specimens of each geometry were machined from the same billet as the specimens used in the small beam testing (see Chapter III), and the previously discussed studies by Marrow *et al.* [88] and Barhli *et al.* [89]. The geometries will be referred to by their notch tip radii, for example KN05 for the sharpest notched geometry, at 0.50 mm.



R [mm]	Number of specimens
0.50	8
1.00	8
2.00	8

Figure 96: Keyhole notched geometries, where the keyhole radius R *was varied as per the inset table. All dimensions in millimetres.*

IV.2.2 Mechanical loading

The specimens were loaded under quasi-static displacement-controlled conditions in the University of Birmingham XCT loading stage described in § III.2.2. The specimens were mounted in a bespoke wedge-loading jig that was used to encourage specimen-wedge alignment (see Figure 97); the jig was designed for these experiments and used by Barhli *et al.* After fixing the specimen height for the X-ray beam and coarse alignment of the wedge with the notch, additional fine alignment (manual and automatic) was achieved by two degrees of freedom in the jig: free rotation of the bearing-mounted wedge and one-dimensional specimen translation, as indicated in Figure 97(b). After applying a slight preload, the linear displacement mechanism assembly in Figure 97(a) enabled the specimen's horizontal position to be gently manipulated to ensure perfect alignment with the wedge, indicated by a minimum registered load. The applied crosshead displacement, δ, of the wedge were recorded by the rig's in-built transducers to a precision 1 μm, while the load, F, was measured by an *Applied Measurements* DDEMF miniature in-line load cell, with a 1 N precision. During loading, data was typically logged at 0.5 s intervals.

Before the tomography experiments the mean peak load, F_M, and critical load, F_C, were measured by fracturing all the specimens, except for one of each of the KN1 and KN2 geometries. F_C was the pop-in load for all the keyhole notch specimens. From the preloaded state, the specimens were loaded at a rate of 1.5 μm.s^{-1} either monotonically to fracture, or up to 50 N, followed by a full unload (with the wedge completely removed) and then reloaded until fracture. No significant differences were observed between the $F(\delta)$ behaviour of the specimens loaded in the two patterns. No *in situ* imaging of these tests was made. An example load-displacement curve is shown in Figure 98 (a) for a load-reload specimen showing both the raw data, and data after 'cleaning' by smoothing using a cubic Savitzky-Golay [172] (implemented in MATLAB®'s SGOLAYFILT function, over a 9-point domain), and then removing the unload cycles using the same algorithm as the beam specimens in § III.3.1 to form a monotonic trace (to failure). The Golay smoothing filter was necessary distinguish the general trends such that the peak detection algorithm could be used accurately. The pop-ins were determined following the criteria in § III.3.1 but averaged over only a 30-point domain due to the lower sampling frequency. Due to the free motion of the wedge mounting, the unload behaviour cannot be determined from this data; the specimen appears to unload instantaneously, followed by a fictitious compressive load. The F_M and F_C values were recorded in Table 15, with $\hat{F}_C$ = 71, 77 and 84 N and $\hat{F}_M$ = 81, 90 and 94 N for the KN05, KN1 and KN2 geometries, respectively.[19]

[19] For one of the KN1 specimens only the F_M value was recorded due to a logging error during loading.

The mean fracture loads informed the target loading of the reserved specimens, which were tested at the DLS on the Joint Engineering, Environmental, and Processing beamline (I12-JEEP) [173] in experiment EE8519-1. Additional unload-reload stages were introduced, with the target loads increasing until crack initiation as 25 N, 50 N, 75 N, 85 N and 95 N. Figure 99 shows the intended and actual loading schedules. The loading was also paused every c. 10 N for *in situ* imaging (radiographs); see § IV.2.3 for further details. The load-displacement traces (incremental loading only) of the two specimens are shown in Figure 98 (b) and (c). For KN1, F_C = 67 N and F_M = 78 N; while the pop-in load was within the statistical estimate of the mean, the maximum value was outside the preliminary 95%CI. For KN2, F_C = 94 N and F_M = 96 N, in agreement with the preliminary 95%CI for this geometry.

To include the additional load data, the updated F_M and F_C distributions are appended to Table 15 for reference, and these distributions plotted in Figure 100 (with the KN05 data) as box and whisker plots. In the box and whisker plots, the interquartile ranges of between 10 N and 20 N were seen for all the geometries and both measures. The KN05 and KN2 distributions appeared approximately symmetric, both with a few data points indicated as outside the 95%ile distributions. The KN1 data appeared to be slightly skewed in favour of high loads. Given the small sample sizes, no effort was made to remove anomalous values. The F_C/F_M ratios in Table 15 indicate that the mean pops in were approximately 11 % lower than the peak loads for all of the geometries, though with significant scatter.

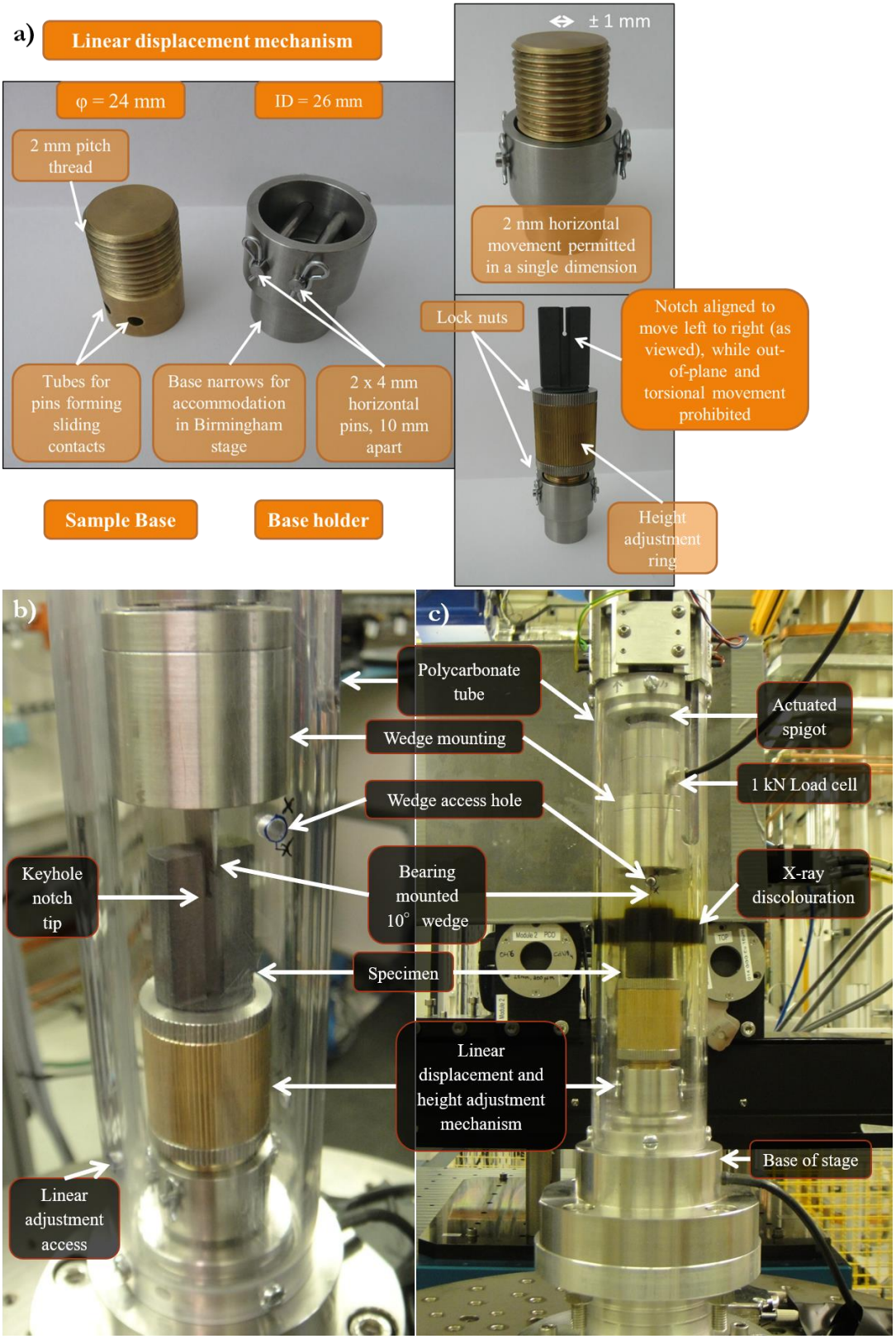


Figure 97: For wedge loading of the keyhole notch specimens the University of Birmingham rig was setup at the Diamond Light Source with the wedge-loading jig and specimen. a) The wedge-loading jig enabled 1-dimensional movement of the specimen via the linear displacement mechanism, at a fixed specimen height. When assembled in the loading stage (b), the specimen position was adjusted beneath the bearing-mounted wedge via the linear adjustment access holes. The loading rig was mounted on the I12 controller stage for in situ X-ray imaging (c) and is viewed along the beam (looking towards the scintillators). The photograph was captured after the experiment, which involved c. 60 hours of X-ray exposure and caused the discolouration band across the tube. The band indicates the location and approximate height of the tomographic region of interest.

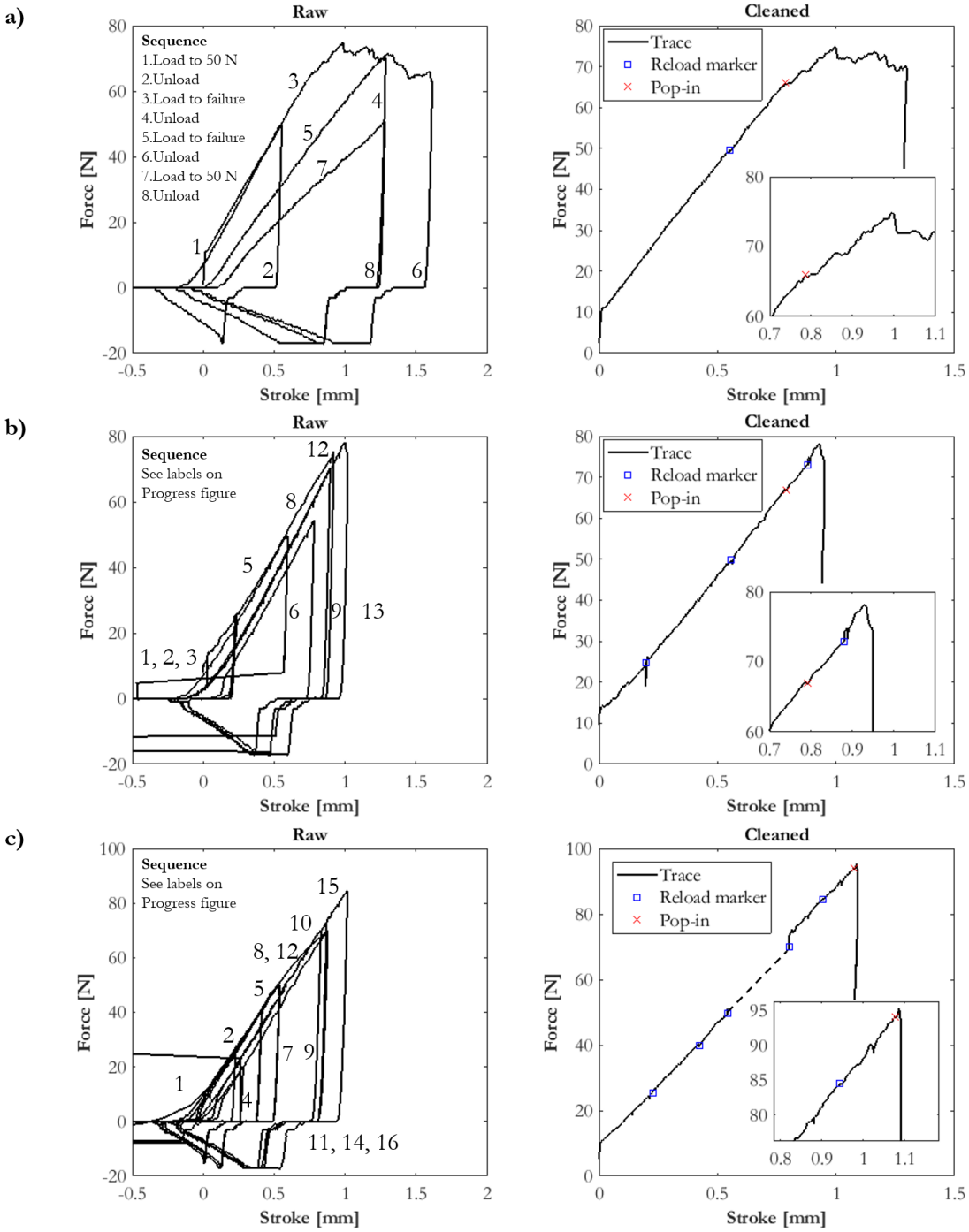


Figure 98: Example load-displacement trace for one specimen in each KN geometry: (a) KN05, (b) KN1, and (c) KN2. The KN05 specimen was loaded under displacement control to 50 N, unloaded and reloaded to failure, while the KN1 and KN2 specimens were loaded as part of the testing at the DLS, with unloading at 50, 75, 85, 78 and 96 N; see Figure 99 for definition of the loading sequence stages. The raw traces in were filtered using a Savitzky-Golay filter (cubic, 9-point window), cleaned to form a monotonic trace to failure and the pop-in detected in. Due to experimental errors, the KN2 loading cycle to 75 N was incorrectly logged, so an estimate of the cleaned trace is given (dashed line).

*Table 15: Fracture load distributions for the KN specimens, also shown in Figure 100. Distributions are described in terms of mean, 95%ile, and 95%CI using the nomenclature defined in § iv. *Distribution recalculated using data from DLS-tested specimens. †For one KN1 specimen, no F_C value is available due to logging errors during experiment.*

Notch tip radius, ***R***	Number of specimens	Load		
		Critical, F_C	Maximum, F_m	Ratio (F_C/F_M)
[mm]	[-]	[N]	[N]	[%]
0.50	8	71 ± 17 (64, 78)	81 ± 16 (74, 88)	89 ± 16 (82, 95)
1.00	7†	77 ± 28 (62, 91)	90 ± 21 (80, 99)	88 ± 31 (71, 104)
2.00	7	84 ± 29 (70, 98)	94 ± 22 (84, 104)	89 ± 19 (80, 99)
1.00*	8†	75 ± 26 (63, 88)	88 ± 21 (79, 97)	87 ± 28 (74, 101)
2.00*	8	85 ± 28 (74, 97)	94 ± 20 (86, 103)	91 ± 19 (82, 99)
Mean	23†	-	-	89 ± 20 (84, 93)

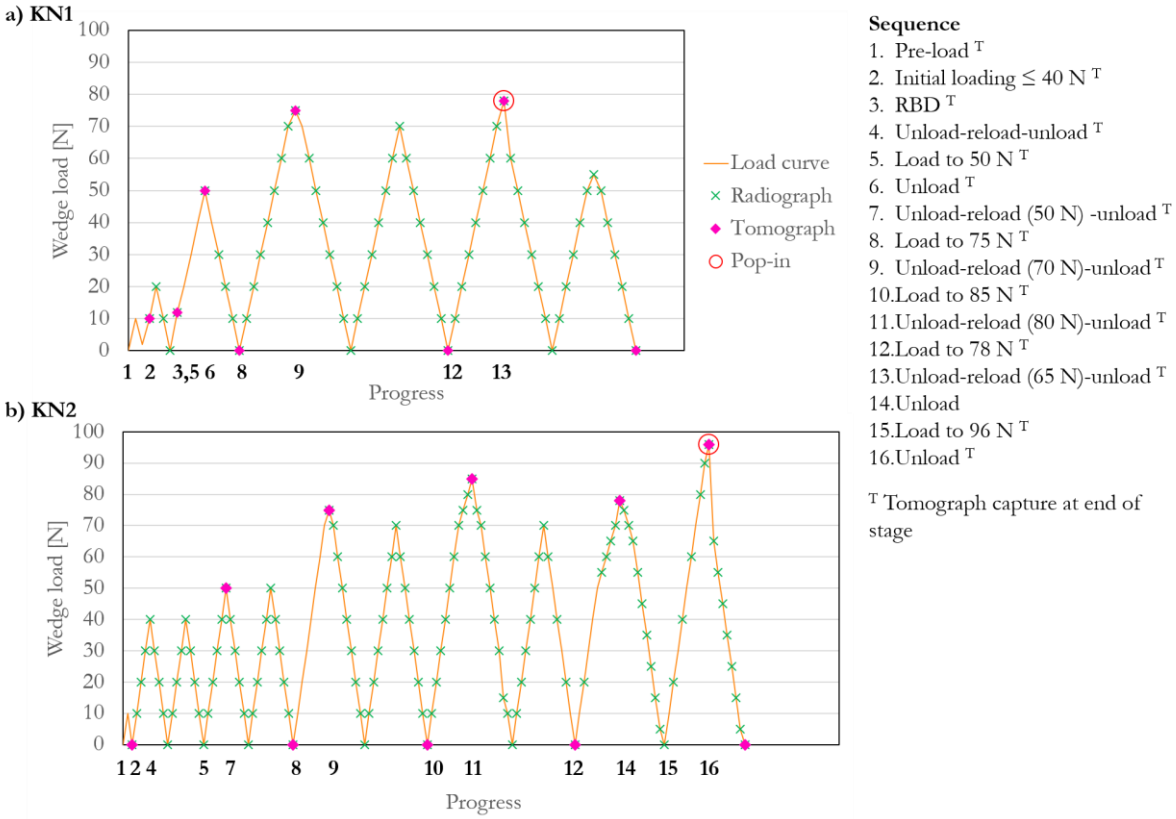


Figure 99: Actual loading and imaging schedule for the tomographed KN specimens, a) KN1 and b) KN2. X-ray radiograph and tomograph imaging points are indicated, as is the tomograph after pop-in. Deformation was displacement-controlled, with the crosshead displacement increasing to attain predetermined target loads, until crack initiation was observed at 78 N and 96 N, respectively.

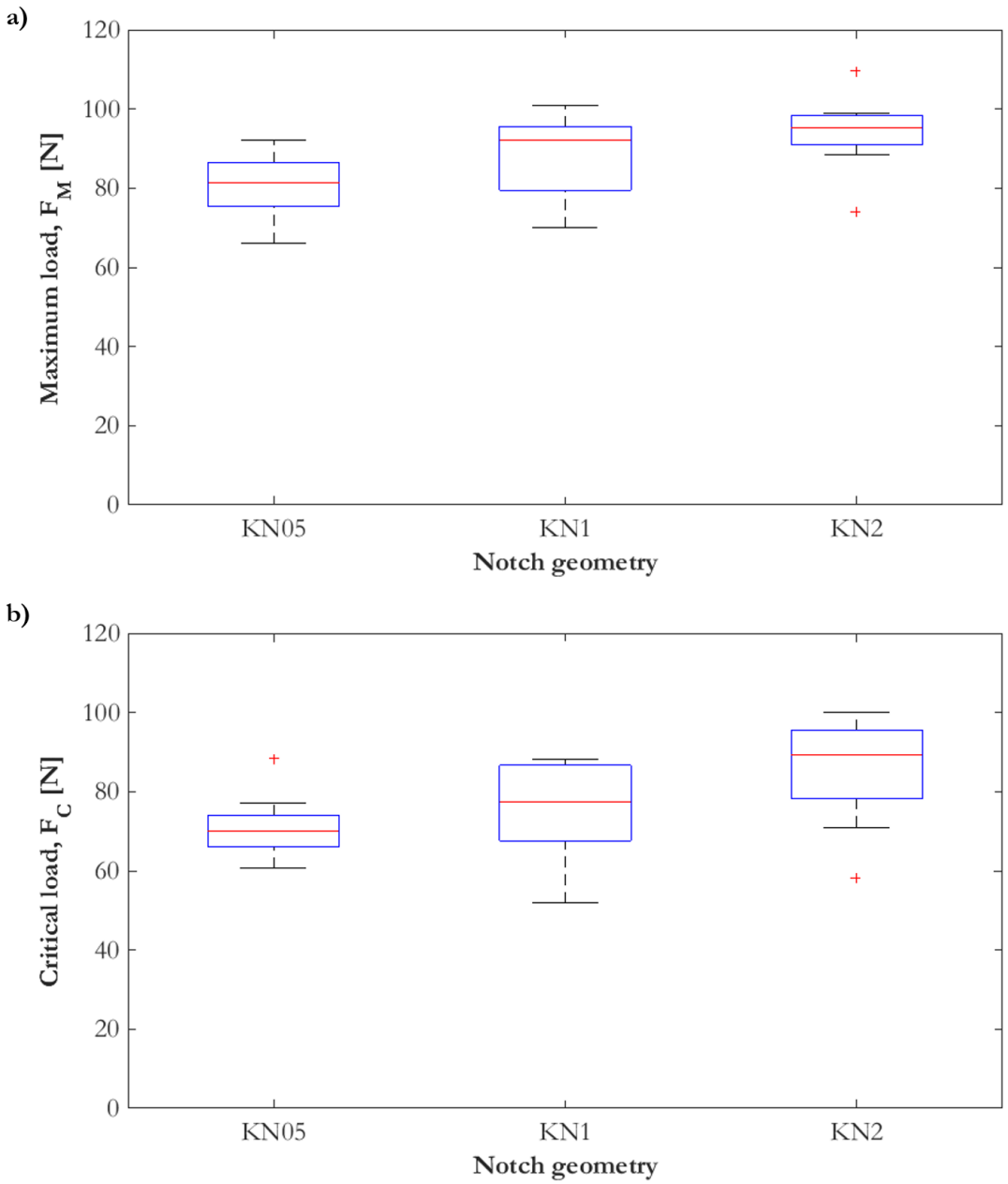


Figure 100: Box and whisker plots of the effect of keyhole notch radius on a) maximum load, F_M, and b) pop-in load, F_P. The centre line indicates the distribution median, and the box bottom and top edges indicate the 25th and 75th percentile, respectively. The whiskers indicate the extent of the data within the 95%ile. Data points outside the 95%ile are indicated by red crosses.

IV.2.3 X-ray imaging

The reserved KN1 and KN2 specimens were X-ray imaged *in situ*: radiographs (single exposure X-ray transmission maps) were taken at 10 N intervals during loading, and volumetric X-ray computed tomographs, XCTs were collected at each of the target loads and subsequent unloads. The imaging schedule is indicated on Figure 99.

For the imaging, a monochromatic X-ray beam energy of 53 keV was used. Small tungsten balls were attached to the specimens as fiducial markers such that the rotational orientation could be determined from the transmission images (see Figure 101(a-b)). The markers were positioned on the upper surface, away from the regions of interest and so did not cast X-ray shadows that would have affected the analysis. The specimen's slot was aligned parallel to beam, such that the opening of the notch faces could be determined by comparing the radiographs (see Figure 101(a-b)). The radiographs were collected at a resolution of 4.9 $\mu m.pixel^{-1}$, and with a maximum usable field of view, FOV, of c. 17 x 12 mm (see Figure 101(c)). To remove imaging artefacts and improve the later quantitative analysis, the radiographs were manipulated as will be described in § IV.2.3.1. Conversely, the XCTs focussed on the material immediately preceding the notch tip, with a resolution of 1.8 $\mu m.voxel^{-1}$ (see Figure 102(a-b)). Each tomograph consisted of 1,800 radiographs captured during a 180° rotation (for example, see Figure 102(c)), and the particulars of the reconstruction procedures will be outlined in § IV.2.3.2. Based on the synchrotron imaging configuration and the specimen geometry, the intended FOV for each tomograph was at least 6.6 x 5.8 x 4.1 mm, but experimental issues with the beamline optics hampered reliable imaging, particularly a monochromator misalignment and scintillator degradation. These limitations reduced the vertical FOV by approximately 50 % for the KN2 specimen tomographs, to approximately 2 mm ahead of the notch. The effect of this degradation on the radiographs for both specimens and the KN1 tomographs was largely insignificant, though increased the noise-to-signal ratio in the vertical direction (*Z*).

During collection of the tomograph of the KN2 specimen in the unloaded state after the 50 N loading, approximately 200 radiographs were not recorded, creating a partial angle tomograph. An attempt at reconstruction was made for this tomograph, though the results were unsuitable for quantitative analysis using digital volume correlation, DVC. Further details are given in § A2.

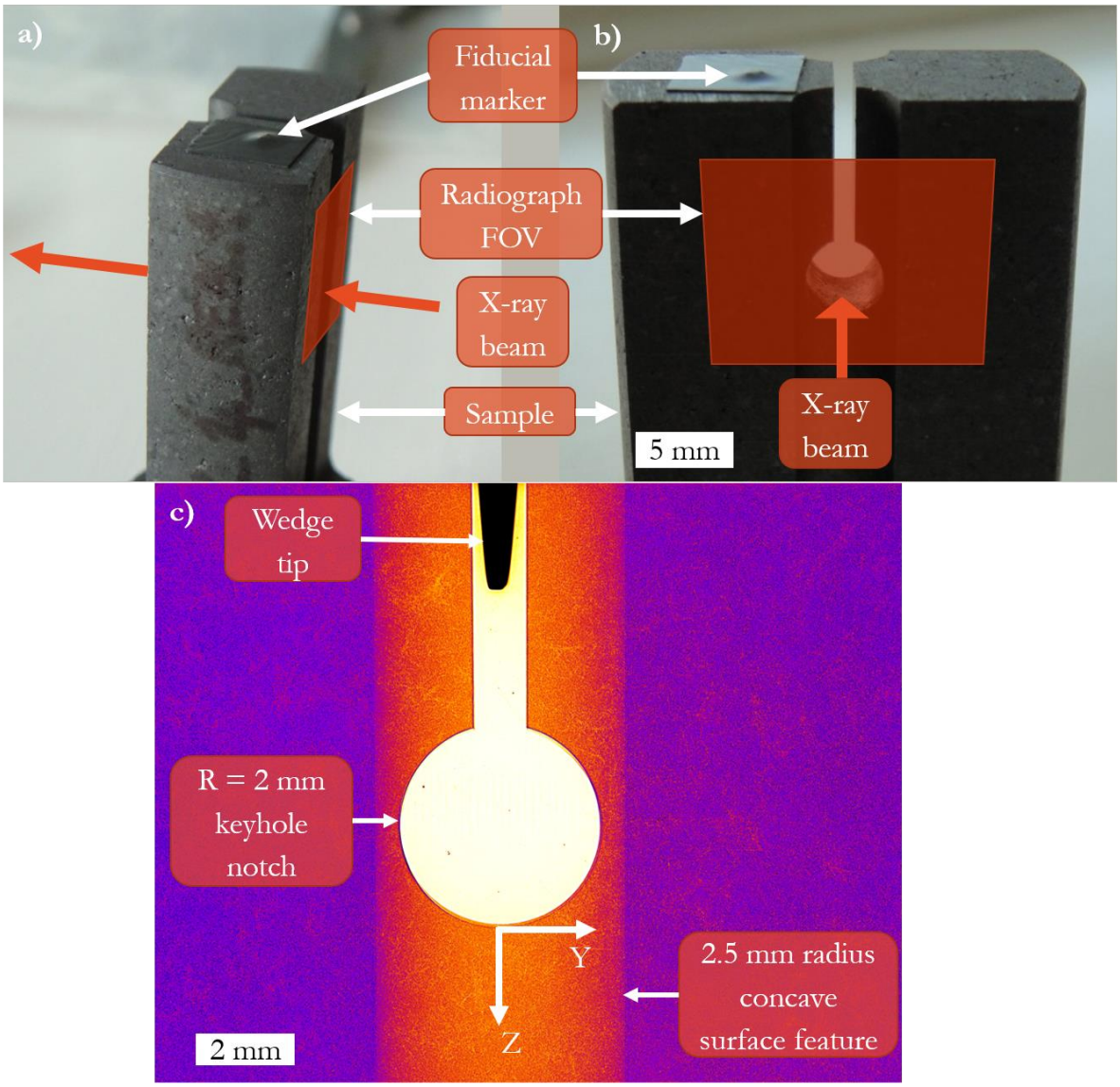


Figure 101: Approximate orientation and FOV of the radiograph imaging for the KN2 specimen, as indicated by the annotations of the photographs from (a) an oblique angle and (b) along the wedge plane, with (c) an example false-coloured radiograph (corrected for background variation), where darker colours indicate lower X-ray transmission, such as the steel wedge. The resolution is 4.9 µm.pixel^{-1}.

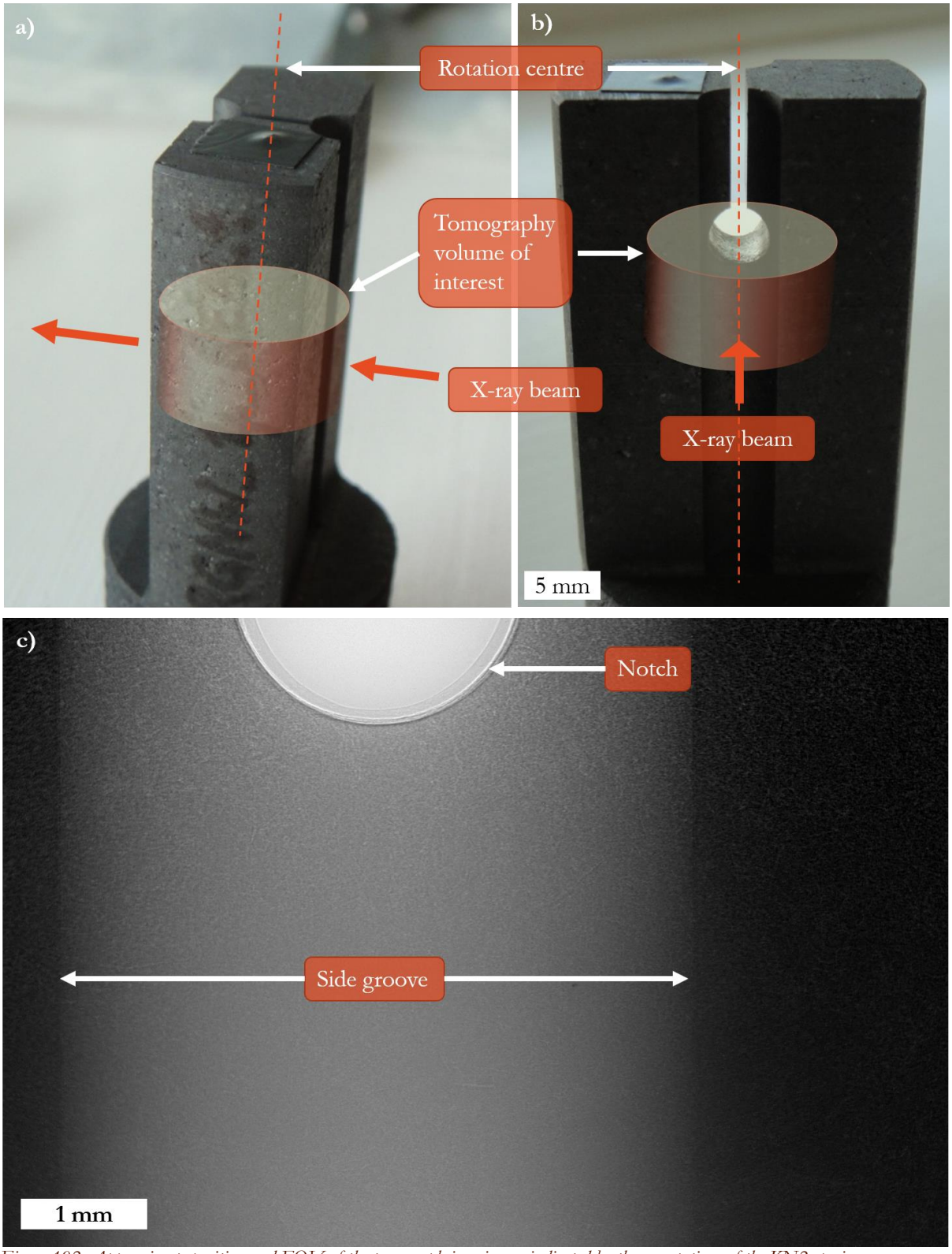


Figure 102: Approximate position and FOV of the tomograph imaging as indicated by the annotations of the KN2 specimen photographs from (a) an oblique angle, and (b) along the wedge plane, with (c) an example tomograph projection (a radiograph corrected for background variation) of the KN1 specimen, imaged along the same imaging orientation as in Figure 101(c). In the projection, darker colours indicate lower X-ray transmission. The resolution is 1.8 μm.pixel^{-1}.

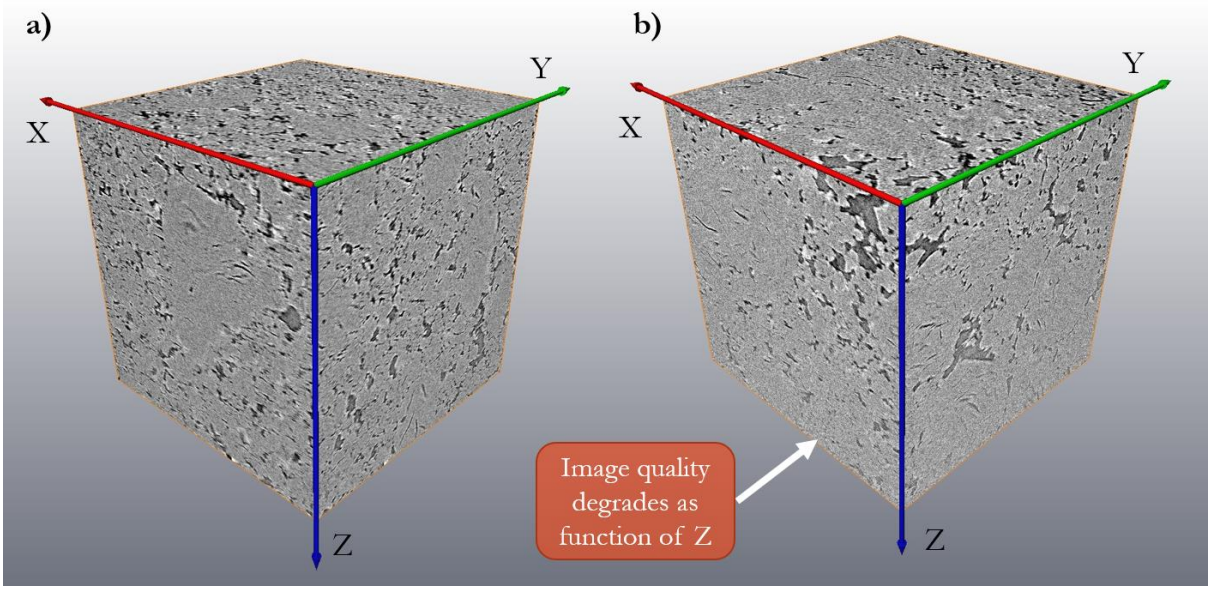


Figure 103: Misalignment of the beamline monochromator and progressive damage to the X-ray optics degraded the tomography quality. The lower halves of the projections of the KN2 tomographs were most significantly degraded; while the microstructural features in the reconstructed KN1 tomograph in (c) can be identified all over the volume, the clarity of the KN2 reconstruction in (d) diminishes rapidly below the centre line as the noise-to-signal ratio increases dramatically. In the reconstructed volumes, darker shades correspond to areas of greater X-ray transmission, such as pores.

IV.2.3.1 Radiograph image treatment

Prior to visualisation and quantitative analyses, the radiographs required manipulation to supress imaging artefacts such as variations in background illumination, detector response, and noise. Processing was performed in ImageJ [161] using a macro that incorporated standard ImageJ tools. The raw radiographs were captured as TIF files at 16-bit image depth, see Figure 104(a). The variation in beam intensity was suppressed by the standard optic correction technique of normalising each radiograph against a bright-field (beam with no specimen) (see Figure 104(b)) and dark-field (no beam) radiographs; the pair of correction radiographs had been captured immediately before each loading sequence. The normalised radiographs were contrast optimised using the ImageJ 'enhance contrast' tool (with a saturation level of 0.05 %) and down-sampled to 8-bit (Figure 104(c)). No spatial filtering was applied. Figure 101(c)) has been prepared following these steps. For the DIC reference images, a geometric mask was then applied, that excluded pixels within the notch and along the image borders where the optics' mountings obscured the image (Figure 104(d)).

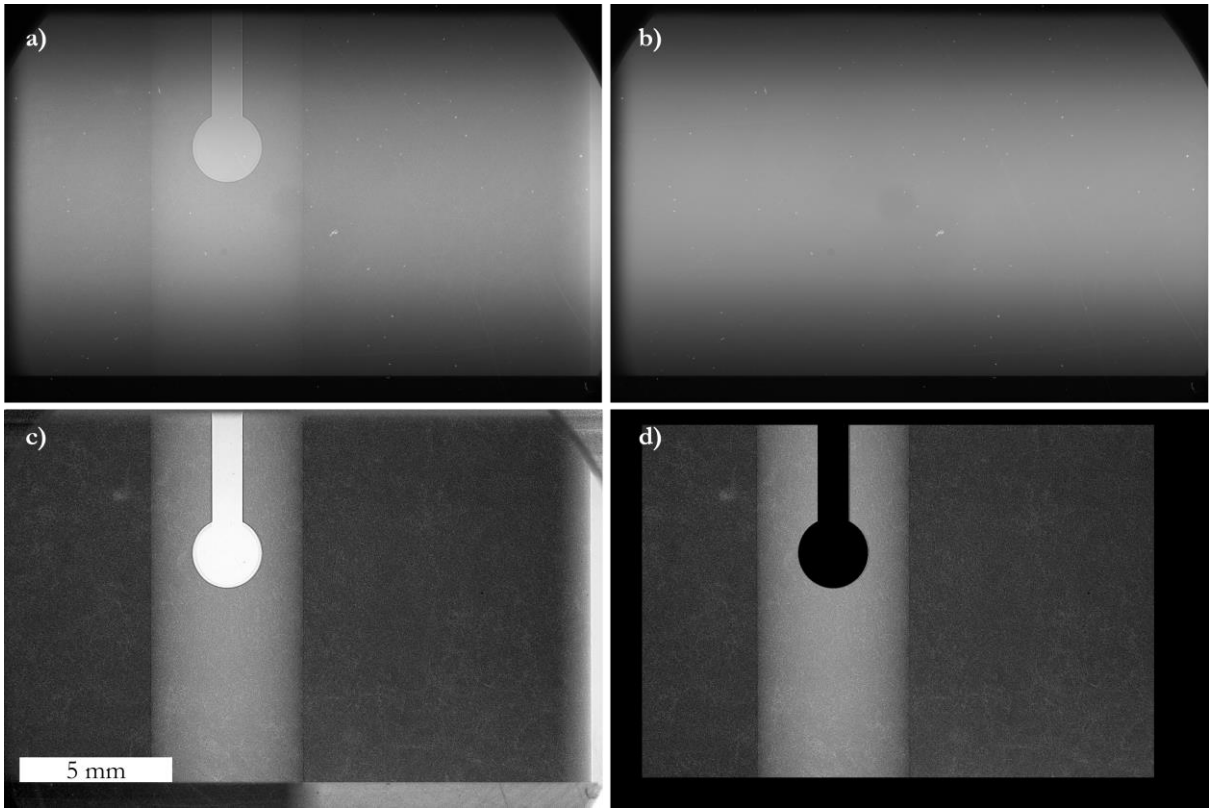


Figure 104: An example radiograph prepared for DIC: (a) raw 16-bit projection, (b) flat-field image, (c) the projection normalised, contrast optimised (0.05 % saturation) and down-sampling to 8-bit, and (d) geometric masking of the notch and border. Notch masking was only applied to the first radiograph (the reference image) in each loading series. All parts shown with maximum contrast range.

IV.2.3.2 Tomography reconstruction

The tomographs were reconstructed using the DLS-implemented back-filtered projection algorithm [174] as TIF images with 32-bit image depth. An example reconstruction of the KN1 specimen is shown as a 3D visualisation in Figure 105(a) and slice ABC of the virtual microstructure in Figure 105(b). The tomography imaging axes were not aligned with the symmetry planes of the specimens, with an angular offset of c. 7° about the Z-axis. Following a similar procedure to the radiographs, the tomograph projections were normalised against ten-frame averaged bright and dark field projections, and contrast optimised (see also § A2 for further details).

The reconstructed tomographs were processed using an ImageJ macro incorporating standard ImageJ tools, with comparable steps to the radiographs: a Gaussian filter (sigma = 1.5 voxel), contrast enhancement and conversion to 8-bit. The tomographs were registered manually and cropped to volumes of 2880 x 2560 x 1792 voxel and 3200 x 2560 x 896 voxel, for the KN1 and KN2 specimens, respectively. This was done to align the notch tips between the reference and each subsequent state; the estimated accuracy of this registration was ± 2 voxel in each direction. For the reference tomographs for DVC, the voxels within the notches and side grooves were also masked assuming cylindrical notches.

Spatial orientation will be described in terms of the axes and orthogonal planes defined in (Figure 105(a)), with the origin at the centre of the notch tip: plane ABC is defined as $Z = 0$ mm, intersecting the notch tip; plane DEF is $Y = 0$ mm, bisecting the notch and parallel with the 'wedge-plane'; and plane GHI is $X = 0$ mm, bisecting the notch. Where possible, analysis was performed on the unrotated data, and then the results rotated for visualisation, to minimise the effects of interpolation artefacts.

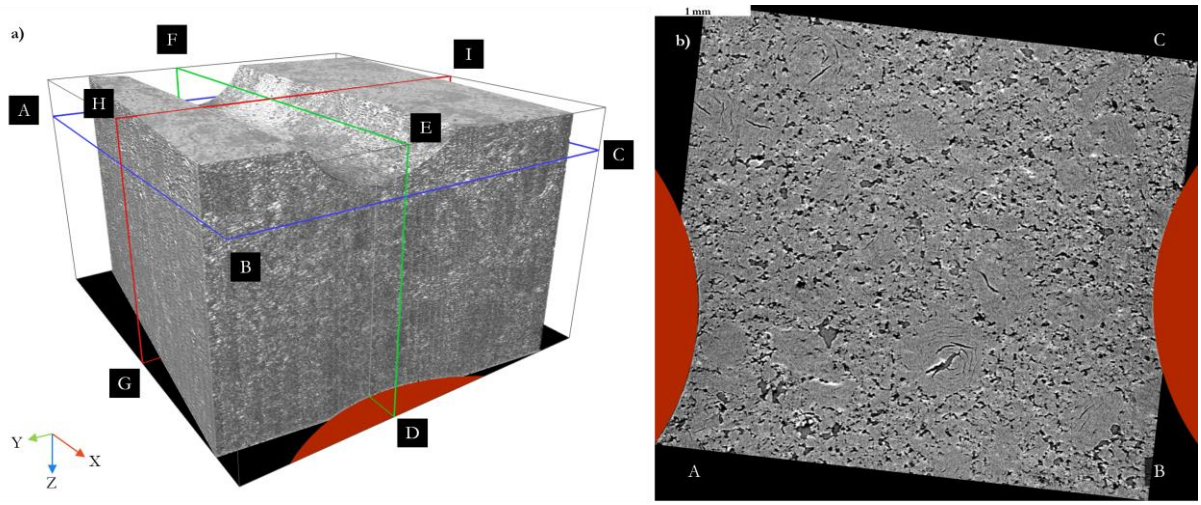


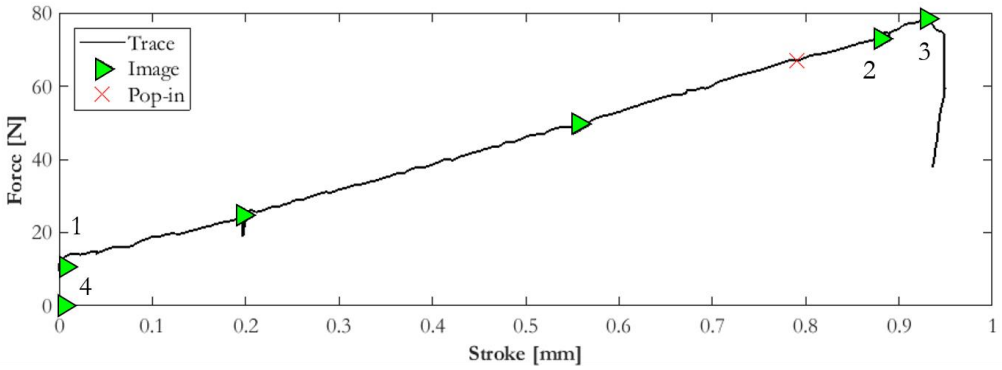
Figure 105: An example reconstruction of the KN1 specimen as: (a) a 3D visualisation in greyscale, rotated to align the symmetry axes with the imaging axes (c. 6.5° about the Z-axis), and with the principal orthogonal planes indicated; and (b) slice ABC of the virtual microstructure. In both images, bright voxels indicated X-ray high absorption. The 2.5 mm radius side grooves are presented in red.

IV.2.4 Observations from tomography

During the experiment crack initiation was monitored from the load-displacement curve and visual inspection of the specimen. Cracking was difficult to distinguish visually from the radiographs, and the time required to reconstruct the tomographs (c. 3 hours each) meant that they were not available for real-time analysis. The fracture behaviour observed during the experiment may be rationalised by considering 2D slices of virtual microstructure extracted from the tomographs immediately ahead of the notch tips.

Figure 106 and Figure 107 show the evolving microstructures at the loading points indicated on the progress curves. In both cases, after the peak load, a full-width crack was observed at the notch tip Figure 106(Image 3) and Figure 107(Image 3). The KN2 specimen fractured in the final 10 % of the loading – no macroscopic cracking was present at 90 %F_M(85 N, Figure 107(Image 2)). In the KN1 specimen, while no cracking was evident at 64 %F_M (at 50 N), an approximately third-width crack had developed by 96 %F_M (75 N, Figure 106(Image 2)). The pop-in load drop was less than 15 N in each case.

From the tomographs immediately following the initiation, the crack path in each specimen is highlighted on Figure 108 on the vertical notch-bisecting planes. In Figure 106 – Figure 108, the path was seen to be tortuous and to deviate from a single plane with a correspondence to the microstructural features. Comparison with the uncracked tomographs demonstrated that the crack tended to follow the pre-existing pore structure, and often passed around the edge of the filler particles.



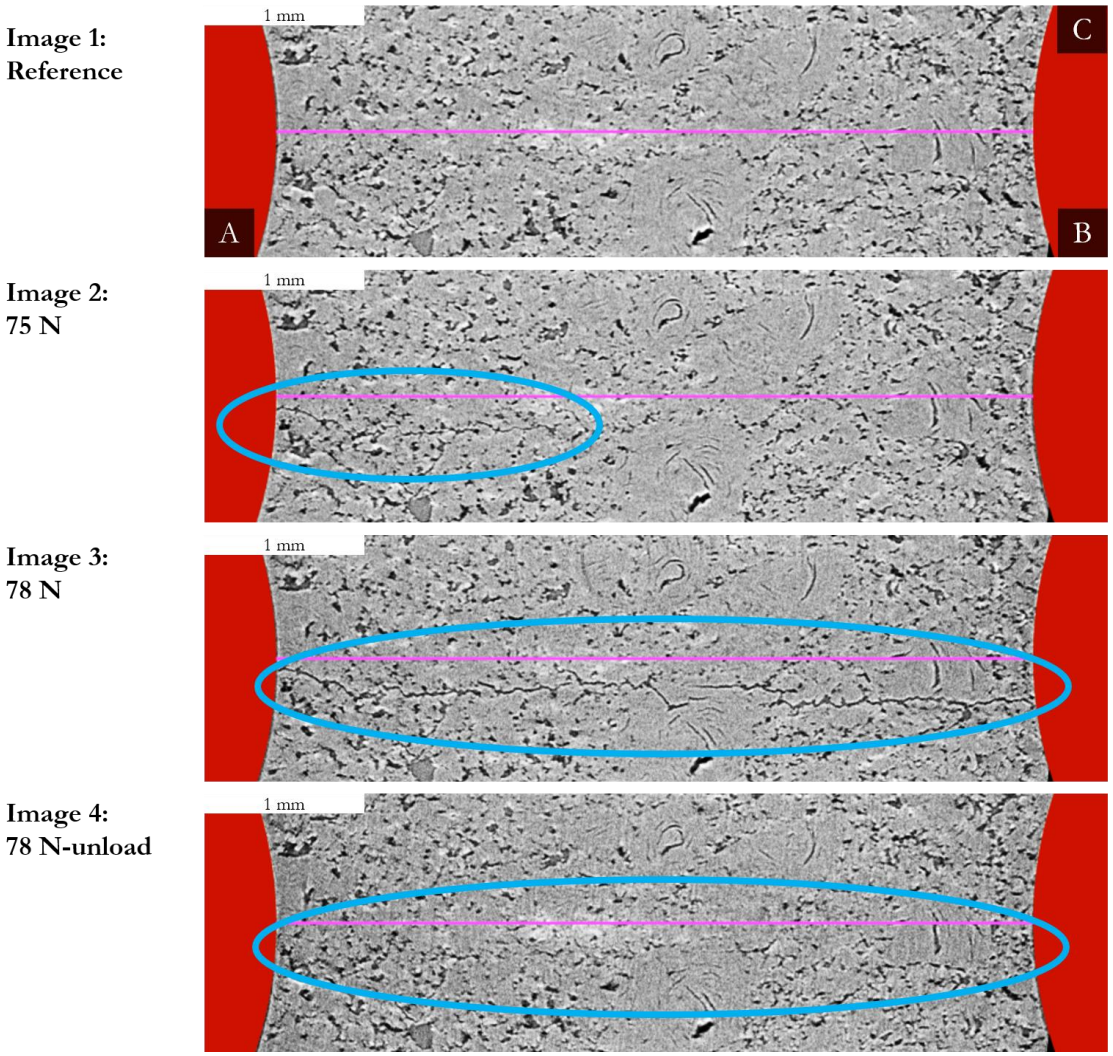
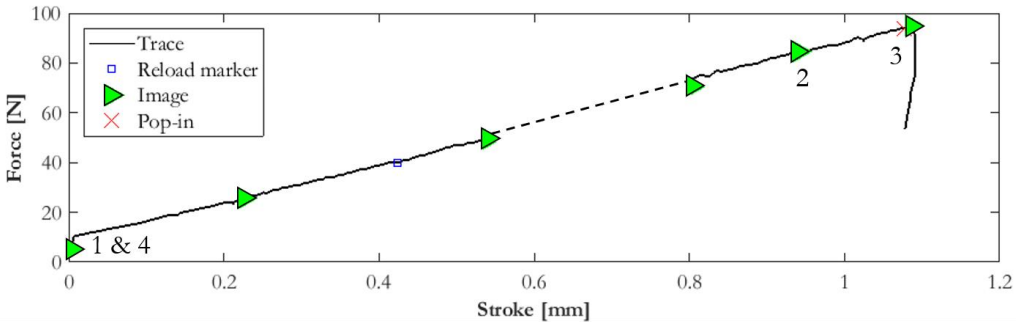


Figure 106: Load-displacement trace for the KN1 specimen indicating the conditions at XCT capture, and virtual slices (from the notch tangent ABC plane) of the evolving microstructure with increasing load. On the virtual slices, the pink line indicates the approximate notch tip, the red regions are the 2.5 mm radius side grooves. The crack path is indicated within the blue ellipses.



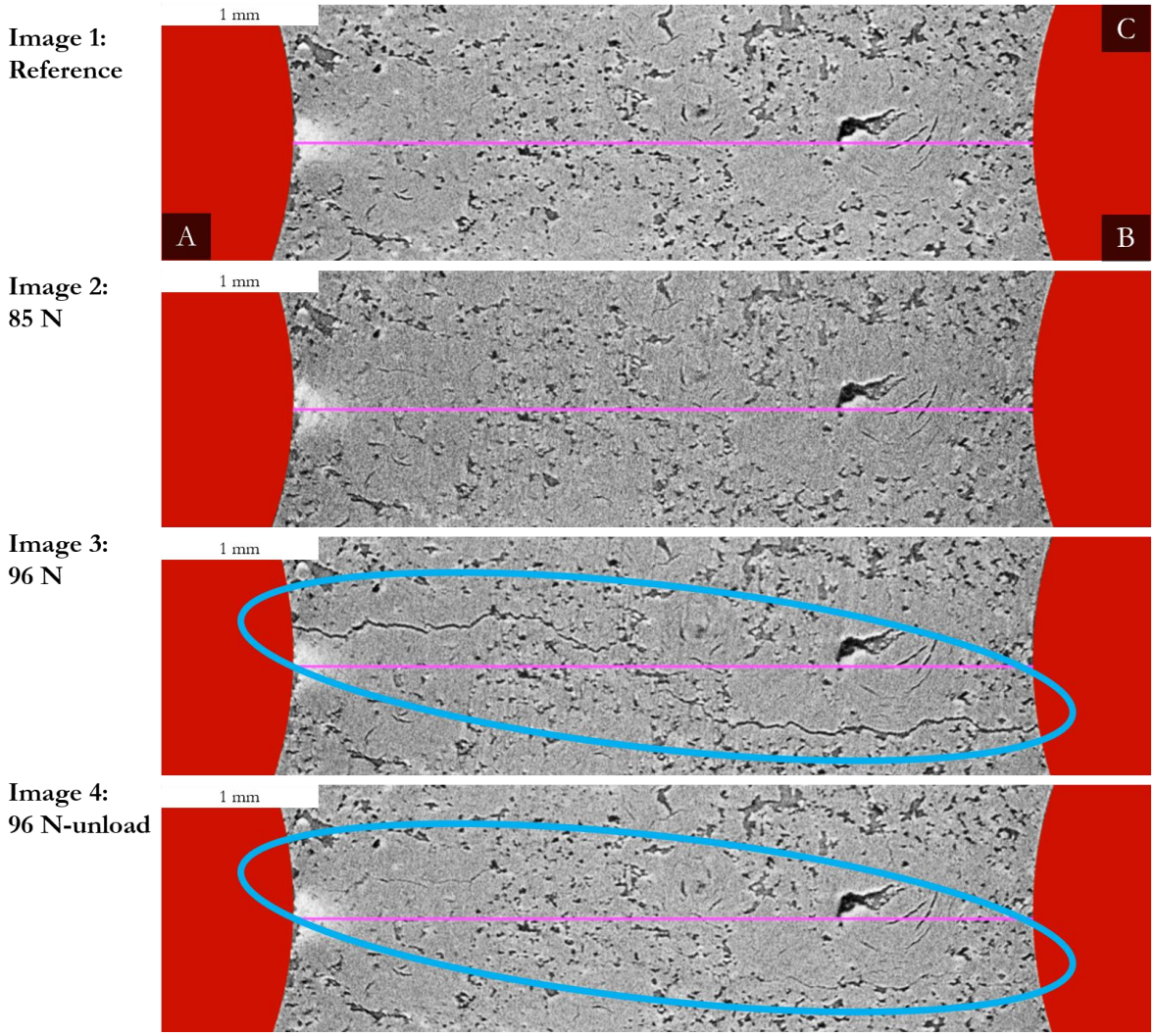


Figure 107: Load-displacement trace for the KN2 specimen indicating the conditions at XCT capture, and virtual slices (from the notch tangent ABC plane) of the evolving microstructure with increasing load. On the virtual slices, the pink line indicates the approximate notch tip, the red regions are the 2.5 mm radius side grooves. The crack path is indicated within the blue ellipses.

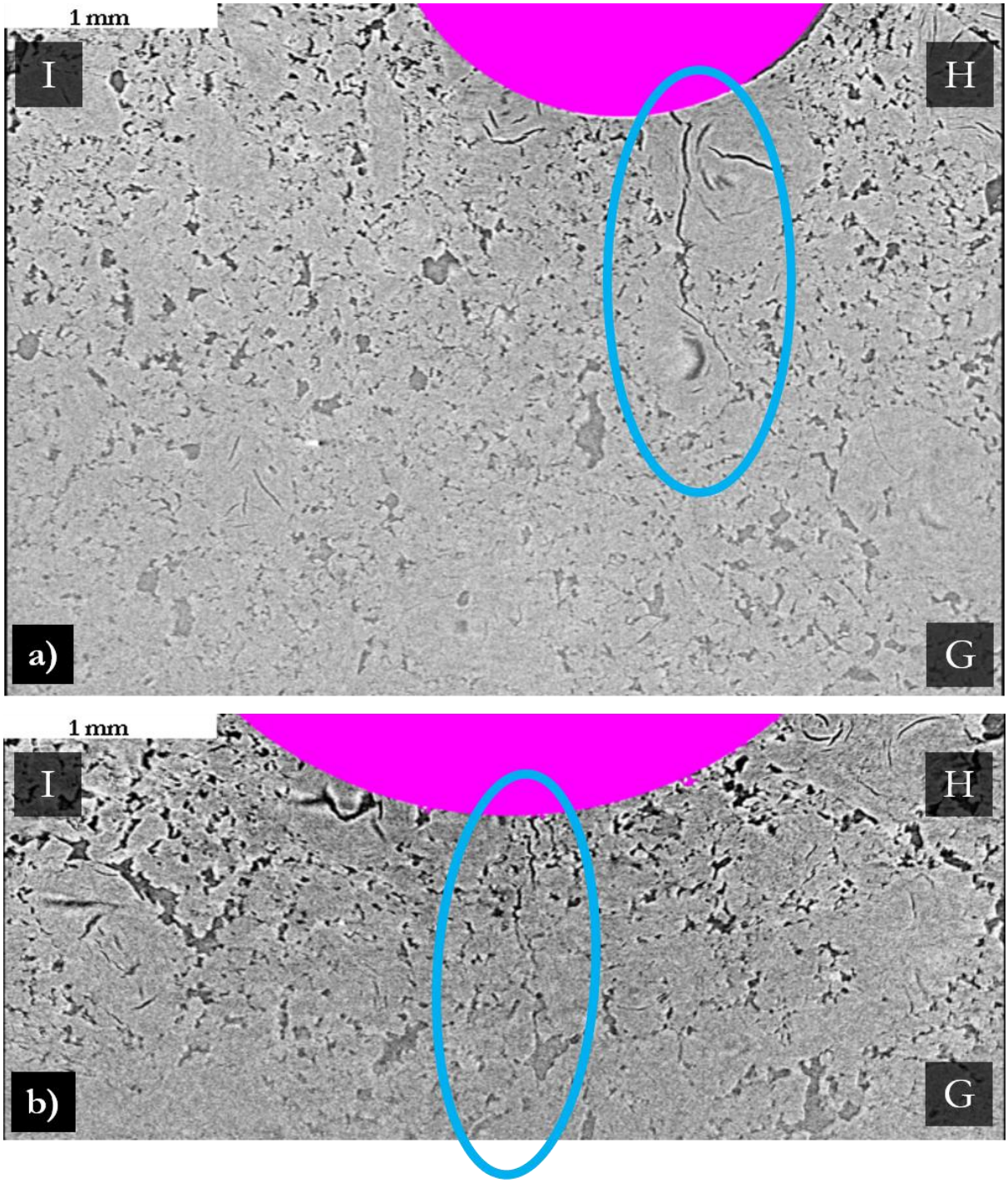


Figure 108: Virtual microstructures of the crack specimens from the tomograph following pop in, viewed on the notch bisecting slices GHI for a) KN1 and b) KN2.

IV.3 Analysis

As with the analysis of the small beam specimens, there were no analytical forms to accurately predict deformations, strains or stresses for the non-standard keyhole notch geometries. Deformations and strains will be measured by image correlation techniques, but the limitations of these techniques in proximity to surfaces has been highlighted in Chapter III. Analysis of the radiograph data is strictly two-dimensional, similar to the monoscopic digital image correlation, DIC, in the previous chapter. The tomographic data is superior to the stereoscopic imaging, in that the correlations are three-dimensional and volumetric, not just of a single plane. The two datasets will be combined in a similar methodology to the small beam analysis, with specimen deformations measured by DIC from the radiographs (§ IV.3.1). This will be used to define the boundary conditions for linear elastic, LE, finite element, FE, simulations (§ IV.3.2). In § III.4.1, the boundary conditions were explicitly defined as contact surfaces between moving components (the rollers), and it was identified that implicit definition of the boundary conditions on the deforming body would be beneficial for improving accuracy in representing the experiment. The high-resolution DVC of the tomography (§ IV.3.3) defines the microstructural response. The spatial deviations of the response from the FE predictions will be calculated and compared to the microstructure, to qualitatively highlight the response of the different phases (§ IV.3.4).

IV.3.1 Radiograph 2D digital image correlation

IV.3.1.1 Radiograph correlation and correction procedure

Displacement vectors originating from coordinate X, $\vec{U}(X)$, were calculated relative to the initial image by the fast Fourier transform, FFT, 2D DIC algorithm in DaVis 8.3.5 using square interrogation windows of reducing size, from (128 pixel)^2 to a (64 pixel)^2 and (32 pixel)^2 for the KN2 and KN1 radiographs respectively (the larger window for the KN2 images was due to an increased noise-to-signal ratio). Vectors with outlier displacements (exceeding 2.5 times the mean of a 5 x 5 kernel) or with correlation coefficients below 0.85 were deleted, and iteratively replaced using DaVis's post processing algorithms. The vectors form the 2D vector field, $U_{RG}^{KNi}(F)$, for geometry KNi, from which the horizontal, $U_{RG,Y}$, and vertical, $U_{RG,Z}$, components were extracted.

The displacement fields were RBM-corrected using the MATLAB®-implemented algorithms described in § III.3.2.2.3. The core regions were selected to avoid the discontinuity caused by the notch, and resultant crack where present. The uncertainty of the radiograph-DIC, and RBM correction was estimated as $\xi_{Corr,RG} = \pm$ 0.08 µm, with the sensitivity to interrogation window size shown in Figure 109.

Example motion-corrected U_{RG}-component fields are shown in Figure 110, for the KN1 specimen loaded to 50 N. Note that the vectors were plotted relative to the displacements of the notch tip.

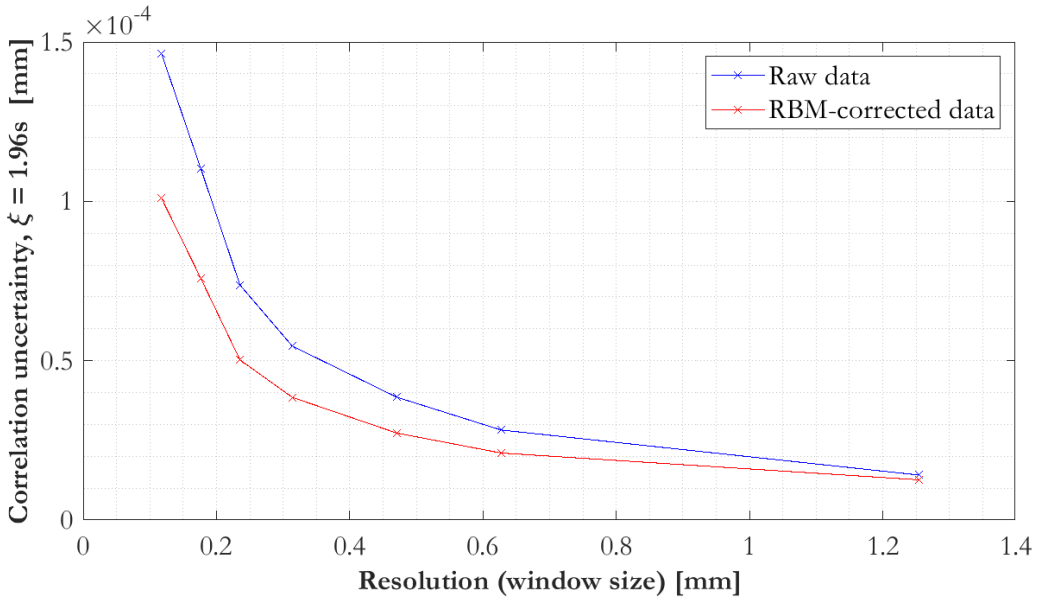


Figure 109:Radiograph-DIC sensitivity based on a rigid body movement.

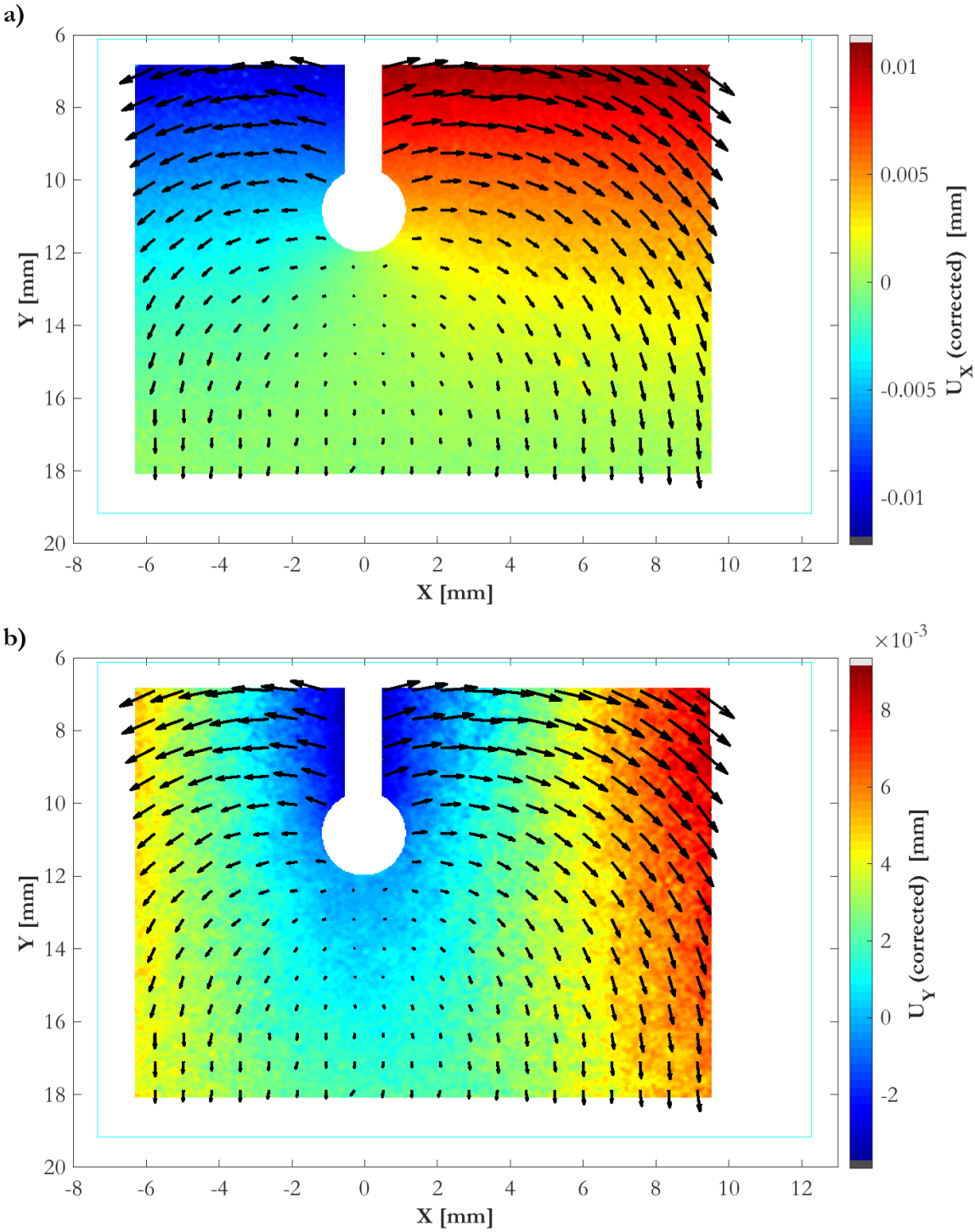


Figure 110: Example motion-corrected DIC maps for the KN1 specimen loaded to 50 N with the colourmaps indicating the components: (a) $U_{RG,Y}$ and (b) $U_{RG,Z}$.

IV.3.1.2 Notch surface deflection

The specimen deflection due to the notch opening was characterised by the displacements of the slot walls. The U_{RG} maps, as in Figure 110, indicated consistent behaviour in both directions in the region adjacent to the slot walls. For the whole series, the $U_{RG,Y}$ contours formed parallel bands of equal width, which spanned each half of the specimen in Figure 110(a). This indicated a linear decrease in $U_{RG,Y}$ with respect to Z-coordinate (which increased away from the notch mouth), as plotted in Figure 111(a), and was insensitive to the vertical profile on which it was measured, so could be measured accurately away from the slot walls. The profiles for the two slot walls are shown separately in Figure 111(a) where the notch mouth opening behaviour is clear. The absolute value of the gradients of the two profiles were similar but not identical, demonstrating that the loading was slightly asymmetric, and that these differences have been fully captured by the analysis.

The more complex $U_{RG,Z}$ behaviour resulted in parabolic-like contours in Figure 110(b), indicating that along a horizontal profile the $U_{RG,Z}(Y)$ displacement peaked at either slot face. In the vertical direction, and $U_{RG,Z}$ decreased in an approximately linear fashion away from the notch mouth (see Figure 111(b)). $U_{RG,Z}$ should therefore have been measured along the vertical profile at the slot walls, but this region was invalid for DIC. To account for this $U_{RG,Z}$ was measured along horizontal profiles and extrapolated to the notch wall coordinates. Minor asymmetry was again observed in the $U_{RG,Z}$ displacements. Due to the noise in the DIC measurement, displacements in both dimensions were characterised as linear fits to the profiles, averaged over at least 618 vectors.

The deformation of the two specimens at each of the load reversal states was determined by this method. The $U_{RG,Z}$ and $U_{RG,Y}$ linear fits that characterised the deflection at the sequential loads indicated the progressive specimen compression and notch opening in Figure 112.

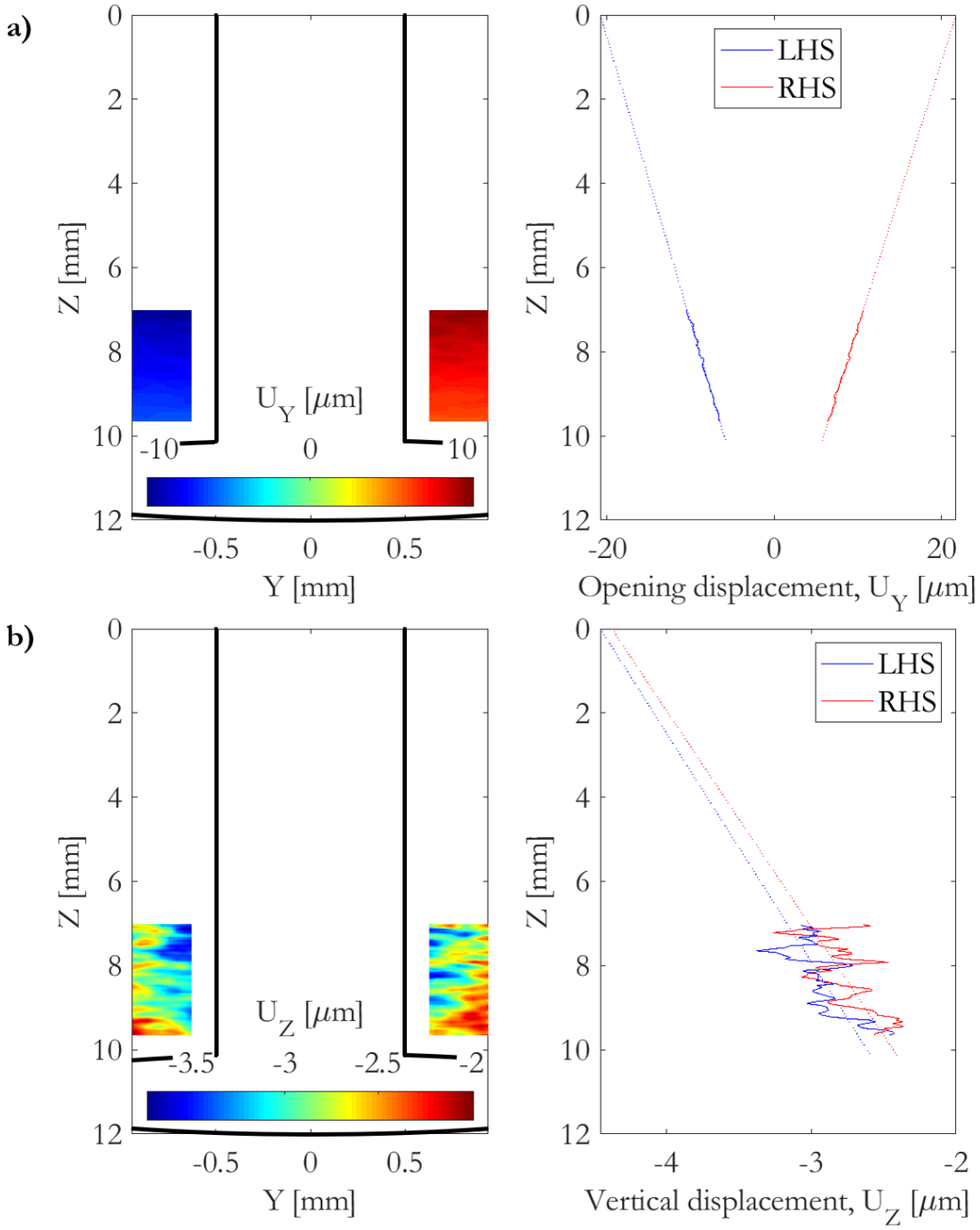


Figure 111: Example characterisation of notch opening behaviour using linear fits shown for the KN1 specimen under 50 N load as a) U_Y and b) U_Z components, as: Left *contour plots of the fitting regions, with the notch boundary indicated in black lines; and* Right *the raw (solid) and linear fits (dotted) to the displacements.*

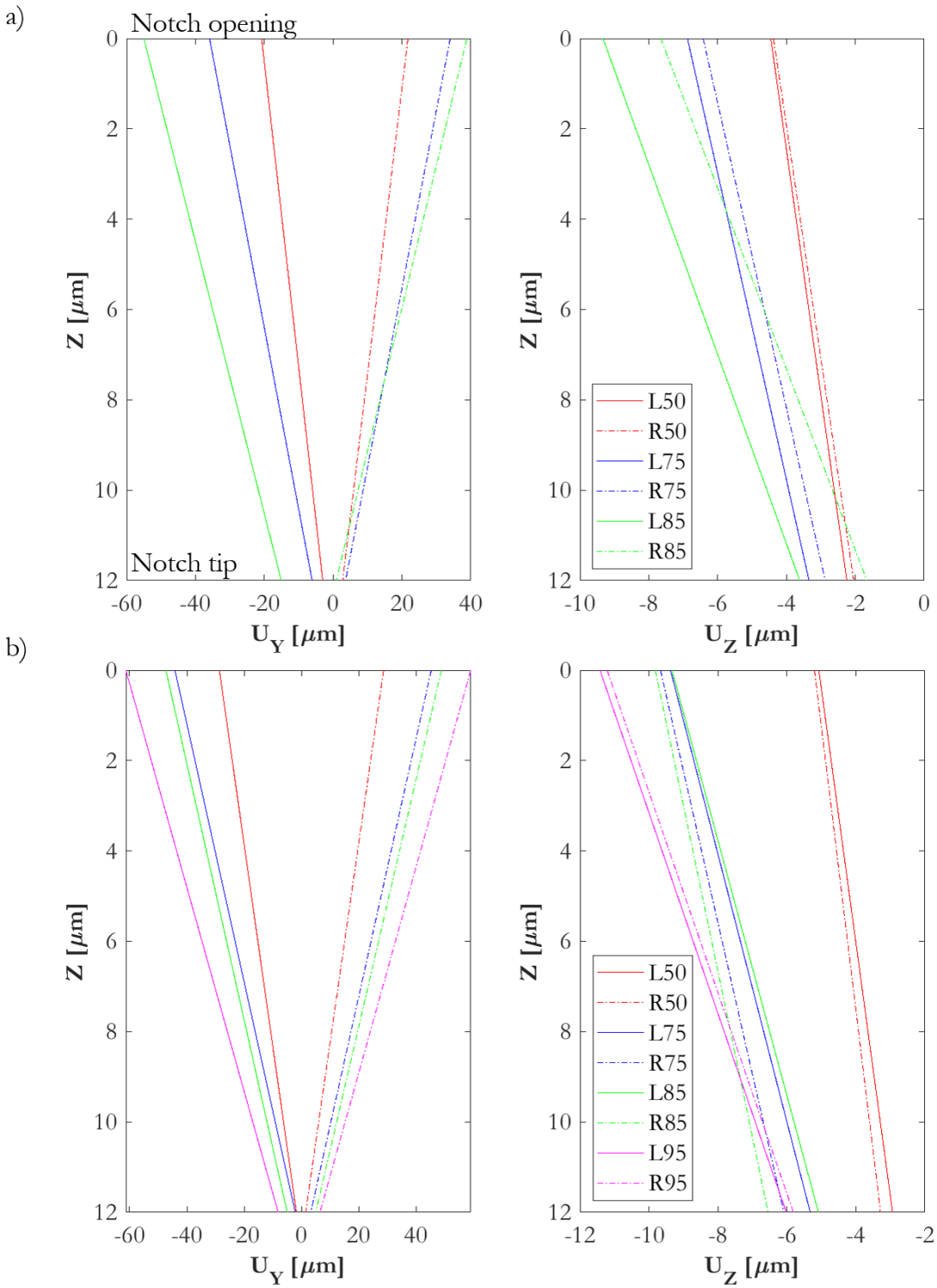


Figure 112: Evolution of the fitted orthogonal components of the opening behaviour for the two faces of the notch with increasing load (left-hand side, "L<load>", and right=hand side, "R<load>") in the two specimens: a) the KN1 specimen and b) the KN2 specimen.

IV.3.2 Keyhole notch finite element simulation

Linear elastic models that closely replicate the experiments (§ IV.3.2.1) will be used to simulate the full-field displacement and strain fields (§ IV.3.2.2) at each of the loaded states. These predictions will be tested against the experimental behaviour determined in § IV.3.3 , to calculate the deviations associated with local differences in experiment from the predictions (§ IV.3.3.2).

IV.3.2.1 Model definition

Half-symmetry models of the Keyhole Notch geometries were created in Simulia's *Abaqus Standard* 6.14.2 to predict the specimen deformation. A mesh of tetrahedral elements with refinement about the notch tip was generated, see Figure 113(a). The fitted radiograph-DIC notch profiles were applied as the boundary conditions to the nodes on the notch faces for each loading state, while boundary conditions reflecting the experimental DOF and measured rigid body displacement were applied to nodes on the base and symmetry face of the model, as in Figure 113(b).

As in § III.4.2.1, linear elastic properties were assumed from Marrow *et al.* [88], using the tensile modulus for this billet, E = 11.93 GPa, and assumed Poisson ratio, ν = 0.21. These values were in line with the values determined for Gilsocarbon by [82, 175]. No attempt was made to fit the reaction loads by adjusting the stiffness.

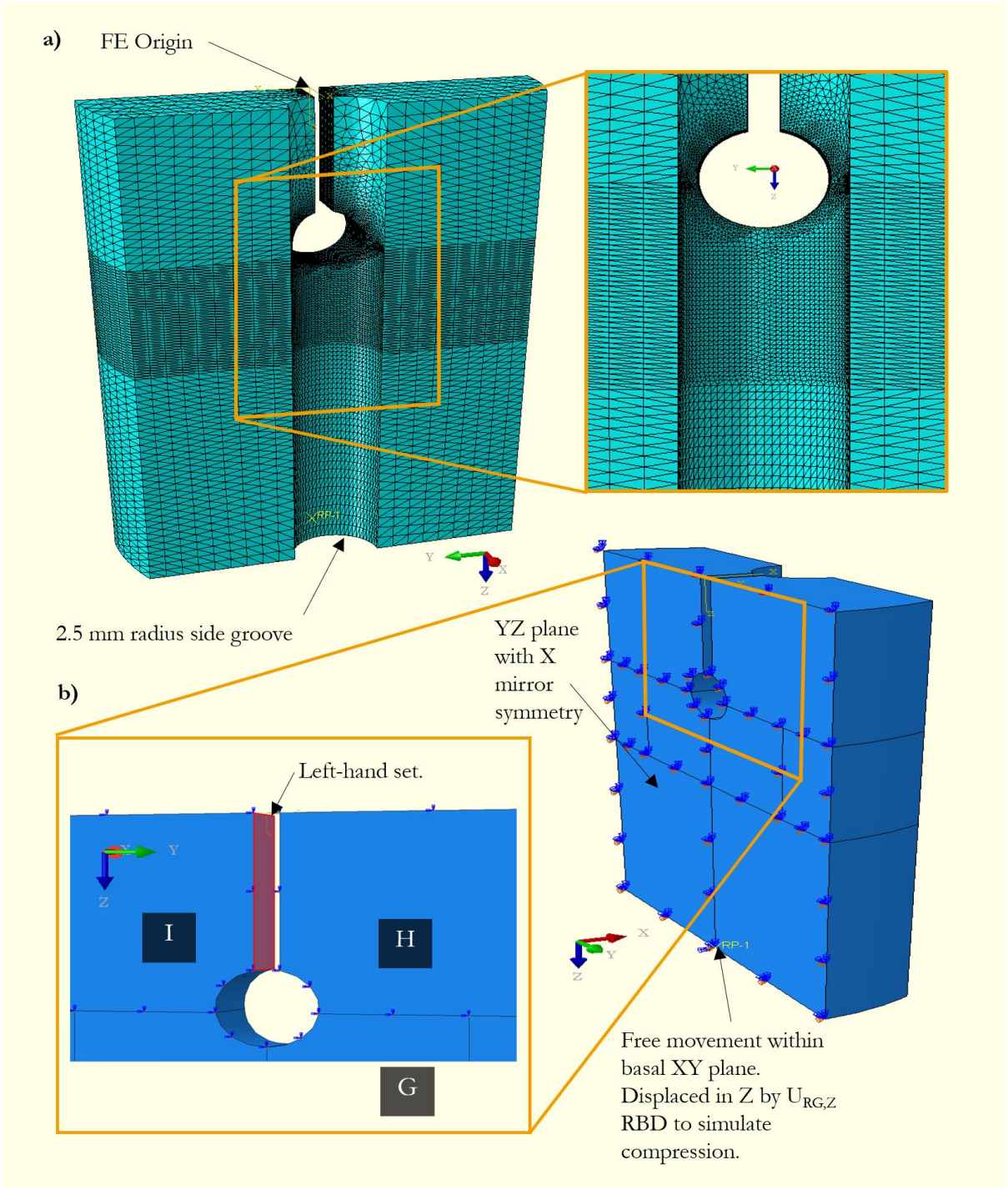


Figure 113: FE simulation half-symmetry definition of the KN2 specimen: a) geometry and mesh, and coordinate origin, b) focus on mesh refinement about the notch tip, c) definition of orthogonal planes boundary conditions and d) node region with load-specific left hand side notch opening boundary conditions defined (the equivalent plane is defined for the right-hand side conditions). Due to the viewing settings, the aspect ratio results in vertical contraction of the simulated images.

IV.3.2.2 Simulation predictions

The KN specimen linear-elastic simulations assume a homogeneous solid to predict the displacement field, $U_{Sim}^{KNi}(F)$, and strain field, $\epsilon_{Sim}^{KNi}(F)$, for each loaded state at load F and for specimen *KNi*. The full-field patterns of evolving deformation and strain with increasing load will be described in § IV.3.2.2.1 . Since linear elasticity was the only material model tested, the predicted behaviour at unload was null fields, that is

$$\vec{U}_{Sim}(F,X) = 0,\ \partial\left(\vec{U}_{Sim}(F,X)\right) = 0,\ \forall X.$$

IV.3.2.2.1 Full-field predictions

Figure 114 and Figure 115 show the principal components $U_{Sim,Y}(50)$ and $U_{Sim,Z}(50)$ for KN1 and KN2, respectively, on the notch bisecting plane GHI. The states shown in Figure 114 were comparable to the radiograph-DIC in Figure 110; the origins of the displacements in the FE had not been adjusted to agree with the DIC so the absolute values of the simulation displacements differed slightly, but the relative magnitudes and patterns of deformation were seen to agree. This confirmed that the boundary conditions were suitably prescriptive to simulate the wedge opening without explicit simulation of the wedge-contact.

The principal deformations were in the notch opening direction (*Y*), which constitutes a Mode I loading. The predicted deformations on the three orthogonal planes during the penultimate loaded tomographs is shown in Figure 116 and Figure 117 for $U_{Sim,Y}^{KN1}(75)$ and $U_{Sim,Y}^{KN2}(85)$. For each plane, an inset shows the corresponding $\epsilon_{Sim,YY}(F)$ predictions; the FOV of the insets correspond to the tomographic FOV, as in Figure 121 for example.

From the displacement maps, the influence of the asymmetric boundary conditions identified in Figure 114 and Figure 115 was apparent in the different contour patterns either side of the notch. Using linear elasticity, the predictions for the earlier loading states were approximately linear scalings of the two states shown, though the degree of asymmetry varied.

The greatest strains were predicted at the notch tip, and particularly where the notch intersected the side grooves of the specimen. In the regions of interest (as approximately indicated in the tomographic FOV), the strains were predominantly tensile ($\epsilon_{YY} > 0$), with the magnitude of any compressive strains dwarfed by the tensile components. The maximum predicted strains in the KN2 specimen were greater than the KN1, though the comparison is not necessarily fair since the simulated KN2 tomograph is relatively closer to the pop-in. A stress concentration zone, SCZ, was observed ahead of both notches. Considering the GHI planes for the penultimate simulations, and taking the boundary as 2.0 mStrain, the zones were seen to be approximately elliptical (extending horizontally in *Y*), centred close to the notch tip, and with geometry dependent sizes: for KN1, the centre was c. 0.1 mm ahead, with radii of c. 0.7 mm and c. 0.4 mm in the major and minor axes respectively; for KN2, the centre was c. 0.3 mm into the notch, with radii of c. 1.3 mm and 1.1 mm in the major and minor axes respectively. Further away from the notch the loci tended to the classic two lobe shape associated with Mode I stress intensity [176].

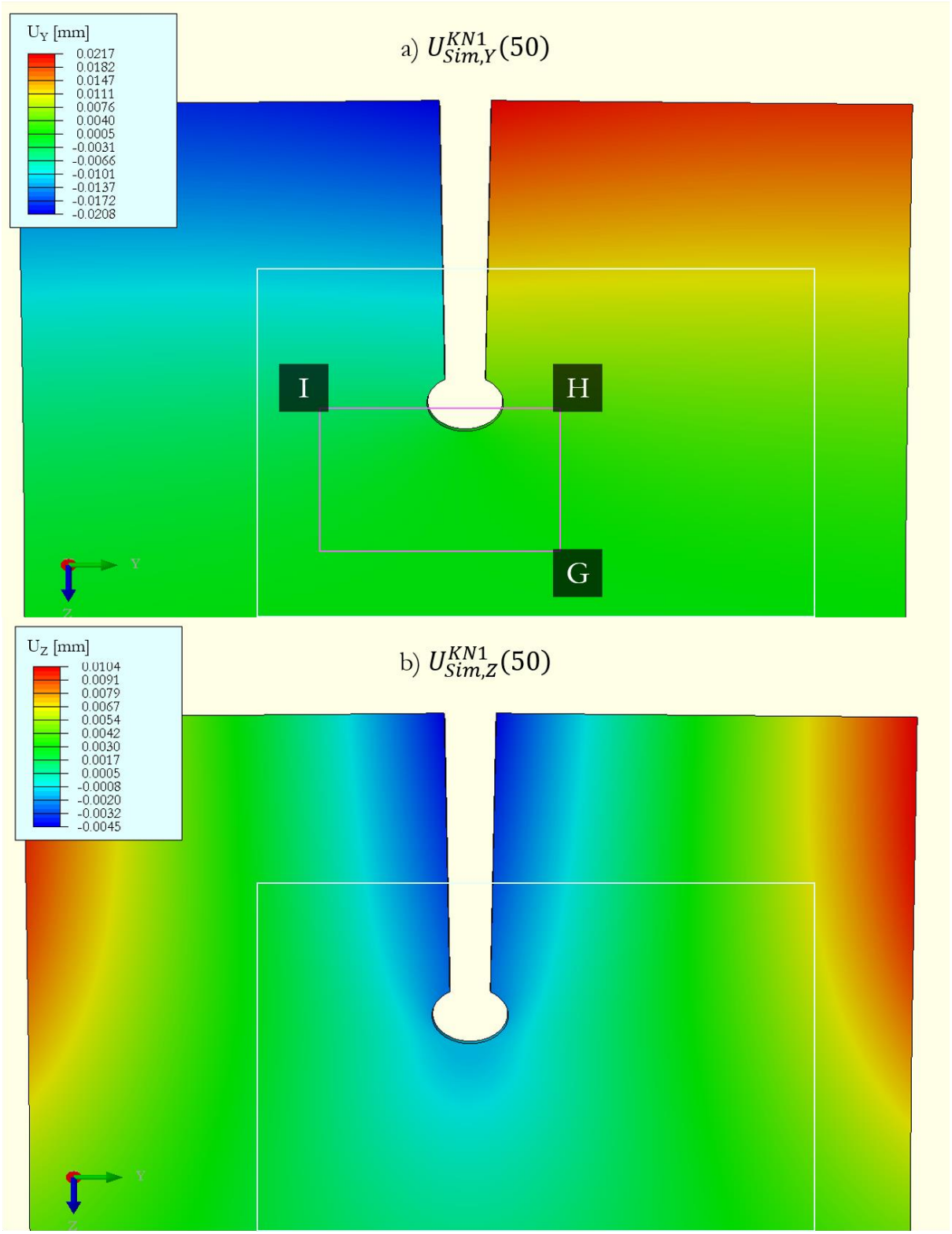


Figure 114: Simulated displacements on the notch-bisecting GHI plane for the KN1 specimen loaded to 50 N: a) $U_{Sim,Y}$ and b) $U_{Sim,Z}$. Deformations are shown with anisotropic scale factor, and note the different ranges of the absolute values of displacement for the separate parts. The pale blue outline corresponds to the radiograph-DIC FOV seen in Figure 110, while the pink outline corresponds to the tomograph-DVC FOV seen in Figure 121, for example. Due to the viewing settings, the aspect ratio results in vertical contraction of the simulated images.

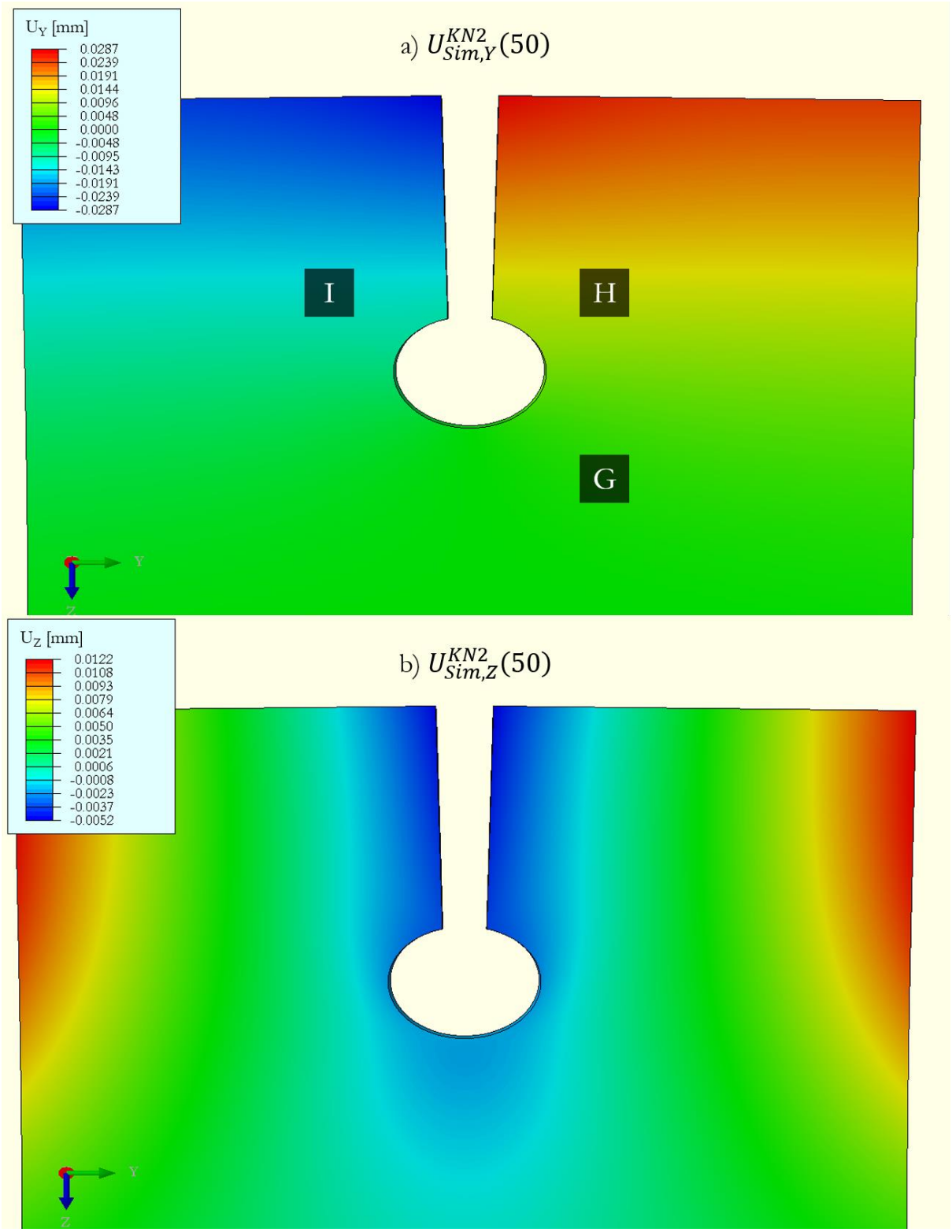


Figure 115: Simulated displacements on the notch-bisecting GHI plane for the KN2 specimen loaded to 50 N: a) $U_{Sim,Y}$ and b) $U_{Sim,Z}$. Deformations are shown with an anisotropic scale factor, and note the different ranges of the absolute values of displacement for the separate parts. Due to the viewing settings, the aspect ratio results in vertical contraction of the simulated images.

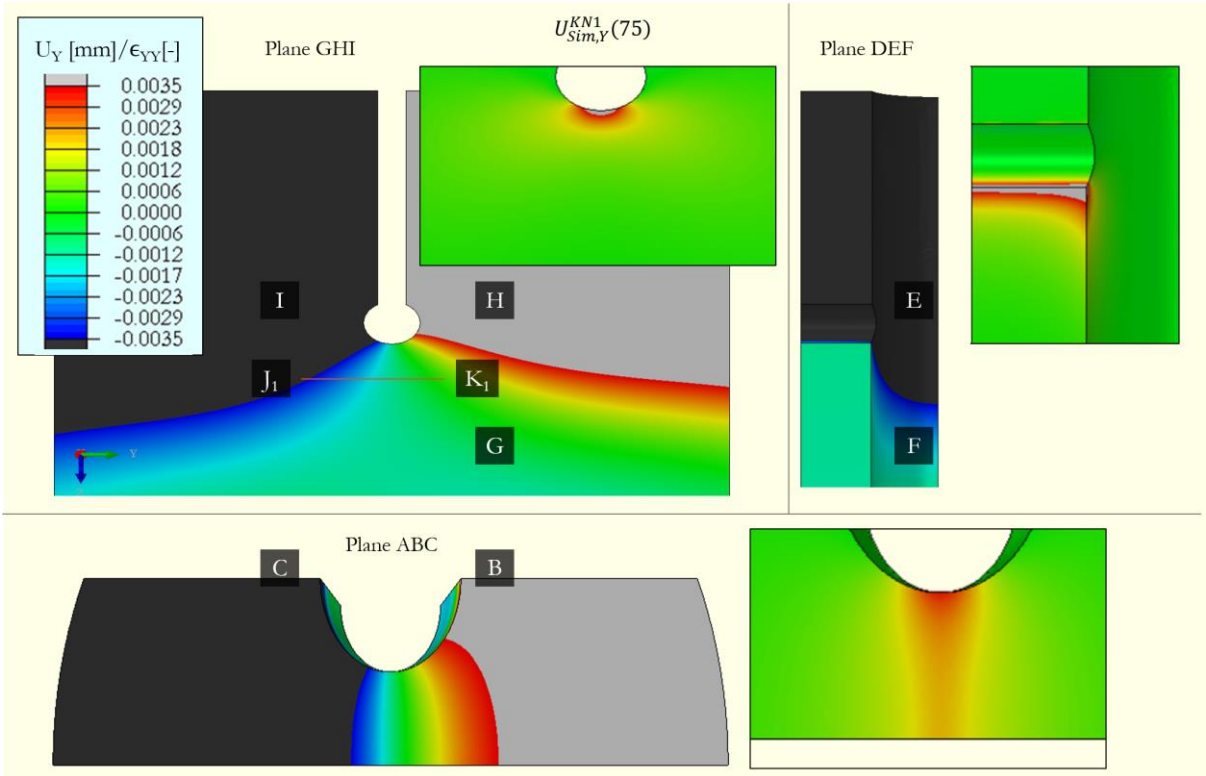


Figure 116: The predicted deformations of the KN1 specimen for the loaded state prior to failure on the three principal orthogonal planes. Each plane shows the displacement field, $U^{KN1}_{Sim,Y}(75)$, with the corresponding strain field $\epsilon^{KN1}_{Sim,YY}(75)$ inset; the strain field FOV corresponds to the tomographic FOV in Figure 121 for example. Displacements and strains are plotted using the same colour scheme, in units of mm and mm/mm respectively; values are capped at ± 3.5 for clarity. Due to the viewing settings, the aspect ratio results in vertical contraction of the simulated images.

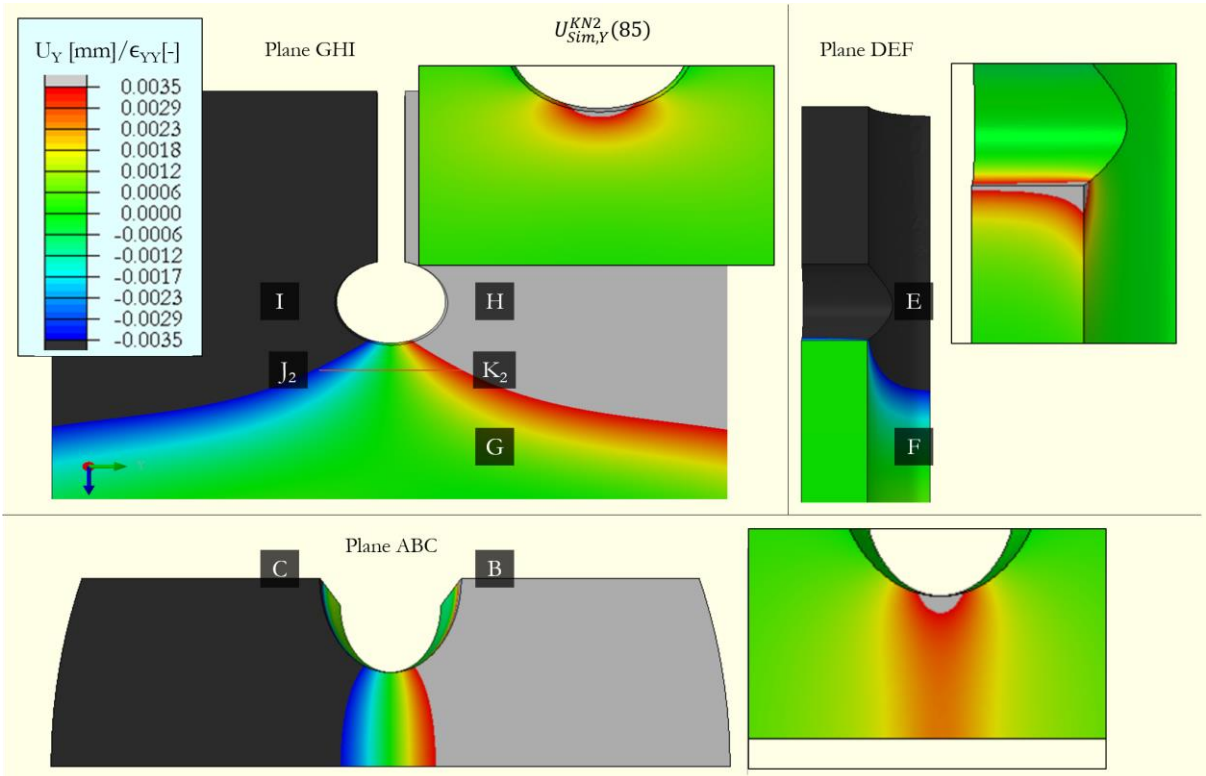


Figure 117: The predicted deformations of the KN2 specimen for the loaded state prior to failure on the three principal orthogonal planes. Each plane shows the displacement field, $U^{KN2}_{Sim,Y}(85)$, with the corresponding strain field $\epsilon^{KN2}_{Sim,YY}(85)$ inset; the strain field FOV corresponds to the tomographic FOV in Figure 121 for example. Displacements and strains are plotted using the same colour scheme, in units of mm and mm/mm respectively; values are capped at ± 3.5 for clarity. Due to the viewing settings, the aspect ratio results in vertical contraction of the simulated images.

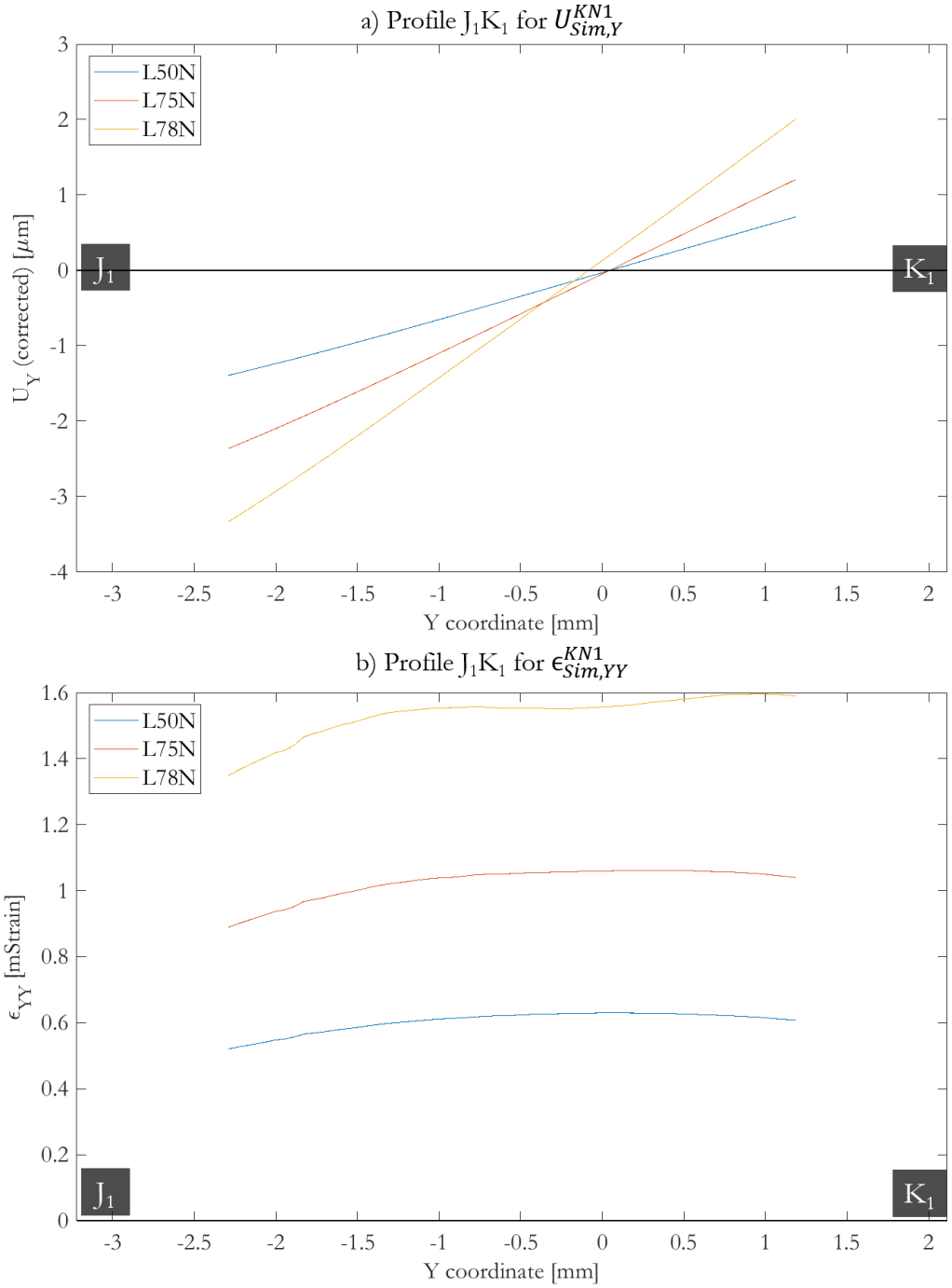


Figure 118: Variation in simulated Mode I (a) displacement and (b) strain, for the KN1 specimen along profile J_1K_1.

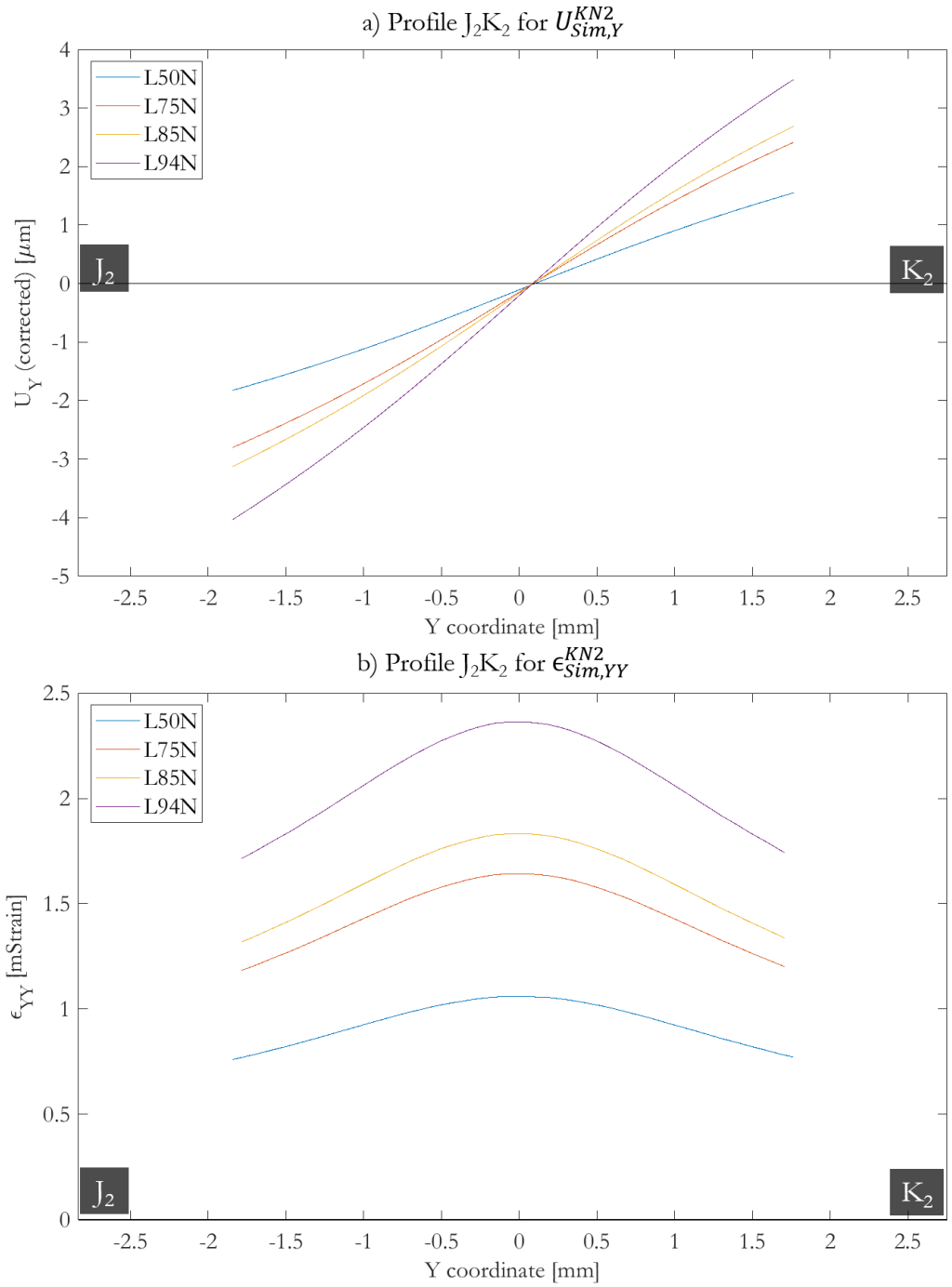


Figure 119: Variation in simulated Mode I (a) displacement and (b) strain, for the KN2 specimen along profile J_2K_2.

IV.3.3 Tomograph 3D digital volume correlation

High-resolution experimental displacement fields, $U_{Exp}^{KNi}(F)$, were calculated by DVC of the tomographs (§ IV.3.3.1). The U_{Exp} fields include the highest resolution and 3D information about the experimental response to the deformation. To identify the history of the datasets for the unloaded states, they are labelled with reference to the previous maximum load and designated as F*; for example, U_{Exp}(50*) is the displacement field measured from the unloaded tomograph having unloaded from 50 N. The evolution at both load and unload will be described in § IV.3.3.2, ahead of the quantitative comparison to the linear elastic simulations in § IV.3.3.2.

IV.3.3.1 DVC correlation and RBM correction

Vectors were calculated by the FFT 3D multi-pass algorithm in DaVis 8.3.1, using cubic interrogation volumes of initial size $(256)^3$ voxel and overlap of 50 %, and a final size of $(128\ \text{voxel})^3$ and overlap of 75 %, with a total of 5 passes. Vectors with correlation coefficients below 0.9 were deleted after each pass. The fields were then RBM-corrected using the MATLAB®-implemented algorithms described in § III.3.2.2.3; the cuboid core region was selected to avoid vectors within 0.5 mm of the image and specimen surfaces. For a pure rigid body displacement, the sensitivity to interrogation volume size for a $(1024\ \text{voxel})^3$ volume is shown in Figure 120, with the correlation uncertainty $\xi_{Corr,DVC} = \pm 0.65$ µm (or 1.96 mStrain) for a final pass using a $(128\ \text{voxel})^3$ (or $(0.23\ \text{mm})^3$) volume.

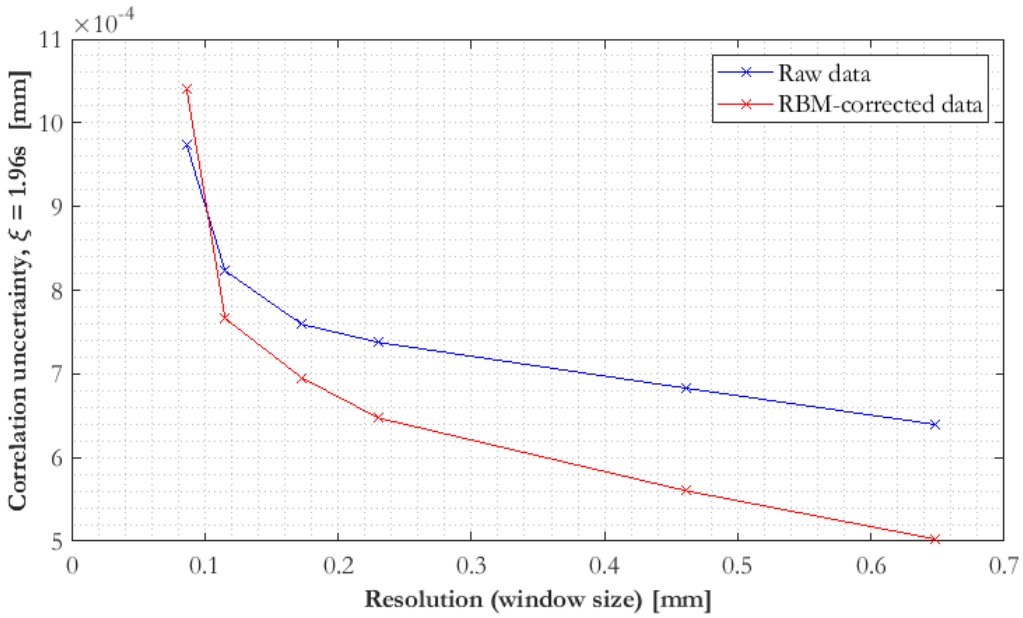


Figure 120: DVC sensitivity to interrogation volume edge dimension (resolution), for a rigid body displacement of a (1024 voxel)³ volume. Interrogation volumes were cubic.

IV.3.3.2 DVC measured behaviour

The DVC behaviour at load and at the subsequent unloads will be considered separately in § IV.3.3.2.1 and § IV.3.3.2.2, respectively. The reference tomographs were collected at 11 N and 0 N for the KN1 and KN2 specimens, respectively. The loaded states will be shown to be comparable to the simulated states in § IV.3.2.2.1. The DVC data will be presented as displacement and strain maps. For brevity, only the mid-slice viewed along the notch axis (slice GHI) will be shown for each load state, and only the Mode I displacement and orthogonal strain component ($U_{Exp,Y}$ and $\epsilon_{Exp,YY}$) will be shown. The displacement maps will be plotted relative to the displacement of the fixed origin set 0.5 mm ahead of the notch tip; the distance from the notch tip is limited by the available volume in the KN2 specimen. For all the plots, coordinates are given relative to the fixed origin.

IV.3.3.2.1 DVC loaded states

The loaded states of the specimens show a clear and progressive Mode I opening in Figure 121 and Figure 122 for the KN1 and KN2 specimens, respectively. Figure 123 and Figure 124 are the complementary $\epsilon_{Exp,YY}$ maps, calculated by central differences using MATLAB®'s GRADIENT function. The $U_{Exp,Y}$ and $\epsilon_{Exp,YY}$ variations along the horizontal profiles J_1K_1 and J_2K_2 were plotted in Figure 125 and Figure 126: for KN1, Y = 0.7 mm for J_1K_1, and for KN2, Y = 0.4 mm for J_2K_2; 1.2 mm and 0.9 mm ahead of the notches, respectively.

Until fracture, $U_{Exp,Y}$ varied in an approximately linear fashion as the deformation increased steadily and consistently across the planes, with the profiles showing the $U_{Exp,Y}(Y)$ gradient rising monotonically. The general trends are in-line with the predicted displacements shown in Figure 114 and Figure 115. Following fracture in both specimens, the location of the discontinuity associated with the crack is clear, with the two halves of the specimen separating in the displacement maps, a step change in the displacement profiles and a corresponding narrow band of high strain. The appearance and size of the partial-width crack observed visually in the KN1 specimen was confirmed by comparison of the displacements with the tomographic images. After macro-crack formation, the simulations were no longer a true representation of the geometry, and so agreement was neither expected nor observed for the states with full width cracks. Detailed comparison of the DVC and FE displacement fields indicated that there were significant fluctuations about the underlying trends ($U_{Exp} \gg \pm \xi_{Corr,DVC}$), resulting in 'hotspots' apparent from the earliest load states; these differences will be explored in § IV.3.4.

From the general form of the strain maps, a strain concentration zone was observed extending approximately 1 mm ahead of the notch; such a zone was expected from the simulations, and the experimental maximum ϵ_{YY} were of a comparable magnitude to the simulations shown in Figure 114 and Figure 115. The proposed ϵCZ locus was estimated by eye from the $\epsilon^{KN1}_{Exp,YY}(50)$ map where the strains appeared to rise rapidly above 1.5 mStrain. The locus was circular, centred on the notch tip, with an approximate radius of R_C = 1.28 mm (the dashed green line in Figure 123(a)). The identical locus appeared suitable for every load state of the KN1 specimen in Figure 123, and also an accurate fit to the ϵCZ in the KN2 maps in Figure 124. For $\epsilon^{KN1}_{Exp,YY}(75)$ the same locus approximately marks the threshold of strains rising above 2.0 mStrain (the definition used for determining the ϵCZ boundary in the simulations), though it is harder to determine the effective threshold for the $\epsilon^{KN2}_{Exp,YY}(85)$ map.

After cracking (Figure 123(c) and Figure 124(d)), the strains within the locus became generally more compressive ($\epsilon_{YY} < 0$) than the surrounding material. Associating the crack with the continuous region of strains exceeding 3.5 mStrain in Figure 123(c), the crack was estimated to extend to the approximate point (0.1, 1.5) on the KN1 GHI slice; this was consistent with the apparent extent of the crack in Figure 108. A second locus was plotted centred on this point (the dotted green line), with the same radius; this locus appeared to contain the region of high tensile strain on that map. The crack appears to extend beyond the KN2 FOV, and so the consistency of this observation could not be tested against the KN2 specimen.

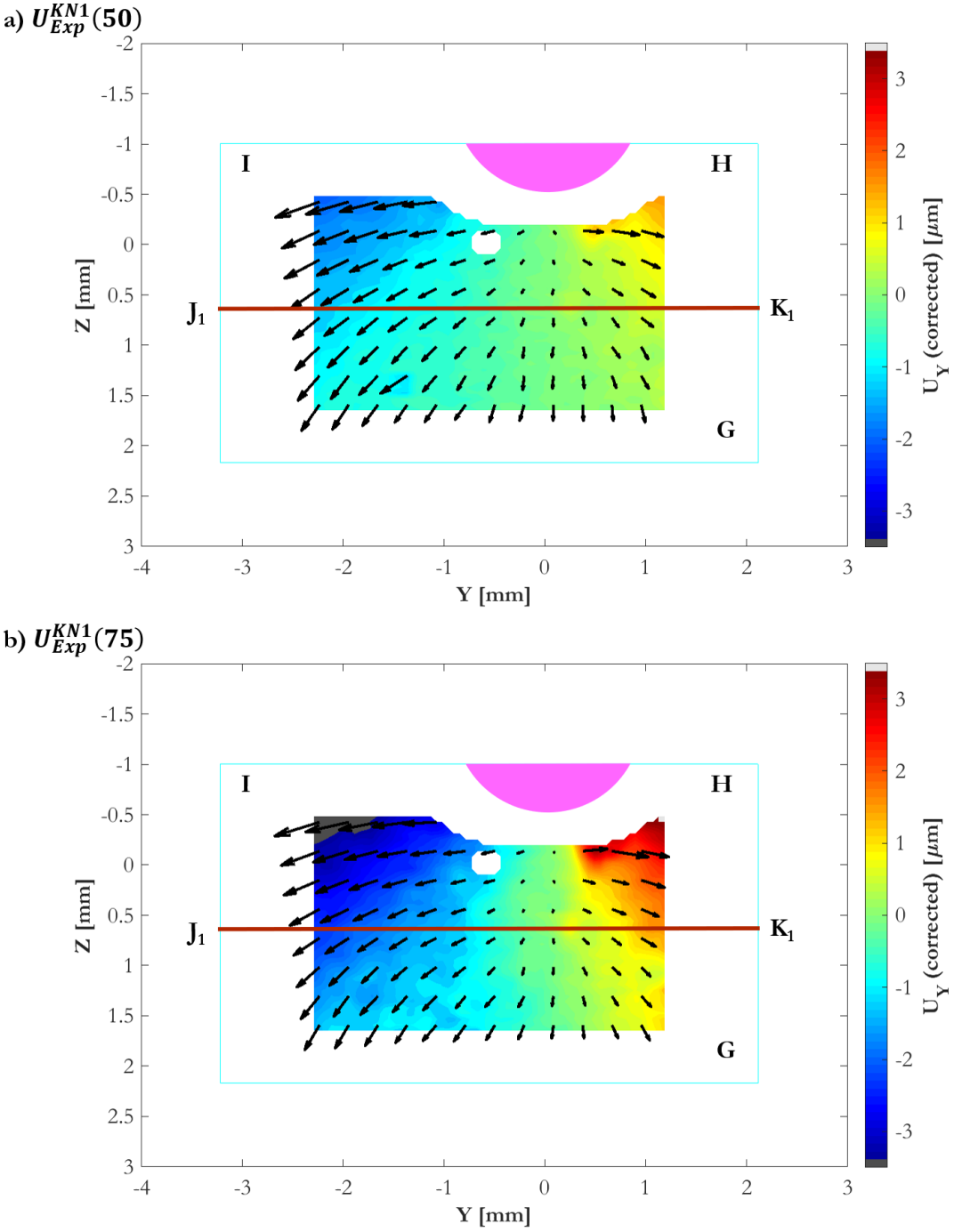
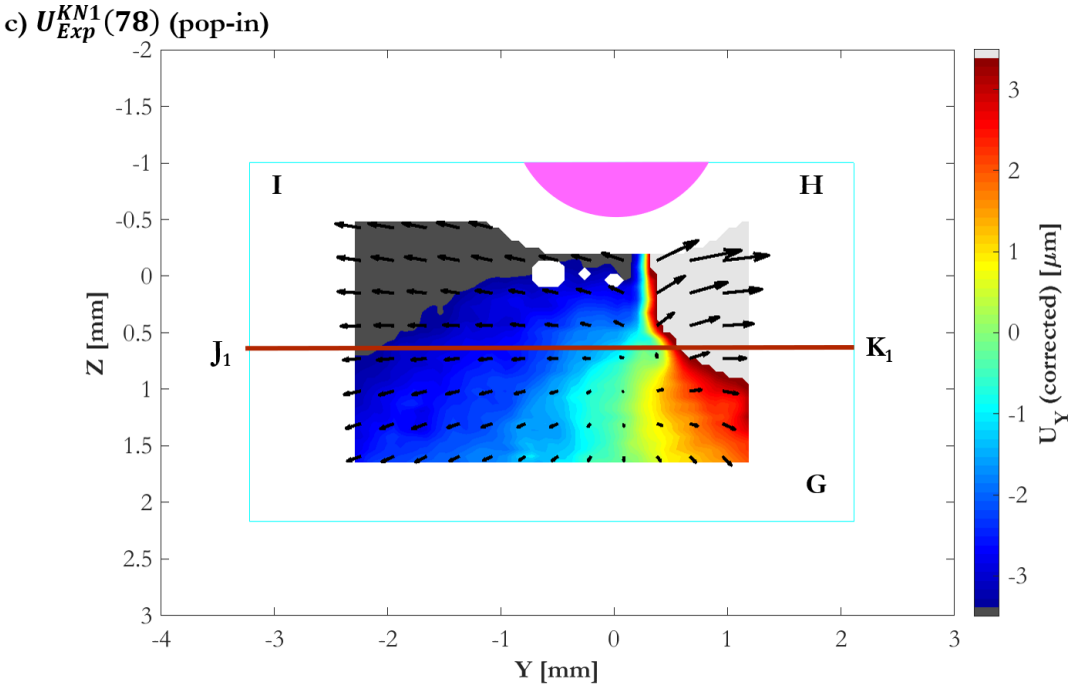


Figure 121: U_Y displacement fields measured from DVC of the KN1 specimen in the loaded states, increasing from (a) 50 N to (c) 78 N (pop-in), the tomograph immediately after pop-in. Presented for the GHI plane, with displacements plotted relative to the vector at (0, 0, 0.5) and extreme values capped at ± 3.5 μm for clarity; vector fields indicate relative displacements compared to the largest displacement in the plane, not absolute values. The notch is indicated in pink and the profile J_1K_1 is shown.



Continued: Figure 121: UY displacement fields measured from DVC of the KN1 specimen in the loaded states, increasing from (a) 50 N to (c) 78 N (pop-in), the tomograph immediately after pop-in. Presented for the GHI plane, with displacements plotted relative to the vector at (0, 0, 0.5) and extreme values capped at ± 3.5 μm for clarity; vector fields indicate relative displacements compared to the largest displacement in the plane, not absolute values. The notch is indicated in pink and the profile J1K1 is shown.

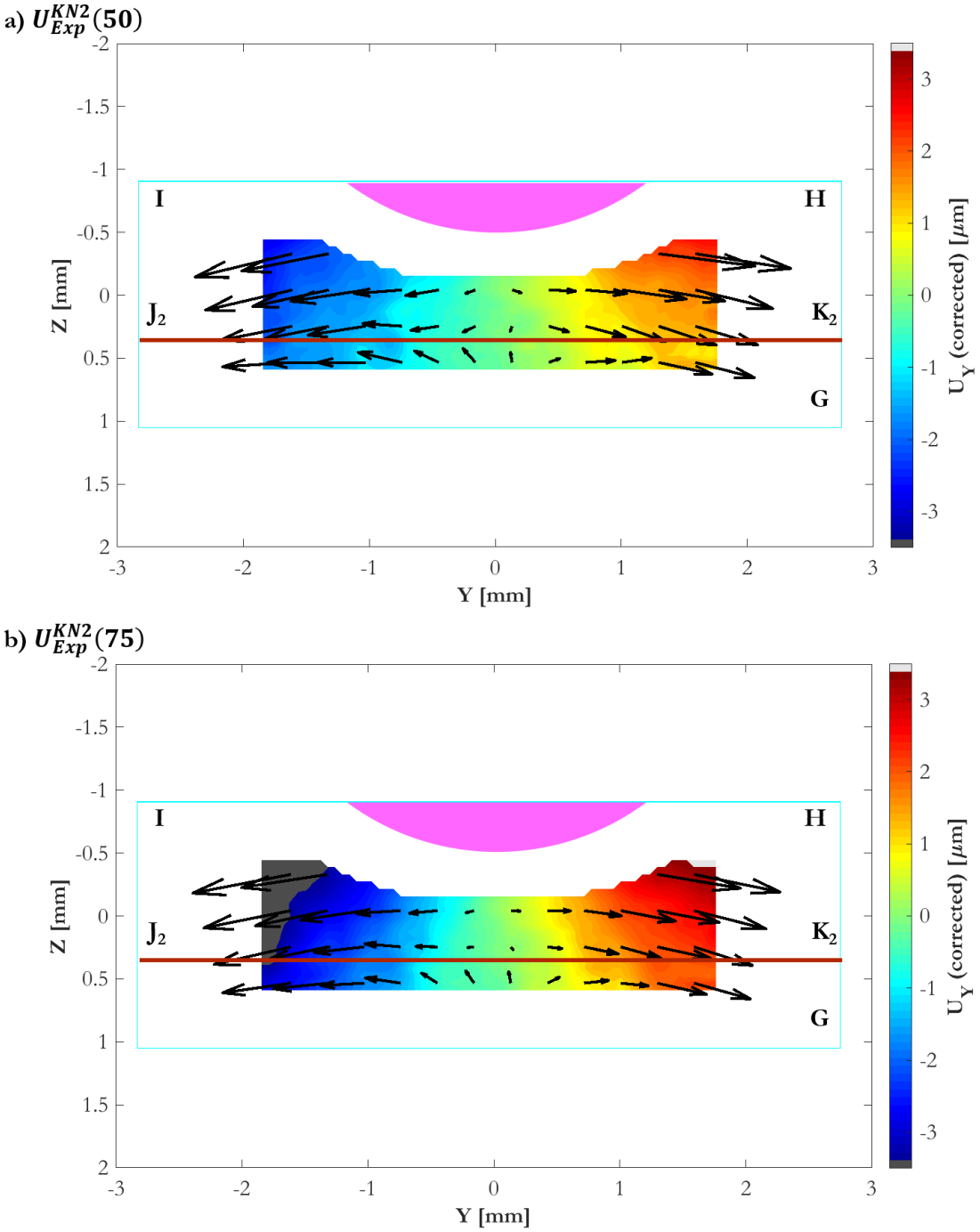
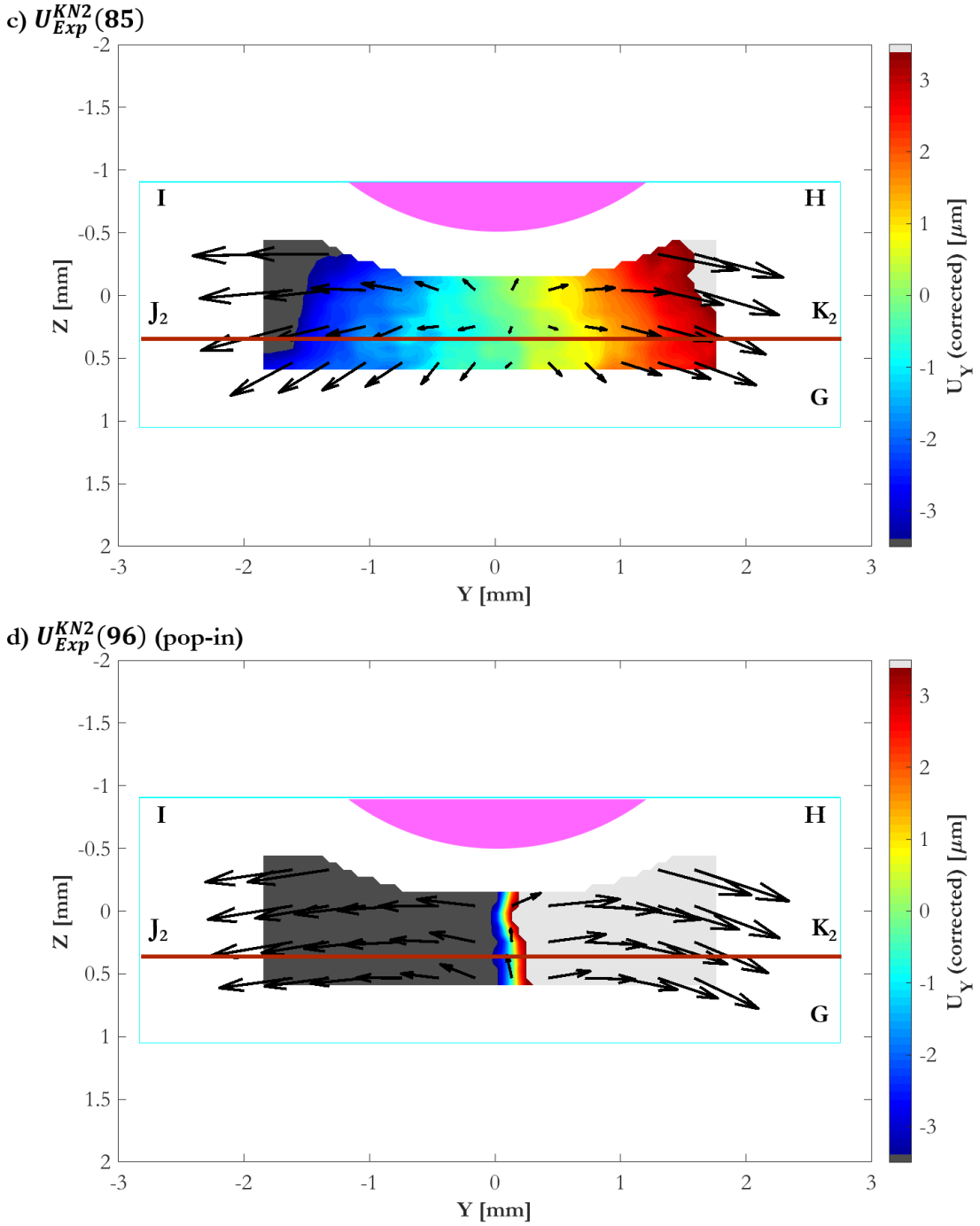


Figure 122: U_Y displacement fields measured from DVC of the KN2 specimen in the loaded states, increasing from (a) 50 N to (d) 96 N (pop-in), the tomograph immediately after pop-in. Presented for the GHI plane, with displacements plotted relative to the vector at (0, 0, 0.5) and extreme values capped at ± 3.5 μm for clarity; vector fields indicate relative displacements compared to the largest displacement in the plane, not absolute values. The notch is indicated in pink and the profile J_2K_2 is shown.



Continued: Figure 122: UY displacement fields measured from DVC of the KN2 specimen in the loaded states, increasing from (a) 50 N to (d) 96 N (pop-in), the tomograph immediately after pop-in. Presented for the GHI plane, with displacements plotted relative to the vector at (0, 0, 0.5) and extreme values capped at ± 3.5 μm for clarity; vector fields indicate relative displacements compared to the largest displacement in the plane, not absolute values. The notch is indicated in pink and the profile J2K2 is shown.

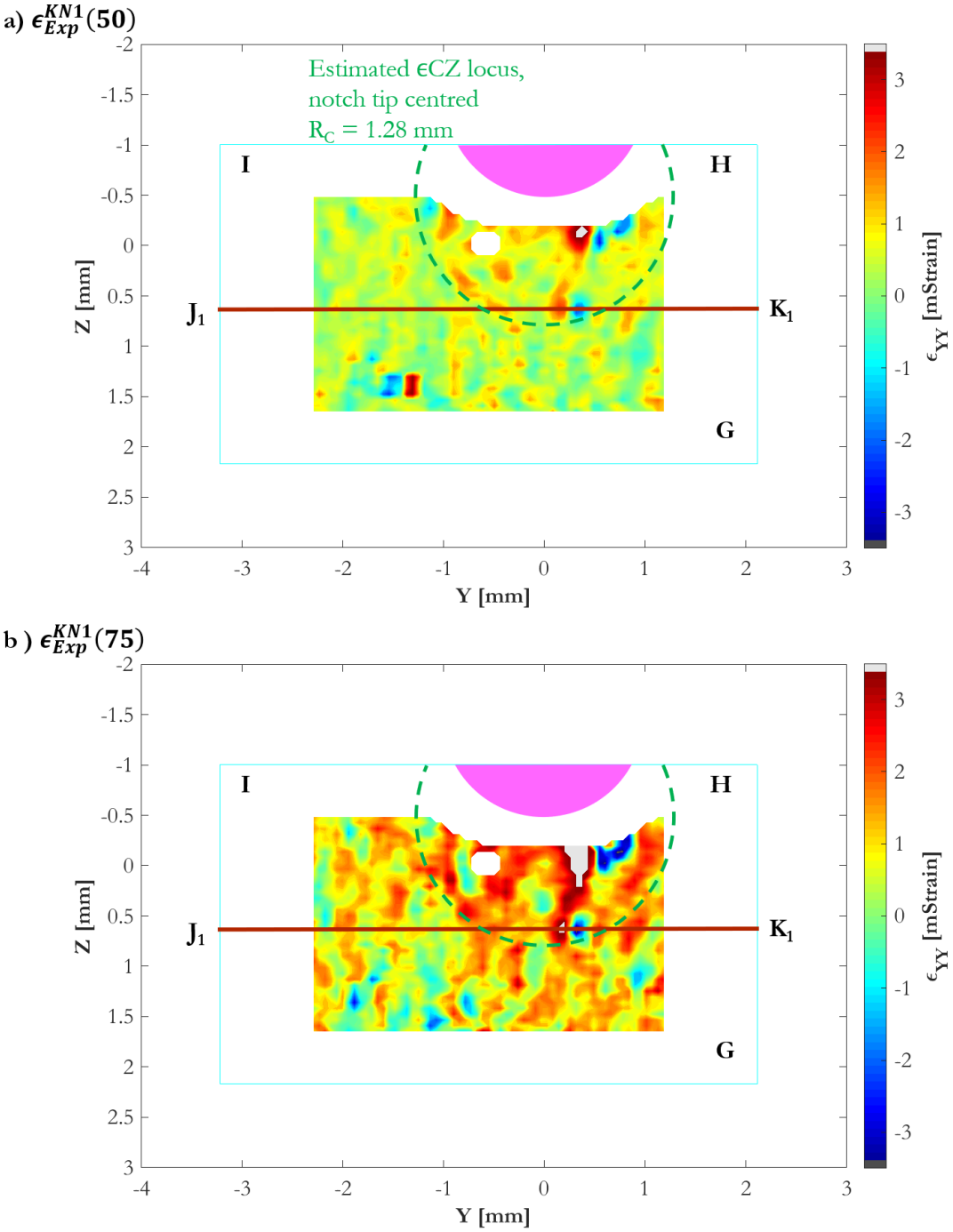
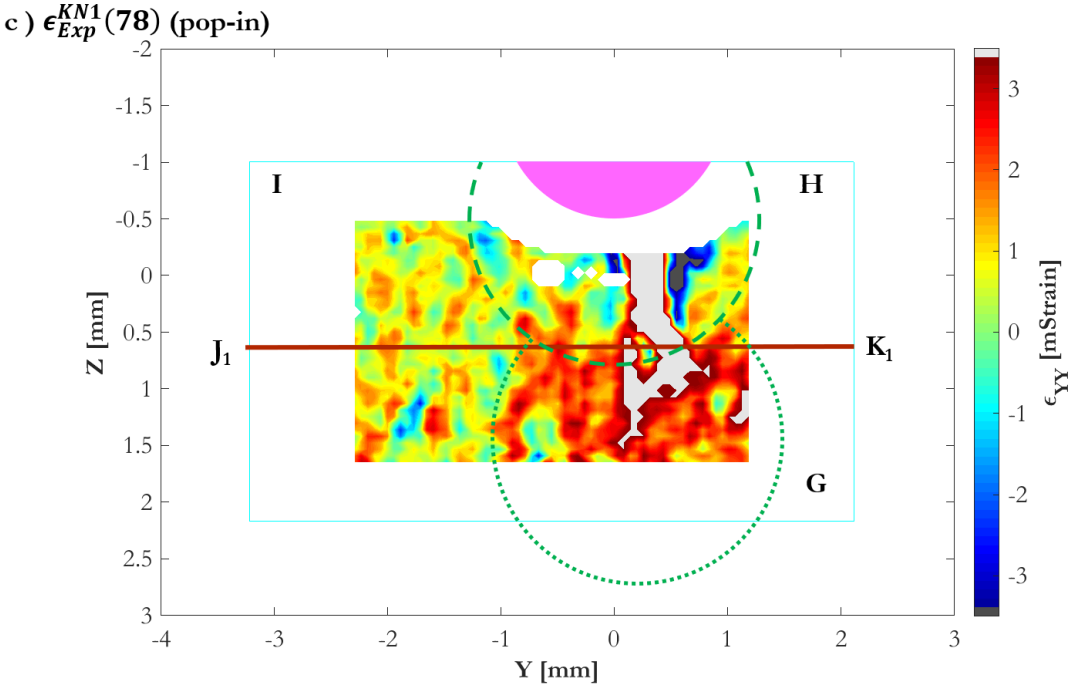


Figure 123: ϵ_{YY} strain fields measured from DVC of the KN1 specimen in the loaded states, increasing from (a) 50 N to (c) 78 N (pop-in), the tomograph immediately after pop-in. Presented for the GHI plane, with strains capped at ± 3.5 mStrain for clarity. The notch is indicated in pink, the profile J_1K_1 is shown, and the estimated ϵCZ locus (green, dashed) is based on (a) ($\epsilon_{Exp}^{KN1}(50)$) for all parts; for (c) an additional locus (green, dotted) of the same radius is shown centred on the estimated crack tip.



Continued: Figure 123: ϵYY strain fields measured from DVC of the KN1 specimen in the loaded states, increasing from (a) 50 N to (c) 78 N (pop-in), the tomograph immediately after pop-in. Presented for the GHI plane, with strains capped at ± 3.5 mStrain for clarity. The notch is indicated in pink, the profile J1K1 is shown, and the estimated ϵCZ locus (green, dashed) is based on (a) ($\epsilon_{Exp}^{KN1}(50)$) for all parts; for (c) an additional locus (green, dotted) of the same radius is shown centred on the estimated crack tip.

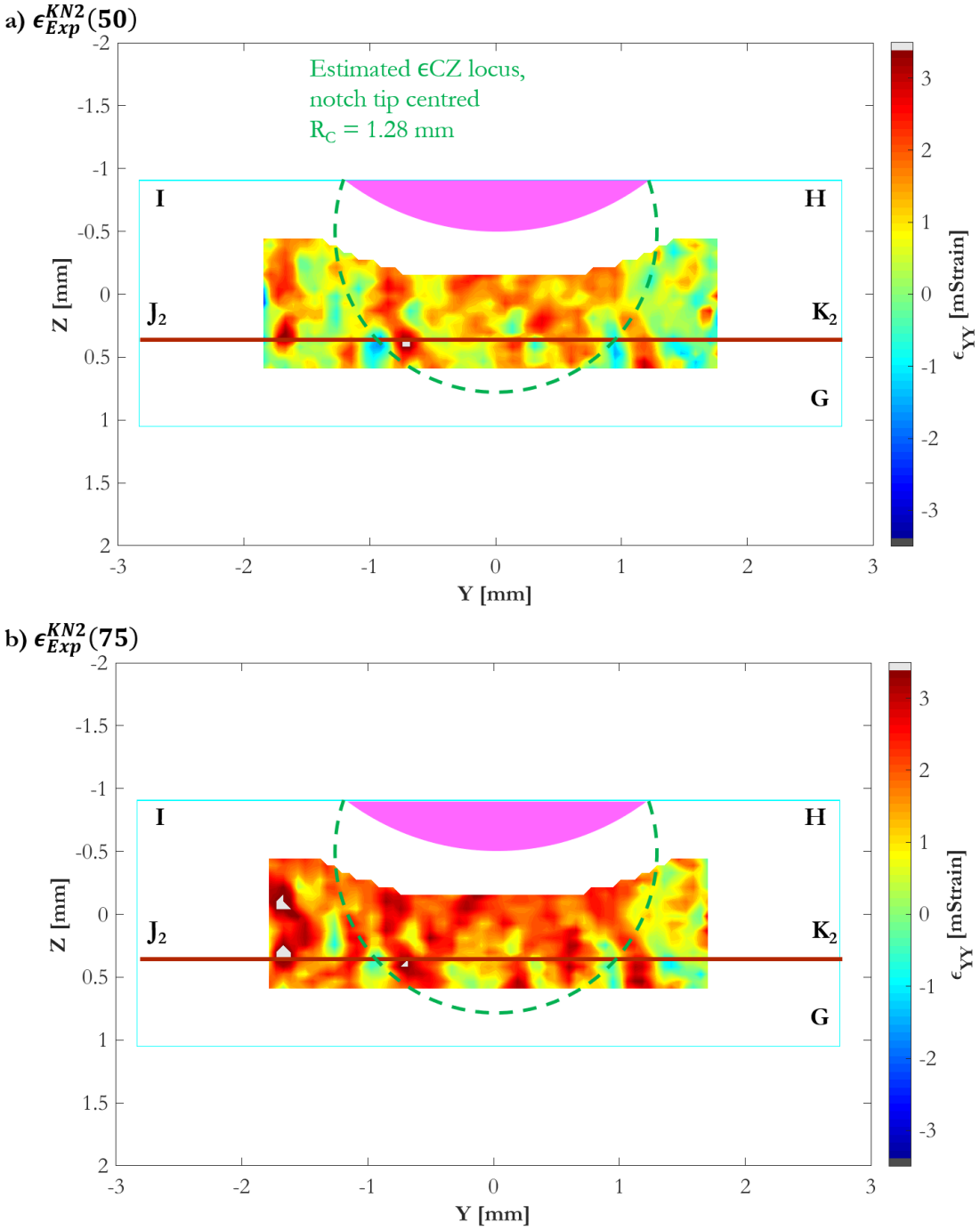
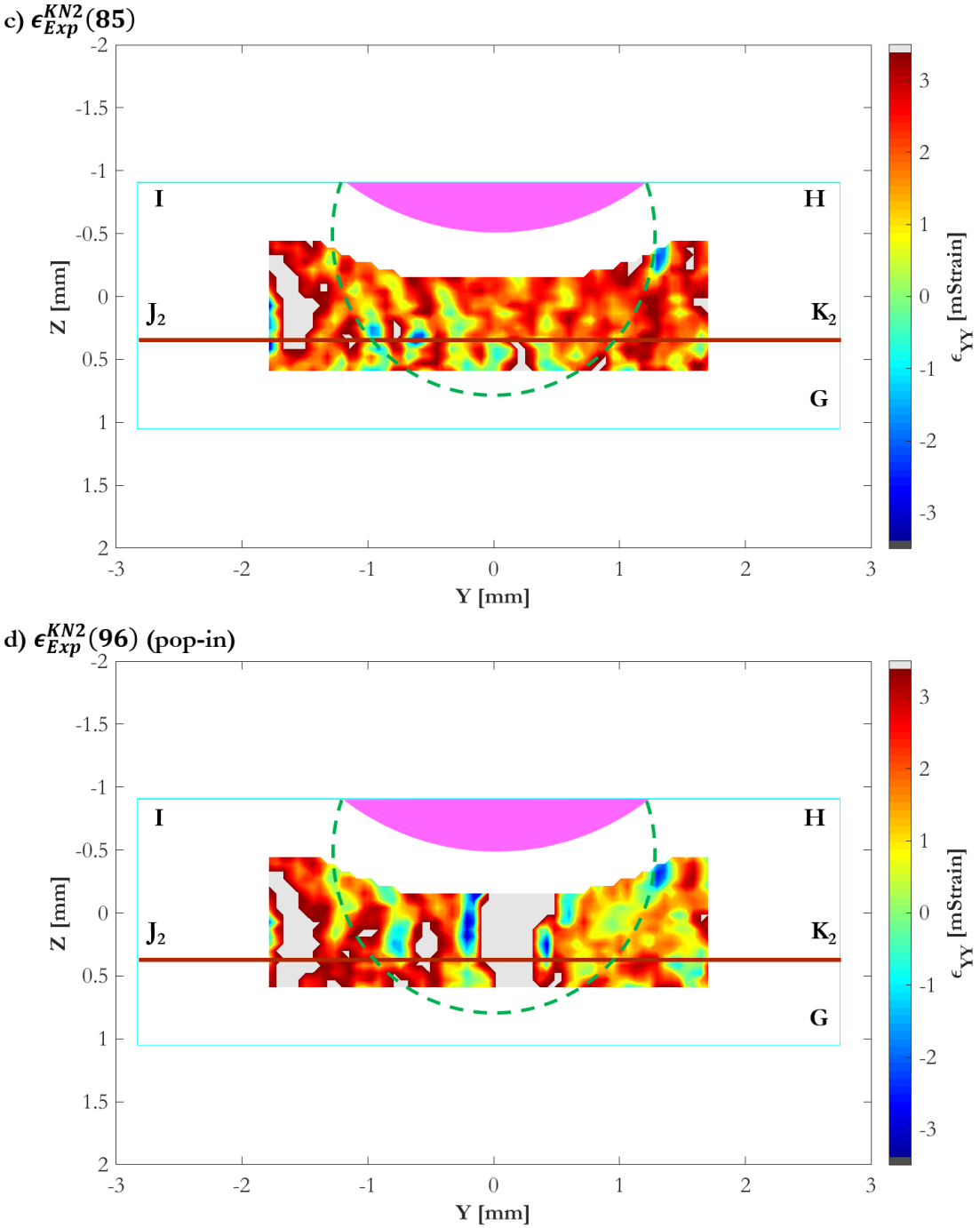


Figure 124: ϵ_{YY} strain fields measured from DVC of the KN2 specimen in the loaded states, increasing from (a) 50 N to (d) 96 N (pop-in), the tomograph immediately after pop-in. Presented for the GHI plane, with strains capped at ± 3.5 mStrain for clarity. The notch is indicated in pink, the profile J_2K_2 is shown and the estimated ϵCZ locus (green, dashed) is based on Figure 123(a) for all parts.



Continued: Figure 124: ϵYY strain fields measured from DVC of the KN2 specimen in the loaded states, increasing from (a) 50 N to (d) 96 N (pop-in), the tomograph immediately after pop-in. Presented for the GHI plane, with strains capped at ± 3.5 mStrain for clarity. The notch is indicated in pink, the profile J2K2 is shown and the estimated ϵCZ locus (green, dashed) is based on Figure 123(a) for all parts.

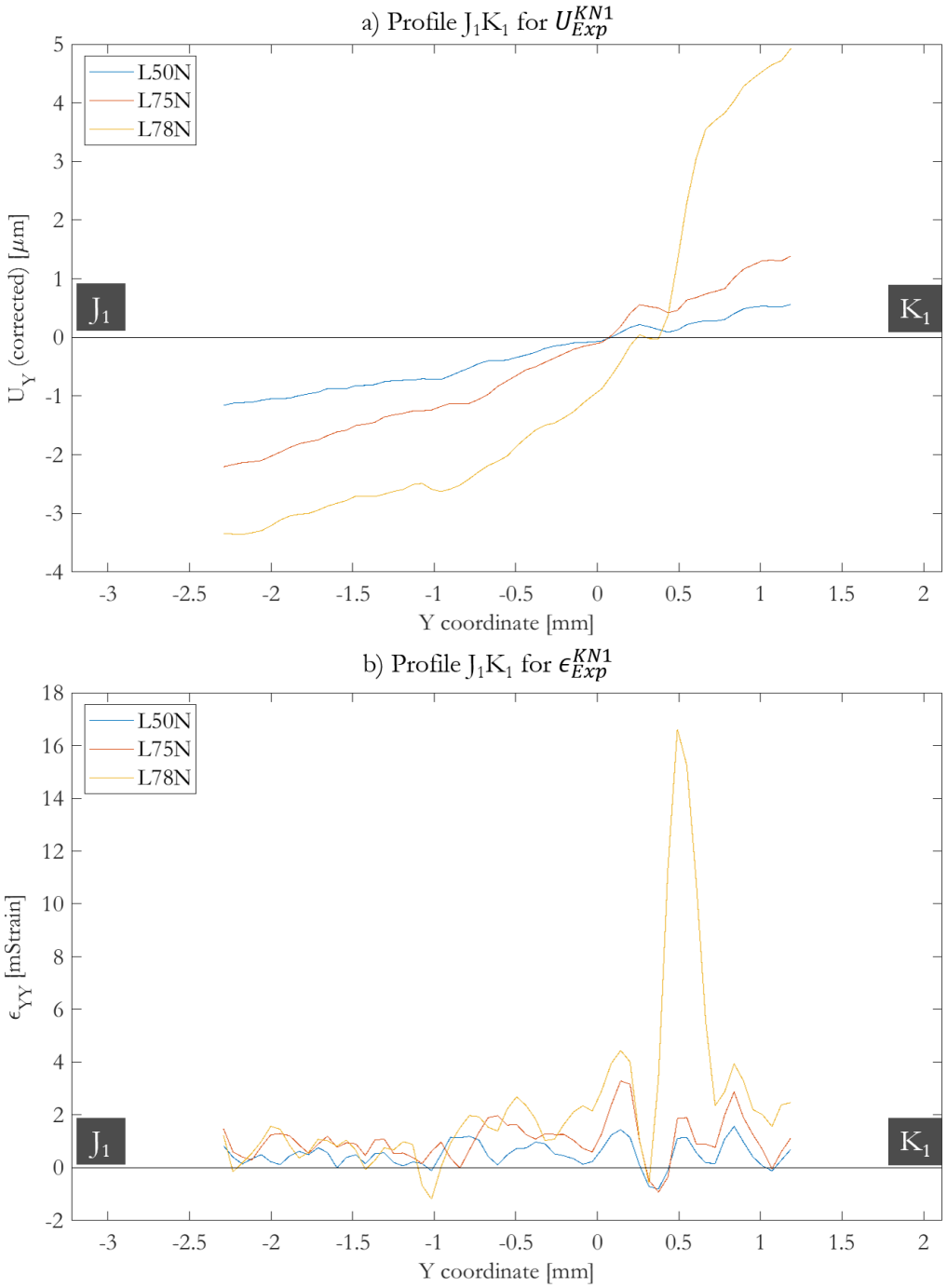


Figure 125: Variation in experimental (DVC) Mode I (a) displacement and (b) strain, for the KN1 specimen in the loaded states along profile J_1K_1.

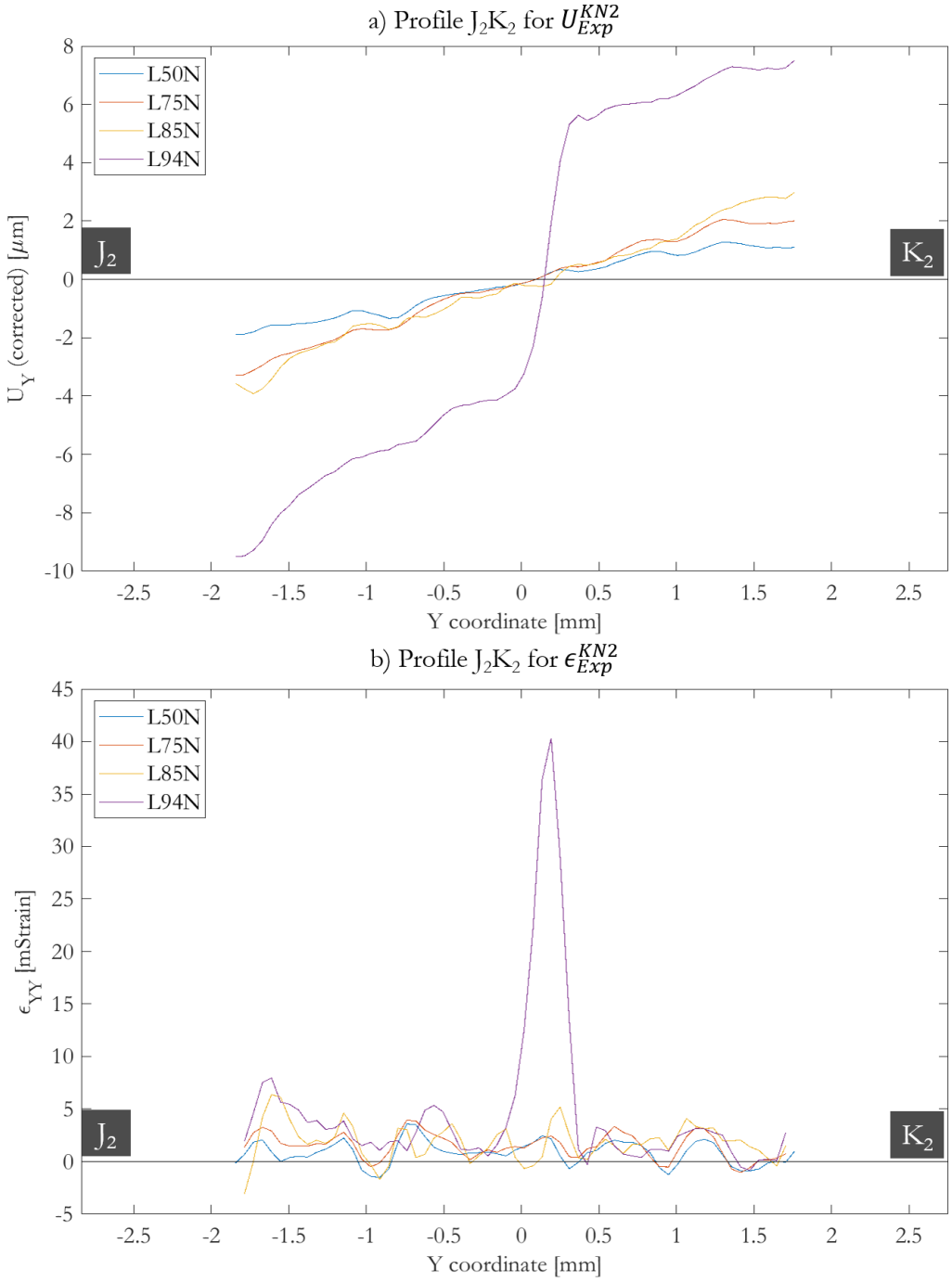


Figure 126: Variation in experimental (DVC) Mode I (a) displacement and (b) strain, for the KN2 specimen in the loaded states along profile J_2K_2.

IV.3.3.2.2 DVC unloaded states

Figure 127 and Figure 128 show the measured displacements in the KN1 and KN2 specimens, respectively, in each unloaded state, with the complementary strain fields in Figure 129 and Figure 130. As with the loaded states, the displacements and strains along the profiles J_iK_i were plotted in Figure 131 and Figure 132 for KN1 and KN2, respectively

From qualitative comparison of the temporal relationship of features in the strain maps, the regions of particularly high and low strain were persistent between successive unload stages, which indicated that the strains were truly associated with features in the correlated bodies, rather than noise.

The displacement fields for the unfractured, unloaded states indicated that there were no significant trends in the unloaded specimens. Minor trends were observed, for example, in Figure 127(a) and (b) where the vectors on the map edges suggested movement towards the origin, but the magnitude of the displacements due to this motion were small ($|U_{Exp,YY}| < \pm 0.7$ μm) in line with $\xi_{Corr,DVC}$. This was likely to be due to the small pre-load on the KN1 specimen (11 N). No corresponding spatial trends were seen in the corresponding strain maps, and no similar pattern was observed in the KN2 data.

Using the same ϵCZ locus as in the loaded states, the volume ahead of the notch appears to have experienced a compressive strain when unloaded, which is particularly notable in the KN2 images. As with the loaded states, hotspots of excessive strain were observed, and will be considered in § IV.3.4.

Following fracture, the crack path was apparent in the unloaded displacement and strain fields for both specimens, significantly displacing either side of the crack and confirming that the cracks permanently deformed the microstructures.

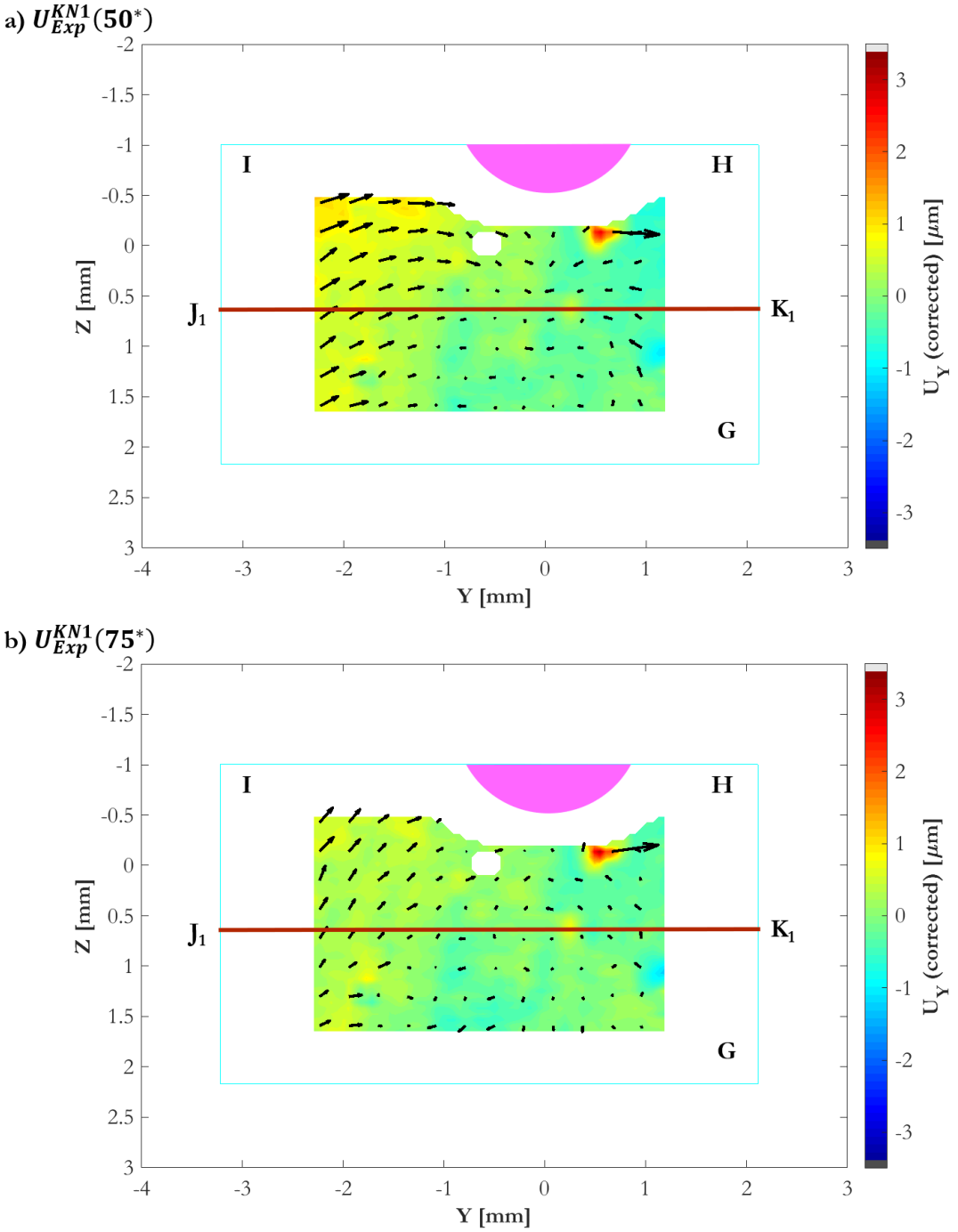
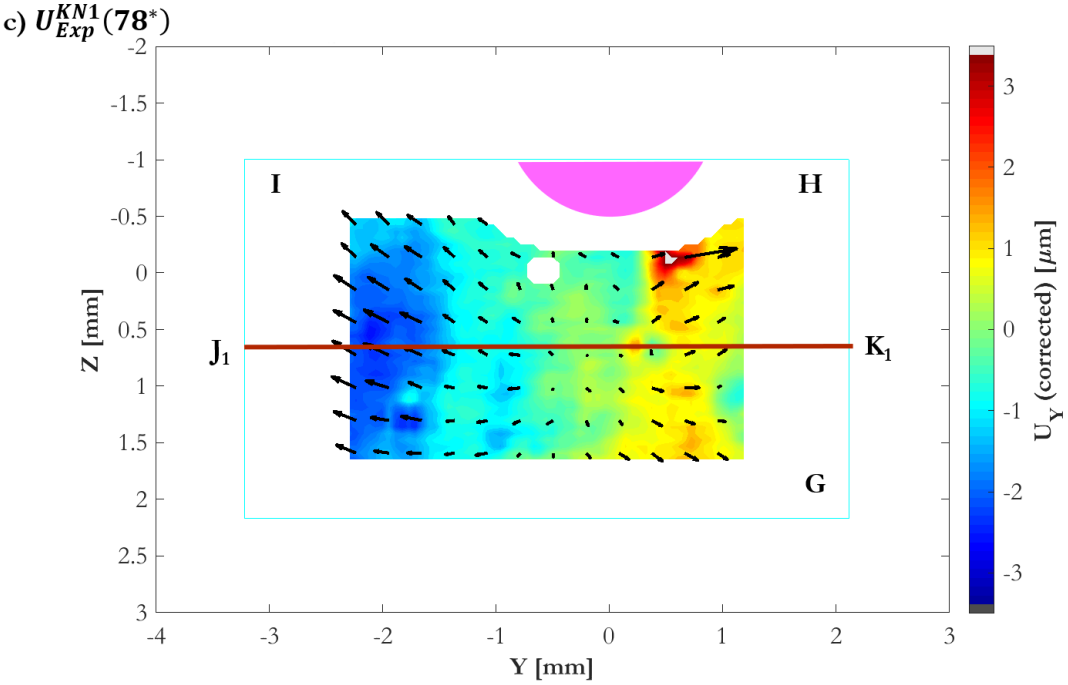


Figure 127: U_Y displacement fields measured from DVC of the KN1 specimen in the unloaded states, increasing from (a) the post-50 N loading to (c) the post-78 N loading. Presented for the GHI plane, and displacements are plotted relative to the vector 0.5 mm ahead of the notch tip, with displacements capped at ± 3.5 µm for clarity; vector fields indicate relative displacements compared to the largest displacement in the plane, not absolute values. The notch is indicated in pink and the profile J_1K_1 is shown.



Continued: Figure 127: UY displacement fields measured from DVC of the KN1 specimen in the unloaded states, increasing from (a) the post-50 N loading to (c) the post-78 N loading. Presented for the GHI plane, and displacements are plotted relative to the vector 0.5 mm ahead of the notch tip, with displacements capped at ± 3.5 μm for clarity; vector fields indicate relative displacements compared to the largest displacement in the plane, not absolute values. The notch is indicated in pink and the profile J1K1 is shown.

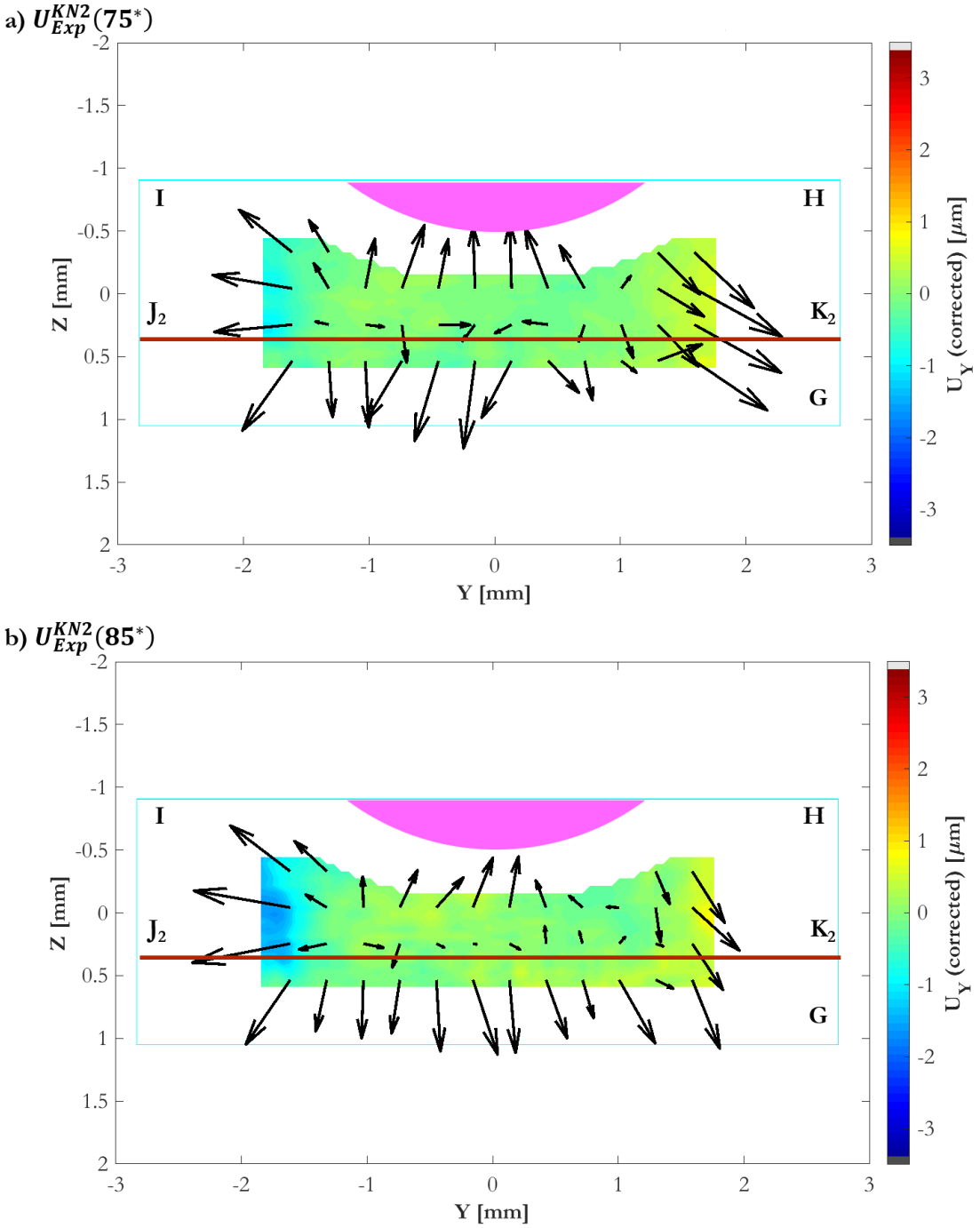
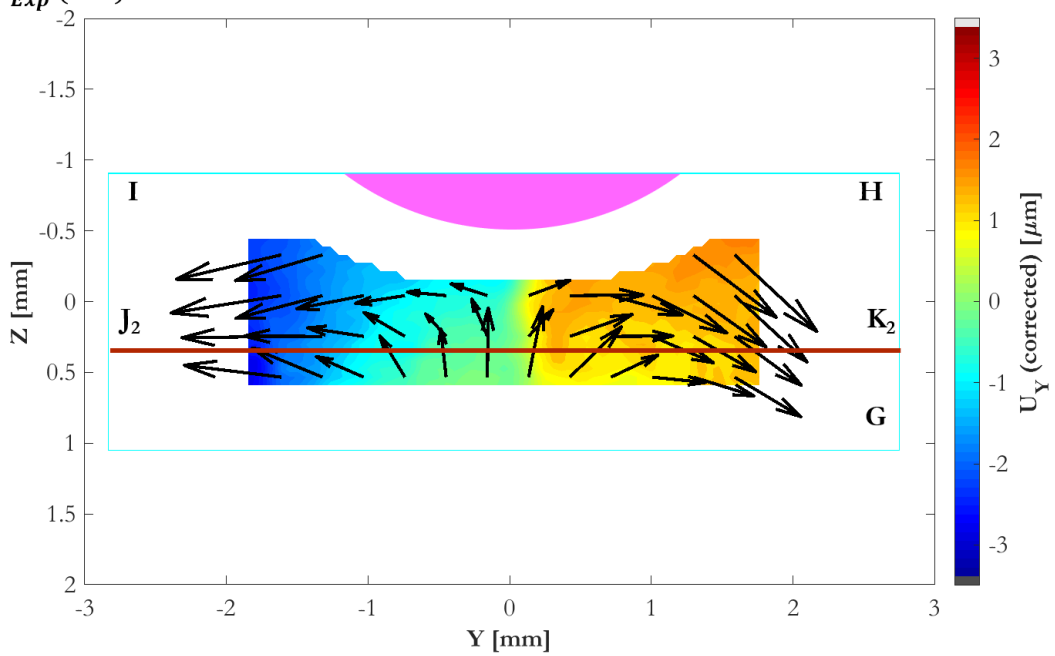


Figure 128: U_Y displacement fields measured from DVC of the KN2 specimen in the unloaded states, increasing from (a) the post-75 N loading to (c) the post-96 N loading. Presented for the GHI plane, and displacements are plotted relative to the vector 0.5 mm ahead of the notch tip, with displacements capped at ± 3.5 μm for clarity; vector fields indicate relative displacements compared to the largest displacement in the plane, not absolute values. The notch is indicated in pink and the profile J_2K_2 is shown.

c) $U_{Exp}^{KN2}(96^*)$



Continued: Figure 128: UY displacement fields measured from DVC of the KN2 specimen in the unloaded states, increasing from (a) the post-75 N loading to (c) the post-96 N loading. Presented for the GHI plane, and displacements are plotted relative to the vector 0.5 mm ahead of the notch tip, with displacements capped at ± 3.5 μm for clarity; vector fields indicate relative displacements compared to the largest displacement in the plane, not absolute values. The notch is indicated in pink and the profile J2K2 is shown.

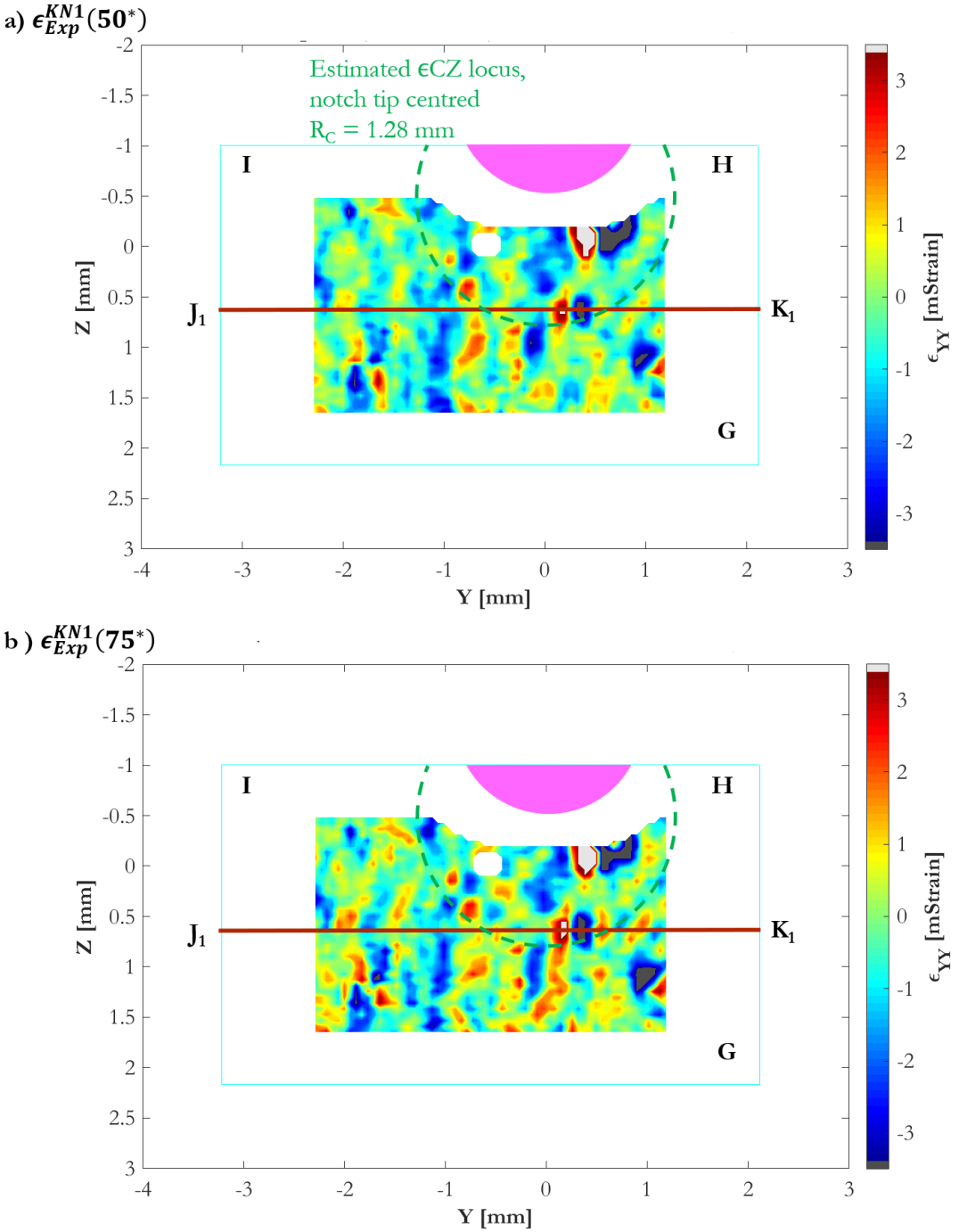
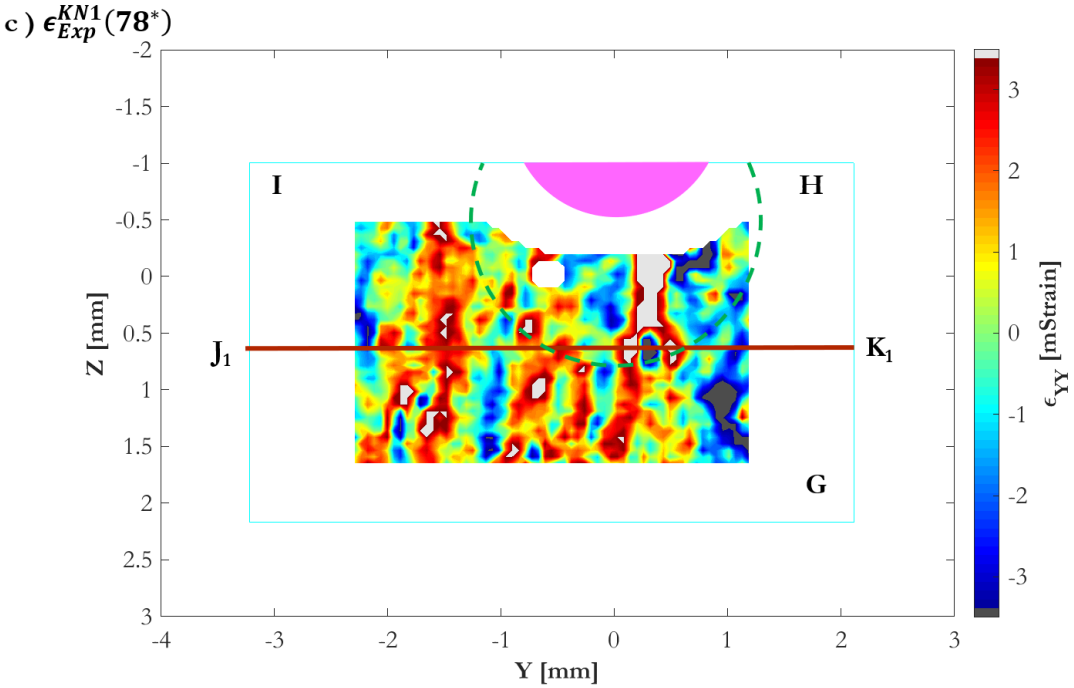


Figure 129: ϵ_{YY} strain fields measured from DVC of the KN1 specimen in the unloaded states, increasing from (a) the post-50 N loading to (c) the post-78 N loading. Presented for the GHI plane, with strains capped at ± 3.5 mStrain for clarity; vector fields indicate relative displacements compared to the largest displacement in the plane, not absolute values. The notch is indicated in pink and the profile J_1K_1 is shown.



Continued: Figure 129: ϵYY strain fields measured from DVC of the KN1 specimen in the unloaded states, increasing from (a) the post-50 N loading to (c) the post-78 N loading. Presented for the GHI plane, with strains capped at ± 3.5 mStrain for clarity; vector fields indicate relative displacements compared to the largest displacement in the plane, not absolute values. The notch is indicated in pink and the profile J1K1 is shown.

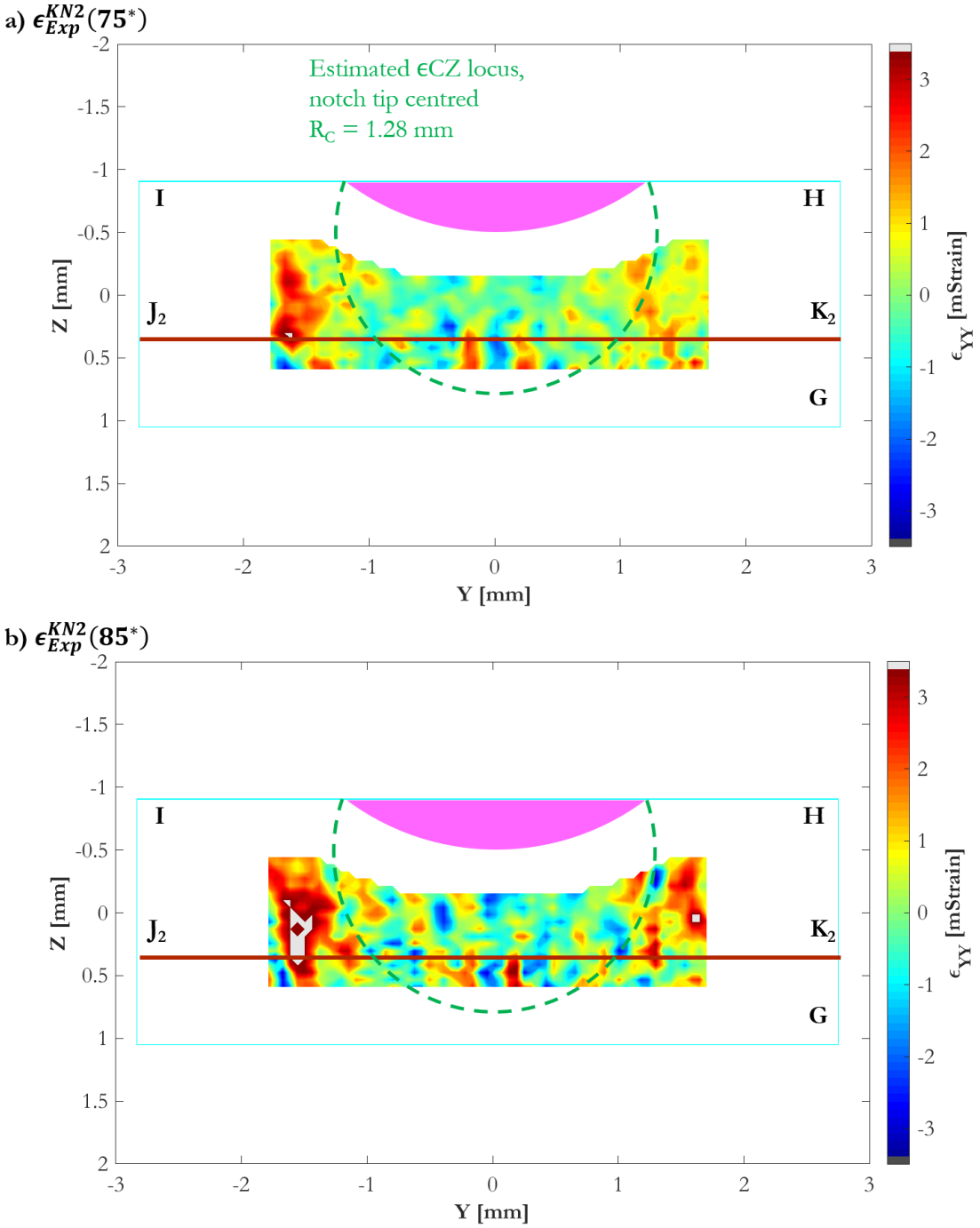
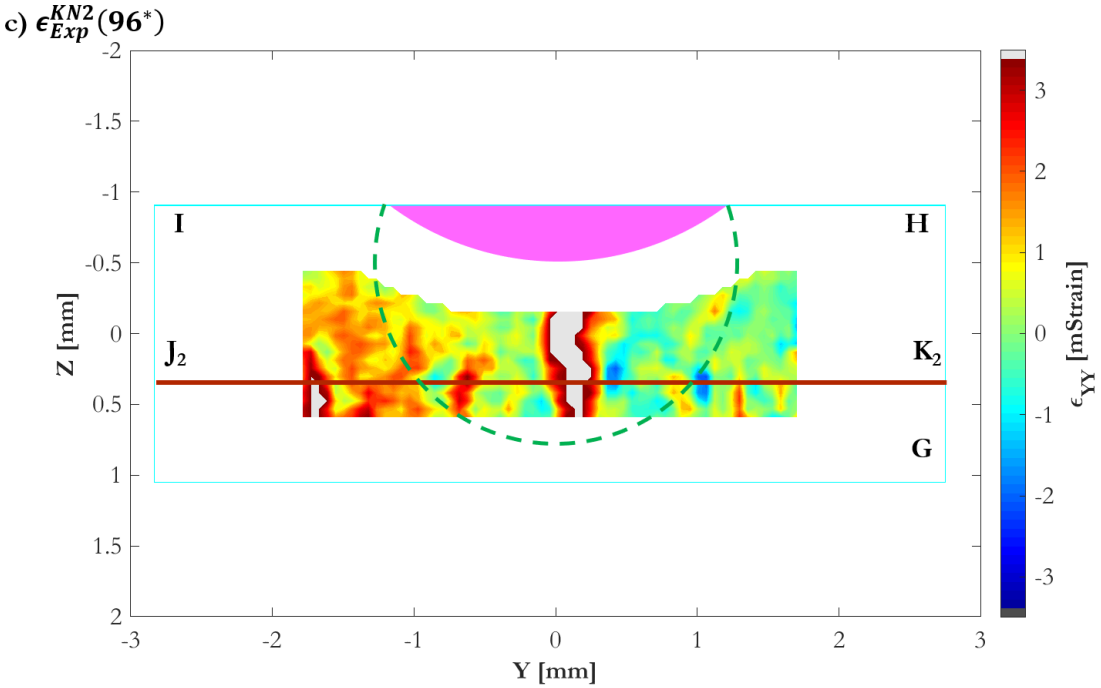


Figure 130: ϵ_{YY} strain fields measured from DVC of the KN2 specimen in the unloaded states, increasing from (a) the post-50 N loading to (d) the post-96 N loading. Presented for the GHI plane, with strains capped at ± 3.5 mStrain for clarity; vector fields indicate relative displacements compared to the largest displacement in the plane, not absolute values. The notch is indicated in pink and the profile J_2K_2 is shown.



Continued: Figure 130: ϵYY strain fields measured from DVC of the KN2 specimen in the unloaded states, increasing from (a) the post-50 N loading to (d) the post-96 N loading. Presented for the GHI plane, with strains capped at ± 3.5 mStrain for clarity; vector fields indicate relative displacements compared to the largest displacement in the plane, not absolute values. The notch is indicated in pink and the profile J2K2 is shown.

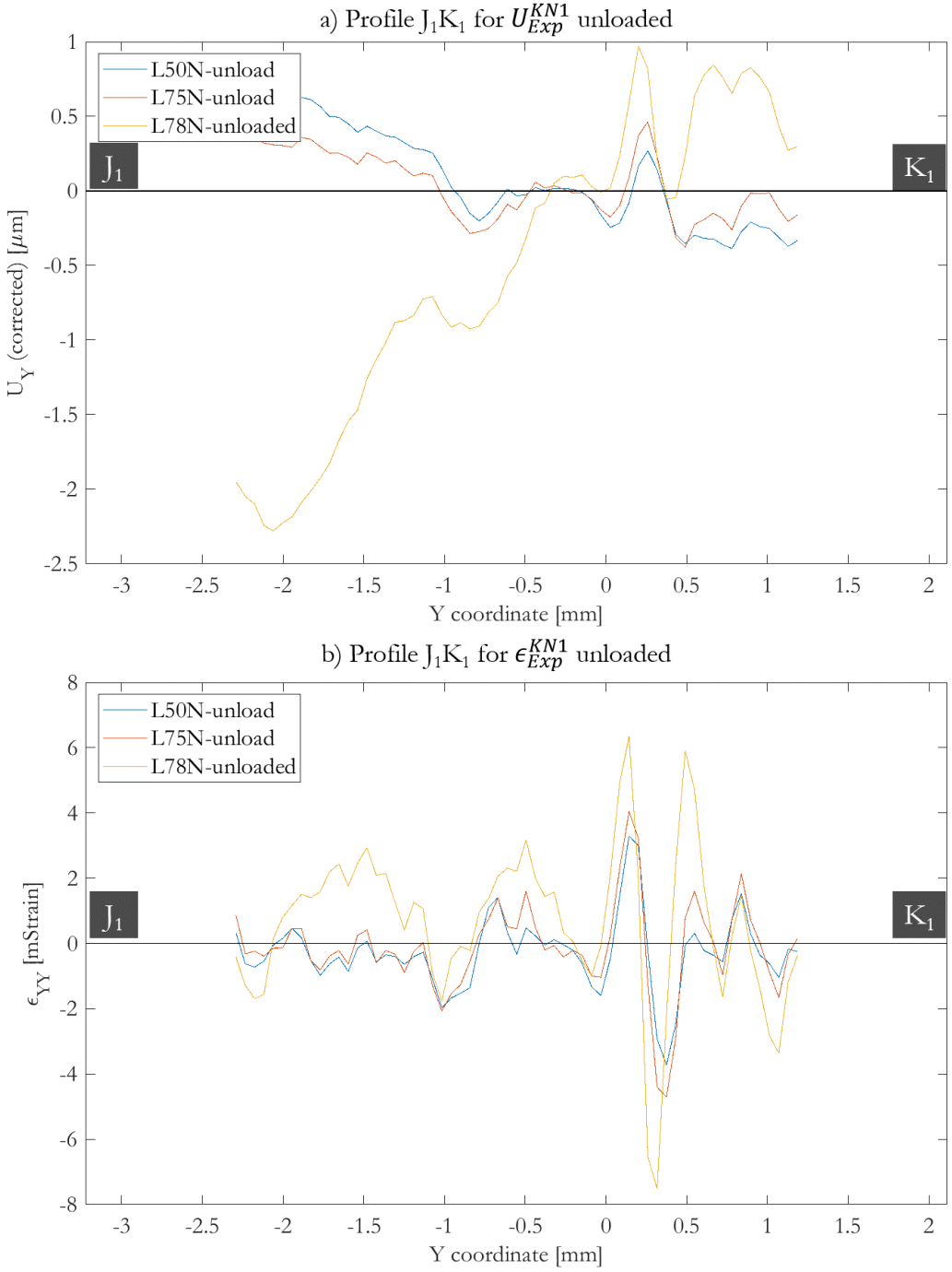


Figure 131: Variation in experimental (DVC) Mode I (a) displacement and (b) strain, for the KN1 specimen in the unloaded states along profile J_1K_1.

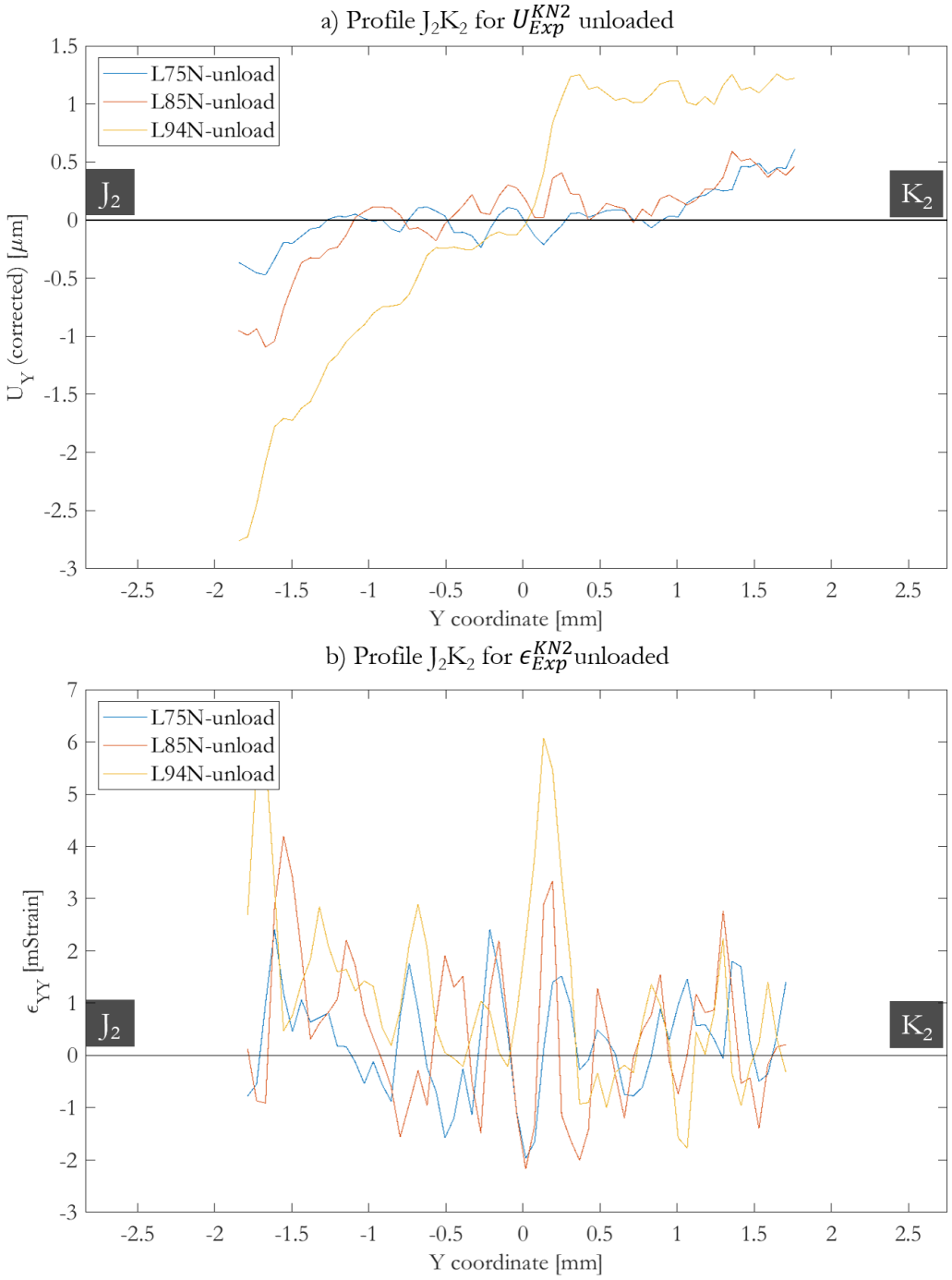


Figure 132: Variation in experimental (DVC) Mode I (a) displacement and (b) strain, for the KN2 specimen in the unloaded states along profile J_2K_2.

IV.3.4 Linear deviations

While the general patterns of measured displacements and strains agreed with the simulated behaviour at a given load in § IV.3.2), significant deviations from the smooth predicted behaviour were observed. Similar hotspots of residual deformation were observed in the measured behaviour at unload in§ IV.3.3. There appeared to exist localised regions that exhibited abnormal levels of displacement, resulting in high strains. To better quantify these deviations, the linear deviation field, $U_{Dev}^{KNi}(F)$, will be calculated (§ IV.3.4.1) as the difference between the experimental and simulation displacements. Trends in the evolution of the U_{Dev} fields and their differentials, $\partial\left(U_{Dev}^{KNi}(F)\right)$ which are equivalent to the difference in the strain fields, will be determined for the entire loading sequence of both specimens and the correspondence between the deviation fields and the microstructural features will be explored (§ IV.3.4.2). For clarity, the differential of the deviations will be referred to as 'deviation strains'. The deviation fields will then be filtered to isolate the statistical hotspots, forming the displacement hotspot fields, $H^{KNi}(F)$, and the complementary deviation strain hotspot fields, $\partial\left(H^{KNi}(F)\right)$, which will be examined in 3D and the evolution of the hotspot fraction quantified (§ IV.3.4.3). The evolution and spatial persistence of the hotspots with applied load will be quantified in (§ IV.3.4.4).

IV.3.4.1 Deviation calculation

To compare the U_{Exp} and U_{Sim} it was required that the two fields were geometrically equivalent. Both fields were highly detailed, each comprised of thousands of vectors, and the vector locations were dissimilar. To align the vectors, the symmetry-reduced U_{Sim} were first expanded to the full geometry, then the coordinate systems were spatially registered by an affine displacement and rotation of U_{Sim}, and the displacement components of the U_{Sim} fields, defined using splines to ensure derivative continuity, were interpolated at the U_{Exp} vector coordinates. This sequence left the U_{Exp} field unaltered, without compromising U_{Sim}.

The interpolation was performed using a 'multiquadric' (second-order) interpolator implemented in the neural network algorithm RBFINTERP that operated with 3D radial basis functions [177] and was incorporated into a bespoke MATLAB® script developed in collaboration with S. Barhli (University of Oxford) to handle the large volume of data and parallelise the calculations. While capable of running to even higher orders of interpolation, the memory and/or time requirements were prohibitive for the thousands of vectors considered here.

The individual vectors in the linear deviation fields, $\vec{U}_{Dev}(F,X)$, were calculated by (28) as point-wise subtractions at a given loading state.

$$\vec{U}_{Dev}(F,X) = \vec{U}_{Exp}(F,X) - \vec{U}_{Sim}(F,X) \tag{28}$$

For the unloaded states, linear elasticity predicted null fields for the displacements and strains, such that maps of the $U_{Dev}(F^*)$ and the corresponding $\partial(U_{Dev}(F^*))$ were identical to the figures in § IV.3.3.2.2; those maps will be replotted for ease of comparison with the deviations in the loaded states. If Gilsocarbon behaved elastically, the distribution of vectors in $U_{Exp}(F^*)$, and hence that of $U_{Dev}(F^*)$, would match the RBD sensitivity measurement derived in § IV.3.3.1, with a 95%ile-width of $\xi_{Corr,DVC}$ = 0.64 μm or 1.96 mStrain.

IV.3.4.2 General deviation behaviour

Considering only the Mode I deformations for clarity, the deviation fields for the 1 mm radius notch, $U_{Dev,Y}^{KN1}$, based on the U_{Exp} data from loaded states in Figure 121 and unloaded states in Figure 127 were plotted in Figure 133, and the $U_{Dev,Y}^{KN2}$ fields (based on Figure 122 and Figure 128) were plotted in Figure 134. The deviation strain fields, $\partial_Y\left(U_{Dev,Y}^{KNi}\right)$ are shown in Figure 135 and Figure 136, for KN1 and KN2, respectively; taking the gradients in the 'normal' directions, these fields were algebraically equivalent to the difference in strains between simulation and experiment (assuming small strains), though calculated as the differential change in deviation displacement for computational accuracy. For brevity, only the fields for the partial differential in the Y direction were presented, equivalent to the difference in ϵ_{YY}. The previously postulated ϵCZ loci have been plotted on each deviation strain map, as have the approximate ellipses that estimate the extent of the simulated ϵCZs (using the 2.0 mStrain limit) for each specimen.

To consider the different deformation behaviour of the microstructural phases, the deviation strain maps for penultimate and final loaded states in Figure 135 and Figure 136 were superimposed on the microstructural GHI slices (as in Figure 108) in Figure 137 and Figure 138 for KN1 and KN2, respectively. From all of the loaded states, line profiles of $U_{Dev,Y}$ and $\partial(U_{Dev,Y})$ along the paths J_iK_i are shown in Figure 139 and Figure 140 (for the unloaded states, the reader is referred to Figure 131 and Figure 132).

The most prominent feature of the maps and profiles is the presence of the discontinuity after fracture; this is seen as a rapid increase in the displacement maps and unreasonably high values in the strain maps, forming a roughly vertical line in the maps. As explained above this was expected since cracking was simulated. Prior to fracture, the maps in Figure 133 and Figure 134 of the loaded states had a relatively consistent background colour (green), indicating that the agreement between simulation and experiment was within error ($\xi_{Corr,DVC}$). Sight horizontal trends were observed in both the maps and profiles for both specimens, consistent with those discussed earlier for the unloaded states (§ IV.3.3.2.2), such that the greatest disparity was at the edges of the tomograph regions (by construction).

The largest deviation strains within the postulated ϵCZ were generally of a higher magnitude than those in the rest of the body. Close inspection of the maps suggested that the deviation strains formed approximately concentric bands, related to the simulated ϵCZ; in a general sense, moving away from the notch tip, the deviation strains were initially negative ($\epsilon_{Exp} < \epsilon_{Sim}$) up to the simulation ϵCZ, then positive ($\epsilon_{Sim} < \epsilon_{Exp}$) up to the postulated ϵCZ locus, and finally falling below $\xi_{\epsilon,Corr,DVC}$ ($\epsilon_{Exp} \approx \epsilon_{Sim}$).

Approximately elliptical regions (of radii up to c. 0.5 mm) with abnormally large displacements (in both a positive and negative sense) were identified in the maps in both specimens, where the magnitude of the deviation appeared to grow progressively with increasing load (the fluctuations identified in the U_{Exp} maps). Comparison with the strain maps show that high deviation strains were measured on the boundaries of these displacement regions, in addition to other narrow regions of high deviation strain. Considering the behaviour at the penultimate load states, from Figure 137 and Figure 138 it was further observed that the most significant deviation strains appeared to be associated with the filler particles. Three filler particles were labelled that were intersected by the profile (FP1-FP3) profile plots, demonstrating their consistently abnormal behaviour, which continued even after fracture. The highest deviation strains appear to be associated with large pores on the periphery of the filler particles; similarly large pores in the binder phase were not highly strained. All the excessive strains in the maps were filler particles or the crack discontinuities. Comparison with the displacement maps indicates that the filler particle displaced as a rigid body, relative to the binder, resulting in high strains at the interfaces, with the strains accommodated mostly by the filler particle rather than the binder.

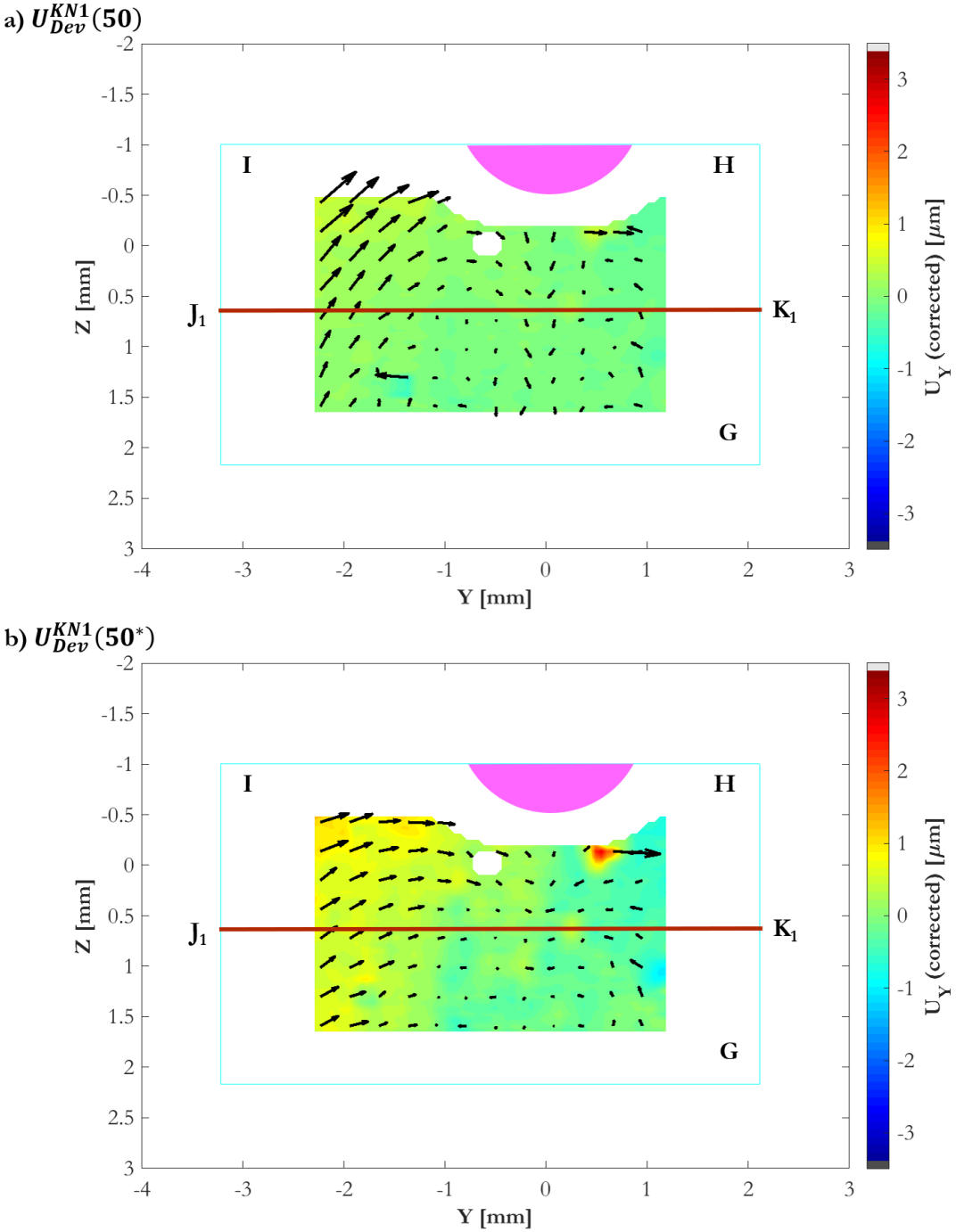
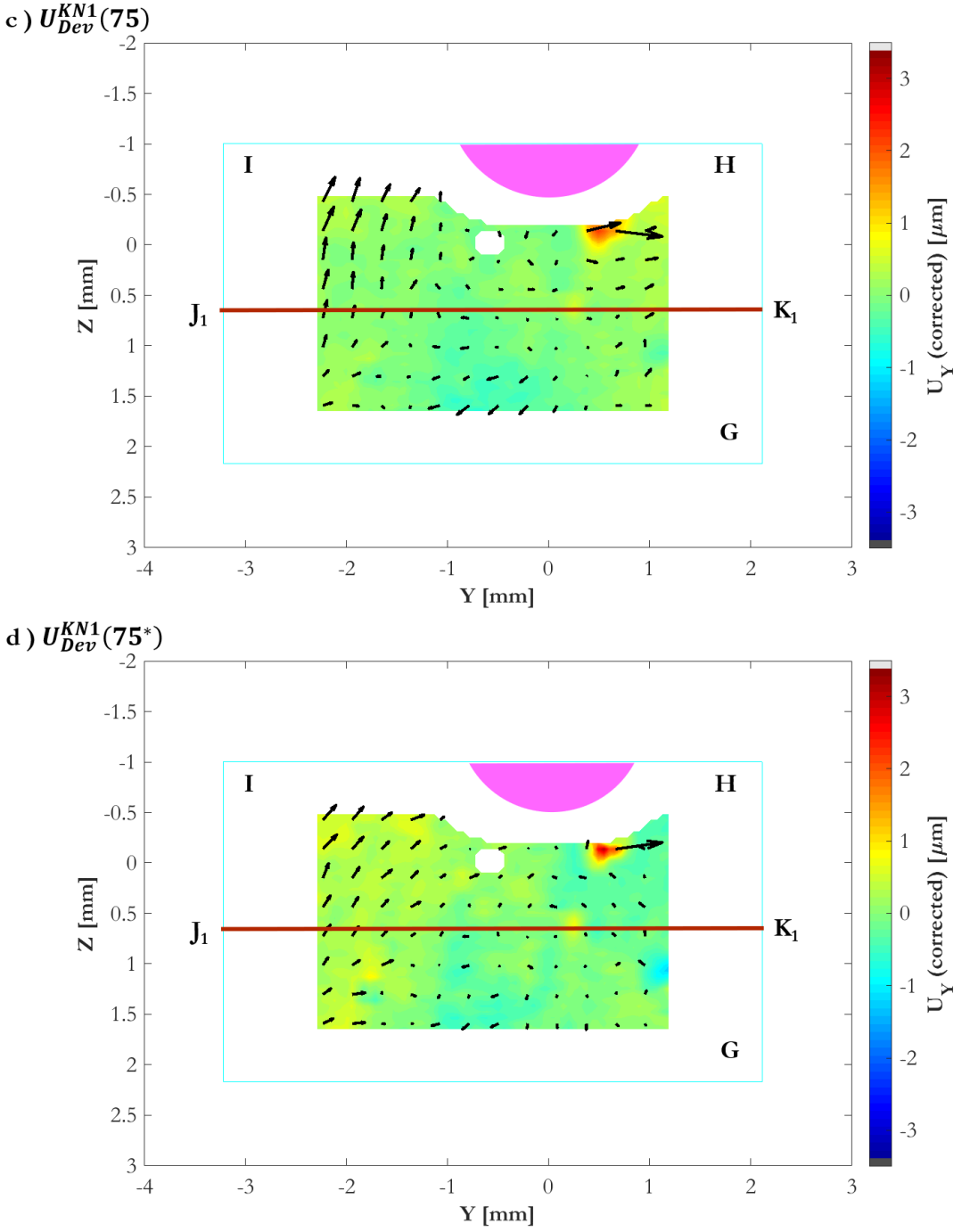
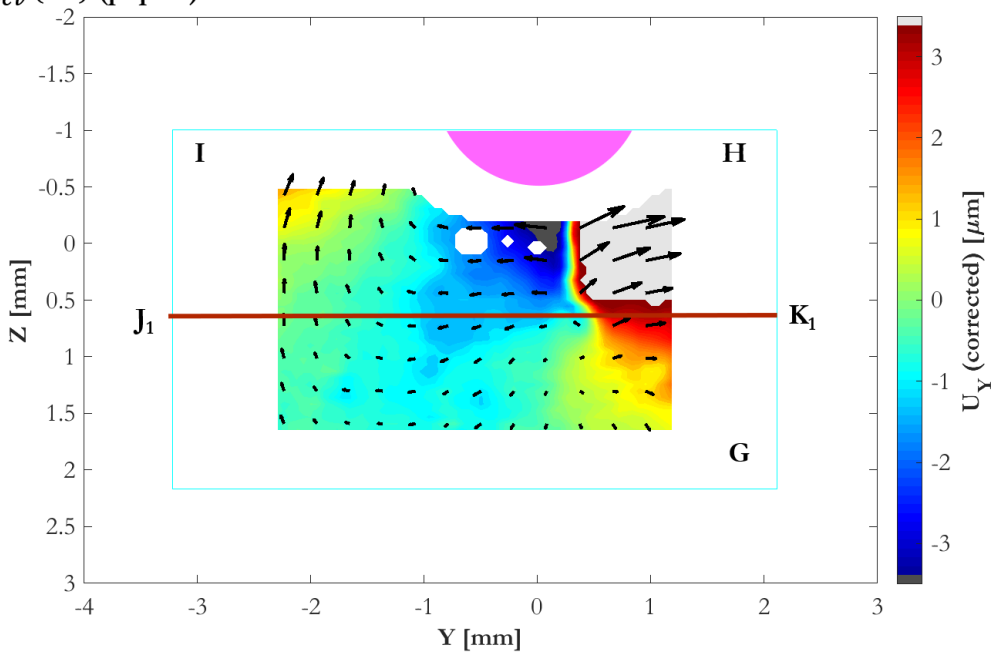


Figure 133: Deviation displacements of the KN1 specimen, progressing from (a) loaded to 50 N to (f) unloaded after the 78 N loading. Presented for the GHI plane, with extreme displacement values capped at ± 3.5 μm for clarity; vector fields indicate relative displacements compared to the largest displacement in the plane, not absolute values. The notch is indicated in pink and the profile J_1K_1 is shown.

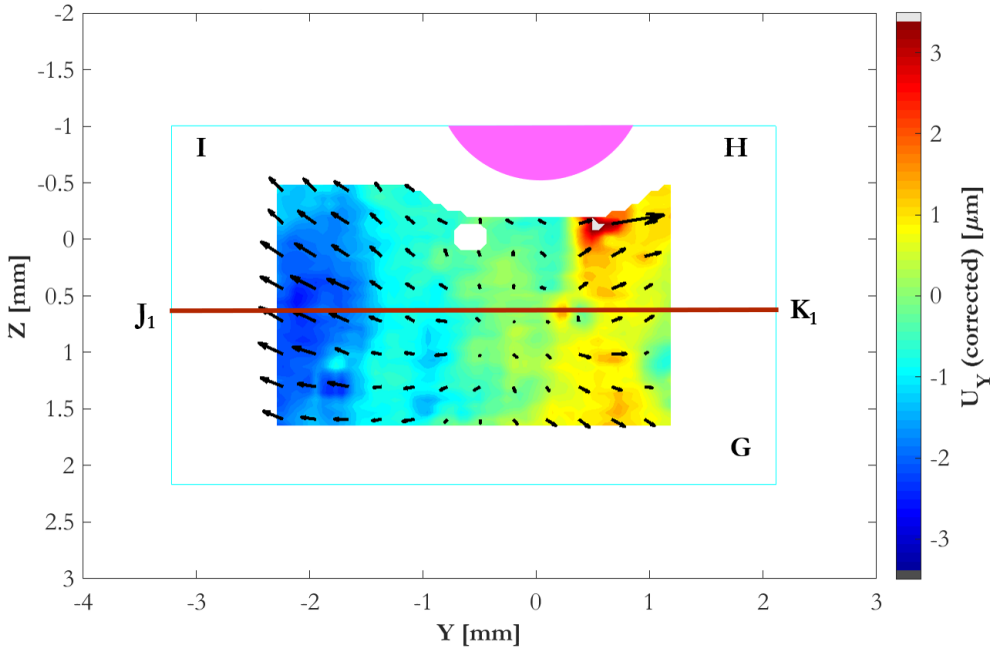


Continued: Figure 133: Deviation displacements of the KN1 specimen, progressing from (a) loaded to 50 N to (f) unloaded after the 78 N loading. Presented for the GHI plane, with extreme displacement values capped at ± 3.5 μm for clarity; vector fields indicate relative displacements compared to the largest displacement in the plane, not absolute values. The notch is indicated in pink and the profile J1K1 is shown.

e) $U_{Dev}^{KN1}(78)$ (pop-in)

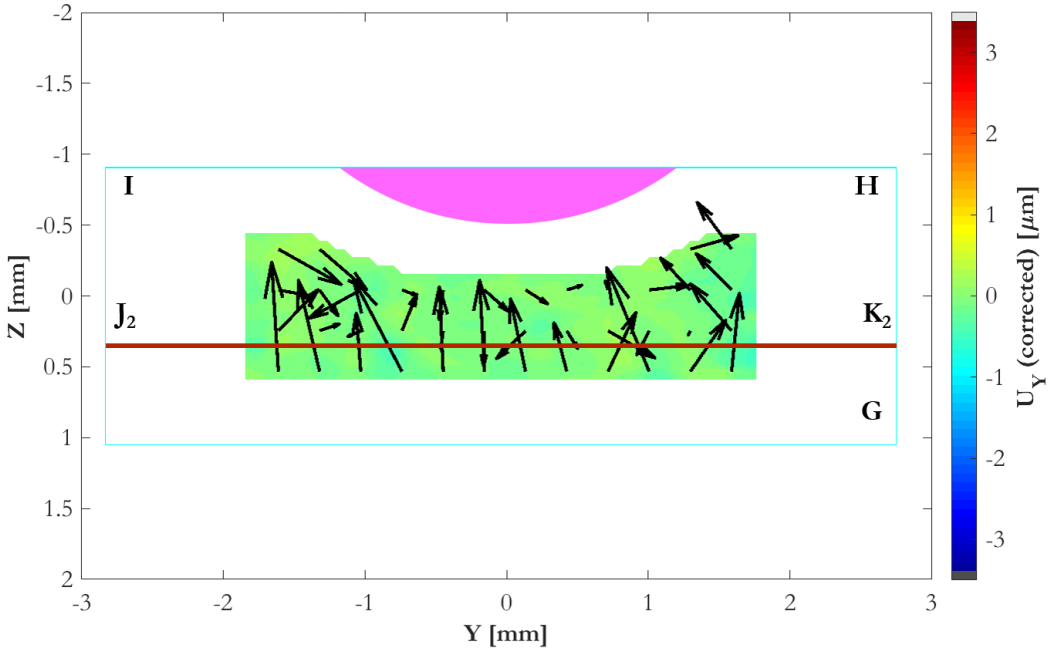


f) $U_{Dev}^{KN1}(78^*)$



Continued: Figure 133: Deviation displacements of the KN1 specimen, progressing from (a) loaded to 50 N to (f) unloaded after the 78 N loading. Presented for the GHI plane, with extreme displacement values capped at ± 3.5 μm for clarity; vector fields indicate relative displacements compared to the largest displacement in the plane, not absolute values. The notch is indicated in pink and the profile J1K1 is shown.

a) $U_{Dev}^{KN2}(50)$

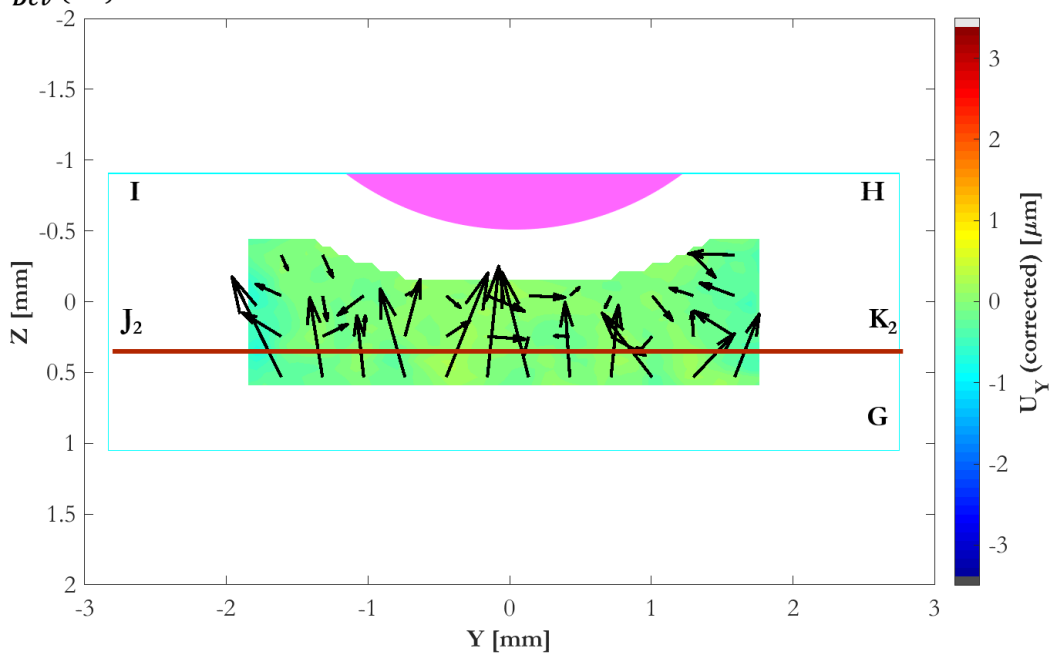


b) $U_{Dev}^{KN2}(50^*)$

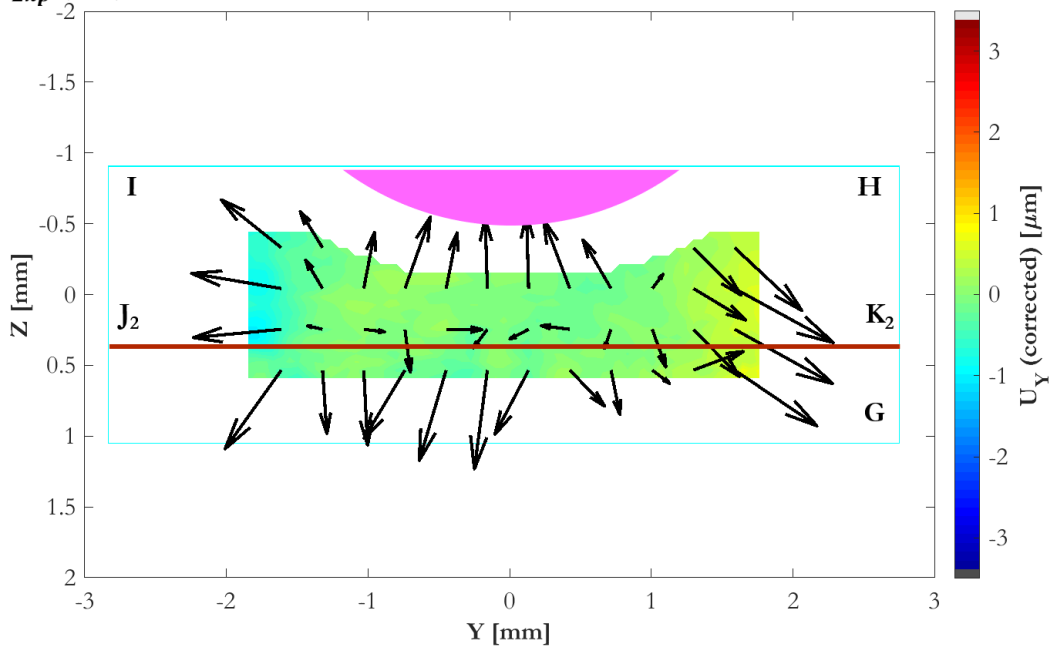
No data presented

Figure 134: Deviation displacements of the KN2 specimen, progressing from (a) loaded to 50 N to (f) unloaded after the 96 N loading. Data for the unload after 50 N is not available; see § A2. Presented for the GHI plane, with extreme displacement values capped at ± 3.5 μm for clarity; vector fields indicate relative displacements compared to the largest displacement in the plane, not absolute values. The notch is indicated in pink and the profile J_2K_2 is shown.

c) $U_{Dev}^{KN2}(75)$

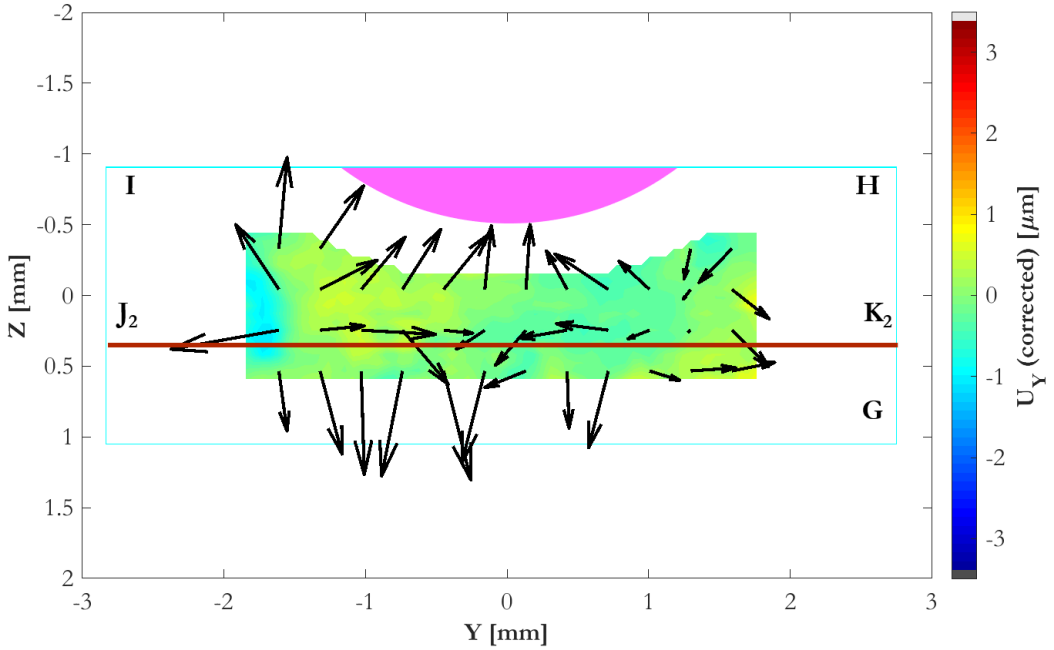


d) $U_{Exp}^{KN2}(75^{*})$

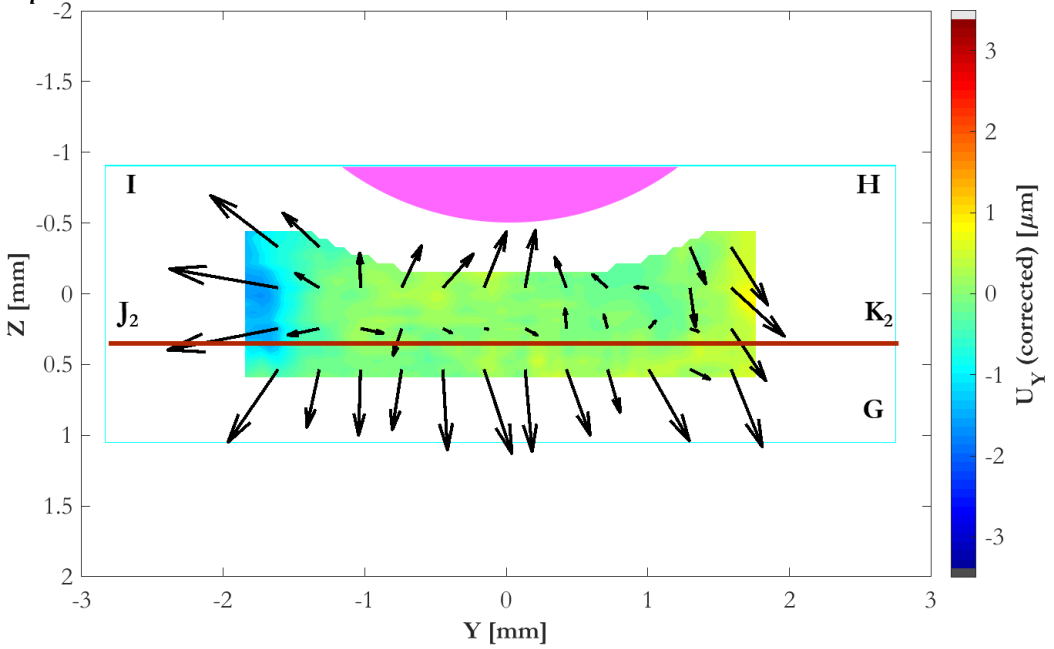


Continued: Figure 134: Deviation displacements of the KN2 specimen, progressing from (a) loaded to 50 N to (f) unloaded after the 96 N loading. Data for the unload after 50 N is not available; see § A2. Presented for the GHI plane, with extreme displacement values capped at ± 3.5 μm for clarity; vector fields indicate relative displacements compared to the largest displacement in the plane, not absolute values. The notch is indicated in pink and the profile J2K2 is shown.

e) $U_{Dev}^{KN2}(85)$

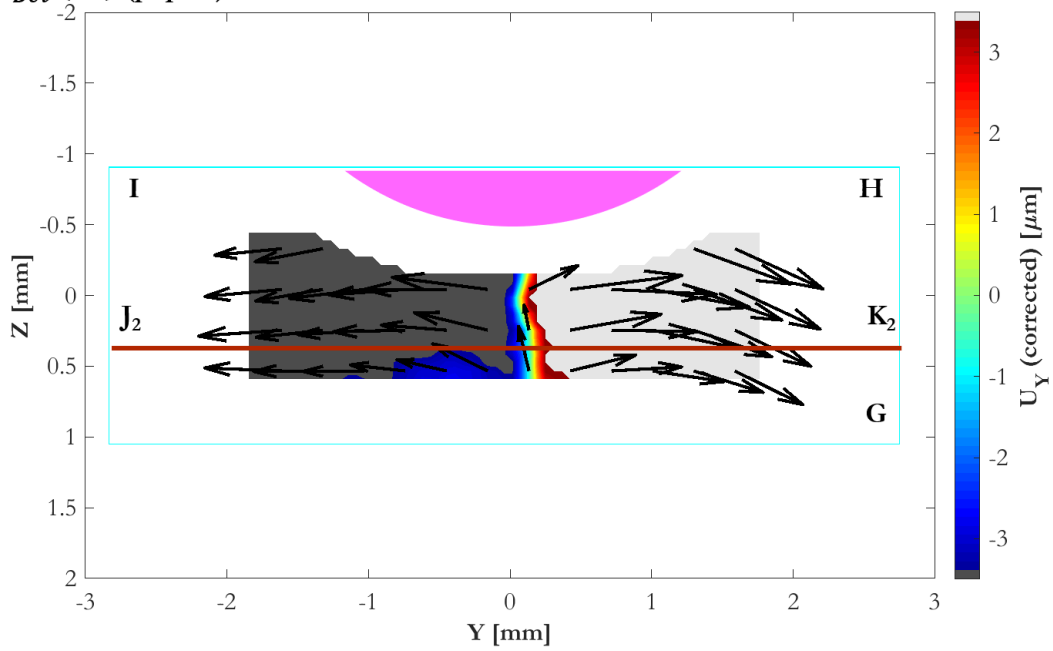


f) $U_{Exp}^{KN2}(85^{*})$

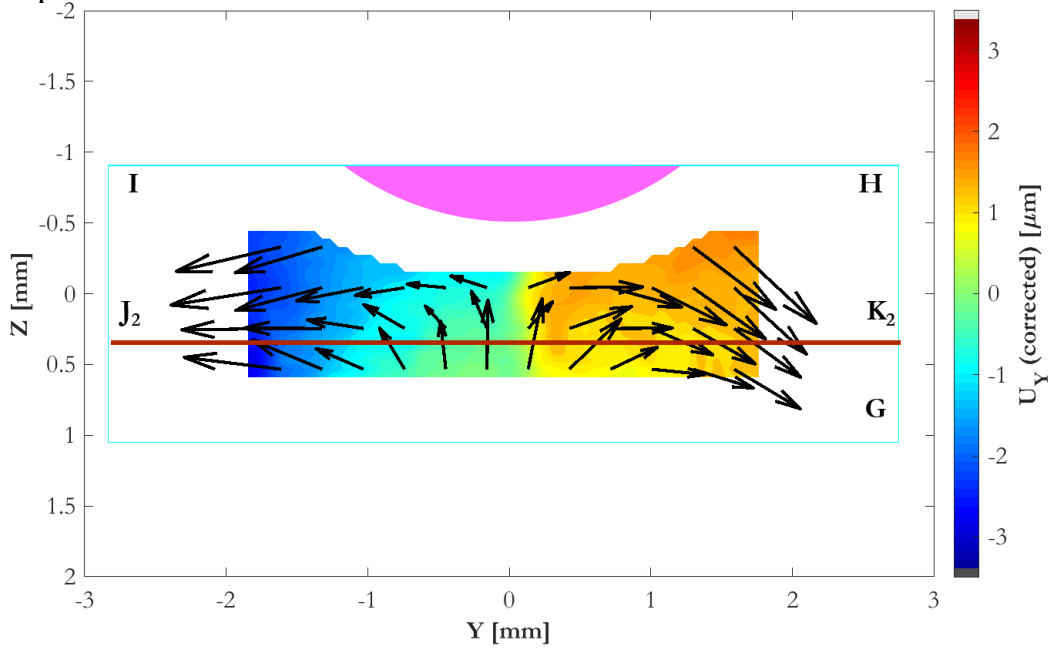


Continued: Figure 134: Deviation displacements of the KN2 specimen, progressing from (a) loaded to 50 N to (f) unloaded after the 96 N loading. Data for the unload after 50 N is not available; see § A2. Presented for the GHI plane, with extreme displacement values capped at ± 3.5 μm for clarity; vector fields indicate relative displacements compared to the largest displacement in the plane, not absolute values. The notch is indicated in pink and the profile J2K2 is shown.

g) $U_{Dev}^{KN2}(96)$ (pop-in)



h) $U_{Exp}^{KN2}(96^*)$



Continued: Figure 134: Deviation displacements of the KN2 specimen, progressing from (a) loaded to 50 N to (f) unloaded after the 96 N loading. Data for the unload after 50 N is not available; see § A2. Presented for the GHI plane, with extreme displacement values capped at ± 3.5 μm for clarity; vector fields indicate relative displacements compared to the largest displacement in the plane, not absolute values. The notch is indicated in pink and the profile J2K2 is shown.

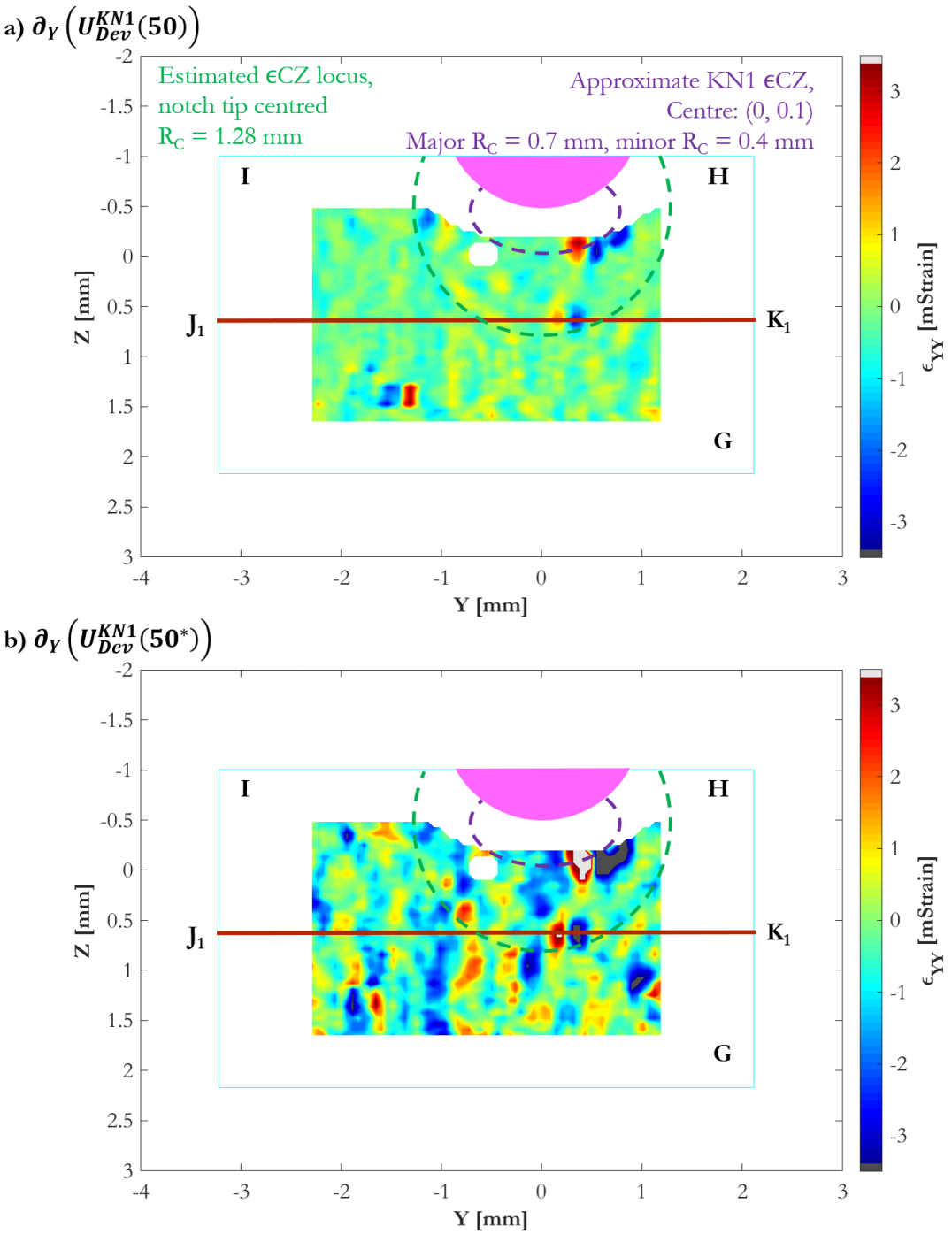
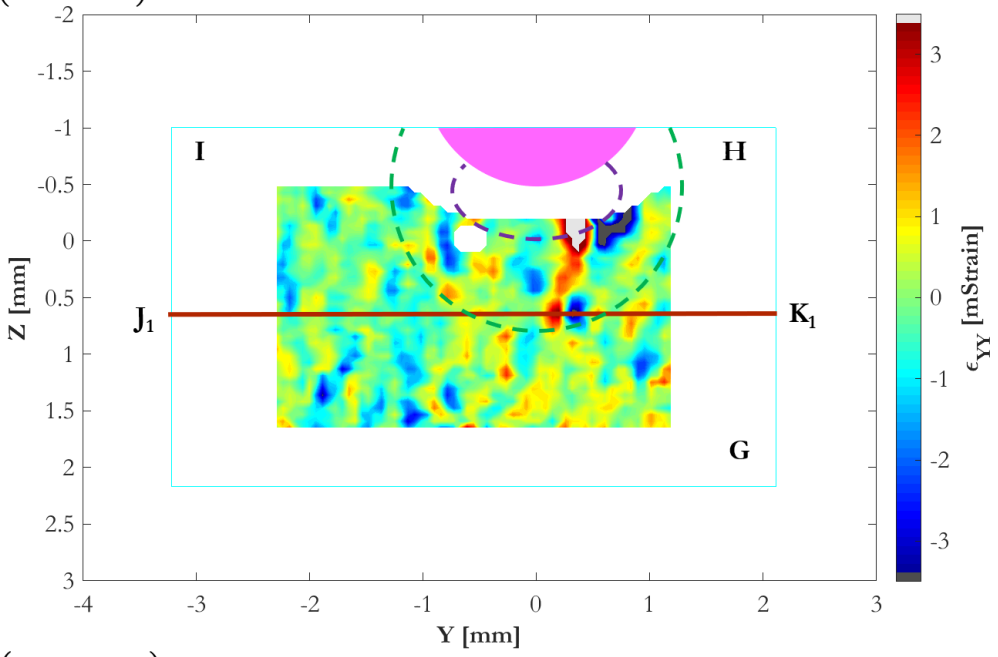
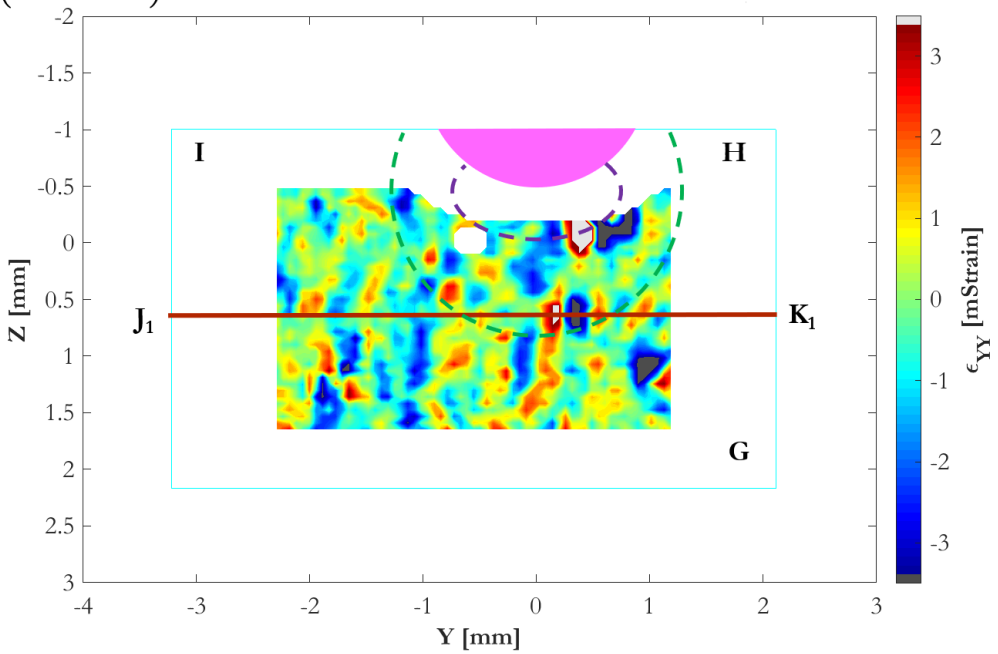


Figure 135: Deviation strains of the KN1 specimen, progressing from (a) loaded to 50 N to (f) unloaded after the 78 N loading. Presented for the GHI plane, with extreme strains values capped at ± 3.5 μm for clarity. The notch is indicated in pink, the profile J_1K_1 is shown, the approximate simulated ϵCZ locus (at 2.0 mStrain) is outlined (purple, dashed) and the postulated ϵCZ locus (green, dashed) is based on $\epsilon_{Exp}^{KN1}(50)$ for all parts; for (e) and (f) an additional locus (green, dotted) of the same radius is shown centred on the estimated crack tip.

c) $\partial_Y \left(U_{Dev}^{KN1}(75) \right)$

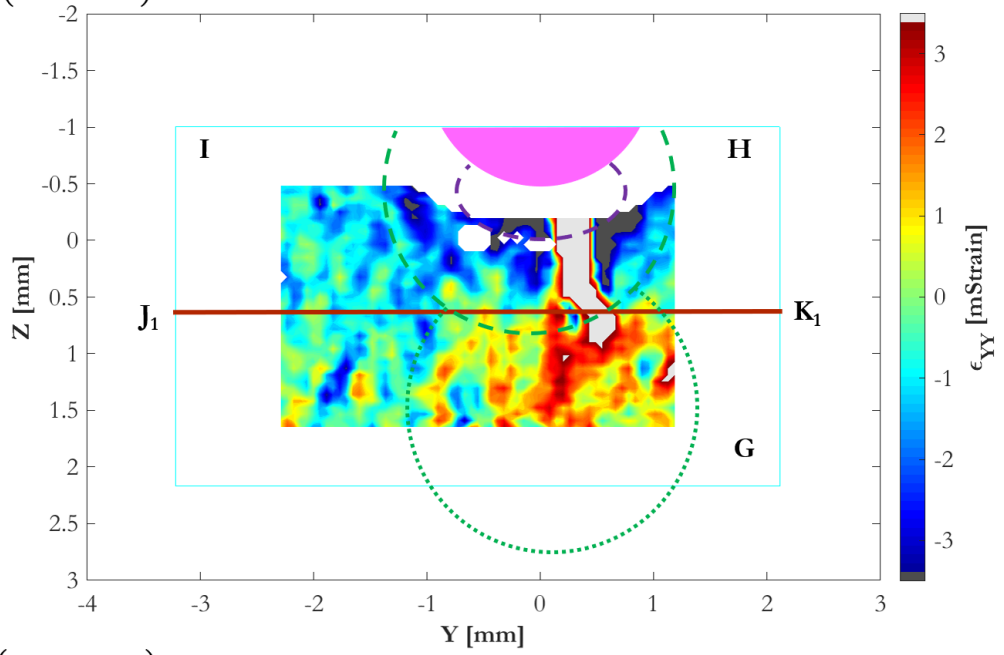


d) $\partial_Y \left(U_{Dev}^{KN1}(75^*) \right)$

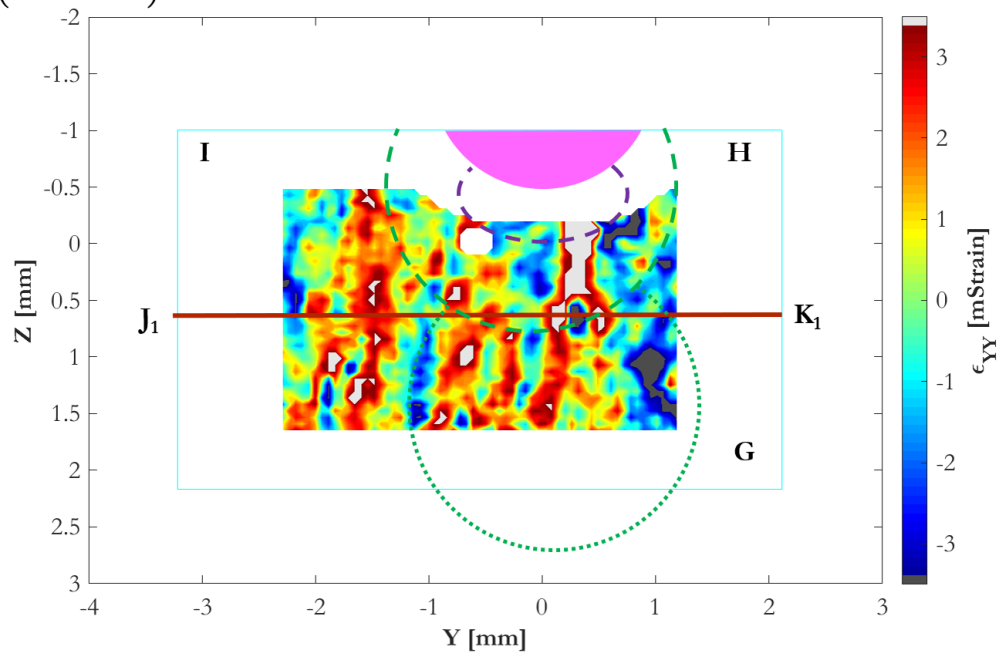


Continued: Figure 135: Deviation strains of the KN1 specimen, progressing from (a) loaded to 50 N to (f) unloaded after the 78 N loading. Presented for the GHI plane, with extreme strains values capped at ± 3.5 μm for clarity. The notch is indicated in pink, the profile J_1K_1 is shown, the approximate simulated ϵCZ locus (at 2.0 mStrain) is outlined (purple, dashed) and the postulated ϵCZ locus (green, dashed) is based on $\epsilon_{Exp}^{KN1}(50)$ for all parts; for (e) and (f) an additional locus (green, dotted) of the same radius is shown centred on the estimated crack tip.

e) $\partial_Y \left(U_{Dev}^{KN1}(78) \right)$ (pop-in)

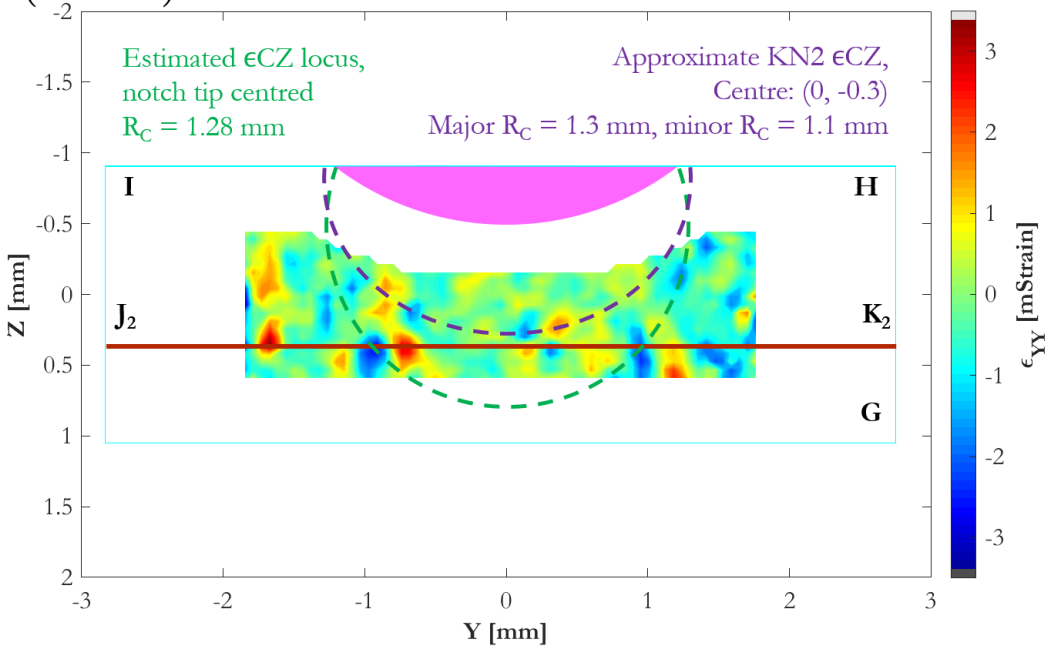


f) $\partial_Y \left(U_{Dev}^{KN1}(78^*) \right)$



Continued: Figure 135: Deviation strains of the KN1 specimen, progressing from (a) loaded to 50 N to (f) unloaded after the 78 N loading. Presented for the GHI plane, with extreme strains values capped at ± 3.5 μm for clarity. The notch is indicated in pink, the profile J_1K_1 is shown, the approximate simulated ϵCZ locus (at 2.0 mStrain) is outlined (purple, dashed) and the postulated ϵCZ locus (green, dashed) is based on $\epsilon_{Exp}^{KN1}(50)$ for all parts; for (e) and (f) an additional locus (green, dotted) of the same radius is shown centred on the estimated crack tip.

a) $\partial_Y \left(U_{Dev}^{KN2}(50) \right)$



b) $\partial_Y \left(U_{Dev}^{KN2}(50^*) \right)$

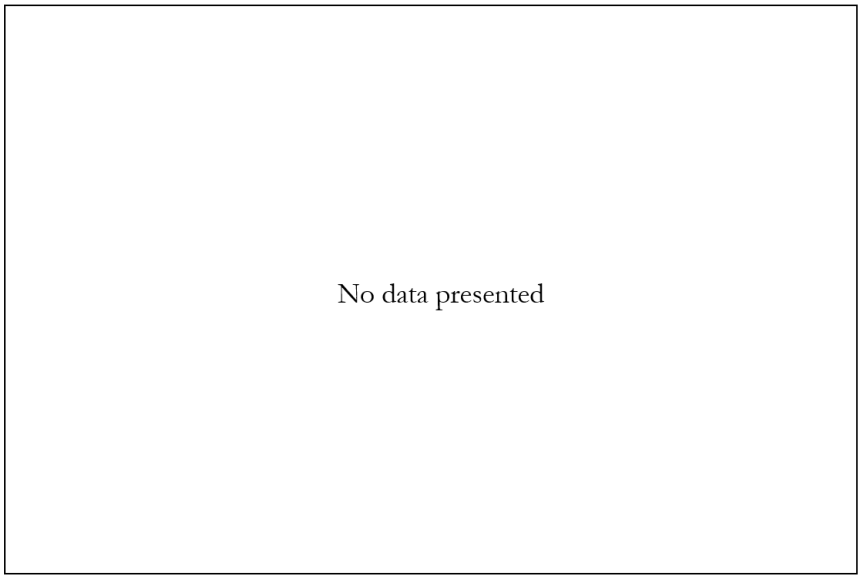
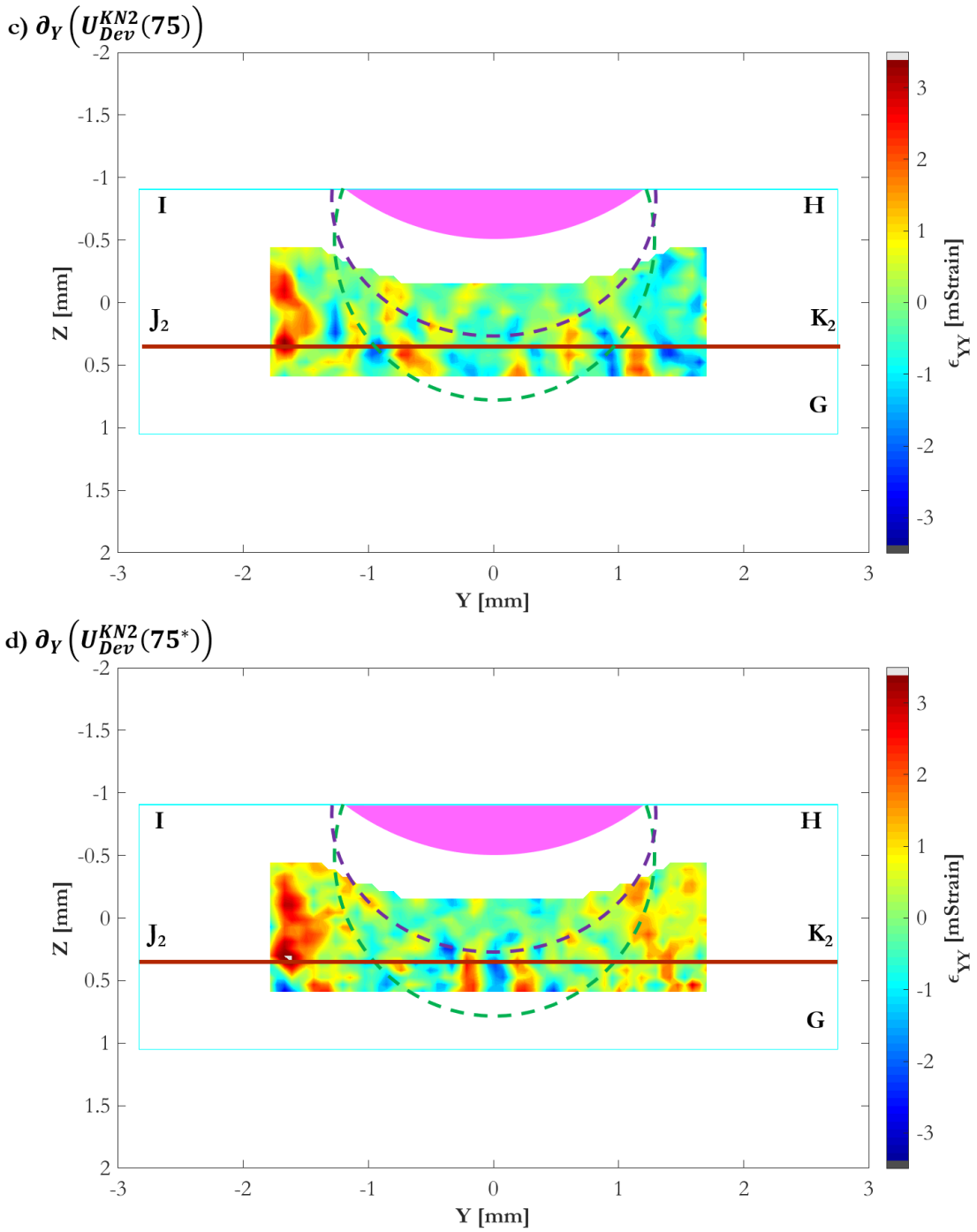
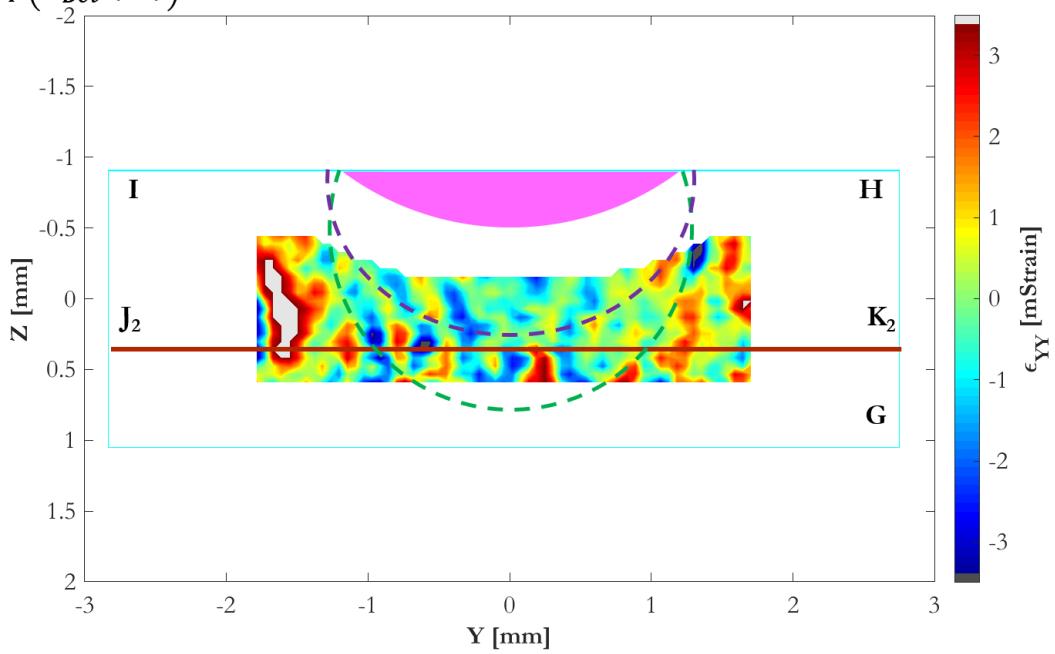


Figure 136: Deviation strains of the KN2 specimen, progressing from (a) loaded to 50 N to (f) unloaded after the 96 N loading. Data for the unload after 50 N is not available; see § A2. Presented for the GHI plane, with extreme strains values capped at ± 3.5 μm for clarity. The notch is indicated in pink, the profile J_2K_2 is shown, the approximate simulated ϵCZ locus (at 2.0 mStrain) is outlined (purple, dashed) and the postulated ϵCZ locus (green, dashed) is based on $\epsilon_{Exp}^{KN1}(50)$ for all parts.

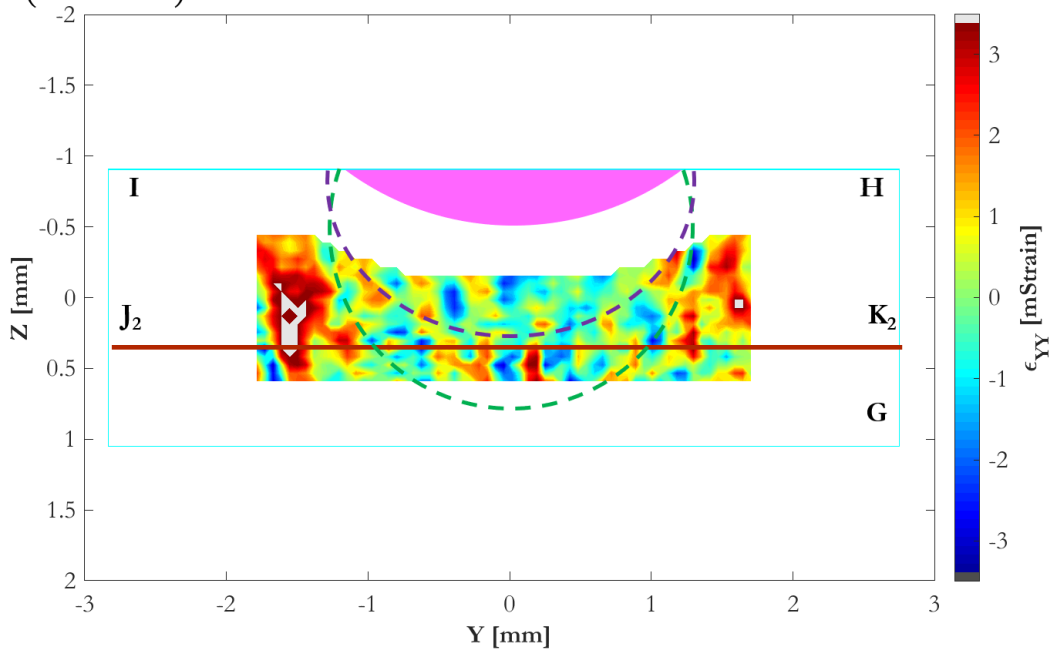


Continued: Figure 136: Deviation strains of the KN2 specimen, progressing from (a) loaded to 50 N to (f) unloaded after the 96 N loading. Data for the unload after 50 N is not available; see § A2. Presented for the GHI plane, with extreme strains values capped at ± 3.5 μm for clarity. The notch is indicated in pink, the profile J_2K_2 is shown, the approximate simulated ϵCZ locus (at 2.0 mStrain) is outlined (purple, dashed) and the postulated ϵCZ locus (green, dashed) is based on $\epsilon_{Exp}^{KN1}(50)$ for all parts.

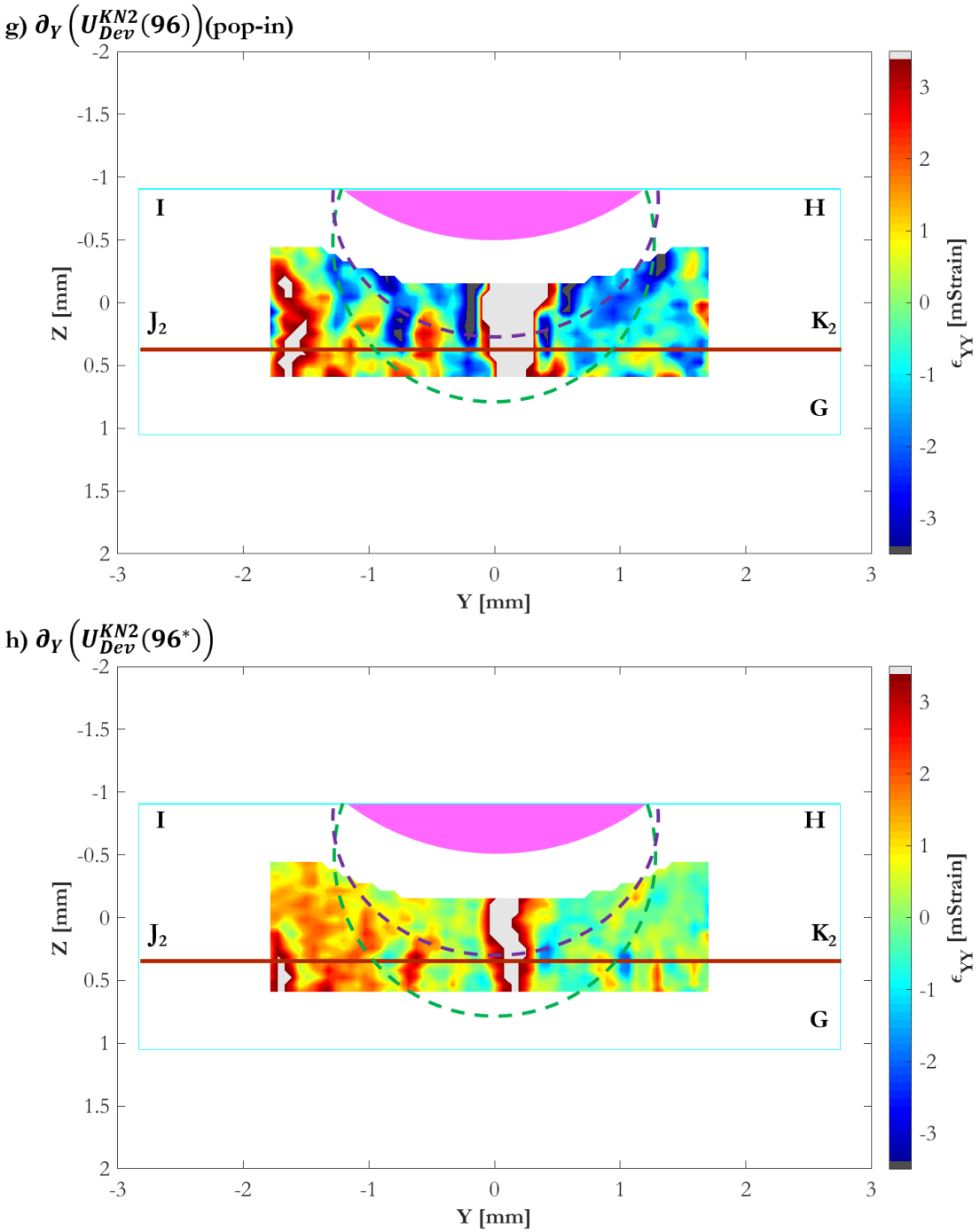
e) $\partial_Y \left(U_{Dev}^{KN2}(85) \right)$



f) $\partial_Y \left(U_{Dev}^{KN2}(85^*) \right)$

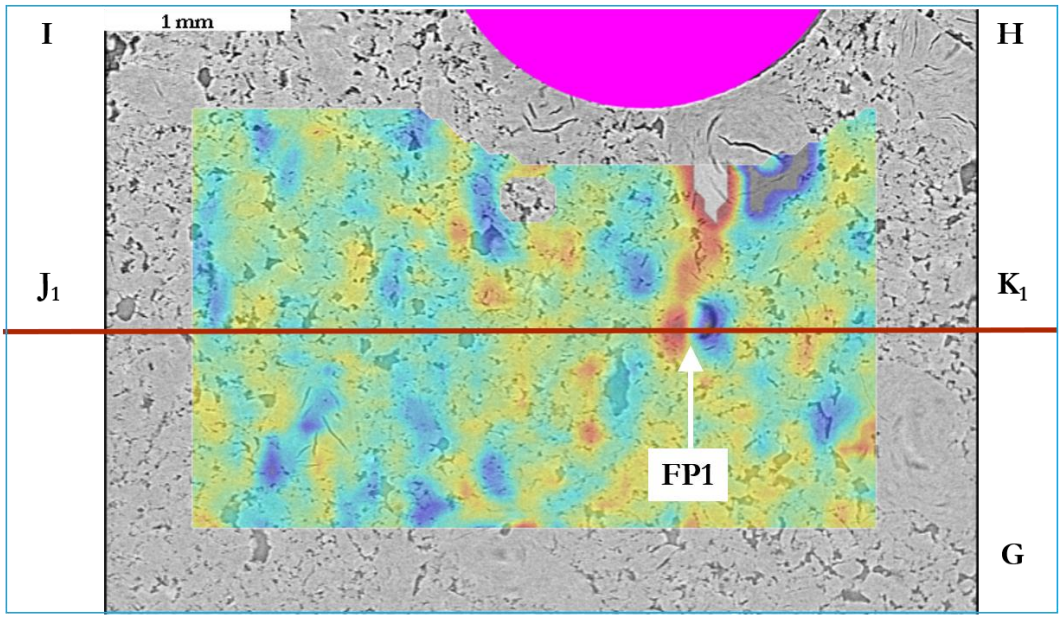


Continued: Figure 136: Deviation strains of the KN2 specimen, progressing from (a) loaded to 50 N to (f) unloaded after the 96 N loading. Data for the unload after 50 N is not available; see § A2. Presented for the GHI plane, with extreme strains values capped at ± 3.5 μm for clarity. The notch is indicated in pink, the profile J_2K_2 is shown, the approximate simulated ϵCZ locus (at 2.0 mStrain) is outlined (purple, dashed) and the postulated ϵCZ locus (green, dashed) is based on $\epsilon_{Exp}^{KN1}(50)$ for all parts.



Continued: Figure 136: Deviation strains of the KN2 specimen, progressing from (a) loaded to 50 N to (f) unloaded after the 96 N loading. Data for the unload after 50 N is not available; see § A2. Presented for the GHI plane, with extreme strains values capped at ± 3.5 μm for clarity. The notch is indicated in pink, the profile J_2K_2 is shown, the approximate simulated ϵCZ locus (at 2.0 mStrain) is outlined (purple, dashed) and the postulated ϵCZ locus (green, dashed) is based on $\epsilon_{Exp}^{KN1}(50)$ for all parts.

a) $\partial_Y \left(U_{Dev}^{KN1}(75) \right)$



b) $\partial_Y \left(U_{Dev}^{KN1}(78) \right)$ (pop-in)

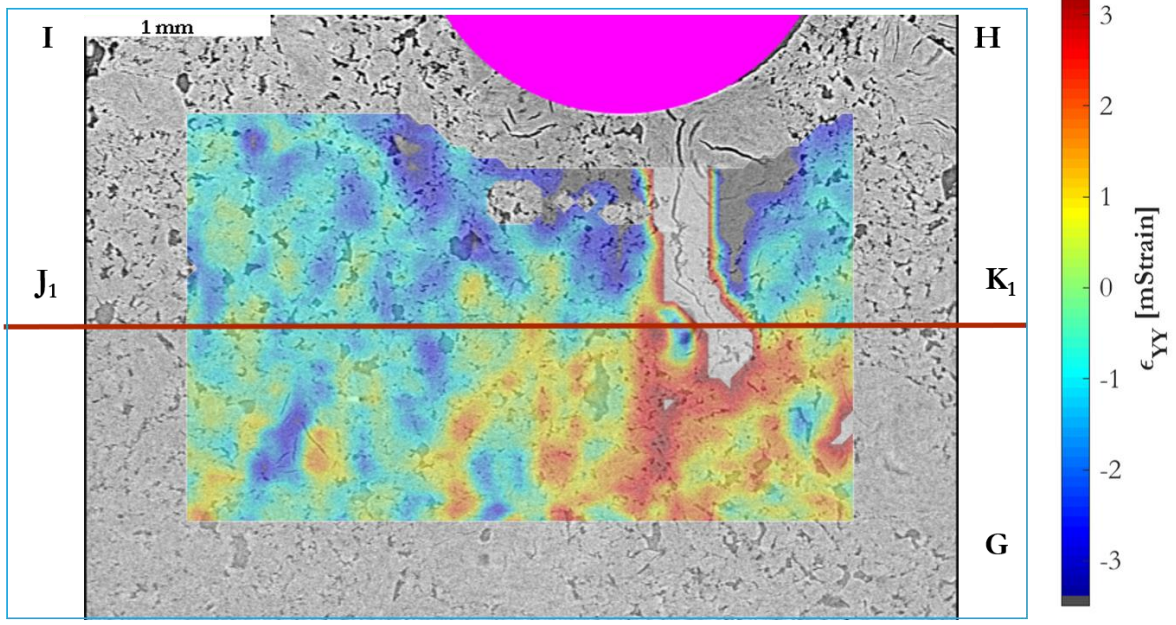


Figure 137: Deviation strains for the KN1 specimen superimposed on the microstructure for the loading states before and after full width cracking: (a) 75 N and (b) 78 N. Presented for the GHI plane, with extreme deviation strain values capped at ± 3.5 µm for clarity. The notch is indicated in pink, the profile J_1K_1 is shown, and filler particle (FP1) on the profile is highlighted. The fractured microstructure was presented in Figure 108(a).

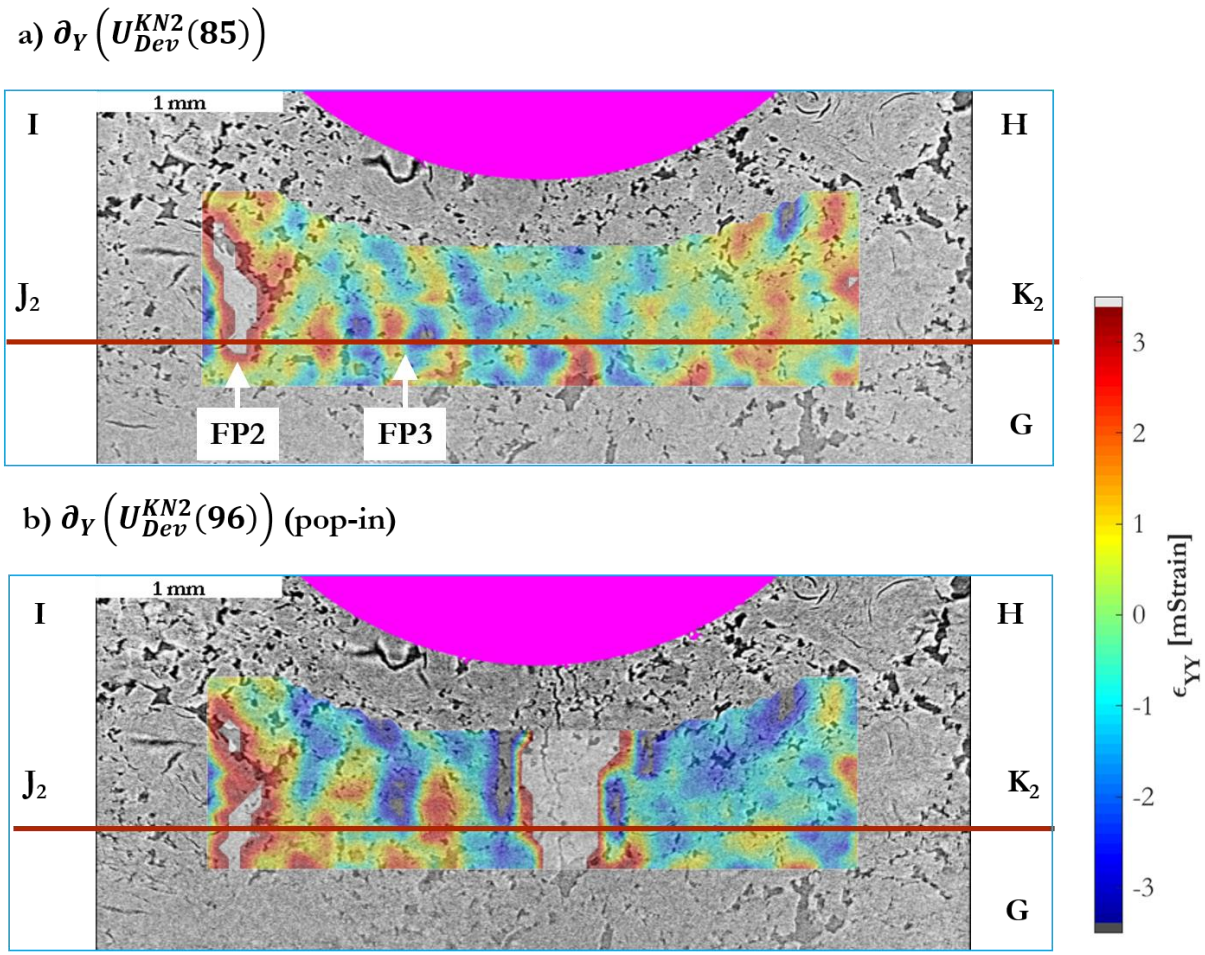


Figure 138: Deviation strains for the KN2 specimen superimposed on the microstructure for the loading states before and after full width cracking: (a) 85 N and (b) 96 N. Presented for the GHI plane, with extreme deviation strain values capped at ± 3.5 µm for clarity. The notch is indicated in pink, the profile J_2K_2 is shown, and filler particles (FP2 and FP3) on the profile are highlighted. The fractured microstructure was presented in Figure 108(b).

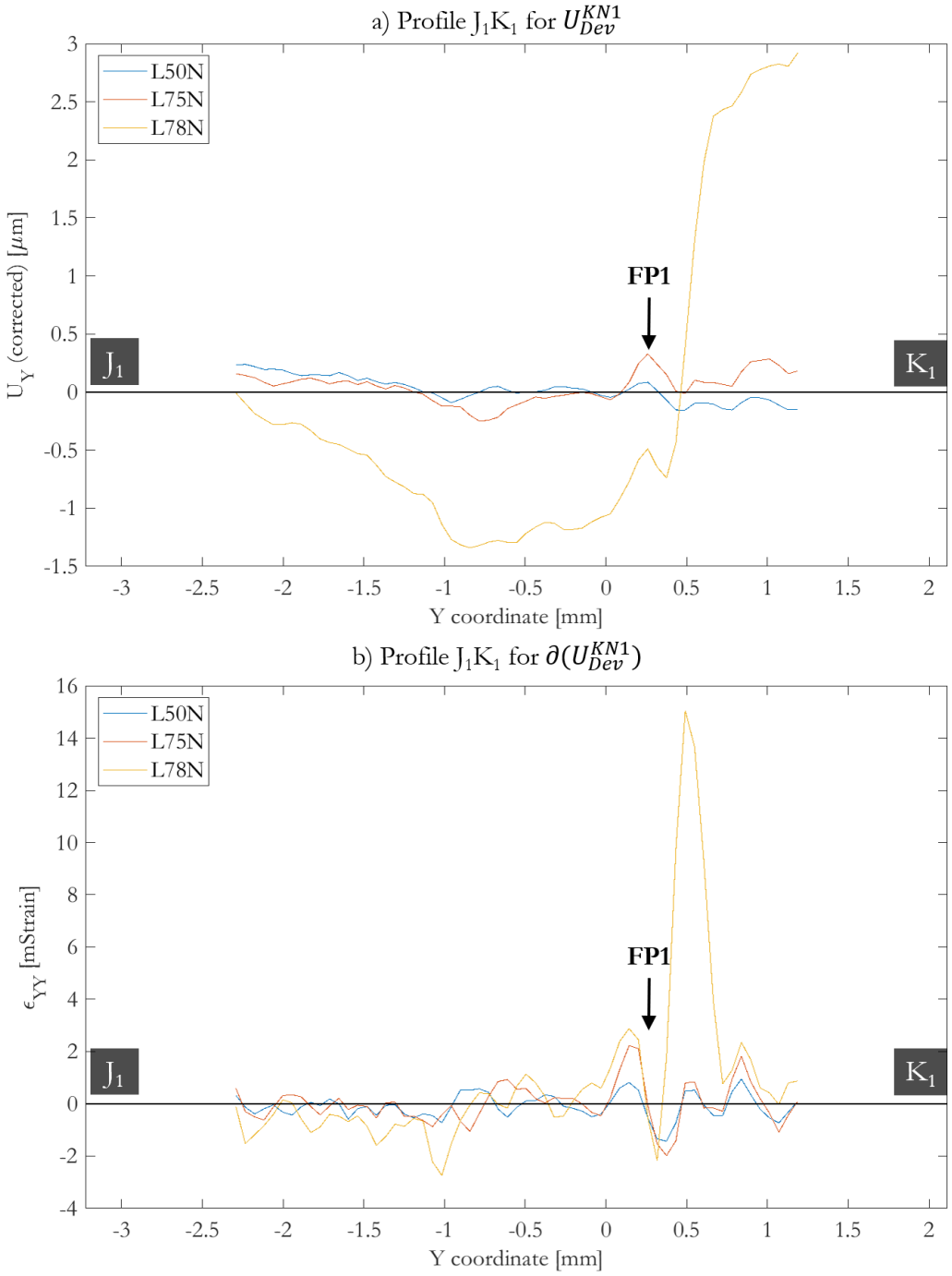


Figure 139: Variation in deviation Mode I (a) displacement and (b) strain, for the KN1 specimen in the loaded states along profile J_1K_1. The location of filler particle FP1 is highlighted.

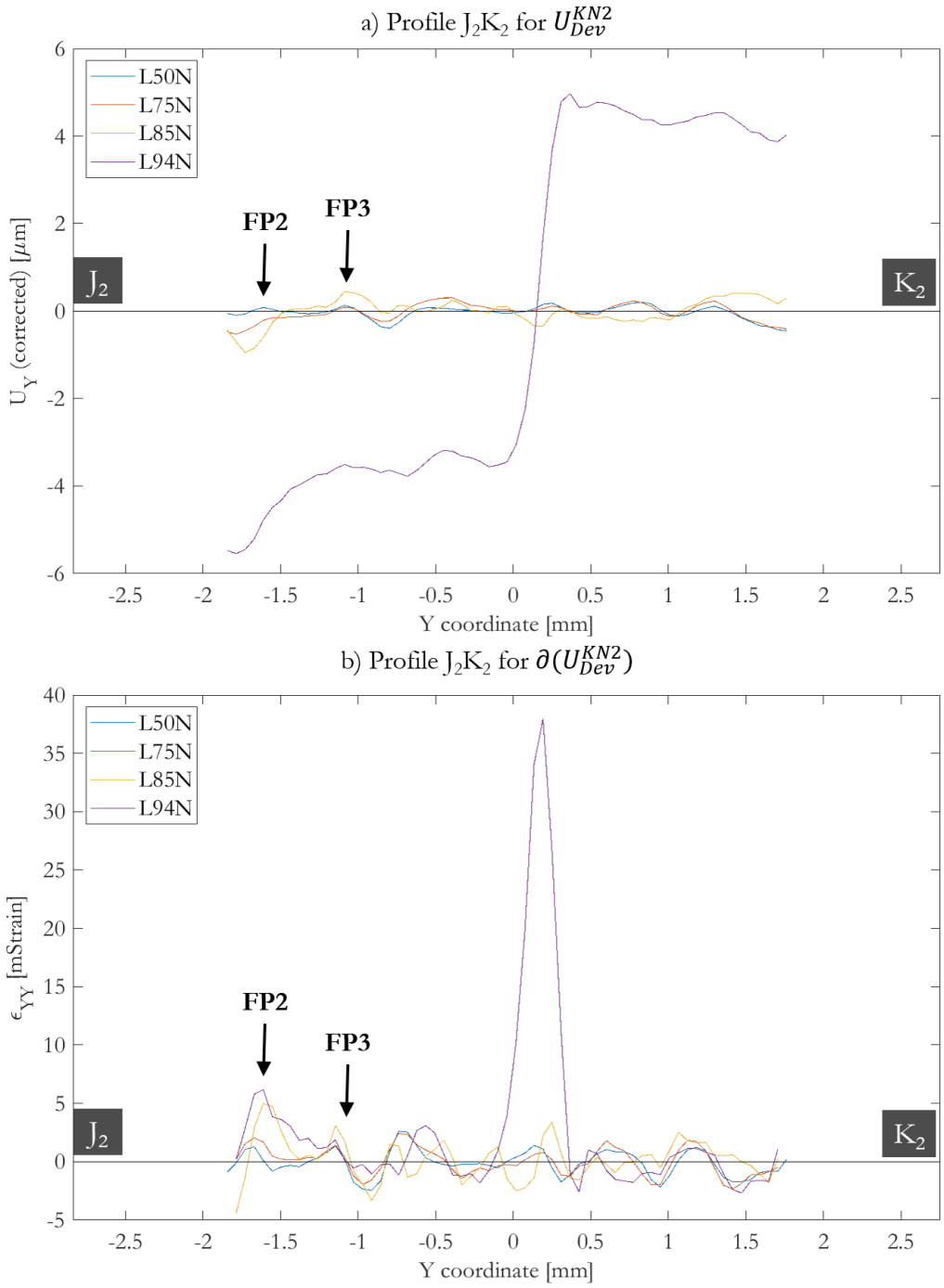


Figure 140: Variation in deviation Mode I (a) displacement and (b) strain, for the KN2 specimen in the loaded states along profile J_2K_2. The location of filler particles FP2 and FP3 are highlighted.

IV.3.4.3 Evolution of deviation hotspots

In § IV.3.3.2 the presence of vectors with notably large displacements and strains magnitudes were identified. Having removed the continuum behaviour, the deviation fields were high-pass filtered to isolate the regions of statistically excessive deformation. Deviation vectors with magnitudes greater than four standard deviations of the experimental uncertainty, (equivalent to the 99.99%ile for a normal distribution), that is $\frac{4}{1.96}\xi_{Corr,DVC}$ = 1.32 µm, were defined as 'hotspots vectors' that belonged to $H^{KNi}(F)$, by (29). The $\partial\left(H^{KNi}(F)\right)$ field was high-pass filtered separately by (30) to isolate differential hotspots, removing vector points where the equivalent of the triaxial maximum principal strain, ϵ_1, was below the four-sigma RBD apparent strain, at $\frac{4}{1.96}\xi_{\epsilon,Corr,DVC}$ = 4.00 mStrain. The H and corresponding ∂H fields for the KN1 and KN2 loading sequences are shown in 3D in Figure 141-Figure 144; the $U_{Sim}(F)$ or $\epsilon_{Sim}(F)$ fields are shown inset for reference. The volume fractions of hotspot vectors within the tomograph regions, f_{Hot}, for both the displacements and strains, at every load state is shown in Figure 145 and Figure 146.

$$\vec{H} = \vec{U}_{Dev}.b \text{ where } b = \begin{cases} 1 \text{ if } \|\vec{U}_{Dev}\| > \frac{4}{1.96}\xi_{U,Corr,DVC} \\ 0 \text{ otherwise} \end{cases} \quad (29)$$

$$\partial(\vec{H}) = \partial(\vec{U}_{Dev}).b \text{ where } b = \begin{cases} 1 \text{ if } |\epsilon_1| > \frac{4}{1.96}\xi_{\epsilon 1,Corr,DVC} \\ 0 \text{ otherwise} \end{cases} \quad (30)$$

The hotspots, particularly in the displacement maps, were clearly identified as clusters of voxels. Until fracture, for both the loaded and unloaded states, the smaller regions were approximately ellipsoidal and disconnected, while the larger regions had more irregular forms. Qualitatively, the regions appear to grow with successive load-unload cycles; this behaviour will be quantified in § IV.3.4.4. The locations and shapes of the hotspot vectors in the loaded states were consistent between successive loads. Similarly, the unloaded states had consistent hotspots, but the locations did not necessarily coincide between the loaded and unloaded states.

From the bar charts, for the early load states in both specimens, displacement hotspots exist at low loads, but $f_{Hot} < 10$ %. f_{Hot} for the KN1 displacements remains low until fracture. In the KN2 specimen there is an increase in the penultimate loaded state (85 N). Once fracture occurs a significant volume of the specimen is deviated, as expected. Considering the unloaded states, f_{Hot} tended to follow the volume fraction at load, consistently increasing slightly for KN1, but decreasing slightly for KN2. From the deviation strains, a more consistent and steady increase was observed with increasing load, with a larger fraction at unload than the previous load for both specimens.

To directly compare the specimens, the hotspot strains within a cuboid region defined by the coordinates [(-2, -1, -0.6), (2, 1, 0.2)] were measured. This volume focused on the material within the proposed ϵCZ region, as shown in Figure 147(a). The measured f_{Hot} were plotted as a function of fractional load relative to the maximum load in Figure 147(b). The evolution of f_{Hot} for the loaded states was seen to be similar for the two specimens rising as an upward curve from $f_{Hot} \approx 15$ % to 70 % over the relative loads of 0.6 to 1. The unload fractions are also indicated on the figure, with each specimen showing a self-consistent trend between the load and subsequent unload comparable to the full volume trends; KN1 rising to a fraction similar to the next loaded state, but KN2 staying at the same f_{Hot}.

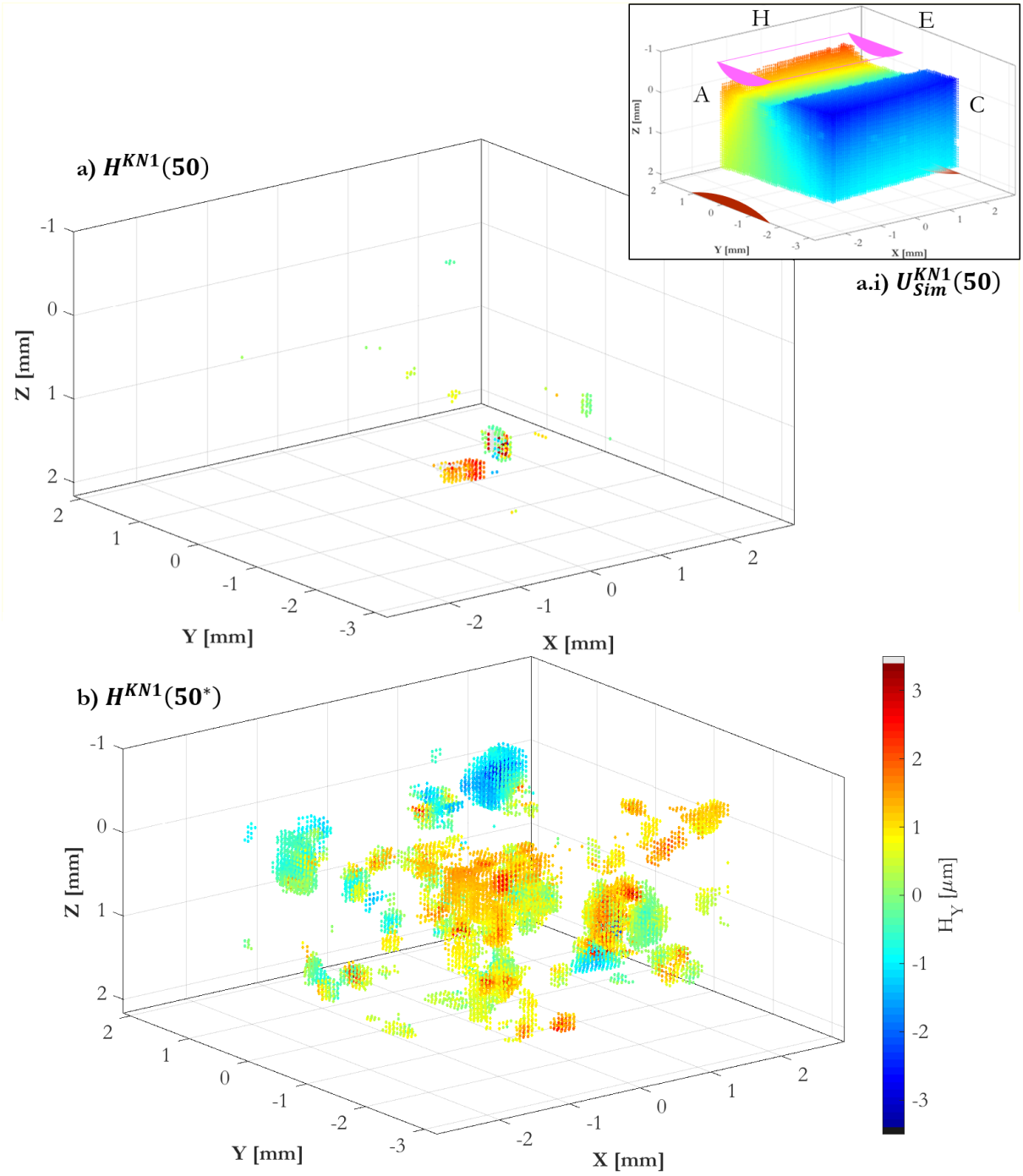
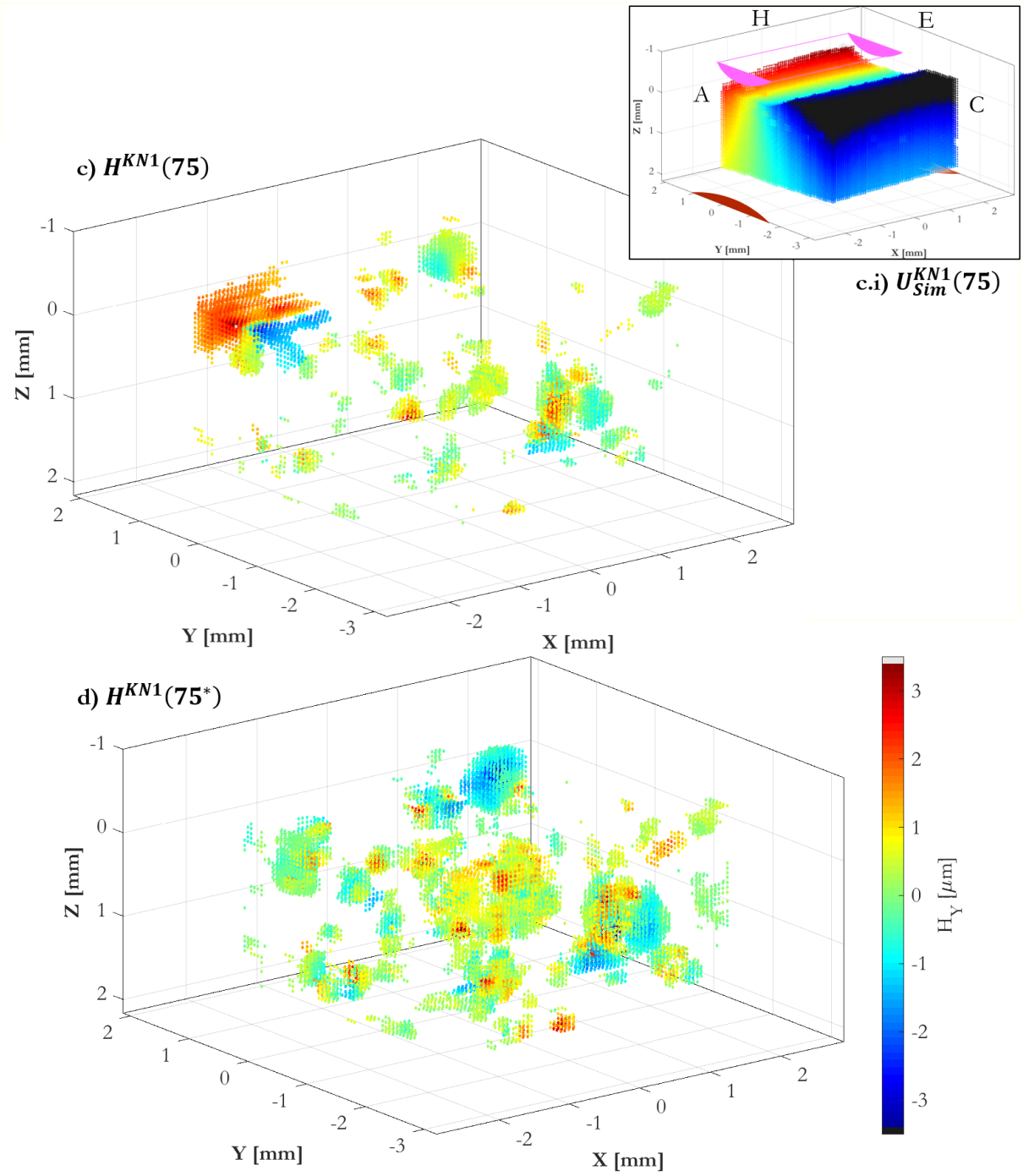
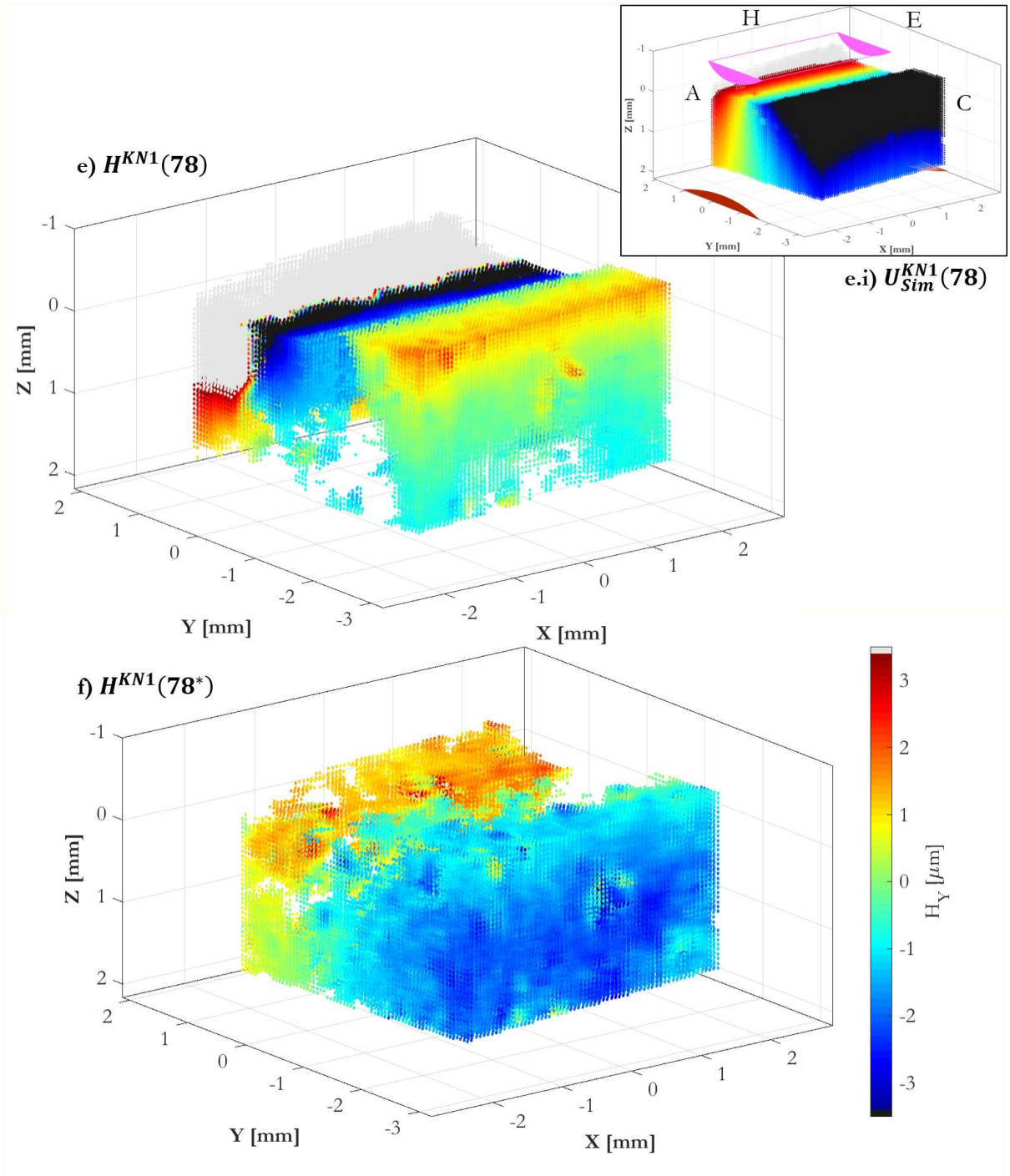


Figure 141: 3D deviation displacement hotspot map of the KN1 specimen, progressing from (a) loaded to 50 N to (f) unloaded after the 78 N loading. The 3D simulated displacements for the loaded states are presented in the insets, using the same colour scale and orientation; extreme displacement values are capped at ± 3.5 µm for clarity. On the insets, the notch is indicated in pink, and the vertical side grooves in brown.



Continued: Figure 141: 3D deviation displacement hotspot map of the KN1 specimen, progressing from (a) loaded to 50 N to (f) unloaded after the 78 N loading. The 3D simulated displacements for the loaded states are presented in the insets, using the same colour scale and orientation; extreme displacement values are capped at ± 3.5 μm for clarity. On the insets, the notch is indicated in pink, and the vertical side grooves in brown.



Continued: Figure 141: 3D deviation displacement hotspot map of the KN1 specimen, progressing from (a) loaded to 50 N to (f) unloaded after the 78 N loading. The 3D simulated displacements for the loaded states are presented in the insets, using the same colour scale and orientation; extreme displacement values are capped at ± 3.5 µm for clarity. On the insets, the notch is indicated in pink, and the vertical side grooves in brown.

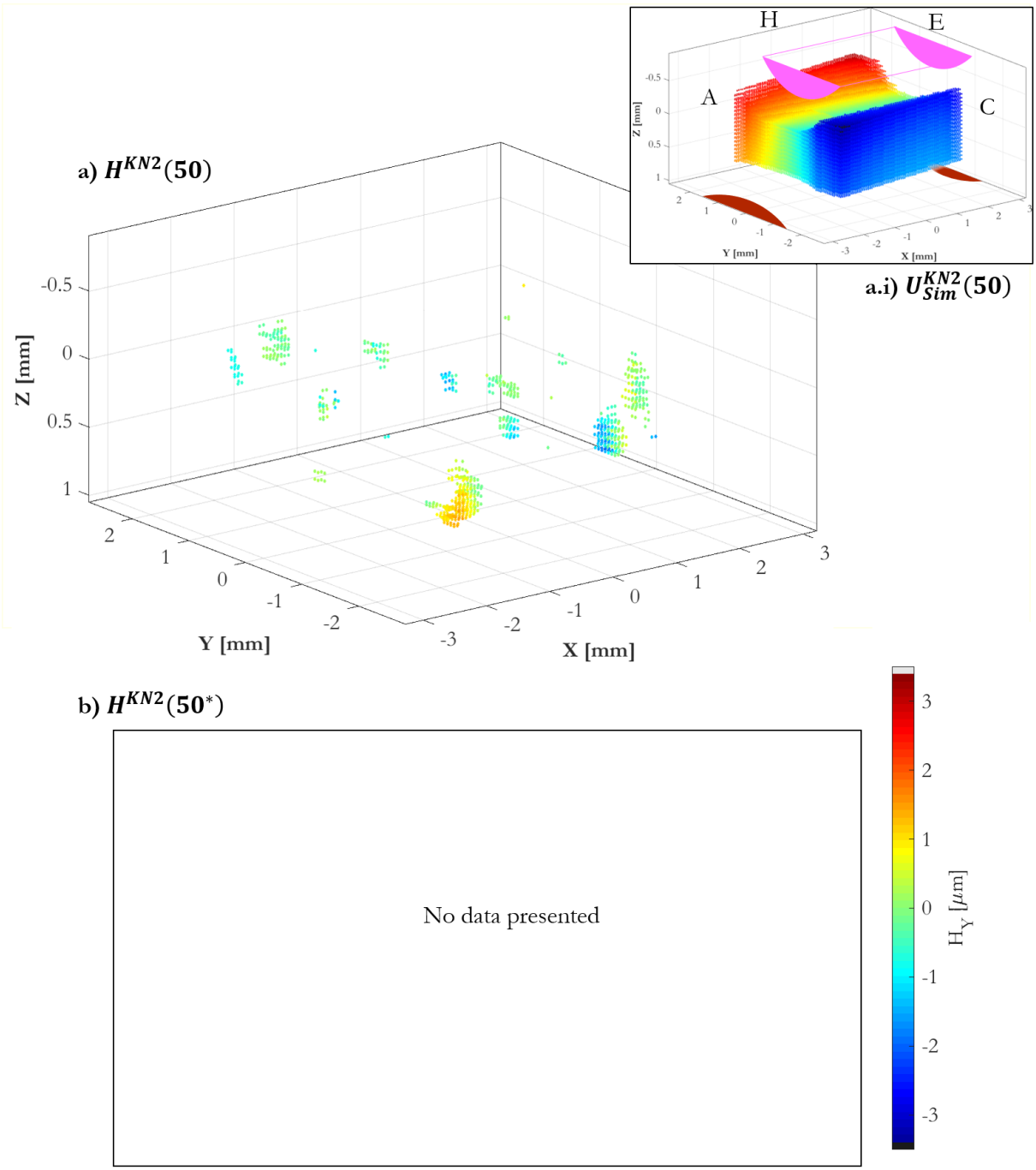
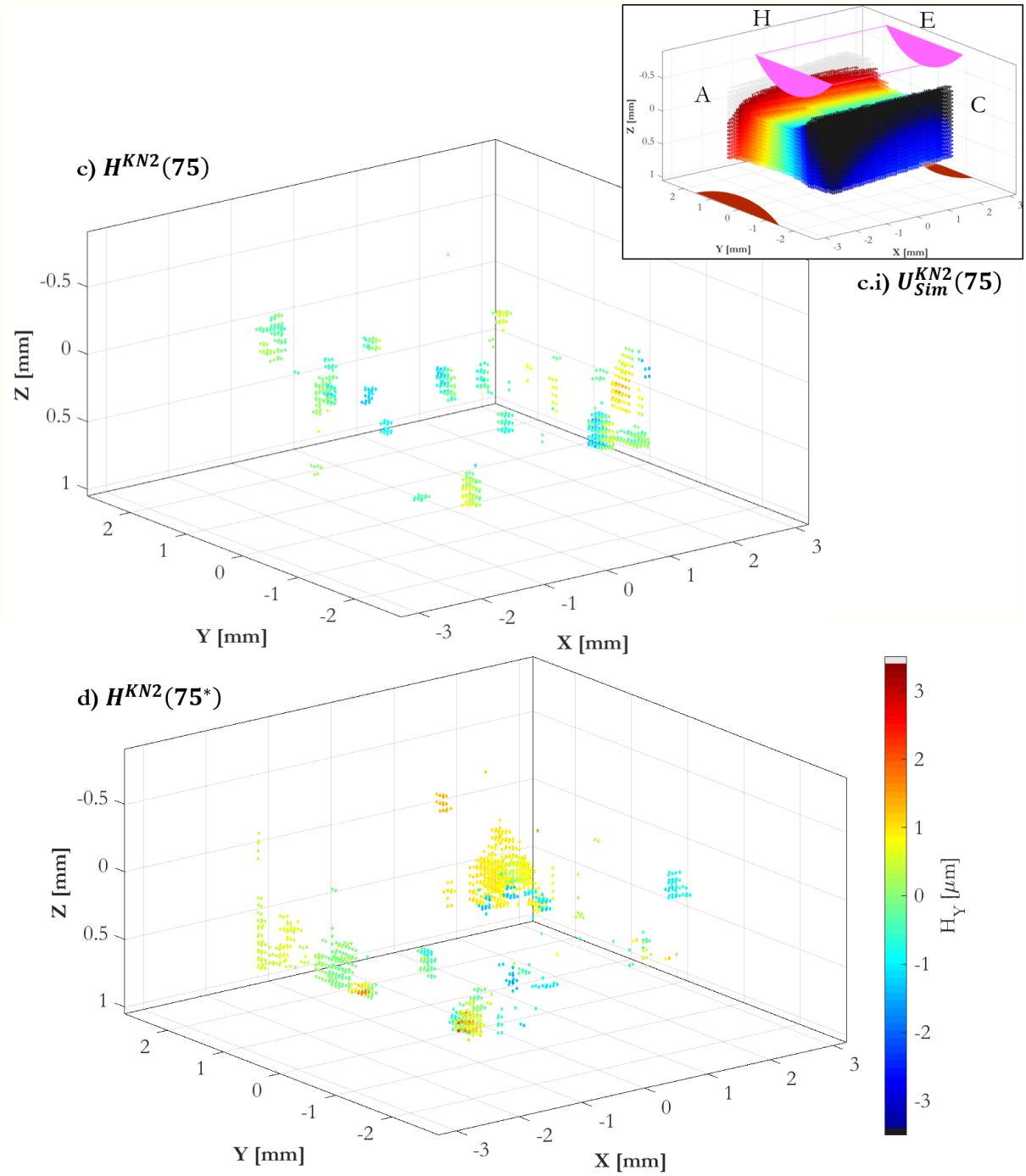
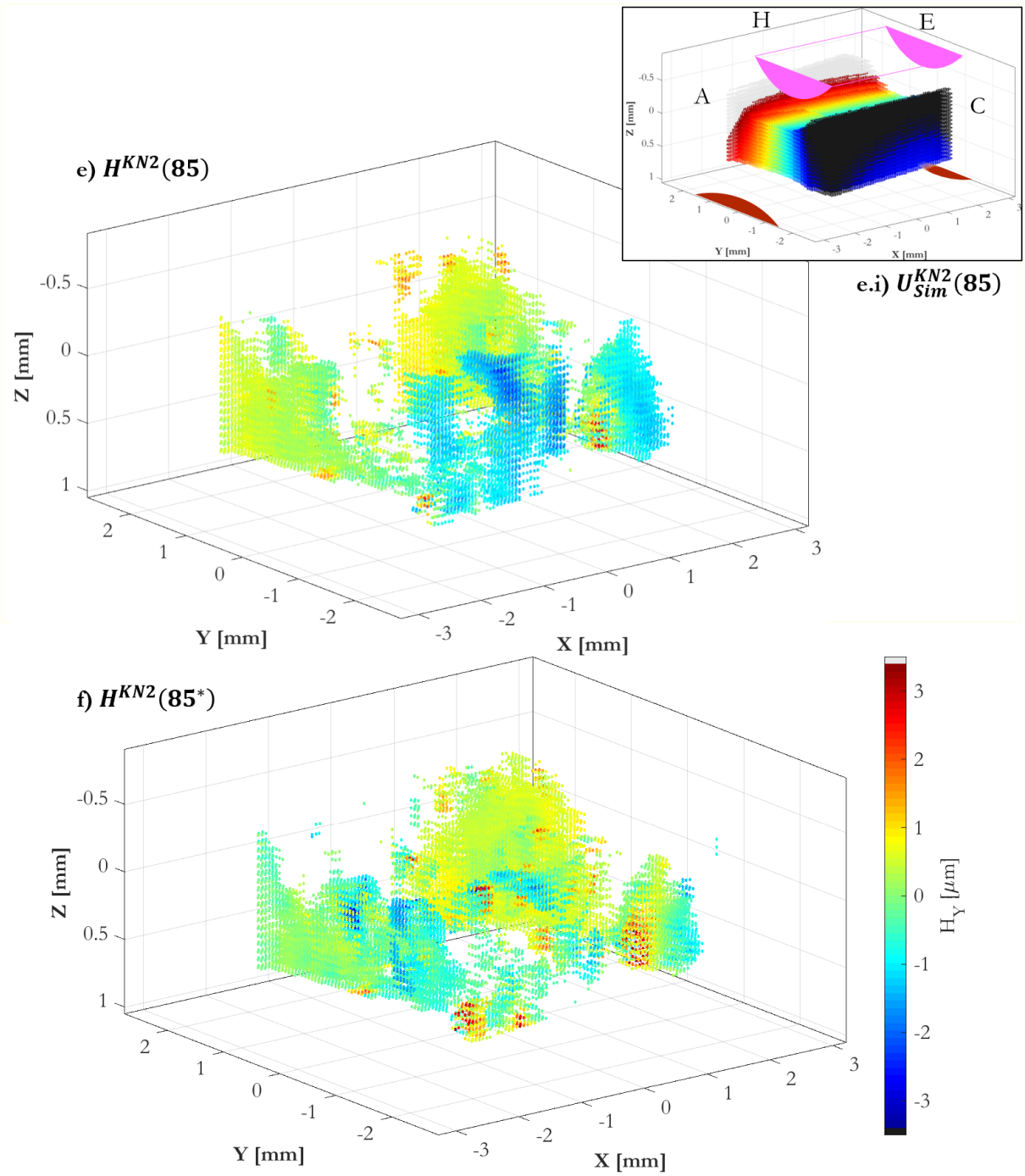


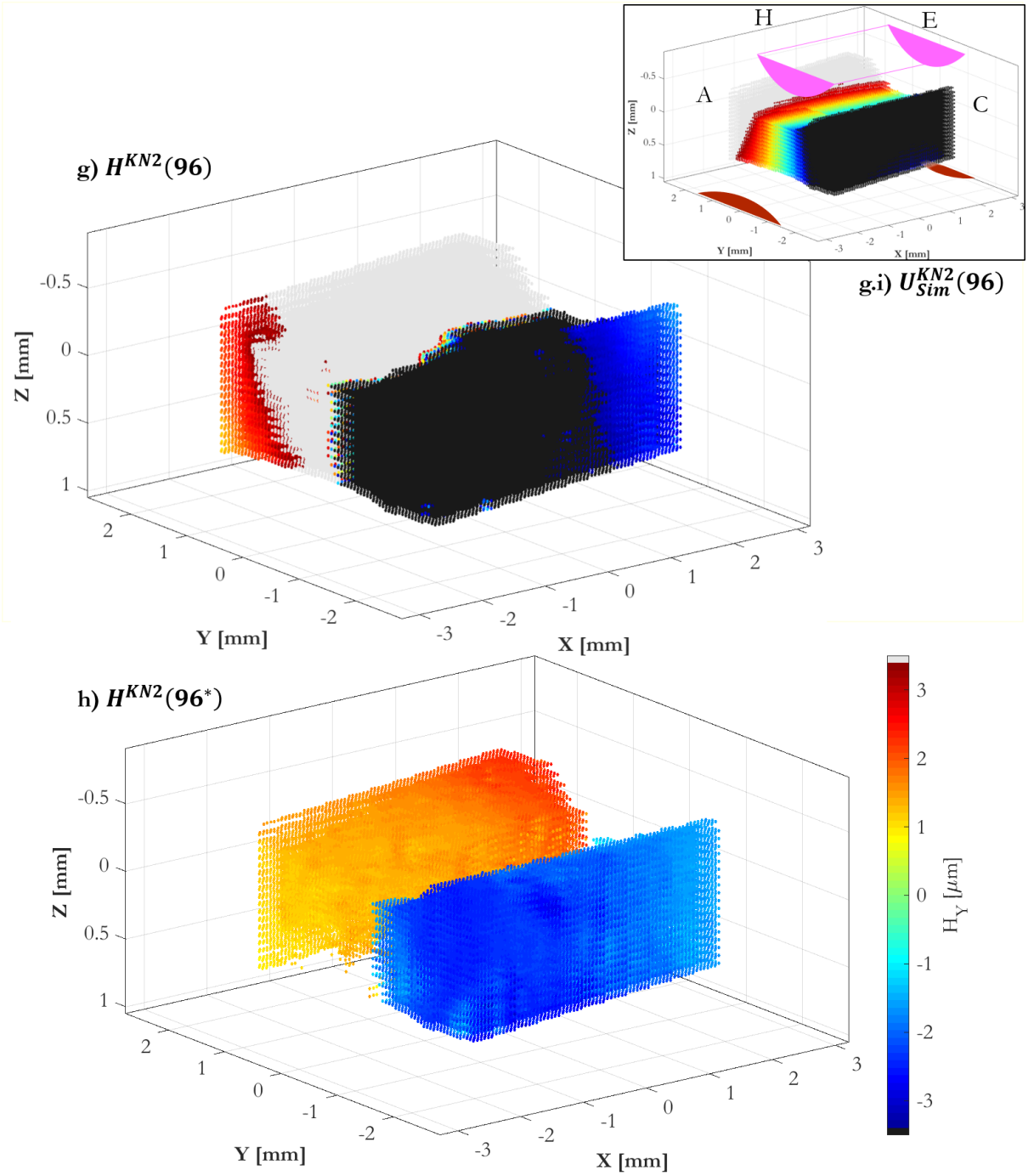
Figure 142: 3D deviation displacement hotspot map of the KN2 specimen, progressing from (a) loaded to 50 N to (b) unloaded after the 96 N loading. Data for the unload after 50 N is not available; see § A2. The 3D simulated displacements for the loaded states are presented in the insets, using the same colour scale and orientation; extreme displacement values are capped at ± 3.5 μm for clarity. On the insets, the notch is indicated in pink, and the vertical side grooves in brown.



Continued: Figure 142: 3D deviation displacement hotspot map of the KN2 specimen, progressing from (a) loaded to 50 N to (h) unloaded after the 96 N loading. Data for the unload after 50 N is not available; see § A2. The 3D simulated displacements for the loaded states are presented in the insets, using the same colour scale and orientation; extreme displacement values are capped at ± 3.5 µm for clarity. On the insets, the notch is indicated in pink, and the vertical side grooves in brown.



Continued: Figure 142: 3D deviation displacement hotspot map of the KN2 specimen, progressing from (a) loaded to 50 N to (h) unloaded after the 96 N loading. Data for the unload after 50 N is not available; see § A2. The 3D simulated displacements for the loaded states are presented in the insets, using the same colour scale and orientation; extreme displacement values are capped at ± 3.5 µm for clarity. On the insets, the notch is indicated in pink, and the vertical side grooves in brown.



Continued: Figure 142: 3D deviation displacement hotspot map of the KN2 specimen, progressing from (a) loaded to 50 N to (h) unloaded after the 96 N loading. Data for the unload after 50 N is not available; see § A2. The 3D simulated displacements for the loaded states are presented in the insets, using the same colour scale and orientation; extreme displacement values are capped at ± 3.5 µm for clarity. On the insets, the notch is indicated in pink, and the vertical side grooves in brown.

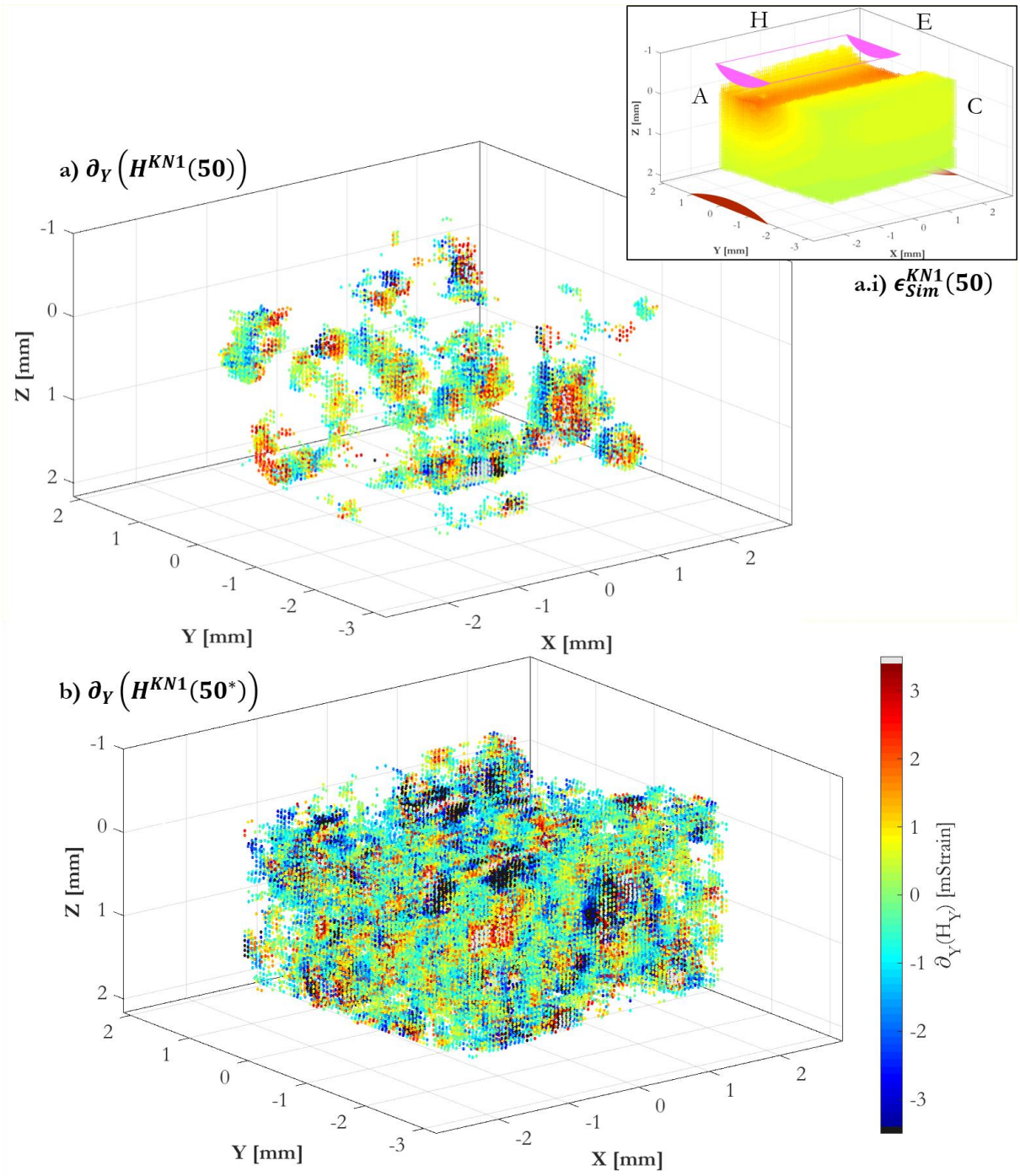
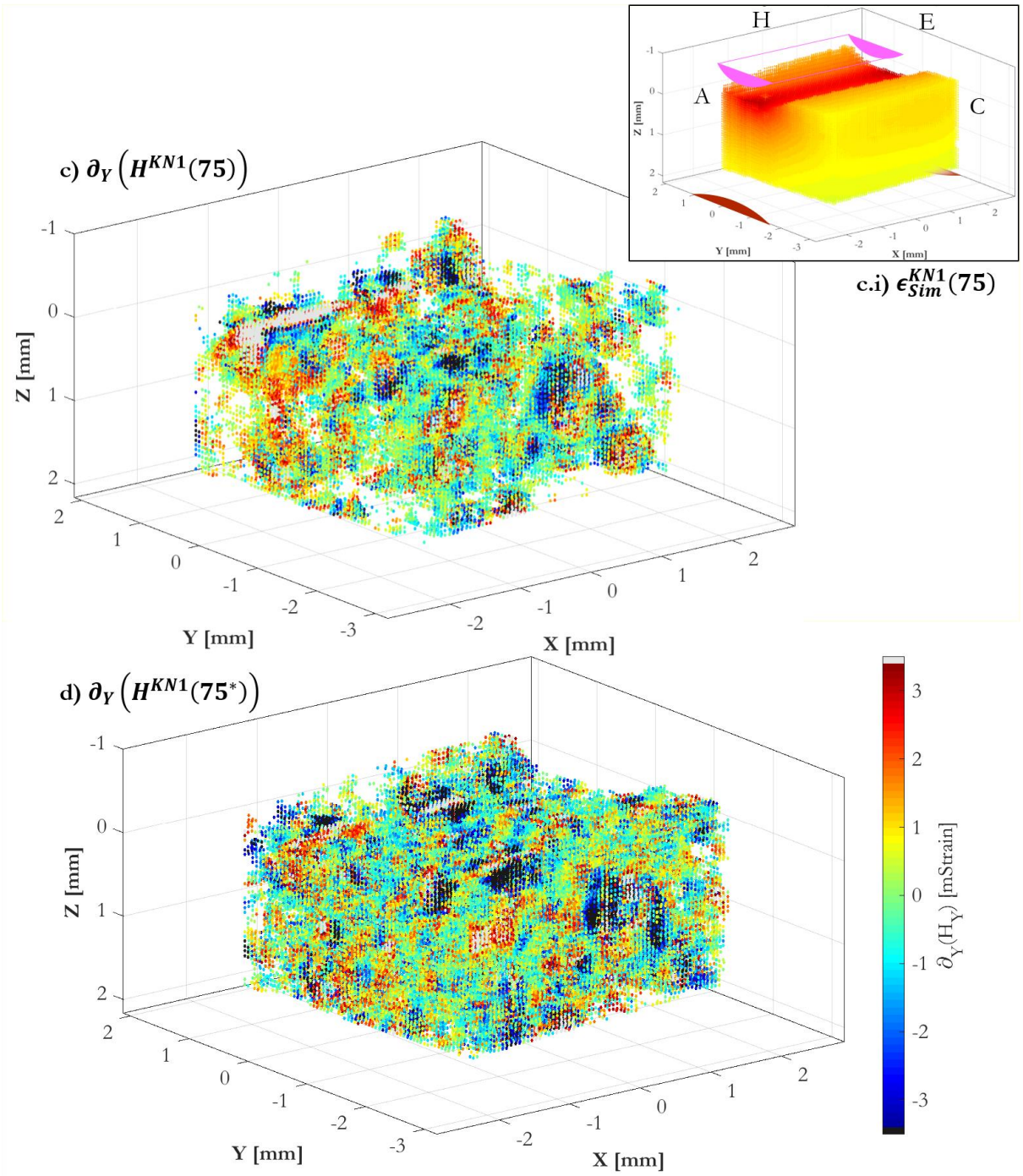
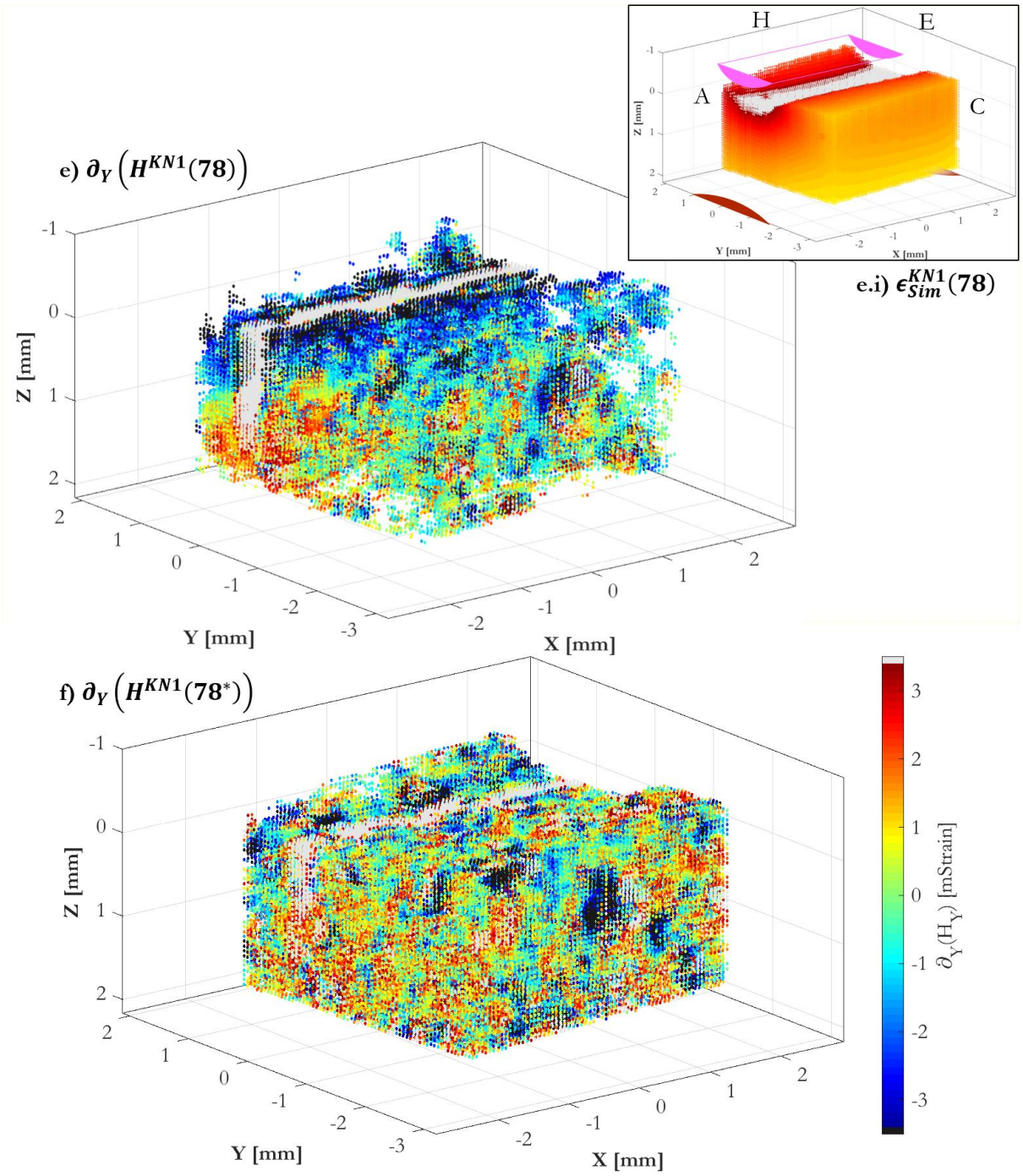


Figure 143: 3D deviation strain hotspot map of the KN1 specimen, progressing from (a) loaded to 50 N to (f) unloaded after the 78 N loading. The 3D simulated strains for the loaded states are presented in the insets, using the same colour scale and orientation; extreme displacement values are capped at ± 3.5 μm for clarity. On the insets, the notch is indicated in pink, and the vertical side grooves in brown.



Continued: Figure 143: 3D deviation strain hotspot map of the KN1 specimen, progressing from (a) loaded to 50 N to (f) unloaded after the 78 N loading. The 3D simulated strains for the loaded states are presented in the insets, using the same colour scale and orientation; extreme displacement values are capped at ± 3.5 μm for clarity. On the insets, the notch is indicated in pink, and the vertical side grooves in brown.



Continued: Figure 143: 3D deviation strain hotspot map of the KN1 specimen, progressing from (a) loaded to 50 N to (f) unloaded after the 78 N loading. The 3D simulated strains for the loaded states are presented in the insets, using the same colour scale and orientation; extreme displacement values are capped at ± 3.5 μm for clarity. On the insets, the notch is indicated in pink, and the vertical side grooves in brown.

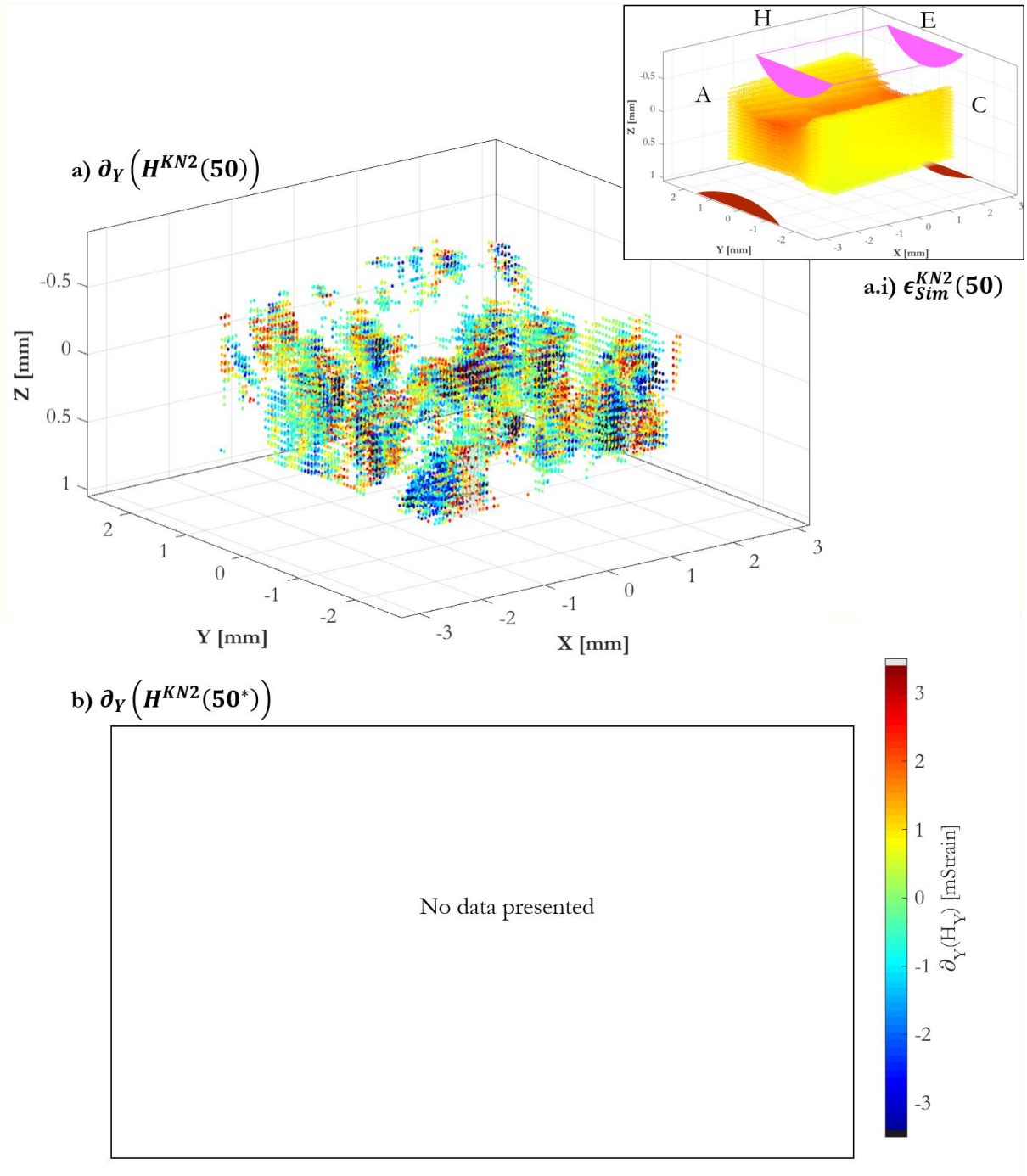
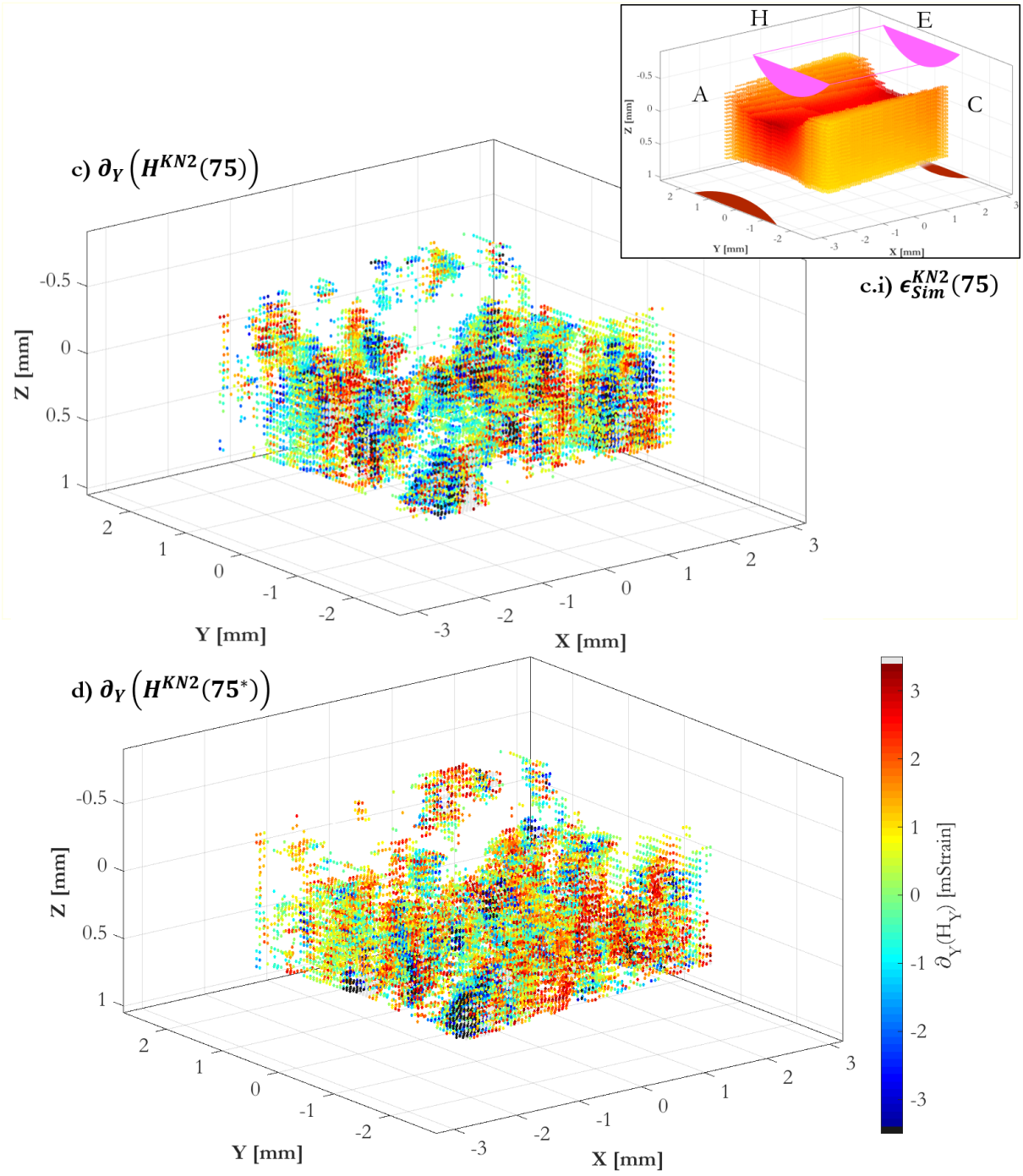
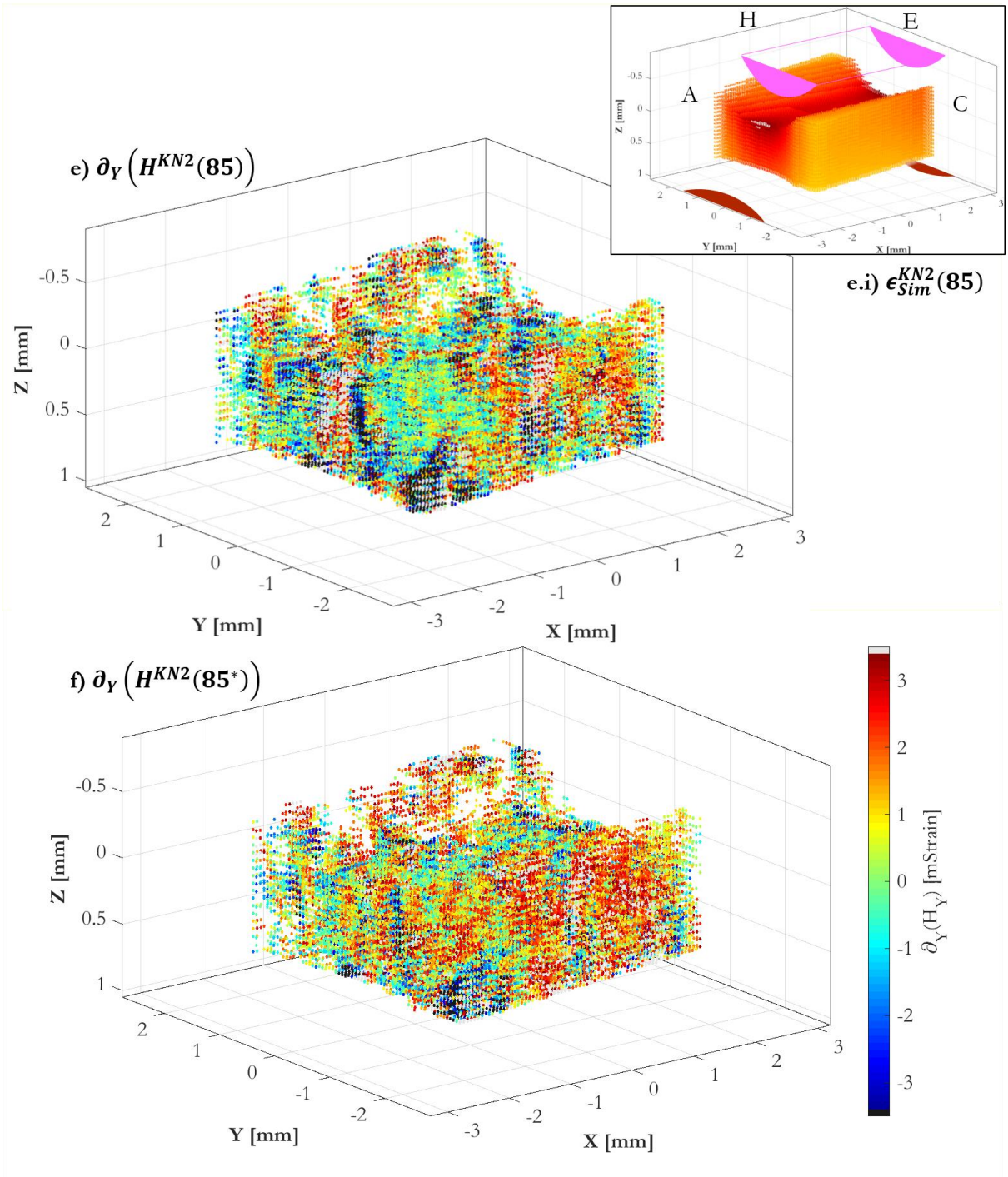


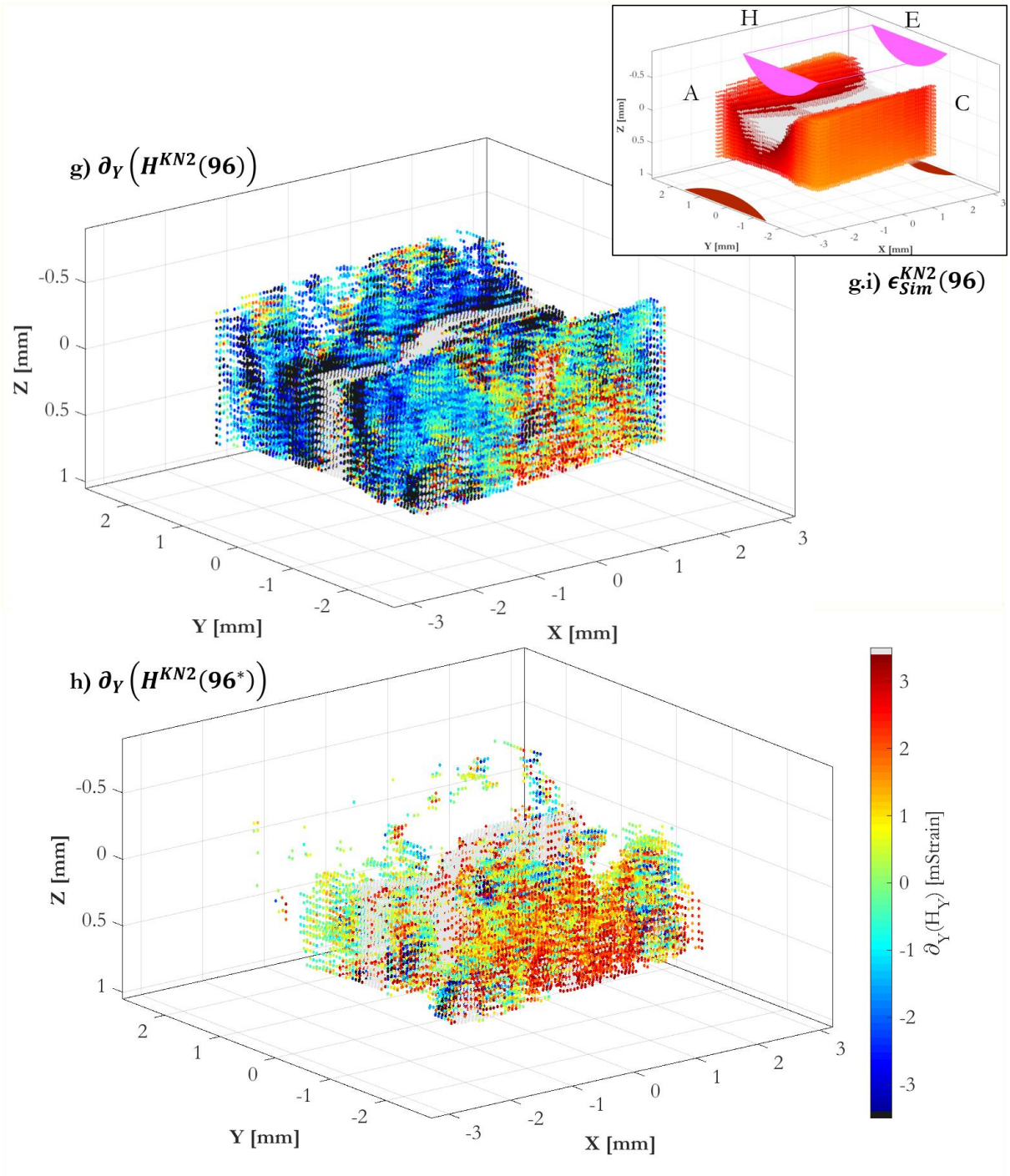
Figure 144: 3D deviation strain hotspot map of the KN2 specimen, progressing from (a) loaded to 50 N to (f) unloaded after the 96 N loading. Data for the unload after 50 N is not available; see § A2. The 3D simulated strains for the loaded states are presented in the insets, using the same colour scale and orientation; extreme displacement values are capped at ± 3.5 μm for clarity. On the insets, the notch is indicated in pink, and the vertical side grooves in brown.



Continued: Figure 144: 3D deviation strain hotspot map of the KN2 specimen, progressing from (a) loaded to 50 N to (f) unloaded after the 96 N loading. Data for the unload after 50 N is not available; see § A2. The 3D simulated strains for the loaded states are presented in the insets, using the same colour scale and orientation; extreme displacement values are capped at ± 3.5 μm for clarity. On the insets, the notch is indicated in pink, and the vertical side grooves in brown.



Continued: Figure 144: 3D deviation strain hotspot map of the KN2 specimen, progressing from (a) loaded to 50 N to (f) unloaded after the 96 N loading. Data for the unload after 50 N is not available; see § A2. The 3D simulated strains for the loaded states are presented in the insets, using the same colour scale and orientation; extreme displacement values are capped at ± 3.5 μm for clarity. On the insets, the notch is indicated in pink, and the vertical side grooves in brown.



Continued: Figure 144: 3D deviation strain hotspot map of the KN2 specimen, progressing from (a) loaded to 50 N to (f) unloaded after the 96 N loading. Data for the unload after 50 N is not available; see § A2. The 3D simulated strains for the loaded states are presented in the insets, using the same colour scale and orientation; extreme displacement values are capped at ± 3.5 μm for clarity. On the insets, the notch is indicated in pink, and the vertical side grooves in brown.

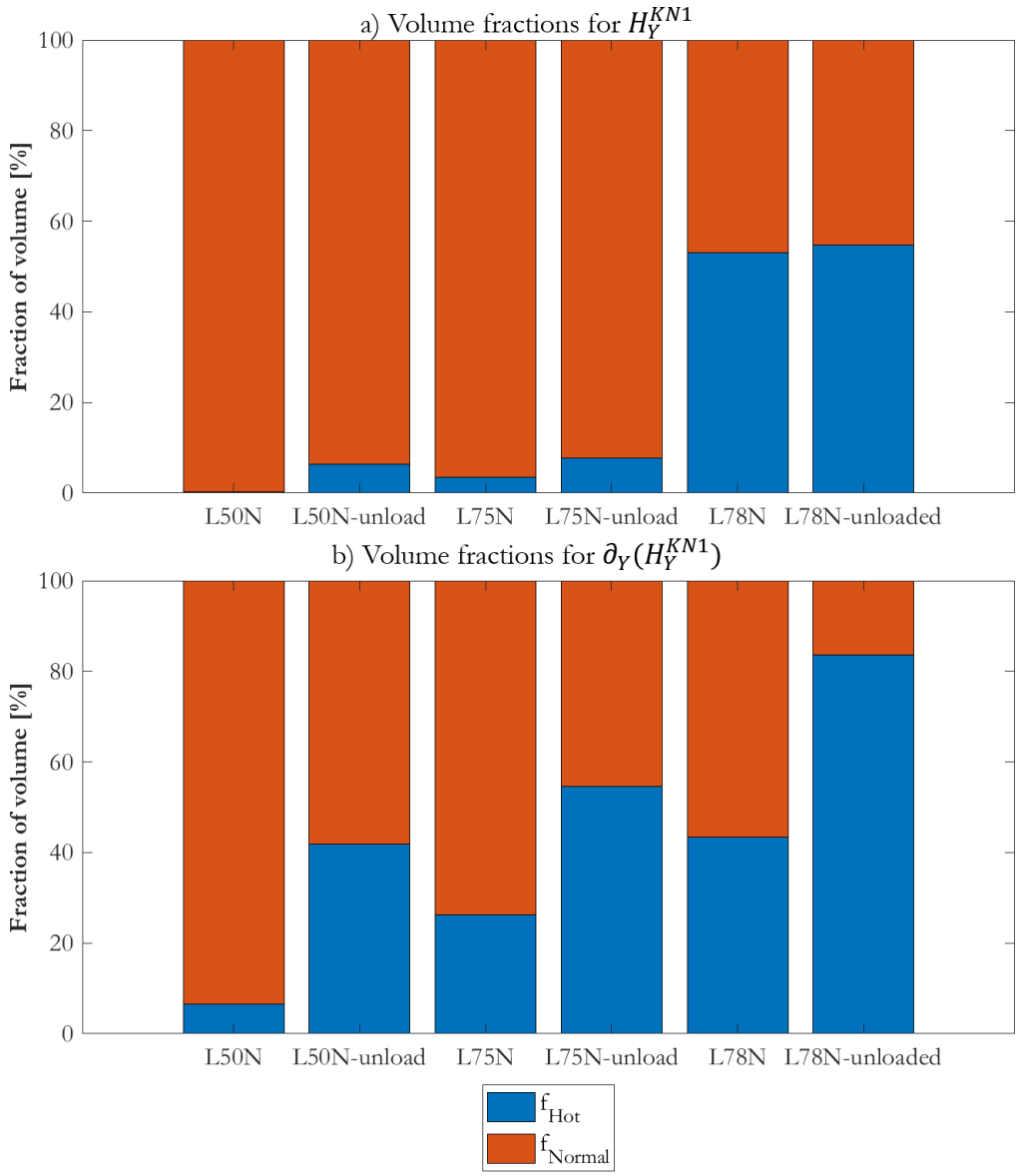


Figure 145: Evolution of deviation hotspot volume fraction (f_{Hot}) for KN1: (a) displacement hotspots, and (b) strain hotspots.

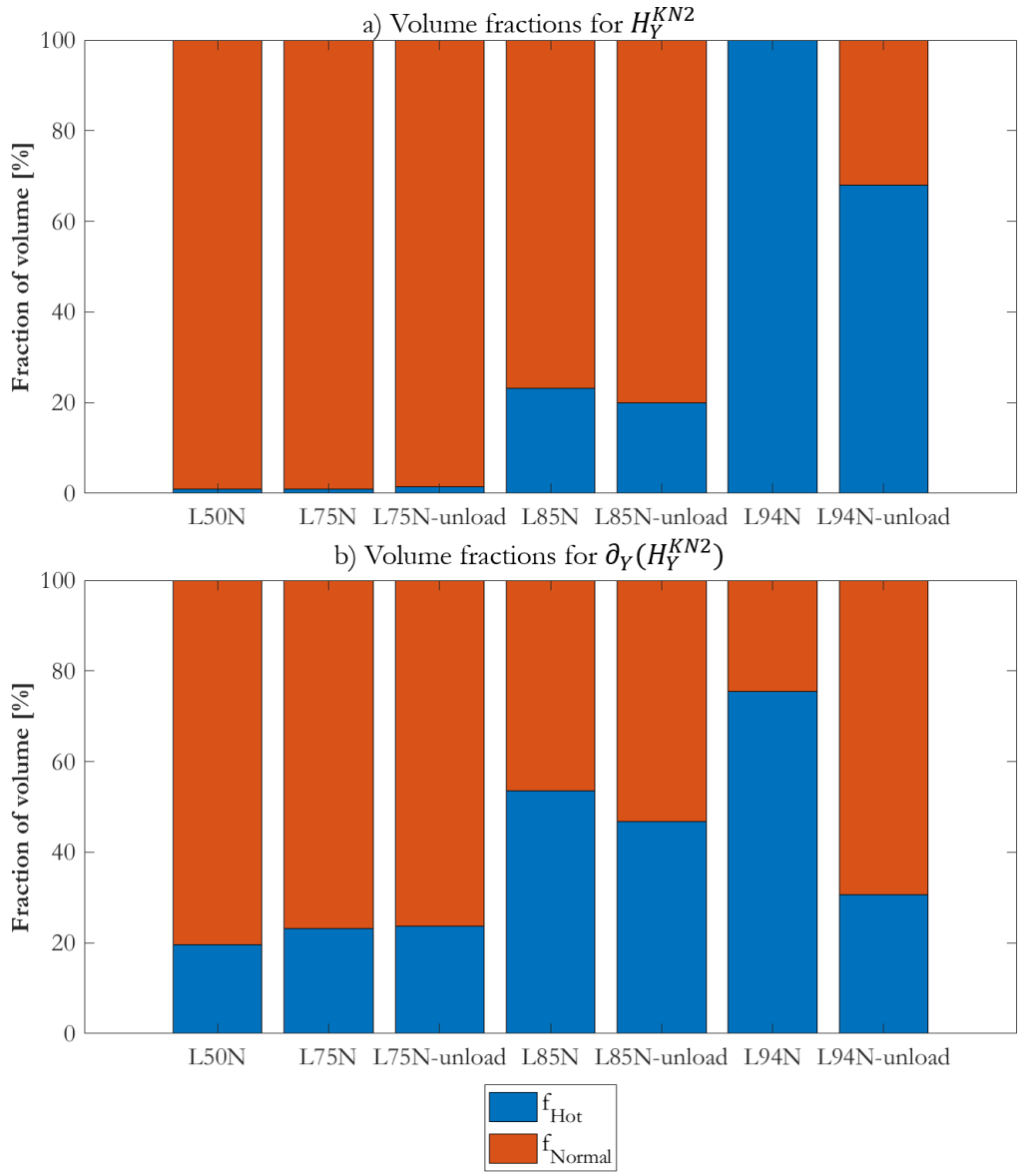


Figure 146: Evolution of deviation hotspot volume fraction (f_{Hot}) for KN2: (a) displacement hotspots, and (b) strain hotspots.

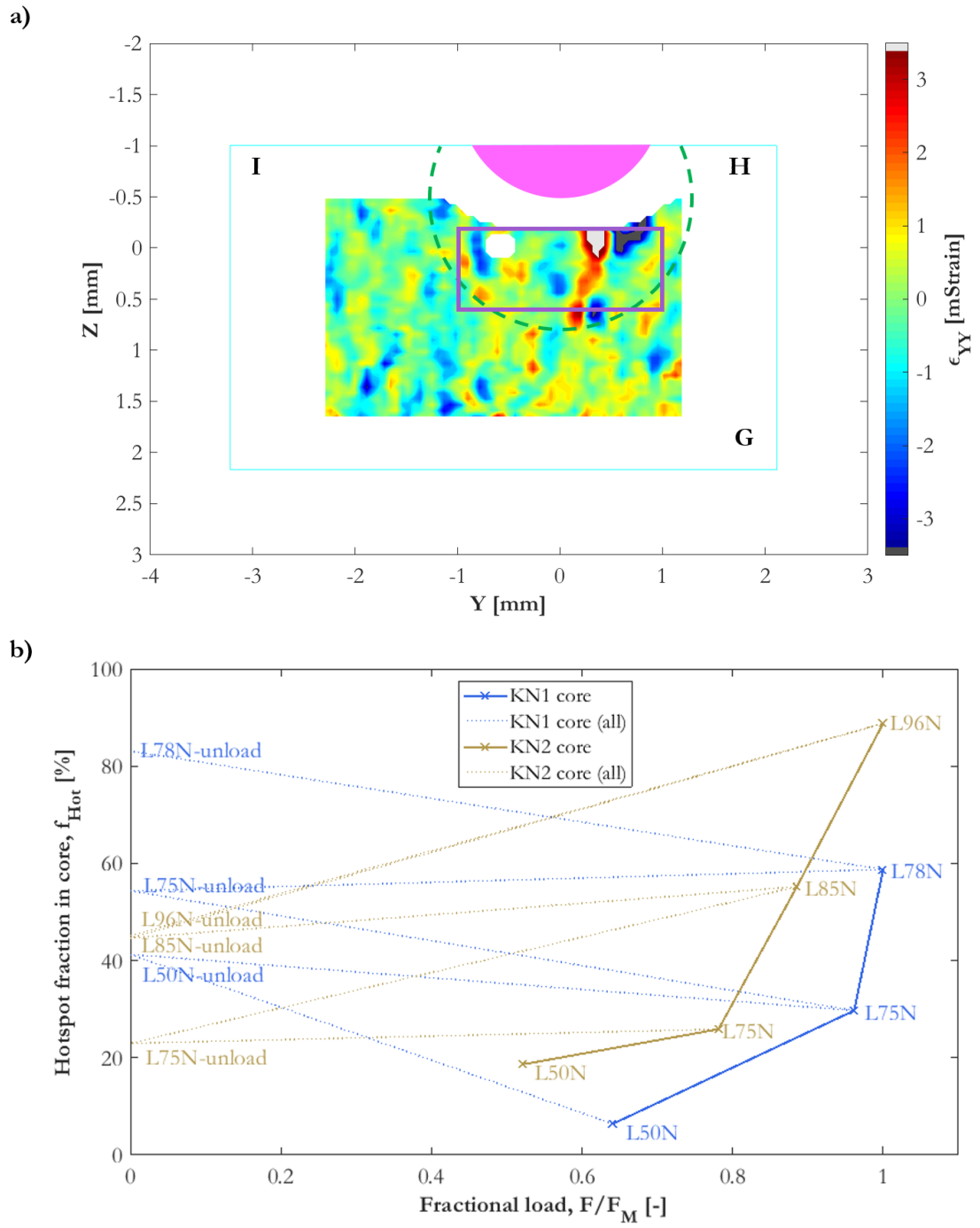


Figure 147: For the notch tip core with coordinates [(-2, -1, -0.6), (2, 1, 0.2)], as indicated by the purple line in (a) on a GHI plane (from Figure 135(c)), the evolving deviation strain hotspot volume fraction (f_{Hot}) is shown in (b) for the two specimens. The dotted lines join all the loaded states in sequence, while the solid lines join only the loaded states, for clarity.

IV.3.4.4 Hotspot persistence

The temporal evolution of individual vector behaviour will now be considered in terms of hotspot behaviour. For example, initially a vector would have a 'normal' level of deviation displacement and strain; and might continue to agree with the simulated displacements during the first load and unload stages, but then during the second stage become a hotspot. On unloading, it might then relax back to the normal state or 'persist' as a hotspot. Depending on the material response, therefore, comparing any two states, the vector might vary between being a hotspot or normal. The changing state of every vector can therefore be described in terms of the four progressions: 'Normal→Normal', 'Normal→Hot', 'Hot→Normal' and the persistent 'Hot→Hot'. The volume fractions for each progression can then be measured.

For KN1 and KN2, respectively, in Figure 148 and Figure 149 the deviation displacements persistence maps for the sequential loading states were plotted, with the accompanying volume fraction bar charts (for both the hotspot strains and displacements) in Figure 150 and Figure 151; the sequential unloaded states and bar charts were compared in Figure 152-Figure 155; and finally, each loaded state was compared to the immediately following unloaded state in Figure 156-Figure 159. For a given pair of states, the 3D maps showed in which state(s) a vector was a hotspot: initial only = red, final only = blue, both = green, or neither = transparent. It was an unfortunate artefact of the visualisation method that the points around the boundaries of the tomograph obscured the behaviour in the centre.

The maps showed a clear trend, particularly at low loads, for clusters of voxels to grow as ellipsoids increasing in volume between sequential stages. In Figure 148(a), for example comparing the 50 N and 75 N states of the KN1 specimen, most of the ellipsoid regions are new hotspots, but it is clear that some of these have formed around persistent hotspots. Some regions of hotspots were initial only, but spatially they were only located at the bottom of the tomograph region. Similar behaviour was observed for both the loaded and unloaded states. At high loads, the hotspots covered more significant regions and appeared to coalesce, such that following the behaviour of individual clusters became difficult. The bar charts show how the different progression fractions varied. The f_{Hot} fractions can be broken down into pre-existing ($f_{Hot\text{-}Hot}$) and new ($f_{Norm.\text{-}Hot}$) hotspot volume by comparing, for example Figure 145 and Figure 150. The net increase in f_{Hot} is the difference between the two transition states. For the loaded states, the displacements show rapid increases for each successive state, while the strains showed a relatively consistent increase in $f_{Norm\text{-}Hot}$, and a consistent decrease in $f_{Hot\text{-}Norm}$. The behaviour of the unloaded states was similar.

For the load-unload comparisons, the ellipsoid nature of the hotspots is clearer than in the load or unload comparisons. It is again apparent that for KN1 f_{Hot} increased substantially on unloading (significant $f_{Norm\text{-}Hot}$ fractions in Figure 158), while for KN2 the net increase was approximately zero for both the displacements and strains in the pre-fracture states (and reduced significantly after fracture) shown in Figure 159.

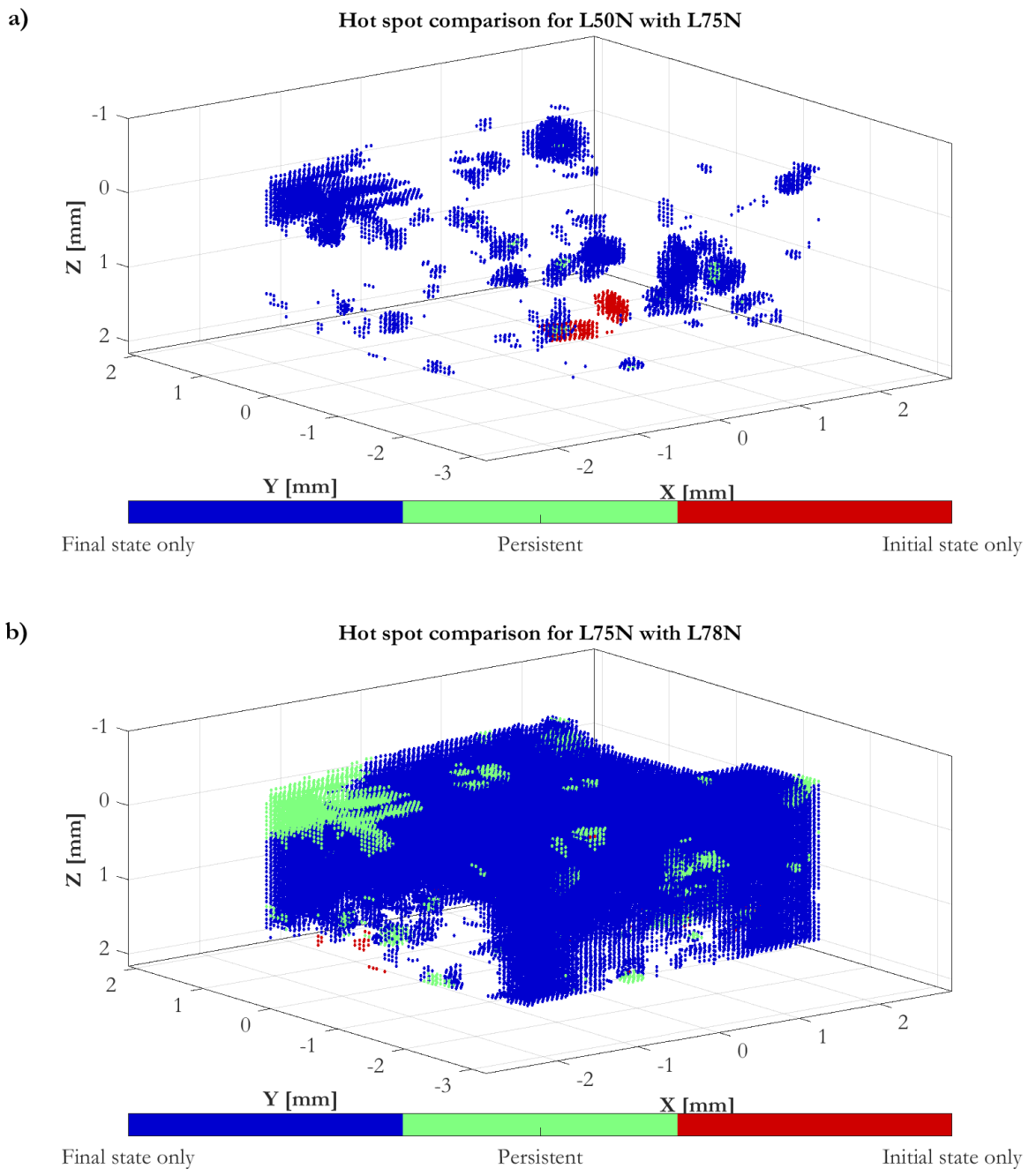


Figure 148: Hotspot persistence plots for the deviation displacements for the sequential KN1 loaded states.

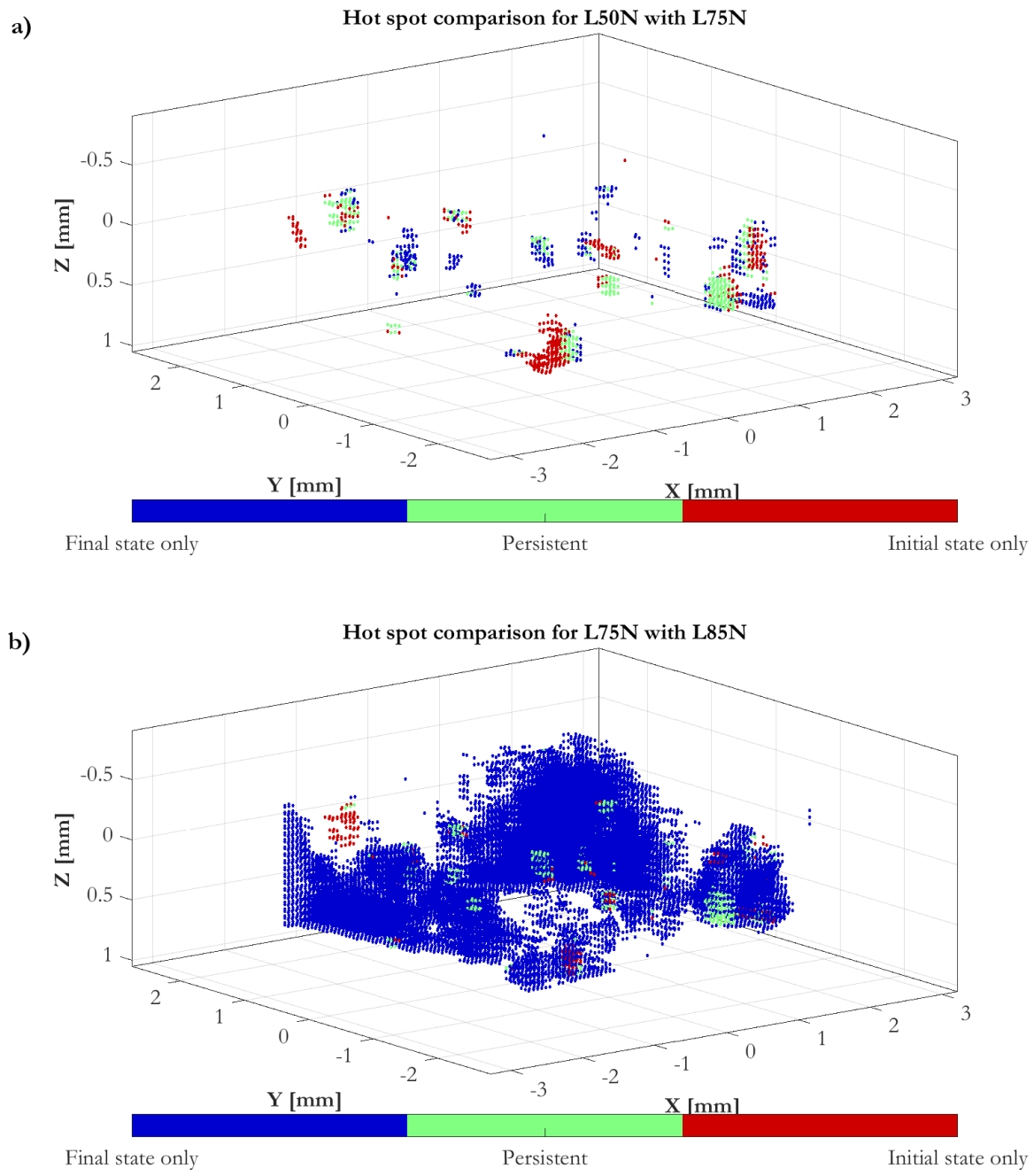
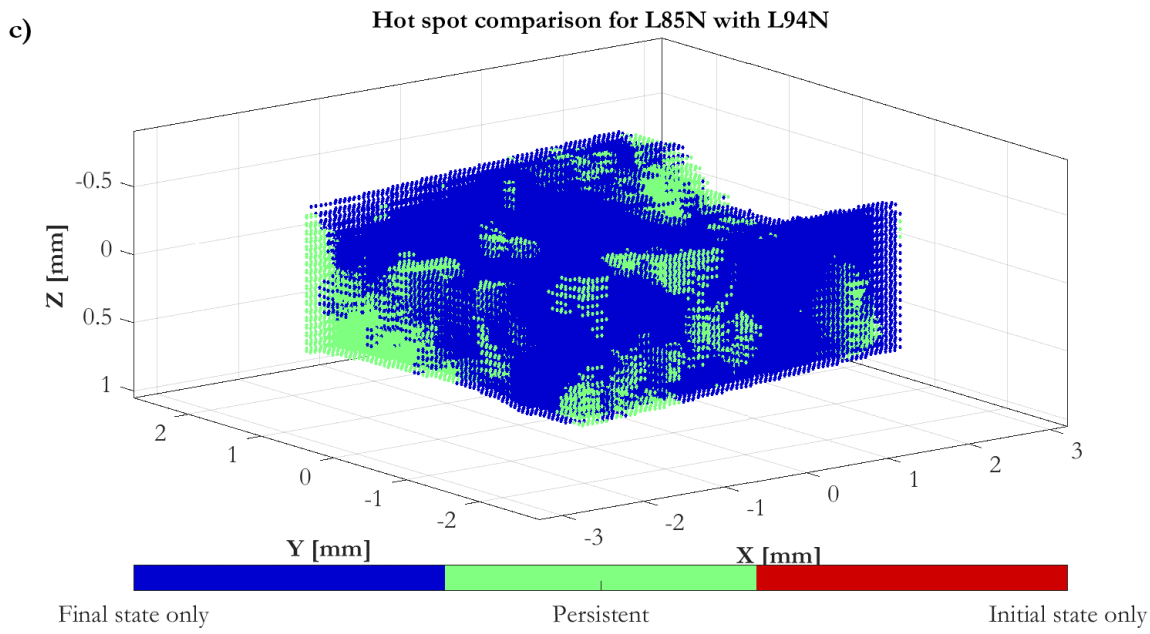


Figure 149: Hotspot persistence plots for the deviation displacements for the sequential KN2 loaded states.



Continued: Figure 149: Hotspot persistence plots for the deviation displacements for the sequential KN2 loaded states.

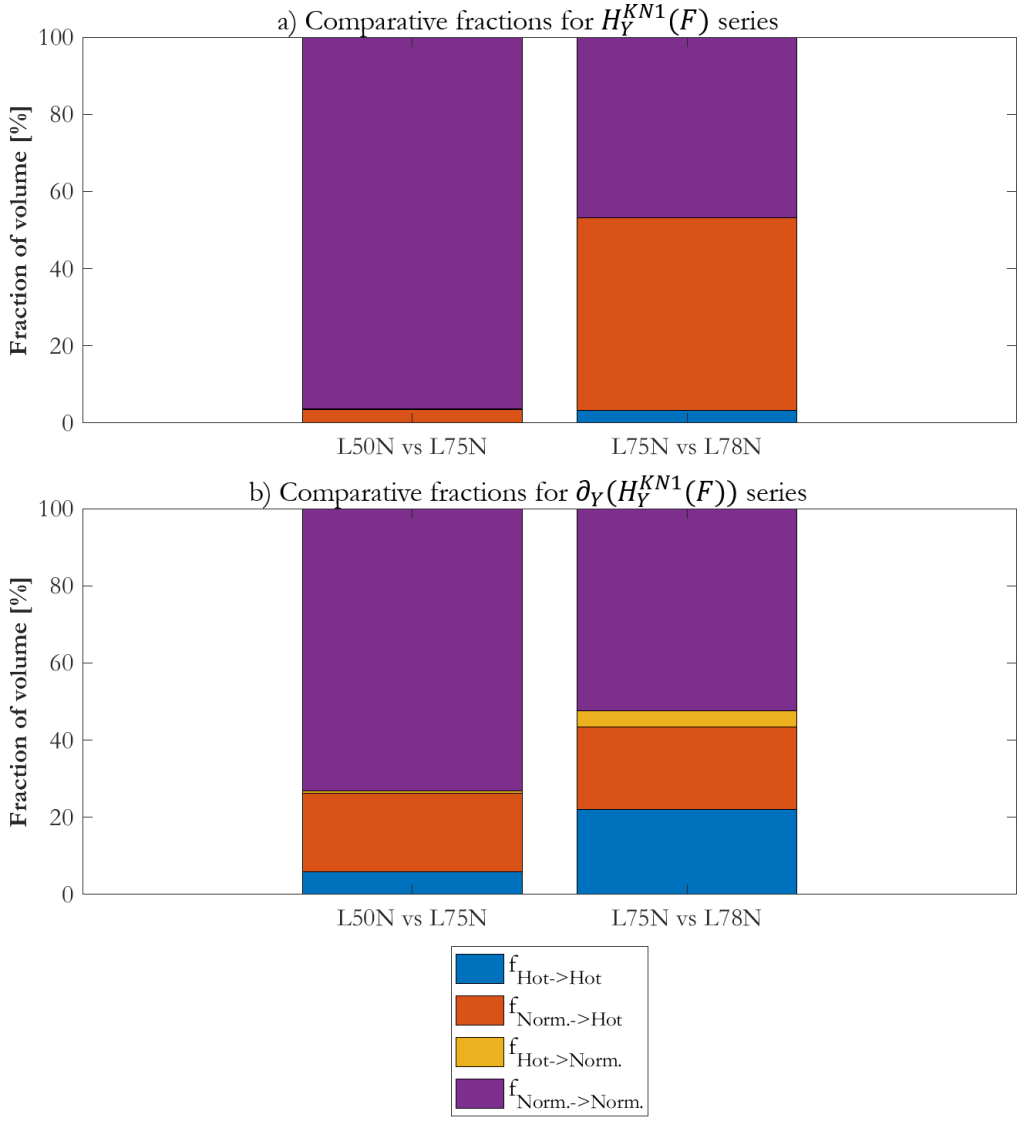


Figure 150: Volume fraction analysis of the hotspot persistence in the sequential KN1 loaded states.

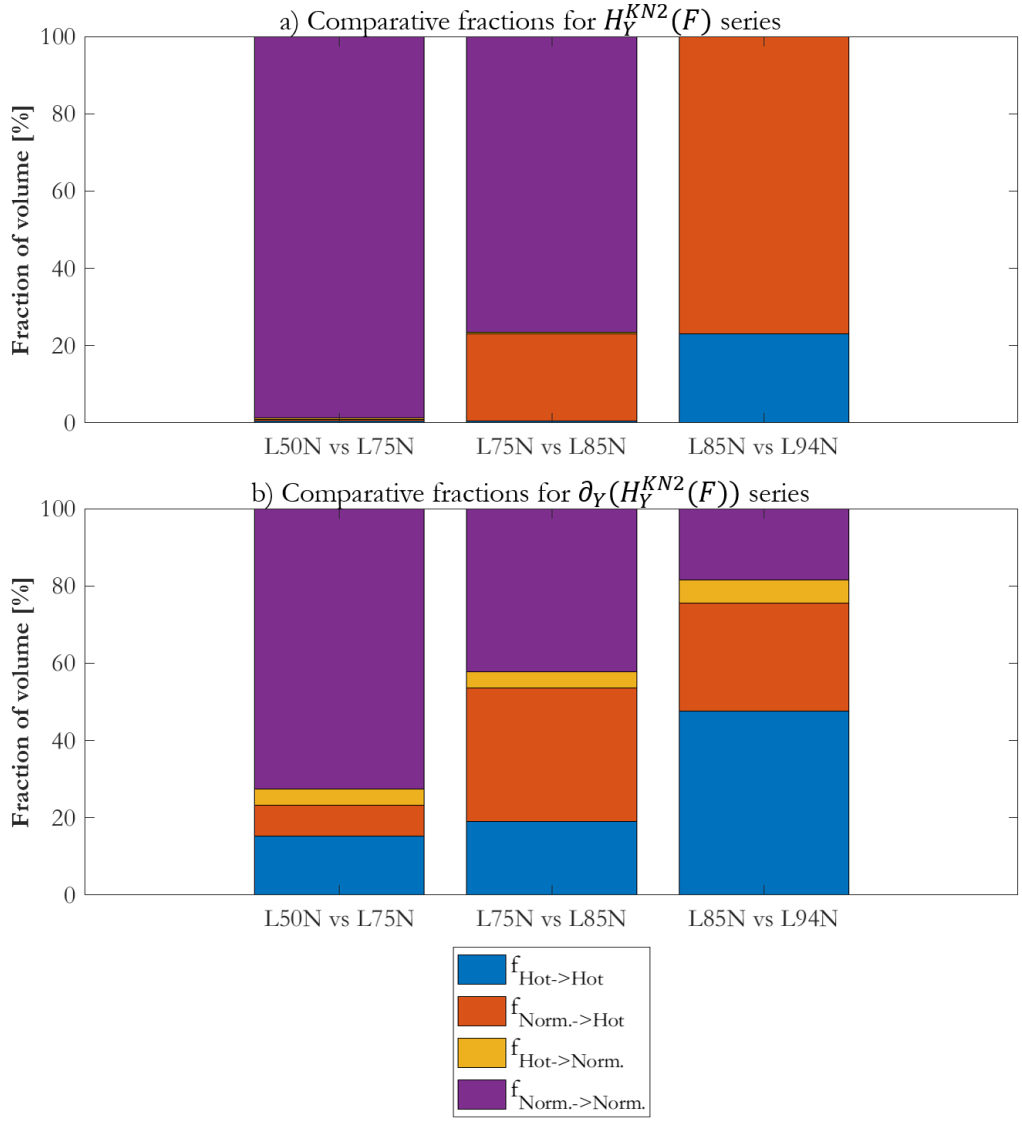
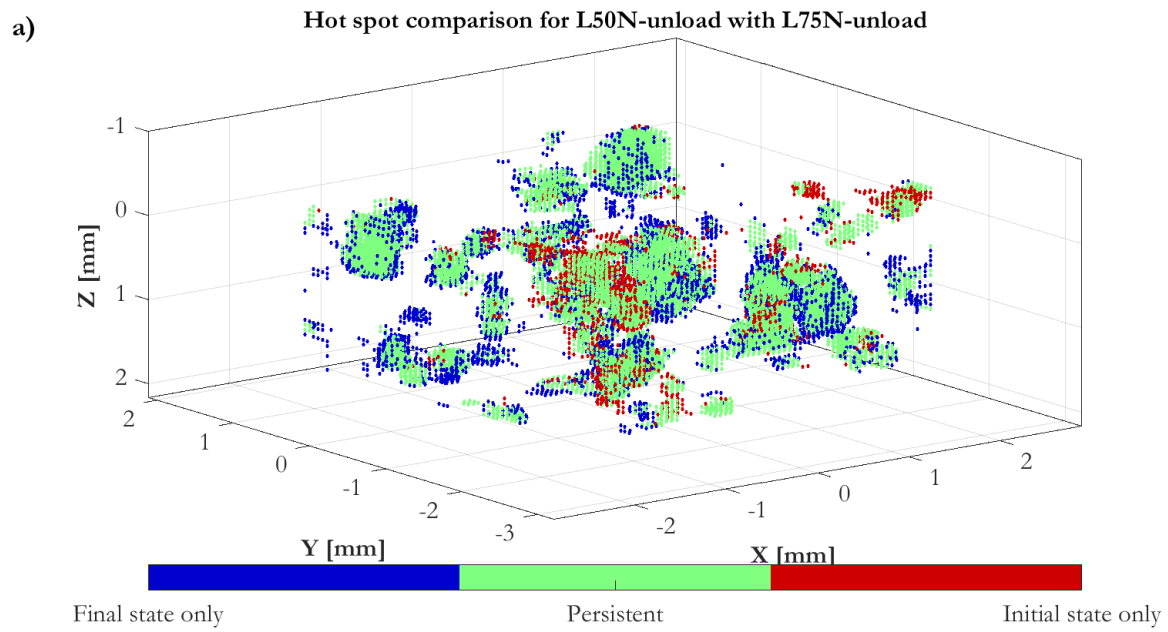


Figure 151: Volume fraction analysis of the hotspot persistence in the sequential KN2 loaded states.



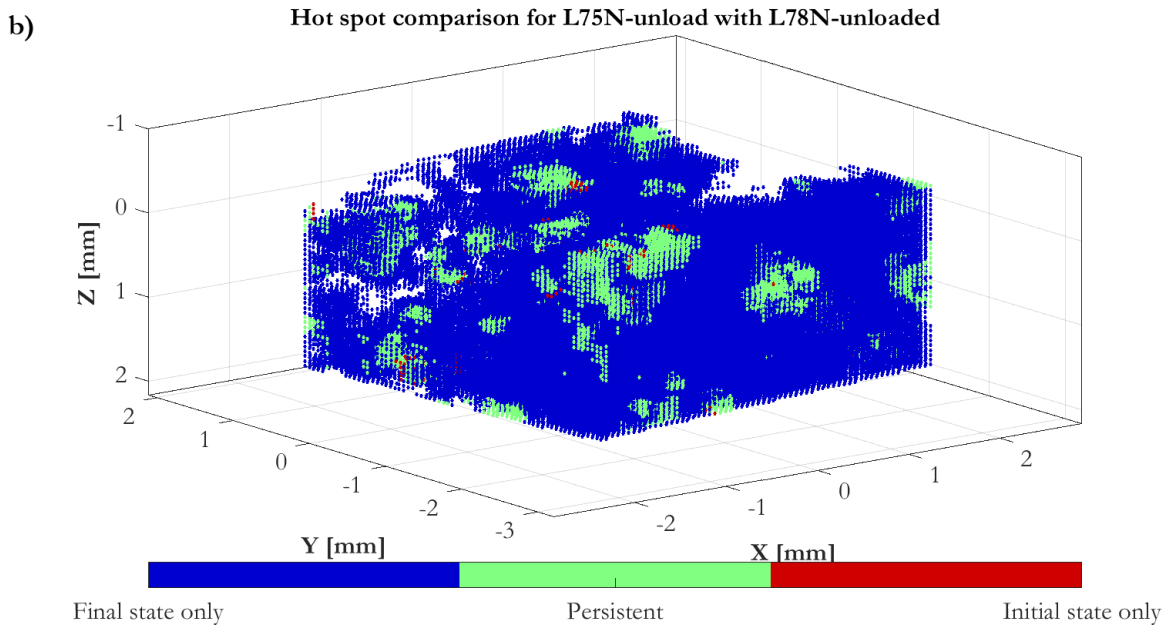


Figure 152: Hotspot persistence plots for the deviation displacements for the sequential KN1 unloaded states.

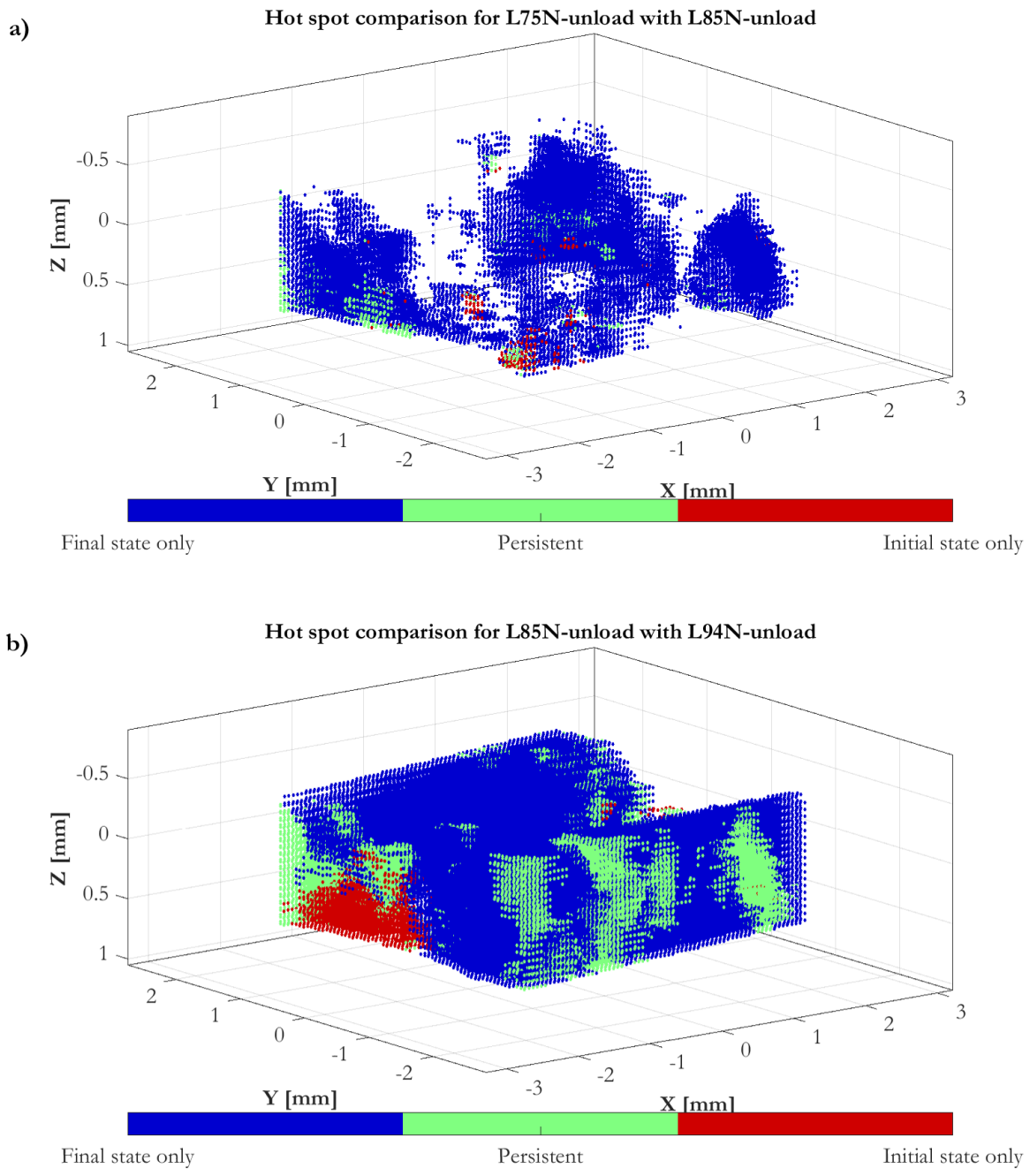


Figure 153: Hotspot persistence plots for the deviation displacements for the sequential KN2 unloaded states.

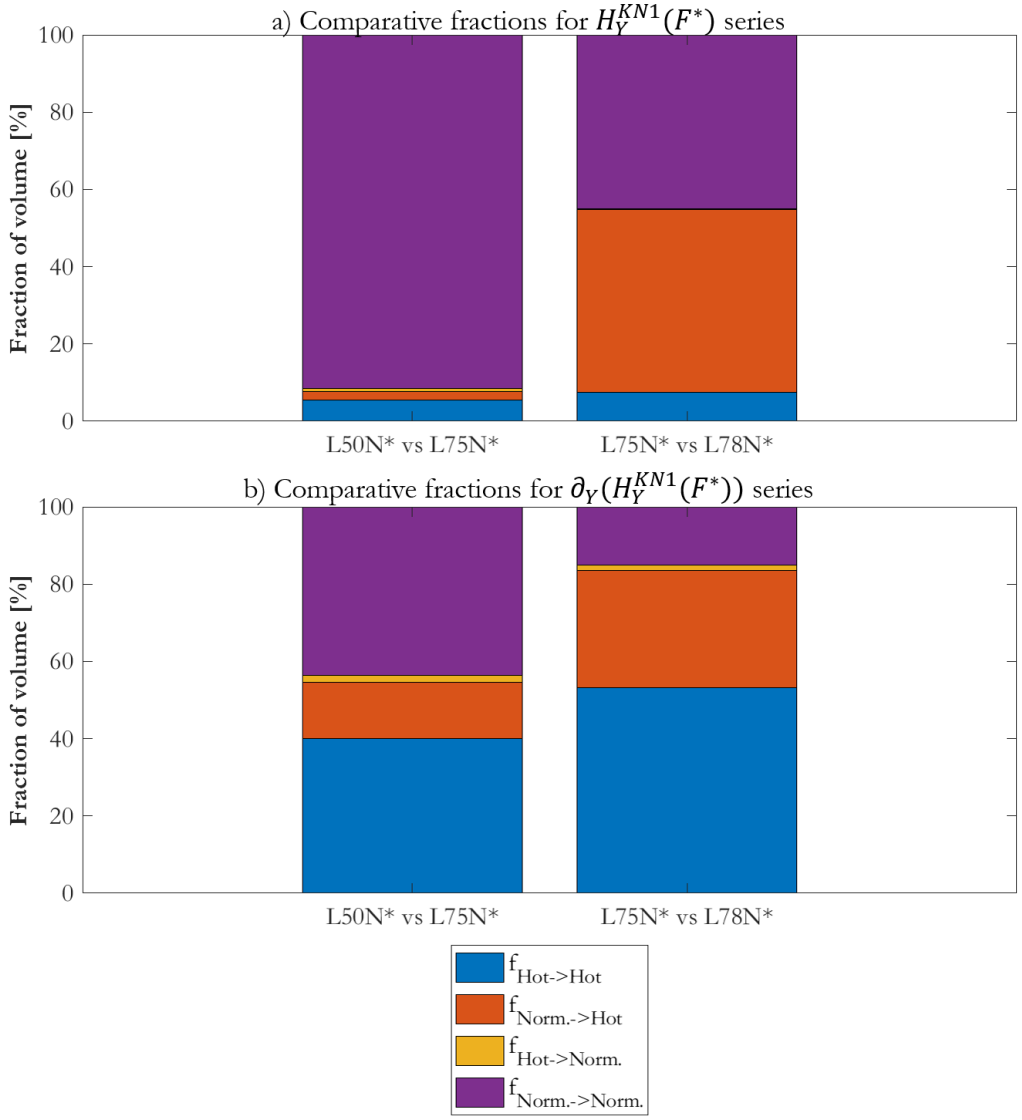


Figure 154: Volume fraction analysis of the hotspot persistence in the sequential KN1 unloaded states

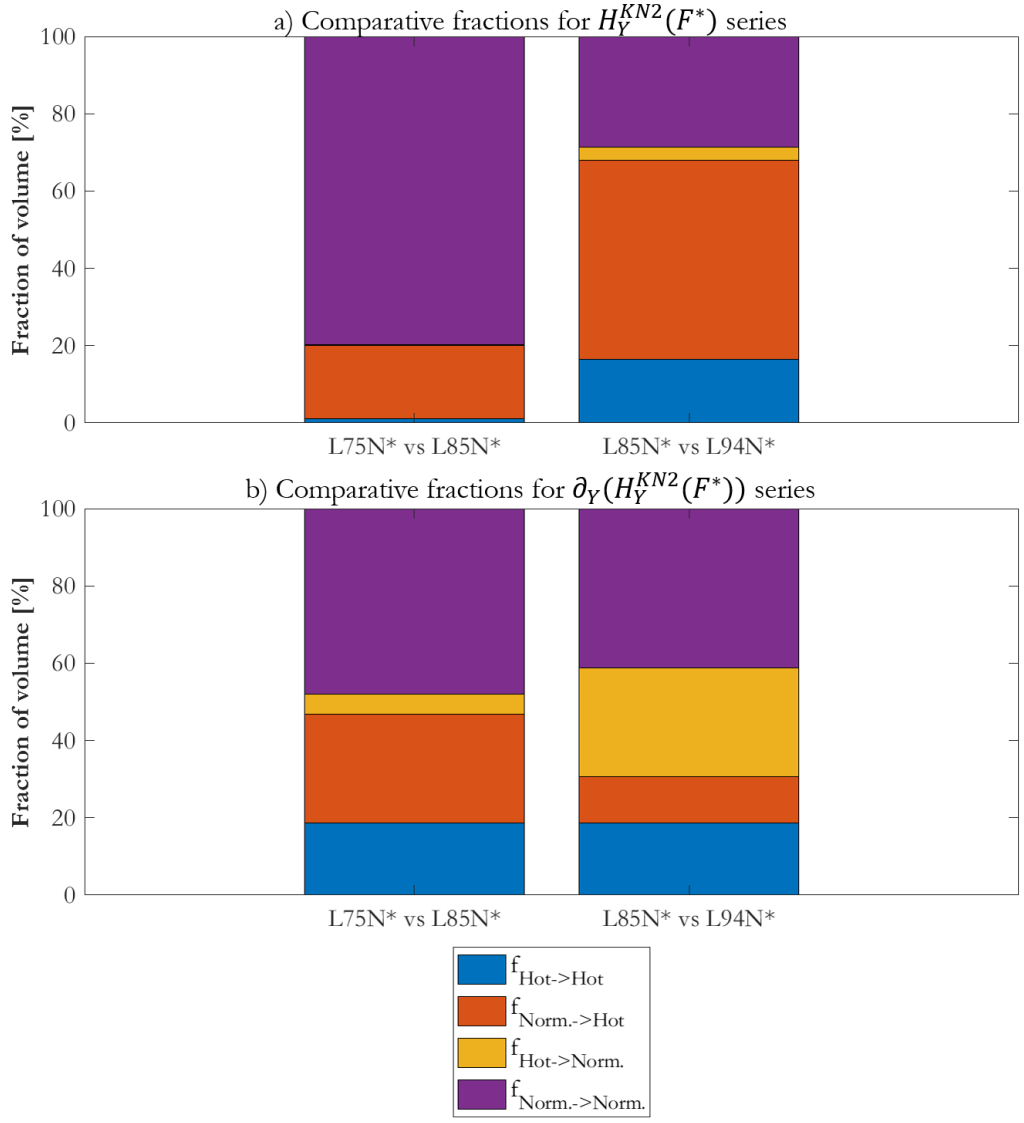


Figure 155: Volume fraction analysis of the hotspot persistence in the sequential KN2 unloaded states

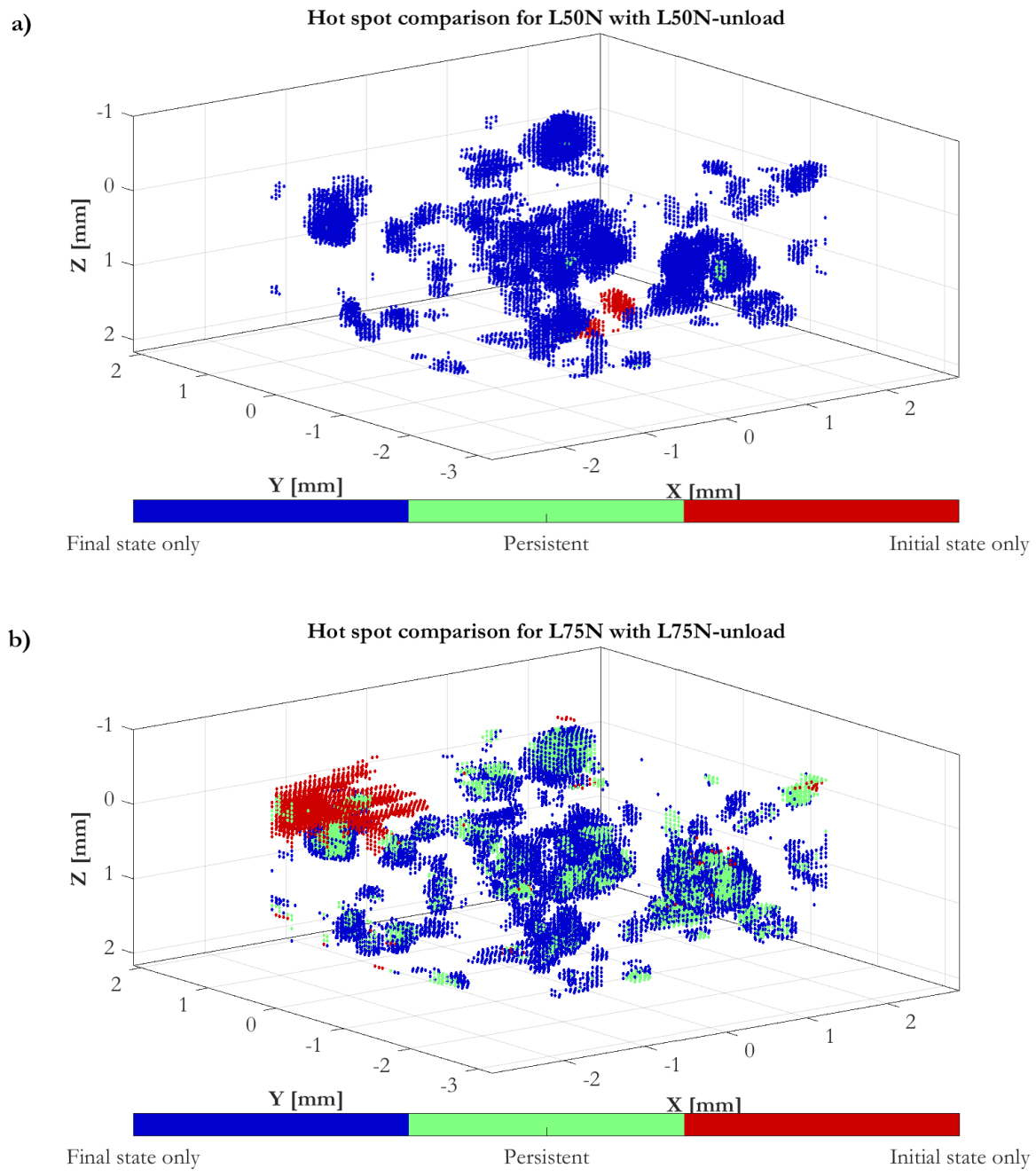
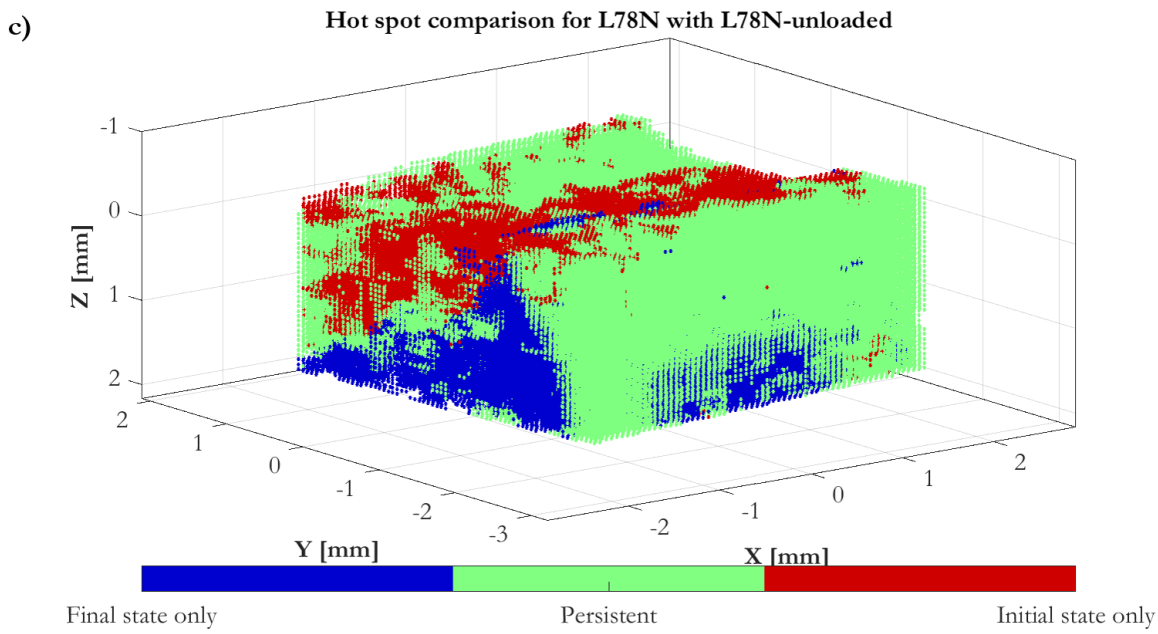


Figure 156: Hotspot persistence plots for the deviation displacements for the sequential KN1loaded states compared with the subsequent unloaded states.



Continued: Figure 156: Hotspot persistence plots for the deviation displacements for the sequential KN1loaded states compared with the subsequent unloaded states.

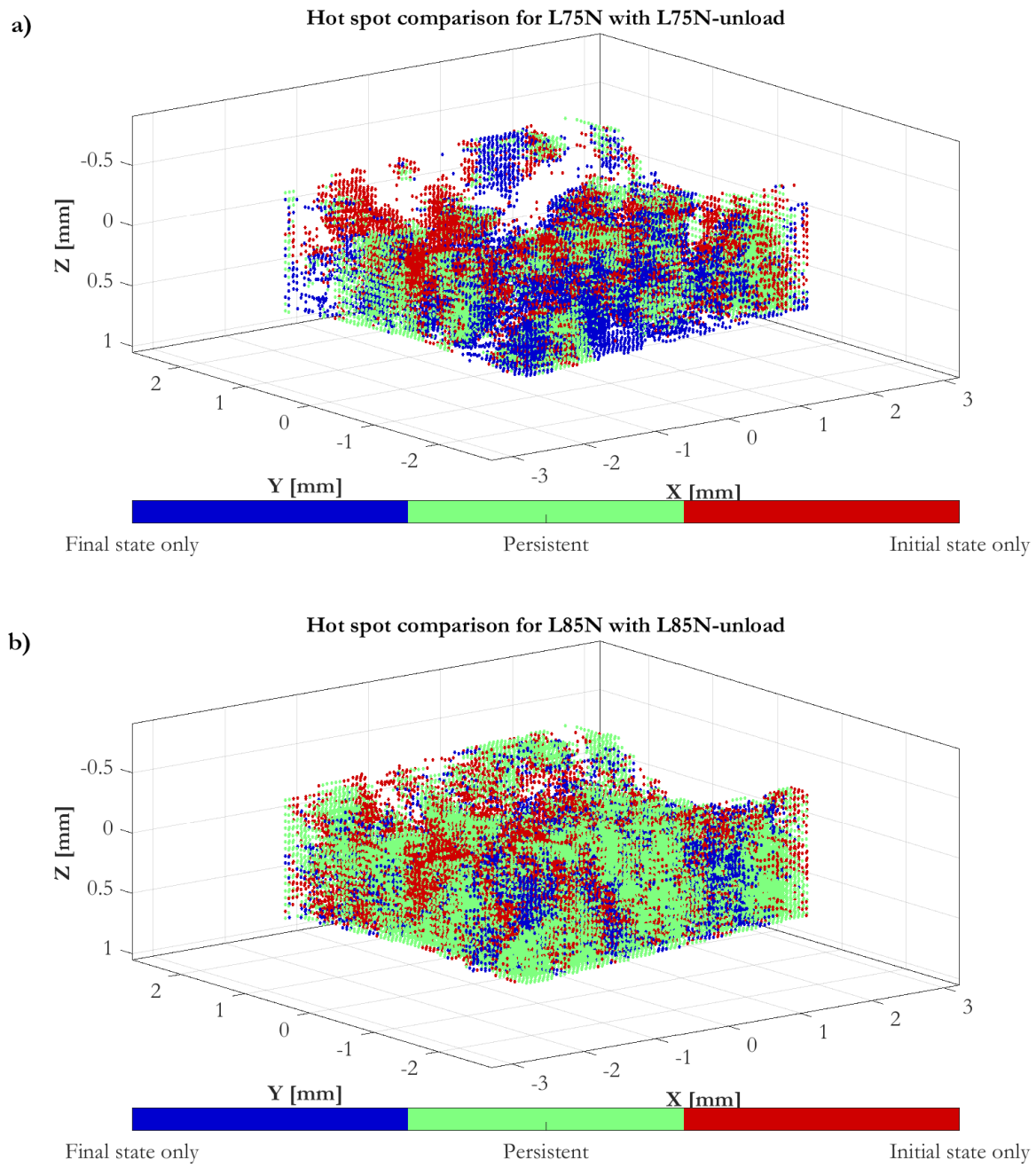
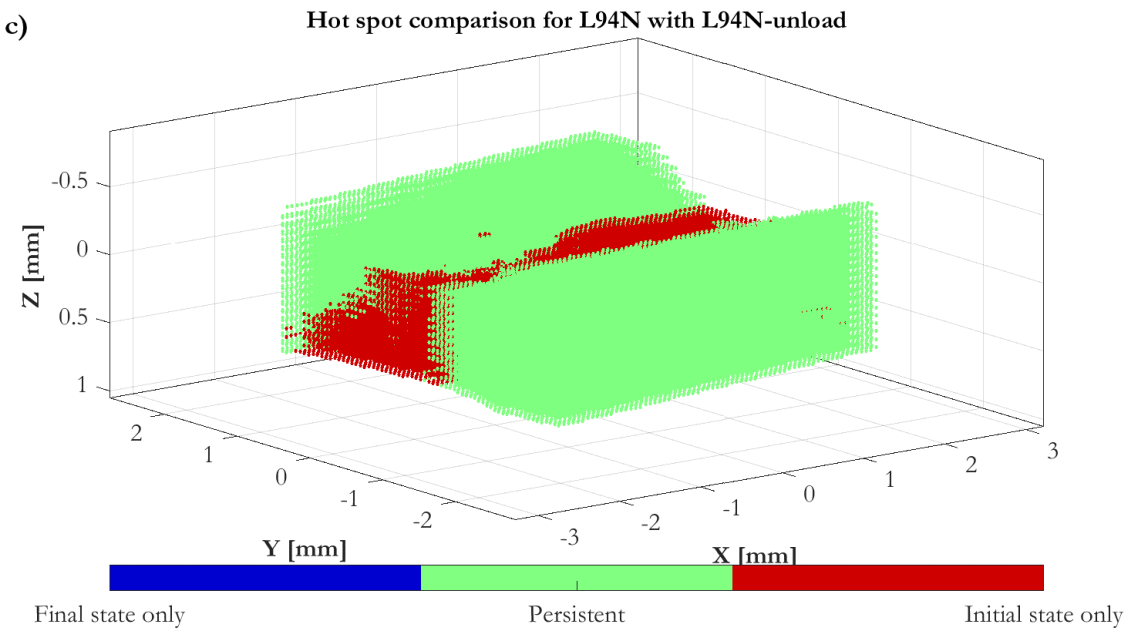


Figure 157: Hotspot persistence plots for the deviation displacements for the sequential KN2 loaded states compared with the subsequent unloaded states.



Continued: Figure 157: Hotspot persistence plots for the deviation displacements for the sequential KN2 loaded states compared with the subsequent unloaded states.

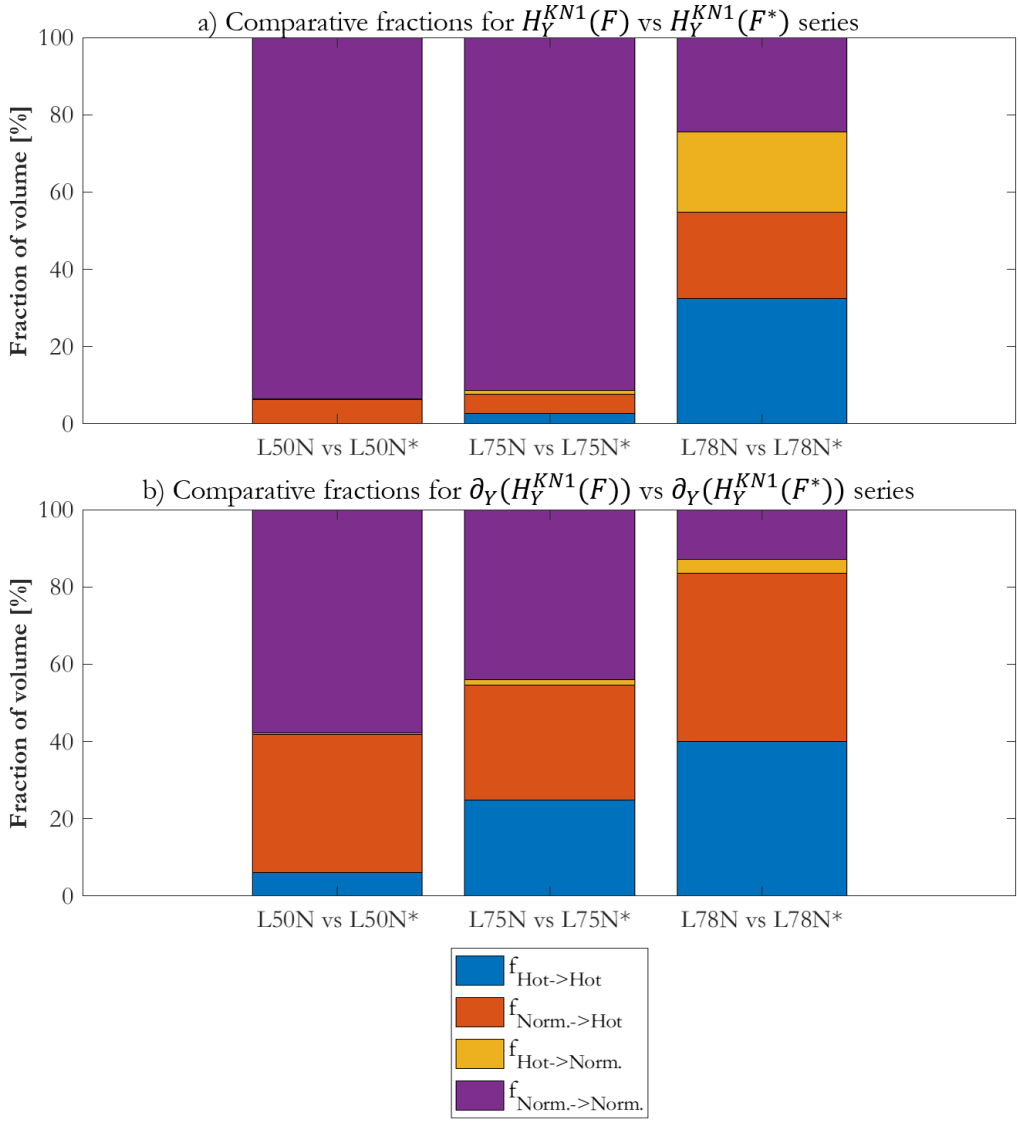


Figure 158: Volume fraction analysis of the hotspot persistence in the sequential KN1 loaded states compared with the subsequent unloaded states.

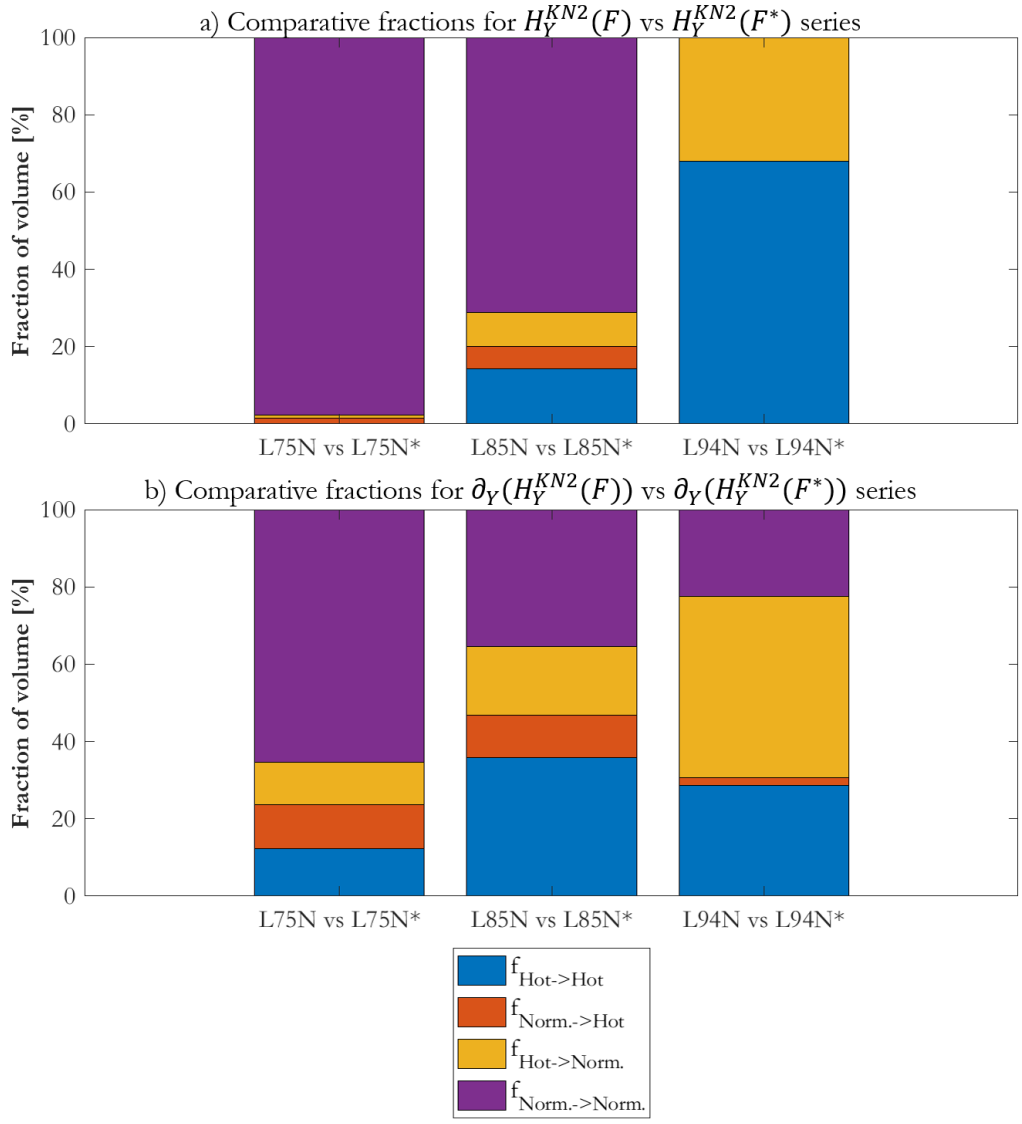


Figure 159: Volume fraction analysis of the hotspot persistence in the sequential KN2 loaded states compared with the subsequent unloaded states.

IV.4 Discussion

The keyhole notch experiments sought to explore the response of the Gilsocarbon microstructure to a concentrated applied strain during crack initiation. Using blunt features of varying radii, heterogeneous behaviour has been observed at two length scales leading to a non-linear and non-recoverable strain response. While the previous chapter focused on demonstrating statistical trends in the behaviour of different notch geometries, only three geometries were considered in this chapter, with only two specimens analysed in detail. The novelty and implications of the experimental and analytical approach will be discussed (§ IV.4.1). The experimental data were compared to predictions from linear elastic simulations. In general, the simulated behaviours were an excellent match for the pre-fracture experimental behaviour at the bulk scale, as evaluated in § IV.3.1.2, § IV.3.2.2.1, § IV.3.3.2.1 and particularly § IV.3.4.2. At smaller length scales (< 10 mm), differences were observed between experiment and prediction, and quantitative comparison by the deviation method demonstrated the advantages of removing the underlying bulk deformation in the detection of non-linear and non-recoverable strains. The presence and implications of the postulated radius-independent ϵCZ is explored (§ IV.4.1.1), as are the evolving behaviour of the filler particles and filler-binder interface that exhibited a statistically anomalous response (§ IV.4.3 and § IV.4.4). Implications for damage modelling in Gilsocarbon and the origins of Gilsocarbon's notch insensitivity will be explained by the observation of a fully-formed FPZ that was consistently defined for both notch radii (§ IV.4.5).

IV.4.1 Experiment set-up and analysis procedure

The novel specimen geometry and bespoke loading jig enabled the controlled crack initiation of ahead of blunt keyhole features. As in Chapter III, by imaging at two length scales both gross deflections and high-resolution information was captured, enabling a multi-scale analysis with finite element simulation. The DIC of the radiographs (§ IV.3.1) demonstrated clear Mode I opening behaviour, with a small degree of Mode II. Displacements contributing to Mode III deformation could not be measured by DIC, but no evidence was found in the subsequent DVC analysis to suspect a significant contribution. The smoothness and consistency of the Mode I and Mode II patterns in Figure 110, demonstrated that the Gilsocarbon behaved in a generally homogeneous manner for length scales greater than 5 mm, without significant shearing, for example. This was in-line with historical component fracture testing, where non-linear brittle or quasi-brittle failure was typically observed such as [126]. The consistent behaviour seen here confirms the suitability of the test method in terms of measuring representable large-scale behaviour of Gilsocarbon.

The observations from the tomography and the load-displacement traces indicated that the pop-ins occurred at around 90 % of the maximum load, where the maximum load corresponds to full-width fracture. From Table 15, the mean failure loads for the three geometries rose consistently with increasing radius, in accordance with the theory of stress concentrations. These findings are in agreement with previous studies on Gilsocarbon outlined in Chapter II, and the findings of Chapter III. The partial-width crack observed in the KN1 specimen before the peak load (Figure 106 at 75N) may be the cause of the statistically low peak load for this specimen, and clearly demonstrates energetically stable (arresting) fracture in this geometry at the component-scale. The quasi-static loading and discrete imaging applied in this experiment prevented identification of the initiation point within the microstructure; the macro-crack was formed during the loading between tomographs.

To model the pre-fracture states, the boundary conditions were applied differently to the finite element simulations than the method described in § III.4.1. For the flexure experiments, the rollers were well-defined and explicit definition was suitable for the geometry. Furthermore, any contact damage would have been spread over a significant area, with an insignificant effect on the deformation patterns. Conversely, for the keyhole notch geometries, the pressure was applied to the very narrow region where the flat wedge surface contacted the upper edges at the slot and caused visible damage to the contact corners. The exact shape of the wedge, progressive damage to the graphite edges, the contact friction of the steel wedge on the graphite, and any slight misalignments of the loading system could therefore have altered the specimen deformation significantly. Capturing these evolving interactions and simulating them *ab initio* was not feasible, and not required since the displacements could be derived from image correlation. The simulation's boundary conditions were therefore defined implicitly for each loading state (§ IV.3.1.2), requiring no iterative modelling nor determination of external fitting parameters, such as wedge displacement or apparent stiffness, and accounting precisely for the minor loading asymmetry identified in Figure 111. This more representative model definition is therefore an alternative to the method in Chapter III, provided that the deformations are adequately defined (that is, multidimensional and suitably constrained).

IV.4.1.1 Deviation calculation

The deviation calculation assumes small strain conditions were valid,[20] and trivially excludes rigid-body motion effects. The natural output from DIC measurement and finite element modelling is the displacement field U_{Corr}, and for the calculation of further derived properties, such as the degree of plastic energy from the J-integral, 'traditional' methods rely on calculation from the raw displacement data [31, 178].[21] Due to the differentiation, the correlation strain field is particularly sensitive to noise in U_{Corr}, where the independent errors in neighbouring vectors compound when determining ϵ_{Exp}. These errors are commonly suppressed by spatial filtering of the raw measurements and/or the calculated strains, but this approach assumes a level of continuity and homogeneity in the fields, at the simplest level, or else requires a model of heterogeneity to be assumed *a priori*.

[20] More complex methods exist to compensate for large strains, for example, considering the Green approximation tensor, using higher order terms and separating linear and non-linear components.
[21] Recent advances, by Barhli *et al.*, Molteno *et al.* and Gonzales *et al.* for example, use strain data as the input, and are more suited for strain-based full-field experimental techniques such as electronic speckle pattern interferometry (ESPI). See:
[179] S.M. Barhli, L. Saucedo-Mora, C. Simpson, T. Becker, M. Mostafavi, P.J. Withers, T.J. Marrow, Obtaining the J-integral by diffraction-based crack-field strain mapping, Procedia Structural Integrity 2 (2016) 2519-2526.
[99] M.R. Molteno, T.H. Becker, Mode I–III Decomposition of the J-integral from DIC Displacement Data, Strain 51(6) (2015) 492-503.
[138] A.R. Torabi, M. Fakoor, E. Pirhadi, Tensile fracture in coarse-grained polycrystalline graphite weakened by a U-shaped notch, Engineering Fracture Mechanics 111 (2013) 77-85.
[180] R. Jones, C. Wykes, Holographic and speckle interferometry : a discussion of the theory, practice, and application of the techniques, (1989).

For the deviation method, accurate representation of the loading in the modelling was required to simulate displacements which could be subtracted from U_{Exp} to remove the bulk deformations. This approach minimised the assumptions imposed on U_{Exp}, and particularly there were no requirements for continuous or homogeneous behaviour, with the potential to achieve a more accurate comparison. The method was more robust to noise and no spatial filtering was required.[22] Boundary condition measurement and model development was the most critical stage, as agreement in the geometry, boundary conditions and material response were vital. While the boundary conditions replicated the experimental loading exactly (at least for Mode I and II), for a generalised technique the geometry definition could be improved: the geometry was assumed to exactly replicate the specimen specification (Figure 96), but from a segmented tomograph it would be possible to define a mesh directly from an object point cloud, for example [181]. Such a procedure was considered of limited value in these experiments due to known geometry and the high quality of the machining but could be useful as part of a PIE technique. Significant internal pores could also be included to capture their effects on deformation.

[22] Spatial filtering could be applied to the deviation field, if desired for visualisation, for example, with less impact on the eventual result since it does not rely on differential results.

For the material model definition, bulk material properties must be derived empirically, though accurate values of stiffness are not needed if only strain predictions are required, and not the stresses. There is no reason that the material response must be linear elastic. In fact, for a material with distinct phases and a known heterogeneous response, such as concrete or composites, the modelling could predict the response given accurate spatial information of the phases; this could be used as a method of validating a multiphase model. At the length scales of interest, assuming a non-linear homogeneous model would be of limited benefit for comparison with a multiphase material like Gilsocarbon. For instance, using Barhli *et al*'s NLE UMAT would be more likely to result in erroneous conclusions. The deviation method is thus a complementary technique for approaching the analysis of fracture mechanics problems, and particularly useful for assessing the behaviour of materials with evolving material properties.

IV.4.2 Strain concentration behaviour

An ϵCZ was predicted in the linear elastic simulations (for example in Figure 116 and Figure 117) with the following behaviour[176]: approximately elliptical or two-lobed patterns extending tangentially to the tip and typical of Mode I loading, centred near to the notch tip, with major and minor axes proportional to $\sqrt{R}$. Ahead of the notch tip, the simulated strains decayed sharply ($\epsilon \propto R^{-0.5}$), from a large tensile value at the notch tip, akin to the strain behaviour for the blunt specimens in § III.4.3.2. The experimental strains clearly did not behave in this fashion.

In the first DVC strain maps (Figure 123), it was identified in that an ϵCZ was present from the earliest loading state. The locus of the postulated region was defined using the simplest suitable geometry, that of a circle centred on the notch tip. The region was defined for the first loaded state ($\epsilon^{KN1}_{Exp,YY}(50)$), where an apparent step change in the level of tensile strain was seen in the figure, with R_C = 1.28 mm. This locus accurately enclosed an area which appeared to be highly strained in the subsequent loaded states, though the strain values were different. Most notably the locus definition was valid for highlighting a similar region in the KN2 specimen (Figure 124); the ϵCZ was apparently insensitive to the 1 mm notch radius. Additionally, around the crack tip in the $\epsilon^{KN1}_{Exp,YY}(85)$ map, the circular locus still appeared valid. Since the crack had arrested this was an energetically metastable state; the body was loaded around a tip of radius $\ll$ 0.5 mm. The focus of this thesis is crack initiation, but this observation may be equally important for simulating crack propagation; 2.0 mStrain at R_C = 1.28 mm is approximately consistent with Barhli *et al.*'s measurements for the strain field ahead of a propagating crack in the same Gilsocarbon billet [89].[23]

The postulated locus was not necessarily circular, but the magnitude of the fluctuations made the assignment of a complex shape nontrivial. The definition would be improved by binning the slices along the X-axis (parallel to the notch) to suppress the correlation noise and removed some of the microstructural contributions. Such a calculation would be a useful extension to this work, though it would be necessary to account for any change in locus definition along this axis due to the transition from plane stress to plane strain.

[23] Barhli *et al.* measured the crystal strains using diffraction techniques and observed a strain profile ahead of a growing crack that was self-consistent between sequential loads and appeared to extend up to 10 mm ahead of the crack tip with the strain decaying $\propto R^{-0.5}$. While this was significantly greater than the region measured here, by calibrating the crystal strains to the bulk strains using the work of Marrow *et al.*, the bulk tensile strain contour at 2.0 mStrain ($\approx$ 0.28 mStrain($d_{00.2}$)) was in the range [1, 2] mm ahead of the crack tip for several of the cycles. See: x
[89] S.M. Barhli, L. Saucedo-Mora, M.S.L. Jordan, A.F. Cinar, C. Reinhard, M. Mostafavi, T.J. Marrow, Synchrotron X-ray characterization of crack strain fields in polygranular graphite, Carbon 124 (2017) 357-371.
[88] T.J. Marrow, D. Liu, S.M. Barhli, L. Saucedo Mora, Y. Vertyagina, D.M. Collins, C. Reinhard, S. Kabra, P.E.J. Flewitt, D.J. Smith, In situ measurement of the strains within a mechanically loaded polygranular graphite, ibid.96 (2016) 285-302.

The dimensions of the contour in the simulations were measured using an estimate of the average strain at the boundary of the ϵCZ in the $\epsilon_{Exp,YY}^{KN1}(75)$ map (2.0 mStrain) (§ IV.3.2.2.1). It is noted that the definition used in this chapter used a lower ϵCZ threshold than the 2.9 mStrain used in § III.4.3.2; using that definition the ϵCZ extended 0.25 mm and 0.35 mm ahead of the notch for KN1 and KN2, respectively. However, the threshold used here was in-line with the abnormal step change in the DVC strains, so is most appropriate for the specimens.

The postulated ϵCZ was significantly larger than predicted for the KN1 specimen, but the radius of the postulated zone with more comparable to the major axis of the simulated KN2 ϵCZ (c. 1.3 mm). Graphically, the relative sizes of the ϵCZs was shown in Figure 135 and Figure 136. For the KN2 zones the shapes differ and the minor axis is less than the postulated radius. The different shapes and sizes of the ϵCZ between simulation and experiment resulted in the banding observed in Figure 135 and Figure 136. The implication is that the microstructure responds to a strain raising feature by distributing strains over a region as wide as if the feature were a 2 mm radius notch, and with an even greater area. While no evidence is available to test larger radii in these experiments, it would be assumed that this is only strictly true for $R \leq 2$ mm.

While the notch tip strains could not be measured by DVC, inside the ϵCZ strains were at a 'consistently' high level, though less than the maximum predicted value, and dropped down to the global level sharply outside the ϵCZ. The banded behaviour seen in Figure 135 and Figure 136 implied that the strains concentrations were more distributed in Gilsocarbon. With reference to the possible crack initiation criteria considered in Chapter III, it is conceivable that this locus (R_C = 1.28 mm, centred on the notch tip) could describe the necessary locus for an area- or volume-averaged criterion. No attempt was made to test this prediction, and it would be an important avenue for further work.

IV.4.3 Non-linear response

The ϵCZ is a phenomenon with length scale of approximately 3 mm. The sub-millimetre length scale can be examined. Considering only the loaded states, outside the ϵCZ the graphite did not behave as a purely linear elastic body but showed hotspots where unusual deformations occurred. By using the RBD uncertainty, the deviation fields of the loaded states were filtered to highlight statistical anomalies. The hotspot displacements were associated with filler particles and were bounded by hotspot strains which were generally contained within the filler particle boundary and often associated with significant pores.

Relative to the bulk, the filler particle cores therefore behaved as undergoing a rigid body motion. The regions were persistent between loaded states, with both the level of displacement and strain within them increasing with greater applied deformation and load. This suggests that the particles behaved in a non-linear manner, or at least a linear manner with a different stiffness, with a related non-linear response of the microstructure. There is insufficient data to be sure whether the filler particle response was linear. The volume fractions of the hotspot vectors (f_{Hot}) also increased, with the volume of individual regions growing at each load stage, and additional regions nucleating. In the volume roughly enclosed by the postulated ϵCZ, the two specimens behaved in a comparable manner, with the f_{Hot} increasing as an exponential-type curve with fractional load (Figure 147). No attempt was made to fit a functional curve, especially since the final state contains a field discontinuity in the form of a crack, where DVC is inaccurate. However, and speculatively, this behaviour might be analogous to a pore network reaching percolation due to oxidation, if it were due to, say, some form of microcracking which coalesced to enable the macro crack to grow.

Larger particles can and do contain larger pores, and these are typically lenticular voids at the particle periphery, or central voids of substantial volume. With no associated stiffness, it is conceivable that the shape and orientation of these pores could accommodate expansion with no deformation (pore opening) in a recoverable manner. The association of higher strains with the larger pores was observed by Joyce *et al.* [81].

IV.4.4 Damage (non-recoverable strain)

Residual deformations were observed on unloading, suggesting non-recoverable strains and hence non-elastic effects. As with the loaded states, the regions of non-recoverable strains were localised and persistent between sequential unloads with the volume fractions consistently growing with increasing peak load. Furthermore, the spatial correlation of the hotspots of non-linear deformation and non-recovered strain (from the load and subsequent unload persistence analysis) suggests that the filler particles were undergoing permanent deformation during load.

On average, the material within the postulated ϵCZ appeared to attain an average compressive strain at unload with $\epsilon \lesssim -\xi_{\epsilon,Corr,DVC}$, while the surrounding material to have residual tensile strains. For this state to exist with no applied load, either (1) the ϵCZ region must have permanently contracted, with no loss of (or a gain in) stiffness, or (2) the surrounding volume would have had to have undergone a volume expansion, compressing a relatively more compliant ϵCZ.

Determining a single mechanism that would explain this behaviour is nontrivial. For (1), the cause of volume contraction within the ϵCZ is unclear, having only been loaded in tension, and the strains cannot be permanent since large tensile strains were observed during subsequent loadings. In contrast, for (2), while permanent damage may have resulted in a compliant ϵCZ, a significant volume increase in material so far from the notch is harder to explain, and if the damage mechanism caused a volume increase, the ϵCZ should have been permanently in tension.

Previous authors have discussed the possibility of a permanent set in Gilsocarbon, where the residual strains from cooling combine with the mechanical strains to exceed the damage criterion. For example, in defining the NLE UMAT, Marrow *et al.* [88] described the onset of a bulk permanent set during initial loading stages of the graphite tensile and flexure specimens, and ascribed it to the significant residual elastic strains that relaxed (via micro-cracking) as tensile strains were applied. Barhli *et al.* [89] later attributed changing compressive strains in the wake of a propagating crack to the residual stress relaxation in Gilsocarbon, which may have directly affected the shape of the fracture process zone. Such a mechanism has been argued to result in an increased compliance of the damaged material, supporting (2). However, this would not explain the volume increase of the material outside the ϵCZ at low strains.

A speculative explanation may be that Gilsocarbon behaves as a particulate composite, with competing damage mechanisms which act independently in tension and compression. The filler particles and binder were shown to behave differently at load, with some evidence that the interface between the two phases is critical. For example, consider a three-phase deformable periphery model containing:

- The binder as a linear elastic foam (deformable, but unsusceptible to damage),
- The filler particle core as a rigid sphere (un-deformable and unsusceptible to damage),
- The filler particle periphery as a plastic shell around the core with a low yield strain, (susceptible to damage, permanently deformed).

On uniaxial loading, the binder stretches, the core location is shifted, and the periphery is stretched into an ellipsoid; appears as a localised tensile strain, around a hotspot displacement. Then on unloading, the periphery retains the deformed shape, but holding the surrounding binder in compression; appears as a localised tensile strain, adjacent to a compressive strain, with the displacement hotspot persisting. On loading to a higher peak load, the periphery deforms further; appearing as a larger, more tensile strained region.

Composites with phases of heterogeneous stiffness are subject to stress redistribution, where the maximum stresses are no longer transmitted uniformly; multiple filler particle cores would then have a stress shielding effect. On loading, two neighbouring cores, separated by binder, would shield one another, causing asymmetric periphery distortion, and protecting the intervening binder; appearing as two (asymmetric) tensile hotspot strains, with the surrounding binder relaxed (due to the periphery distortion), and intervening binder in tension, but to a lower degree than if the particles were absent. On unloading, the distorted peripheries compress the surrounding binder, which acts to compress the intervening binder. This behaviour would account for the extended tensile ϵCZ at load, and the compressive strain, with hotspots at unload.

This model is far from complete but has general agreement with the measured properties. There is no accounting for any permanent set. The binder did not behave as a pure linear elastic solid, since the macro crack will form eventually, and this was seen to pass through the binder in preference to the filler particles.

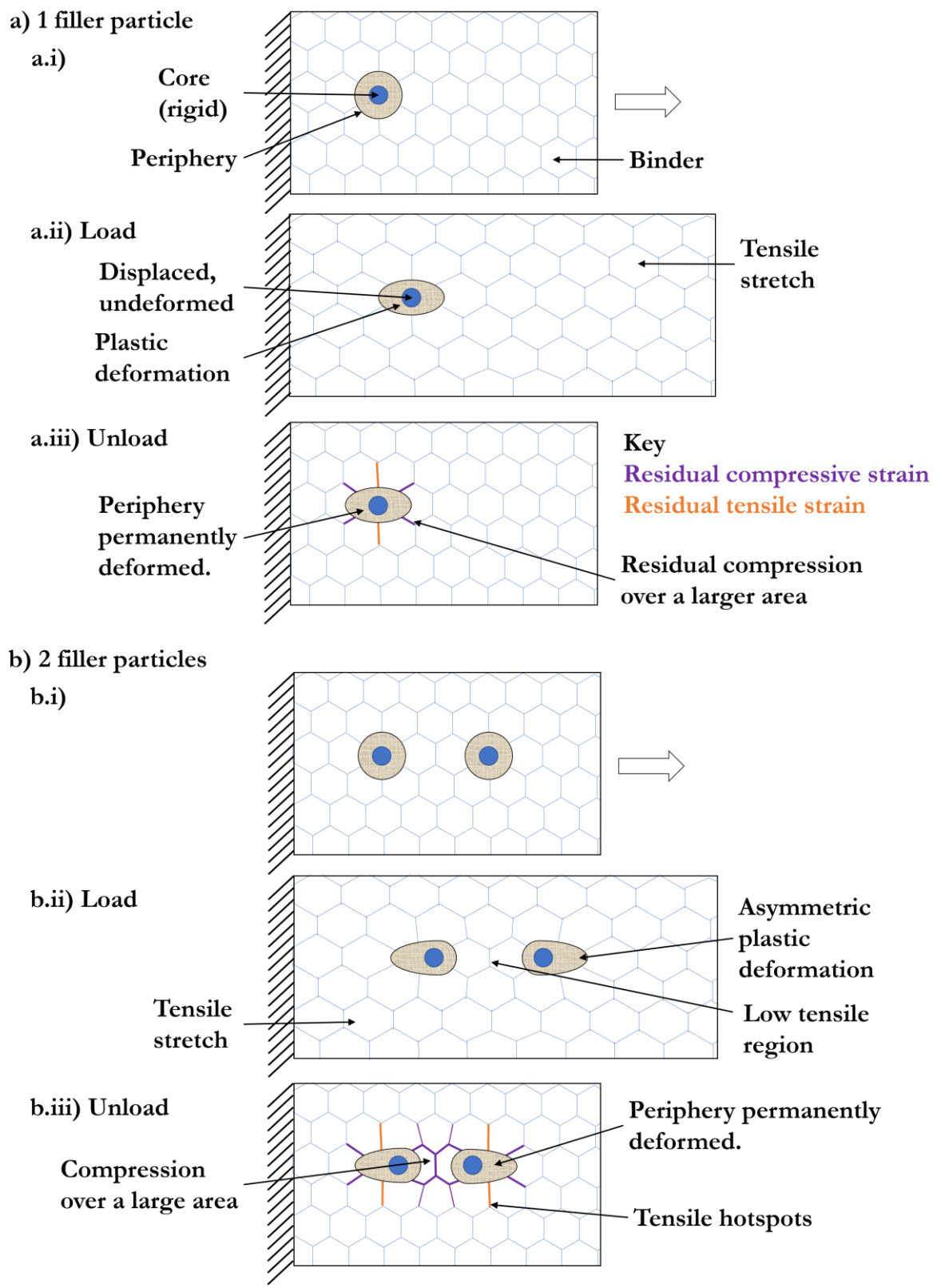


Figure 160: Three-phase deformable periphery model for Gilsocarbon damage.

IV.4.5 Implications for damage modelling

From the above arguments, the damage in Gilsocarbon can and should be considered at different length scales, though these mechanisms are not independent. Identifying the length scales to which each behaviour is relevant is important for simulating Gilsocarbon fracture initiation (and propagation).

At the submillimetre (filler particle) length scale it is necessary to distinguish between filler and binder. Between two phases the levels of crystallinity and crystal orientation are distinctly different, as are the associated pore structures. To generate the observed high-strain regions surrounding RBD behaviour of the filler particles, they should be modelled with the ability to deform the periphery without weakening their core – a 'soft shell' model, possibly mediated by extension of, or deformation around, the lenticular cracks. The binder phase should behave in a more linear elastic fashion and be capable of eventual fracture such that cracks can form between existing pores. The interface between the phases should accommodate some form of damage, for example microcracking, such that the apparent f_{Hot} fraction can increase in an exponential like manner. The majority of microcracks that might form must be subcritical for the material.

At the millimetre-to-centimetre length scale, regardless of the explanation for the origin of the compressive strains within the ϵCZ at unload, its persistence means that the ϵCZ may be identified as a FPZ. FPZs are formed in other plastic materials, when the damage generally acts to blunt or delay crack formation due to a rising R-curve. Typically, such a zone would grow with increasing load (until fracture) as the strain level increases and more and more volume of material is subjected to stresses beyond a yield stress. It is notable therefore that the FPZ was identified from the very earliest loading states with its final dimensions.

From the consistent form of the FPZ it is possible to explain the mechanism of virgin Gilsocarbon's notch insensitivity as follows. Under an applied deformation, strains concentrate ahead of a concave geometric feature. If $R \leq 2$ mm, an FPZ forms as though $R = 2$ mm. The heightened strains (and associated stresses and strain energies) are then distributed over the large FPZ, rather than concentrating at the notch tip. The average strain then continues to build with increasing load. Once the fracture criterion is exceeded, the crack propagates, and the strains are relieved in the ϵCZ; the ϵCZ is weakened to an extent that is no longer load-bearing.

To understand the relatively large statistical spread of the strength and notch sensitivity measurements in Chapter III, and join up the understanding of the sub-millimetre- and FPZ-scale observations, the distributions of the microstructural phases should be considered. The filler particles have a size distribution, are essentially randomly dispersed and have varying degrees of filler-binder interface; these properties combined explain the significant statistical spread in fracture properties outlined in Chapter III. The discrete nature of the phases means that the damage mechanisms do not operate in a connected fashion, but instead are activated as the stress pattern changes within the Gilsocarbon evolve. The bulk stress raising feature would continue to be a stress raiser, though less effective than in a brittle material. To properly predict crack initiation in virgin Gilsocarbon, a model would be required to realistically simulate the filler particle size distribution and spatial dispersion, and the different material properties of the binder and particle phases, which in turn would depend on the filler particle sizes. These simulations would be required to completely understand the notch sensitivity of graphite when measured in small specimens.

IV.5 Conclusions

The novel geometry of the keyhole notch specimens enabled loading by wedge-opening for specimens with three notch radii of 0.50, 1.00 and 2.00 mm. Eight specimens of each geometry were fractured with one specimen of each 1.00 mm and 2.00 mm radii were tested with *in situ* X-ray imaging, and particularly tomography, at the Diamond Light Source. From the tomography, internal displacements were mapped non-destructively, such that the behaviour could be compared to experiment-realistic finite element simulations to calculate deviation behaviour. The experimental strain fields were calculated, and an approximately circular strain concentration zone ahead of the notch tip was identified, that was shown to be significantly larger than the simulation predictions for the 1 mm notch but comparable to the 2 mm notch radius. The quantitative assessment of the deviation behaviour demonstrated hotspot regions at both load and unload, with a degree of persistence and which were qualitatively associated with microstructural features, notably the filler particles and the filler-binder interfaces. These hotspot deviations were attributed to one or more heterogeneous damage mechanisms that enabled the filler particles to accommodate significant deformations in a non-linear fashion with residual deformation on unloading. It was suggested that this behaviour enabled the Gilsocarbon to withstand greater deflections than a homogeneous brittle solid, with the range of filler particle behaviours acting to shield the binder from high straining, and thus minimising the damage to the binder phase. This shielding spread the strains over a large fracture process zone that was fully formed from early loading with a shape that was insensitive to notch radii below 2 mm. Understanding from these observations will inform modelling of crack initiation and inform the constraints for developing a notch sensitivity test using small specimens.

V Progress Towards a Notch Sensitivity Test

V.1 Assessment of challenges in implementing the general methodology

In Chapter I a general methodology was outlined for predicting the initiation of axial cracks due to the presence of stress raising features. A series of material science considerations were outlined for implementing such a methodology, including the need to develop a test suitable for AGR post irradiation examination for measuring Gilsocarbon's notch sensitivity behaviour. Having reviewed the available evidence for Gilsocarbon in Chapter II, a series of material-specific challenges were outlined in § II.6. This chapter will review the experimental and theoretical results presented in the previous two chapters, in the context of addressing those challenges. Potential methods of addressing these challenges, and the current progress towards them, will also be outlined.

The matrix in § V.1.1 briefly highlights the progress towards a method for resolving each challenge, limitations of the work to date and the outstanding understanding required. This list is intended to give the reader an idea of the remaining difficulties in implementing a reliable PIE test for notch sensitivity and is neither exhaustive nor prescriptive. Further detail on some of the outstanding challenges will be reviewed in § V.2.

V.1.1 Assessment matrix

For brevity, the challenges in the following table are reduced to keywords, and numbered (#1, #2 etc.) as in § II.6. The reader should refer to the full text in that section for further detail. In the matrix Roman numerals (II, III, and IV) refer to the related chapter, and alphabetic characters (a, b etc.) refer to the limitation notes.

Challenge	Progress	Comments on and limitations of presented work	Outstanding challenges
#1 PIE test constraints	Gross dimensions: Geometries constrained by extractable material, currently c. ϕ 19 x70 mm [II, III, a] Notch: Two significantly notch different geometries are required (e.g. notched and smooth, or different radii) [II, III, b] $a > 1$ mm [II] $0.5 < R < 2$ mm [IV, b]	a. A significant density gradient exists in these trepanned cores, modifying the properties, potentially further constraining specimen dimensions. b. Notch sensitivity was observed in virgin material for $R < 2$ mm. For $R < 0.5$ mm notch tip radius could not be guaranteed due to porosity. $R = 1$ mm seems a suitable compromise. To quantify changing behaviour a comparison must be made between relatively sharp and blunt notches; the blunt notch could be a smooth specimen as already used.	Analytical expressions for mechanical properties cannot be reliably applied to constrained test geometries with dimensions below recognised geometries. Advanced full field analyses should be used to identify anomalous behaviour until analytical expressions for small specimens, with potential test property gradients, are available and validated for Gilsocarbon.
#2 Prototype PIE test	Notched 6 x 6 19 mm beams were tested in flexure, with notch geometries varied [III, a] Specimen geometry: 3PB or 4PB appeared acceptable [II, III, a] $W > 6$ mm [III, b] $a/W < 0.5$ [II, III, c]	a. 4PB was used in III due to well-defined 'critical volume', and absence of compressive force ahead of notch. For $W = 6$ mm 3PB testing [98] the same complete notch insensitivity from was observed (all using the same reduced-ligament formulation) , though they were testing reactor extracted material, so this is not directly comparable. b. A size effect appears to constrain W for virgin specimens (compared to historical results) and low weight loss specimens (compared to larger parent specimens). It is unknown whether this is a smooth or discontinuous effect.	Use scaled sample testing to better understand the size effect in notched flexure (see § V.2). Determine whether any size effect is observed in radiolytically-oxidised graphite. No size effect might enable the use of the $W = 6$ mm tests consistent with current PIE.

Challenge	Progress	Comments on and limitations of presented work	Outstanding challenges
		c. Relative notch depth alters the interaction of the ϵCZ and neutral axis. For large specimens, a minima in sensivity may exist around $a/W = 0.3$, though evidence in Gilsocarbon is inconclusive. $a/W = 0.75$ was more sensitive than $a/W = 0.5$, but could not be satisfactorily analysed.	If larger specimens ($W > 6$ mm) are machined from trepanned cores, they would be cut with density gradients running along beam axis, potentially affecting flexural curvature.
#3 Obtain statistical data	Over 100 specimens from a single virgin billet were tested in 7 geometries, generating statistical distributions flexural failure forces [III, a, b] Failure stress distributions were extrapolated using LE properties [III, c] Notch insensitivity confirmed by statistical testing [III, d]	a. Due to lack of confidence in $a/W = 0.75$, analysis with full field techniques only considered 78 specimens in 5 geometries. This is still a statistically significant number of tests, suitable for comparison against future datasets b. Only statistical data for flexure was generated. c. The geometric relations enabled confident extrapolation for LE behaviour. This was not possible for non-linear formulations, hence only estimated properties rather than distributions could be made for the UMAT, limiting comparison with future datasets, especially due the numerical instability in the simulation. d. As noted for #2, the $W = 6$ mm geometry may be unsuitable, limiting comparison with future datasets.	Measure statistical distributions in other loading modes (see § V.2.1). Calculate stress (and other failure criteria, e.g. energetic) distributions for non-linear models.
#4 Measure brick-applicable multiaxial and multimodal behaviour	Keyway roots have a triaxial stress state (tensile hoop, compressive axial and a gradient of radial stresses), subjecting them to principally Mode I loading. Brick distortion might cause Mode III loading on its neighbours Measurements in 4PB, with tensile strain across notch [III, a]	a. Flexure with standard geometries is Mode I and results in unstable cracking. Centre-notched 4PB with $a/W \lesssim 0.4$ remains Mode I. Squat 4PB may be generate 'diagonal shear', which may be enhanced by notching. Heterogeneous microstructures may distort applied loading and accentuate certain modes e.g. increased shear stress. Deep notching ($a/W = 0.75$) was included as an attempt to introduce biaxial stresses where the notch crosses the neutral axis of a smooth beam (see also #2c). The deformation modes were defined by 2D boundary condisiton and the contact surfaces, so may not have fully captured the multiaxial and multimodal behaviour.	Small specimen testing of additional loading axes required, particularly focusing on biaxial stress tension-compression (see § V.2.1). Small specimen testing of additional loading modes required, particularly focusing on bimodal Mode I-III Small notched test geometries will need full-field 3D boundary condition volumetric strain analyses to fully identify modal states of loading (see § V.2.2).

Challenge	Progress	Comments on and limitations of presented work	Outstanding challenges
	Indentation-like measurements with tensile strain across notch [IV, b]	b. The Keyhole Notch (KN) geometry is principally a Mode I tensile opening, with a compression element.The Mode II displacements were also captured realistically, but Mode III variations could not be applied. While the deformations were accurate, the compressive loads were poorly reproduced by simulation. This was probably due to the inadequate material response definition (linear elastic), but may also reflect the multimodal behaviour. Cracking was stable, with no neutral axis interaction.	
#5 Measure mechanical properties, crack initiation criteria of individual phases	The multiscale analysis approaches allowed high-resolution imaging of the microstructure A heterogeneous response was observed, with the filler particles showing potential biphase properties with the periphery and filler-binder interface deforming independently of the core [IV, a]	a. Phases could only be assessed in intimate contact and not independently, such that the responses were constrained. b. Behaviour attributed to filler particles and binder qualitatively. A robust mechanism to identify filler particles tomographs would allow quantitative association of the properties.	Microscale experiments might be able to interrogate properties of indiviual phases, but isolating the phases without causing damage would be nontrivial. Furthermore, the highly connected pore structures which extend throughout the bulk would be necessarily reduced. Algorithmic identification of filler particles and association with measured behaviours (see § V.2.3). Effective insight might be gained from further volumetric Deviation analysis (see § V.2.2).
#6 Identify phase interaction mechanisms and critical length scales	LEFM was insufficient to predict strain and stress behaviour [II, III, IV] NLE simulations predicted formation of a notch-tip dependent ϵCZ of up to 0.5 mm 'radius' [II, III, IV, a]	a. The only non-linear elastic (NLE) model used was Barhli *et al.*'s UMAT, which while specific for the billet, modified only the Young's modulus (not the entire stiffness tensor), was reversible ('damaged' material could recover its stiffness at later stages), and resulted in numerical instabilities that prevented the simulations achieving the correct deflection. As such the predictions from the UMAT simulations were under-deformed. Nevertheless the presence of a broadened ϵCZ as a result of the degrading stiffness was qualitatively predicted.	Make further observations of the interaction mechanisms through further investigation, both empirical and simulation. Testing of analogous materials could be insightful, but would require careful construction to ensure the correct mechanisms were replicated.

Challenge	Progress	Comments on and limitations of presented work	Outstanding challenges
	Qualitative image analysis indicated the presence of a FPZ, with dimensions greater than the simulated ϵCZ [IV, b] Strain analysis suggested formation of an FPZ ahead of the notches [IV, c]	b. The ϵCZ at load was postulated as a circular locus centred on the notch tip with R_0 = 1.28 mm, much larger than the region ahead of the 1 mm notch predicted by LE, and more circular than the 2 mm notch prediction. Limited evidence suggested that the definition was consistent for a crack. The ϵCZ was defined based on analysis of only two specimens, one of which had severely degraded tomographs. c. As the same ϵCZ was observed at unload, this was identified as non-recoverable strain within an FPZ, and sugested an energy dissipating and crack blunting was active. The origin of the compressive strains at unload was unresolved.	Validate the presence of the FPZ and its invariance to notch radius for $R < 2$ mm through further fracture testing with *in situ* volume imaging
#7 Identify the critical path for failure	The identification of a significant FPZ indicates microstructural interactions capable of absorbing energy and blunting cracks [IV] Filler particle periphery and interface failure appears to be important to bulk crack initiation and interface [IV] A notch radius independent FPZ could explain the notch insensitivity of Gilsocarbon [III, IV, a, b] A theory for filler particle deformation and interaction was outlined [IV, b]	a. A notch radius independent FPZ is an important result, and could provide a clear explanation of the limited notch sensitivity of Gilsocarbon below the R = 2 mm limit. However, no larger radii samples were tested to validate that the FPZ dimensions change above this limit. b. In the context of the notch geometry critical SED, the FPZ radius (1.28 mm) was approximately half the SED ROI locus (2.0 mm for plane strain). It is possible that using this radius for critical SED could be an appropriate criterion for crack initiation. This hypothesis could not be tested against either the notched beam or KN specimens due to the lack of DIC data in this region and/or the identification of failings of the material models used for simulation. b. This theory relies on the filler particles having a two phase nature and acting to stress-shield the intermediate binder phase. The theory is oversimplified and requires further definition. No account is made of pore shapes and sizes, or multi-axial, or multi-modal response.	Demonstrate the FPZ dimension notch radius independence through futher fracture tests with large radius notches. Identify a consistent FPZ and notch sensitivity effect in other loading geometries through further fracture testing with *in situ* imaging. Confirmation or disproving the notch geometry critical SED would be a valuable result, but requires accurate strain data adjacent to the notch tip, ideally in 3D. Application of the postulated theory would require further definition and testing against empirical data. The different phases could be simulated empirically using 'ideal material' composites, eg stiff foam for the binder.

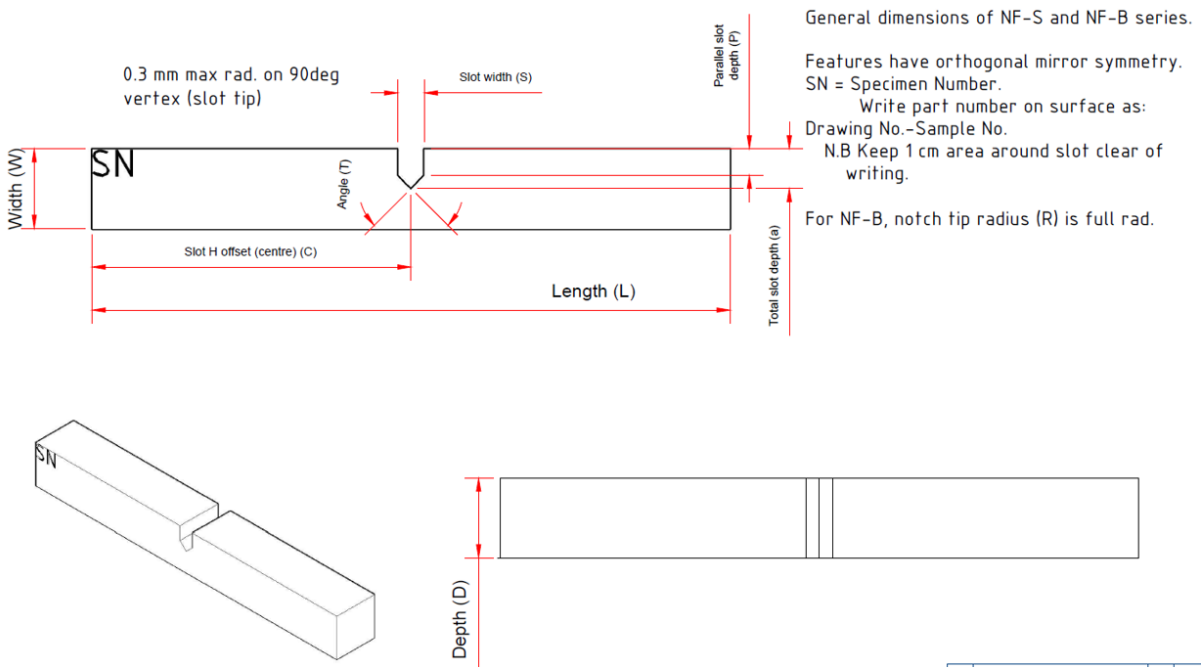
Challenge	Progress	Comments on and limitations of presented work	Outstanding challenges
#8 Develop a microstructurally-realistic and scalable simulation	Understanding of the interaction of the phases, and understanding of the critical path for fracture initiaiton is a fundamental basis for fracture simulation [IV] Detailed datasets (either volumetric or statistically) provide validation cases for simulations [III, IV, a]	a. An accurate simulation must be able to predict both small specimen results and axial cracking in the bricks, or else have a size limit defined on the application. To be a suitable model for all scales, the $W = 6$ mm notch insensitivity, and $W > 12$ mm limited sensitivity must be predicted, otherwise the results cannot be translated from the PIE test to the reactor.	Develop a model capable of statistical predictions with sufficient fidelity to simulate the individual phases, including filler particle breakdown, and yet simulate multiple bricks in reasonable computation time. (see § V.2.4).
#9 Determine expected behaviour in nuclear environment	If applicable lengthscale for notch sensitivity is FPZ radius, significant oxidation might lessen the filler particle interaction [IV, a]	a. In a speculative assesment, any residual strains from manufacture would be relieved early in reactor life. Prior to turn around the bulk shrinkage would reduce the FPZ dimension, potentially increasing notch sensitivity. After turn around, when the binder is preferentially oxidised, the physical connection between the filler particles would lose stiffness (absolute, and relative to the particles) and eventually disintegrate. The change in effective notch size and radius due to surface contacting porosity will be ignored. With less binder, filler particle distortion, if still active, would be less prevalent and the material would be less able to dissipate strain energy. The likely result is persisting notch insensitivity, but due to a different mechanism.	The complexity of the response in virgin material, and complications due to the nuclear environment, require 3D volumetric analyses. It is necessary to ensure that analysis techniques remain valid for irradiated and oxidised material. Significant changes could degrade DVC accuracy, and this should be checked before any fracture testing commences (see § V.2.2).

Challenge	Progress	Comments on and limitations of presented work	Outstanding challenges
			Measuring trends in notch sensitivity behaviour of reactor-extracted material requires: sufficient monlithic volumes of material that are suitable for maching machining into the required geometries; multiple geometries for testing different loading configurations and modal behaviour; a sufficient number of specimens to generate statistically relevant results across the dose-weight loss envelope; and sufficient analytical detail to understand the behaviour.
#10 Refine test for industrial application	From the prototype test the requirements for a PIE test have been refined, and a potential comparison dataset for virgin material created [III, a]	a. The principal limitation is avoiding any size effect due to $W = 6$ mm, but also the benefits and limitations of 3PB versus 4PB, or in the use of flexure, as outlined above	Demonstrating that any technique arising from solving the above challenges is industrially viable in terms of remote handling and set up, robust analysis protocols and clearly defined thresholds for pass and fail behaviour, or use of the calculated properties in simulations.

V.2 Size effect tests in notched four-point bend

The notch geometry study in Chapter III used squat four-point bend geometries, that would be incompatible with industrial-standard specimens. Compared to historical testing, a size effect was indicated. For other PIE tests, such as strength, the scaling effect is known to be continuous, and may be compensated for using an appropriate correction factor. For this approach to be valid for notch sensitivity specimens using the 6 x 6 x 19 mm beams, it would first be necessary to demonstrate whether the effect is continuous or discontinuous with reducing dimensions.

Designing a suitable size effect study requires scaling from recognised geometries down to the small-specimen geometry proposed. Scaling could be linear, volumetric or elsewise. Since notch insensitivity is not observed for large radius notches, the specimens in Figure 161 are proposed for a future study. The largest beam proposed is 24 x 24 x 192 mm and would be compliant with ASTM C651 (as a smooth beam), for a graphite with a 1 mm microstructural scale. The proposed notch tip geometries are consistent with the small half-depth notch geometries. For the other geometries (except the squat beams already tested) all other dimensions are scale linearly, with the scaling factor reducing to a 6 x 6 x 48 mm slender beam. Each geometry would be tested with a complementary smooth beam from which the NSF and notch sensitivity factors would be calculated.



W, D	[mm]	24.00	12.00	6.00	6.00
L	[mm]	192.00	96.00	48.00	19.00
a *(a/W = 0.5)*	[mm]	12.00	6.00	3.00	3.00
a *(a/W = 0.75)*	[mm]	18.00	9.00	4.50	4.50

Figure 161: Proposed flexural geometries for studying the potential size effect associated with small beam (6 x 6 x 19 mm) notch sensitivity.

V.2.1 Statistical distributions from other loading modes

To extend the understanding from the small sample beams in Chapter III to further loading modes, a double ligament edge notched tensile, DLENT, geometry was designed. Plate samples were double notched symmetrically, with separate ligaments using the same notch geometries and *a/W* ratios as the small beam testing, as shown in Figure 162. As with the small beam tip geometries, the intention was to measure both uniaxial and biaxial stress concentrating effects. Preliminary LE-FE simulations (see § A3) suggested that the stress profile ahead of the deep notches (from the notch tip to the 'lozenge face') would be significantly altered, with increasing biaxial behaviour, summarised as:

1. For a given a/W, at any distance ahead of the notch > 0.005 mm, the stresses are higher ahead of the blunt geometry in both the loading and transverse directions
2. At a given distance, the stress range covered by the blunt geometry is broader than for the sharp geometry
3. The peaks of transverse stress curves are always nearer the notch tip and show less variation in peak stress for the a/W range than the blunt
4. There is no compressive stress parallel to the loading direction along this path for $a/W < 0.6$, whereas for larger a/W the back face is under increasingly strong compression

Samples were machined from the same Gilsocarbon billet as used throughout this thesis, as well as the machinable ceramic Macor® and the filter carbon PC45. Macor® is very fine-grained with zero porosity and fails in a linear elastic brittle fashion. PC45 is a highly porous carbon with non-linear failure behaviour. Three Macor®, and eight Gilsocarbon and PC45 specimens were machined in each geometry, and tested to failure using pin mountings to ensure alignment as in Figure 163. A similar three-camera imaging set-up was used as in Chapter III. The normalised failure load distributions are shown in Figure 164. Due to out of plane movement, high-resolution DIC was not possible, and efforts are ongoing to extract usable boundary conditions for finite element simulation for comparison.

Taking the Macor® data as the definitive response, the sharp notch failure loads were c. 70 % of the blunt notched specimens, and the smaller ligaments failed at loads c. 35 % of the larger. The half-depth notches in Gilsocarbon had similar behaviour to the Macor®, but the smaller ligament was insensitive to the notch radius. For the blunt notches, the strength was comparable to the relative reduction in the Macor®. The more porous PC45 had similar median values to the Gilsocarbon but showed greater scatter. The relative reduction for the smaller ligaments was greater, and instead was comparable to the reduction seen for the Macor® sharp tip sample with $a/W = 0.75$.

The consistent change in the Macor® with notch radius supports the designation as a notch sensitive material, which is relatively insensitive to biaxial stress. The radius insensitivity of Gilsocarbon with a small ligament is in line with the flexural behaviour, but the comparable sensitivity of Gilsocarbon with $a/W = 0.5$ deserves further investigation, as does the cause of the change in apparent behaviour. The more porous PC45 was perhaps more susceptible to the biaxial stress, but further experiment and simulation work would be required to properly understand this behaviour.

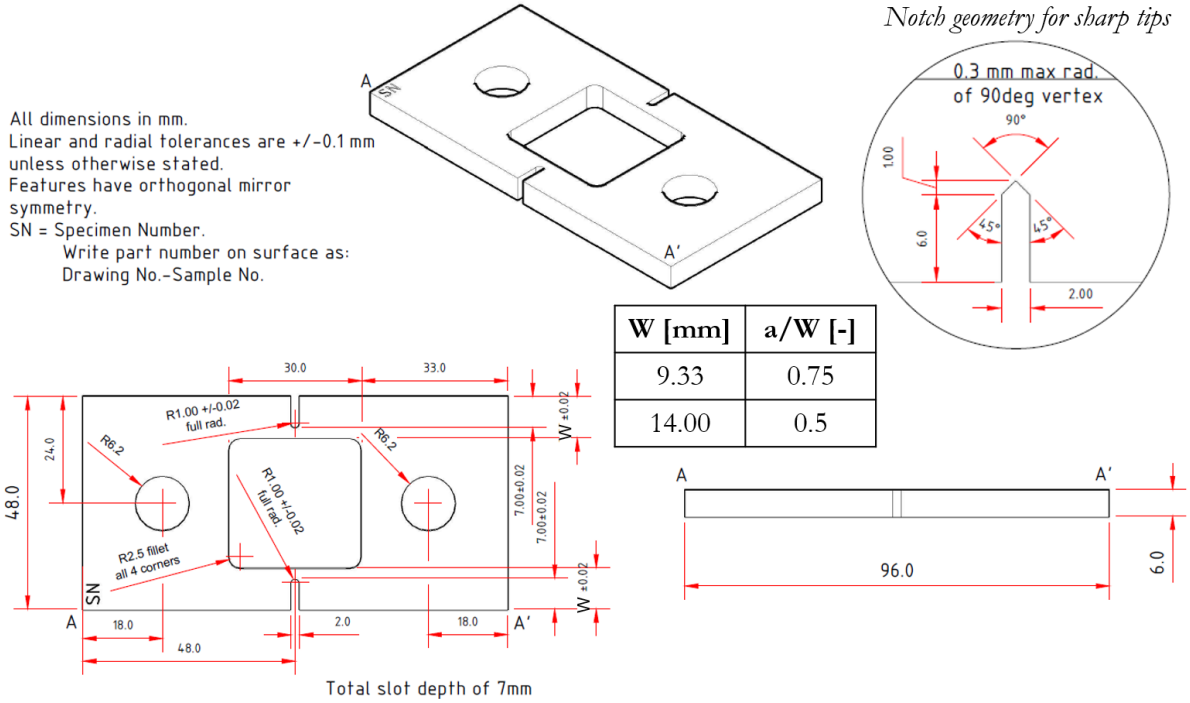


Figure 162: Double ligament edge notched tensile, DLENT, geometry, with notch variables of W (see inset table) and tip geometry of either full-radius blunt or 90° V sharp (see inset).

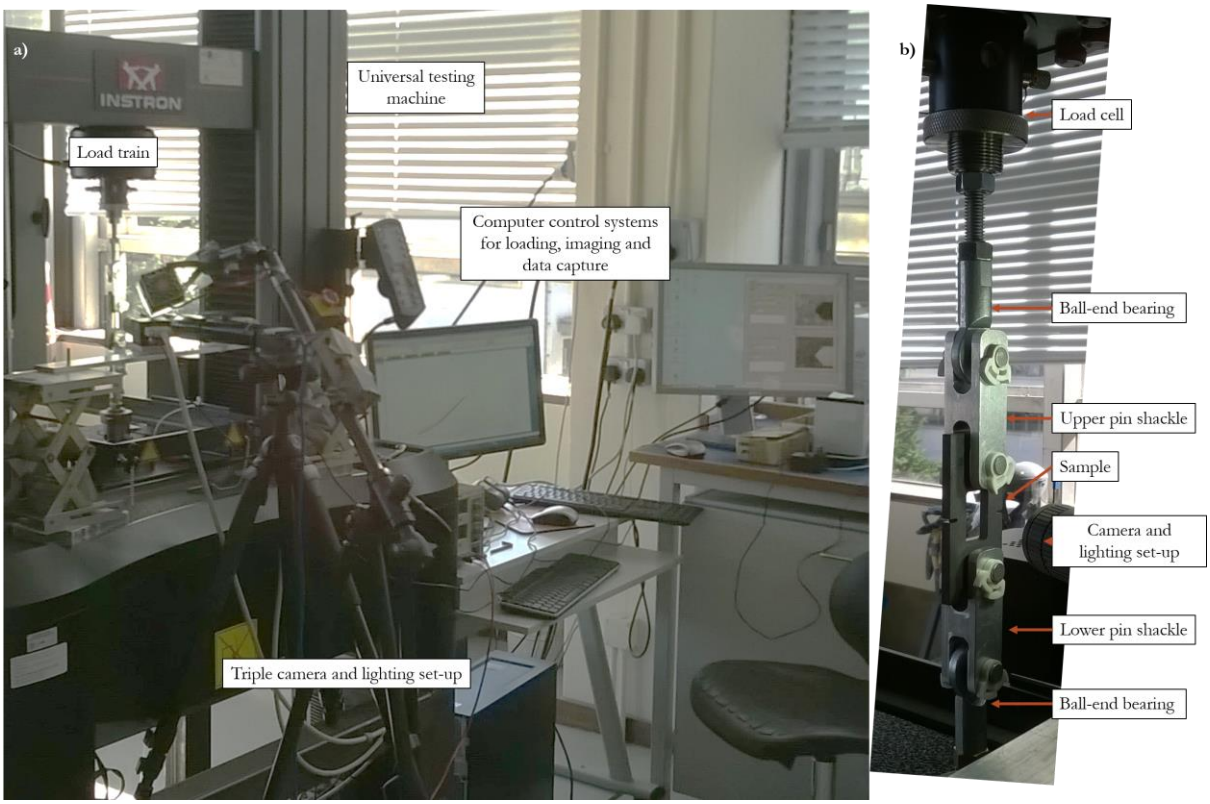


Figure 163: Loading and imaging setup for the DLENT sample testing: (a) around an instream universal test machine a three camera (a Toshiba Teli stereo pair, and Grasshopper 3) and lighting system were arranged with dual computer control to image the sample contained in the load train (b) comprising the load cell, a pair of ball-end bearings and clevis pin shackles such that the samples were loaded in pure tension.

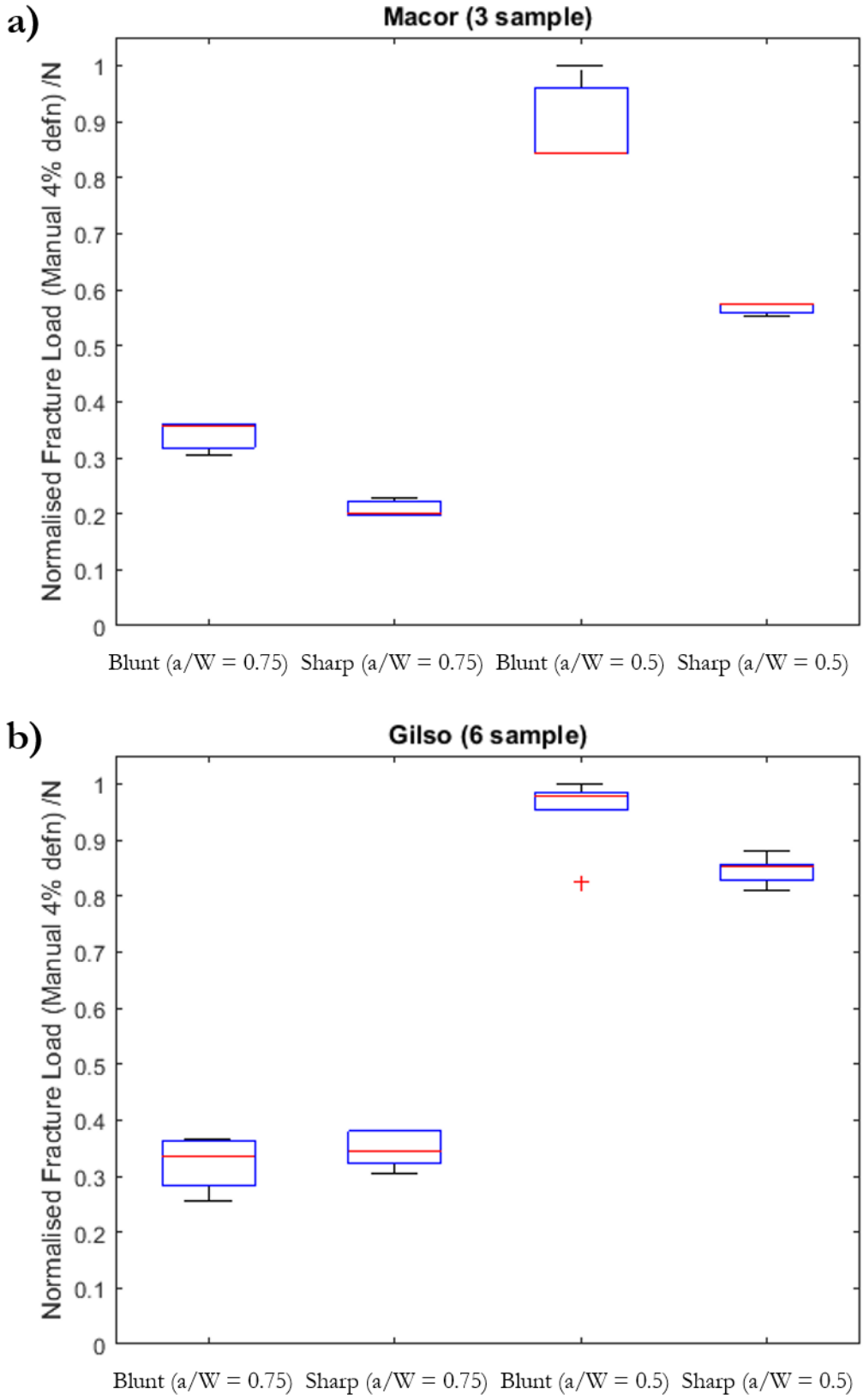
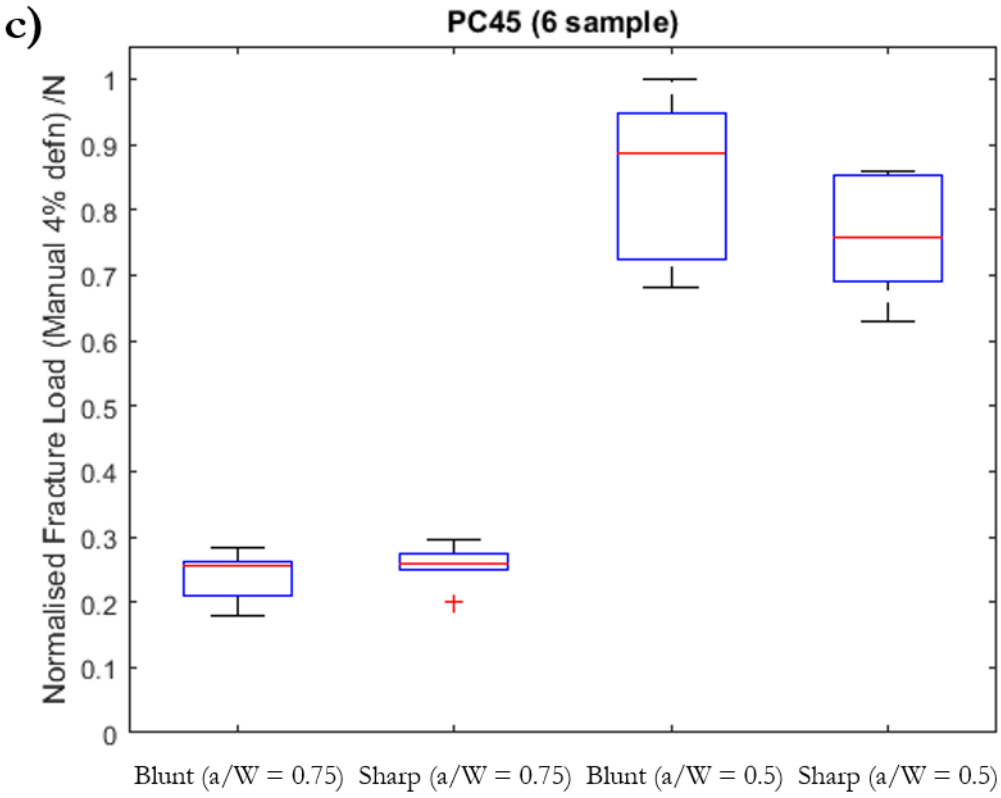


Figure 164: Normalised fracture load distributions for the DLENT specimens (normalised relative to the maximum load in each material) in the three materials: (a) Macor (3 specimens per geometry), (b) virgin Gilsocarbon (6 specimens per geometry) and (c) PC45 (6 specimens per geometry). The median is indicated by the red line, the blue box indicates the interquartile range, the whiskers show the extent of the data within c. ± 2.7 standard deviations of the median (wider than used elsewhere in this thesis), and outliers are indicated by crosses.



Continued: Figure 164: Normalised fracture load distributions for the DLENT specimens (normalised relative to the maximum load in each material) in the three materials: (a) Macor (3 specimens per geometry), (b) virgin Gilsocarbon (6 specimens per geometry) and (c) PC45 (6 specimens per geometry). The median is indicated by the red line, the blue box indicates the interquartile range, the whiskers show the extent of the data within c. ± 2.7 standard deviations of the median (wider than used elsewhere in this thesis), and outliers are indicated by crosses.

V.2.2 Full field 3D boundary conditions volumetric analyses

To compare full-field empirical strains with simulations, as in the Deviation technique, it is vital that the simulations accurately reflect the experimental loading. In Chapter III the finite element simulations were fitted using a trial and error approach to match a profile relying on multi-body contact definitions. In Chapter IV two-dimensional boundary conditions were calculated directly from experiment data and used as input data for a 3D model. This approach was an improvement on the multi-body contact, but the reduced dimensionality meant that out-of-plane motion was unconstrained. A more complete simulation would take three-dimensional boundary conditions from the periphery of a DVC analysed body, and put these as finite element boundary conditions, and compare the behaviours in the central region of interest.

To demonstrate the use of XCT-derived full field boundary conditions, the tomography data captured as part of the experiments in § A1 was analysed with DVC. The displacements of the vectors in half cylinders (of radius 2 mm) beneath the inner rollers and planes either side of the notch were smoothed and set as boundary conditions in the notched beam simulation shown in Figure 165. The outer rollers were outside the tomograph region, hence the definition on planes either side of the notch. Excellent agreement was seen between the displacement maps for the simulation and empirical data, Figure 166. Further analysis of this data will seek to complete the deviation fields in order to identify strain concentration behaviour, the heterogeneous response and confirm the presence of a radius-independent FPZ.

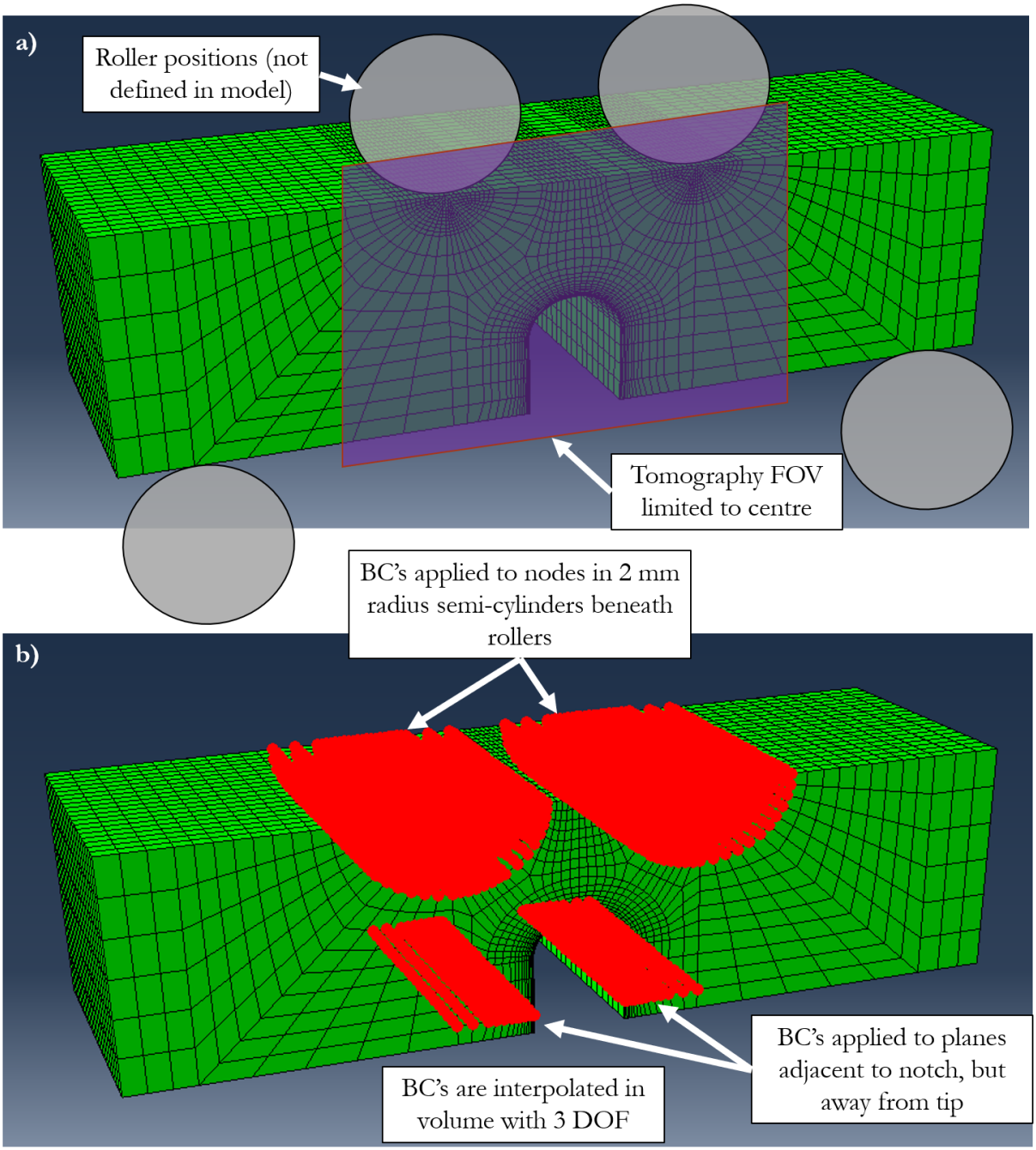


Figure 165: FE model definition for analysing the four-point bend tomography data in § A1, using boundary conditions (BC's) derived from DVC with three degrees of freedom. The geometry and mesh are shown in (a) indicating the position of the rollers and the approximate tomography field of view. In (b) the nodes on which the boundary conditions are applied (beneath the rollers and adjacent to the notch) are shown.

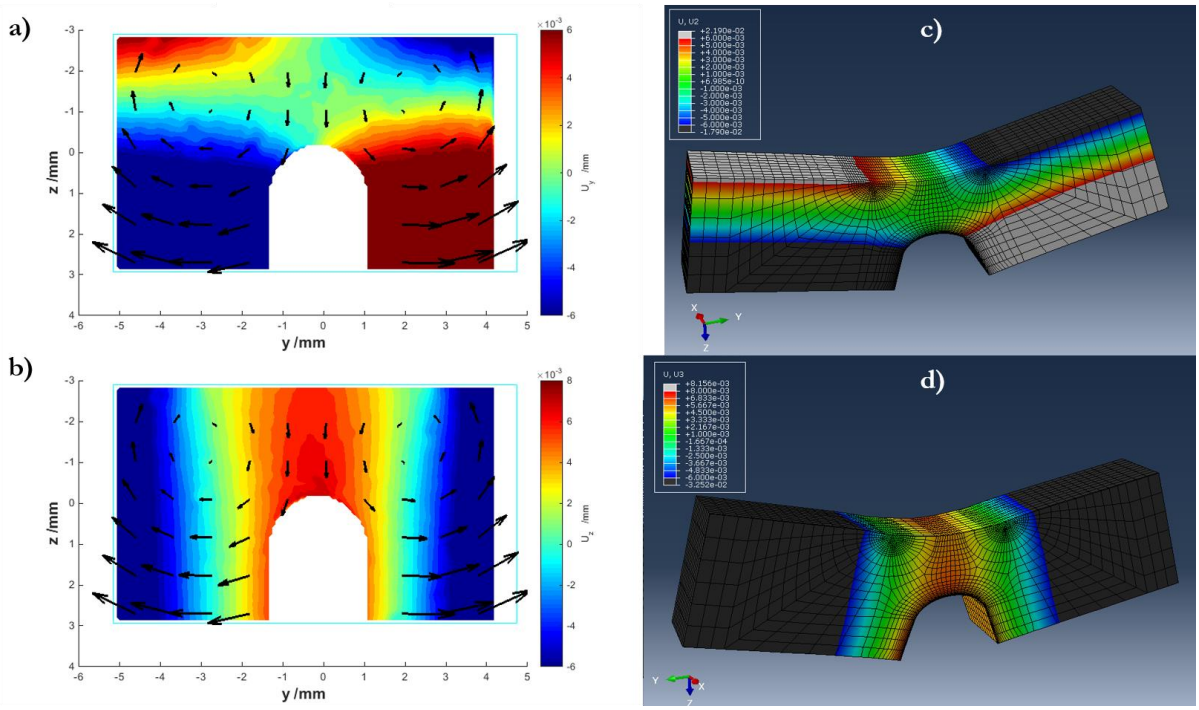


Figure 166: Empirical and simulated displacement responses of the half-depth blunt notch beams tested in § A1, showing good qualitative agreement: a) Uy from DVC, b) Uz from DVC, c) Uy from LE-FE, b) Uz from LE-FE.

V.2.3 Filler particle identification

To confirm that the peak hotspot deviation strains are truly attributed to the particles, a statistical comparison is required, to compare the locations of all the filler particles and all the hotspot strains. Filler particle segmentation, separate from the binder, is a computationally-difficult problem due to the lack of contrast difference between the two phases and the wide-ranging pore structures. Particles may be identified manually, but this is time-consuming and somewhat subjective. Vertyagina and Marrow [75] used a manual segmentation approach to isolate filler particle and binder from the KN1 tomograph in Chapter IV and applied a fractal-based assessment to identify the filler particles (see Figure 167). Reasonable results were achieved in both the virgin and radiolytically-oxidised states. Comparing this dataset with the hotspot deviation strains would be an insightful further work.

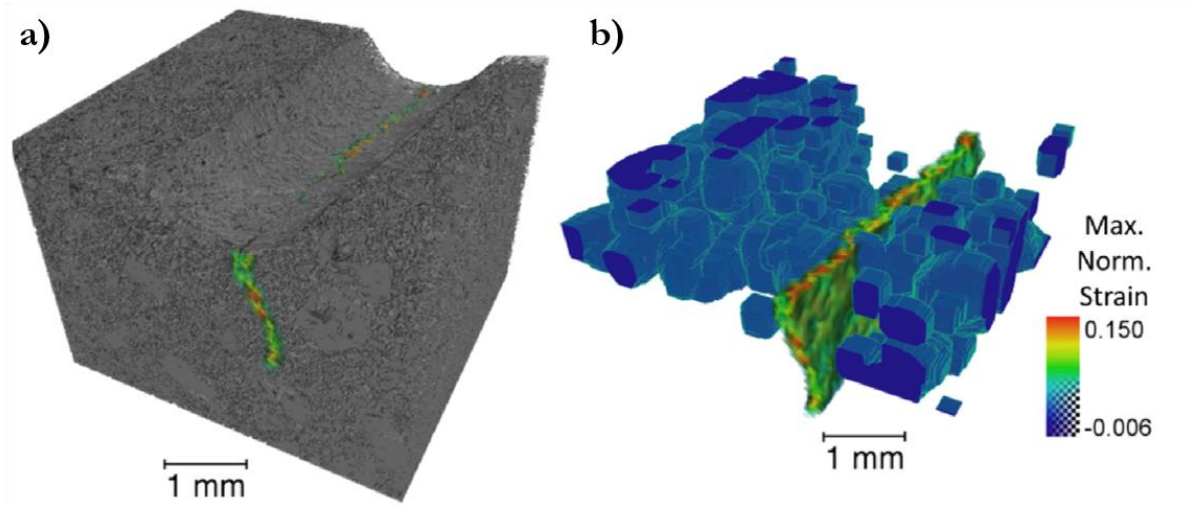


Figure 167: Using a multi-fractal formulation Vertyagina and Marrow segmented the KN1 tomograph(a) to identify the filler particles in (b), and compared this to the crack profile isolated by DVC maximum normal strain. Reprinted from [75] with permission from Elsevier.

V.2.4 Multi-scale simulation of Gilsocarbon crack initiation

In § II.5.2.2, the CA-FEMME model was identified as a potential multiscale model that incorporated statistical distributions of fracture prediction. L. Saucedo-Mora applied the CA-FEMME approach to solve the FE models defined in Chapter IV, using a random distribution of filler particles and porosity that matched real-world distributions. Under the experimental boundary conditions, crack initiation was simulated (see Figure 168). In the stages prior to fracture, disperse localised 'damage' was observed. These regions joined up to form a macroscopic crack with a feasible crack path. This type of multiscale simulation is an important stage in developing a scalable simulation for predicting axial crack initiation.

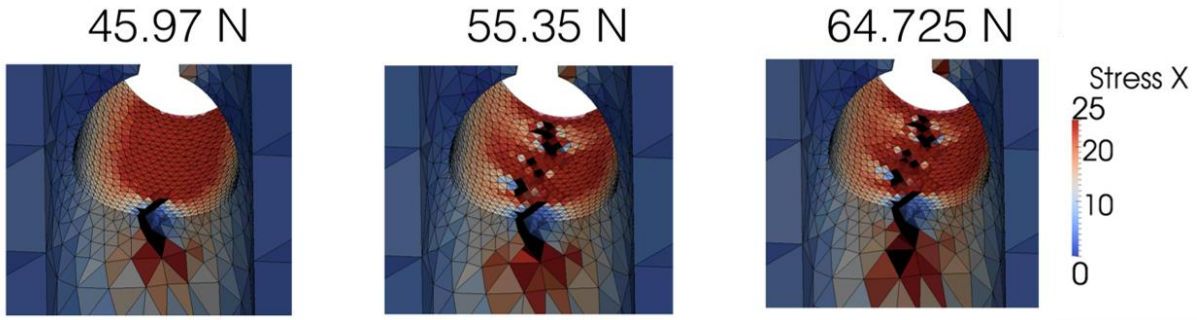


Figure 168: Predictions for fracture formation due to isolated damage coalescence simulated using the CA-FEMME approach applied to the (full symmetry) simulations created for the KN2 sample, with experiment realistic boundary conditions. Image courtesy of L. Saucedo-Mora.

V.2.5 DVC sensitivity dependence on oxidation

Combined volumetric imaging and 3D analysis of the small specimen fracture tests has been a vital tool in understanding the behaviour. To ensure this behaviour is consistent with radiolytic oxidation, or understand any differences, it is necessary to first verify that the techniques applied here can be applied to the degraded material. Progressive radiolytic oxidation opens the pore structure which could make detection of features more difficult at high weight losses.

A preliminary study was conducted, to verify that the sensitivity of XCT-DVC remains viable for *in situ* studies. Six PIE samples (of 6 mm square cross-section) from the Hinkley Point B and Hunterston B sister stations were selected covering the weight loss range w = [9, 40] %. For each specimen a pair of active sample X-ray tomographs were captured with a 50 µm rigid body displacement, at a resolution of 2.98 µm.voxel^{-1}. Example slices of the virtual microstructures are shown in Figure 169, clearly showing the preferential oxidation of the binder by the coarsening of the equiaxed pores. A DVC sensitivity study using the FFT algorithm was conducted, similar to that described in § IV.3.3.1. The sensitivity curve is plotted in Figure 170, along with the curve for the 3.24 µm.voxel^{-1} beam specimen XCT-imaged at the DLS in § A1 (see also § V.2.2).

No degradation of DVC sensitivity was observed with progressive oxidation. Conversely, the curves become flatter suggesting a better detection of the small features, with no significant loss of sensitivity to the large features. The improved small feature sensitivity is possibly due to the preferential oxidation of the small pores that were below the X-ray tomography limit in the virgin material. XCT-DVC is therefore a viable method for studying the damage mechanisms in radiolytically-oxidised graphite, at least to moderate weight losses.

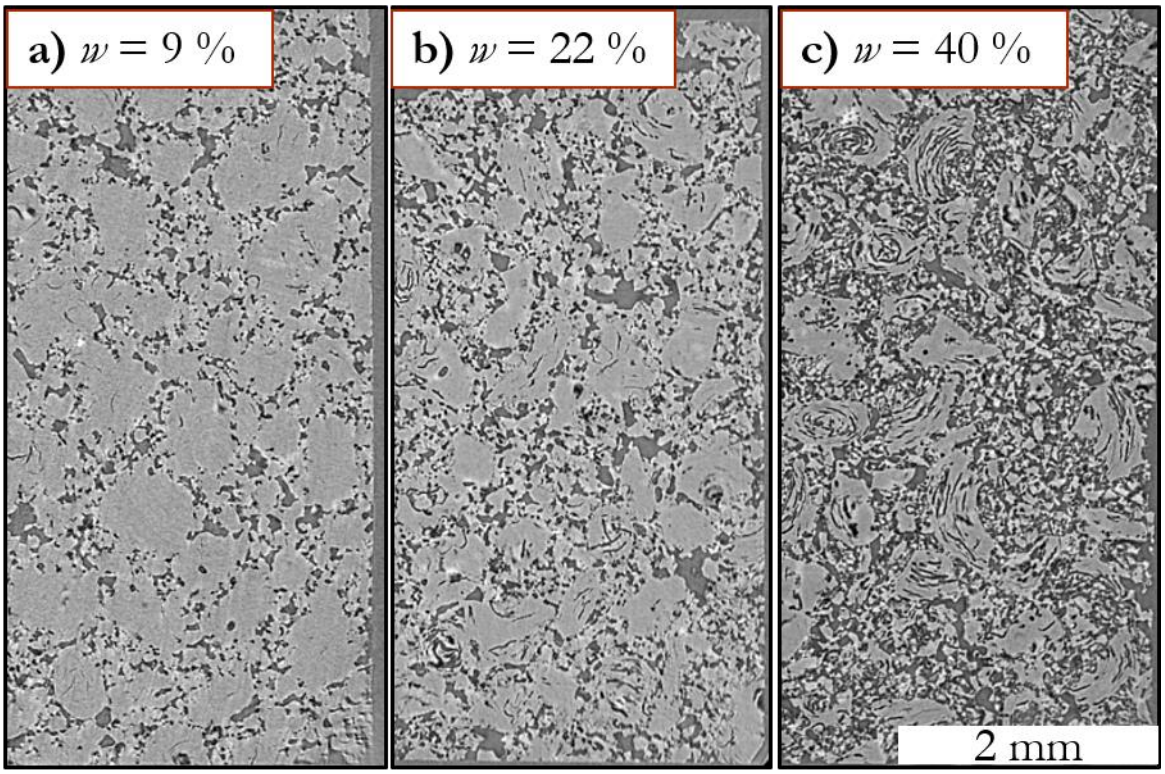


Figure 169: Example slices of virtual microstructure from XCT imaging of radiolytically-oxidised Gilsocarbon (from Hinkley Point B and Hunterston B stations) with weight loss increasing from (a) w = 9 % to (c) w = 40 %. Images are cropped to a 3 × 6 mm with a sample edge included to indicate the surface quality.

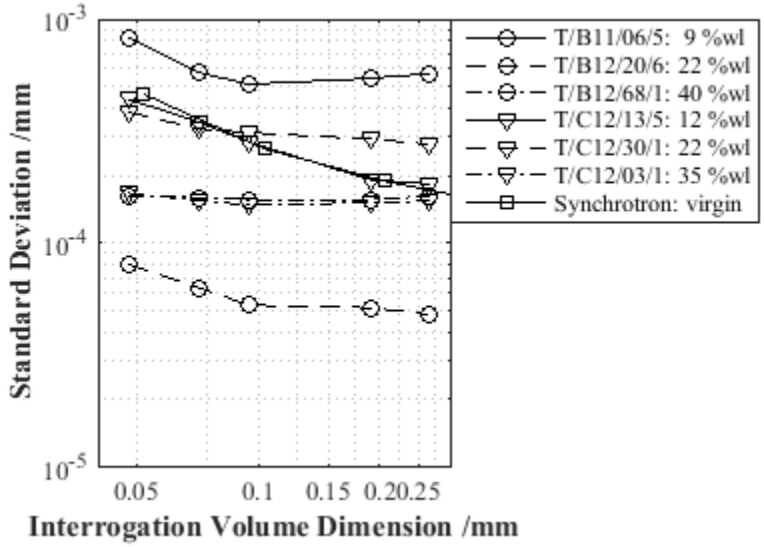


Figure 170: XCT-DVC sensitivity analysis of reactor extracted Gilsocarbon with weight losses up to 40% (from Hinkley Point B, coded T/B, and Hunterston B, coded T/C) and the virgin sample XCT-imaged at the DLS in § A1.

V.3 Summary

This thesis has considered how the response of nuclear graphite to stress concentrations might be measured, to build further confidence in the predictions of axial crack initiation. The focus has been addressing the material science challenges in developing a suitable PIE test method for notch sensitivity. Firstly, historical results related to stress concentration and notch sensitivity in industrial graphite were reviewed. These results indicated the complexities in measuring the properties of Gilsocarbon, especially once it is subjected to fast neutron irradiation and radiolytic oxidation. A small specimen PIE test based on notched 6 x 6 x 19 mm beams was prototyped, and virgin material was tested in four-point bend, with over 100 beams machined with seven different notch geometries.

Full-field measurements were collected based on multi-scale, multi-camera *in situ* imaging. Digital image correlation and finite element simulation was used to calculate the stress, strain and energy states of the specimens at fracture. Stress and energy-based approaches to considering the fracture criteria and notch strengthening effect were evaluated, including calculating the notch strengthening factors and strain energy density. Using historical analysis methods of calculating notch strengthening factors from a reduced-ligament formulation that assumed linear elasticity, a relative insensitivity to notch radius (from 0.05 mm to 2.00 mm), and the effect of notch depth (up to 4.5 mm) were demonstrated. Compared to the historical results, the 6 mm samples were shown to underestimate notch sensitivity. Furthermore, it was shown that linear elasticity and the reduced-ligament theories were deficient, and a non-linear material model is required. A non-linear elastic model, previously fitted to Gilsocarbon's empirical behaviour, was tested with predictive success, though not fully evaluated due to numerical instability in the simulations. Additionally, consistent behaviours were shown between the SED measurements from simulation and DIC, despite incomplete empirical data. These are important results in the development of PIE techniques and raises the potential for the real-time monitoring of graphite components. The heterogeneous behaviour of the microstructure was characterised by utilising *in situ* volumetric imaging during crack initiation. By further combining multi-scale image correlation and simulation, the presence of sub-millimetre heterogeneous behaviour of the microstructure was demonstrated to deviate from the predicted linear elastic response. A non-linear non-recoverable stress-strain response was observed, with deformation due to residual strains identified and associated with microstructural features. Furthermore, the formation of a strain concentration zone – extending over several millimetres – was argued to be the origin of the insensitivity of Gilsocarbon to notch radii less than 2 mm.

A significant degree of progress was therefore shown in addressing the material science challenges in developing a PIE notch sensitivity test. The outstanding challenges and potential future work were also identified. From the work presented in this thesis, the requirements for a suitable PIE test have been outlined and constrained, and significant advances in understanding the crack initiation processes in Gilsocarbon have been achieved.

VI Appendices

A1. Determining the minimum number of short beam specimens

To determine whether a notch tip geometry impacts on the crack initiation in a specimen, a sufficient number of specimens in each geometry must be fractured, such that the distributions in the measured properties belong to demonstrably different populations. The combination of Gilsocarbon's inhomogeneous microstructure and the experimental errors results in property distributions that may mask underlying effects. It is necessary to exclude results that are false positives (identifying a trend where none exists) and false negatives (failing to identify a real trend) from the analysis. The geometric properties of interest were notch tip geometry and notch depth. Notch depth is a continuous property, but tip geometry depends on not only the tip radius, but also the notch width and tip shape (sharp or blunt); it was considered as a discrete variable. To accommodate these two types of variable, the required number of specimens was estimated using two methods: by Student's t-test and a linear regression analysis.

Experimental

Six of each the half-depth sharp and blunt specimens were prepared for the Preliminary testing, with specimens labelled SS# and BS#, respectively. The loading geometry was identical to the main series testing ($2l_{in}$ = 5.33 mm, $2l_{out}$ = 16 mm, ϕ 4 mm steel rollers), but used a different loading jig, designed for compatibility for an XCT-compatible stage. The stage was loaned from the University of Birmingham (see Figure 171) and is a tension-compression rig with no supporting columns that would otherwise have blocked the X-ray beam at particular angles. The specimen was mounted in a bespoke jig to encourage specimen-wedge self-alignment through multiple mechanical degrees of freedom and the rollers were greased to reduce specimen-roller contact friction, as shown in Figure 172 (a). The applied crosshead displacement, δ, was recorded by the rig's in-built transducers to a precision of 1 μm, while the load was measured by an *Applied Measurements* DDEMF miniature 1 kN in-line load cell, with a 1 N precision. The force required to accommodate the mechanical slack was determined as less than 25 N.

All tests were conducted under quasi-static conditions with a principal loading rate of 1.5 $\mu m.s^{-1}$. Four specimens of each geometry were tested in a cyclic load-unload fashion, increasing the peak load until failure, whilst the remaining specimens (BS1, BS2, SS1 and SS2) were loaded monotonically, pausing to take *in situ* tomographs at loads of 25, 80, 100, 110 and 120 N. The tomographs were taken on the I12: Joint Engineering, Environmental, and Processing (I12-JEEP) beamline at the Diamond Light Source as part of experiment EE9478-1. Using a 53 keV monochromatic beam, the specimens were imaged with a voxel size of $(3.24\ \mu m)^3$ and reconstructed volume of approximately 8 x 8 x 7 mm. For each 180° scan, 1,800 projections were collected with an exposure of 0.1 s.

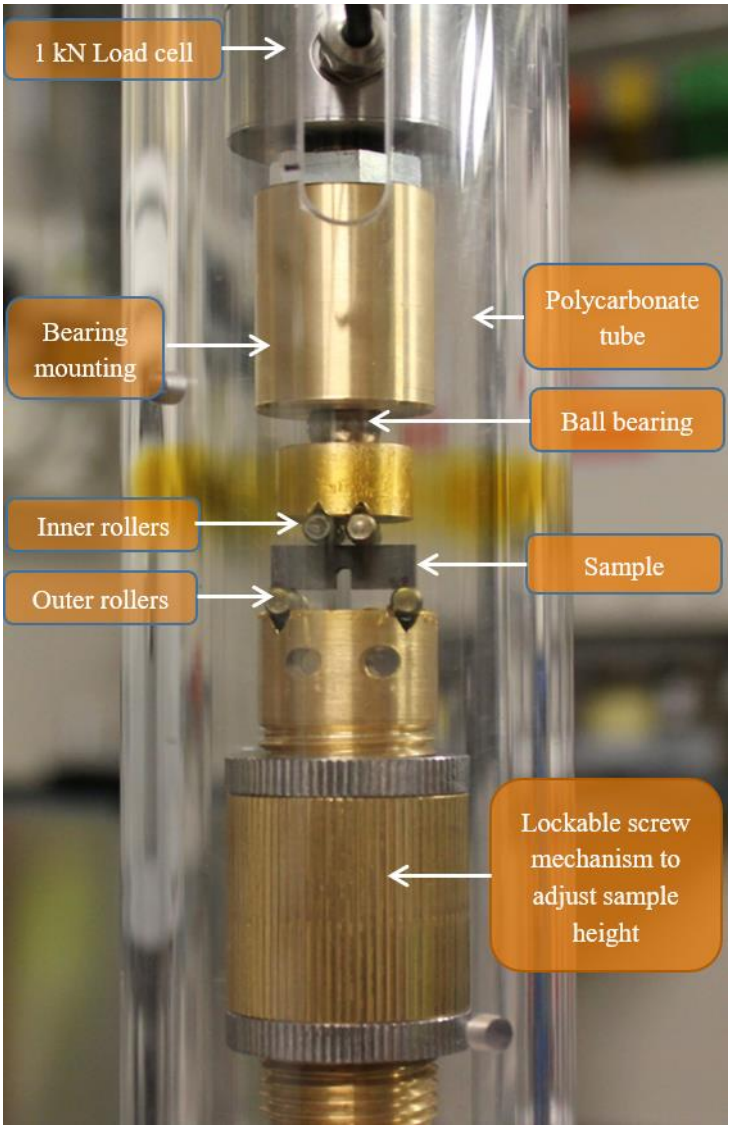


Figure 171: University of Birmingham XCT compatible loading stage used for the small notched beam preliminary testing on beamline I12 (JEEP) at the Diamond Light Source (a), with the load train including a bespoke four point bend loading jig in (b) (see also Figure 172).

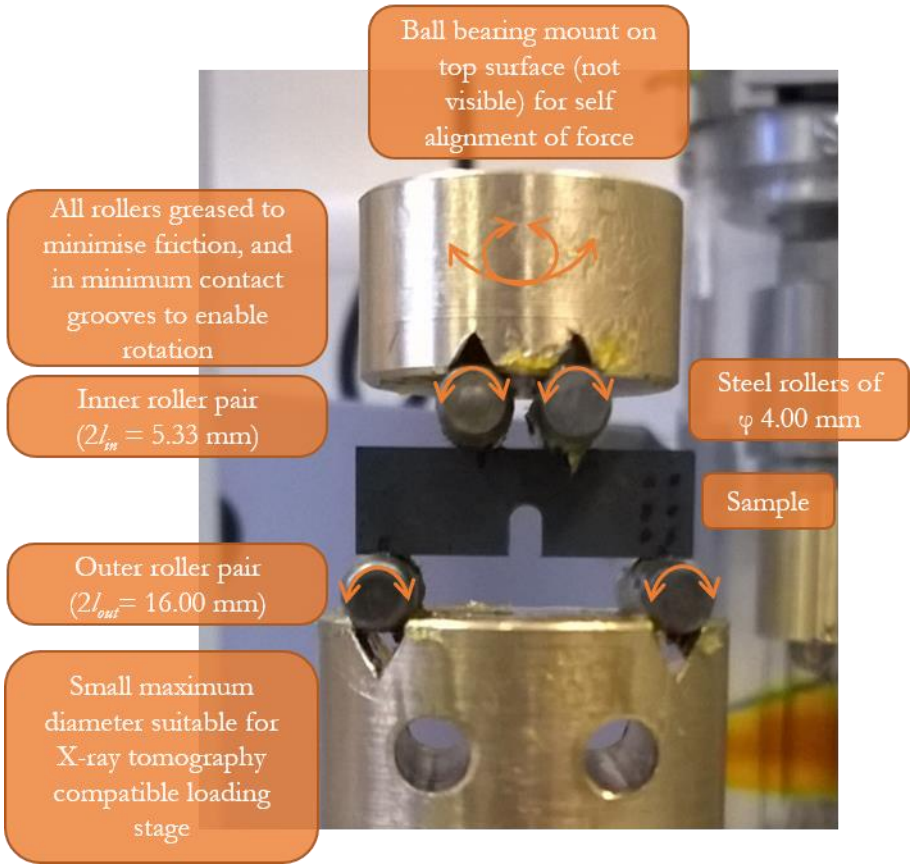


Figure 172: Four-point flexure jig used during the preliminary tests. Rotational degrees of freedom are indicated by the orange arrows.

Analysis

The preliminary testing demonstrated that the short notched-beams could be tested successfully in four-point bend, though also highlighted areas of variability to be accounted for during the Main Campaign testing. These areas were: (1) notch machining, where the depths were found to be overcut by an average of 0.04 mm; (2) specimen alignment; and (3) the fracture load distributions.

The load-displacement traces for all of the blunt and sharp notch-tip preliminary specimens are shown in Figure 173(a) and (b), respectively. The traces for the specimens that were imaged by tomography are replotted in Figure 174 for clarity. The load drops observed in the curves on Figure 174 correspond to when the tomography scans were performed; the drop in load was attributed to a settling of the apparatus, due to mechanical vibration, rather than da mage to the microstructure. From the profiles in Figure 173, the maximum load, F_M, and the 'elastic' compliance were measured. F_M was greater than 90 N for all the specimens. The compliance was defined as the curve gradient in the [35, 60] N range.

The impact of specimen misalignment, particularly rotation about the beams' long axis, was highlighted by comparing the beam orientation with the F_M and the compliance values for each specimen. Figure 173 indicates a bimodal property distribution in both F_M and compliance for both geometries. The low strength (and compliance) values in each geometry arose from two blunt and three sharp specimens, so by excluding these specimens, a 'higher-F_M' set was defined. For each geometry, the F_M and compliance distributions are summarised in Table 16, calculated for all the specimens and separately for the higher-F_M set. In general, the blunt specimens failed at a greater $\hat{F}_M$, but with a greater scatter: within the higher-F_M set, $\hat{F}_{M,blunt} = 134$ N with a 7 % range, compared to $\hat{F}_{M,sharp} = 119$ N with a 9 % range. The compliance distributions were comparable between the two geometries and measuring only the higher-F_M set resulted in a consistent mean increase (to 1.6 N.μm^{-1}).

Figure 175 shows horizontal (perpendicular to the loading axis) slices from the reconstructed tomographs, which intersect the notch tips of the two blunt specimens. While the notch in the image for the specimen BS2 (Figure 175(a)) shows a symmetric intersection, where the notch width appears constant across the specimen (edges are parallel), the BS1 specimen image (Figure 175(b)) lacks the symmetry, suggesting the notch tip was at an angle to the horizontal plane. Both optical microscopy and the 3D tomography indicate that the notches were cut parallel to the specimen surfaces, and therefore BS1 specimen must have been rotated, resulting in misalignment with the rollers and hence the applied force. Comparable observations were made for the sharp specimens. In Figure 174 the profiles for the rotated samples (BS1 and SS2) both have a lower compliance, and belong to the specimens excluded from higher-F_M.

With distinct bimodal properties, particularly respecting the compliances, it was therefore inferred that the rig used in these experiments could result in either a correct alignment, or a specific misalignment. The distributions of the higher-F_M specimens will therefore be used to determine the minimum number of specimens required based on a Student's t-test and separately a regression analysis.

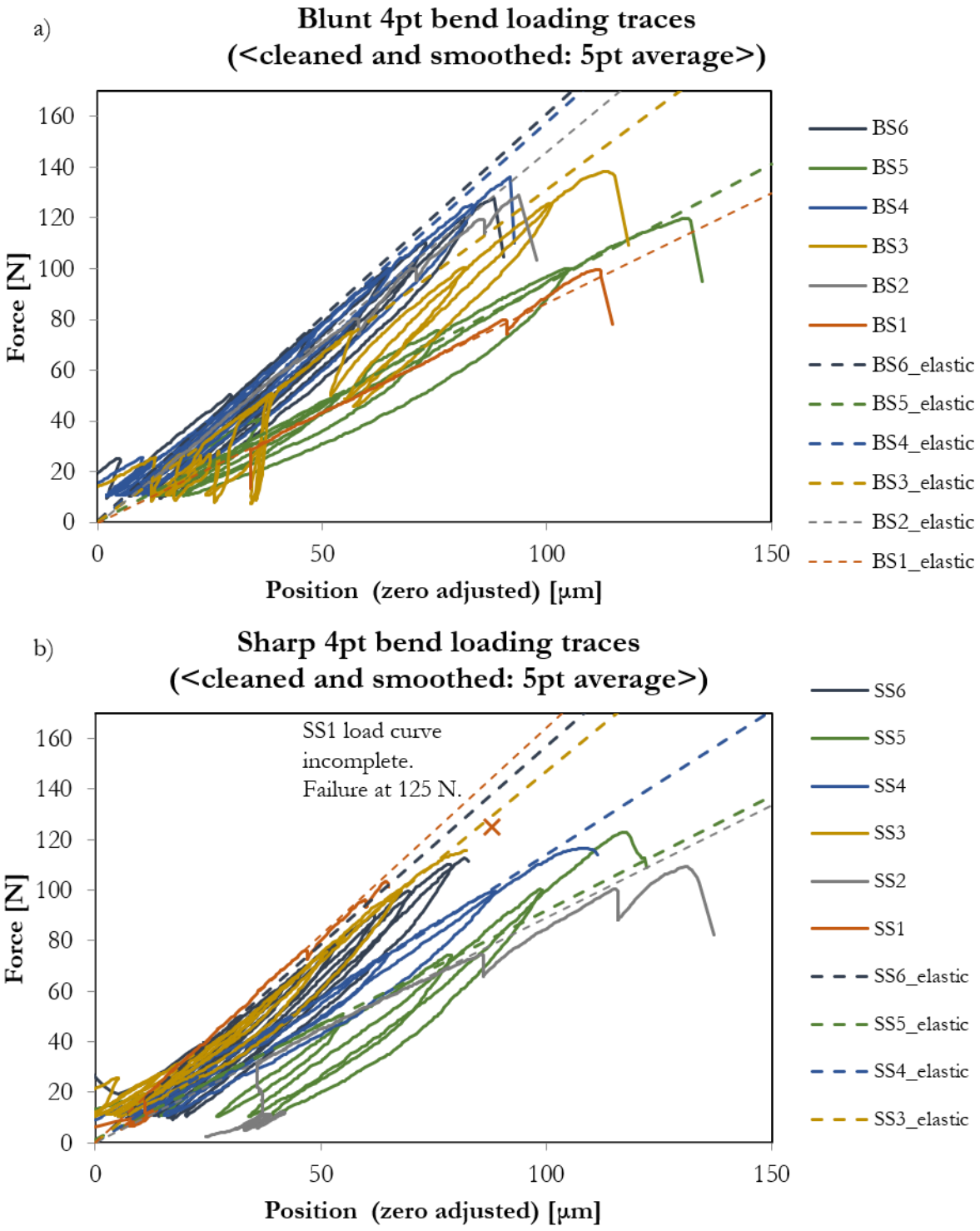


Figure 173: Preliminary sample load-displacement traces for the (a) blunt and (b) sharp samples. For clarity, traces have been smoothed with a 5-point moving average. Linear gradients indicating the elastic compliance were fitted over the [35, 60] N range.

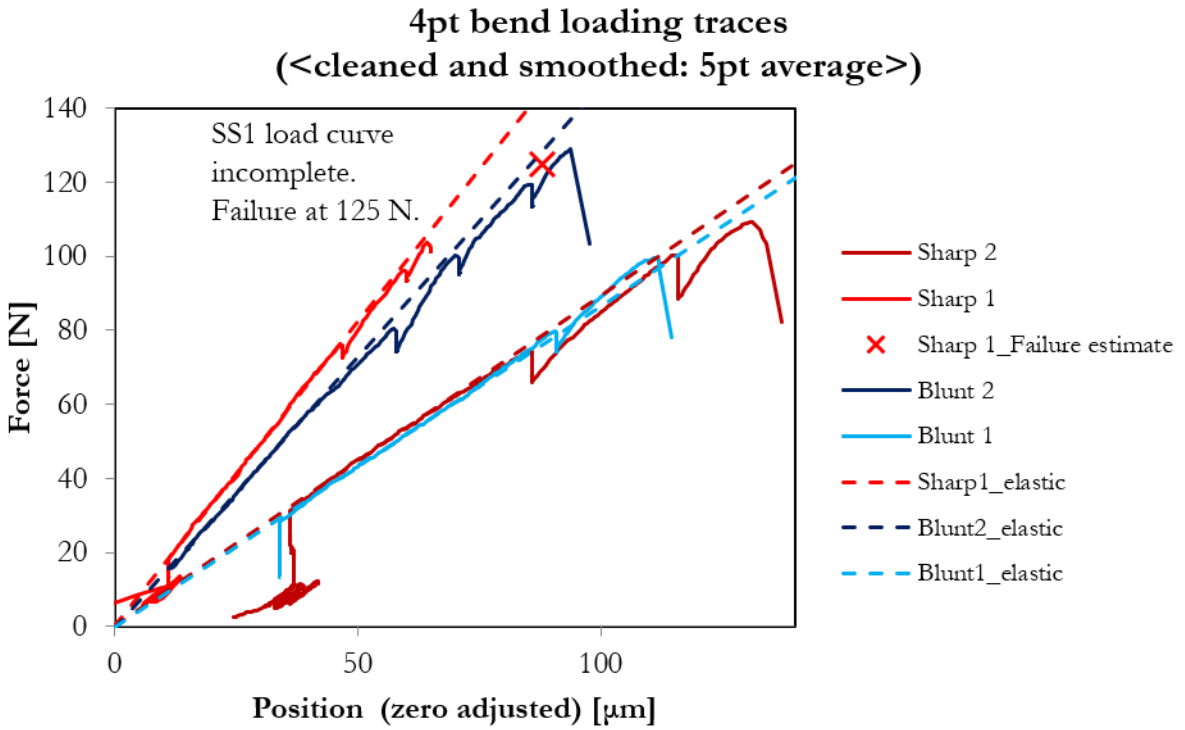


Figure 174: Preliminary sample load-displacement traces only the samples tested at the DLS, with Sharp notch-tip samples in red and blunt notch tip samples in blue. For clarity, traces have been smoothed with a 5-point moving average. Load drops are caused by movement of the stage for tomographic imaging, and were not fracture events. Linear gradients indicating the elastic compliance were fitted over the [35, 60] N range.

Table 16: Statistical data on the failure loads and 'elastic' gradients of the samples tested as part of EE9478. The "'Aligned' only" data refers only to samples with the higher gradient values. The Percentage Difference (% Diff.) column is calculated row-wise as $\left(\frac{|[sharp]-[blunt]|}{[blunt]}\right)$ *for the absolute values. In-cell percentage values relate to the appropriate average value* $\left(\frac{[Cell\ value]}{[average]}\right)$.

		Peak Loads [N]			Gradients (35-60N) [N.µm^{-1}]	
		Sharp	**Blunt**	**% Diff.**	**Sharp**	**Blunt**
All data	Average	118	126	6	1.3	1.3
	Sample standard deviation, *s*	6 (5 %)	14 (11 %)	57	0.3 (23 %)	0.3 (23 %)
	Range	15 (13 %)	38 (30 %)	60	0.8 (62 %)	0.7 (54 %)
'Aligned' only (3/4 samples, respectively)	Average	119	134	11	1.6	1.6
	Range	11 (9 %)	10 (7 %)	10	0.2 (13 %)	0.1 (6 %)

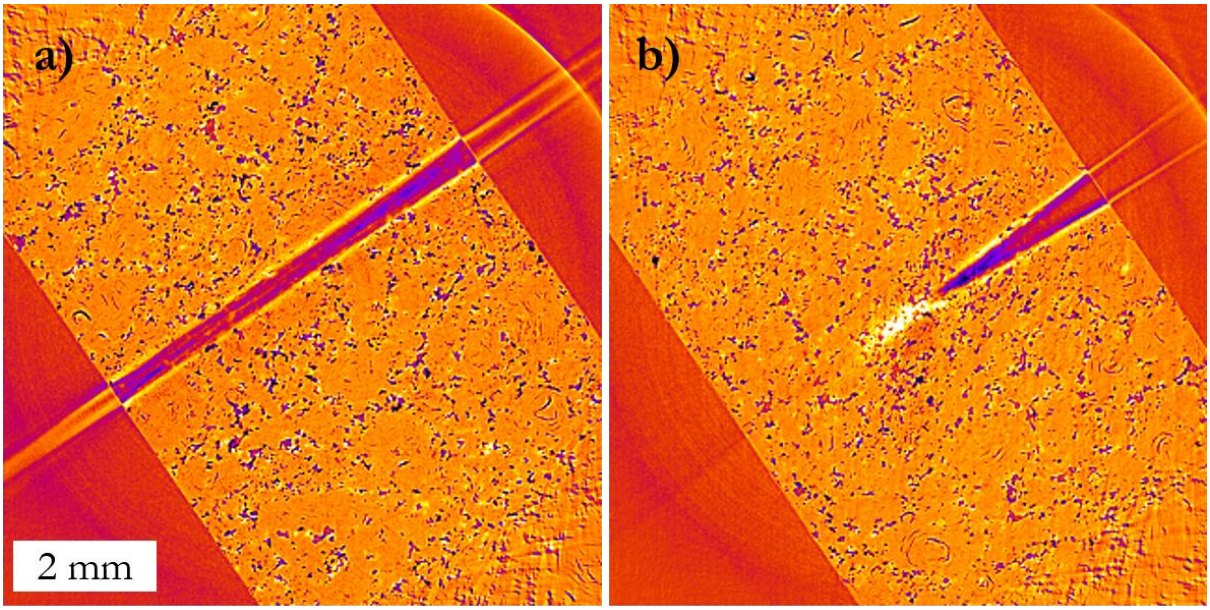


Figure 175: Virtual X-Y slices from the tomographs of preliminary specimens. The slice position intersects notch tip and shows examples of (a) an aligned sample where the notch tip has parallel sides and so appears symmetric with respect to the beam, and (b) a sample rotated about the beam long axis, so that the notch sides are non-parallel, and the tip appears asymmetric.

Student's t-test

The null hypothesis to be tested is that the statistical distributions of the maximum loads for the two notch-tip geometries belong to the same parent distribution. Student's t-test can be used to determine the minimum number of specimens *per geometry*, n, required to demonstrate this hypothesis to be false. From (31) the difference in the mean maximum loads for the geometries, $\Delta\hat{F}_M = 15$ N, using the higher-F_M distributions in Table 16. The two-sided t-test was employed for comparing specimens from independent populations, as in (32)[182]; the symmetric assumption increased the number of samples required.

(31) $$\Delta\hat{F}_m = \hat{F}_{m,Blunt} - \hat{F}_{m,Sharp}$$

(32) $$n = \frac{t(\alpha,\beta)^2 \left(s_{p,Blunt}{}^2 + s_{p,Sharp}{}^2\right)}{(\Delta\widehat{F_m})^2}$$

The small sample size in the higher-F_M set limited the validity of calculating the standard deviations for the specimens, so the ranges were substituted as a measure of statistical spread; it is notable that the higher-F_M range values were comparable to the standard deviations calculated for all the specimens. A significance level and statistical power were used equivalent to requiring a 95 % certainty that observed trends are real, $\alpha = 0.05$, and an 80 % power to corroborate that a true hypothesis is that people measurable, $\beta = 0.2$. These were converted by (33) to an acceptable probability based on the critical values, $t(a,\beta)$, of the t-test distribution.

$$t(\alpha,\beta) = t_{1-\frac{\alpha}{2}} + t_{1-\beta}. \tag{33}$$

By this analysis, $n \gtrsim 8$ specimens would be required per notch tip geometry to distinguish the maximum loads with confidence, though this does not consider notch depth.

Regression series

The *total* number of specimens in the study, N, was also estimated based on the statistical significance on the effect of both notch tip geometry and depth assuming that F_M is a smooth function of depth a. There were to be six control variables, m, ('predictors') in the study: two notch tip geometries and four notch depths (a = 0.00, 1.50, 3.00 and 4.50 mm). For this type of problem a regression-type analysis would be appropriate, and the rule-of-thumb described in (34) was selected to calculate N, which Green supported as suitable when $m < 7$ [183].

$$N \geq 50 + 8\,m \tag{34}$$

The main series tests should therefore have N ≥ 98 specimens, which if divided equally between the seven unique test specifications (three notch depths in the two geometries plus one un-notched), equates to $n \geq 14$ specimens per geometry. This was comparable to the requirement from Student's t-test, though more conservative.

Conclusions and recommendations

The preliminary testing demonstrated that the short notched-beams could be tested successfully in four-point bend, though also highlighted the following areas of variability to be accounted for during the main series testing:

1. Notch machining, where the depths were found to be overcut by an average of 0.04 mm
2. Specimen alignment can make a significant different to the mean strengths measured
3. The fracture load distributions are significant for Gilsocarbon.

To mitigate (1), all sample dimensions should be measured and modelled precisely for accurate comparison.

To mitigate (2), alignment through manual preload adjustment and self-alignment during loading should be achieved using a robust rig with multiple degrees of freedom.

To mitigate (3), at least 14 specimens should be prepared for the main series tests in each geometry, totalling based on the statistical analyses comparing peak loads.

A2. Tomograph projection normalisation and partial angle tomography

Use of frame-average radiographs

As with the radiographs described in § IV.2.3.1, every projection needed to be normalised during reconstruction against a bright-field and dark-field projection collected with the tomograph. The same pair of correction projections were applied to all 1800 imaging projections, so it was vital that they accurately captured the imaging conditions. For each tomograph, a mean bright- and dark-field projection was created by pixel-wise averaging of over ten sequential exposures in each configuration. This reduced the impact of random energy fluctuations on the correction pair. At the time of the experiment (May 2013), standard practice at the DLS was to use only a single exposure bright- and dark-field projection during reconstruction; as a result of this experiment, using mean bright- and dark-field projections became the norm. In several mean bright-field projections, some of the pixels within the detector's charge-coupled device, CCD, were saturated due to excessive exposures, particularly affecting the earliest tomographs of the 2 mm notch specimen. Saturation resulted in periodic vertical stripes in the bright-field projections and caused strong 'ring' artefacts in the tomographs. Ring artefacts are invariant under specimen motion, and so interfere with digital volume correlation. Saturated bright-fields were therefore sympathetically substituted with unsaturated images collected from as close a time a possible. This correction significantly reduced the occurrence of ring artefacts.

Reconstruction of partial angle tomograph

The partial angle tomograph of the KN2 specimen was missing c. 200 radiographs. A simple interpolation was attempted for the missing projections by duplicating the projection immediately before and after, each filling half the gap. This approximation allowed the fine detail of the microstructure to be generated for the whole volume, but resulted in a distinct striping artefact along the axis of the missing projections with a width of the interpolation angular range, as seen in Figure 176. The fine detail of the tomograph confirms no cracking was present at 50 N, but the reconstruction artefact prevents more quantitative analysis.

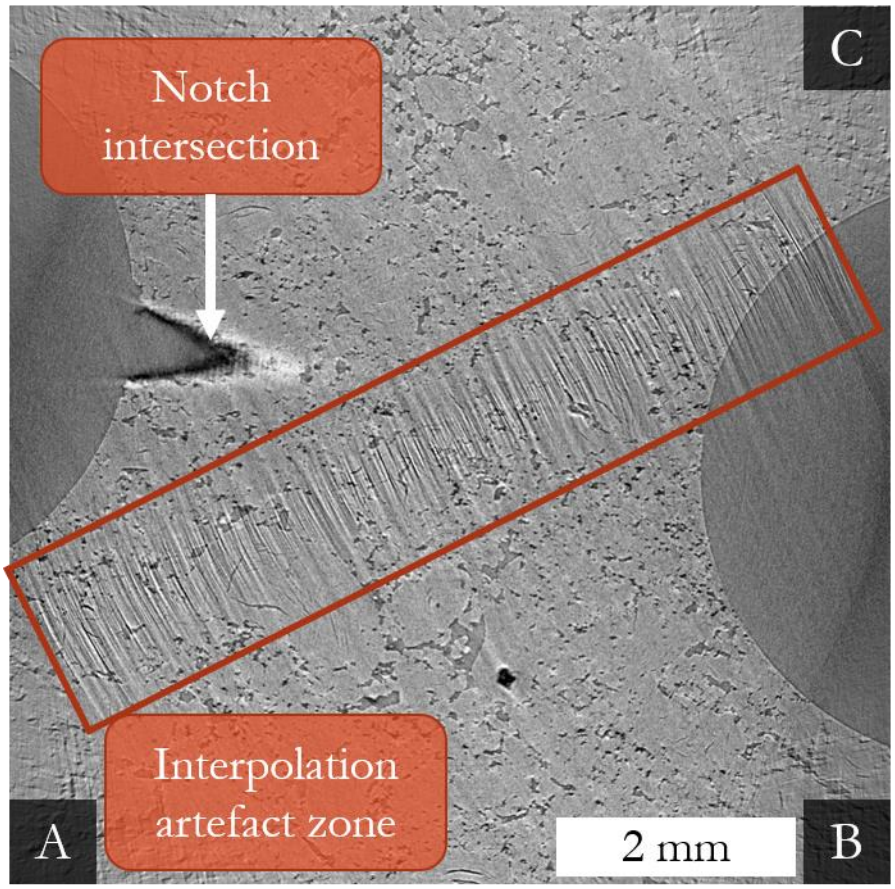


Figure 176: Virtual microstructure of the KN2 specimen on the slice ABC for the unloaded state following the 50 N loading. 200 tomograph projections were not recorded, creating a partial angle tomograph which was reconstructed using a simple interpolation method, resulting in the interpolation zone artefact. For the slice displayed, a small region of the notch is visible where the 'horizontal slice' intersected.

A3. Linear elastic predictions for DLENT geometries

3D FE modelling has been used to predict the failure loads of the DLENT sample. The dependence on ligament ($W - a$) was considered with the ligament varying over [0.78, 17.50] mm. A $1/8^{th}$ model of DLENT (three orthogonal planes of symmetry, Figure 177) was used, with loading achieved via the vertical displacement of ϕ 12 mm pin in a ϕ 12.4 mm hole (for compatibility with existing loading rigs). The simulations used an essentially linear elastic model with a critical tensile stress criterion for failure, which is considered to under-predict fracture loads. Displacement increments of ≤ 1 μm (≤ 2 μm by symmetry) were applied, with the reaction force on pin calculated at each step.

Calculation of effective stress

The effective stress, σ_{eff}, was calculated by (35)

$$\sigma_{eff} = \frac{Reaction\ force\ on\ pin\ [x\ 4]}{Ligament\ (0.78 \leq L \leq 17.50)\ x\ model\ thickness\ (3)\ [x\ 4]} \quad (35)$$

Where […] indicates a symmetry multiplier.

The yield point was determined as the first step in which the Abaqus Equivalent Plastic Energy, PEEQ, measure is non-zero. PEEQ is based around the von Mises yield condition, and a critical stress of 16 MPa was chosen, based on the tensile data of Marrow *et al.* [88]. σ_{eff} for both geometries is shown in Figure 178 with the error due to the discrete steps in pin displacement. It should be noted that the von Mises criterion was employed for ease of implementation and not because it is the most likely condition of yield.

To achieve the failure at the notch consistently, the model had to be adapted for the large ligament samples, as the von Mises criterion favoured crushing above the pin. The top section was modelled as infinitely linearly elastic, while the lower section was elastic-plastic. This assumption should be valid where compressive strengths are more than twice tensile strengths (as in graphite).

On the plots, the a/W value and ligament size was adjusted for the sharp geometry to take account of the assumed 0.3 mm radius tip, that is, the notch was shorter and the ligament longer than expected. This was to replicate likely machining tolerances.

Calculation of stress reduction factor

In this discussion, the effect on the effective loading stress is considered, as opposed to the concentration of stresses around the notch tip. Therefore, the results are described in terms of a stress reduction factor, SRF, that is the mathematically inverted NSF.

Equivalent strain stress reduction factor

Once the yield point was determined, the yield strain (ϵ_y) was calculated by (36).

$$\epsilon_y = \frac{Displacement\ [x\ 2]}{Distance\ from\ pin\ contact\ surface\ to\ symmetry\ plane\ [x\ 2]} \tag{36}$$

A cuboid with the same cross-sectional dimensions as the ligament and the length of the inter-pin distance was strained to the equivalent strain (ϵ_y, by construction). The resultant stress in the loading direction was the unnotched stress (σ_u) from which the 'equivalent strain SRF' ($SRF(\frac{a}{W})_{ES}$) was calculated by (37) and shown on Figure 178.

$$SRF(\frac{a}{W})_{ES} = \frac{\sigma(a/W)_{eff}}{\sigma(a/W)_u} \tag{37}$$

Note that σ_u was the simplest component of the stress tensor and may be calculated trivially in all cases (verified by FE modelling) by (38).

$$\sigma(a/W)_u = E\ .\epsilon(a/W)_y \tag{38}$$

Equivalent yield condition (stress) SRF

An alternative SRF was calculated by taking the un-notched bar described above, straining it until the yield condition was met and then calculating the axial load. FE modelling demonstrated that for all a/W considered, the Poisson contraction has negligible influence on the yield (the von Mises yield stress was < 0.1 % different from the axial stress). Therefore, the un-notched failure stress (and strain) was known exactly (16 MPa). It was more convenient to work in stresses than loads (assuming constant cross-section), so the SRF became (39). With a constant σ_c, the SRF data are scaled values of the yield stresses shown in Figure 178, and so the data are not re-plotted; $SRF_{YC} < 1$ in all cases and increases with a/W.

(39) $$SRF\left(\frac{a}{W}\right)_{YC} = \frac{\sigma(a/W)_{eff,y}}{\sigma_c\ (=16\ MPa)}$$

Surface stresses

The surface stresses in the loading direction (S22) and transverse direction (S11) were predicted. The surface stress state immediately before yield is plotted in Figure 179 (S22) and Figure 180 (S11), for the shortest surface path from the notch tip to the back face. In the linear elastic case, the stress is directly proportional to the strain (with E = 10 GPa), and so these plots represent the differences that might be resolvable in actual testing using DIC. There are four particular features of note in these figures:

1. For a given a/W, at any distance ahead of the notch > 0.005 mm, the stresses are higher ahead of the blunt geometry in both *S11* and *S22*
2. At a given distance, the stress range covered by the blunt geometry is broader than for the sharp geometry
3. The peaks of *S11* curves are always nearer the notch tip and show less variation in peak stress for the a/W range than the blunt
4. There is no compressive *S22* stress for $a/W < 0.6$ along this path, whereas for larger a/W the back face is under increasingly strong compression

Considering Figure 179 and Figure 180 the differences in blunt and sharp geometries should be measurable by surface DIC with a submicron correlation uncertainty and features of the strain patterns used to differentiate the geometries and notch depths.

Implications for future work

Using a linear-elastic model with von Mises failure criterion used is known to be unrealistic for quasi-brittle Gilsocarbon, under-predicting the strength. With no inelastic deformation, the model is insensitive to the effects of the predicted 'biaxial' stresses. The model also makes no account for the known notch insensitivity of scale effects. Predictions given above are therefore deemed insufficient to predict the outcome of the experimental series, but provide a guide as to the range of behaviour (e.g. relative initiation loads) that would be expected.

The DLENT samples are an unproven geometry for fracture testing, but with significant potential for understanding tensile fracture. The planar surface is suitable for measuring surface strains using imaging techniques. The dual ligament geometry prevents the bending moment around the notch tip (as would be observed in a single notch plate specimen). Furthermore, as the strain states around the notch tips will be nearly identical during loading and the ligaments will fail at different instances, the 'exact' strain to failure (at the notch) may be determined, without direct interaction of the notches.

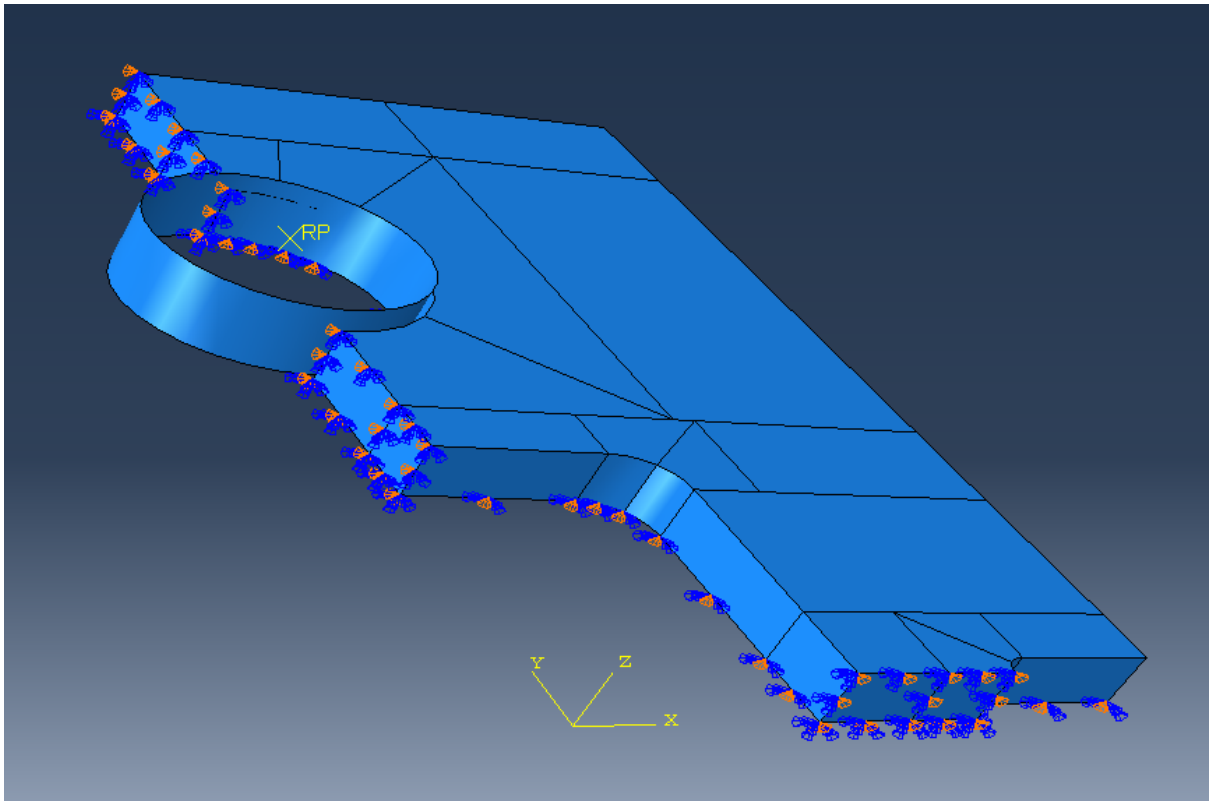


Figure 177: 1/8th DLENT model, showing three orthogonal mirror planes. The loading is applied by a ϕ 12 mm pin in ϕ 12.4 mm hole.

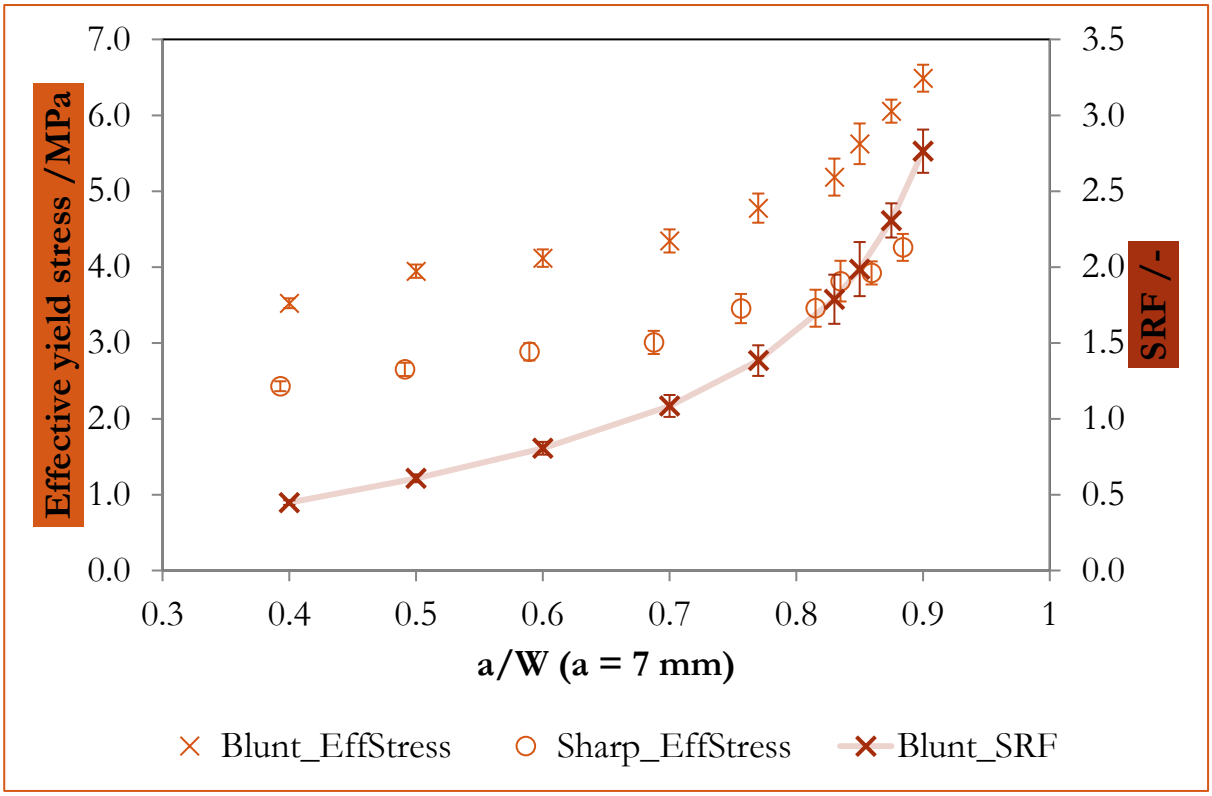


Figure 178: Predictions of effective yield stress (reaction force per ligament area) and SRF for 'Sharp' and 'Blunt' notch geometries as a function of a/W.

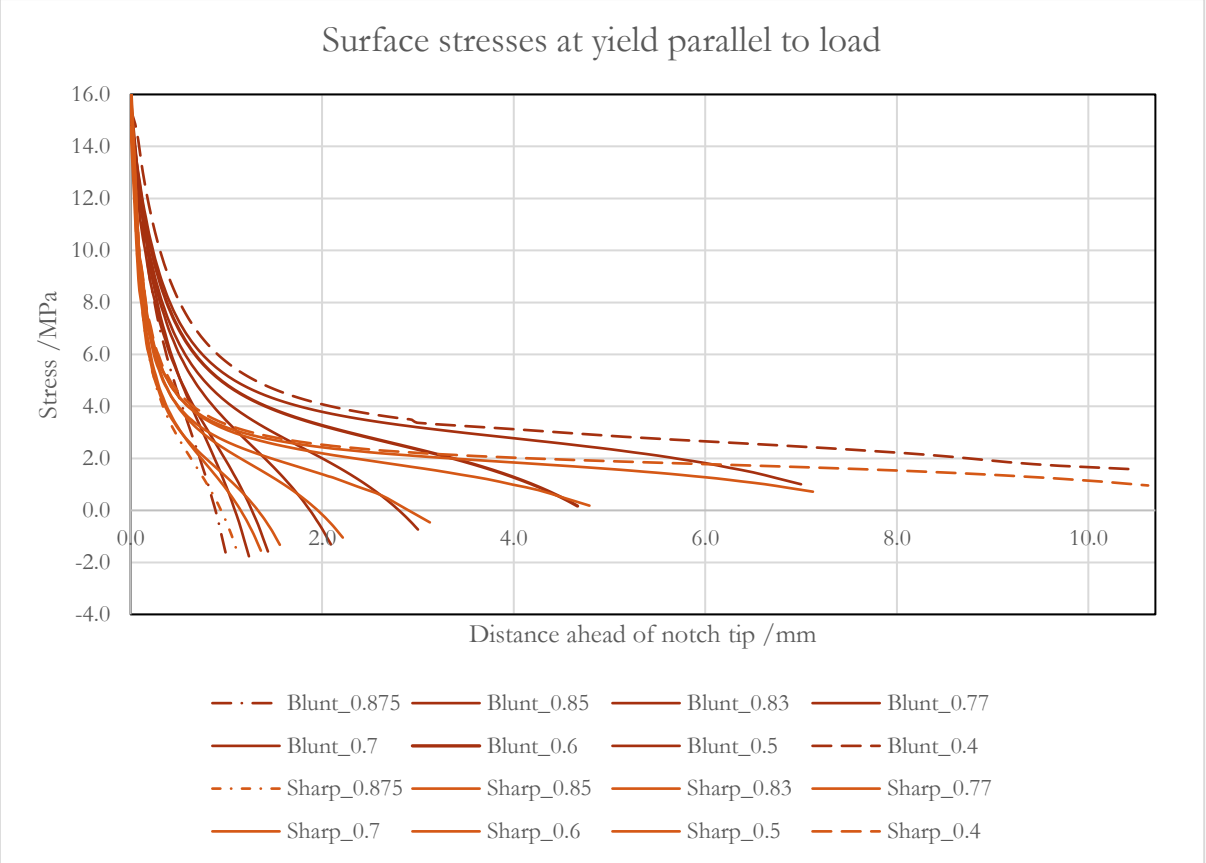


Figure 179: Surface stress component in loading direction along profile ahead of notch tip for Blunt and Sharp geometries. Numbers in dataset entries refer to a/W ratio (a = 7 mm for all geometries).

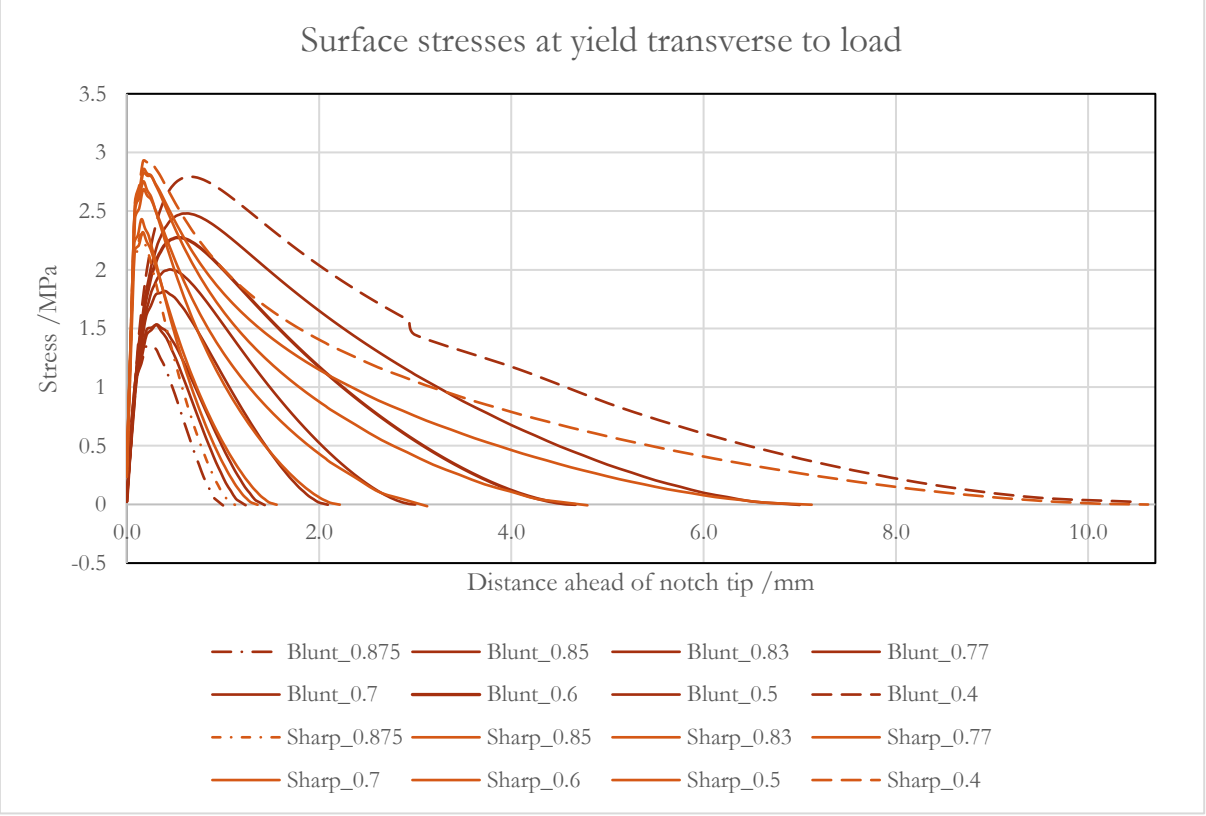


Figure 180: Surface stress component in transverse direction along profile ahead of notch tip for Blunt and Sharp geometries. Numbers in dataset entries refer to a/W ratio (a = 7 mm for all geometries).

VII References

[1] K. Keane, Hunterston B: Pictures show cracks in Ayrshire nuclear reactor [Online], BBC News, BBC, 8 March 2019.
[2] E. Energy, Hunterston Graphite Inspections – December 2018 EDF Energy, 2018.
[3] J.V. Best, W.J. Stephen, A.J. Wickham, Radiolytic graphite oxidation, Progress in Nuclear Energy 16(2) (1985) 127-178.
[4] F. Fox, TNPG report 727, 1970.
[5] T.J. Marrow, Notch Sensitivity and Fatigue in Nuclear Graphite, University of Manchester, The, Manchester, 2006.
[6] G. Locatelli, M. Mancini, N. Todeschini, Generation IV nuclear reactors: Current status and future prospects, Energy Policy 61 (2013) 1503-1520.
[7] L.L. Snead, Chapter 12 - Fusion Energy Applications, in: D.B. Timothy (Ed.), Carbon Materials for Advanced Technologies, Elsevier Science Ltd, Oxford, 1999, pp. 389-427.
[8] W. Penney, B.F.J. Schonland, J.M. Kay, J. Diamond, D.E.H. Peirson, Report on the accident at Windscale No. 1 Pile on 10 October 1957, Journal of Radiological Protection 37(3) (2017) 780-796.
[9] Atomic Power Construction Ltd., Dungeness 'B' Nuclear Power Station (Active Core Block -Standard), 1986, p. Design drawing of core block in Dungeness 'B' power station.
[10] National Nuclear Corporation Limited (NNC), Reactor System Detail of Basic Fuel Brick Component 201 Layers 2-9, 1979, p. Design drawing of core block in Heysham II and Torness power stations.
[11] The Nuclear Power Group Limited, Detail of Polygonal Brick Component No 202 1969, p. Design drawing of core block in Hunterston 'B' and Hinkley Point 'B' power stations.
[12] GEC Reactor Equipment Ltd., Layer 5 Standard Bricks Inner Zone, 1973, p. Design drawing of core block in Hartlepool power station.
[13] B.T. Kelly, Radiation damage in graphite and its relevance to reactor design, Progress in Nuclear Energy 2(4) (1978) 219-269.
[14] Y.-S. Lim, S.-H. Chi, K.-Y. Cho, Change of properties after oxidation of IG-11 graphite by air and CO2 gas, J Nucl Mater 374(1–2) (2008) 123-128.
[15] B.J. Marsden, G.N. Hall, 4.11 - Graphite in Gas-Cooled Reactors, in: J.M.K. Editor-in-Chief: Rudy (Ed.), Comprehensive Nuclear Materials, Elsevier, Oxford, 2012, pp. 325-390.
[16] M.S.L. Jordan, P. Ramsay, K.E. Verrall, T.O. van Staveren, M. Brown, B. Davies, A. Tzelepi, M.P. Metcalfe, Determining the electrical and thermal resistivities of radiolytically-oxidised nuclear graphite by small sample characterisation, J Nucl Mater 507 (2018) 68-77.

[17] A. Tzelepi, P. Ramsay, A.G. Steer, J. Dinsdale-Potter, Measuring the fracture properties of irradiated reactor core graphite, J Nucl Mater 509 (2018) 667-678.
[18] H. Salih, N. McLachlan, SALCOR Simulation of Local AGR Core Region with Multiple Singly and Doubly Cracked Fuel Bricks and Potential Key Disengagement, in: P.E.J. Flewitt, A.J. Wickham (Eds.) The 5th EDF Energy Nuclear Graphite Conference – Science and Engineering in Collaboration to Support Safe Operation of the Graphite Reactor Cores, EMAS Publishing, Southampton, 2017, pp. 255-263.
[19] J. Reed, The 5th EDF Energy Nuclear Graphite Conference: Welcome [Presentation only], in: P.E.J. Flewitt, A.J. Wickham (Eds.) The 5th EDF Energy Nuclear Graphite Conference – Science and Engineering in Collaboration to Support Safe Operation of the Graphite Reactor Cores, Southampton, 2017.
[20] W.J.M. Rankine, W.J. Millar, P.G. Tait, Miscellaneous scientific papers, C. Griffin, London, 1881.
[21] W.T. Kelvin, P.G. Tait, Treatise on natural philosophy, Cambridge University Press, Cambridge; New York, 2009.
[22] M. Filonenko-Borodich, M. Konaeva, [Теория упругости.] Theory of Elasticity. (Translated by M. Konayeva.). Moscow, Foreign Languages Pub. House, 1963.
[23] G.S. Holister, Experimental stress analysis : principles and methods, Cambridge University Press, London, United Kingdom, 1967.
[24] G. Irwin, Analysis of stresses and strains near the end of a crack traversing a plate, Journal of Applied Mechanics 24 (1957) 361–364.
[25] W.C.c. Twisp, Fracture modes v2, in: F.m. v2.svg (Ed.) Inkscape, Wikimedia Commons, the free media repository., https://commons.wikimedia.org/wiki/File:Fracture_modes_v2.svg, 21 January 2008, pp. Three fracture modes, inspired by Mode.jpg.
[26] A.A. Griffith, The Phenomena of Rupture and Flow in Solids, Philosophical Transactions of the Royal Society of London. Series A, Containing Papers of a Mathematical or Physical Character 221 (1921) 163-198.
[27] B.S. Institution, BS 7910:2013+A1:2015 Guide to methods for assessing the acceptability of flaws in metallic structures, 2015, p. 490.
[28] S.M. Barinov, M. Sakai, The work-of-fracture of brittle materials: Principle, determination, and applications, Journal of Materials Research 9(06) (1994) 1412-1425.
[29] T.H. Becker, T.J. Marrow, R.B. Tait, Damage, crack growth and fracture characteristics of nuclear grade graphite using the Double Torsion technique, J Nucl Mater 414(1) (2011) 32-43.
[30] G.P. Cherepanov, The propagation of cracks in a continuous medium, Journal of Applied Mathematics and Mechanics 31(3) (1967) 503-512.
[31] J.R. Rice, A Path Independent Integral and the Approximate Analysis of Strain Concentration by Notches and Cracks, Journal of Applied Mechanics 35 (1968) 379-386.
[32] F. Berto, P. Lazzarin, F.J. Gómez, M. Elices, Fracture assessment of U-notches under mixed mode loading: two procedures based on the ‘equivalent local mode I’ concept, International Journal of Fracture 148(4) (2008) 415-433.
[33] E. Barati, Y. Alizadeh, J.A. Mohandesi, Relationship between J-integral and averaged strain-energy density for U-notches in the case of large control volume under Mode I loading, Engineering Fracture Mechanics 78(6) (2011) 1317-1322.
[34] F. Berto, P. Lazzarin, M.R. Ayatollahi, Brittle fracture of sharp and blunt V-notches in isostatic graphite under pure compression loading, Carbon 63 (2013) 101-116.
[35] F. Berto, P. Lazzarin, C. Marangon, Brittle fracture of U-notched graphite plates under mixed mode loading, Materials & Design 41 (2012) 421-432.
[36] BSI, Advanced technical ceramics. Mechanical properties of ceramic composites at ambient temperature. Evaluation of the resistance to crack propagation by notch sensitivity testing, BSI, UK, 2006.

[37] D.R. Steinmetz, T. Jäpel, B. Wietbrock, P. Eisenlohr, I. Gutierrez-Urrutia, A. Saeed–Akbari, T. Hickel, F. Roters, D. Raabe, Revealing the strain-hardening behavior of twinning-induced plasticity steels: Theory, simulations, experiments, Acta Materialia 61(2) (2013) 494-510.
[38] H.K.D.H. Bhadeshia, TRIP-Assisted Steels?, ISIJ International 42(9) (2002) 1059-1060.
[39] F. Wakai, N. Kondo, Y. Shinoda, Ceramics superplasticity, Current Opinion in Solid State and Materials Science 4(5) (1999) 461-465.
[40] A. Pineau, T. Pardoen, 2.06 - Failure of Metals, in: I.M. Editors-in-Chief: , R.O. Ritchie, B. Karihaloo (Eds.), Comprehensive Structural Integrity, Pergamon, Oxford, 2007, pp. 684-797.
[41] Tsuji, Iwase, Ando, An investigation into the location of crack initiation sites in alumina, polycarbonate and mild steel, Fatigue Fract Eng M 22(6) (1999) 509-517.
[42] N.G. Tsouvalis, K.N. Anyfantis, Determination of the fracture process zone under Mode I fracture in glass fiber composites, J Compos Mater 46(1) (2012) 27-41.
[43] M.O. Tucker, A.P.G. Rose, T.D. Burchell, The fracture of polygranular graphites, Carbon 24(5) (1986) 581-602.
[44] F.E. Amparano, Y. Xi, Y.-S. Roh, Experimental study on the effect of aggregate content on fracture behavior of concrete, Engineering Fracture Mechanics 67(1) (2000) 65-84.
[45] W.D. Pilkey, D.F. Pilkey, Peterson's Stress Concentration Factors, Third Edition, John Wiley & Sons, Inc.2008.
[46] J.E. Brocklehurst, R.G. Brown, Fatigue, Notch Sensitivity and Work of Fracture Studies on Isotropic Graphite, Springfields, 1973.
[47] R.G. Brown, M. Birch, C. Stainthorpe, P. Rosen, A study of the notch sensitivity and the effect of specimen size on the strength of a wide range of graphites, Springfields Nuclear Power Development Laboratories, 1986.
[48] A. Carpinteri, P. Cornetti, N. Pugno, A. Sapora, On the most dangerous V-notch, International Journal of Solids and Structures 47(7–8) (2010) 887-893.
[49] S. Hanawa, M. Ishihara, Y. Motohashi, Analytical study on biaxial strength of structural ceramics under tension-compression condition, Advances in Fracture and Strength, Pts 1- 4 297-300 (2005) 40-46.
[50] D.A. Hills, D. Dini, Characteristics of the process zone at sharp notch roots, International Journal of Solids and Structures 48(14-15) (2011) 2177-2183.
[51] G.D. Quinn, Mechanical Testing of Ceramics, in: K.H.J.B. Editors-in-Chief: , W.C. Robert, C.F. Merton, I. Bernard, J.K. Edward, M. Subhash, V. Patrick (Eds.), Encyclopedia of Materials: Science and Technology (Second Edition), Elsevier, Oxford, 2001, pp. 5274-5276.
[52] K. Duan, X. Hu, F.H. Wittmann, Scaling of quasi-brittle fracture: Boundary and size effect, Mechanics of Materials 38(1–2) (2006) 128-141.
[53] BSI, Fracture mechanics toughness tests. Method for determination of fracture resistance curves and initiation values for stable crack extension in metallic materials, BSOL, 1997.
[54] F.M. Sánchez-Arévalo, G. Pulos, Use of digital image correlation to determine the mechanical behavior of materials, Mater Charact 59(11) (2008) 1572-1579.
[55] F. Corbani, P. Delvò, L. Fiorina, C.M.e.M.L. Rizzi, Speckle interferometry, fibre optic sensors and laser induced ultrasounds as solutions to industrial demands, Optics and Lasers in Engineering 37(4) (2002) 369-383.
[56] L. Salvo, P. Cloetens, E. Maire, S. Zabler, J.J. Blandin, J.Y. Buffière, W. Ludwig, E. Boller, D. Bellet, C. Josserond, X-ray micro-tomography an attractive characterisation technique in materials science, Nuclear Instruments and Methods in Physics Research Section B: Beam Interactions with Materials and Atoms 200 (2003) 273-286.

[57] L. Salvo, M. Suéry, A. Marmottant, N. Limodin, D. Bernard, 3D imaging in material science: Application of X-ray tomography, Comptes Rendus Physique 11(9–10) (2010) 641-649.
[58] M. Mostafavi, S.A. McDonald, P.M. Mummery, T.J. Marrow, Observation and quantification of three-dimensional crack propagation in poly-granular graphite, Engineering Fracture Mechanics (0) (2013).
[59] M. Mostafavi, T.J. Marrow, Quantitative in situ study of short crack propagation in polygranular graphite by digital image correlation, Fatigue Fract Eng M 35(8) (2012) 695-707.
[60] K. Triconnet, K. Derrien, F. Hild, D. Baptiste, Parameter choice for optimized digital image correlation, Optics and Lasers in Engineering 47(6) (2009) 728-737.
[61] T.D. Burchell, Carbon Materials for Advanced Technologies, Elsevier Science1999.
[62] F. Brown, J. Palmer, P. Wood, Derivation of a radionuclide inventory for irradiated graphite-chlorine-36 inventory determination, 2001.
[63] X. Luo, S. Yu, X. Sheng, S. He, Temperature effect on IG-11 graphite wear performance, Nuclear Engineering and Design 235(21) (2005) 2261-2274.
[64] D.W. Olson, Graphite, in: U.S.G. Survey (Ed.) 2011 Minerals Handbook, U.S. Department of Interior, 2013.
[65] R.E. Nightingale, Nuclear graphite, J Nucl Mater 10(3) (1963) 263-264.
[66] R.E. Nightingale, CHAPTER ONE - Graphite in the Nuclear Industry, in: R.E. Nightingale (Ed.), Nuclear Graphite, Academic Press2013, pp. 1-20.
[67] K. Lafdi, S. Bonnamy, A. Oberlin, Tem studies of coal tars: Crude tar and its insoluble fractions, Carbon 28(1) (1990) 57-63.
[68] U. Świetlik, S. Jasieńko, A. Wolski, Carbonization and graphitization processes of pitch from coal liquid and its fractions, Carbon 31(3) (1993) 461-466.
[69] S.S. Jones, E.M. Woodruff, Microstructure of carbon blacks in pitch-bonded graphites and structural changes produced by gas—graphite oxidation reactions, Carbon 9(3) (1971) 259-264.
[70] A. Hodgkins, Crack propagation in nuclear graphite, Faculty of Engineering and physical sciences, University of Manchester, Manchester, 2006.
[71] B. McEnaney, T.J. Mays, Characterization of macropores using quantitative microscopy, in: F.R.-R.K.S.W.S. J. Rouquerol, K.K. Unger (Eds.), Studies in Surface Science and Catalysis, Elsevier1994, pp. 327-337.
[72] S. Fazluddin, Crack Growth Resistance in Nuclear Graphite, Lambert Academic Publishing2010.
[73] H. Marsh, Introduction to carbon science, 1989.
[74] K.Y. Wen, T.J. Marrow, B.J. Marsden, The microstructure of nuclear graphite binders, Carbon 46(1) (2008) 62-71.
[75] Y. Vertyagina, T.J. Marrow, Multifractal-based assessment of Gilsocarbon graphite microstructures, Carbon 109 (2016) 711-718.
[76] G. Hall, B.J. Marsden, S.L. Fok, The microstructural modelling of nuclear grade graphite, J Nucl Mater 353(1–2) (2006) 12-18.
[77] K. Shen, S. Yu, F. Kang, The microstructure and texture of Gilsocarbon graphite, Carbon 153 (2019) 428-437.
[78] J.W. Anthony, Handbook of mineralogy, Mineral Data Publ.1990.
[79] M. Ströck (mstroeck), Eight Allotropes of Carbon, in: E.A.o. Carbon.png (Ed.) iMol for Mac OS X and Photoshop CS2, Wikipedia (C) Creative Commons License 2008, the free encyclopedia, 2006.
[80] M. Caragiu, S. Finberg, Alkali metal adsorption on graphite: a review, Journal of Physics: Condensed Matter 17(35) (2005) R995-R1024.

[81] M.R. Joyce, T.J. Marrow, P. Mummery, B.J. Marsden, Observation of microstructure deformation and damage in nuclear graphite, Engineering Fracture Mechanics 75(12) (2008) 3633-3645.
[82] S.D. Preston, Variation of material properties within a single brick of the Heysham 2/Torness moderator graphite, Springfields Nuclear Power Development Laboratories, 1988.
[83] I.B. Mason, R.H. Knibbs, The Young's modulus of carbon and graphite artefacts, Carbon 5(5) (1967) 493-506.
[84] T. Tsuzuku, Mechanical energy losses due to motion of dislocations in graphite and carbons, Carbon 1(1) (1963) 25-32.
[85] A.M. Barrachin, G. Jouquet, G. Micaud, F. Pattou, Effet de la porosite et de l'orientation cristalline sur le module d'young du graphite artificiel, J Nucl Mater 20(3) (1966) 294-302.
[86] F. Roberts, I.B. Mason, M.S.T. Price, J. Bromley, Progress in Nuclear Technlogy, Pergamon Press1961, p. 105.
[87] I.B. Mason, R.H. Knibbs, Variation with Temperature of Young's Modulus of Polycrystalline Graphite, Nature 188(4744) (1960) 33-35.
[88] T.J. Marrow, D. Liu, S.M. Barhli, L. Saucedo Mora, Y. Vertyagina, D.M. Collins, C. Reinhard, S. Kabra, P.E.J. Flewitt, D.J. Smith, In situ measurement of the strains within a mechanically loaded polygranular graphite, Carbon 96 (2016) 285-302.
[89] S.M. Barhli, L. Saucedo-Mora, M.S.L. Jordan, A.F. Cinar, C. Reinhard, M. Mostafavi, T.J. Marrow, Synchrotron X-ray characterization of crack strain fields in polygranular graphite, Carbon 124 (2017) 357-371.
[90] W.D. Callister, D.G. Rethwisch, Fundamentals of Materials Science and Engineering: An Integrated Approach, Wiley2012.
[91] J.E. Brocklehurst, 1977.
[92] R.H. Knibbs, Fracture in polycrystalline graphite, J Nucl Mater 24(2) (1967) 174-187.
[93] J.E. Brocklehurst, Chemistry and physics of carbon : a series of advances. Vol. 13, M. Dekker, New York; Basel, 1977.
[94] M. Birch, R.G. Brown, J.E. Brocklehurst, Defining the effective inherent defect size of graphite for fracture mechanics applications., 16th Biennial Conference on Carbon, University of California, San Diego, California, 1983, p. 404.
[95] I.B. Mason, The Fifth Carbon Conference (1961), Pergamon Press, Pennsylvania, 1963, p. 597.
[96] W.L. Greenstreet, J.E. Smith, G.T. Yahr, Mechanical properties of EGCR-type AGOT graphite, Carbon 7(1) (1969) 15-45.
[97] M.P. Metcalfe, N. Tzelepi, D. Wilde, Effect of Test Specimen Size on Graphite Strength Graphite Testing for Nuclear Applications: The Significance of Test Specimen Volume and Geometry and the Statistical Significance of Test Specimen Population, ASTM International, West Conshohocken, PA, 2014.
[98] N. Tzelepi, J. Dinsdale-Potter, M.S.L. Jordan, H. Preston, G. Copeland, M. Crelling, T. McGrady, S. Wilkinson, P. Ramsay, Innovate-UK Project: Influence of Creep and Geometry on Strength of Irradiated Graphite Components - Work Package 1: Measurements of Strength and Fracture Properties on Irradiated Graphite, 2017.
[99] M.R. Molteno, T.H. Becker, Mode I–III Decomposition of the J-integral from DIC Displacement Data, Strain 51(6) (2015) 492-503.
[100] M. Mostafavi, N. Baimpas, E. Tarleton, R.C. Atwood, S.A. McDonald, A.M. Korsunsky, T.J. Marrow, Three-dimensional crack observation, quantification and simulation in a quasi-brittle material, Acta Materialia 61(16) (2013) 6276-6289.
[101] D.K. Bazaj, E.E. Cox, Stress-concentration factors and notch-sensitivity of graphite, Carbon 7(6) (1969) 689-697.

[102] M.O. Tucker, The application of fracture mechanics to the notch sensitivity of graphite, IAEA Technical committee meeting on mechanical behaviour of graphite for High Temperature reactors, IAEA, Gif sur Yvette, France, 1987.
[103] J.E. Brocklehurst, M.I. Darby, Concerning the fracture of graphite under different test conditions, Materials Science and Engineering 16(1–2) (1974) 91-106.
[104] P. Marshall, E.K. Priddle, Room temperature fatigue crack propagation in reactor graphites, Carbon 11(5) (1973) 541-546.
[105] I.M. Pickup, B. McEnaney, R.G. Cooke, Fracture processes in graphite and the effects of oxidation, Carbon 24(5) (1986) 535-543.
[106] A. Hodgkins, T.J. Marrow, P. Mummery, B. Marsden, A. Fok, X-ray tomography observation of crack propagation in nuclear graphite, Mater Sci Tech-Lond 22(9) (2006) 1045-1051.
[107] H.Y. Li, J. Duff, T.J. Marrow, In-Situ Observation of Crack Nucleation in Nuclear Graphite by Digital Image Correlation, Proceedings of the Asme Pressure Vessels and Piping Conference - 2008, Vol 6, Pt a and B (2009) 813-820.
[108] J.D. Arregui-Mena, L. Margetts, D.V. Griffiths, L. Lever, G. Hall, P.M. Mummery, Spatial variability in the coefficient of thermal expansion induces pre-service stresses in computer models of virgin Gilsocarbon bricks, J Nucl Mater 465 (2015) 793-804.
[109] R. Taylor, R.G. Brown, K. Gilchrist, E. Hall, A.T. Hodds, B.T. Kelly, F. Morris, The mechanical properties of reactor graphite, Carbon 5(5) (1967) 519-531.
[110] T.D. Burchell, Nuclear Graphite and Radiation Effects, in: K.H.J.B. Editors-in-Chief: , W.C. Robert, C.F. Merton, I. Bernard, J.K. Edward, M. Subhash, V. Patrick (Eds.), Encyclopedia of Materials: Science and Technology (Second Edition), Elsevier, Oxford, 2001, pp. 6310-6319.
[111] S. Yoda, M. Eto, T. Oku, Change in dynamic young's modulus of nuclear-grade isotropic graphite during tensile and compressive stressing, J Nucl Mater 119(2–3) (1983) 278-283.
[112] J.E. Brocklehurst, Fracture of Polycrystalline Graphite: A Review, Springfields, 1976.
[113] B. Allard, D. Rouby, G. Fantozzi, D. Dumas, P. Lacroix, Fracture behaviour of carbon materials, Carbon 29(3) (1991) 457-468.
[114] M.I. Darby, A fracture mechanics approach to the failure of graphite in laboratory tests, International Journal of Fracture 12(5) (1976) 745-757.
[115] T.D. Burchell, 4.10 - Radiation Effects in Graphite, in: R.J.M. Konings (Ed.), Comprehensive Nuclear Materials, Elsevier, Oxford, 2012, pp. 299-324.
[116] J.C. Bell, H. Bridge, A.H. Cottrell, G.B. Greenough, W.N. Reynolds, J.H.W. Simmons, Stored Energy in the Graphite of Power-Producing Reactors, Philosophical Transactions of the Royal Society of London. Series A, Mathematical and Physical Sciences 254(1043) (1962) 361-395.
[117] B.S. Gray, J.E. Brocklehurst, A.A. McFarlane, The irradiation induced plasticity in graphite under constant stress, Carbon 5(2) (1967) 173-180.
[118] B.T. Kelly, T.D. Burchell, The analysis of irradiation creep experiments on nuclear reactor graphite, Carbon 32(1) (1994) 119-125.
[119] M.A. Davies, M. Bradford, A revised description of graphite irradiation induced creep, J Nucl Mater 381(1–2) (2008) 39-45.
[120] A. Hodgkins, T.J. Marrow, M.R. Wootton, R. Moskovic, P.E.J. Flewitt, Fracture behaviour of radiolytically oxidised reactor core graphites: a view, Mater Sci Tech-Lond 26(8) (2010) 899-907.
[121] B.T. Kelly, J.E. Brocklehurst, B.W. Ashton, W.H. Martin, Fourth Conference on Industrial Carbons and Graphites 1974, SCI, London, 1976, p. 172.
[122] B.T. Kelly, Physics of Graphite, Applied Science Publishers1981.

[123] T.D. Burchell, I.M. Pickup, B. McEnaney, R.G. Cooke, The relationship between microstructure and the reduction of elastic modulus in thermally and radiolytically corroded nuclear graphites, Carbon 24(5) (1986) 545-549.
[124] L. Babout, P.M. Mummery, T.J. Marrow, A. Tzelepi, P.J. Withers, The effect of thermal oxidation on polycrystalline graphite studied by X-ray tomography, Carbon 43(4) (2005) 765-774.
[125] H. Matsuo, K. Fujii, H. Imai, T. Kurosawa, Effect of oxidation on physical properties of nuclear grade graphites, J Nucl Mater 136(2–3) (1985) 229-237.
[126] R. Adam, Notch sensitivity studies related to CAGR bricks, , 1988.
[127] B.T. Kelly, R.L. Faircloth, J.V. BEST, 77 Reduction in the strength of graphite by radiolytic oxidation in carbon dioxide, 1982.
[128] I.M. Pickup, R.G. Cooke, B. McEnaney, 15th Biennial Conference on Carbon, 15th Biennial Conference on Carbon, American Carbon Society, Philadelphia, Pennsylvania, 1981, p. 556.
[129] R. Adam, J.E. Brocklehurst, Mechanical tests on graphite with simulated radiolytic oxidation gradients (UKAEA, ND-R-853(S) (AB 7/26300)), UKAEA, 1983.
[130] British Energy, Core Graphite Data Sheet, Stress Strain Relationship: Young's Modulus, CSDMC/P28, Core Graphite Data Sheet, British Energy, 2003.
[131] British Energy, Core Graphite Data Sheet, Strength, CSDMC/P28, Core Graphite Data Sheet, British Energy, 2003.
[132] Y.V. Petrov, U.V. Taraban, On process-zone-size fracture criteria for brittle solids, Mater Sci 35(1) (1999) 129-131.
[133] D. Taylor, Predicting the fracture strength of ceramic materials using the theory of critical distances, Engineering Fracture Mechanics 71(16–17) (2004) 2407-2416.
[134] F.J. Gómez, M. Elices, Fracture loads for ceramic samples with rounded notches, Engineering Fracture Mechanics 73(7) (2006) 880-894.
[135] Z. Bažant, B.H. Oh, Crack band theory for fracture of concrete, Mat. Constr. 16(3) (1983) 155-177.
[136] Z. Yosibash, A. Bussiba, I. Gilad, Failure criteria for brittle elastic materials, International Journal of Fracture 125(3-4) (2004) 307-333.
[137] P. Lazzarin, F. Berto, Some Expressions for the Strain Energy in a Finite Volume Surrounding the Root of Blunt V-notches, International Journal of Fracture 135(1) (2005) 161-185.
[138] A.R. Torabi, M. Fakoor, E. Pirhadi, Tensile fracture in coarse-grained polycrystalline graphite weakened by a U-shaped notch, Engineering Fracture Mechanics 111 (2013) 77-85.
[139] F.J. Gómez, M. Elices, F. Berto, P. Lazzarin, Local strain energy to assess the static failure of U-notches in plates under mixed mode loading, International Journal of Fracture 145(1) (2007) 29-45.
[140] D. Radaj, State-of-the-art review on the local strain energy density concept and its relation to the J-integral and peak stress method, Fatigue Fract Eng Mater Struct 38(1) (2015) 2-28.
[141] S.M.J. Razavi, M.R.M. Aliha, F. Berto, Application of an average strain energy density criterion to obtain the mixed mode fracture load of granite rock tested with the cracked asymmetric four-point bend specimens, Theoretical and Applied Fracture Mechanics 97 (2018) 419-425.
[142] A.P.G. Rose, M.O. Tucker, A fracture criterion for nuclear graphite, J Nucl Mater 110(2–3) (1982) 186-195.
[143] M.O. Tucker, N. Mclachlan, Fracture and Microstructure of Graphites, J Phys D Appl Phys 26(6) (1993) 893-907.
[144] T.D. Burchell, A microstructurally based fracture model for polygranular graphites, Carbon 34(3) (1996) 297-316.

[145] A. Hillerborg, Fracture mechanics concepts applied to moment capacity and rotational capacity of reinforced concrete beams, Engineering Fracture Mechanics 35(1–3) (1990) 233-240.
[146] J. Lubliner, J. Oliver, S. Oller, E. Oñate, A plastic-damage model for concrete, International Journal of Solids and Structures 25(3) (1989) 299-326.
[147] E. Smith, Size effect relations associated with cohesive zone type fracture at a blunt stress concentration, International Journal of Fracture 95(1-4) (1999) 41-50.
[148] D.S. Dugdale, Yielding of steel sheets containing slits, Journal of the Mechanics and Physics of Solids 8(2) (1960) 100-104.
[149] G.I. Barenblatt, The mathematical theory of equilibrium cracks in brittle fracture, Advances in applied mechanics 7 (1962) 55-129.
[150] DassaultSystèmes, Abaqus Analysis User's Manual, Simulia, 2010.
[151] R. de Borst, Fracture in quasi-brittle materials: a review of continuum damage-based approaches, Engineering Fracture Mechanics 69(2) (2002) 95-112.
[152] Z. Zou, S.L. Fok, B.J. Marsden, S.O. Oyadiji, Numerical simulation of strength test on graphite moderator bricks using a continuum damage mechanics model, Engineering Fracture Mechanics 73(3) (2006) 318-330.
[153] Z. Zou, S.L. Fok, S.O. Oyadiji, B.J. Marsden, Failure predictions for nuclear graphite using a continuum damage mechanics model, J Nucl Mater 324(2–3) (2004) 116-124.
[154] L. Saucedo-Mora, T.J. Marrow, FEMME: A multi-scale Finite Element Microstructure MEshfree fracture model for quasi-brittle materials with complex microstructures, Engineering Fracture Mechanics 147 (2015) 355-372.
[155] L. Saucedo Mora, M. Mostafavi, D. Khoshkhou, C. Reinhard, R. Atwood, S. Zhao, B. Connolly, T.J. Marrow, 3D cellular automata finite element (CAFE) modelling and experimental observation of damage in quasi-brittle nuclear materials: Indentation of a SiC-SiC(fibre) ceramic matrix composite, Third International Workshop on Structural Materials for Innovative Nuclear Systems (SMINS-3), Idaho Falls, USA, 2013.
[156] L. Saucedo-Mora, M. Mostafavi, D. Khoshkhou, C. Reinhard, R. Atwood, S. Zhao, B. Connolly, T.J. Marrow, Observation and simulation of indentation damage in a SiC-SiC fibre ceramic matrix composite, Finite Elements in Analysis and Design 110 (2016) 11-19.
[157] Y. Vertyagina, T.J. Marrow, A multi-scale three-dimensional Cellular Automata fracture model of radiolytically oxidised nuclear graphite, Carbon 121 (2017) 574-590.
[158] L. Saucedo-Mora, T. James Marrow, Method for the explicit insertion of microstructure in Cellular Automata Finite Element (CAFE) models based on an irregular tetrahedral Finite Element mesh: Application in a multi-scale Finite Element Microstructure MEshfree framework (FEMME), Finite Elements in Analysis and Design 105 (2015) 56-62.
[159] ASTM, ASTM C651-17, Standard Test Method for Flexural Strength of Manufactured Carbon and Graphite Articles Using Four-Point Loading at Room Temperature, 2017.
[160] T.M. Inc, MATLAB Release 2018a, The MathWorks Inc, Natick, Massachusetts, United States, 2018.
[161] C.A. Schneider, W.S. Rasband, K.W. Eliceiri, NIH Image to ImageJ: 25 years of image analysis, Nature Methods 9 (2012) 671.
[162] G.S. Holister, Experimental Stress Analysis: Principles and Methods, Cambridge University Press, Cambridge, UK, 1967.
[163] M. Mostafavi, D.M. Collins, B. Cai, R. Bradley, R.C. Atwood, C. Reinhard, X. Jiang, M. Galano, P.D. Lee, T.J. Marrow, Yield behavior beneath hardness indentations in ductile metals, measured by three-dimensional computed X-ray tomography and digital volume correlation, Acta Materialia 82 (2015) 468-482.
[164] K. Shoemake, III.5. - Euler Angle Conversion, in: P.S. Heckbert (Ed.), Graphics Gems, Academic Press1994, pp. 222-229.

[165] T.M. Inc, MATLAB and OptimizationToolbox 2018a, The MathWorks Inc, 2018a, pp. A "nonlinear least-squares solver".
[166] D.R. Lide, CRC Handbook of Chemistry and Physics, CRC Press, Boca Raton, Florida, United States, 1994.
[167] B.L. Welch, The generalization of 'Student's' problem when several different population variances are involved, Biometrika 34(1-2) (1947) 28-35.
[168] A. Hodgkins, T.J. Marrow, P. Mummery, B.J. Marsden, A.S.L. Fok, Crack propagation resistance and damage mechanisms in nuclear graphite, Roy Soc Ch (309) (2007) 127-133.
[169] P.J. Heard, M.R. Wootton, R. Moskovic, P.E.J. Flewitt, Crack initiation and propagation in pile grade A (PGA) reactor core graphite under a range of loading conditions, J Nucl Mater 401(1-3) (2010) 71-77.
[170] B. Šavija, G.E. Smith, P.J. Heard, E. Sarakinou, J.E. Darnbrough, K.R. Hallam, E. Schlangen, P.E.J. Flewitt, Modelling deformation and fracture of Gilsocarbon graphite subject to service environments, J Nucl Mater 499 (2018) 18-28.
[171] A. Farsi, A.D. Pullen, J.P. Latham, J. Bowen, M. Carlsson, E.H. Stitt, M. Marigo, Full deflection profile calculation and Young's modulus optimisation for engineered high performance materials, Scientific Reports 7 (2017) 46190.
[172] A. Savitzky, M.J.E. Golay, Smoothing and Differentiation of Data by Simplified Least Squares Procedures, Analytical Chemistry 36(8) (1964) 1627-1639.
[173] M. Drakopoulos, T. Connolley, C. Reinhard, R. Atwood, O. Magdysyuk, N. Vo, M. Hart, L. Connor, B. Humphreys, G. Howell, S. Davies, T. Hill, G. Wilkin, U. Pedersen, A. Foster, N. De Maio, M. Basham, F. Yuan, K. Wanelik, I12: the Joint Engineering, Environment and Processing (JEEP) beamline at Diamond Light Source, Journal of Synchrotron Radiation 22(3) (2015) 828-838.
[174] A.C. Kak, M. Slaney, Principles of computerized tomographic imaging, Society for Industrial and Applied Mathematics, Philadelphia, Pa, 2001.
[175] S.D. Preston, B.J. Marsden, Changes in the coefficient of thermal expansion in stressed Gilsocarbon graphite, Carbon 44(7) (2006) 1250-1257.
[176] H.L. Ewalds, R.J.H. Wanhill, Fracture mechanics, E. Arnold ; Delftse Uitgevers Maatschappij, London; Delft, Netherlands, 1984.
[177] A. Chirokov, Scattered Data Interpolation and Approximation using Radial Base Functions (rbf_interp) version 1.0.0.0, MathWorks(R) File Exchange https://uk.mathworks.com/matlabcentral/fileexchange/10056-scattered-data-interpolation-and-approximation-using-radial-base-functions, last updated: 9 Oct 2006.
[178] G.P. Cherepanov, Crack propagation in continuous media: PMM vol. 31, no. 3, 1967, pp. 476–488, Journal of Applied Mathematics and Mechanics 31(3) (1967) 503-512.
[179] S.M. Barhli, L. Saucedo-Mora, C. Simpson, T. Becker, M. Mostafavi, P.J. Withers, T.J. Marrow, Obtaining the J-integral by diffraction-based crack-field strain mapping, Procedia Structural Integrity 2 (2016) 2519-2526.
[180] R. Jones, C. Wykes, Holographic and speckle interferometry: a discussion of the theory, practice, and application of the techniques, (1989).
[181] G. Nikishkov, Y. Nikishkov, A. Makeev, Finite element mesh generation for composites with ply waviness based on X-ray computed tomography, Advances in Engineering Software 58 (2013) 35-44.
[182] P. Armitage, G. Berry, Statistical Methods in Medical Research. 3rd Ed., Blackwell Scientific Publications, Oxford, 1994.
[183] S.B. Green, How Many Subjects Does It Take To Do A Regression Analysis, Multivariate Behavioral Research (1991) 499-510.